

# **Polypyrrole Modified with Macrocycles for the Detection of Aqueous Pollutants and Carbon Membranes for the Separation of Gases.**



**NUI MAYNOOTH**

Ollscoil na hÉireann Má Nuad

**Sinéad Mc Dermott, B.Sc.**

**Department of Chemistry  
National University of Ireland, Maynooth  
May 2010**

**Thesis submitted to the National University of Ireland in fulfilment of the  
requirements for the Degree of Doctor of Philosophy**

**Supervisors: Prof. Carmel Breslin and Dr. Denise Rooney**

**Head of Department: Prof. John Lowry**

---

**Table of Contents**

<b>Table of contents</b> .....	i
<b>Declaration</b> .....	vi
<b>Acknowledgements</b> .....	vii
<b>Dedication</b> .....	ix
<b>Abstract</b> .....	x
<b>Chapter 1 - Introduction and Literature Review</b> .....	1
1.1 Introduction.....	1
1.2 Conducting Polymers .....	4
1.2.1 Definition of a Conducting Polymer .....	4
1.2.2 Formation and Synthesis of Conducting Polymers .....	6
1.2.3 Applications of Conducting Polymers .....	8
1.3 Polypyrrole .....	8
1.3.1 Polymerisation of Pyrrole .....	9
1.3.2 Parameters Influencing the Electropolymerisation of Py.....	11
1.3.3 Electro-activity of PPy.....	14
1.4 Supramolecular Systems.....	15
1.4.1 Cyclodextrins .....	15
1.4.2 Inclusion Complexes .....	19
1.4.3 Applications of Cyclodextrins.....	21
1.4.4 Calixarenes .....	22
1.4.5 Synthesis and Properties of Calixarenes.....	24
1.4.6 Inclusion Complexes of Calxarenes .....	25
1.4.7 Applications of Calixarenes .....	26
1.4.8 Methods for Determining Inclusion Complex Association Constant.....	27
1.5 Paraquat and Diquat.....	28
1.5.1 Environmental Technologies for Sensing Paraquat and Diquat.....	30
1.6 Membrane Technology and Gas Separation .....	31
1.6.1 Membranes.....	32
1.6.2 Current Applications of Membranes .....	33
1.6.3 Mechanism of Separation .....	34
1.6.4 Types of Membranes.....	36
1.6.5 Configurations of Carbon Membranes .....	39
1.6.6 Gas Separation .....	40
1.6.7 Aging .....	41
1.6.8 Regeneration .....	42

---

1.7 References .....	44
<b>Chapter 2 - Experimental</b> .....	<b>52</b>
2.1 Introduction.....	52
2.2 Chemicals and Solutions.....	52
2.3 Electrochemical Cell and Electrode Preparation.....	53
2.4 Electrochemical Techniques.....	55
2.4.1 Cyclic Voltammetry .....	56
2.4.2 Pulse Voltammetry .....	59
2.4.3 Differential Pulse Voltammetry (DPV).....	59
2.4.5 Rotating Disc Voltammetry (RDV) .....	60
2.4.6 Potentiostatic Techniques (Chronoamperometry).....	63
2.5 Spectroscopic Techniques .....	64
2.5.1 UV-Vis Spectroscopy .....	65
2.5.2 Fluorescence Spectroscopy .....	66
2.5.3 Nuclear Magnetic Resonance (NMR) Spectroscopy.....	67
2.6 Scanning Electron Microscopy and Energy Dispersive X-ray Analysis.....	69
2.7 Methods of Analysis.....	69
2.7.1 Job's Plot .....	70
2.7.2 Evaluation of Association Constant, $K_a$ .....	70
2.7.2.1 Electrochemical Analysis.....	71
2.7.2.2 UV-Vis and Fluorescence Methods .....	72
2.7.2.3 $^1\text{H}$ NMR Analysis.....	73
2.7.3 Michaelis Menten Kinetics and Lineweaver-Burk Analysis.....	74
2.8 Carbon Molecular Sieve Membranes (CMSMs) .....	75
2.8.1 Module Assembly .....	76
2.8.2 Gas Testing.....	79
2.8.3 Gas Permeation Test.....	80
2.8.4 Leak Test.....	81
2.8.5 Aging Study.....	82
2.8.5.1 Dynamic Aging Study .....	82
2.8.5.2 Static Aging Study .....	84
2.8.6 Electro-regeneration.....	85
2.9 References .....	86
<b>Chapter 3 - Cyclodextrin Modified Polypyrrole for the Detection of Paraquat</b> .....	<b>88</b>
3.1 Introduction.....	88
3.2 Electrochemistry of Paraquat.....	89

---

3.3 Formation and Characterisation of PPy/sul- $\beta$ CD films.....	95
3.3.1 Influence of the Dopant on Polymerisation.....	97
3.3.2 Parameters Influencing Polymer Growth.....	100
3.3.3 Effect of Charge/Film Thickness on the Polypyrrole films .....	104
3.3.4 SEM and EDX.....	106
3.4. Paraquat at the Modified Electrode Surface .....	111
3.5 Optimisation of Paraquat at the Polymer Film .....	114
3.5.1 Effect of pH and Potential Window on the Paraquat signal.....	115
3.5.2 Influence of Applied Potential in Forming the Polymer .....	116
3.5.3 Electropolymerisation Charge .....	118
3.5.4 Influence of the supporting electrolyte .....	119
3.5.5 Optimum Conditions.....	121
3.6 Calibration study.....	122
3.6.1 Cyclic Voltammetry .....	122
3.6.2 Differential Pulse Voltammetry.....	123
3.6.3 Constant Potential Amperometry.....	125
3.6.4 Michaelis-Menten Kinetics and Lineweaver-Burk Analysis .....	129
3.7 Comparative study of PPy doped with SDS.....	133
3.7.1 Differential Pulse Voltammetry.....	133
3.8 Interference Studies .....	135
3.8.1 Interference of Ametryn.....	135
3.8.2 Interference of Diquat.....	137
3.9 Summary of Results.....	140
3.10 References .....	142
<b>Chapter 4 - Calixarene Modified Polypyrrole for the Detection of</b>	
<b>Paraquat.....</b>	<b>146</b>
4.1 Introduction.....	146
4.2 Formation and Characterisation of the PPy/sul-calix[4] films.....	147
4.2.1 SEM and EDX.....	150
4.3 Paraquat at the Modified Electrode .....	154
4.4 Optimisation of Paraquat at the Polymer film .....	156
4.4.1 Potential Window.....	157
4.4.2 Applied Potential for the Polymerisation of Py.....	158
4.4.3 Electropolymerisation Charge .....	159
4.4.4 Effect of pH on the Paraquat signal.....	160
4.4.5 Influence of Scan Rate .....	161

---

4.4.6 Optimum conditions .....	164
4.5 Calibration Study.....	165
4.5.1 Cyclic Voltammetry .....	165
4.5.2 Constant Potential Amperometry.....	167
4.6 Michaelis-Menten Kinetics and Lineweaver-Burk analysis .....	170
4.7 Interference Study.....	173
4.7.1 Interference of Diquat .....	173
4.8 Summary of Results.....	176
4.9 References .....	178
<b>Chapter 5 - Complexation of Sulfonated Calix[4]arene with Diquat and Paraquat.....</b>	<b>180</b>
5.1 Introduction.....	180
5.2 Interaction of $V^{2+}$ and Sul-calix[4] using CV.....	182
5.3 Stoichiometry of $V^{2+}$ and Sul-calix[4].....	187
5.4 Evaluation of the association constant, $K_a$ , for sul-calix[4] and $V^{2+}$ .....	189
5.4.1 Evaluation of $K_a$ for Sul-calix[4] with $V^{2+}$ using RDV.....	190
5.4.2. Evaluation of $K_a$ for Sul-calix[4] with $V^{2+}$ using UV-Vis Spectroscopy..	198
5.4.3 Evaluation of $K_a$ for Sul-calix[4] and $V^{2+}$ using Fluorescence Spectroscopy.....	202
5.4.4 Role of Charge and Ionic Strength.....	204
5.5 Conformations of Sul-calix[4] .....	208
5.5.1 Structural Interaction of $V^{2+}$ and Sul-calix[4] .....	210
5.5.2 Quantitative Interaction of $V^{2+}$ and Sul-calix[4] .....	215
5.6 Interaction of $MV^{2+}$ and Sul-calix[4] .....	217
5.6.1 Stoichiometry of the Interaction of $MV^{2+}$ and Sul-calix[4] .....	217
5.6.2 Evaluation of $K_a$ for the Interaction of $MV^{2+}$ and Sul-calix[4] using CV.	219
5.6.3 Evaluation of $K_a$ for the Interaction of $MV^{2+}$ and Sul-calix[4] using RDV .....	222
5.6.4 Structural Interaction of $MV^{2+}$ and Sul-calix[4] .....	227
5.6.5 Evaluation of $K_a$ of $MV^{2+}$ and Sul-calix[4] using $^1H$ NMR.....	232
5.7 Interaction of $V^{2+}$ and $MV^{2+}$ with Calix[4]arene .....	233
5.8 Summary of results .....	236
5.9 References .....	238
<b>Chapter 6 - Complexation of Sulfonated <math>\beta</math>-Cyclodextrin with Paraquat and Diquat.....</b>	<b>241</b>
6.1 Introduction.....	241
6.2 Stoichiometry of Sul- $\beta$ CD and Paraquat .....	242

---

6.3 Evaluation of $K_a$ for Sul- $\beta$ CD and $MV^{2+}$ .....	245
6.3.1 Evaluation of $K_a$ for Sul- $\beta$ CD and $MV^{2+}$ using CV .....	246
6.3.2 Evaluation of $K_a$ for Sul- $\beta$ CD and $MV^{2+}$ using RDV .....	248
6.3.3 $^1H$ NMR Studies on the Interaction of $MV^{2+}$ and sul- $\beta$ CD .....	255
6.4 Interaction of $MV^+$ and $MV^0$ with Sul- $\beta$ -CD and $\beta$ -CD .....	259
6.5 Influence of pH .....	264
6.6 Interaction of Diquat and sul- $\beta$ CD .....	266
6.6.1 Stoichiometry of $V^{2+}$ with sul- $\beta$ CD .....	266
6.6.2 Evaluation of $K_a$ for Sul- $\beta$ -CD and Diquat.....	267
6.7 Summary of Results .....	272
6.8 References .....	274
<b>Chapter 7 - Aging and Electro-regeneration of Carbon Membranes</b> .....	<b>276</b>
7.1 Introduction.....	276
7.2 Characterisation of CMSMs .....	277
7.3 Permeation of $CO_2$ and $N_2$ .....	284
7.4 Influence of Aging on Carbon Membranes.....	288
7.4.1 Dynamic Study .....	288
7.4.2 Intermediate Study.....	292
7.4.3 Static Study.....	293
7.5 Electro-regeneration of Carbon Membranes.....	296
7.5.1 Electro-regeneration of CMSMs.....	297
7.6 Summary of Results .....	301
7.7 References .....	303
<b>Chapter 8 - Conclusions</b> .....	<b>305</b>
8.1 General Conclusions .....	305
8.2 Conference Presentations.....	309
8.3 References .....	309

**Declaration**

I hereby certify that this thesis, which I now submit for assessment on the programme of study leading to the award of PhD has not been submitted, in whole or part, to this or any other University for any degree and is, except where otherwise stated the original work of the author.

Signed : \_\_\_\_\_

### **Acknowledgements**

Firstly, I would like to express my sincere thanks to my supervisors Prof. Carmel Breslin and Dr. Denise Rooney. Carmel and Denise have been instrumental in their support and encouragement over the past three years and I am extremely grateful for all your assistance.

I would like to acknowledge Science Foundation Ireland (SFI) and the Norwegian Research Council for the funding during this project. In particular, I would like to thank Prof. May-Britt Hägg and all those in the Memfo research group at the Norwegian University of Science and Technology. I had a wonderful experience in Norway and will treasure the memories of my time there. A word of thanks to the Tyndall institute and the National Access Programme for the SEM micrographs. Also, I would like to express my gratitude to the academic and technical staff in the department for their generosity to the endless number of fundraiser events! A big thank you, to Dr. John Colleran for your help over the last few months.

To all the postgrads and postdocs, past and present, you've certainly made my time in Maynooth memorable. A particular word of thanks to Gillian, Claire, Catherine, Eoin, Declan, John, Eimear, Richard, Denis, Ciaran, Rob, Linda, Theresa, Fiachra and Niall. Cheers for all the support over the last few months. I've been extremely fortunate in having the pleasure of working with three of the most wonderful people over the last three years! Enrico, Adelaide and Valeria, I cannot thank you enough for all your help. Enrico, you are a great friend and I wish you every success in the future. Don't forget to "help yourself"!! Adelaide, you have been fantastic over the last few weeks! Your expertise on computers has saved me a lot of time of which I am so grateful. Valeria, I have been blessed with your friendship over the last three years. I am so happy that we have finished this together and cannot wait for the celebrations!!

To Edel, Ciara, Sarah, Liz, Deirdre, Theresa and Sarah Lyons. You are truly great friends and I appreciate all the encouragement you've given me!

Finally, to my Mam and Gabriel. Your encouragement to explore new aspects of life has made me the person I am today. I am eternally grateful for all the advice you've given me and hope that some day, I can return the favour.

*Dedicated to my Mam and Gabriel  
Thank you for all your support*

---

**Abstract**

The development of environmental technologies and their applications in aqueous and gaseous systems are essential in combating pollution. The formation and detailed characterisation of a polypyrrole (PPy) film modified with anionic macrocycles of either sulfonated- $\beta$ -cyclodextrin (sul- $\beta$ CD) or sulfonated-calix[4]arene (sul-calix[4]) were carried out. These composite modified electrodes were used as electrochemical sensors for the detection of the harmful herbicide, paraquat. These polymer films were highly conducting and due to the immobilisation of the large anionic dopants within the PPy matrix they exhibited cation exchange behaviour on reduction. Cyclic voltammetry (CV), differential pulse voltammetry (DPV) and constant potential amperometry (CPA) were the techniques employed to evaluate the sensitivity of PPy/sul- $\beta$ CD and PPy/sul-calix[4] towards the redox states of  $MV^{2+}$ ,  $MV^+$  and  $MV^0$  of paraquat. A limit of detection of  $1.28 \times 10^{-5} \text{ mol dm}^{-3}$  and  $3.48 \times 10^{-6} \text{ mol dm}^{-3}$  for the reduction of  $MV^{2+}$  was evaluated using CPA for PPy/sul- $\beta$ CD and PPy/sul-calix[4], respectively.

Additional studies were carried out to probe the nature of the complex interaction between the macrocyclic structures of sul- $\beta$ CD and sul-calix[4] and the analytes, paraquat and diquat. Electrochemical and spectroscopic techniques were used to quantify the association constant,  $K_a$ . The data obtained from these techniques was consistent with electrostatic interactions as the major driving force in complex formation. In the case of the sul-calix[4] system the magnitude of  $K_a$  was influenced by ionic strength. The  $K_a$  values decreased from  $10^6$  to  $10^3 \text{ mol}^{-1} \text{ dm}^3$  for the complex of diquat and sul-calix[4] in the absence and presence of  $0.1 \text{ mol dm}^{-3} \text{ Na}_2\text{SO}_4$ , respectively.

Carbon molecular sieve membranes (CMSMs) were employed for the separation of gases. CMSMs displayed selective permeation of  $\text{CO}_2$  over  $\text{N}_2$  by a factor of 24.7:1.0. Reduction in the permeability of the membrane was observed with aging. This was restored using an electro-regeneration procedure.

### Introduction and Literature Review

#### 1.1 Introduction

The goal of the project outlined in this thesis was to investigate and develop new environmental technologies suitable for pollution remediation. In recent years, the increase in climate change has ignited an awareness of the rapid damage caused by water and air pollution, which is harming the environment. On a national level, the Environmental Protection Agency (EPA) launched its science, technology, research and innovation for the environment (STRIVE) programme to tackle the problem of climate change. This began in 2007 and will proceed until 2013. Internationally, the Kyoto Protocol developed in 1997 is aimed at combating global warming. In compliance with these initiatives, there are now technologies required to minimise these problems. The primary focus of this work was to develop a sensor technology for an aqueous based system. In addition, a short project was carried out to develop a technology for separating CO<sub>2</sub> from N<sub>2</sub> gas.

The work outlined in Chapter 3 is based on the formation of an electrochemical sensor, consisting of a modified polypyrrole (PPy) film doped with supramolecular cages of sulfonated- $\beta$ -cyclodextrins (sul- $\beta$ CD). PPy is a well-known conducting polymer with a wide range of applications, in particular that of electrochemical sensors<sup>1,2</sup>. Following a description of characterisation of the sensor, the conditions required for optimal sensing of the harmful herbicide, methyl viologen are outlined. More commonly known as paraquat (PQ), methyl viologen is a dangerous herbicide used in controlling weed growth. It degrades slowly and can leach from soil into water over time<sup>3</sup>. The performance of the sensor is analysed in a solution of paraquat. The selectivity of the sensor is also examined in the presence of diquat (DQ), the main interfering compound for paraquat.

The attraction of paraquat to the modified polymer film is based on an electrostatic interaction, as paraquat is positively charged and the supramolecular cage of sul- $\beta$ CD is negatively charged. The research described in Chapter 4, is based on incorporating another macrocyclic compound, sulfonated calix[4]arene (sul-calix[4]) into the PPy matrix. This macrocyclic cage was chosen as previous studies have shown it has a high affinity for paraquat<sup>4,5</sup>. Aside from the anionic charge on the macrocyclic structures, both cyclodextrins and calixarenes have an internal cavity which is important in the formation of inclusion complexes. Thus, not only does the presence of charge offer a means of interaction but, the formation of an inclusion complex is proposed as a method of removing the harmful substance from solution. Following optimisation of the polymer sensor for the detection of paraquat, a titration was carried out. A range of techniques were used to determine a detection limit for paraquat at the modified PPy film, including cyclic voltammetry (CV), differential pulse voltammetry (DPV) and constant potential amperometry (CPA). These techniques were also employed to assess the selectivity of the sensor in the presence of equivalent concentrations and large excesses of diquat, relative to a fixed concentration of paraquat.

In Chapter 5, work carried out in order to study the inclusion complex formed between diquat and sul-calix[4] in solution is discussed. The promising results in Chapter 4, regarding the response of diquat at the modified PPy film with incorporated sul-calix[4] indicated the formation of a strong inclusion complex. Inclusion complexes in solution are also known as host-guest interactions. In this research, the macrocyclic cage is the host and the analyte of paraquat or diquat is referred to as the guest. Electrochemical and spectroscopic methods were used to quantify the strength of the inclusion complex and determine the structural interaction of diquat with sul-calix[4]. These results are presented in Chapter 5. A comparative study of the interaction of paraquat and sul-calix[4] is also carried out.

There is quite a variation in the electrochemical response of paraquat at the modified substrate of PPy doped with sul- $\beta$ CD and PPy doped with sul-calix[4].

This indicates the nature of the interaction is different. To the best of our knowledge, no previous research has been carried out on the inclusion complex of paraquat and sul- $\beta$ CD or diquat and sul- $\beta$ CD in solution. Hence, in Chapter 6 the complex of paraquat and sul- $\beta$ CD is investigated. This chapter serves as a comparative study to the data presented in Chapter 5, in which the stoichiometry and measure of association between paraquat and sul- $\beta$ CD are discussed. A similar study is carried out assessing the interaction of diquat and sul- $\beta$ CD and the results are presented in Chapter 6.

In Chapter 7, work is described on the development of a technology for the separation of CO<sub>2</sub> from N<sub>2</sub> gas, using carbon molecular sieve membranes (CMSMs). This work was carried out during a five month visit to the Memfo Research Group at the Norwegian University of Science and Technology, Trondheim, Norway. Membranes have a wide range of applications and in the last two decades, they have been used for separating CO<sub>2</sub> from gases, such as nitrogen (N<sub>2</sub>) and methane (CH<sub>4</sub>)<sup>6</sup>. There are a wide range of membranes which can be applied to gas separation as is described in Section 1.6.4. On comparing the variety of membranes, CMSMs have a definitive advantage over others as a result of their durability. However, they are susceptible to aging over time. This can be attributed to exposure to the atmosphere. Thus, in Chapter 7 the influence of a dynamic and static air source on the performance of the membrane, is investigated. Also, work is carried out regarding the process of electro-regeneration, which is a relatively new technique developed by Lie *et al.*<sup>7</sup> to combat aging.

In this introductory chapter, concepts behind both technologies and an account of the harmful pollutants of paraquat and diquat are explained. The opening section outlines the background to conducting polymers, followed by details of the properties and the electrochemical synthesis of PPy. Detailed descriptions of the supramolecular cages which are incorporated into the polymer film are then presented. The properties of these hazardous pollutants are discussed. The final section of this chapter introduces membrane technology and the theory behind this relatively new technique for the separation of CO<sub>2</sub> from N<sub>2</sub> gas.

## 1.2 Conducting Polymers

Polymers are high molecular weight components built up from a number of basic units, known as monomers<sup>8</sup>. Generally, organic polymers are considered non-conducting. However, a number of organic polymers can be conducting. The following section delves into the properties and applications of conducting polymers.

### 1.2.1 Definition of a Conducting Polymer

According to Chandrasekhar<sup>9</sup>, conducting polymers (CPs) are not polymers with conductive fillers, but conducting polymers are intrinsically conducting due to  $\pi$ -conjugation. Conducting polymers date back to the early 1900s with reports of 'aniline black' and 'pyrrole black'. However, at this time the synthetic routes only produced black powders and much of this early work was discarded<sup>9</sup>. Significant developments came about in 1977 when MacDiarmid *et al.*<sup>10</sup> reported a 10 million-fold increase in the conductivity of polyacetylene, upon doping it with iodine. In the year 2000, MacDiarmid, Shirakawa and Heeger were awarded the Nobel Prize in Chemistry for this research. Now, conducting polymers are used in a wide range of applications, including electronics and biosensors<sup>2,11-13</sup>. In general CPs are comprised of C and H atoms along with heteroatoms, such as N or S, as illustrated in Figure 1.1, which shows the repeating units of the monomer for the polymers, polyaniline (Pani), polypyrrole (PPy) and polythiophene (PT).

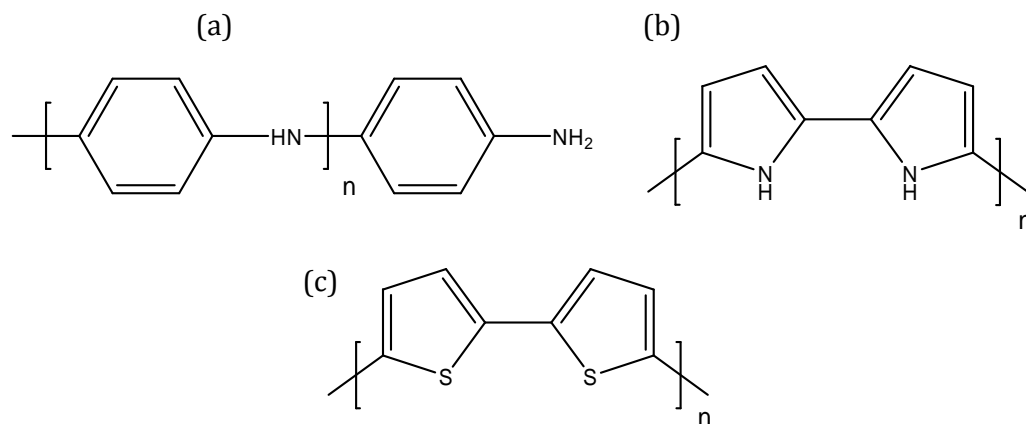


Figure 1.1: Conducting polymers of (a) polyaniline (Pani), (b) polypyrrole (PPy) and (c) polythiophene (PT).

Materials are generally classified as insulators, semi-conductors or conductors using the band gap energy model. In this analysis there are two energy bands, valence (VB) and conductance bands (CB). A valence band corresponds to the occupied electronic energy levels and a conductance band is equivalent to the unoccupied energy levels. The separation between these two bands is referred to as the band gap energy ( $E_g$ ). As depicted in Figure 1.2,  $E_g$  for insulators is large, it is lower for semi-conductors, and for conductors, the bands overlap. Conductivity arises due to the transition of electrons from the valence (occupied orbital) to the conductance band (unoccupied orbital), however if the gap is large, the electronic transition will not occur. If the band gap is greater than 10 eV, the electronic transitions do not occur and this is indicative of an insulator. A band gap of approximately 1 eV corresponds to a semi-conductor.

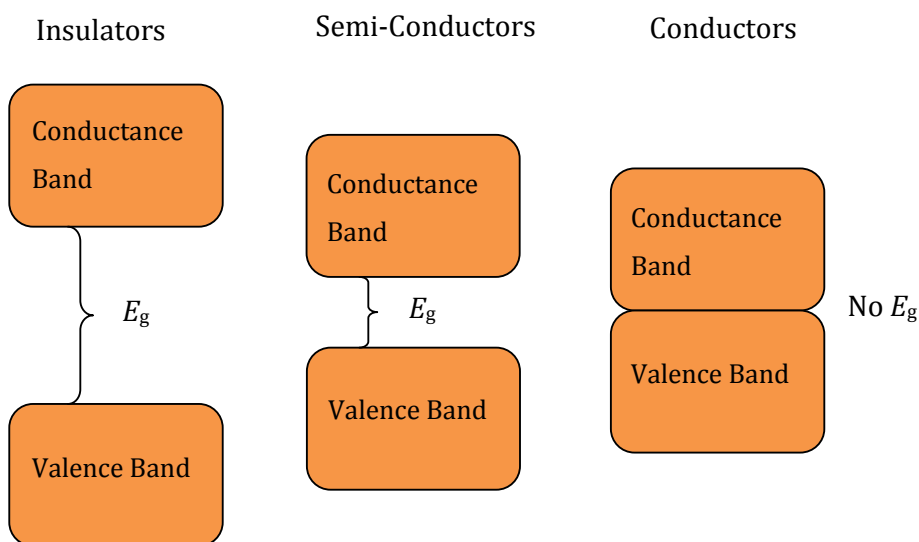


Figure 1.2: Schematic illustrating the band gap energy model, showing the band gap energy ( $E_g$ ) for insulators, semi-conductors and conductors.

Bredas and Street<sup>14</sup> published on the nature of CPs in terms of the energy band gap model using an analogy similar to that employed to describe inorganic semiconductors. In a polymer, the monomer units interact with their corresponding neighbours to form the valence and conductance bands. It was proposed that upon doping the polymer an electronic transition occurred between VB and CB. However, this was challenged when applying this model to

the polymers: polyacetylene (PA)<sup>15</sup>, polyparaphenylene (PPP)<sup>16</sup> and polypyrrole (PPy)<sup>17-19</sup>.

Although there is still some debate about the exact nature of conduction, it is now generally accepted that the conducting nature of the polymers is due to the presence of mobile charge carriers<sup>2</sup>. These charge carriers are termed polarons and bipolarons. As the polymer is oxidised (for example polypyrrole) an electron is removed producing a free radical and a positive charge. The radical and cation are coupled via local resonance of the charge. This combination of a charged site and a radical is called a polaron. Upon further oxidation, a bipolaron is formed. This is of lower energy than two separate polarons. These charges are mobile due to the conjugated polymer backbone and it is this movement of charge along the polymer backbone that gives rise to the electrical conductivity of the polymer<sup>2</sup>.

In order to maintain neutrality of the polymer backbone structure, the positive charges (polarons and bipolarons in the case of polypyrrole) are counter balanced by the incorporation of anions from the electrolyte solution. These anions are termed dopants and the process is known as doping.

In terms of the energy gap model, the polaron is equivalent to the generation of localised electronic energy states in the forbidden energy gap, with the lower energy state being occupied by single unpaired electrons. Generation of the bipolaron gives more electronic energy states. As more of these states are generated, the upper and lower bipolaron bands merge with the CB and VB to produce partially filled bands approaching metallic-like conductivity. Also, the smaller the  $E_g$  is, the more conductive the polymer.

### **1.2.2 Formation and Synthesis of Conducting Polymers**

Polymerisation can be carried out in two ways, using either chemical synthesis or electrochemical methods. The formation of a polymer, involves oxidation of the monomer unit which forms a radical cation. This radical ion then gives rise to the formation of oligomers, which finally assemble to give a polymer chain.

Chemical polymerisation occurs in solution with the presence of relatively strong oxidising agents, like ammonium peroxydisulfate (APS), ferric ions, permanganate or dichromate anions or hydrogen peroxide<sup>20</sup>. Typically, the synthesis occurs by addition polymerisation, i.e., chain growth polymerisation and the oxidising agent generally acts as the dopant. Following initial radical generation, rather than radical-radical coupling, interaction occurs between the radical and the monomer which yields dimers, oligomers and finally polymers. Polymerisation occurs in the bulk solution and the resulting polymers precipitate.

Electrochemical polymerisation dates back to when “pyrrole black” was formed as a precipitate on a platinum electrode by exposing an aqueous solution of pyrrole and sulphuric acid to an oxidation potential<sup>21</sup>. Electrochemical synthesis differs from chemical polymerisation, in that following radical generation upon oxidising the monomer, propagation occurs by radical-radical recombination, which causes the loss of two electrons and hence the formation of a dimer. Oxidation of this dimer generates an oligomeric radical which combines with other oligomeric radicals to generate a polymeric structure.

A range of electrochemical techniques can be used to carry out electropolymerisation<sup>22</sup>. These include constant current or galvanostatic, potentiostatic or cyclic voltammetry. Depending on the technique used, a range of polymer morphologies can be achieved. Similar to chemical polymerisation, a bulk solution of monomer, dopant and suitable solvent are used, but the precipitated polymer deposits on a conducting surface. This offers a significant advantage over chemical polymerisation in that the polymer is tailored to the desired thickness and offers a more organised molecular structure<sup>23</sup>. The appeal of preparing the polymer electrochemically with respect to controlling the properties of thickness and morphology, has provided opportunities to investigate the development of sensors, one of the many applications of conducting polymers nowadays<sup>24,25</sup>. On the other hand, all polymers can be prepared using chemical synthesis, however electrochemical synthesis is

confined to monomers which can be oxidised on the application of a potential to form the radical ion intermediates for polymerisation<sup>2</sup>.

### 1.2.3 Applications of Conducting Polymers

According to Ahuja *et al.*<sup>26</sup>, in recent years, there has been a growing interest in conducting polymers because of their wide range of potential applications in areas such as rechargeable batteries<sup>27,28</sup>, gas separation membranes<sup>29</sup>, EMI shielding<sup>30</sup> and electrochromic display<sup>31</sup>. Adhikari and Majumdar<sup>32</sup> published a review in 2004 on the applications of polymers for sensor development. Within this article, it was highlighted that conducting polymers have been extensively applied in the field of artificial sensors with the goal of mimicking natural sense organs. In addition, there is a wide range of conducting polymer sensors for environmental applications for both aqueous and gaseous based systems. For example, Panasyuk-Delaney *et al.*<sup>33</sup> used the technique of graft polymerisation to prepare thin films of molecularly imprinted polymers on the surface of polypropylene membranes and on a hydrophobised gold surface, for the detection of a herbicide. Also, conducting polymers have been employed as amperometric sensors<sup>32</sup>. They have also been used to detect hazardous gases and vapours<sup>34,35</sup>.

Polypyrrole (PPy) was the conducting polymer chosen in this thesis. It was chosen for the detection of herbicides in water. In the following section, the formation and properties of PPy are discussed and the benefits of using PPy as a sensor are highlighted.

### 1.3 Polypyrrole

Polypyrrole (PPy) is synthesised from the monomer pyrrole, shown in Figure 1.3. The molecular structure consists of a 5-membered ring, with a N heteroatom. Similar to other organic molecules, polymerisation occurs upon oxidation of the monomer. A conjugated polymer chain with overlapping  $\pi$ -orbitals and a positive charge along the backbone forms as a result of oxidation<sup>36</sup>. PPy was first synthesised chemically in 1916<sup>37</sup> and cited literature show that the earliest electrochemical synthesis of PPy by Dallolio *et al.*<sup>21</sup>, was

in 1968. Moreover, in 1979, Kanazawa and co-workers<sup>38</sup> also synthesised continuous and freestanding PPy films electrochemically, using platinum electrodes and from this they revived the electrochemical approach for the synthesis of conducting polymers. Nishizawa *et al.*<sup>39</sup> discussed the advantages and appeal of using PPy. It has a large surface area owing to its fibrous structure and thus is a high-capacity electrode material. Furthermore, the ease of preparation, inherent electrical conductivity, high stability in air and aqueous media, controllability of surface biochemical properties and biocompatibility make PPy a promising interfacial material<sup>39,40</sup>. Thus, PPy is an ideal candidate for sensor development in environmental technologies. The following sections discuss the electrochemical oxidation of Py to form PPy and the electroactivity of this conducting polymer.

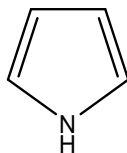


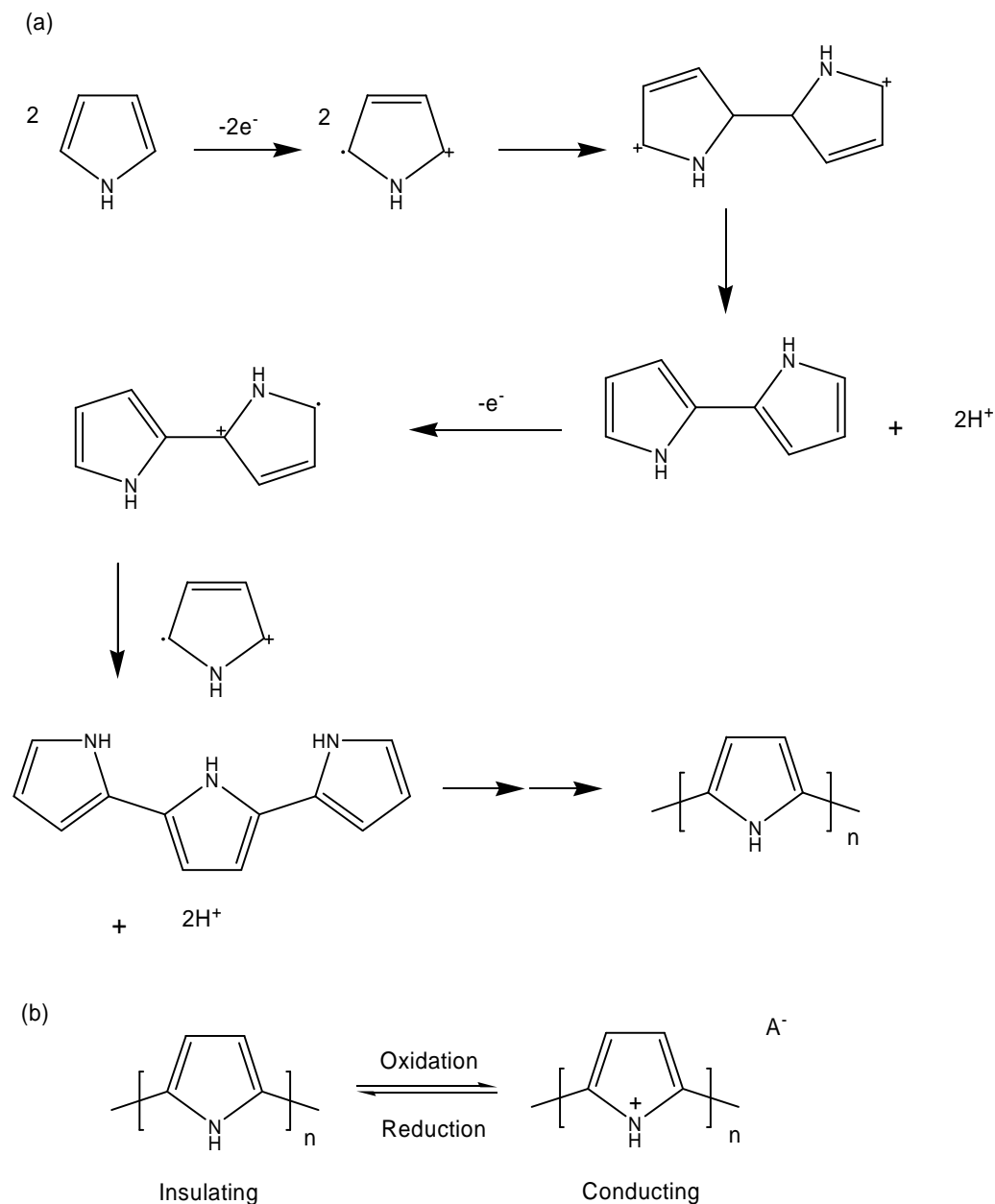
Figure 1.3: Molecular structure of the pyrrole (Py) monomer.

### 1.3.1 Polymerisation of Pyrrole

Like all conducting polymers, PPy can be synthesised using chemical or electrochemical means. Chemical synthesis is used when large quantities of material are required and involves mixing a strong oxidising agent with a monomer solution<sup>41,42</sup>. PPy synthesised using this method, is insoluble in common solvents because of the strong inter-chain interactions, unless suitable doping agents are used to increase solubility<sup>1</sup>. Common oxidants that have been used include ferric chloride<sup>43,44</sup>, ferric perchlorate<sup>45</sup> and ammonium peroxydisulfate<sup>1,46</sup>. Although similar to electrochemical polymerisation, the mechanism of polymerisation is slightly different. In chemical polymerisation, the propagation step is controlled by the fact that the monomer is in large excess of the radical cation and therefore couples with the cation to form a dimer<sup>20</sup>. On the other hand, in electro-polymerisation, the anodic potential

generates a much larger excess of radical cations relative to monomer units and the radical cations couple to each other to generate a radical dimer<sup>47</sup>.

The electrochemical synthesis of PPy occurs when an anodic potential is applied and following initiation, propagation and termination, a polymer chain is formed, as shown in Scheme 1.1. There is still some debate on the exact mechanism of electropolymerisation, but the mechanism proposed by Diaz and Castillo<sup>48</sup> and explained later by Henry *et al.*<sup>49</sup> is generally taken as the accepted mechanism. The process involves a one-electron oxidation of the pyrrole monomer to generate a radical cation. Two such radicals react to form a bond linking the two pyrrole rings. Subsequent loss of two protons yields an overall two-proton, two-electron oxidation reaction to give a neutral dimer. The dimer is then oxidised to generate a radical species, which couples with another radical cation to give a trimer. Propagation continues to give the polymer. The resulting polymer mainly contains structural units of 2,5-linkages<sup>50</sup> as shown by the trimer in Scheme 1.1 (a). As illustrated in this mechanism, the polymer appears in a neutral state. However, intrinsic conductivity results from the formation of charge carriers upon oxidising the conjugated backbone using an anodic potential. As discussed by Lange *et al.*<sup>51</sup>, oxidation of the neutral polymer causes the generation of localised electronic states and the formation of polarons. This leads to the formation of bipolarons and so a positive charge is located along the polymer backbone. Moreover, negatively charged counter-ions must be present in solution to maintain charge balance within the polymer, since positive charges usually on the nitrogen atom are developed along the PPy backbone, as shown in Scheme 1.1 (b)<sup>52</sup>. PPy is oxidised at lower potentials than its corresponding monomer and approximately one in every three to four rings carries a positive charge<sup>50,53</sup>. The growth of PPy depends on its electrical characteristics, i.e., if it was non-conducting its growth would be self-limiting, producing very thin films similar to that of polyphenol<sup>54</sup>. However, PPy growth is virtually unlimited due to its inherent conductivity. The next section outlines the factors that influence PPy growth, followed by the electro-activity of this inherently conducting polymer.



Scheme 1.1: (a) Mechanism for the electrochemical polymerisation of PPy and (b) redox states of PPy.

### 1.3.2 Parameters Influencing the Electropolymerisation of Py

In general, electrochemical polymerisation of pyrrole is carried out in a conventional three-electrode cell, with a surface for polymer deposition, known as the working electrode and a solution of dopant and monomer. This process will be discussed further in Chapter 2, Sections 2.2 and 2.3. The advantages of

electrochemical deposition of PPy are that films can be prepared simply with a one-step procedure and exact control of thickness<sup>55</sup>. Parameters such as the nature of the solvent<sup>56-59</sup>, temperature<sup>60</sup>, potential or current density<sup>61</sup>, pH, and the nature of the working electrode<sup>55</sup> all have a strong effect on the rate of electropolymerisation and on the properties of the resulting polymer .

In electrochemical doping, the electrode supplies the redox charge to the conducting polymer, while ions diffuse into (or out of) the polymer structure from the nearby electrolyte to compensate for the electronic charge<sup>36</sup>. The conductivity of the PPy films is usually related to the degree of doping by the counter-anions, which also contributes to the rate of formation<sup>58</sup>. Provided the dopant is sufficiently conducting, it also serves as the supporting electrolyte. During oxidation of pyrrole, nucleation of the oligomers in solution occurs, followed by a rapid increase in charge density due to gradual PPy growth<sup>62</sup>. According to Almario and Cacera<sup>63</sup>, the doping agents play a key role in the polymerisation process, producing different induction times, mechanisms of nucleation and polymer growth. Therefore, the polymerisation rate varies with each dopant.

It has been shown that the higher the initial conductivity of a PPy film, the less prone it is to attack by oxygen<sup>64</sup>. Thus, the greater the doping level, the more conjugation and the more stable the polymer matrix is. Diaz and Clarke<sup>65</sup> reported that as PPy growth proceeds from the initial stages to a polymer chain, the oxidation potential for the oxidation reaction shifts towards more negative values. This relates to the reactivity of each species towards air, which increases as the oxidation potential becomes more positive and the corresponding conjugation length becomes shorter<sup>57</sup>. Increased oxygen content within the PPy film can lead to over-oxidation. This disturbs the conjugation and lowers the conductivity<sup>66-68</sup>. Although, as reported by Thieblemont *et al.*<sup>44</sup> PPy shows good stability and undergoes only slow degradation in ambient atmosphere.

PPy films can be prepared from aqueous or organic solutions. It is suggested that water reduces the solubility of oligomers and this reduced solubility gives

rise to a faster deposition of the polymer on the electrode<sup>69</sup>. Also, given the high dielectric constant of water, this reduces the coulombic repulsion between the radical cations and consequently facilitates the radical-radical coupling<sup>70-72</sup>. Diaz and Hall<sup>73</sup> investigated the effect of the addition of water to acetonitrile solutions on the conductivity of PPy. They found that the conductivity and the mechanical properties of PPy films greatly depend on the water concentration since the addition of water into acetonitrile resulted in a decrease of the conductivity and mechanical properties. Similarly, Sutton and Vaughan<sup>74</sup> reported that the addition of methanol into water also leads to a drop in the conductivity of PPy films.

The electropolymerisation temperature has a substantial influence on the kinetics of polymerisation as well as on the conductivity, redox properties and mechanical characteristics of the films<sup>75</sup>. As the temperatures increases, there is a decrease in the redox properties. Thus, higher conductivities are obtained at lower temperatures in aqueous solutions<sup>76</sup>.

Electropolymerisation can be carried out using cyclic voltammetry, galvanostatic or potentiostatic methods<sup>22</sup>. Zhou and Heinze<sup>77</sup> and indeed others<sup>78,79</sup> have shown that the electrochemical method controls the structural form of the electrodeposited PPy. Films prepared using cyclic voltammetry or potentiostatic methods are usually compact and smooth, whereas polymers prepared galvanostatically are porous and rough. A comparative study was carried out by Li *et al.*<sup>55</sup> using different electrochemical techniques for PPy formation, to which they investigated the redox properties of PPy. They found that galvanostatic deposition produced PPy films of higher electrochemical reactivity in comparison to those prepared using cyclic voltammetry or grown potentiostatically.

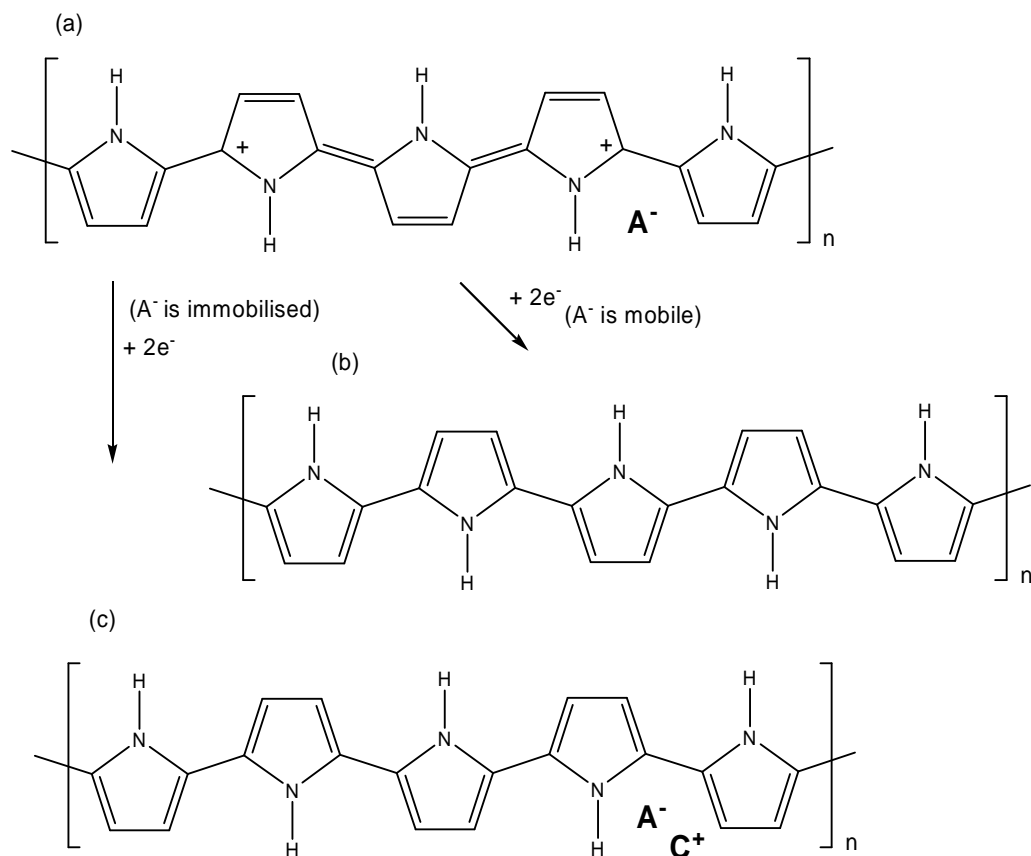
The pH of the monomer solution has an influence on the conductivity and electropolymerisation of pyrrole. It is well known that the electropolymerisation of pyrrole at pH values higher than 7.0 is hindered and the conductivity of the films drop dramatically<sup>80-82</sup>. At the other end of the pH

scale, PPy prepared in a highly acidic pH solution produces polymers with weak conductivity due to the acid catalysed formation of non conjugated trimers<sup>75</sup>. These trimers react further to form a partly conjugated PPy film.

The nature of the electrode surface at which electro-deposition of PPy occurs must be inert to its oxidation potential. In the event that substrates used are susceptible to oxidation, this will further hinder the oxidation and polymerisation of pyrrole. Commonly used anodes are gold, platinum or glassy carbon. Another type of substrate is indium tin oxide (ITO), which can be used for spectroscopic applications, as it is a transparent substrate.

### 1.3.3 Electro-activity of PPy

PPy has been widely studied for its high conductivity, stability in the oxidised form and the ability to be electrochemically switched between the conducting and the insulating states<sup>83</sup>. In the reduced state, PPy is insulating and maintains a neutral oxidation state. Then, in the oxidised state it is highly conducting and positively charged, as shown in Scheme 1.2 (a). A review of the literature revealed that PPy films synthesised in solutions with small dopants such as Cl<sup>-</sup>, ClO<sub>4</sub><sup>-</sup>, NO<sub>3</sub><sup>-</sup>, etc., mainly exhibit anion exchange behaviour due to the high mobility of these ions in the polymer matrix<sup>84</sup>. This implies that upon reduction of PPy to a neutral state, the mobile anions are expelled from the polymer film, as illustrated in Scheme 1.2 (b). Reduction of PPy doped with large anions, such as polyvinylsulfonate and polystyrenesulfonate does not result in the release of these dopants<sup>85</sup>. Under these conditions cation exchange can take place. Thus, the influx of cations is required to neutralise the overall negative charge of the PPy matrix, as shown in Scheme 1.2 (c).



Scheme 1.2: PPy in a (a) oxidised state, (b) reduced state, as an anion exchanger and (c) reduced state, as a cation exchanger.  $A^-$  represents the dopant anion, while  $C^+$  represents a cation.

## 1.4 Supramolecular Systems

A supramolecular system consists of two or more molecular entities held together and organised by means of inter-molecular, non-covalent binding interactions<sup>86,87</sup>. One such system is a host-guest interaction, whereby an inclusion complex is formed. In general, host molecules are cyclic structures and the guest molecule is favourably inserted into the ring structure as a result of a particular driving force, e.g., an electrostatic interaction. Some examples of well known host molecules in supramolecular chemistry are crown ethers, cryptates, calixarenes and cyclodextrins (CDs)<sup>88</sup>.

### 1.4.1 Cyclodextrins

Cyclodextrins (CDs) are a series of natural cyclic oligosaccharides consisting of six, seven or eight glucopyranose units linked by  $\alpha$ -(1,4) bonds<sup>89</sup>. These

structures correspond to  $\alpha$ ,  $\beta$  and  $\gamma$ CD, respectively and are shown in Figure 1.4. Although, CDs have an identical height of 7.9 Å, the variation in the number of linked glucopyranose units dictates the size of the internal cavity. According to Astray *et al.*<sup>90</sup> and Szejtli<sup>91</sup>, the cavity diameters are 5.7, 7.8 and 9.8 Å for  $\alpha$ ,  $\beta$  and  $\gamma$ CD, respectively. The earliest discovery of CDs was in 1891 by Villiers<sup>92</sup>, when in addition to reducing dextrans a small amount of crystalline material was obtained from starch digest of *Bacillus amylobacter*. Research continued on isolating and identifying the macrocyclic structures and in 1942,  $\alpha$  and  $\beta$ CD were determined by X-ray crystallography<sup>93</sup>. Then in 1948, the X-ray structure of  $\gamma$ CD was determined<sup>89</sup>. The X-ray crystal structures show that CDs adopt a hollow truncated cone structure with all glucopyranose units in the  ${}^4C_1$  chair conformation, as illustrated in Figure 1.5. Song *et al.*<sup>88</sup> stated that in CDs the secondary hydroxyl groups (C<sub>2</sub> and C<sub>3</sub>) are located on the wide edge of the ring, which is termed the secondary rim, while the primary hydroxyl groups (C<sub>6</sub>) are found on the other edge, the primary rim. The apolar C<sub>3</sub> and C<sub>5</sub> hydrogens and ether-like oxygens are at the inside of the torus-like molecules. Thus, the molecule has a hydrophilic exterior, which can dissolve in water and a hydrophobic interior<sup>94</sup>.

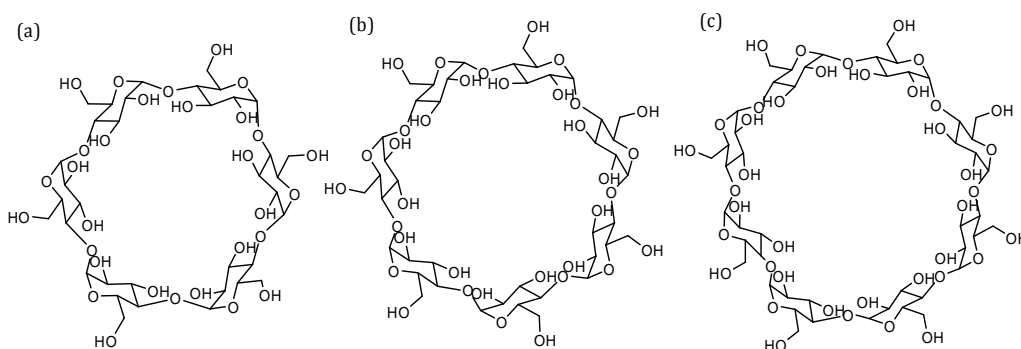


Figure 1.4: Molecular structures of (a)  $\alpha$ CD, (b)  $\beta$ CD and (c)  $\gamma$ CD.

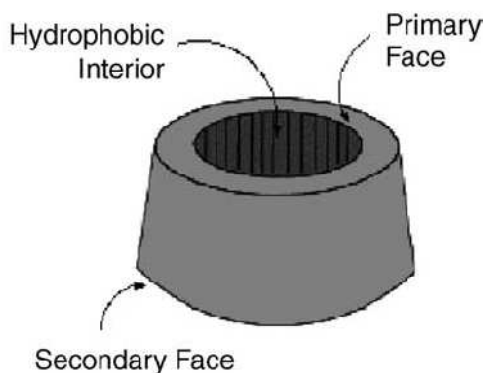


Figure 1.5: Schematic illustrating the truncated cone structure of CD.

Bender and Komiyama<sup>95</sup> showed that treatments of starches with amylase from *Bacillus macerans* gives a crude mixture of  $\alpha$ CD,  $\beta$ CD and  $\gamma$ CD, together with small amounts of CDs with more than eight glucopyranose units. Although, difficult to purify, advances in biotechnology and genetic engineering made possible the isolation of different types of cyclodextrin glucosyl transferases (CGTases)<sup>96</sup>. This improvement in purity and production meant that CDs could be used by pharmaceutical companies. In 1970,  $\beta$ CD was only available as a fine chemical at a price of about \$2,000 per kg. Today, the annual  $\beta$ CD production is close to 10,000 tons and the commodity price is now about \$5 per kg<sup>97</sup>. CDs containing a greater number of glucopyranose units than the common  $\alpha$ ,  $\beta$  or  $\gamma$ CDs have been purified and characterised from enzymes<sup>98</sup>. However, the low solubility of these larger CDs implies that they are not suitable for important applications, such as, solubilisers for drugs<sup>97</sup>. CDs containing less than six glucopyranose units have been synthesised chemically, as they have not been possible to produce enzymatically<sup>99</sup>.

In general, the solubility in water of naturally occurring CDs is limited. This is due to the relatively strong intramolecular hydrogen bonding in the crystal lattice. Substitution of any of the hydrogen bond-forming hydroxyl groups results in a dramatic improvement of their aqueous solubility<sup>100</sup>.  $\beta$ CD contains 7 hydroxyl groups on the primary face and 14 on the secondary face and a number of these hydroxyl groups can be functionalised.

The modified CD used in this work is the commercially available sulfonated- $\beta$ CD (sul- $\beta$ CD). The degree of substitution where the corresponding hydroxyl groups are substituted with sulfonate groups ( $\text{SO}_3^-$ ) is between 7 and 11. The chemical structure corresponding to one of the seven glucopyranose units of sul- $\beta$ CD is illustrated in Figure 1.6. As described by Chen *et al.*<sup>101</sup> and Amini *et al.*<sup>102</sup>, complete sulfonation occurs at the C-6 position, while the C-2 secondary hydroxyls are partially sulfonated. This gives rise to the presence of 7  $\text{SO}_3^-$  groups on the primary face. The complete sulfonation at C-6 is expected due to the higher reactivity of the primary alcohol. As proposed by Ueno and Brelson<sup>103</sup>, sulfonation of the secondary hydroxyls occurs selectively at C-2 only, indicative of the higher acidity of the hydroxyl at the C-2 compared to the C-3 position. Also, the preferential sulfonation at the C-6 position may sterically prevent or reduce the accessibility to the C-3 hydroxyl. Sulfonation occurs at the C-2 equatorial hydroxyl position located at the rim of the wider opening (secondary rim) of the CD, leaving regiospecific C-3 hydroxyls available for potential hydrogen-bonding with guest molecules.

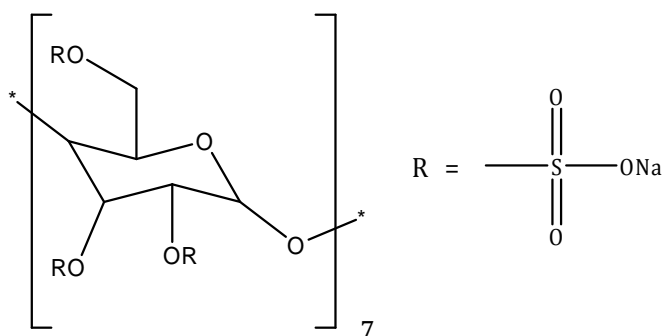


Figure 1.6: Chemical structure corresponding to a one of the seven glucopyranose units of sul- $\beta$ CD, in which the degree of sulfonation of the hydroxyl groups is between 7 and 11.

An important feature of CDs is their ability to form inclusion complexes with a wide range of solid, liquid and gaseous compounds<sup>104</sup>. Hence, the following section discusses the process of inclusion and the parameters which dictate the measure of inclusion.

### 1.4.2 Inclusion Complexes

It is generally accepted that in aqueous solutions CDs form what are called “inclusion complexes”, where water molecules located within the lipophilic central cavity are replaced by a lipophilic guest molecules<sup>96</sup>. CDs are typical host molecules<sup>97</sup>. The type of bond established between the guest and host is non-covalent<sup>98</sup>. Complex formation in solution is a dynamic equilibrium process which is depicted in Equation 1.1, where  $CD$  is the host molecule,  $G$  is the guest molecule and  $CD-G$  is the host-guest complex formed. The stability of the inclusion complex can be described in terms of an association constant ( $K_a$ ) and is governed by a thermodynamic equilibrium, as illustrated in Equation 1.2<sup>90,91</sup>. Large guest molecules give rise to a slower formation and dissociation of the inclusion complex. The process is energetically favoured by the interaction of the guest molecule with the solvated hydrophobic cavity of the host<sup>90</sup>.



$$K_a = \frac{[CD - G]}{[CD][G]} \quad (1.2)$$

Several hypothesis have been proposed to explain the driving force for the formation of CD inclusion complexes<sup>98</sup>. These include electrostatic interactions, hydrogen-bonding interaction, Van der Waals forces and hydrophobic interactions<sup>100,105-108</sup>. The formation cannot be explained by any one of these factors alone, since several of these forces are evident in the inclusion complex<sup>105,109</sup>.

A review article published by Liu and Guo<sup>110</sup> on the driving forces of inclusion, explained an electrostatic interaction as the energy of interaction between the undistorted charge distribution of the two molecules interacting with each other. It includes all electrostatic forces between permanent charges, dipoles and higher multipoles present in the system. Usually three types of electrostatic interactions are important. These are: ion-ion interactions, ion-dipole interactions and dipole-dipole interactions. Ion-ion interactions occur when the CD is appropriately substituted<sup>111</sup> and both the guest and host are charged. An

ion-dipole interaction is the interaction of an ion with a polar molecule. This is an expected interaction in the case of neutral CDs, as CDs are polar molecules. However, this can be difficult to observe in aqueous solutions, as the interaction between the guest and water will also be strong. Finally, dipole-dipole interactions occur between molecules with a dipole moment. In 1988, Chujo and co-workers<sup>112</sup> modelled the complexation of  $\alpha$ CD with substituted benzenes, e.g., benzoic acid and *p*-nitrophenol. It was found that in the complexes the dipoles of the guest molecules were antiparallel to that of the host. As the magnitude of the guest dipole increased, the value of the CD dipole increased but in the opposite direction. The authors concluded that the dipole-dipole interaction plays an essential role in stabilising the complex as well as determining its orientation.

A hydrogen bond may be regarded as a particular kind of dipole-dipole interaction in which, a hydrogen atom attached to an electronegative atom is attracted to a neighbouring dipole on an adjacent molecule or functional group<sup>113</sup>. In particular, in aqueous systems there is some controversy as to the contribution hydrogen bonding can have on complexation. As hydrogen bonds can form with the guest and water molecules, this can inhibit the formation of an inclusion complex<sup>114</sup>. It has been proposed that the hydrogen at the C-6 position is involved in hydrogen bonding as it is flexible and can rotate around the C-5 bond<sup>110</sup>.

Van der Waals interactions can also be referred to as induction and dispersion forces<sup>109</sup>. These forces depend on polarizability, which is also related to molecular size and electron density<sup>113</sup>. These forces result in weak electrostatic interactions. In an aqueous environment, both water and the CD molecule are polar. However, the polarizability of water is much lower than that of the organic components lining the CD cavity and so it is expected that the Van der Waals forces should be stronger between the CD and the guest, as opposed to water and the guest. It was reported by Casu and Ravu<sup>115</sup> in 1966, that induction forces are the main driving force for complexation.

Hydrophobic effects relate to the association of non-polar molecules in water. This interaction is usually associated with a positive enthalpy and positive entropy. In many cases negative enthalpy and entropy changes are computed on formation of the inclusion complex, thus suggesting that hydrophobic effects have little impact on the measure of inclusion<sup>110</sup>. However, this simple analysis has limitations. It is well known that increasing the hydrophobicity of the substituent of the guest molecule enhances complexation as a result of hydrophobic interactions<sup>89</sup>.

### 1.4.3 Applications of Cyclodextrins

The ability of cyclodextrins to encapsulate guest molecules makes them suitable for applications in separation technologies, electrochemistry, environmental technologies, the food industry and in pharmaceutical chemistry<sup>116</sup>. Five of the major areas where CDs are applied are outlined as follows:

#### 1. Separation Methodologies:

CDs are used extensively in separation methodologies because of their ability to discriminate between positional isomers, functional groups, homologues and enantiomers<sup>117</sup>. Analytically, they are used in capillary electrophoresis (CE), which is a useful technique for chiral separation. As documented by Amini *et al.*<sup>102</sup>, charged CDs often contribute to higher chiral resolving capabilities at lower concentrations than neutral CDs. In particular, sul- $\beta$ CD has been used for the determination of the enantiomeric purity of (1*R*,2*S*)-ephedrine<sup>102</sup>.

#### 2. Electrochemical Applications

CDs and functionalised CDs have also been used to modify electrode surfaces<sup>118</sup>. They can then offer an increased surface area for the detection of analytes. This modification usually involves the formation of CD monolayers on the electrode surface<sup>119</sup>.

#### 3. Adsorption and Removal of Pollutants

CDs can be used for the solubilisation of organic contaminants, enrichment and removal of organic pollutants and heavy metals from the environment<sup>116</sup>.

Wastewaters containing dangerous aromatic compounds such as phenol can be significantly reduced if treated with  $\beta$ CD<sup>94</sup>. CDs also decrease the toxicity resulting in an increase in microbial and plant growth. The low cost, biocompatible and effective degradation makes  $\beta$ CDs a useful tool for bioremediation processes<sup>116</sup>.

#### 4. Food Industry

In the early 1970s when expanding the industrial applications of CDs, areas where CDs became very popular were the food, cosmetic and pharmaceutical industries. CDs were investigated as stabilizers for flavouring agents and to reduce unpleasant odour and taste<sup>96</sup>. CDs act as molecular encapsulants, protecting the flavour throughout many rigorous food-processing methods of freezing, thawing and microwaving. This then allows the flavour quality and quantity to be preserved to a greater extent and provides longevity to the food item.

#### 5. Pharmaceutical Industry

A classic application of CDs is in the field of pharmaceuticals. The ability of CDs to form inclusion complexes with active ingredients, e.g., drugs, gives rise to the stabilization, enhanced solubility and bioavailability of the drug. Moreover, CDs have been employed in drug delivery systems and are potential drug delivery candidates in many applications because of their ability to alter the physical, chemical and biological properties of guest molecules through the formation of inclusion complexes<sup>120</sup>.

#### **1.4.4 Calixarenes**

Calixarenes are similar to CDs in that they are torus shaped and are involved in forming inclusion complexes. Unlike CDs, calixarenes are totally synthetic, but the history of calixarenes began in the 19<sup>th</sup> century also. In 1872, Adolph von Baeyer<sup>121</sup> heated aqueous formaldehyde with phenol and observed a reaction that yielded a hard resinous, noncrystalline product. However, the advances in chemistry were not sufficient to characterise the product. Some years later in the 1900s, Baekeland<sup>122</sup> devised a process to synthesise the phenol-

formaldehyde compound in a controlled manner. This homogeneous material consisted of linked phenol molecules joined by methylene bridging units, which were ortho to the phenolic hydroxyl groups. Then in 1942, a cyclic structure was proposed, but it was not until 1972, that Gutsche<sup>123</sup> named the cyclic tetramer, calixarene. The chalice shaped appearance of these molecules resembled a type of Greek vase, known as a *calix-crater*, hence the name “calixarenes”. Each structure is distinguishable by inserting the number of phenolic units within brackets and it is inserted between the prefix -calix and the suffix -arene. Hence, calix[4]arene is composed of 4 phenolic units and is often referred to as a tetramer. The structure is illustrated in Figure 1.7 (a). A similar nomenclature is used for the pentamer and hexamer to give calix[5]arene and calix[6]arene, respectively. These are illustrated in Figure 1.7 (b) and (c), respectively.

Calixarenes are generally non-polar prior to functionalisation at the para position to the hydroxyl group of the phenolic rings. Similar to CDs, functionalisation increases solubility. Ungaro and co-workers<sup>124</sup> were the first to achieve water soluble calixarenes, when they prepared calixarenes containing carboxylate groups. Soon after, Shinkai *et al.*<sup>125,126</sup> described sulfonated calixarenes.

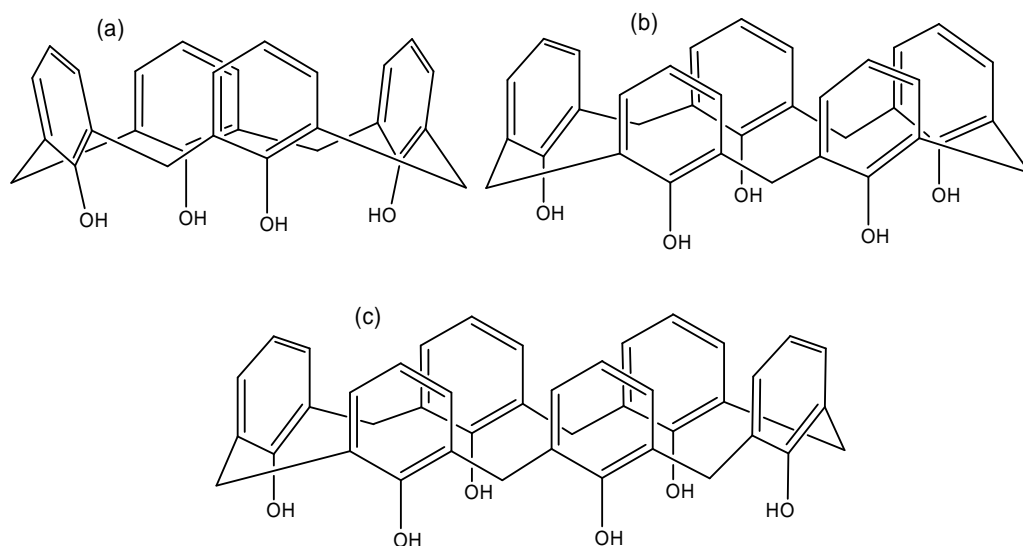
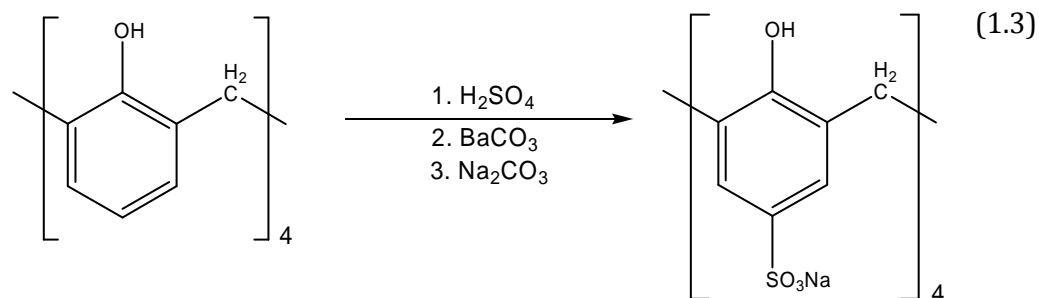


Figure 1.7: Chemical structures of (a) calix[4]arene, (b) calix[5]arene and (c) calix[6]arene.

### 1.4.5 Synthesis and Properties of Calixarenes

The synthesis of calixarenes is now well established. As an example, the synthesis of sulfonated-calix[4]arene, which is used in this work, is described below.

The synthesis of sulfonated-calix[4]arene (sul-calix[4]) was published by Shinkai and co-workers<sup>126</sup>, according to the reaction given in Equation 1.3. The starting material of calix[4]arene is prepared by the debutylation of *p*-*t*-butylcalix[4]arene. Following this, calix[4]arene is mixed with a concentrated solution of sulphuric acid (H<sub>2</sub>SO<sub>4</sub>) to yield a precipitate. After cooling the precipitate is then filtered and neutralised with barium carbonate (BaCO<sub>3</sub>). Following further purification, the product is then adjusted to a pH of 8.0 using sodium carbonate (Na<sub>2</sub>CO<sub>3</sub>).



An interesting feature of calixarenes in contrast to CDs is their ability to interchange between conformers. As a result of the relatively low inversion energy barrier of aromatic rings, the conformational flexibility of the calixarene scaffold provides a variety of three-dimensional structures<sup>127</sup>. Thus, calixarenes have conformational isomers called “cone” and “alternate”<sup>128,129</sup>. The cone conformation in calix[4]arene and its derivatives can be conveniently discriminated from others using <sup>1</sup>H NMR spectroscopy. These conformations are depicted in Figure 1.8 (a) and (b), respectively. By observing the resonances arising from the ArCH<sub>2</sub>Ar methylene protons, one can detect a pair of doublets for cone calixarenes under slow exchange conditions, whereas it becomes a singlet at higher temperatures<sup>128-130</sup>. The temperature at which interconversion between the cone and alternate structure occurs at a sufficiently

rapid rate that the signals of the methylene protons coalesce into a single signal, is known as the coalescence temperature ( $T_c$ ). It was determined by Gutsche and Bauer<sup>131,132</sup>, that a high  $T_c$  is obtained in aprotic solvents, such as chloroform and toluene, but the  $T_c$  is lowered in basic solvents, e.g., acetone and pyridine. These results indicate that the cone conformation is stabilised by intramolecular hydrogen-bonding interactions among OH groups, which compete with intermolecular hydrogen-bonding interactions with solvent molecules. Hence, intermolecular hydrogen-bonding interactions can reduce the conformational freedom in calixarenes. A template effect can also occur upon the formation of an inclusion complex. When the guest molecule is adequately bound with the macrocyclic structure, this can restrict the movement of the calixarene and hence force it to remain in one conformation. In general for the tetramer, it remains in the cone conformation upon formation of an inclusion complex.

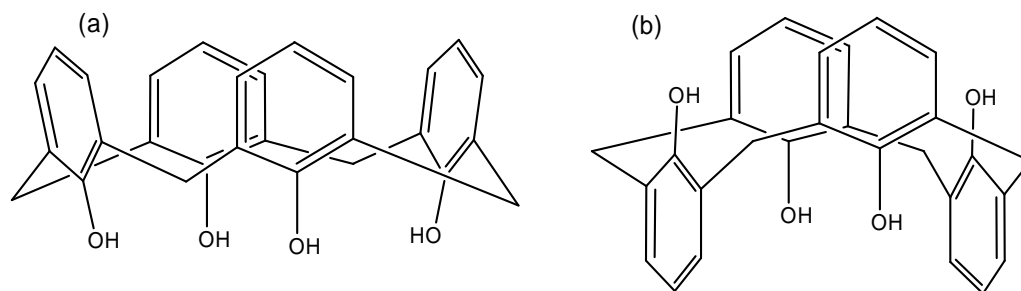


Figure 1.8: (a) Cone conformation and (b) alternate conformation of calix[4].

#### 1.4.6 Inclusion Complexes of Calixarenes

As mentioned previously, calixarenes prior to functionalisation are quite insoluble in water. Hence, functionalisation of these macrocycles is quite common. For sulfonated calixarenes, the two main possible binding interactions arise from electrostatic interactions with a charged cationic guest and or  $\pi$ - $\pi$  interactions with an aromatic guest<sup>5</sup>.

Bonal *et al.*<sup>133</sup> and Morel *et al.*<sup>134</sup> reported on the binding affinities and thermodynamics of sul-calix[4] with a range of metals. They found that divalent

cations were strongly bound in contrast to the monovalent cations, e.g.,  $\text{Na}^+$  and  $\text{Ag}^+$ . This was concluded from thermodynamic changes. The complexation of sul-calix[4] is enthalpy driven accompanied with negative or small positive entropy changes, but the complexation with divalent and trivalent cations is entropy driven with unfavorable enthalpy changes. The monovalent cations are included within the cavity and are bound by cation- $\pi$  interactions. On the other hand, multivalent metal ions interact with sul-calix[4] outside the cavity and this involves electrostatic interactions. The positive entropy and enthalpy changes originate from the partial desolvation of  $\text{Na}^+$  and  $\text{SO}_3^-$  ions upon interaction with the cations and from the consequent release of water molecules.

Arena *et al.*<sup>135,136</sup> studied the interactions between alcohols with sul-calix[4] using  $^1\text{H}$  NMR. They found that the apolar aliphatic portions of the guest were included into the host hydrophobic cavity with the terminal polar groups directed towards the polar sulfonate groups of the host and to the solvent. For the binding of alcohols with sul-calix[4], the interaction is mainly due to Van der Waals forces. The interaction of sul-calix[4] with aromatic substrates was studied by Baur *et al.*<sup>137</sup>, in which they found the driving force for inclusion to be  $\pi$ - $\pi$  interactions. For substituted aromatic guest molecules the ring was inserted within the cavity, while the functional group was positioned outside the cavity.

#### 1.4.7 Applications of Calixarenes

There are a wide range of applications for the usage of calixarenes, ranging from sensor technology<sup>138</sup>, radioactive waste management, pharmaceutical sciences<sup>139</sup> and analytical applications<sup>140-142</sup>. Similar to CDs, an important application of calixarenes is in chemical sensors. As for CDs, the means of detection is based on the calixarenes ability to form inclusion complexes. Aoki *et al.*<sup>143</sup> used fluorescent calixarene systems as ion sensors. Their study was based on a functionalised calixarene containing a pyrene group and a *p*-nitrobenzyl quencher located on the lower rim of the functionalised calixarene. This molecule showed no fluorescence. The formation of an inclusion complex with a cation, caused the lower rim to expand and forced the quencher and the fluorophore spatially apart, enabling the compound to fluoresce again.

### 1.4.8 Methods for Determining Inclusion Complex Association Constant

The determination of the inclusion complex association constant ( $K_a$ ) between host molecules of either sul- $\beta$ CD or sul-calix[4] is important for understanding the type of interaction occurring.

Prior to quantifying this value, the stoichiometry of the interaction is required. This can be done using a continuous variation method, often called Job's method<sup>144,145</sup>. The experimental procedure consists of preparing a series of solutions of host and guest subject to the condition that the sum of the total host and guest concentration is constant<sup>146</sup>. A variety of methods can be used to carry out a Job's plot, in which some property whose value changes in forming the host-guest complex is measured. The maximum of this property is related to the stoichiometric ratio<sup>146</sup>.

A range of methods can be used to evaluate  $K_a$ . Spectroscopic methods are based on the changes in absorbance<sup>147-150</sup>, fluorescence<sup>150-153</sup> and changes in the chemical shifts obtained from  $^1\text{H}$  NMR spectroscopy<sup>154-156</sup>. Electrochemical methods can also be used, such as cyclic voltammetry<sup>157</sup> or rotational disc voltammetry<sup>158</sup>. For all of the above methods, the data to determine the  $K_a$  value are acquired by carrying out a host-guest titration. This involves maintaining the concentration of one of the species constant, usually the guest and varying the host concentration. Upon addition of increasing amounts of host concentration, the response of the guest changes and these changes are monitored. These changes arise because of the shift in equilibrium from uncomplexed to complexed species, as depicted in Equation 1.1. In addition to measuring the quantitative value of the interaction, it is also useful to obtain structural information about the inclusion complex.  $^1\text{H}$  NMR spectroscopy is the best method of obtaining data about the structure of an inclusion complex in solution. Each proton has a signal on the NMR spectrum and the change in the chemical shift can provide information on the position of that proton in relation to the host. This gives vital information as to the geometry of the complex, which can be useful in interpreting the strength of inclusion based on the  $K_a$  value. Takhashi *et al.*<sup>159</sup> illustrated the use of  $^1\text{H}$  NMR spectroscopy to evaluate

the measure of binding between Aspartame and  $\beta$ CD in solution. They evaluated a  $K_a$  value of  $60 \text{ mol}^{-1} \text{ dm}^3$  from the changes in chemical shifts of the respective protons. They proposed that the phenyl ring was included within the CD cavity. Yunyou *et al.*<sup>160</sup> used fluorescence and  $^1\text{H}$  NMR spectroscopy to quantify the interaction between dopamine and sul-calix[4]. They found that increasing concentration of sul-calix[4] in the presence of a fixed concentration of dopamine caused a decrease in the dopamine fluorescence and when a sufficient excess was added the fluorescence was quenched. The  $K_a$  value was  $4.06 \times 10^3 \text{ mol}^{-1} \text{ dm}^3$  and the large downfield shifts obtained from the  $^1\text{H}$  NMR data for the aromatic protons of dopamine indicated inclusion within the cavity.

### 1.5 Paraquat and Diquat

Paraquat and diquat are chemically known as 1,1'-dimethyl-4,4'-bipyridinium and 1,1'-ethylene-2,2'-bipyridinium, respectively. Their chemical structures are shown in Figure 1.9 (a) and (b) and both molecules are bipyridilium pesticides and are extremely hazardous for human health<sup>161</sup>. They are quaternary ammonium herbicides named "quats" and have been widely used in agricultural applications<sup>162</sup>.

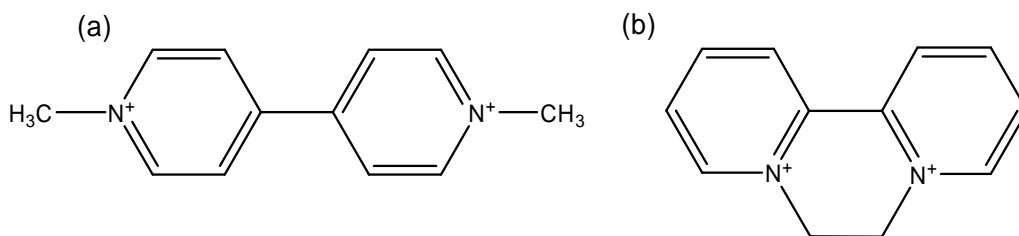
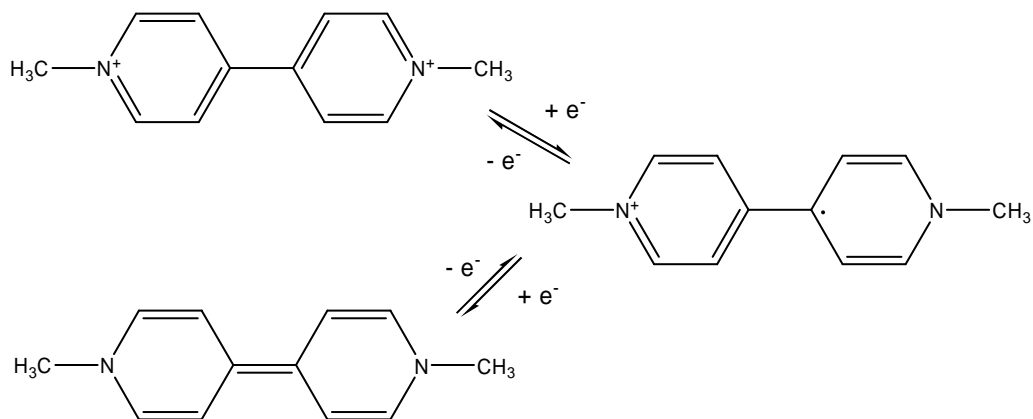


Figure 1.9: Chemical structures of (a) paraquat and (b) diquat.

Paraquat, also known as methyl viologen, is a member of a class of chemicals called the "viologens". Viologens have a long history as redox indicators in biological studies and some have important herbicidal properties, such as paraquat<sup>163</sup>. Paraquat is a quaternary nitrogen herbicide that is widely used in broadleaf weed control. It is a quick acting, non-selective compound that destroys green plant tissue on contact and by translocation within the plant<sup>164</sup>.

Paraquat is harmful to humans also, in which the toxicity occurs almost exclusively through ingestion. The major danger of paraquat is to the lungs. The lungs are mainly affected by direct aspiration, either as the irritative substance is swallowed or by regurgitation from the stomach during vomiting<sup>165</sup>. Due to its toxicity, the United States Environmental Protection Agency (USEPA) has outlined a maximum concentration level for paraquat at  $3 \mu\text{g} / \text{L}$  ( $1.2 \times 10^{-8} \text{ mol dm}^{-3}$ ) in drinking water<sup>166</sup>. Viologens are a class of compounds that readily undergo electron transfer<sup>167</sup>. There are three common redox states as illustrated in Scheme 1.3. The most stable is the colourless dication. Reductive electron transfer to viologen dications forms the radical cations. The stability of the cations is attributable to the delocalisation of the radical electron throughout the  $\pi$ -framework of the bipyridyl moiety and the 1 and 1' substituents also carry some charge<sup>163</sup>. The reduction of the dication is also coupled with a colour change, in which a blue/violet colour is observed upon formation of the radical. Further reduction of the radical cation, forms a neutral species, displaying a yellow/brown colour.



Scheme 1.3: Redox states of paraquat (methyl viologen).

Diquat, similar to paraquat is a widely used bipyridylium herbicide effective in the control of aquatic weeds<sup>168</sup>. Diquat is chemically reduced in the plant by replacing NADP as an electron acceptor in photosynthesis and when oxidised, highly phytotoxic hydrogen peroxide is produced<sup>169</sup>. According to Lopez-Paz *et*

*al.*<sup>170</sup>, when diquat is released into the environment it adheres strongly to soil particles which protect it from microbiological degradation. As a result of this, it increases the risk of contamination. It is also toxic for humans and poisoning from diquat can cause acute renal failure, toxic liver damage, respiratory difficulty and brain haemorrhage. Concentration limits of 20 µg / L ( $7.8 \times 10^{-8}$  mol dm<sup>-3</sup>) in drinking water are outlined by the USEPA<sup>166</sup>. Diquat has a similar chemistry to paraquat, in that it is dicationic and can undergo a two step redox process, similar to that shown in Scheme 1.3. When reduced, diquat gives a relatively stable free radical which has an intense green colour<sup>171</sup>. Diquat usually occurs in the presence of paraquat and is referred to as an interfering compound. A particular aim of this research is to selectively detect and remove paraquat from solution in the presence of diquat.

### 1.5.1 Environmental Technologies for Sensing Paraquat and Diquat

Given the highly toxic nature of paraquat and diquat even at low concentrations, continued use of these herbicides will produce major environmental problems<sup>172</sup>. New methods must therefore be developed to detect and quantify these compounds in water. A range of analytical techniques have been applied to the analysis and detection of paraquat in solution.

Shivhare and Gupta<sup>165</sup> used UV-visible spectroscopy to monitor the detection of the radical cation of paraquat, which absorbs at 600 nm. In this paper, paraquat was reduced in the presence of ascorbic acid to produce the radical cation. The concentration of paraquat as a function of absorbance was plotted and a detection limit in the range of  $1.2 - 9.6 \times 10^{-6}$  mol dm<sup>-3</sup> was evaluated. Taguchi *et al.*<sup>166</sup> investigated the determination of paraquat in water using liquid chromatography and electron ionization mass spectrometry. Paraquat was isolated on a solid phase extraction disk using trifluoroacetic acid. Following this, paraquat was re-dissolved into the mobile phase and it was analysed by liquid chromatography. Quantitatively, mass spectrometry was used to determine the concentration. Using this method an impressive detection limit of  $8.0 \times 10^{-10}$  mol dm<sup>-3</sup> was obtained.

Electrochemically, a range of techniques has been used to optimise the detection of paraquat and diquat. This is quite a desirable technique to use as it eliminates the number of sample handling steps in contrast to the previously discussed techniques<sup>173</sup>. Walcarius and Lamberts<sup>174</sup> examined the use of square wave voltammetry (SWV) for the detection of paraquat and diquat. Using a static mercury drop electrode, a limit of detection of  $1.5 \times 10^{-8}$  mol dm<sup>-3</sup> was obtained. They found that enhanced signals were due to the adsorption of the analytes on the working electrode, however, this method showed non-selective activity between paraquat and diquat. Another aspect of electrochemical detection is to modify the working electrode. As published by Zen *et al.*<sup>175</sup>, a glassy carbon electrode was modified with clay colloids and appropriate amounts of Nafion. The film was spin coated onto the electrode surface and was used to detect paraquat in solution. This method proved very successful and they obtained a detection limit of  $5.0 \times 10^{-10}$  mol dm<sup>-3</sup>. Similarly, Lu and Sun<sup>176</sup> obtained a detection limit of  $5.0 \times 10^{-10}$  mol dm<sup>-3</sup> for paraquat in solution using a glassy carbon electrode that was modified with Nafion. Even though, similar working electrodes were used to detect paraquat at the modified surface, variations in electrolyte solvent and pH induce a different response of the sensor in detecting the analyte. The increased response observed for the detection of paraquat and diquat at the modified electrode in contrast to the bare electrode, is the underlining principle that is used throughout this thesis work. However, as well as focusing on the detection of paraquat at the modified electrode, this research investigates the removal of paraquat and diquat through the formation of complexes with sul- $\beta$ CD or sul-calix[4] as dopants in PPy films.

## 1.6 Membrane Technology and Gas Separation

The latter section of this thesis focuses on the development of another technology, suitable for environmental remediation. As mentioned in the introductory section, Section 1.1, CO<sub>2</sub> emissions have been associated with global warming. Therefore, in order to reduce CO<sub>2</sub> emissions, there is currently an interest in the development of CO<sub>2</sub> sequestration technologies. The first step in such a technology is CO<sub>2</sub> separation from other gases. The following section

discusses the types of membranes, their properties and their use in gas separation according to the literature to date.

### 1.6.1 Membranes

A membrane is defined as a layer which acts as a permselective barrier and has the ability to discriminate between two molecules and separate a mixture based on size or chemical structure<sup>8</sup>. Separation is possible as a result of energy supplied in the form of heat or mechanical work, e.g., the process of osmosis occurs in the presence of a concentration gradient<sup>177</sup>. Figure 1.10 depicts a simple illustration by Kanchan and Benny<sup>178</sup> of the mechanism of a membrane. The driving force in gas separation is the pressure gradient. Thus, the left side of the membrane is under high pressure and the right side is at low pressure. The left and right side are known as the feed and permeate side, respectively. The feed (upstream phase) is partly transported through the membrane and the resulting permeate (downstream phase) is then collected at low pressure. The permeate that flows through the membrane usually contains the desired product<sup>8</sup>. Moreover, the remainder of the feed stream which does not permeate through the membrane and only through the vessel encasing the membrane is known as the retentate<sup>179</sup>. This is illustrated in Figure 1.11.

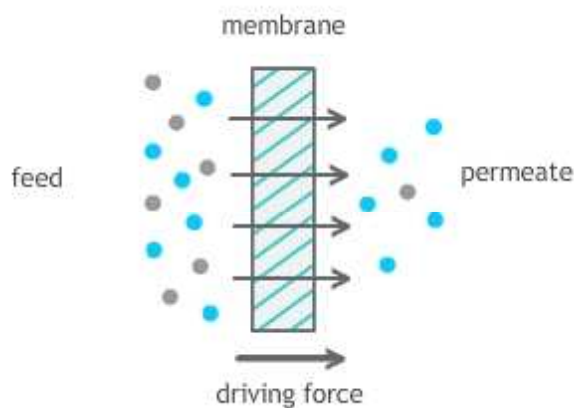


Figure 1.10: Illustration of the dead-flow pattern of gaseous molecules through a membrane in which the principal force of flow is due the presence of a pressure gradient.

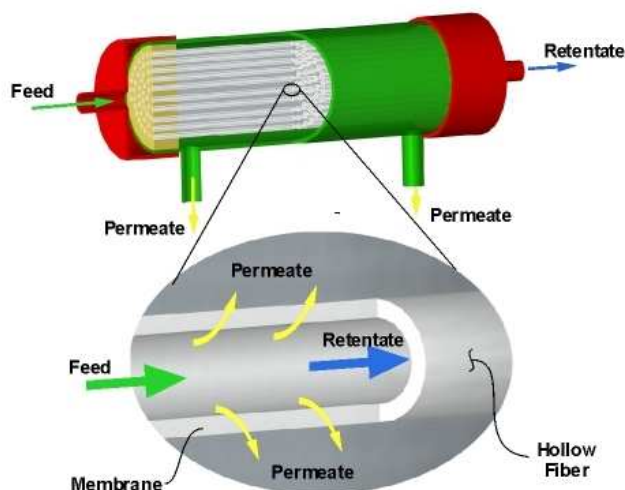


Figure 1.11: Schematic depicting the separation of a mixture, using a cross-flow pattern through the membrane. The permeate is collected perpendicular to the direction of flow of the feed stream and the retentate is collected with the direction of flow.

Membranes can be categorized according to their morphology and the materials used to synthesise them, i.e., organic or inorganic compounds. These parameters will dictate the performance of the membranes in terms of selectivity ( $\alpha$ ) and permeability ( $P$ )<sup>180</sup>. Also, the success of a membrane is dependent on improving its cost effectiveness<sup>181-183</sup>. The research outlined in this thesis investigates carbon molecular sieve hollow fibre membranes and their potential to separate CO<sub>2</sub> from gas mixtures. This work is discussed in Chapter 7.

### 1.6.2 Current Applications of Membranes

Membranes can be utilised in a wide variety of applications. Table 1.1 highlights the applications of membranes throughout the past century. The spectrum of applications varies from biological, chemical, medical and environmental uses. As can be seen from Table 1.1, it is only since the 1980s that the process of hydrogen recovery marked a new era for membrane technology, i.e., gas separation. Although, there was technical curiosity since the 1960s, it was only in the 1980s that intense research activity and commercialisation of membrane technology occurred<sup>183</sup>.

Table 1.1: Details of membrane processes and their corresponding application. The list outlines the country of origin and the year of development as illustrated by Mulder<sup>8</sup>.

Membrane process	Country	Year	Application
Micro-filtration <sup>ζ</sup>	Germany	1920	laboratory use (bacteria filter)
Ultra-filtration <sup>ζ</sup>	Germany	1930	laboratory use
Hemodialysis <sup>ζ</sup>	Netherlands	1950	artificial kidney
Electrodialysis <sup>#</sup>	USA	1955	desalination
Reverse osmosis <sup>#</sup>	USA	1960	sea-water desalination
Ultra-filtration <sup>#</sup>	USA	1979	conc. of macromolecules
Gas separation <sup>#</sup>	USA	1981	hydrogen recovery
Membrane distillation <sup>ζ</sup>	Germany	1981	concentration of aqueous solutions
Pre-evaporation <sup>#</sup>	Germany/ Netherlands	1982	dehydration of organic solvents

ζ Small scale

# Industrial scale

### 1.6.3 Mechanism of Separation

As mentioned in Section 1.6.1, permeability and selectivity are controlled by the morphology of the membrane<sup>180</sup>. This is also linked to the means by which the gas is transported through the membrane and is dependent on a number of parameters, including pore size, presence of ions, selectivity, flux and temperature<sup>184</sup>. Separation can be passive (with the gradient) or active (against the gradient)<sup>8</sup>. In the case of carbon molecular sieve membranes, the transport is passive and the pore size is tailored to provide the desired separation. The process of separation can then be carried out by several different mechanisms including, Knudsen diffusion, selective surface diffusion, capillary condensation or molecular sieving. Figure 1.12<sup>185</sup> indicates the different separation mechanisms which occur due to different pore sizes<sup>186,187</sup>.

Knudsen flow occurs when the pore diameter is greater than  $20 \text{ \AA}^{188,189}$ . It refers to the collisions of the gaseous molecules with themselves and with the pore wall. The measure of these collisions ( $\lambda$ ) within a mean path is dependent on pressure and temperature<sup>190</sup>. Knudsen's number can be calculated in accordance with Equation 1.4<sup>184</sup>, where  $\lambda$  is the measure of these collisions and  $d_p$  is the pore diameter. A value of ten or greater indicates Knudsen flow<sup>189</sup>. Although Knudsen flow shows a high permeability for all gases, due to the large pore sizes, there is very poor selectivity between gases, as all gases can permeate through the membrane due to the large pore size.

$$N_{kn} = \lambda/d_p \quad (1.4)$$

Selective surface diffusion (SSD) occurs when the pore size is in the range of 5-7  $\text{\AA}^{191,192}$ . Gaseous molecules which are larger and more selective to the membrane material surface are adsorbed readily in favour of non-selective gas and then diffuse across the membrane<sup>193</sup>. As described by Lindbråthen and Hägg<sup>194</sup>, SSD is used for selectivity of larger molecules and thus smaller molecules do not permeate through the membrane.

Capillary condensation is a separation technique for membranes with a pore size of 20-30  $\text{\AA}^{184}$ . Schematically it looks similar to the SSD, however the main difference is the pore size and the molecules can exist in two phases, either as a liquid or gas<sup>195</sup>. This occurs when the selective gas adsorbs within the membrane pores and pressure conditions are relatively close to the partial pressure for gas condensation, hence both phases can exist simultaneously<sup>196</sup>. The challenge in quantifying the permeance of the selective gas combined with six possible flow regimes, as proposed by Park *et al.*<sup>197</sup>, which implies that capillary condensation does not serve as a viable transport technique<sup>195</sup>.

Molecular sieving is the dominant transport mechanism where carbon molecular sieve membranes (CMSMs) are applied<sup>184</sup>. With a pore size of 3-5  $\text{\AA}$ , the membranes contain constrictions that approach the molecular dimensions

of the absorbing species<sup>198</sup>. In this manner, they are able to separate gas molecules with similar sizes effectively<sup>193</sup>.

The above mechanisms of separation pertain specifically to carbon membranes. There are other methods of separation depending on the type of membrane. As documented by Lie *et al.*<sup>199</sup> there is a particular type of polymeric membrane, known as a fixed-site carrier membrane (FSCM) which contains active amine groups on the polymer backbone. The means of separation of CO<sub>2</sub> over other gases is based on these amine groups acting as carriers for the CO<sub>2</sub>/H<sub>2</sub>O complex formed upon permeation<sup>199</sup>.

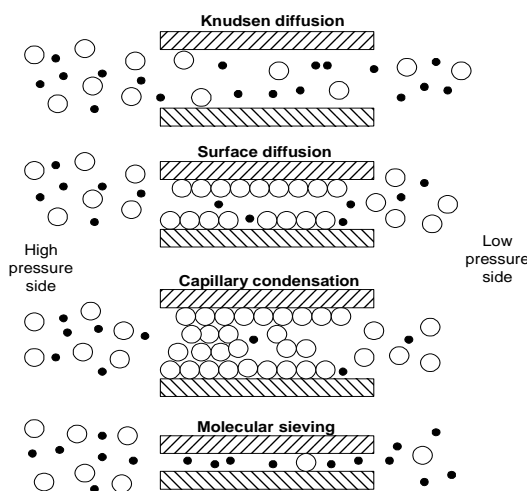


Figure 1.12: Different mechanisms for gas separation using membranes<sup>185</sup>.

#### 1.6.4 Types of Membranes

There are two main types of membranes, biological and synthetic<sup>8</sup>. A further sub-category of membrane classification is done according to their morphology (thick or thin, homogenous or heterogeneous), transport process employed (active or passive) and whether they are neutral or charged. The following is a brief description of the various types of membranes.

Biological membranes are those that are naturally occurring. They are complex structures that carry out specific functions. A well-known and simple example is the plasma or cell membrane, as illustrated in Figure 1.13. This lipid/plasma bi-

layer is composed of an outer hydrophilic region and an inner hydrophobic region<sup>200</sup>. Although the bi-layer is impermeable to molecules, e.g., vitamins and minerals, embedded proteins facilitate the required transport<sup>8</sup>. The transport can be either passive or active. Passive permeation is where the solute permeates through the membrane according to the concentration gradient<sup>201</sup>. Active transport is when the solute permeates against the concentration gradient (i.e. from low to high) and requires energy<sup>201</sup>. Adenosine triphosphate (ATP) is the required energy for this process.

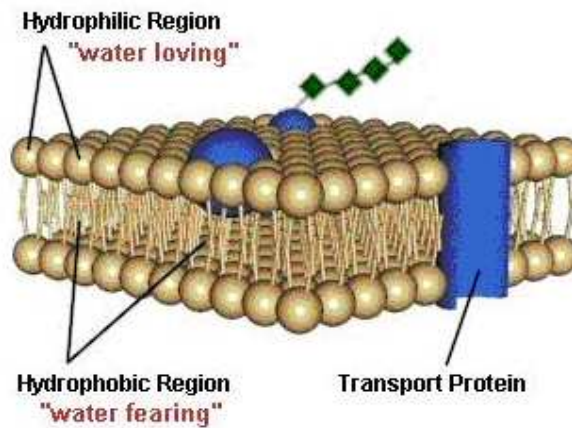


Figure 1.13: Schematic illustration of a biological, cell membrane.

Synthetic membranes can be subdivided into a range of categories. They can be either organic or inorganic, which can be sub-divided into non-porous or porous. The porous membranes can be further categorised into symmetric or asymmetric.

Polymeric membranes are synthetic membranes that can be porous or non-porous, symmetric or asymmetric. A polymer has a high molecular weight and this large molecule is made of multiple monomer units<sup>202</sup>. Polymerisation occurs when the units link, and depending on the monomer and the interaction, will cause variation among polymers of similar monomer structure<sup>8</sup>. The choice of polymer is also important to its permeation. As described by Scholes *et al.*<sup>6</sup> there are two types of polymers, rubber and glassy. Rubber state polymer chains exhibit greater flexibility than glassy polymers. According to Bley *et al.*<sup>203</sup>

thermal energy can change the polymer from glassy to a rubber state, when it reaches a specific temperature known as its glass transition temperature ( $T_g$ ). In general, glassy polymeric membranes exhibit low permeance due to a high  $T_g$ , but show a high selectivity. In contrast, rubber polymeric membranes have good permeance but lower selectivity. For gas separation, glassy polymers are the favoured choice, in particular those with a high  $T_g$ <sup>178</sup>. They show high selectivity and high thermal resistance, e.g., polyoxadiazoles and polytriazoles<sup>8</sup>.

There are many types of inorganic membranes ranging from ceramic, glass, metal and carbon<sup>193</sup>. Similar to organic membranes they can be porous or non-porous. Also porous membranes can be asymmetric or symmetric. Asymmetric membranes are very successful as they combine both a dense selective top layer and a porous sub-layer, achieving good selectivity and permeability<sup>204</sup>. Inorganic membranes are more resistant to thermal and chemical effects in contrast to organic polymeric membranes, in which their morphology can be changed significantly by high temperature, high pressure and exposure to corrosive reagents<sup>193</sup>.

As mentioned, inorganic membranes have a greater appeal in contrast to polymeric membranes due to their resistance to temperature and pressure. Rao *et al.*<sup>205</sup> also indicated that they show superior separation properties when compared to polymeric membranes. Factoring this information into account, inorganic membranes were the chosen material for gas separation. There are many types of inorganic membranes ranging from silica, zeolites and carbon. Silica and zeolites exhibit molecular sieving properties and display good permeability and selectivity. However, silica is insufficient in separating gases of similar sizes, e.g., oxygen and nitrogen<sup>206</sup>. Moreover, zeolites can separate isomers, but it is difficult to obtain a crack-free zeolite membrane<sup>193</sup>. On the other hand, carbon molecular sieve membranes (CMSMs) have been recognized as attractive gas separation materials due to their high flux and selectivity<sup>180,193,207-212</sup>. Carbon membranes differ from polymeric membranes, as they undergo a post synthesis treatment known as carbonisation or pyrolysis<sup>193</sup>. This is a heating process whereby all functional groups are removed from the

carbon precursor, contributing to a large weight loss<sup>207</sup>. The membrane material forms disrupted graphite sheets, which are arranged to form pores, as shown in Figure 1.14. The dimensions of the pores can be tailored by varying the heating process, which optimises the selectivity of the fibre for a certain gas.

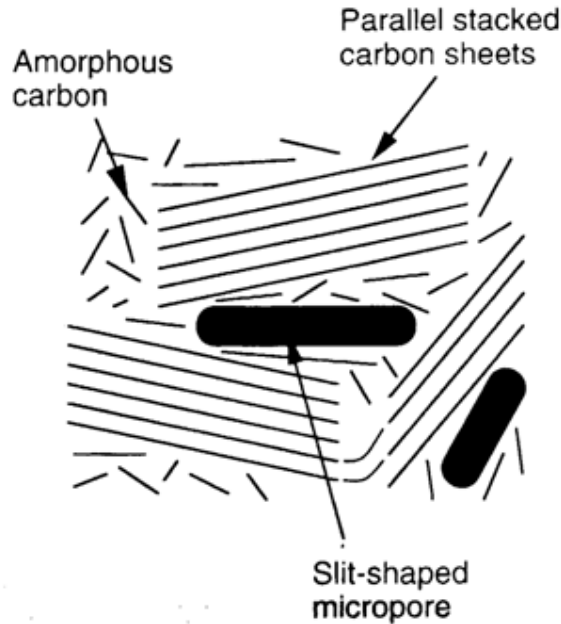


Figure 1.14: Micropore of carbon molecular sieve membrane (CMSM)<sup>210</sup>.

### 1.6.5 Configurations of Carbon Membranes

There are four possible conformations for carbon membranes; these are flat sheet, tubular, hollow fibre and capillary<sup>184</sup>. Flat sheet and hollow fibres have similar pore sizes of 3-5 Å and are both self-supporting. However, they differ in their overall structure, in which flat membranes are sheets and hollow fibres are tubular structures with an outer diameter of less than 1.5 mm. A handbook of definitions issued by the European Society of Membrane Science and Technology<sup>179</sup> states that hollow fibres differ from tubular membranes which, are normally formed inside a porous stainless steel, ceramic or plastic supporting tube with the diameter of the tube being more than 5 mm. Tubular membranes are non-self supporting membranes. Finally, capillary membranes

are tubular shaped, self-supporting membranes with an outer diameter between 1.5 and 5 mm<sup>179</sup>.

All of these carbon membrane configurations apply the same method of separation, molecular sieving, provided the pore size is within the range of 3-5 Å. Although, a different technique is used to prepare the membranes the principal of formation is identical, which is that of phase inversion. Phase inversion is a technique whereby the carbon precursor, i.e., polymer is transformed from a liquid to a solid state<sup>8</sup>. The process of solidification occurs as a result of liquid-liquid de-mixing.

The variation in carbon membrane configurations offers advantages in different aspects, e.g., the ease of preparation or their ability to be used on an industrial scale. Self supporting membranes are of greater appeal than non-self supporting, with simple preparation of a module prior to gas testing. Furthermore, the surface area of a module filled with hollow fibre carbon membranes, in contrast to flat sheet membranes, is much higher. Thus, for membrane technology on an industrial scale, hollow fibres are a premier choice. The remainder of this chapter and subsequently the results in Chapter 7 will discuss the use of carbon molecular sieve hollow fibre membranes for the selective permeation of CO<sub>2</sub> over N<sub>2</sub>, for the potential application of flue gas separation.

### 1.6.6 Gas Separation

Membranes act as filters to separate one or more gases from a feed mixture and generate permeate, rich in the specific gas(es). According to Scholes *et al.*<sup>6</sup>, the characteristics that dictate membrane performance is permeability and selectivity. Based on this, gas separation experiments can involve either a single gas or gas mixtures. With respect to the work outlined in Chapter 7, a series of single gas tests was carried out. The permeabilities of single gas tests using gases such as CO<sub>2</sub>, N<sub>2</sub> or CH<sub>4</sub> are compared to interpret the selectivity of the membrane. The selectivity of the membrane to a particular gas is quantified in accordance with Equation 1.5, which considers the ratio of the permeability of

gases A and B, respectively. The selectivity of carbon hollow fibre membranes can be specifically tailored. In this case, the membranes showed selectivity for CO<sub>2</sub>. The dense top layer was selective for this gas over molecules similar in size, i.e., CH<sub>4</sub> and N<sub>2</sub>. As the gas permeated through the porous sub layer, the selectivity of the dense layer to CO<sub>2</sub> inhibited the permeation of other gases through to the permeate side. Thus, when carrying out mixed gas tests, in theory, it should be possible to separate mixtures of CH<sub>4</sub> and CO<sub>2</sub>. Due to the pore size of these membranes, CO<sub>2</sub> permeates through the membrane by molecular sieving, which is normally used for separation by size.

$$\alpha_{A/B} = \frac{P_A}{P_B} \quad (1.5)$$

### 1.6.7 Aging

The biggest challenge with carbon membranes is combating aging, i.e., the membranes decreasing ability to allow gases to permeate. This occurs due to exposure to differential pressure, temperature and contaminants on top of their natural and physical aging behaviour<sup>213,214</sup>. The carbon membranes produced in this work are selective for CO<sub>2</sub>, but the permeability of CO<sub>2</sub> is compromised over time due to aging. During the intervening time between carbonisation and gas testing, the fibres are most susceptible to physical and chemical adsorption<sup>215</sup>, i.e., directly after carbonisation, there are many sites available at which adsorption can occur.

Physical adsorption is the intermolecular interactions caused by the adsorption of water molecules from moisture in the atmosphere in the carbon matrix of the membrane<sup>216</sup>. As hypothesised by Menendez and Fuertes<sup>215</sup>, water can be removed using a low-pressure vacuum or the application of temperatures above 100 °C. In contrast, aging due to chemical adsorption is not so easily resolved. Chemical adsorption is the adsorption of O<sub>2</sub> and the formation of covalent C-O bonds, which are significantly stronger than Van der Waals forces or hydrogen bonds of physically adsorbed H<sub>2</sub>O onto the membrane<sup>216,217</sup>. The adherence of either molecule can compromise the permeance of the membranes, as pores

become unavailable for permeating gases as they are essentially blocked by either O<sub>2</sub> or H<sub>2</sub>O molecules<sup>218</sup>.

Membranes can also be affected by hydrocarbons, e.g., butane and aromatics, such as, toluene. Given the organophilic nature of carbon membranes, they are excellent adsorbents for organics<sup>215,219</sup>. Whether in a laboratory or in an industrial setting, the membranes will have a certain amount of exposure to these molecules. Similar to H<sub>2</sub>O or O<sub>2</sub>, these species adsorb onto the membrane, reducing the number of pores available for gas separation.

Various techniques have been researched to minimise aging. This is of great importance for the up-scaling process from laboratory to industry, as replacing the membranes on a regular basis due to aging would prove costly and not a feasible option. Thus, as well as producing a successful permeating membrane, it is equally as important to sustain productivity. Regeneration is a method used to enhance the productivity of an aged membrane to within a close range of its original permeability.

### **1.6.8 Regeneration**

Regeneration is a method used to restore the membranes productivity to its original state, through the removal of adsorbed contaminants<sup>219</sup>. There are four types of regeneration techniques for carbon materials which have been investigated to date, namely: thermal<sup>215</sup>, chemical<sup>219-221</sup>, microwave<sup>222</sup> and electrical regeneration<sup>7,223</sup>.

Thermal regeneration is the application of heat to an aged membrane in order to remove adsorbed molecules from the membrane. As discussed earlier, temperatures above 100 °C remove physically adsorbed molecules, such as H<sub>2</sub>O molecules<sup>215</sup>. However, higher temperatures are required to remove chemically adsorbed molecules, such as O<sub>2</sub>. Menendez and Fuertes<sup>215</sup> investigated the effect of treating carbon membranes under vacuum at 120 °C for 3 hours. The results showed partial restoration of permeance values. As demonstrated by Vu *et al.*<sup>216</sup>, to remove chemically adsorbed molecules from the membrane,

temperatures from 600-800 °C are required. However, at temperatures between 700-800 °C the morphology and porosity of the carbon membrane material and its transport properties are changed. As well as potentially damaging the membrane, economically this is not a feasible option for industrial use. Thus, other methods of regeneration are required.

Chemical regeneration is a method which involves exposing the membrane to a hydrocarbon, which acts as a cleaning agent, removing any unwanted adsorbed material. Considering the large number of hydrocarbons tested, it has been reported in the literature, that propylene is the most efficient at restoring the membranes performance<sup>219</sup>. Hydrocarbons containing 6 carbons or higher are not suitable chemicals for regeneration. Hexane tends to form a monolayer over the membrane. Even though this prevents further physical and chemical adsorption, it essentially blocks the pores from permeating gases. However, the disadvantage of using smaller hydrocarbons is that if the exposure time is too short, the adsorbed materials will not be removed completely. Conversely, when the membrane is left exposed to the hydrocarbon for too long, it is reported to widen the pores thus, altering the selectivity of the CMSMs<sup>220,221</sup>.

Similar to thermal and chemical regeneration, microwave regeneration is the removal of adsorbents using microwave energy. However, this technique has yet to be tested on carbon hollow fibre membranes, but has been demonstrated to work successfully on carbon adsorption beds. Coss and Cha<sup>222</sup> showed that granular activated carbon (GAC) readily adsorbs solvents, but these solvents can be desorbed and collected following regeneration. The advantage of microwave regeneration is that it does not require as much energy as the thermal process. However, for regeneration to occur on the carbon absorbent beds, it took up to 20 cycles of applying microwave energy to do this<sup>222</sup>. Thus, similar to thermal regeneration, this may not be a viable option for carbon membranes in industry given the cost needed to supply continuous amounts of microwave energy. The final method that proves the most promising and has been investigated previously by Lie *et al.*<sup>7</sup> on flat sheet carbon membranes is electro-regeneration.

Electro-regeneration is the application of an electric current to a CMSM in order to regenerate the permeability of the membrane to its original state. Similar to microwave regeneration it removes adsorbed material due to aging or previous gas testing of the membrane. It is still a relatively new technique, in which only research on flat sheet carbon membranes has been carried out<sup>7,223</sup>. Thus, in Chapter 7, analysis and results of the electro-regeneration of aged carbon hollow fibre membranes will be presented.

### 1.7 References

1. E. J. Oh, K. S. Jang, and A. G. MacDiarmid, *Synth. Met.*, **125**, 267, (2001).
2. N. K. Guimard, N. Gomez, and C. E. Schmidt, *Prog. Polym. Sci.*, **32**, 876, (2007).
3. E. Halfon, S. Galassi, R. Brüggemann, and A. Provini, *Chemosphere*, **33**, 1543, (1996).
4. D. S. Guo, L. H. Wang, and Y. Liu, *J. Org. Chem.*, **72**, 7775, (2007).
5. D. S. Guo, K. Wang, and Y. Liu, *J. Inclusion Phenom. Macroyclic Chem.*, **62**, 1, (2008).
6. C. A. Scholes, S. E. Kentish, and G. W. Stevens, *Recent Patents on Chemical Engineering* **1**, 52, (2008).
7. J. A. Lie and M. B. Hagg, *J. Membr. Sci.*, **284**, 79, (2006).
8. M. Mulder, *Basic Principles of Membrane Technology*, Kluwer Academic Publishers, Dordrecht, 1996.
9. P. Chandrasekhar, *Conducting Polymers, Fundamentals and Applications, A Practical Approach*, Kluwer Academic Publishers, Boston / Dordrecht / London, 1999.
10. H. Shirakawa, E. J. Louis, A. G. Macdiarmid, C. K. Chiang, and A. J. Heeger, *J. Chem. Soc., Chem. Commun.*, 578, (1977).
11. K. Gurunathan, A. V. Murugan, R. Marimuthu, U. P. Mulik, and D. P. Amalnerkar, *Mater. Chem. Phys.*, **61**, 173, (1999).
12. J. N. Turner, W. Shain, D. H. Szarowski, M. Andersen, S. Martins, M. Isaacson, and H. Craighead, *Exp. Neurol.*, **156**, 33, (1999).
13. J. D. Weiland and D. J. Anderson, *IEEE Trans. Biomed. Eng.*, **47**, 911, (2000).
14. J. L. Bredas and G. B. Street, *Acc. Chem. Res.*, **18**, 309, (1985).
15. S. Ikehata, J. Kaufer, T. Woerner, A. Pron, M. A. Druy, A. Sivak, A. J. Heeger, and A. G. Macdiarmid, *Phys. Rev. Lett.*, **45**, 1123, (1980).
16. M. Peo, S. Roth, K. Dransfeld, B. Tieke, J. Hocker, H. Gross, A. Grupp, and H. Sixl, *Solid State Commun.*, **35**, 119, (1980).
17. G. B. Street, T. C. Clarke, M. Krounbi, K. Kanazawa, V. Lee, P. Pfluger, J. C. Scott, and G. Weiser, *Mol. Cryst. Liq. Cryst.*, **83**, 1285, (1982).
18. J. C. Scott, J. L. Bredas, K. Yakushi, P. Pfluger, and G. B. Street, *Synth. Met.*, **9**, 165, (1984).
19. J. C. Scott, J. L. Bredas, J. H. Kaufman, P. Pfluger, G. B. Street, and K. Yakushi, *Mol. Cryst. Liq. Cryst.*, **118**, 163, (1985).
20. A. Malinauskas, *Polymer*, **42**, 3957, (2001).

21. A. Dallolio, G. Dascola, V. Varacca, and V. Bocchi, *Comptes Rendus Hebdomadaires Des Seances De L Academie Des Sciences Serie C*, 267, 433, (1968).
22. W. Schuhmann, C. Kranz, H. Wohlschlager, and J. Strohmeier, *Biosens. Bioelectron.*, 12, 1157, (1997).
23. M. Gerard, A. Chaubey, and B. D. Malhotra, *Biosens. Bioelectron.*, 17, 345, (2002).
24. K. S. V. Santhanam, *Pure Appl. Chem.*, 70, 1259, (1998).
25. S. Ta, *Handbook of conducting polymer*, Basel, New York, 1997.
26. T. Ahuja, I. A. Mir, D. Kumar, and Rajesh, *Biomaterials*, 28, 791, (2007).
27. K. A. Mauritz, I. D. Stefanithis, S. V. Davis, R. W. Scheetz, R. K. Pope, G. L. Wilkes, and H. H. Huang, *J. Appl. Polym. Sci.*, 55, 181, (1995).
28. R. C. D. Peres, M. A. Depaoli, S. Panero, and B. Scrosati, *J. Power Sources*, 40, 299, (1992).
29. K. Suri, S. Annapoorni, A. K. Sarkar, and R. P. Tandon, *Sens. Actuators, B*, 81, 277, (2002).
30. A. Kaynak, J. Unsworth, G. E. Beard, and R. Clout, *Mater. Res. Bull.*, 28, 1109, (1993).
31. G. A. Sotzing, J. R. Reynolds, and P. J. Steel, *Chem. Mater.*, 8, 882, (1996).
32. B. Adhikari and S. Majumdar, *Prog. Polym. Sci.*, 29, 699, (2004).
33. T. Panasyuk-Delaney, V. M. Mirsky, M. Ulbricht, and O. S. Wolfbeis, *Anal. Chim. Acta*, 435, 157, (2001).
34. J. R. Stetter, P. C. Jurs, and S. L. Rose, *Anal. Chem.*, 58, 860, (1986).
35. A. B. Benrashed, D. R. Bull, and G. J. Harris, *Sens. Actuators, B*, 24, 248, (1995).
36. A. J. Heeger, *Synth. Met.*, 125, 23, (2001).
37. A. Angeli, *Gazz. Chim. Ital.*, 46, 279, (1916).
38. K. Keiji Kanazawa, A. F. Diaz, W. D. Gill, P. M. Grant, G. B. Street, G. Piero Gardini, and J. F. Kwak, *Synth. Met.*, 1, 329, (1980).
39. M. Nishizawa, H. Nozaki, H. Kaji, T. Kitazume, N. Kobayashi, T. Ishibashi, and T. Abe, *Biomaterials*, 28, 1480, (2007).
40. S. Carquigny, O. Segut, B. Lakard, F. Lallemand, and P. Fievet, *Synth. Met.*, 158, 453, (2008).
41. S. P. Armes, *Synth. Met.*, 20, 365, (1987).
42. J. Duchet, R. Legras, and S. Demoustier-Champagne, *Synth. Met.*, 98, 113, (1998).
43. R. E. Myers, *J. Electron. Mater.*, 15, 61, (1986).
44. J. C. Thieblemont, A. Brun, J. Marty, M. F. Planche, and P. Calo, *Polymer*, 36, 1605, (1995).
45. K. Nishio, M. Fujimoto, O. Ando, H. Ono, and T. Murayama, *J. Appl. Electrochem.*, 26, 425, (1996).
46. C. Cassignol, P. Olivier, and A. Ricard, *J. Appl. Polym. Sci.*, 70, 1567, (1998).
47. A. Malinauskas, J. Malinauskiene, and A. Ramanavicius, *Nanotechnology*, 16, R51, (2005).
48. A. F. Diaz and J. I. Castillo, *J. Chem. Soc., Chem. Commun.*, 397, (1980).
49. M. C. Henry, C. C. Hsueh, B. P. Timko, and M. S. Freund, *J. Electrochem. Soc.*, 148, D155, (2001).
50. A. Deronzier and J. C. Moutet, *Acc. Chem. Res.*, 22, 249, (1989).

51. U. Lange, N. V. Roznyatouskaya, and V. M. Mirsky, *Anal. Chim. Acta*, **614**, 1, (2008).
52. D. D. Ateh, H. A. Navsaria, and P. Vadgama, *J. R. Soc. Interface*, **3**, 741, (2006).
53. K. K. Kanazawa, A. F. Diaz, W. D. Gill, P. M. Grant, G. B. Street, and G. P. Gardini, *Synth. Met.*, **1**, 329, (1980).
54. S. Eddy, K. Warriner, I. Christie, D. Ashworth, C. Purkiss, and P. Vadgama, *Biosens. Bioelectron.*, **10**, 831, (1995).
55. C. M. Li, C. Q. Sun, W. Chen, and L. Pan, *Surf. Coat. Technol.*, **198**, 474, (2005).
56. K. Imanishi, M. Satoh, Y. Yasuda, R. Tsushima, and S. Aoki, *J. Electroanal. Chem.*, **260**, 469, (1989).
57. R. Cervini, R. J. Fleming, B. J. Kennedy, and K. S. Murray, *J. Mater. Chem.*, **4**, 87, (1994).
58. J. Ouyang and Y. F. Li, *Polymer*, **38**, 1971, (1997).
59. J. Tietje-Girault, C. Ponce de Leon, and F. C. Walsh, *Surf. Coat. Technol.*, **201**, 6025, (2007).
60. W. B. Liang, J. T. Lei, and C. R. Martin, *Synth. Met.*, **52**, 227, (1992).
61. D. S. Maddison and J. Unsworth, *Synth. Met.*, **30**, 47, (1989).
62. A. A. A. Almario and R. L. Vieira, *J. Chil. Chem. Soc.*, **51**, 971, (2006).
63. A. A. A. Almario and R. L. T. Caceres, *J. Chil. Chem. Soc.*, **54**, 14, (2009).
64. R. Cervini, R. J. Fleming, and K. S. Murray, *J. Mater. Chem.*, **2**, 1115, (1992).
65. A. F. Diaz and T. C. Clarke, *J. Electroanal. Chem.*, **111**, 115, (1980).
66. J. C. Thieblemont, J. L. Gabelle, and M. F. Planche, *Synth. Met.*, **66**, 243, (1994).
67. J. T. Lei and C. R. Martin, *Synth. Met.*, **48**, 331, (1992).
68. T. L. Tansley and D. S. Maddison, *J. Appl. Phys.*, **69**, 7711, (1991).
69. A. J. Downard and D. Pletcher, *J. Electroanal. Chem.*, **206**, 139, (1986).
70. F. Beck, M. Oberst, and R. Jansen, *Electrochim. Acta*, **35**, 1841, (1990).
71. F. Beck, *Electrochim. Acta*, **33**, 839, (1988).
72. F. Beck and M. Oberst, *Synth. Met.*, **28**, C43, (1989).
73. A. F. Diaz and B. Hall, *IBM J. Res. Dev.*, **27**, 342, (1983).
74. S. J. Sutton and A. S. Vaughan, *Synth. Met.*, **58**, 391, (1993).
75. S. Sadki, P. Schottland, N. Brodie, and G. Sabouraud, *Chem. Soc. Rev.*, **29**, 283, (2000).
76. M. Satoh, K. Kaneto, and K. Yoshino, *Synth. Met.*, **14**, 289, (1986).
77. M. Zhou and J. Heinze, *Electrochim. Acta*, **44**, 1733, (1999).
78. T. F. Otero and E. Delarreta, *Synth. Met.*, **26**, 79, (1988).
79. T. Hernandez-Perez, M. Morales, N. Batina, and M. Salmon, *J. Electrochem. Soc.*, **148**, C369, (2001).
80. M. Zhou and J. Heinze, *J. Phys. Chem. B*, **103**, 8443, (1999).
81. S. Asavapiryanont, G. K. Chandler, G. A. Gunawardena, and D. Pletcher, *J. Electroanal. Chem.*, **177**, 229, (1984).
82. S. Kuwabata, J. Nakamura, and H. Yoneyama, *J. Chem. Soc., Chem. Commun.*, 779, (1988).
83. C. Ehrenbeck and K. Juttner, *Electrochim. Acta*, **41**, 511, (1996).
84. M. Karthikeyan, K. K. Satheeshkumar, and K. P. Elango, *J. Hazard. Mater.*, **167**, 300, (2009).

85. C. Weidlich, K. M. Mangold, and K. Juttner, *Electrochim. Acta*, 47, 741, (2001).
86. J. M. Lehn, *Angewandte Chemie-International Edition in English*, 27, 89, (1988).
87. F. Diederich, *J. Chem. Educ.*, 67, 813, (1990).
88. L. X. Song, L. Bai, X. M. Xu, J. He, and S. Z. Pan, *Coord. Chem. Rev.*, 253, 1276, (2009).
89. E. M. M. Del Valle, *Process Biochem.*, 39, 1033, (2004).
90. G. Astray, C. Gonzalez-Barreiro, J. C. Mejuto, R. Rial-Otero, and J. Simal-Gandara, *Food Hydrocolloids*, 23, 1631, (2009).
91. J. Szejtli, *Chem. Rev.*, 98, 1743, (1998).
92. A. Villiers, *Comptes Rendus de l'Académie des sciences*, 112, 536, (1891).
93. H. J. Buschmann and E. Schollmeyer, *J. Cosmet. Sci.*, 53, 185, (2002).
94. J. Szejtli, *Trends Biotechnol.*, 7, 170, (1989).
95. M. L. Bender and M. Komiyama, *Cyclodextrin Chemistry*, Springer-Verlag, Berlin, 1978.
96. T. Loftsson and D. Duchene, *Int. J. Pharm.*, 329, 1, (2007).
97. M. E. Brewster and T. Loftsson, *Adv. Drug Delivery Rev.*, 59, 645, (2007).
98. K. L. Larsen and W. Zimmermann, *J. Chromatogr. A*, 836, 3, (1999).
99. T. Nakagawa, K. Ueno, M. Kashiwa, and J. Watanabe, *Tetrahedron Lett.*, 35, 1921, (1994).
100. J. Szejtli, *Cyclodextrin Technology*, Kluwer Academic Publisher, Dordrecht, 1988.
101. F. T. A. Chen, G. Shen, and R. A. Evangelista, *J. Chromatogr. A*, 924, 523, (2001).
102. A. Amini, T. Rundlof, M. B. G. Rydberg, and T. Arvidsson, *J. Sep. Sci.*, 27, 1102, (2004).
103. A. Ueno and R. Breslow, *Tetrahedron Lett.*, 23, 3451, (1982).
104. S. D. Eastburn and B. Y. Tao, *Biotechnol. Adv.*, 12, 325, (1994).
105. K.-H. Fromming and J. Szejtli, *Cyclodextrins in Pharmacy*, Kluwer, Dordrecht, 1994.
106. J. F. Wojcik, *Bioorg. Chem.*, 12, 130, (1984).
107. Y. Matsui, T. Nishioka, and T. Fujita, *Top. Curr. Chem.*, 128, 61, (1985).
108. R. J. Clarke, J. H. Coates, and S. F. Lincoln, *Adv. Carbohydr. Chem. Biochem.*, 46, 205, (1988).
109. K. A. Connors, *Chem. Rev.*, 97, 1325, (1997).
110. L. Liu and Q. X. Guo, *J. Inclusion Phenom. Macrocyclic Chem.*, 42, 1, (2002).
111. Y. Matsui and A. Okimoto, *Bull. Chem. Soc. Jpn.*, 51, 3030, (1978).
112. M. Kitagawa, H. Hoshi, M. Sakurai, Y. Inoue, and R. Chujo, *Bull. Chem. Soc. Jpn.*, 61, 4225, (1988).
113. J. W. Steed and J. L. Atwood, *Supramolecular Chemistry*, John Wiley & Sons, Ltd, Chichester, New York, Weinheim, Brisbane, Singapore and Toronto, 2000.
114. D. W. Griffiths, M. L. Bender, and H. P. a. P. B. W. D.D. Eley, in *Advances in Catalysis*, Vol. 23, Academic Press, 1973, p. 209.
115. B. Casu and L. Rava, *Ric. Sci.*, 36, 733, (1966).
116. M. Singh, R. Sharma, and U. C. Banerjee, *Biotechnol. Adv.*, 20, 341, (2002).
117. S. M. Han, *Biomed. Chromatogr.*, 11, 259, (1997).

118. C. Camacho, J. C. Matias, B. Chico, R. Cao, L. Gomez, B. K. Simpson, and R. Villalonga, *Electroanalysis*, 19, 2538, (2007).
119. H. X. Ju and D. Leech, *Langmuir*, 14, 300, (1998).
120. K. Uekama, F. Hirayama, and T. Irie, *Chem. Rev.*, 98, 2045, (1998).
121. A. v. Baeyer, *Ber.*, 5, 1094, (1872).
122. L. H. Baekeland, *J. Ind. Eng. Chem.*, 5, 506, (1913).
123. C. D. Gutsche and R. Muthukrishnan, *J. Org. Chem.*, 43, 4905, (1978).
124. A. Arduini, A. Pochini, S. Reverberi, and R. Ungaro, *J. Chem. Soc., Chem. Commun.*, 981, (1984).
125. S. Shinkai, S. Mori, T. Tsubaki, T. Sone, and O. Manabe, *Tetrahedron Lett.*, 25, 5315, (1984).
126. S. Shinkai, K. Araki, T. Tsubaki, T. Arimura, and O. Manabe, *J. Chem. Soc. Perkin. 1*, 2297, (1987).
127. E. Bukhaltsev, I. Goldberg, and A. Vigalok, *Organometallics*, 24, 5732, (2005).
128. C. D. Gutsche, *Acc. Chem. Res.*, 16, 161, (1983).
129. C. D. Gutsche, *Top. Curr. Chem.*, 123, 1, (1984).
130. K. Araki, S. Shinkai, and T. Matsuda, *Chem. Lett.*, 581, (1989).
131. C. D. Gutsche and L. J. Bauer, *Tetrahedron Lett.*, 22, 4763, (1981).
132. C. D. Gutsche and L. J. Bauer, *J. Am. Chem. Soc.*, 107, 6052, (1985).
133. C. Bonal, Y. Israeli, J. P. Morel, and N. Morel-Desrosiers, *J. Chem. Soc., Perkin Trans. 2*, 1075, (2001).
134. J. P. Morel and N. Morel-Desrosiers, *Organic & Biomolecular Chemistry*, 4, 462, (2006).
135. G. Arena, A. Casnati, A. Contino, D. Sciotto, and R. Ungaro, *Tetrahedron Lett.*, 38, 4685, (1997).
136. G. Arena, A. Contino, F. G. Gulino, A. Magri, D. Sciotto, and R. Ungaro, *Tetrahedron Lett.*, 41, 9327, (2000).
137. M. Baur, M. Frank, J. Schatz, and F. Schildbach, *Tetrahedron*, 57, 6985, (2001).
138. D. Diamond and K. Nolan, *Anal. Chem.*, 73, 22A, (2001).
139. E. Da Silva, A. N. Lazar, and A. W. Coleman, *J. Drug Delivery Sci. Technol.*, 14, 3, (2004).
140. R. Ludwig, *Microchimica Acta*, 152, 1, (2005).
141. S. K. Menon and M. Sewani, *Rev. Anal. Chem.*, 25, 49, (2006).
142. L. Mutihac, H. J. Buschmann, R. C. Mutihac, and E. Schollmeyer, *J. Inclusion Phenom. Macrocyclic Chem.*, 52, 135, (2005).
143. I. Aoki, T. Sakaki, S. Tsutsui, and S. Shinkai, *Tetrahedron Lett.*, 33, 89, (1992).
144. A. Dimitrovska, B. Andonovski, and K. Stojanoski, *Int. J. Pharm.*, 134, 213, (1996).
145. C. Y. Huang, R. X. Zhou, D. C. H. Yang, and P. B. Chock, *Biophys. Chem.*, 100, 143, (2003).
146. A. Sayago, M. Boccio, and A. G. Asuero, *Int. J. Pharm.*, 295, 29, (2005).
147. K. Kitamura and N. Imayoshi, *Anal. Sci.*, 8, 497, (1992).
148. S. E. Brown, J. H. Coates, C. J. Easton, S. F. Lincoln, Y. Luo, and A. K. W. Stephens, *Aust. J. Chem.*, 44, 855, (1991).
149. R. Deponti, C. Torricelli, A. Motta, and M. Crivellente, *Eur. J. Pharm. Biopharm.*, 37, 106, (1991).

150. S. Letellier, B. Maupas, J. P. Gramond, F. Guyon, and P. Gareil, *Anal. Chim. Acta*, 315, 357, (1995).
151. S. Ishiwata and M. Kamiya, *Chemosphere*, 34, 783, (1997).
152. I. DuranMeras, A. M. DelaPena, F. Salinas, and I. R. Caceres, *Appl. Spectrosc.*, 51, 684, (1997).
153. Y. L. Loukas, V. Vraka, and G. Gregoriadis, *J. Pharm. Pharmacol.*, 49, 127, (1997).
154. G. Endresz, B. Chankvetadze, D. Bergenthal, and G. Blaschke, *J. Chromatogr. A*, 732, 133, (1996).
155. B. Chankvetadze, G. Endresz, G. Schulte, D. Bergenthal, and G. Blaschke, *J. Chromatogr. A*, 732, 143, (1996).
156. Y. L. Loukas, *J. Pharm. Pharmacol.*, 49, 944, (1997).
157. G.-C. Zhao, J.-J. Zhu, J.-J. Zhang, and H.-Y. Chen, *Anal. Chim. Acta*, 394, 337, (1999).
158. E. Coutouli-Argyropoulou, A. Kelaidopoulou, C. Sideris, and G. Kokkinidis, *J. Electroanal. Chem.*, 477, 130, (1999).
159. S. Takahashi, E. Suzuki, and N. Nagashima, *Bull. Chem. Soc. Jpn.*, 59, 1129, (1986).
160. Z. Yunyou, L. Chun, Y. Huapeng, X. Hongwei, L. Qin, and W. Lun, *Spectrosc. Lett.*, 39, 409, (2006).
161. D. De Souza and S. A. S. Machado, *Electroanalysis*, 18, 862, (2006).
162. O. Nunez, E. Moyano, L. Puignou, and M. T. Galceran, *J. Chromatogr. A*, 912, 353, (2001).
163. R. J. Mortimer, *Electrochim. Acta*, 44, 2971, (1999).
164. M. A. El Mhammedi, M. Bakasse, and A. Chtaini, *J. Hazard. Mater.*, 145, 1, (2007).
165. P. Shivhare and V. K. Gupta, *Analyst*, 116, 391, (1991).
166. V. Y. Taguchi, S. W. D. Jenkins, P. W. Crozier, and D. T. Wang, *J. Am. Soc. Mass Spectrom.*, 9, 830, (1998).
167. B. Zhao, K. G. Neoh, F. T. Liu, E. T. Kang, and K. L. Tan, *Synth. Met.*, 123, 263, (2001).
168. I. R. Schultz, W. L. Hayton, and B. H. Kemmenoe, *Aquat. Toxicol.*, 33, 297, (1995).
169. H. G. Peterson, C. Boutin, K. E. Freemark, and P. A. Martin, *Aquat. Toxicol.*, 39, 111, (1997).
170. J. L. Lopez-Paz, M. Catala-Icardo, and B. Anton-Garrido, *Analytical and Bioanalytical Chemistry*, 394, 1073, (2009).
171. A. Calderbank, C. B. Morgan, and S. H. Yuen, *Analyst*, 86, 569, (1961).
172. M. Luque, A. Rios, and M. Valcarcel, *Analyst*, 123, 2383, (1998).
173. U. M. F. de Oliveira, J. Lichtig, and J. C. Masini, *J. Braz. Chem. Soc.*, 15, 735, (2004).
174. A. Walcarius and L. Lamberts, *J. Electroanal. Chem.*, 406, 59, (1996).
175. J. M. Zen, S. H. Jeng, and H. J. Chen, *Anal. Chem.*, 68, 498, (1996).
176. T. H. Lu and I. W. Sun, *Talanta*, 53, 443, (2000).
177. K. Heister, P. J. Kleingeld, and J. P. Gustav Loch, *Geoderma*, 136, 1, (2006).
178. G. Kanchan and D. F. Benny, *Polym. Adv. Technol.*, 5, 673, (1994).
179. E. S. o. M. S. Technology, *Nomenclature & Symbols in Membrane Science & Technology*, 1995.
180. W. J. Koros and R. Mahajan, *J. Membr. Sci.*, 175, 181, (2000).

181. W. J. Koros and G. K. Fleming, *J. Membr. Sci.*, 83, 1, (1993).
182. S. A. Stern, *J. Membr. Sci.*, 94, 1, (1994).
183. L. M. Robeson, *J. Membr. Sci.*, 62, 165, (1991).
184. M. B. Hagg, J. A. Lie, and A. Lindbrathen, *Adv. Membr. Tech.*, 984, 329, (2003).
185. H. L. Fleming, in Planning Conference Proceedings, Business Communications Co., Co. Cambridge, MA., 1986.
186. J. D. Way and D. L. Roberts, *Sep. Sci. Technol.*, 27, 29, (1992).
187. A. J. Burggraaf, *J. Membr. Sci.*, 155, 45, (1999).
188. M. B. Rao and S. Sircar, *J. Membr. Sci.*, 110, 109, (1996).
189. C. J. Geankoplis, Transport Processes and Unit Operations, Prentice-Hall, Englewood Cliffs, 1993.
190. S. Gruener and P. Huber, *Phys. Rev. Lett.*, 100, (2008).
191. S. Sircar, M. Rao, and C. Thaeron, *Sep. Sci. Technol.*, 34, 2081, (1999).
192. A. B. Fuertes, *J. Membr. Sci.*, 177, 9, (2000).
193. A. F. Ismail and L. I. B. David, *J. Membr. Sci.*, 193, 1, (2001).
194. A. Lindbråthen and M.-B. Hägg, *J. Membr. Sci.*, 259, 154, (2005).
195. F. Ahmad, H. Mukhtar, Z. Man, and B. K. Dutta, *Chem. Eng. Process.*, 47, 2203, (2008).
196. P. Uchytíl, R. Petrickovic, S. Thomas, and A. Seidel-Morgenstern, *Sep. Purif. Technol.*, 33, 273, (2003).
197. K. H. Lee and S. T. Hwang, *J. Colloid Interface Sci.*, 110, 544, (1986).
198. C. W. Jones and W. J. Koros, *Ind. Eng. Chem. Res.*, 34, 158, (1995).
199. J. A. Lie, T. Vassbotn, M. B. Hagg, D. Grainger, T. J. Kim, and T. Mejdell, *Int. J. Greenhouse Gas Control*, 1, 309, (2007).
200. S. J. Singer and G. L. Nicolson, *Science*, 175, 720, (1972).
201. B. Szachowicz-Petelska, Z. Figaszewski, and W. Lewandowski, *Int. J. Pharm.*, 222, 169, (2001).
202. J. McMurry and R. C. Fay, Chemistry, Second Edition, Prentice-Hall, Upper Saddle River, New Jersey, 1998.
203. O. Bley, J. Siepmann, and R. Bodmeier, *Eur. J. Pharm. Biopharm.*, 73, 146, (2009).
204. J. Y. Zhang, J. J. Lu, W. M. Liu, and Q. J. Xue, *Thin Solid Films*, 340, 106, (1999).
205. P. S. Rao, M. Y. Wey, H. H. Tseng, I. A. Kumar, and T. H. Weng, *Microporous Mesoporous Mater.*, 113, 499, (2008).
206. J. Hayashi, H. Mizuta, M. Yamamoto, K. Kusakabe, and S. Morooka, *J. Membr. Sci.*, 124, 243, (1997).
207. S. M. Saufi and A. F. Ismail, *Carbon*, 42, 241, (2004).
208. N. Kishore, S. Sachan, K. N. Rai, and A. Kumar, *Carbon*, 41, 2961, (2003).
209. J. N. Barsema, N. F. A. van der Vegt, G. H. Koops, and M. Wessling, *J. Membr. Sci.*, 205, 239, (2002).
210. K. Kusakabe, M. Yamamoto, and S. Morooka, *J. Membr. Sci.*, 149, 59, (1998).
211. Y. D. Chen and R. T. Yang, *Ind. Eng. Chem. Res.*, 33, 3146, (1994).
212. N. Itoh and K. Haraya, *Catal. Today*, 56, 103, (2000).
213. T. S. Chung and S. K. Teoh, *J. Membr. Sci.*, 152, 175, (1999).
214. W. H. Mazur and M. C. Chan, *Chem. Eng. Prog.*, 78, 38, (1982).
215. I. Menendez and A. B. Fuertes, *Carbon*, 39, 733, (2001).

216. D. Q. Vu, W. J. Koros, and S. J. Miller, *Ind. Eng. Chem. Res.*, 42, 1064, (2003).
217. C. G. Hill, An Introduction to Chemical Engineering Kinetics & Reactor Design, John Wiley & Sons, New York, 1977.
218. S. Lagorsse, F. D. Magalhaes, and A. Mendes, *J. Membr. Sci.*, 310, 494, (2008).
219. C. W. Jones and W. J. Koros, *Carbon*, 32, 1427, (1994).
220. Y. Finkelstein, A. Saig, A. Danon, and J. E. Koresh, *Langmuir*, 19, 218, (2003).
221. J. E. Koresh, *J. Chem. Soc., Faraday Trans.*, 89, 935, (1993).
222. P. M. Coss and C. Y. Cha, *J. Air Waste Manage. Assoc.*, 50, 529, (2000).
223. J. A. Lie, in Chemical Engineering, NTNU, Trondheim, 2005.

**Experimental****2.1 Introduction**

This chapter outlines the experimental techniques and procedures carried out during this research project. Details regarding solutions and chemicals and on the preparation of the electrodes, are provided in Sections 2.2 and 2.3, respectively. The electrochemical techniques used to synthesise and characterise the polymer sensor are described in Section 2.4. In addition to the voltammetric experiments, a number of spectroscopic techniques were used to measure the level of complexation between two species. These spectroscopic techniques are described in Section 2.5. The recorded spectroscopic and electrochemical data were then used to quantify the measure of the complex interaction in accordance with the methods described in Section 2.7. Section 2.8.1 illustrates the procedures required in preparing the carbon membranes for gas testing. The techniques used in monitoring the performance of the carbon membranes are discussed in Section 2.8.2, 2.8.3 and 2.8.4, respectively. The procedures in carrying out an aging study and the technique of electro-regeneration on the carbon membranes are discussed in Section 2.8.5 and 2.8.6, respectively.

**2.2 Chemicals and Solutions**

All chemicals for this project work were obtained from Sigma-Aldrich and used as received. However, pyrrole (Py) was modified further. The bulk solution of Py was distilled and stored at temperatures below 0 °C, in the dark prior to experimental use. Solutions were prepared in distilled H<sub>2</sub>O unless otherwise stated. In general, for electrochemical analysis, 0.1 mol dm<sup>-3</sup> Na<sub>2</sub>SO<sub>4</sub> was used as the supporting electrolyte. Other electrolyte solutions used for comparative purposes included NaCl, KCl, CaCl<sub>2</sub> and NH<sub>4</sub>Cl, all of which were 0.1 mol dm<sup>-3</sup>. To measure the conductivity of these solutions, a Jenway 4510 conductivity meter was used. Prior to using the instrument, it was calibrated with a standard 0.1

mol dm<sup>-3</sup> KCl solution. For UV-Vis and fluorescence spectroscopy, H<sub>2</sub>O was the chosen solvent. All <sup>1</sup>H NMR experiments were carried out using deuterated water (D<sub>2</sub>O) as the solvent. In the event that a change in pH was required, it was adjusted accordingly using an acidic or a basic solution. H<sub>2</sub>SO<sub>4</sub> was used to maintain an acidic pH and NaOH was used to maintain a basic pH. The pH was measured using an Orien Model 720A pH meter, which was calibrated with buffer solutions of pH 4.0 and 7.0, respectively, prior to use. These buffer solutions were obtained from Sigma-Aldrich.

### 2.3 Electrochemical Cell and Electrode Preparation

All electrochemical techniques were carried out using a conventional three-cell electrode system, as shown in Figure 2.1. This system comprises of a working electrode (WE), a counter or auxiliary electrode (CE/AE) and a reference electrode (REF), within a glass cell containing an electrolyte solution. The working electrode (WE) is the interface at which the redox reaction occurs. The working electrode, shown in Figure 2.2, was prepared by securing the bulk electrode material, e.g., gold (Au), glassy carbon (GC) or platinum (Pt) within a Teflon rod. The metal was held within the Teflon holder using epoxy resin. In order to pass current through the working electrode, a conducting wire was secured to the bulk metal using conducting epoxy resin and the wire was threaded through the Teflon rod. Au, GC or Pt were the chosen working electrode used during electrochemical experiments, each measuring 3 mm, 4 mm and 4 mm in diameter, respectively. The counter electrode (CE) for all electrochemical experiments was a platinum wire, approximately 1 mm in diameter with a large surface area. The CE facilitates the movement of electrons to and from the WE. The final part of the three-cell system is the reference electrode (REF). The chosen REF electrode for all experiments was a saturated calomel electrode (SCE). When not in use, the reference electrode was stored in a saturated solution of potassium chloride (KCl), to prevent the porous frit at the tip of the electrode from drying out. The REF electrode was rinsed with distilled water between experiments to avoid contamination between solutions. The WE was polished using diamond paste to give a smooth surface and to remove any polymer or excess analyte that may have deposited on the surface.

The paste used was a Buehler® diamond suspension with particles ranging from 1  $\mu\text{m}$ – 30  $\mu\text{m}$ . The higher sized diamond particles (15  $\mu\text{m}$  and 30  $\mu\text{m}$ ) were used to remove deposited polymer on the surface, followed by the lower grade (1  $\mu\text{m}$ ) to polish and give a smooth electrode surface. The polished electrodes were rinsed in water and sonicated for about 30 seconds to remove any diamond particles. A Branson 1510 sonicator was used to remove the diamond particles. The CE was cleaned using 1200 grade carbide paper. The purpose of the paper was similar to that of the diamond suspension, i.e., fine graded carbide paper would provide a smooth surface on the wire surface, along with removing any deposited material. The platinum wire was then rinsed with distilled water prior to experimental use.

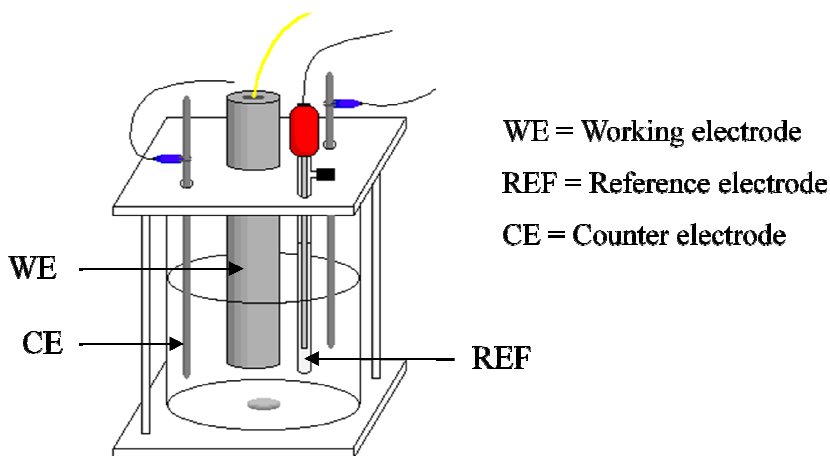


Figure 2.1: Three-cell electrode system.

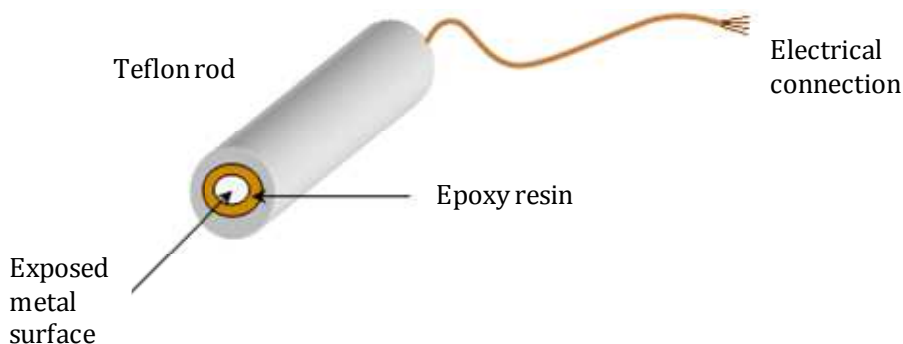


Figure 2.2: Schematic illustration of a working electrode (WE).

## 2.4 Electrochemical Techniques

All electrochemical techniques were carried out using a Solartron potentiostat (Model SI 1285), with the exception of differential pulse voltammetry (DPV). The latter technique was carried out using a Chi440 potentiostat (Model 400). The majority of electrochemical experiments carried out throughout this research were based on the application of a potential to the working electrode (WE), which resulted in the mass transport of new materials to the electrode surface and the generation of current<sup>1</sup>. Software was used to interface the potentiostat and the cell to the computer, as illustrated in Figure 2.3. The software package for the Solartron potentiostat was CorrWare for Windows 98/NT/2000/XP, Version 2.9c and for the CHI440 potentiostat, Chi440 software, Version 2.0.6 was employed. From each of these software packages, data were then transferred and further analysis was carried out. CorrView 2, Version 2.9.c was used to assess the recorded data from CorrWare and Excel for Microsoft Windows was used to analyse the data recorded using the Chi440 potentiostat.

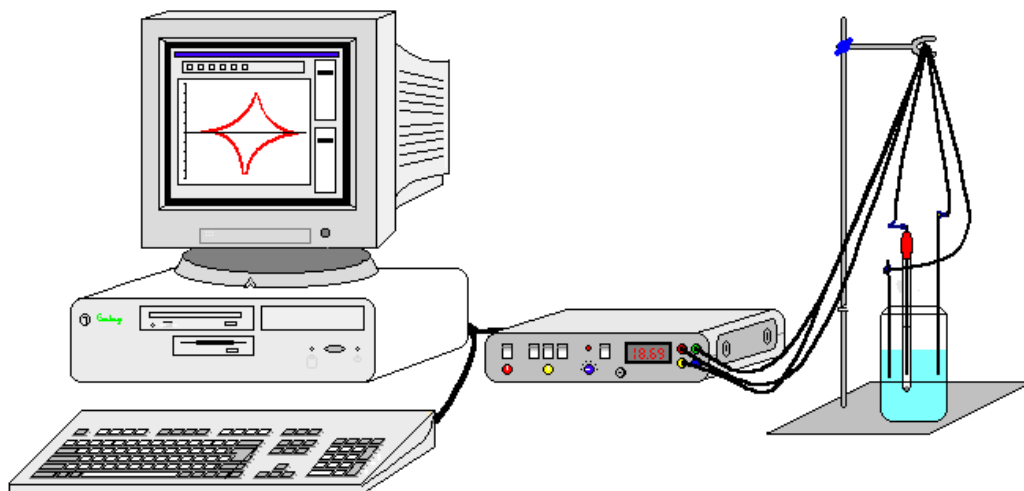


Figure 2.3: Experimental set-up of potentiostat connected to the three-cell electrode system and the data recorded using computer software.

### 2.4.1 Cyclic Voltammetry

This technique is often referred to as an extension of linear potential sweep voltammetry<sup>2</sup>. Cyclic voltammetry (CV) occurs when a potential is applied between initial ( $E_i$ ) and final ( $E_f$ ) limits. A constant scan rate is applied and unlike linear potential sweep voltammetry, which only scans in the forward direction from initial to final potentials, CV sweeps in both a forward and reverse direction. Thus, with a constant scan rate, the potential is cycled from initial to final potentials, also known as a potential window. The number of desired cycles, scan rate and potential window can be set prior to carrying out the experiment. Figure 2.4 illustrates a typical cyclic voltammogram (CV) for the redox couple of  $\text{Fe}^{2+} \rightarrow \text{Fe}^{3+}$ . The reduction of  $\text{Fe}^{3+}$  to  $\text{Fe}^{2+}$  occurs at the cathode ( $E_p^C$ ) and is identifiable on the CV by the trace going from a positive to negative potential. On the other hand, the oxidation of  $\text{Fe}^{2+} \rightarrow \text{Fe}^{3+}$  takes place at the anode ( $E_p^A$ ) and the current can be monitored as the potential goes from a negative to positive potential. The current is recorded as a function of the applied potential<sup>3</sup>. There are many useful properties of the analyte which can be obtained from cyclic voltammetry. Two such properties are the diffusion of the analyte in aqueous systems and the reversibility of the reaction.

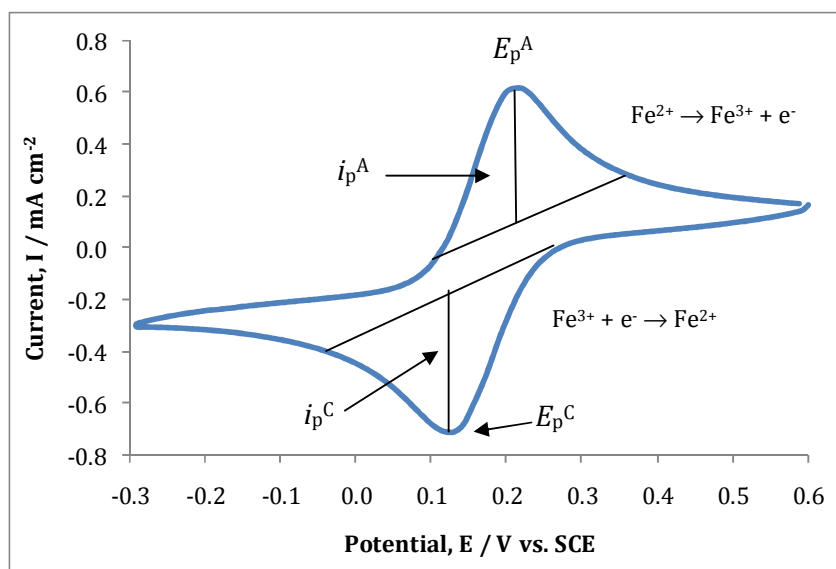


Figure 2.4: Cyclic voltammogram of the redox couple  $\text{Fe}^{2+} \rightarrow \text{Fe}^{3+}$  at a scan rate of  $50 \text{ mV s}^{-1}$ . The potential window is from  $-0.3 \text{ V} \rightarrow 0.6 \text{ V}$  vs. SCE at Au.

In electrochemistry, for a reversible reaction, the process of kinetics and electron transfer of a redox reaction is described as fast and the ratio of the anodic and cathodic peak currents is unity. Also, the peak separation,  $\Delta E_p$ , is given by Equation 2.1<sup>3</sup>, in which the number of electrons,  $n$ , transferred can be calculated.

$$\Delta E_p = E_p^A - E_p^C = \frac{59}{n} mV \quad (2.1)$$

At a constant temperature of 25°C, for  $n$  electrons,  $\Delta E_p$  is 59/ $n$  mV. The diffusion of the analyte can be calculated in accordance with the Randles-Sevcik equation<sup>4</sup>, Equation 2.2. The peak current,  $i_p$ , is measured in A,  $D_c$  is the diffusion coefficient in cm<sup>2</sup> s<sup>-1</sup>,  $n$  is the number of electrons transferred,  $c$  is the analyte concentration in mol cm<sup>-3</sup>,  $A$  is the surface area of the electrode in cm<sup>2</sup> and  $\nu$  is the scan rate in V s<sup>-1</sup>. This equation is valid for a reversible reaction in which the peak current is proportional to the concentration of the electroactive species and to the square root of the scan rate. A linear plot of peak current as a function of the square root of the scan rate indicates that the redox reaction is a diffusion-controlled process, free from adsorption.

$$i_p = 2.686 \times 10^5 n^{3/2} A c D_c^{1/2} \nu^{1/2} \quad (2.2)$$

For irreversible processes, electron transfer is slow and often displays a forward peak with the absence of a reverse peak. Also, with increasing scan rate, the rate of mass transport is comparable to the rate of electron transfer and in general, peak separation increases, coupled with a slight decrease in peak current. For an irreversible system, the peak current is proportional to the concentration, the square root of the scan rate and also the square root of the transfer coefficient,  $\alpha_c n_\alpha$  as illustrated in Equation 2.3<sup>3</sup>.

$$i_p = (2.99 \times 10^5) n (\alpha_c n_\alpha)^{1/2} c D^{1/2} \nu^{1/2} \quad (2.3)$$

In contrast to a reversible system, the peak potential varies with scan rate for irreversible redox reactions. At 25°C, the potential shifts by  $30/\alpha_c n_\alpha$  mV for each decade change in  $v$ . The shape factor is for the peak potential and the half-wave potential is given by Equation 2.4.

$$E_p - E_{p/2} = \frac{48}{\alpha_c n_\alpha} mV \quad (2.4)$$

An intermediate process between reversible and irreversible is known as quasi-reversible. In this case, the kinetics are neither too slow nor too fast and is within the boundaries of the following reaction rate, Equation 2.5, where  $k^\theta$  is the standard rate constant. The peak current increases with the square root of the scan rate, but is not proportional to it. The ratio of the anodic and cathodic peak currents is unity, provided that  $\alpha_c$  and  $\alpha_A$  are 0.5. The peak separation is greater than  $59/n$  mV and increases with increasing scan rate. Finally, the peak potential at the cathode shifts negatively with increasing scan rate<sup>3</sup>.

$$0.3v^{1/2} \geq k^\theta \geq 2 \times 10^{-5}v^{1/2} cm s^{-1} \quad (2.5)$$

Throughout this research, CV was used as a means of characterising the polymers of polypyrrole doped with either sulfonated- $\beta$ Cyclodextrin (sul- $\beta$ CD) or sulfonated calix[4]arene (sul-calix[4]), i.e., PPy/sul- $\beta$ CD or PPy/sul-calix[4]. Secondly, it was used to monitor the current response of paraquat or diquat at the modified electrode of PPy/sul- $\beta$ CD or PPy/sul-calix[4]. Finally, it was used to investigate and quantify the strength of the complex interactions in solution, for either sul- $\beta$ CD or sul-calix[4] with paraquat or diquat. In general, CVs were carried out in the potential window from -0.1  $\rightarrow$  -1.4 V vs. SCE, at a scan rate of either 50 or 100 mV s<sup>-1</sup>, for 10 cycles. A data point was recorded every second at Au, GC or Pt. Moreover, in all of the results chapters, the experimental conditions will be given in the captions of the relevant figures.

### 2.4.2 Pulse Voltammetry

Pulse voltammetry records the difference in the rate of decay of the capacitance current and faradaic current after a potential step or “pulse” is applied. Capacitance or background current is due to the build up of charge on the electrode interface and in solution. Faradaic current corresponds to the sum of the oxidation and reduction current of the analyte. Similar to linear sweep voltammetry, a potential window is chosen at a fixed scan rate. However, there are some additional parameters which are important for pulse voltammetry. They are pulse amplitude, which is the magnitude of the potential, pulse width, the duration of the potential pulse, the sample period and the time frame at the end of the pulse when the current is measured. There are many types of pulse voltammetry experiments ranging from differential, normal to square-wave. The benefits of pulse voltammetry are that it can increase the sensitivity of detection of an analyte in comparison to linear sweep or cyclic voltammetry.

### 2.4.3 Differential Pulse Voltammetry (DPV)

This method of voltammetry involves a slightly different approach to measuring the current. Instead of measuring the difference between faradaic and charge decay, the current is measured before the pulse is applied and then again at the end of the pulse. The significance of recording the current before the pulse is applied is to consider the non-faradaic current. The current then measured at the end of the pulse ensures that the charging current has decayed and the true faradaic current can be obtained. It is this value that is plotted against the applied potential. The potential pulse is fixed, i.e., constant amplitude, hence the stairwell shape of the schematic, as shown in Figure 2.5.

DPV was used to improve the current response of paraquat at the modified PPy/sul- $\beta$ CD film and also paraquat at the modified PPy/SDS film, in which SDS represents the anionic dopant of sodium dodecyl sulfate (SDS). These experiments were carried out within a potential window of -0.1  $\rightarrow$  -1.4 V vs. SCE. for 1 cycle under the optimised conditions, shown in Table 2.1.

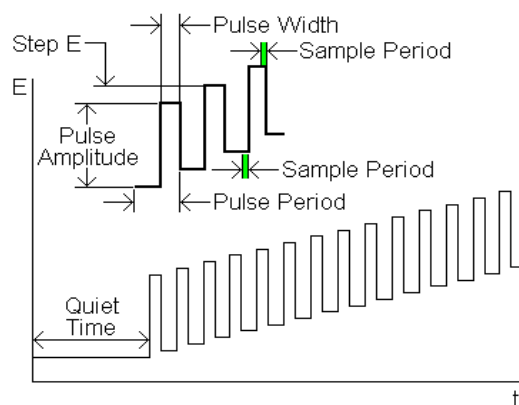


Figure 2.5: Schematic representation of DPV.

Table 2.1: Optimal parameters used in DPV experiments.

Parameter	PPy/sul- $\beta$ CD	PPy/SDS
Amplitude	50.00 mV vs. SCE	50.00 mV vs. SCE
Pulse Width	0.10 s	0.09 s
Sample Width	0.06 s	0.06 s
Pulse Period	0.30 s	0.30 s
Increment	3.00 mV vs. SCE	2.00 mV vs. SCE

### 2.4.5 Rotating Disc Voltammetry (RDV)

Rotating disc voltammetry (RDV) is a variation of cyclic voltammetry, in which the working electrode, instead of remaining stationary within the glass cell, is rotated about its own axis. Similar to CV, the set-up comprises of a three-electrode system, as shown in Figure 2.6. However, for RDV the working electrode has a slightly different design. Although retaining the properties of the bulk surface, i.e. GC or Au, the connection of the electrode to the potentiostat is by means of an electrical connection attached to a rotor spindle. Thus, when RDV is carried out, the working electrode is rotating at a fixed rate depending on the pre-set rotation speed. Analysis of RDV includes monitoring the redox activity and investigating the kinetics of the electrochemical reaction. The working electrode is often referred to as a hydrodynamic electrode. In contrast to CV, the diffusion of the analyte is no longer time dependant in RDV and can be

controlled by setting the angular frequency,  $\omega$ , measured in  $\text{rad s}^{-1}$ . This angular frequency controls the process of diffusion by convection and not by mass transport, which is the predominant feature of CV.

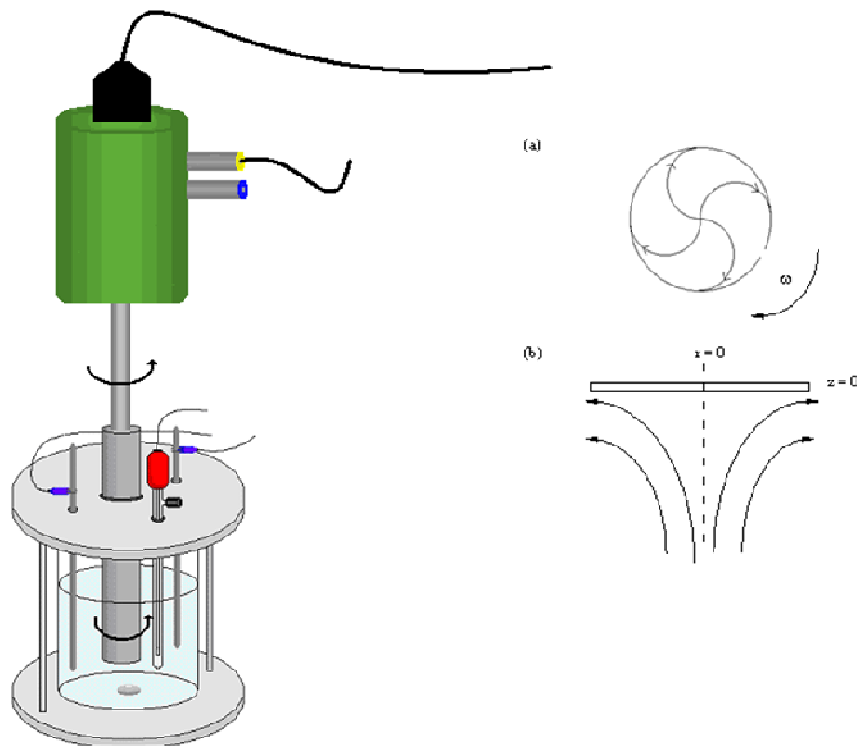


Figure 2.6: Schematic illustration of the RDV set-up, with the three-cell electrode system and the working electrode attached to an electrical rotor to aid rotation. The means of flow at the electrode surface is shown in (a) and the flow of solution to the electrode surface within the cell is shown in (b).

Convection is the transport of species due to external mechanical forces<sup>3</sup>. The movement of the solution near the electrode surface during rotation is often called streamlines, as illustrated in Figure 2.6 (b)<sup>5</sup>. These lines represent the direction of the flow of the solution due to a centrifugal force. The solution is then pumped to and from the electrode surface continuously, in what is known as laminar flow. In general this is the desired flow rate for carrying out RDV. Another motion, which is rigorous and significantly faster than laminar, is turbulent flow. This can ensure a uniform mixture, but can lead to no net movement of the solution as the motion is too fast<sup>3</sup>. To calculate the motion of

the solution, the Reynolds number is evaluated, using Equation 2.6. If the angular velocity is greater than 1,000 rad s<sup>-1</sup>, then the flow is turbulent, if it is less than 1,000 rad s<sup>-1</sup>, the flow is laminar. In Equation 2.6,  $Re$  is the Reynolds number,  $\omega$  is the angular velocity in rad s<sup>-1</sup>,  $r_o$  is the radius of the disc in cm and  $\nu$  is the kinematic viscosity in cm<sup>2</sup> rad s<sup>-1</sup> of the electrolyte.

$$Re = \frac{\omega r_o^2}{\nu} \quad (2.6)$$

Given that the diffusion layer is held constant during RDV experiments, this ensures that the analyte can access the entire area of the WE. In light of this, provided a sufficient oxidation or reduction potential is applied, all species on the electrode surface can be completely oxidised or reduced, thus a limiting current ( $i_L$ ) is recorded upon oxidation or reduction. The currents recorded for RDV are generally higher than for that of CV, due to the increased transport of electroactive species to the surface, thus allowing for greater sensitivity and reproducibility<sup>4</sup>. The limiting current depends on the angular velocity and is given by the Levich equation, shown in Equation 2.7, where  $n$  is the number of electrons transferred through oxidation or reduction,  $F$  is the Faraday's constant, 96485.3415 C mol<sup>-1</sup>,  $A$  is the surface area in cm<sup>2</sup>,  $\nu$  is kinematic viscosity in cm<sup>2</sup> rad s<sup>-1</sup>,  $c$  is the concentration of the analyte in mol cm<sup>-3</sup>,  $\omega$  is the angular velocity in rad s<sup>-1</sup> and  $D_c$  is the diffusion coefficient in cm<sup>2</sup> s<sup>-1</sup>.

$$i_L = 0.621nFAD_c^{2/3}\nu^{-1/6}c\omega^{1/2} \quad (2.7)$$

Experimentally, the Levich equation was used to calculate the diffusion coefficients of the free and complexed analytes of paraquat or diquat, with either sul- $\beta$ CD or sul-calix[4]. In general, for complex interactions the analyte concentration is maintained constant and the concentration of the other species is varied. It is the changes in the analyte chemistry that are monitored and analysed to evaluate an association constant,  $K_a$ . A predominant pattern for complex interactions is that the diffusion coefficient of the analyte decreases with the addition of another species to the solution. It is these changes in

diffusion combined with potential shifts ( $\Delta E_p$ ) that are used to evaluate and measure the association constant,  $K_a$ . More details regarding the calculation of  $K_a$  are given in Section 2.7.2.

In addition to calculating the diffusion coefficient of the free and complexed analyte in solution using RDV, the rate constant,  $k$ , of the analyte can also be calculated. The rate constant corresponds to the kinetics of heterogeneous electron transfer at the interface upon either oxidation or reduction<sup>6</sup>. The rate constant,  $k$ , can be calculated in accordance with Equation 2.8<sup>7</sup>, the Koutechy-Levich equation. From a linear plot of  $1/i_L$  as a function of  $1/\omega^{1/2}$ , the rate constant,  $k$ , is obtained from the intercept value. In this equation  $i_L$  is the limiting current in A,  $\omega$  is the angular velocity in  $\text{rad s}^{-1}$ ,  $n$  is the number of electrons transferred,  $F$  is the Faraday's constant,  $96485.3415 \text{ C mol}^{-1}$ ,  $A$  is the surface area in  $\text{cm}^2$ ,  $\nu$  is the kinematic viscosity in  $\text{cm}^2 \text{ s}^{-1}$ ,  $c$  is the concentration, in  $\text{mol dm}^{-3}$ ,  $D_c$  is the diffusion coefficient in  $\text{cm}^2 \text{ s}^{-1}$  and  $k$  is the rate constant in  $\text{cm s}^{-1}$ .

$$\frac{1}{i_L} = \frac{1}{nFAkc} + \frac{1.61}{nFA\nu^{-1/6}D^{2/3}\omega^{1/2}c} \quad (2.8)$$

In this work, the Koutechy-Levich equation was used to evaluate the rate constant values for diquat in the presence and absence of sul-calix[4] and for free and complexed paraquat with either sul-calix[4] or sul- $\beta$ CD, in solution.

#### 2.4.6 Potentiostatic Techniques (Chronoamperometry)

This electrochemical technique involves applying a constant potential and monitoring the change in current,  $I$ , with respect to time,  $t$ . The potential can be applied for a fixed period of time or until a desired charge is reached. Chronoamperometry was used in the formation of PPy, doped with either sul- $\beta$ CD, sul-calix[4] or SDS. In general, the monomer solution was prepared with  $0.20 \text{ mol dm}^{-3}$  Py monomer and  $0.02 \text{ mol dm}^{-3}$  dopant. An anodic potential of between 0.5 and 0.7 V vs. SCE was applied until a charge of 25 mC was reached. This method was also used in the detection of paraquat at the modified

electrode, in which the polymer was conditioned in a solution of paraquat at -0.2 V vs. SCE for 15 min prior to recording the current response of the analyte at the modified electrode using CV.

Finally, this technique was used in Constant Potential Amperometry (CPA). CPA is a technique where a constant potential sufficient to oxidise or reduce the analyte of interest, is applied to the electrode and the current is monitored. This served as another technique to optimise the detection of paraquat at the modified electrode of PPy/sul- $\beta$ CD and PPy/sul-calix[4]. This involved maintaining the polymer film at a constant potential of -0.9V vs. SCE in an electrolyte solution of 0.10 mol dm<sup>-3</sup> Na<sub>2</sub>SO<sub>4</sub>, until the capacitive current decayed and a steady state was reached. Aliquots of a 2.0 × 10<sup>-3</sup> mol dm<sup>-3</sup> paraquat solution were then added to the electrochemical cell and the change in current was monitored according to each addition of analyte. The working electrode was rotated at high speeds of 2,000 rpm during this experiment and upon completion of the paraquat additions, a step-wise curve was recorded. A limit of detection was quantified from these data, along with the kinetics of the interaction of paraquat at the polymer film using Michaelis-Menten kinetics and the Lineweaver-Burk plot. Details of this analysis are given in Section 2.7.3.

## 2.5 Spectroscopic Techniques

There are many types of spectroscopic techniques and the following types were carried out during this experimental work; ultraviolet-visible (UV-Vis) absorption spectroscopy, fluorescence spectroscopy and nuclear magnetic resonance (NMR) spectroscopy. The underlying principle of spectroscopy is the absorption and emission of energy. The energy effect on the sample is measured by a detector and saved by means of a recorder. The purpose of using the above mentioned techniques was to investigate complex interactions in aqueous based solutions. The data collected by the recorder were further analysed using appropriate equations to evaluate the degree of complexation. The theory of evaluating the association constant,  $K_a$ , is discussed in Section 2.7.2. Moreover, the following section is a more detailed explanation of each technique used.

### 2.5.1 UV-Vis Spectroscopy

The absorption of UV-Vis energy gives rise to the electronic transition of occupied energy levels to unoccupied energy levels. More specifically, energy transitions from the HOMO (highest occupied molecular orbital) to the LUMO (lowest unoccupied molecular orbital)<sup>8</sup>. The UV-Vis radiation source has wavelengths in the range of 200 to 800 nm, with the UV range going from 200-400 nm and the visible range extending from 400-800 nm. In general, species that absorb in the UV region appear colourless and species that absorb in the visible region are coloured. The wavelength at which the maximum absorption occurs is known as  $\lambda_{\max}$ . At this fixed wavelength, the absorbance changes in accordance with concentration. This relationship is known as the Beer-Lambert law, which states that absorbance is proportional to concentration at a fixed wavelength, as shown in Equation 2.9, where  $A$  is the absorbance,  $\epsilon$  is the molar extinction coefficient in  $\text{mol}^{-1} \text{cm}^2$ ,  $c$  is the concentration in  $\text{mol cm}^{-3}$  and  $l$  is the path length in cm.

$$A = \epsilon cl \quad (2.9)$$

During this research, a Varian Cary spectrometer was used. The spectrometer comprises of a Xenon lamp with a maximum scan rate of 24,000 scans per minute. Sample solutions were placed in a quartz cuvette, with a path length of 1 cm and volume of approximately 3  $\text{cm}^3$ . All samples were colourless, thus the absorption measurements were confined to the UV region of 200-400 nm. The data were recorded using Scan Software, Version 3.00 and analysis was done using Microsoft Excel for Windows.

UV-Vis spectroscopy was used to determine the stoichiometry between diquat and sul-calix[4] by means of a Job's plot. It was also used to evaluate the association constant,  $K_a$ , for the complex interaction of diquat and sul-calix[4]. All solutions were prepared in either distilled  $\text{H}_2\text{O}$  or varying concentrations of  $\text{Na}_2\text{SO}_4$ , in which concentrations in the range of  $10^{-5} \text{ mol dm}^{-3}$  diquat were used and the concentration of sul-calix[4] varied from  $10^{-6} \rightarrow 10^{-5} \text{ mol dm}^{-3}$ .

### 2.5.2 Fluorescence Spectroscopy

The fundamentals of fluorescence spectroscopy focus on the emission of absorbed energy. In contrast to UV-Vis spectroscopy, the detector records light emission as opposed to light absorbed. The schematic illustration shown in Figure 2.7 illustrates that the absorbed light is emitted at right angles to the absorbed light from the sample. The emitted light is then detected, recorded and appears as a spectrum of intensity versus wavelength in nm. The theory of fluorescence is based on the absorption of photons of light, at a particular wavelength. This is known as the excitation wavelength. The absorption of light causes an electronic transition from the lowest vibrational level in the ground state to the lowest vibrational level in the excited state. The lifetime of this excited state is usually very short and then relaxation occurs, which is the process of emission. Emission occurs at a longer wavelength than excitation. The intensity of the emission bands changes linearly with concentration. Also, the intensity of the fluorescence is generally high for compounds containing aromatic functional groups with low-energy  $\pi \rightarrow \pi^*$  transition levels, along with aliphatic and alicyclic carbonyl structures or highly conjugated double-bond structures<sup>9</sup>. Hence, diquat was chosen for this reason, due to the presence of three aromatic rings. Paraquat, on the other hand has less aromaticity than diquat and therefore the intensity of fluorescence was much less. This made it quite difficult to assess the complex interaction between paraquat and sulcalix[4], thus an alternative technique was required, i.e., CV or <sup>1</sup>H NMR spectroscopy.

All fluorescent experiments were carried out using a Cary Eclipse fluorescence spectrophotometer and data were recorded using complimentary software, Scan Software Version 1.1. Data were further analysed using Microsoft Excel for Windows. Similar to UV-Vis spectroscopy, the solution sample was placed in a quartz cuvette of path length 1 cm. The instrument was then programmed with a single excitation wavelength and an emission range. In general, the emission wavelengths were 5 -10 nm longer than that of the excitation wavelength and the sample was monitored within the UV range, not exceeding 400 nm. The slit widths of the excitation and emission monochromator remained constant

throughout all experiments. It is important to keep the slit widths as small as possible without compromising the intensity, as the intensity increases with slit width. However, increasing the slit width also reduces the resolution of the emission band.

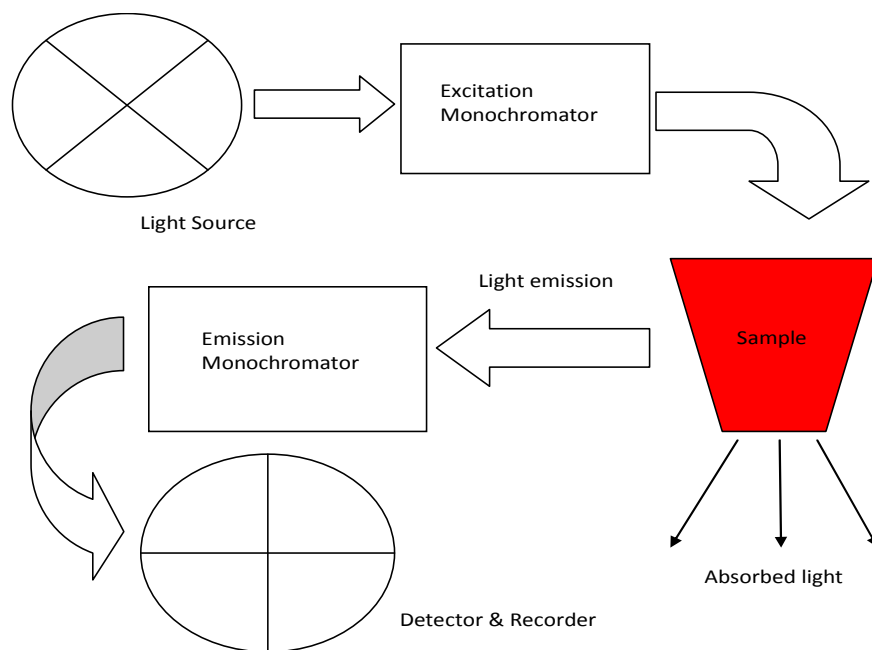


Figure 2.7: Schematic illustration of fluorometer and the method of detection and recording.

Similar to UV-Vis spectroscopy, fluorescence was used to quantify the measure of complexation of diquat and sul-calix[4]. All solutions were prepared in either distilled H<sub>2</sub>O or varying concentrations of Na<sub>2</sub>SO<sub>4</sub>, in which a concentration in the range of 10<sup>-5</sup> mol dm<sup>-3</sup> diquat was used and the concentration of sul-calix[4] varied from 10<sup>-6</sup>→10<sup>-5</sup> mol dm<sup>-3</sup>. An excitation wavelength of 310 nm was applied and the emission data was recorded in the range of 320-420 nm.

### 2.5.3 Nuclear Magnetic Resonance (NMR) Spectroscopy

Nuclear magnetic resonance (NMR) is a technique useful for identifying molecular structures of novel compounds. Aside from structural analysis, it was also used as a complementary technique to evaluate association constants ( $K_a$ ) and to evaluate the stoichiometry of the complex. To ensure concurrence

between electrochemical and spectroscopic techniques, the trends observed were compared as well as the quantitative values measuring complexation.

$^1\text{H}$  NMR spectroscopy provides a “map” of the carbon-hydrogen framework of an organic molecule<sup>10</sup>. The principle of  $^1\text{H}$  NMR spectroscopy relies on applying an external magnetic field which causes an energy difference between the spin states of the proton. This combined with a beam of radiation gives rise to resonance absorption of energy. Depending on the type of nucleus, e.g.,  $^1\text{H}$  or  $^{13}\text{C}$ , there is a characteristic resonance frequency<sup>11,12</sup>. In conjunction to an applied magnetic field, there is a local magnetic field surrounding the molecule. This is due to the electron clouds surrounding each atom. These local fields can then shield the molecule from the applied magnetic field<sup>10</sup>. As each atom of a molecule has a varying arrangement of electrons, the degree of shielding can differ. This is then translated onto a  $^1\text{H}$  NMR spectrum with a unique signal, known as a chemical shift ( $\delta$ ), measured in parts per million (ppm).

$^1\text{H}$  NMR spectra were recorded from 0 to 10 ppm. The greater the effect of shielding, the smaller the chemical shift, thus the closer the  $^1\text{H}$  NMR signal is to 0 ppm. Thus, a highly shielded molecule appears upfield on a  $^1\text{H}$  NMR spectrum. The reverse is the case for a poorly shielded molecule; it has a larger chemical shift and appears downfield on the spectrum.

Investigations regarding the complex interactions of sul- $\beta$ CD, sul-calix[4] and calix[4] with guests diquat and paraquat, were analysed using a  $^1\text{H}$  NMR titration and a Job’s plot. For complex titrations, the concentration of paraquat or diquat remained constant at  $1.0 \times 10^{-3} \text{ mol dm}^{-3}$  and the concentration of sul- $\beta$ CD or sul-calix [4] was varied from  $1.0 \times 10^{-3}$  to  $1.0 \times 10^{-2} \text{ mol dm}^{-3}$ . The change in chemical shift ( $\delta$ ) of the analyte was monitored, with respect to the absence and presence of the cyclodextrin or calixarene in solution. All solutions were prepared in a solution of  $0.1 \text{ mol dm}^{-3}$  KCl and deuterium oxide ( $\text{D}_2\text{O}$ ) to maintain a constant ionic strength. For the Job’s plot, concentrations of both

species remained fixed at  $1.0 \times 10^{-3}$  mol dm<sup>-3</sup>. All <sup>1</sup>H NMR experiments were carried out using a Bruker 300 MHz spectrophotometer at 293 K.

### **2.6 Scanning Electron Microscopy and Energy Dispersive X-ray Analysis**

Scanning electron microscopy (SEM) is a type of an electron microscope that is used to view solid materials on a macro to submicron range. It uses electrons to record images instead of light. Electrons are ejected from an electron gun under vacuum. These electrons interact with atoms of the sample and X-rays, backscattered electrons and secondary electrons emitted from the sample are collected by the detector and converted into an image. As the electrons are expelled from the electron gun under vacuum, it is important that the samples are free from H<sub>2</sub>O, as it would vaporise in the vacuum and subsequently may have an impact on the materials morphology. All samples for SEM must be conductive. For non-conductive materials, the sample is sputter coated with a layer of gold coating. Another feature of SEM is energy dispersive X-ray (EDX) analysis. This technique identifies the elemental composition of the sample according to the X-rays emitted following the bombardment of the sample with electrons from the electron gun.

In this research, SEM was used to obtain information regarding the morphology of PPy/sul-βCD, PPy/sul-calix[4] and PPy doped with Cl<sup>-</sup>, i.e., PPy/Cl<sup>-</sup>. EDX analysis was used to obtain information regarding the chemical composition of the latter polymers upon applying an oxidation and a reduction potential to them. All samples were prepared on a GC flat disc electrode and the samples were dried and sputter coated prior to obtaining the image. SEM images were obtained from an Avalon 8,000, Princeton Gamma Technology and sputter coated using an Emitech K550x.

### **2.7 Methods of Analysis**

The complex interactions of cyclodextrins or calixarenes with paraquat or diquat are discussed in Chapters 5 and 6, respectively. The following section provides information regarding the analytical techniques used, firstly, to

determine the stoichiometry of the complex using a Job's plot and secondly to evaluate its  $K_a$  value. Also, the theory regarding Michaelis-Menten kinetics and the Linweaver-Burk plot is used to establish the strength of the interaction of paraquat at the modified electrode of PPy/sul- $\beta$ CD and PPy/sul-calix[4]. These results are presented in Chapter 3 and 4, respectively.

### 2.7.1 Job's Plot

The method of continuous variation, often called Job's method, provides a means of establishing the ratio of the substrate S and ligand L within the complex,  $SL^{13}$ . In this case, it was used to establish the stoichiometry for complex interactions. A range of techniques can be used to implement this study of which CV, UV-Vis and  $^1H$  NMR were the chosen techniques during this research. The experimental procedure consisted of preparing a series of solutions, subject to the condition that the sum of the total of the concentration of each species was constant. The mole fraction of the analyte was calculated in accordance with Equation 2.10. The changes in absorbance, current and chemical shift were calculated in accordance with Equations 2.11, 2.12 and 2.13, respectively, in which  $a$  denotes the analyte, either paraquat or diquat,  $c$  denotes either sul- $\beta$ CD or sul-calix[4] and  $com$  is indicative of the complex formed. The product of the latter changes were plotted as a function of the mole fraction of the analyte, either paraquat or diquat. The plotted data generated a curve at which the maximum value of the curve at the x-coordinate depicted the stoichiometry of the complex.

$$\frac{n_a}{n_a + n_c} \quad (2.10)$$

$$\Delta A = A_a - A_{com} \quad (2.11)$$

$$\Delta I = I_a - I_{com} \quad (2.12)$$

$$\Delta \delta = \delta_a - \delta_{com} \quad (2.13)$$

### 2.7.2 Evaluation of Association Constant, $K_a$

Complexation is governed by the equilibrium in Equation 2.14. The association constant,  $K_a$ , for this relationship is then defined by Equation 2.15, in which  $[A]$

and  $[C]$  correspond to the equilibrium concentrations of the analyte (paraquat or diquat) and either sul- $\beta$ CD or sul-calix[4].  $K_a$  values were calculated for the complex of sul- $\beta$ CD and sul-calix[4] with paraquat and diquat using electrochemical techniques of CV and RDV and spectroscopic techniques of UV-Vis, fluorescence and  $^1\text{H}$  NMR spectroscopy. This was done by carrying out a titration, whereby the analyte concentration was maintained constant and the concentration of sul- $\beta$ CD or sul-calix[4] was varied. The changes of the analyte chemistry with respect to the addition of either sul- $\beta$ CD or sul-calix[4] were the parameters used to evaluate  $K_a$ . The following section outlines the theory behind the analysis of the latter techniques.



$$K_a = \frac{[A - C]}{[A][C]} \quad (2.15)$$

### 2.7.2.1 Electrochemical Analysis

Paraquat and diquat are electroactive species in which their redox activity occurs at negative potentials. The electro-activity of these species was monitored in the absence and presence of either sul- $\beta$ CD or sul-calix[4]. The characteristic feature for the formation of a complex is a decrease in peak current for the redox reactions and also a shift in redox potential. In general, the peak potential shift is negative for reduction and positive for oxidation. This shift in potential indicates the increased potentials required to oxidise or reduce the species, as it is bound by a large macrocyclic structure, i.e., sul- $\beta$ CD or sul-calix[4]. Using CV to quantify the measure of the complex interaction, the change in current is monitored and plotted in accordance with Equation 2.16<sup>14</sup>. In this equation,  $K_a$  is the association constant,  $[C]$  is the concentration of either sul- $\beta$ CD or sul-calix[4] in  $\text{mol dm}^{-3}$ ,  $A$  is a proportional constant,  $i$  is the peak current of the complex formed in solution in  $\text{A cm}^{-2}$  and  $i_0$  is the peak current of analyte in solution in  $\text{A cm}^{-2}$ .

$$1/[C] = K_a \frac{(1-A)}{1-i/i_0} - K_a \quad (2.16)$$

Using RDV as a means of analysis to quantify  $K_a$ , the change in current combined with the shift in peak potential in accordance with Equation 2.17 to evaluate the measure of complexation. As discussed in Section 2.4.5, the Levich equation, Equation 2.7<sup>15</sup> is used to evaluate the diffusion coefficient of the free ( $D_f$ ) and complexed analyte ( $D_c$ ) species. These values along with the potential shifts for the half-wave potentials of the analyte species in the absence and presence of a macrocycle were used to compare and further verify the validity of using electrochemical methods to quantify  $K_a$ .

$$\left(\frac{F}{RT}\right) \left\{ (E_1)_{app} - (E_1)_f \right\} = \ln(1 + K[sul - calix[4]]) + \ln\left(\frac{D_c}{D_f}\right)^{1/2} \quad (2.17)$$

### 2.7.2.2 UV-Vis and Fluorescence Methods

As discussed in Section 2.5.2, UV-Vis and fluorescence are complimentary to each other, in that UV-Vis absorption measures absorbed light and fluorescence records emitted light following absorption. It is important for this analysis that both species do not have overlapping absorption or emission wavelengths. As previously mentioned for complex interactions, the concentration is maintained constant and changes are monitored with respect to the presence of either sul- $\beta$ CD or sul-calix[4]. Diquat does not have an overlapping  $\lambda_{max}$  with sul- $\beta$ CD or sul-calix[4] however, paraquat does. Also, diquat is fluorescent whereas paraquat is weakly fluorescent. Hence, the evaluation of  $K_a$  using UV-Vis absorption and fluorescence was confined to the complex of diquat and sul-calix[4]. A general trend for the formation of complexes is a decrease in the absorption or emission intensity. As depicted by Li *et al.*<sup>16</sup> the fluorescence of L-tryptophan was quenched upon the addition of sul-calix[4]. The quantitative changes are necessary in calculating  $K_a$  in accordance with Equation 2.18, commonly known as the Heildebrand-Bensei equation<sup>17</sup>. Here,  $A$  and  $A_0$  are the absorbances of diquat in the presence and absence of sul-calix[4], respectively.

$\epsilon_H$  and  $\epsilon_G$  are the extinction coefficients of sul-calix[4] and diquat, respectively and  $K_a$  is the association constant in  $\text{mol}^{-1} \text{dm}^3$ . Moreover, a plot of  $A_0/A-A_0$  as a function of the inverse of sul-calix[4], yields a straight line in which the slope and intercept are used to calculate  $K_a$ . Similar methodology is applied for the quantification of  $K_a$  using fluorescence spectroscopy, in which the absorbance terms are replaced by emission intensity.

$$\frac{A_0}{A - A_0} = \frac{\epsilon_G}{\epsilon_{H-G} - \epsilon_G} + \frac{\epsilon_G}{\epsilon_{H-G} - \epsilon_G} \times \frac{1}{K_a[\text{sul} - \text{calix}[4]]} \quad (2.18)$$

### 2.7.2.3 $^1\text{H}$ NMR Analysis

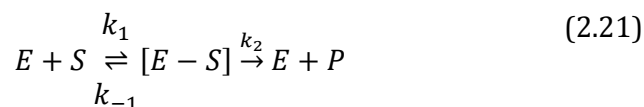
For complex interactions,  $^1\text{H}$  NMR is commonly used to obtain structural information regarding the complex. Quantitative information can also be obtained based on the changes in chemical shift of the analyte proton signals. Similar to the other methods of analysis, the evaluation of  $K_a$  is made easier if the signals of the both species are independent of each other. Paraquat and diquat have characteristic signals separate from those of sul- $\beta$ CD or sul-calix[4]. Hence, a  $^1\text{H}$  NMR titration was carried out with the latter molecules. Similar concentrations of the analyte and either sul- $\beta$ CD or sul-calix[4] molecules were used for the  $^1\text{H}$  NMR analysis and the electrochemical analysis. Thus, as a means of comparing the two techniques the  $K_a$  value calculated using CV and RDV and the maximum change in chemical shift of the protons of the analyte in the absence and presence of the largest excess of either sul- $\beta$ CD or sul-calix[4] was used to simulate a non-linear curve fit, in accordance with Equation 2.19, where  $b$  was calculated from Equation 2.20. In these equations,  $R$  is the ratio of the concentrations of either sul- $\beta$ CD or sul-calix[4] to analyte (paraquat and diquat),  $[C]_0$  is the concentration of the analyte in  $\text{mol dm}^{-3}$ ,  $\delta_a$  is the chemical shift of the analyte in ppm,  $\delta$  is the chemical shift of the analyte in the presence of either sul- $\beta$ CD or sul-calix[4] in ppm and  $\Delta\delta$  is  $\delta - \delta_a$ , in ppm. The experimental data recorded for the complex interactions were plotted and the degree of correlation between the recorded data and simulated data was an indication of the accuracy of using CV, RDV and  $^1\text{H}$  NMR to evaluate  $K_a$ .

$$|\delta - \delta_a| = \left| \left( \frac{\Delta\delta}{2} \right) \left( b - \sqrt{b^2 - 4R} \right) \right| \quad (2.19)$$

$$b = 1 + R + \frac{1}{(K[C]_0)} \quad (2.20)$$

### 2.7.3 Michaelis Menten Kinetics and Lineweaver-Burk Analysis

Michaelis-Menten kinetics measure the rate of catalytic conversion of the enzyme-substrate complex,  $E-S$ , to form the product,  $P$ , as depicted in Equation 2.21<sup>18</sup>. The rate constants for the association and dissociation of the enzyme and the substrates are  $k_1$  and  $k_{-1}$ , respectively, and  $k_2$  is the rate constant for the conversion of the enzyme substrate complex to form the product. Two assumptions are made upon applying Michaelis-Menten kinetics. Firstly, the enzyme concentration remains unchanged and secondly, the enzyme substrate complex concentration remains constant. This indicates that the rate of association and dissociation of  $E$  and  $S$  are equal, obeying steady-state conditions.



From these kinetics, the Michaelis-Menten equation is derived as shown in Equation 2.22<sup>18</sup>.  $V$  is the initial reaction rate,  $S$  is the substrate concentration, and  $V_{\max}$  is the rate at which the enzyme has been “saturated” by an infinite concentration of substrate or the maximum conversion rate as expressed in Equation 2.23<sup>18</sup>. The Michaelis constant,  $K_m$  is the substrate concentration corresponding to half  $V_{\max}$ .  $K_m$  is also related to the rate constants of Equation 2.20 and can be expressed as shown in Equation 2.24<sup>19,20</sup>.

$$V = \frac{V_{\max}[S]}{K_m + [S]} \quad (2.22)$$

$$V_{\max} = k_2([E] + [E - S]) \quad (2.23)$$

$$K_m = \frac{k_{-1} + k_2}{k_1} \quad (2.24)$$

A Michaelis-Menten plot has a characteristic hyperbolic curve, in which  $V$  is plotted as a function of  $S$ . The initial linear response represents the catalytic first-order reaction. A continued increase in substrate concentration results in a slower rate of conversion and is indicative of the transition from first to zero-order kinetics<sup>20,21</sup>. The  $V_{\max}$  asymptote is never reached and so this method estimates an approximate value of  $V_{\max}$  and  $K_m$ , in which  $K_m$  correlates the strength of binding between the enzyme and the substrate<sup>22</sup>. A large value of  $K_m$  indicates weak binding and a small value is consistent with a strong interaction<sup>22</sup>. Another form of analysis for Michaelis-Menten kinetics is the Lineweaver-Burk analysis and is given by Equation 2.25<sup>23</sup>. This is reciprocal of the initial rate of conversion,  $V$  and the substrate concentration,  $[S]$ . From a linear plot of  $1/V$  as function of  $1/[S]$ ,  $V_{\max}$  and  $K_m$  can be determined using both the slope and the intercept.

$$\frac{1}{V} = \frac{1}{V_{\max}} + \frac{K_m}{V_{\max} [S]} \quad (2.25)$$

In this research, both Michaelis-Menten kinetics and the Lineweaver-Burk analysis were used to determine the measure of binding of paraquat at the modified electrode of PPy/sul- $\beta$ CD and PPy/sul-calix[4]. Although, sul- $\beta$ CD and sul-calix[4] are not enzymes, this analysis can be applied to the interactions of paraquat with sul- $\beta$ CD and paraquat with sul-calix[4].

## 2.8 Carbon Molecular Sieve Membranes (CMSMs)

Carbon molecular sieve membranes are prepared from a polymeric material, cellulose acetate. Unlike polymeric membranes, CMSMs differ in that they undergo a post treatment of carbonisation following synthesis of the membrane. The underlying principle of separation is the same for all types of membranes, which is described in Chapter 1, Section 1.6.3. The following sections outline the techniques involved post synthesis of the membranes, from module assembly to the various types of gas testing. The variations in the gas tests are important in understanding the properties of the membrane and optimising the process of gas separation. The outlined techniques are described according to their

performance, the theory concerning the techniques and their contribution towards successful gas separation is detailed in Chapter 1, Section 1.6.6-1.6.8.

### 2.8.1 Module Assembly

There were 3 different types of modules required for gas testing and electro-regeneration. The method of preparation remained the same but the varying parameters distinguishing the 3 modules was the epoxy resin or the tubing the fibres were housed in. Module A involved placing the selected hollow fibres into a steel module in which the fibre ends were sealed in place with epoxy resin (Araldite® 2012). The materials for assembling this module were stainless steel Swagelok® unions and tubing. The module was assembled by attaching a tee union and a straight union on either end of the steel tubing. The length of the module was determined by the length of the steel tubing and initially by the length of the fibres to be tested. The procedure for preparing the modules is described as follows along with Figure 2.8 which shows the schematic representation of this process.

The fibres were handled with great care as they were quite brittle following carbonisation. The length of the fibre inserted was usually 6 cm longer than that of the tubing to accommodate for the additional adapter unions that were placed at the dead and permeate end which were approximately 3 cm in length, as shown in Figure 2.8 (b). The fibres were extended at either end so that in the event of excessive force being applied when screwing on the unions or applying the resin, breakage of the fibres could be seen from above the unions, as shown in Figure 2.8 (d).

In order to prevent the glue (epoxy resin) from leaking, filter paper was placed at the base of each end, thus preventing the glue from flowing further down the steel tubing. The fibres were thread through holes in the filter paper of similar diameter. These holes were punctured using a needle. Figure 2.9 shows the location of the filter paper within the module laterally and Figure 2.8 (a) illustrates the disc of filter paper with holes for fibre insertion. Approximately 1-2 ml of glue was required per seal, as shown in Figure 2.8 (c). The sealant

used was Araldite® 2012, an epoxy resin composed of bisphenol-A-epinchlorhydrin and a curing agent of 1,3-propylenediamine. Equal quantities of resin and curing agent were used in preparing the epoxy resin. The curing time for the resin was approximately 2-3 hours at room temperature. Once the glue was added, additional Swagelok® adapter unions were attached to the tee-union and straight union. These are referred to as the dead and permeate end, respectively. Perpendicular to the dead end is the feed end. It is here that the gas permeates through the membrane. This was done prior to the resin cross-linking as it was not possible to screw on the unions once the glue had begun to set. A Swagelok® cap was then screwed onto the union at the dead end. Thus, this part of the module was closed off to any permeating gases.

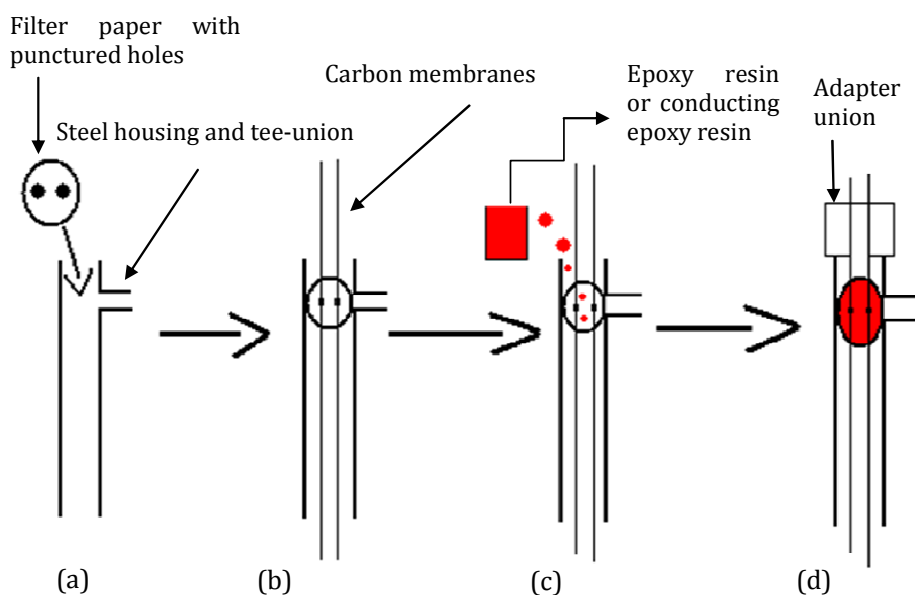


Figure 2.8: Schematic representation of module assembly, in part (a), the filter paper with the punctured holes is first placed at the base of the tee-union. The membranes are then threaded through the paper; (b) and sealed in place using the epoxy resin (c). Finally, an adapter union is placed above the tee-union (d). An identical process is carried out at the other end of the module, in which there is a straight union instead of a tee-union.

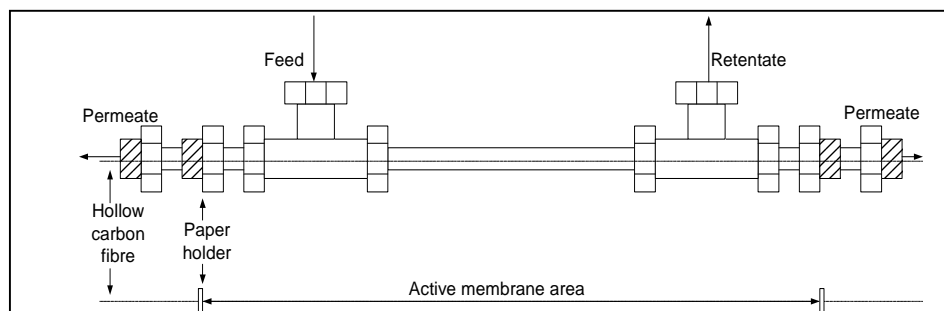


Figure 2.9: Illustration of the module, with the feed and permeate end at either side of the steel tubing.

For modules B and C, a conductive epoxy resin was used. This epoxy resin was a silver, thixotropic paste which was combined with a curing agent. As this was a thicker and more viscous adhesive in comparison to the Araldite<sup>®</sup> epoxy resin, toluene was used as a thinning agent to make for easier application. Once prepared, the module was cured at 60-80 °C under vacuum for several hours to remove any toluene that may not have evaporated at room temperature. Module B was prepared using the identical method for module A. Conducting epoxy resin was used instead of epoxy resin to seal the fibres within the module. Module C was prepared using non-conductive tubing; PMMA (polymethyl methacrylate) between the dead and permeate end and conducting epoxy resin to seal the fibres in place. The significance of using insulating tubing was that upon application of an electric current, only the carbon fibres would be conducting. This served as another method of comparison to investigate the influence of current on the membranes performance. The non-conductive material used was PMMA (polymethyl methacrylate). This material was thermally tested to ensure that it could withstand temperatures of up to 80 °C. A pressure test was also carried out on the material, which showed that it could withstand up to 2 bar ( $2 \times 10^6$  Pa). 1 bar was the chosen pressure and this was the maximum pressure used in the experiments. The Swagelok<sup>®</sup> tee union and straight union were attached to the plastic tubing using epoxy resin as shown in Figure 2.10. Upon curing the module, a Swagelok<sup>®</sup> cap was placed on the dead end after which the module was then placed in the gas permeation unit.



Figure 2.10: Picture showing the prepared plastic module with both permeate and tee unions attached using Araldite® epoxy resin.

### 2.8.2 Gas Testing

The module (A, B or C) was mounted between the high and low-pressure vessels as shown in Figure 2.11. The feed end was connected closest to valve 2 (V2), thus it was closest to the high-pressure vessel. The permeate end was then connected closest to valve 5 (V5) and closest to the low-pressure vessel. The gas permeation rig was constructed using  $\frac{1}{4}$ " stainless steel tubes and Swagelok® VCO tube fittings<sup>24</sup>. The schematic shown in Figure 2.11 illustrates the tubing connecting the feed and permeate vessels, an external line to the gas supply and a vacuum pump which was necessary for evacuating the unit.

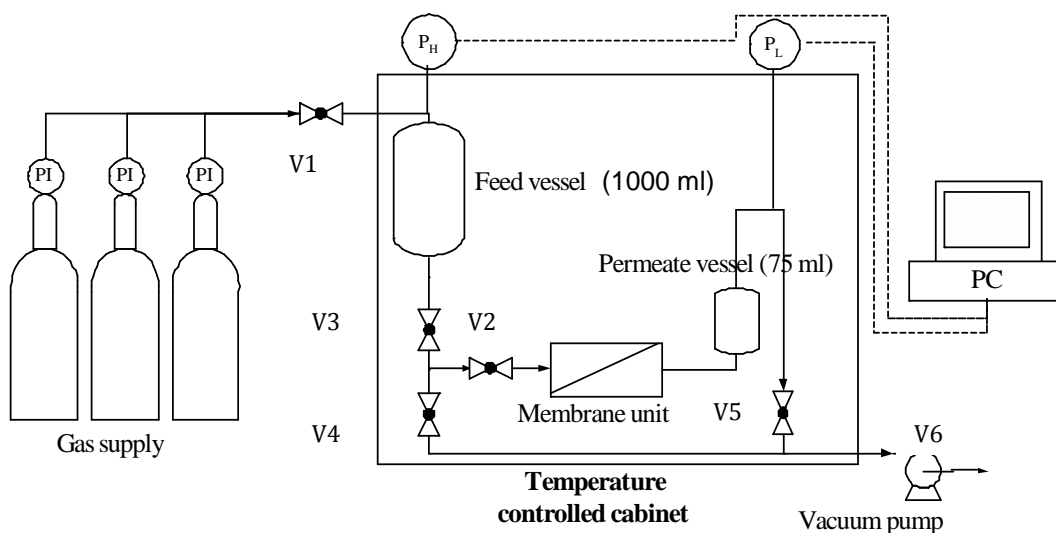


Figure 2.11: Schematic illustration of the gas permeating unit, containing the feed vessel and the high pressure side and the permeate vessel on the low pressure side.

The external line to the gas supply was controlled by valve 1 (V1). Valve 3 (V3) and valve 4 (V4) controlled the high-pressure (feed) and V5 the low-pressure (permeate) side. Valve 6 (V6) controlled the vacuum pump connection to the entire rig and V2 controlled permeation of the gas to the membrane. The cabinet used for gas permeation and electro-regeneration contained a dual module system. Although gas tests on each module were performed on an individual basis, evacuation of the two modules was carried out simultaneously. This was made possible by placing gas valves, ¼" SVA at the feed and permeates side of each module inside the cabinet.

Upon mounting the module into the unit, the rig was first evacuated overnight to remove any gaseous molecules within the rig and module. The protocol for evacuating the rig was as follows. The vacuum pump was switched on and the high-pressure side was evacuated initially. The pump used throughout this experimental work was an RV3 pump with a zeolite trap from BOC Edwards. V1 remained closed for the whole evacuation process. V3, V4 and V6 were opened until the pressure decreased to approximately 0.01 mbar. The feed pressure transducer (0-16 bar Industrie Mess Technik GmbH, Germany) was used to monitor the change in pressure on the feed side. V5 on the low-pressure (permeate) side was then opened slowly so the high vacuum would not damage the fibres within the module. Following a decrease in pressure on the permeate side (< 1 mbar), valve 2 was then opened. The pressure was monitored on the permeate side by a MKS 626A Baratron® 0-100 mbar pressure transducer. V2 was opened slowly to prevent damage to the fibres as a result of high vacuum. The pressure transducers were attached to a computer and monitored using the software Labview™, a program specific for recording pressure data.

### 2.8.3 Gas Permeation Test

Following a prolonged period of evacuation, e.g. 10 hours, the valves either side of the membrane (V2 and V5) were closed. In order to fill the feed side with the desired gas, i.e., H<sub>2</sub>, N<sub>2</sub>, CO<sub>2</sub> or CH<sub>4</sub>, the line attached to V1 (on the outside of the permeation rig), was attached to the gas cylinder as shown in Fig. 2.11. To begin a gas test, the following procedure was carried out. V2 was closed and after

some minutes V5 was then closed. V1 was opened to evacuate the line between the rig and the gas cylinder for approximately five minutes. V1 was then closed along with V4 and V6 and the vacuum pump was turned off. The gas cylinder was opened with the pressure set to approximately 1 bar. V1 was then opened and the high-pressure vessel was filled to 1 bar. The pressure transducers were used to monitor this increase in pressure. All experiments were carried out at 1 bar, i.e., 1 atmosphere of pressure on the feed (high pressure) side. V2 was then opened. This marked the start of the permeation test. The pressure in the permeate vessel was recorded as a function of time. The pressures in the feed and permeate vessel were noted at the beginning and end of each gas test. The gas tests were all carried out at approximately 30 °C. This temperature was maintained within the cabinet using an electrical heating element and thermostat.

#### 2.8.4 Leak Test

After completion of the gas tests, a leak test was carried out in order to obtain an accurate measurement of the loss in permeance due to leaking gas as it is virtually impossible to obtain a leak free system and module. This value can then be accounted and compensated for when comparing data from experiment to experiment. This test was carried out similar to a normal gas test with the only difference being that there was no gas present in the high-pressure side. Thus, the increase in pressure in the permeate vessel was as a result of a poor sealant within the rig and air leaking into the system. Similarly, this test was carried out over a period of time, e.g., 5-6 hours. As the leak rate was generally quite low, the time taken to establish linear curvature was longer than for a gas test. The true permeability was calculated as the difference between the leak rate and the permeance of the tested gas. The slope value which was a measure of permeance, was used to calculate the permeability of each gas in accordance with Equation 2.26, where  $P$  is the permeability in  $\text{m}^3(\text{STP})\text{m}/\text{m}^2 \text{ bar}/\text{s}$  or Barrer,  $l$  is the thickness of the membrane wall in m,  $V$  is the collection volume in  $\text{m}^3$ ,  $A$  is the effective membrane area in  $\text{m}^2$ ,  $T$  is the experimental temperature in K,  $dp/dt$  is the pressure rate at which the gas goes through the membrane in  $\text{mbar}/\text{s}$  and  $p$  is the feed gas pressure in bar. From the permeability values of

each gas, the selectivity was calculated as the ratio of the permeability values using Equation 2.27, where  $\alpha_{A/B}$  is the selectivity of gas A with respect to gas B,  $P_A$  is the permeability of gas A in  $\text{m}^3(\text{STP})\text{m}/\text{m}^2 \text{ bar s}$  and  $P_B$  is the permeability of gas B in  $\text{m}^3(\text{STP})\text{m}/\text{m}^2 \text{ bar/s}$ .

$$P = \frac{273.15 \times 10^{10} V l}{76 A T (p \times 75)} \left( \frac{dp}{dt} \times \frac{0.075}{60} \right) \quad (2.26)$$

$$\alpha_{A/B} = \frac{P_A}{P_B} \quad (2.27)$$

### 2.8.5 Aging Study

The focus of this study was to examine the effects of air on the membranes performance over time. It is found that the permeability of carbon membranes decrease with time due to adsorbed  $\text{O}_2$  molecules, as discussed in Chapter 1, Section 1.6.7. This study proved to be a useful comparative to investigate the influence of a dynamic air-flow versus static air-flow and to calculate which air-flow system had a greater impact on the membranes performance. This study also proved beneficial in evaluating the level of degeneration of the membranes and thus the required level of regeneration using electricity, which is explained further in Section 2.8.6.

#### 2.8.5.1 Dynamic Aging Study

Fibres were taken from the same batch and modules were prepared using an approach similar to that described for module A. There was a slight variation introduced: the module did not have a screw cap on the tee-union also known as the dead end and this was connected to the permeate side of the gas line. Two identical modules, 1 and 2, were prepared in this way, each containing two fibres. The modules were assembled immediately after carbonisation and were mounted approximately 6 hours later in the gas permeation rig. The procedure of placing the modules within the dual testing cabinet was slightly different also to previously mounted modules A, B and C. The orientation of the module was reversed, with the straight union being placed on the feed side and the tee-union being placed on the permeate side. Thus, for this dynamic aging study, air

was pumped continuously from the feed to the open outlet, also known as the retentate. The permeance of the membrane was measured accordingly on the permeate side. Figure 2.12 illustrates the flow of air throughout the module.

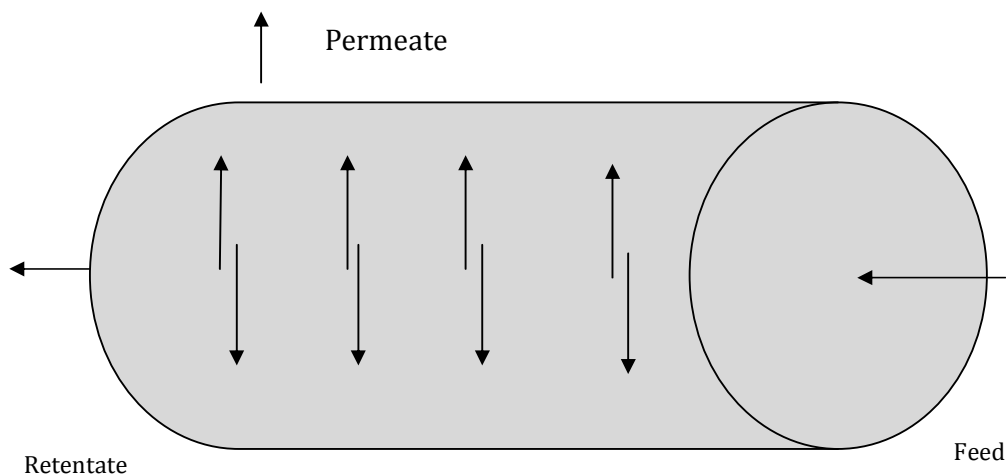


Figure 2.12: Schematic illustration of the air flow throughout the membrane. Air was pumped between the feed and the retentate, however the permeance of the air through the membrane was recorded through the permeate.

Once mounted, the rig was evacuated for 10 min until a vacuum of 0.1 mbar was obtained on the permeate side. A small pump was then activated on the feed side to provide an over pressure of 1.4 bar which enabled a constant flow of air to both modules. To prevent the build up of air in the low-pressure vessel, the vacuum pump was left on for the duration of the study.

Gas permeation tests were carried out in the following way. For module 1, initially V6, closest to the vacuum pump, was closed. The permeate valve of module 2 was then closed. The increase in permeance was then monitored for approximately 10-15 min. The permeate valve and V6 were then opened again. Once a vacuum of approximately 0.1 mbar on the permeate side was established, module 2 was tested. Similar to module 1, V6 was initially closed. The permeate valve to module 1 was then closed. The increase in permeance

with respect to time was monitored for approximately 10-15 min. Upon completion, V6 and the permeate valve to module 1 was re-opened again. Gas tests were carried out at the following time intervals; 0, 6, 21, 36, 45, 52, 70, 75, 90, 114, 124, 142, 149, 165, 173, 189, 198, 217, 239, 265, 285 and 650 hrs. The permeability was then plotted against time, in which the permeability was calculated in accordance with Equation 2.26. The effect of dynamic aging was then evaluated.

#### **2.8.5.2 Static Aging Study**

The focus of this study was to examine the effect of a static atmosphere on the membranes performance over time. The following procedure was carried out. A module identical to type 1 and 2 was prepared. Module 3 was assembled with two carbon fibres from the same batch that had aged for approximately 10 days. The module was then mounted in the gas permeation rig in an identical manner to module 1 and 2. Once mounted, the rig was evacuated for approximately 20 min, until a vacuum of approximately 0.1 mbar was established on the permeate side. Once evacuated, the air test was carried out using the same method as for carrying out the leak test, as previously explained in Section 2.8.4. As the dead end was unsealed, i.e. no screw cap, the leak rate was quite high and after 10 min the test was complete as a linear relationship had been acquired. Once finished, all valves with the rig were closed and the vacuum pump was switched off. This was to prevent the unnecessary absorption of air molecules onto the entirety of the rig. The module was then disconnected at the feed end so that the air flow between the feed and retentate was static; similar to the air flow of the dynamic aging study however, no pump was employed for this method. Thus, the only attached part of the module was to the permeate end of the module. The module was left in the rig for a further 18 days after which a second air test was carried out. The permeability was then calculated, comparing the permeance of the membrane on day 10 to the permeance on day 28.

Following the evaluation of both the dynamic and static aging studies, a comparison between the two methods themselves was then carried out to evaluate the impact of air on the membranes performance.

### 2.8.6 Electro-regeneration

The experimental procedures and equipment set-up for investigating the electro-regeneration of carbon fibres was almost identical to that of gas testing, explained in Section 2.8.2, with the exception of a modification to the module design and the addition of electrical equipment to deliver the electrical current to the membrane. There were three different experimental modules designed for applying the current to the module and the fibres within. In the first case, which was referred to as module A, this module was assembled using steel tubing (Swagelok®) and non-conducting epoxy resin; hence the current was only applied to the conducting metal housing surrounding the fibres. The second module, module B, was made of steel tubing (Swagelok®) and silver conducting epoxy resin. In this case, the current was delivered to both the fibres and the module housing. The final module, module C, was constructed using plastic tubing and silver conducting epoxy resin. Thus, when the current was applied, it was only delivered to the fibres.

As steel is highly conducting, a resistor was inserted in series with the circuit to prevent short-circuiting of the system for modules A and B. It was also important to maintain the electrical charge to the module only and not to the entire gas permeation rig, therefore plastic tubing replaced the previous steel unions between the feed and permeate vessels. A 56 V power-pack was used to supply the electrical charge to the system and crocodile clips were attached to the perimeter of the Swagelok® unions at both the feed and permeate end, to complete the circuit.

The following protocol was observed in the case of the electro-regeneration experiments: Following carbonisation, the fibres were aged for approximately one week, either pre- or post-assembly. Aging was simply carried out by leaving the membranes exposed to air. Each module was prepared using two identical fibres from the same batch, using one of the three module assemblies described above. The completed module was placed in the gas permeation rig in the conventional manner, as described previously. Crocodile clips were placed at the feed and permeate end of the module, i.e., at the tee-union and straight

union attached to either the steel tubing or plastic tubing. This was done prior to commencing gas tests. The circuit was completed using a multi-meter, a power-pack and in the event module A or B being used, a resistor. The gas test proceeded using the same methodology, as previously described in Section 2.8.2. Following a lag time, an electric charge of 5 V was applied for approximately 1 hr. Following the 1 hr duration, the power-pack was turned off and the permeance was measured during all these steps.

A comparative test was carried out on two identical modules that were mounted and tested at the same time. In this respect, the only variable between the two modules was the application of electricity to one module over the other. Thus, the module with no electricity applied to it was referred to as the reference module. The specific parameters of voltage applied, the time intervals of application, during which gas test the electro-regeneration took place are detailed further in Chapter 7. Finally, a leak test was carried out on both modules to obtain an accurate permeance of each gas through the membrane.

## 2.9 References

1. F. A. Settle, Handbook of Instrumental Techniques for Analytical Chemistry, Prentice Hall PTR, New Jersey, 1997.
2. P. H. Rieger, Electrochemistry, Chapman & Hall, Inc., New York, 1994.
3. S. E. Group, Instrumental Methods in Electrochemistry, Eilis Horwood Limited, 1985.
4. C. M. A. Brett and A. M. O. Brett, Electrochemistry: Principles, Methods and Applications, Oxford University Press, 1993.
5. P. M. S. Monk, C. Turner, and S. P. Akhtar, *Electrochimica Acta*, 44, 4817, (1999).
6. N. K. Bhatti, M. S. Subhani, A. Y. Khan, R. Qureshi, and A. Rahman, *Turk. J. Chem.*, 30, 165, (2006).
7. F. Brusciotti and P. Duby, *Electrochimica Acta*, 52, 6644, (2007).
8. C. E. Housecroft and E. C. Constable, Chemistry: An integrated approach, Addison Wesley Longman Limited, 1997.
9. D. A. Skoog, F. J. Holler, and T. A. Nieman, Principles of Instrumental Analysis, Thomson Learning, 1997.
10. J. McMurray, Fundamentals of organic chemistry, Brooks/Cole Publishing Company, 1986.
11. F. A. Carey, Organic Chemistry, McGraw-Hill Companies, 2000.
12. C. N. Banwell and E. M. McCash, Fundamentals of Molecular Spectroscopy, McGraw-Hill Companies, 1994.
13. A. Sayago, M. Boccio, and A. G. Asuero, *Int. J. Pharm.*, 295, 29, (2005).

14. G.-C. Zhao, J.-J. Zhu, J.-J. Zhang, and H.-Y. Chen, *Analytica Chimica Acta*, 394, 337, (1999).
15. E. Coutouli-Argyropoulou, A. Kelaidopoulou, C. Sideris, and G. Kokkinidis, *Journal of Electroanalytical Chemistry*, 477, 130, (1999).
16. W. Y. Li, H. Li, G. M. Zhang, J. Bin Chao, L. X. Ling, S. M. Shuang, and C. Dong, *J Photoch Photobio A*, 197, 389, (2008).
17. H. A. Benesi and J. H. Hildebrand, *J. Am. Chem. Soc.*, 71, 2703, (1949).
18. S. W. Runge, B. J. F. Hill, and W. M. Moran, *CBE-Life Sciences Education*, 5, 348, (2006).
19. J. E. Dowd and D. S. Riggs, *J. Biol. Chem.*, 240, 863, (1965).
20. K. Kosmidis, V. Karalis, P. Argyrakakis, and P. Macheras, *Biophys. J.*, 87, 1498, (2004).
21. P. Wang, S. Q. Li, and J. Q. Kan, *Sens. Actuators, B*, 137, 662, (2009).
22. E. A. Khudaish and W. R. Al-Farsi, *Electrochim. Acta*, 53, 4302, (2008).
23. C. J. Halkides and R. Herman, *J. Chem. Educ.*, 84, 434, (2007).
24. J. A. Lie, in Chemical Engineering, NTNU, Trondheim, 2005.

**Cyclodextrin Modified Polypyrrole for the Detection of Paraquat****3.1 Introduction**

Methyl viologen or 1,1'-dimethyl-4,4'-bipyridilium is a common herbicide used in agricultural treatments to boost productivity<sup>1</sup>. It is widely used for broadleaf weed control, as it is a quick acting, non-selective compound that destroys green plant tissue on contact and by translocation within the plant<sup>2</sup>. As discussed in Chapter 1, Section 1.5, methyl viologen is more commonly referred to as paraquat and is a quaternary nitrogen herbicide that was introduced commercially in 1962<sup>2-4</sup>. However, paraquat was initially produced in 1932 at the Rockfellar Institute by Michaelis and Hill<sup>4</sup>. It serves as an oxidation-reduction indicator, due to its ability to change colour depending on the oxidation state. Hence the name methyl viologen, as the reduced radical of paraquat is violet or blue in colour. Paraquat, as a herbicide, is a toxic pollutant even at low concentrations of  $1.2 \times 10^{-8}$  mol dm<sup>-3</sup> and due to its long residence time, acceptable concentration limits have been outlined by both the Environmental Protection Agency (EPA) and the European Union<sup>1,5</sup>. Thus, it is important to detect and quantify levels of paraquat within water.

A wide range of analytical techniques are used to monitor paraquat levels within the environment, from spectrophotometric<sup>6-10</sup> to chromatographic<sup>3,11</sup>. Electrochemistry is also another method of detection, as paraquat is electrochemically active. There have been many electrochemical sensors designed for the detection of paraquat from those based on anionic crown ethers to ion exchangers<sup>6,12-14</sup>. However, these sensors have limitations in the presence of counter ions. Thus, it was proposed that a sensor of polypyrrole (PPy) doped with sulfonated- $\beta$ -cyclodextrin (sul- $\beta$ CD) would be employed to detect paraquat. The advantage of using a charged cyclodextrin is two-fold in terms of sensing paraquat. Given the presence of anionic charges located on the rim of the cyclodextrin, electrostatic detection of the cationic paraquat species

may be possible. Also, it is well known that the presence of the hydrophobic cavity within the macrocyclic cage facilitates the formation of inclusion complexes<sup>15-17</sup> and therefore an inclusion complex may form between sul- $\beta$ CD and paraquat. Thus, the purpose of this research was to develop a sensor for the detection and inclusion of paraquat in water at a PPy interface functionalised with sul- $\beta$ CD.

Prior to any sensing work, the electrochemistry of paraquat was evaluated at the bare electrode. The modified polymer was then characterised according to its formation and properties as explained in Section 3.3. The results obtained from the electrochemistry of paraquat and the properties of the polymer were combined to assess the redox activity of paraquat at the modified polymer surface, as depicted in Section 3.4. The sensor was then optimised for the detection of paraquat in solution. This is discussed in Section 3.5. The detection limit of this sensor was then evaluated through a calibration study in which a range of techniques were used to improve sensitivity and reduce the capacitance current. A comparative study, using another dopant of sodium dodecyl-sulfate (SDS) incorporated into the polymer matrix was carried out and its sensitivity was compared to the sensitivity of PPy doped with sul- $\beta$ CD. This is illustrated in Section 3.7. Finally, the selectivity of the sensor through an interferent study, which was carried out with respect to two common interferents for paraquat, diquat and ametryn is discussed in Section 3.8.

### 3.2 Electrochemistry of Paraquat

As documented by Walcarius *et al.*<sup>3</sup>, paraquat is electrochemically active and can be cycled between three different oxidation states,  $MV^{2+} \rightleftharpoons MV^+ \rightleftharpoons MV^0$ . These redox events are shown in Figure 3.1, with the reduction of  $MV^{2+}$  to  $MV^+$  at approximately -0.7 V vs. SCE and the conversion of  $MV^+$  to  $MV^0$  at about -1.1 V vs. SCE. However, upon close inspection of the redox couple of  $MV^+ + e^- \rightarrow MV^0$  it is evident that there are two oxidation peaks for every one reduction peak. This indicates that there is another process occurring upon oxidation of  $MV^0$ ,  $MV^0 \rightarrow MV^+ + e^-$ .

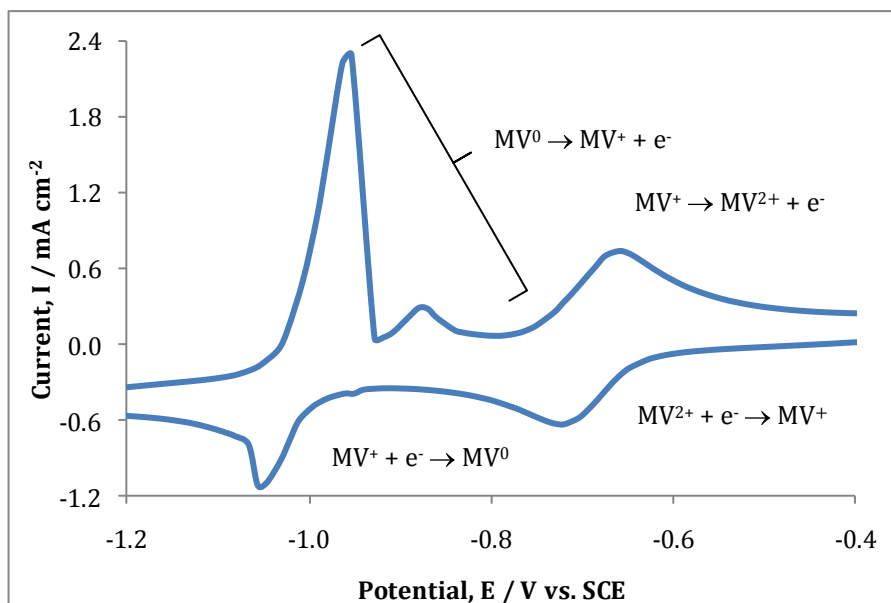
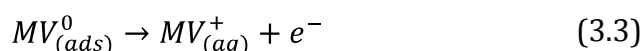
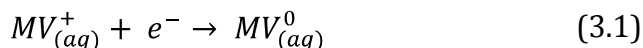


Figure 3.1: CV of  $2.5 \times 10^{-3} \text{ mol dm}^{-3}$  paraquat in  $0.1 \text{ mol dm}^{-3} \text{ Na}_2\text{SO}_4$ . The potential was swept from  $-0.1 \rightarrow -1.4 \text{ V vs. SCE}$  at  $100 \text{ mV s}^{-1}$  at GC. The second redox couple at approximately  $-1.1 \text{ V vs. SCE}$  shows a single reduction wave for  $\text{MV}^{2+} + \text{e}^- \rightarrow \text{MV}^+$  and two corresponding oxidation peaks on the reverse sweep.

The complexity of the second redox process has been well documented in the literature<sup>18-21</sup>. In particular, Xiao *et al.*<sup>19</sup> have explained these unusual features in terms of adsorbed  $\text{MV}^0$ . Equations 3.1 and 3.2 represent the reduction and oxidation in solution of  $\text{MV}^+$  and  $\text{MV}^0$ , respectively. The neutral species of paraquat ( $\text{MV}^0$ ) is sparingly soluble in solution and when a sufficient concentration of  $\text{MV}^0$  is generated, this reduced species can adsorb onto the electrode surface. When a more electropositive potential is applied, the adsorbed species is oxidised, as shown in Equation 3.3. However, the redox potentials of the  $\text{MV}^+/\text{MV}^0_{(\text{ads})}$  and  $\text{MV}^+/\text{MV}^0_{(\text{aq})}$  are different and accordingly two oxidation waves are generated.



Another well known reaction is the conproportionation of  $MV^0$ , as depicted in Equation 3.4<sup>20</sup>. This has often been identified as the second oxidation peak. Although, there is no free electron transferred between the working and counter electrodes during this reaction and it is difficult to explain the oxidation wave in terms of Equation 3.4. However,  $MV^{2+}$  and  $MV^0$  are susceptible to reduction and oxidation and so the degree of conproportionation can have a contributing effect on the redox activity of  $MV^0$  and  $MV^{2+}$ . Thus, prior to analysing the interaction of paraquat at the modified electrode surface, the redox peaks in Figure 3.1 were identified. This was done by varying the scan rate, the concentration of paraquat in the solution and by using both CV and RDV techniques.

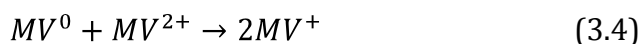


Figure 3.2 illustrates the CV of  $2.5 \times 10^{-3} \text{ mol dm}^{-3}$  paraquat in  $0.1 \text{ mol dm}^{-3}$   $\text{Na}_2\text{SO}_4$  at varying scan rates. At  $10 \text{ mV s}^{-1}$ , the oxidation peak at  $-0.85 \text{ V vs. SCE}$  corresponds to the oxidation of the adsorbed species, as shown in Equation 3.3<sup>19</sup>. At this slow scan rate, the neutral species has sufficient time to adsorb onto the electrode surface and then become oxidised on the reverse sweep<sup>18</sup>. However, the adsorbed layer minimises the oxidation of the  $MV^0$  species in solution, hence only the oxidation of the adsorbed species is recorded. Upon increasing the scan rate to  $100 \text{ mV s}^{-1}$ , two oxidation peaks were recorded for the oxidation of  $MV^0$ . At this scan rate, the reduced species still has sufficient time to precipitate out of solution and form an adsorbed layer at the interface. However, the surface coverage of the adsorbed layer is not as large in comparison to that at the slower scan rate, and so  $MV^0$  in solution can diffuse to the interface and become oxidised, hence two oxidation peaks are recorded. At the faster scan rate of  $250 \text{ mV s}^{-1}$ , there is little time for the reduced species to adsorb onto the electrode surface, thus only one oxidation peak, corresponding to the oxidation of the  $MV^0$  in solution, in accordance with Equation 3.2, is observed. The assignment of the oxidation waves at  $-0.96$  and  $-0.85 \text{ V vs. SCE}$  to Equations 3.2 and 3.3, respectively, was further verified by varying the concentration of paraquat, as the presence of the adsorbed species is

concentration dependent. In addition, RDV experiments were carried out, as this technique eliminates the time dependent process of mass transport.

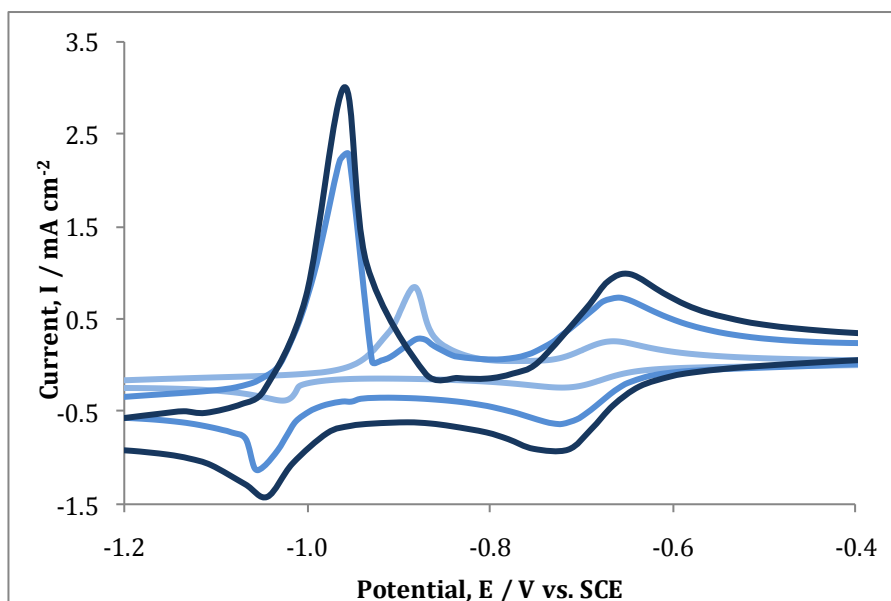


Figure 3.2: CVs of  $2.5 \times 10^{-3} \text{ mol dm}^{-3}$  paraquat in  $0.1 \text{ mol dm}^{-3} \text{ Na}_2\text{SO}_4$ . The potential was swept from  $-0.1 \rightarrow -1.4 \text{ V vs. SCE}$  at scan rates of (—) 10, (—) 100 and (—) 250  $\text{mV s}^{-1}$  at GC.

Figure 3.3 depicts the CVs of varying concentrations of paraquat cycled within the same potential window, at an identical scan rate and at the same GC substrate. However, it is clear from both traces that the oxidation of  $\text{MV}^0$  to  $\text{MV}^+$  is different at the varying concentrations, indicating that the formation of an adsorbed layer on the electrode surface is concentration dependent. At the lower concentration of paraquat, the adsorbed layer is less prominent, as the concentration of  $\text{MV}^0$  produced during the forward reduction wave is not sufficiently high to generate the precipitated  $\text{MV}^0_{(\text{ads})}$  species.

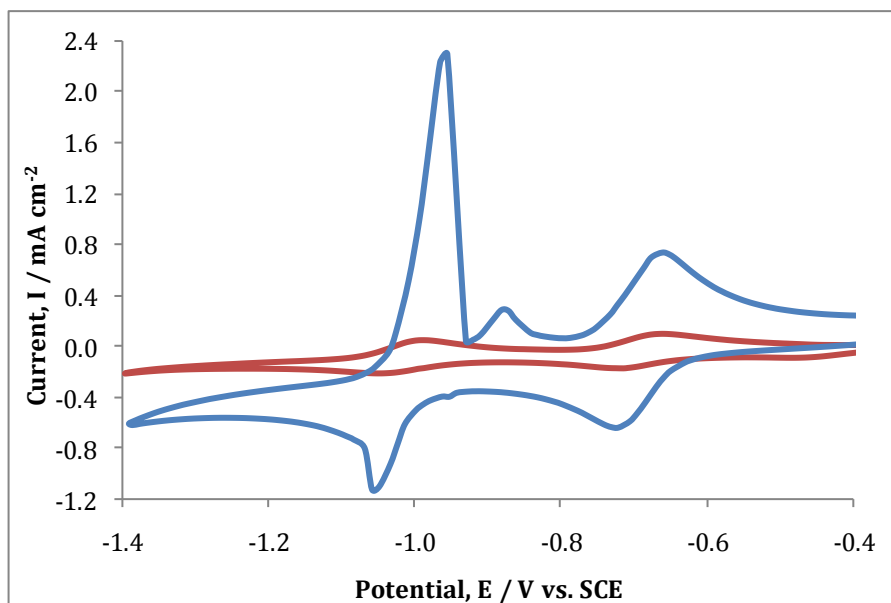


Figure 3.3: CVs of (—)  $2.5 \times 10^{-3}$  mol dm<sup>-3</sup> and (—)  $5.0 \times 10^{-4}$  mol dm<sup>-3</sup> paraquat in 0.1 mol dm<sup>-3</sup> Na<sub>2</sub>SO<sub>4</sub>. The potential was swept from -0.1 → -1.4 V vs. SCE at 50 mV s<sup>-1</sup> at GC.

To further verify that the peak observed at -0.85 V vs. SCE was oxidation of the adsorbed species, RDV experiments were carried out and the results compared with the CV data, as shown in Figure 3.4. Similar concentrations of paraquat were used in an identical potential window and at the same scan rate. However, the working electrode for RDV was rotated. The blue trace in Figure 3.4 shows the RDV data, while the red trace illustrates the CV of the stationary electrode. As RDV is a more sensitive technique in comparison to CV, the currents recorded using RDV are larger than those for CV<sup>22</sup>. Also, the capacitance current is minimised, and all solution species transported to the electrode surface by convection are oxidised or reduced and expelled immediately back into solution<sup>23</sup>. Under these conditions, only the oxidation of the adsorbed species is observed, as the MV<sup>0</sup> in solution is expelled from the interface. Thus, the large peak recorded at -0.85 V vs. SCE is that of the adsorbed MV<sup>0</sup> species being oxidised to MV<sup>+</sup>. This is in good agreement with the data presented in Figures 3.1, 3.2 and 3.3 and provides conclusive evidence that the oxidation peak observed at -0.85 V vs. SCE is indeed the oxidation of the MV<sup>0</sup><sub>(ads)</sub> species.

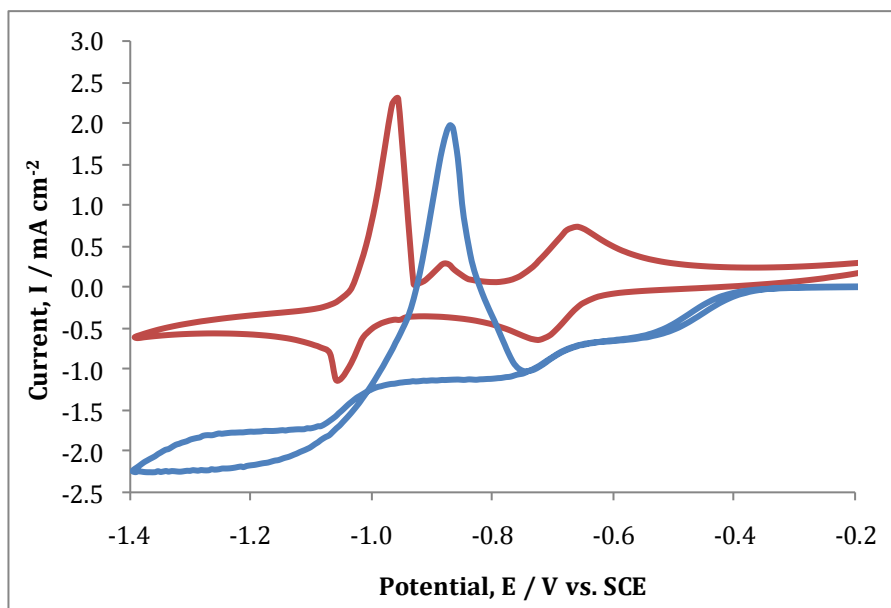


Figure 3.4: CV of (—)  $2.5 \times 10^{-3} \text{ mol dm}^{-3}$  paraquat and RDV of (—)  $1.0 \times 10^{-3} \text{ mol dm}^{-3}$  paraquat in  $0.1 \text{ mol dm}^{-3} \text{ Na}_2\text{SO}_4$ . The potential was swept from  $-0.1 \rightarrow -1.4 \text{ V}$  at  $50 \text{ mV s}^{-1}$  at GC. The RDV was recorded with the working electrode rotating at a frequency of 2,000 rpm.

Once all the peaks were assigned for each redox process, it was then possible to assess the behaviour of paraquat at the modified electrode. To our knowledge, no previous study has been carried out on the detection of paraquat using a polypyrrole film functionalised with an anionic dopant of sul- $\beta$ CD. Saad *et al.*<sup>24</sup> prepared polymer films modified with neutral cyclotetrasiloxanes and recorded a detection limit of  $12.9 \text{ mg L}^{-1}$  ( $5.1 \times 10^{-5} \text{ mol dm}^{-3}$ ) for paraquat. Thus, functionalising the polymer with a negatively charged species may enhance the detection of the positively charged paraquat species as a result of an electrostatic interaction. Also, the hydrophobic cavity of cyclodextrins offers a host for host-guest interactions and the formation of inclusion complexes<sup>15-17</sup>. As documented by Mirzoin *et al.*<sup>25</sup> the adsorption process of  $\text{MV}^0$  at the electrode surface is minimised by the inclusion of  $\text{MV}^0$  and a cyclodextrin host. Hence, modifying the polymer may have a two-fold advantage over a metallic interface with regards to the detection and trapping of the harmful species of paraquat.

### 3.3 Formation and Characterisation of PPy/sul- $\beta$ CD films

As discussed in Chapter 1, Section 1.2.3, polypyrrole (PPy) is one of the most extensively used conducting polymers<sup>26</sup>. The most important property of conducting polymers is that chemical recognition elements, i.e., dopants can be introduced into these polymers during the polymerisation step<sup>27</sup>, as shown in Figure 3.5 (a). In our case, the chosen dopant was sul- $\beta$ CD, however any negatively charged ion can be used. Polymerisation occurs electrochemically with the application of an anodic potential. The anodic potential gives rise to oxidation of the monomer and the formation of the radical cation. The radicals form dimers, which in turn form oligomers and finally a polymer chain deposits on the electrode surface<sup>28</sup>. The backbone of the polymer is positively charged at approximately every 3 to 4 monomer units of Py<sup>26,29</sup>. In order to counter-balance the positively charged polymer, the anionic dopant is required to satisfy electron-neutrality within the polymer matrix<sup>27</sup>.

The polymer film is reduced to a neutral state on the application of an appropriate cathodic potential. In order to maintain neutrality within the polymer film, the small anions are expelled into solution. However, in the case of large anions, they remain trapped within the polymer, as depicted in Figure 3.5 (b). Zanganeh *et al.*<sup>27</sup> reported similar findings upon the reduction of PPy doped with Eriochrome Blue-black. This approach can be used to induce cation-selective sensors, as the cation diffuses to the polymer film to maintain a neutral charge<sup>30,31</sup>. As sul- $\beta$ CD is a considerably larger anion than, for example, Cl<sup>-</sup> or SO<sub>4</sub><sup>2-</sup>, as shown in Figure 3.6, the sul- $\beta$ CD will remain within the polymer upon applying a reduction potential. This in turn will give the polymer cation exchange properties making it attractive for the sensing of the cationic parquat species.

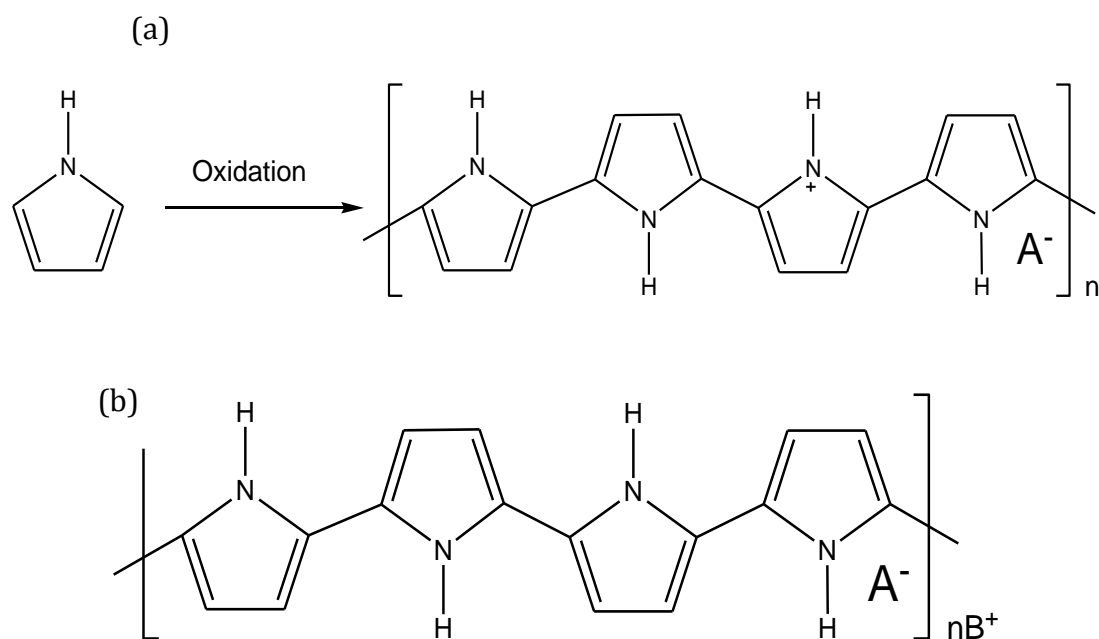


Figure 3.5: Schematic of (a) oxidation of the Py monomer to form PPy with an anionic dopant incorporated to balance the positively charged polymer and (b) reduced PPy film in a neutral state with the anionic dopant immobilised due to its large size.

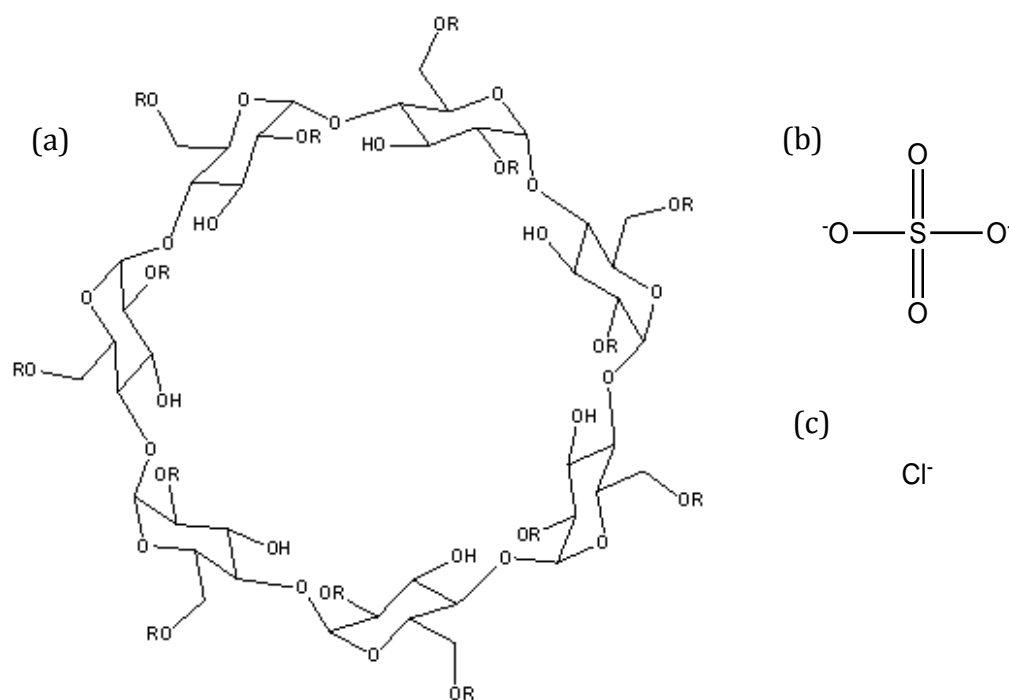


Figure 3.6: Schematic representation of (a) sul- $\beta$ CD in which  $R = \text{SO}_3^-$  or  $\text{H}^+$ , in which the degree of substitution is between 7 and 11 hydroxyl groups, (b) sulfate anion and (c) chloride anion.

### 3.3.1 Influence of the Dopant on Polymerisation

The electropolymerisation of Py was carried out potentiostatically. This method involves applying a constant potential and monitoring the change in current as outlined in Chapter 2, Section 2.4.6. Other methods suitable for polymerisation are galvanostatic and cyclic voltammetry. All techniques result in uniform conducting polymer films, however films prepared galvanostatically are generally thicker and used for transport studies<sup>32</sup>. Polymerisation using cyclic voltammetry usually generates uniform layers<sup>33</sup>, however as thickness of the polymer is related to the charge, the polymer thickness can be more easily controlled by applying a constant potential until a fixed charge is consumed. As documented by Hernandez-Perez *et al.*<sup>33</sup> potentiostatic methods in forming the polymer allow better monitoring and control during film growth.

Figure 3.7 illustrates the current-time plots for the electropolymerisation of pyrrole with various dopants. The plot clearly shows a higher current for the preparation of PPy doped with sul- $\beta$ CD, as depicted by the green trace. Interestingly, the Cl<sup>-</sup> doped polymer gives the lowest currents. It is anticipated that the small size of the chloride ion, in contrast to other dopants, would give rise to better diffusion to the polymer surface and a higher rate of electropolymerisation. However, it should be noted that the PPy was formed at 0.60 V vs. SCE in the chloride-containing solution and this will give rise to a lower rate of polymer growth. Also the concentration of the chloride anion is higher than the other dopants, making a direct comparison difficult. Nevertheless, it is clear that the PPy doped with sul- $\beta$ CD grows with considerable ease. As shown in Figure 3.7, there is a sharp decrease in the current during the first few seconds, mainly due to the decreasing capacitance current. However, nucleation and growth of the polypyrrole occurs during the same period. This is observed as increasing current generating a final constant current of approximately 5 mA cm<sup>-2</sup>. This trend is confirmed in the analysis of the charge-time plots, shown in Figure 3.8.

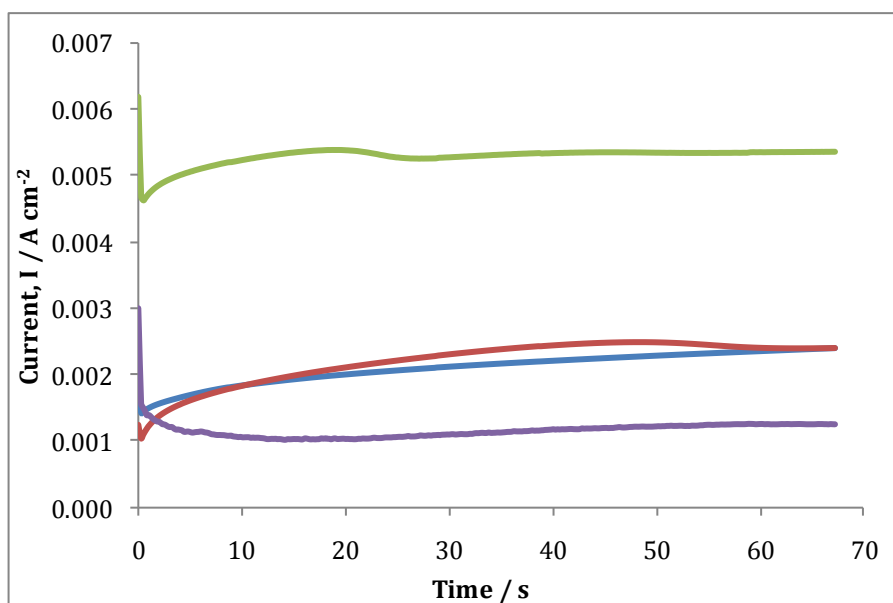


Figure 3.7: Current-time plots for the polymerisation of  $0.20 \text{ mol dm}^{-3}$  Py at Au in the presence of (—)  $0.02 \text{ mol dm}^{-3}$  sul- $\beta$ CD at  $0.65 \text{ V vs. SCE}$ , (—)  $0.02 \text{ mol dm}^{-3}$  PSS<sup>-</sup> at  $0.65 \text{ V vs. SCE}$ , (—)  $0.02 \text{ mol dm}^{-3}$  SDS<sup>-</sup> at  $0.65 \text{ V vs. SCE}$  and (—)  $0.10 \text{ mol dm}^{-3}$  Cl<sup>-</sup> at  $0.60 \text{ V vs. SCE}$ .

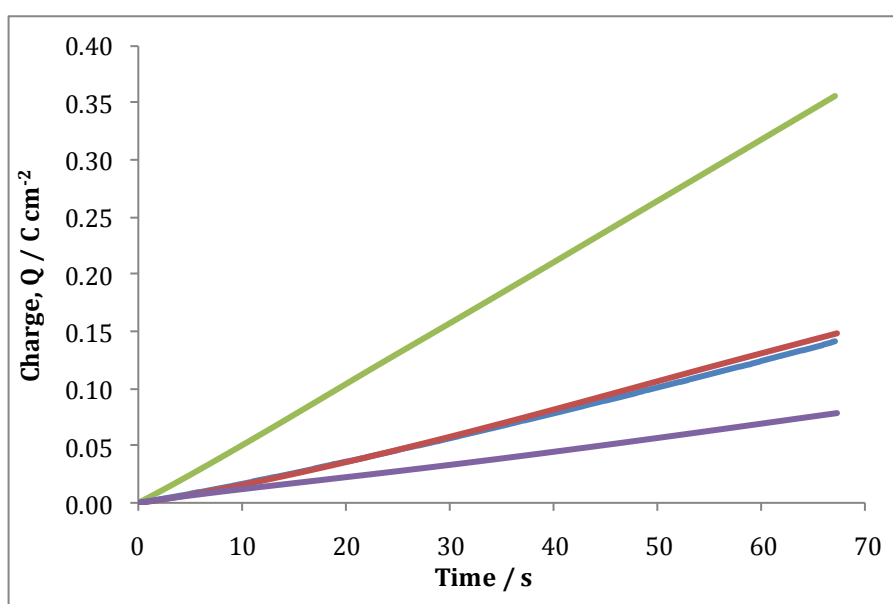


Figure 3.8: Charge-time plots for the polymerisation of  $0.20 \text{ mol dm}^{-3}$  Py at Au in the presence of (—)  $0.02 \text{ mol dm}^{-3}$  sul- $\beta$ CD at  $0.65 \text{ V vs. SCE}$ , (—)  $0.02 \text{ mol dm}^{-3}$  PSS<sup>-</sup> at  $0.65 \text{ V vs. SCE}$ , (—)  $0.02 \text{ mol dm}^{-3}$  SDS<sup>-</sup> at  $0.65 \text{ V vs. SCE}$  and (—)  $0.10 \text{ mol dm}^{-3}$  Cl<sup>-</sup> at  $0.60 \text{ V vs. SCE}$ .

The slope of the charge-time plot is considerably higher in the presence of the sul- $\beta$ CD. The slope values were calculated as  $5.3 \times 10^{-3}$ ,  $2.3 \times 10^{-3}$ ,  $2.1 \times 10^{-3}$  and  $1.1 \times 10^{-3}$  C cm<sup>-2</sup> s<sup>-1</sup> for the sul- $\beta$ CD, polystyrene sulfonate (PSS<sup>-</sup>), SDS<sup>-</sup> and Cl<sup>-</sup> dopants, respectively. As mentioned earlier, the bulky sul- $\beta$ CD anions are not as mobile as a simple Cl<sup>-</sup> anion, however the increased charge on the sul- $\beta$ CD, in which approximately 7 of the sulfonated groups are ionised, generates a solution with a high conductivity and contributes to a faster rate of electropolymerisation.

Given the size difference between sul- $\beta$ CD and Cl<sup>-</sup> anions, further analyses were carried out regarding conductivity and ionic strength to understand the larger currents recorded during the polymerisation of Py in the presence of sul- $\beta$ CD. Tables 3.1 and 3.2 display the ionic strength and conductivity values of the sul- $\beta$ CD and Cl<sup>-</sup> anions, respectively. The ionic strength and conductivity were calculated in accordance with Equations 3.5<sup>34</sup> and 3.6<sup>35</sup>. Although the variation in concentration is five-fold, the conductivity values are only slightly lower for sul- $\beta$ CD, confirming the presence of ionised groups on the modified cyclodextrin. The influence of the ionised sulfonated groups on the sul- $\beta$ CD are clearly evident from the ionic strengths; the ionic strength is 5.6 times greater for the sul- $\beta$ CD when compared with NaCl. In this analysis, a total of 7 sulfonated groups (SO<sub>3</sub><sup>-</sup>) were taken as the degree of substitution. Clearly the charged nature of the dopant has an influencing factor on the rate of electropolymerisation.

The results recorded during the electropolymerisation of Py with the highly charged sul- $\beta$ CD showed promise. Not alone did the polymer form easily but there was no need for any additional supporting electrolyte ensuring that the polymer was only doped with the anionic sul- $\beta$ CD. Moreover, the increasing number of negative sites incorporated within the polymer matrix may enhance the detection of the cationic paraquat species at the modified surface. Hence, further analysis of the polymer was carried out regarding the influence of other parameters on polymer growth.

Table 3.1: Ionic strength values of 0.02 mol dm<sup>-3</sup> sul-βCD and 0.10 mol dm<sup>-3</sup> NaCl.

Dopant	Ionic Strength / mol dm <sup>-3</sup>
Sul-βCD	0.56
Cl <sup>-</sup>	0.10

Table 3.2: Conductivity measurements of 0.02 mol dm<sup>-3</sup> sul-βCD and 0.10 mol dm<sup>-3</sup> NaCl in a 0.20 mol dm<sup>-3</sup> monomer solution of Py.

Dopant	Concentration / mol dm <sup>-3</sup>	Conductivity / Ω <sup>-1</sup> m <sup>-1</sup>
Sul-βCD	0.02	8.48
Cl <sup>-</sup>	0.10	10.50

$$I = \frac{1}{2} \sum_{i=0}^n c_i z_i^2 \quad (3.5)$$

$$k = \left(\frac{1}{R}\right) \frac{L}{A} \quad (3.6)$$

### 3.3.2 Parameters Influencing Polymer Growth

As concluded from Figure 3.7, the rate of electropolymerisation is enhanced in the presence of the highly charged sul-βCD. However, the Py concentration and the applied potential are also important parameters that influence the kinetics of polymerisation. Figure 3.9 illustrates the influence of potential on the time required for the polymer to reach a fixed charge density of 0.35 C cm<sup>-2</sup>. It is clearly evident that as the applied potential increases from 0.5 to 0.6 V vs. SCE, the time required to reach the charge density increases approximately ten-fold. Also, upon the application of potentials of 0.8 V vs. SCE and above, the rate of polymerisation is approximately constant at 10 seconds.

Similar profiles were obtained on varying the concentrations of Py and sul-βCD. On increasing the concentrations of the monomer or dopant, an increase in the rate of electropolymerisation was observed. For example, at a constant applied potential of 0.5 V vs. SCE, the electropolymerisation period varied from 3000 s

for  $0.01 \text{ mol dm}^{-3}$  Py to about 400 s for  $0.10 \text{ mol dm}^{-3}$  Py. Higher concentrations had little influence on the rate of polymer growth. Likewise, the sul- $\beta$ CD dopant had a significant effect at concentrations lower than  $2 \times 10^{-3} \text{ mol dm}^{-3}$ , but at concentrations of  $8 \times 10^{-3} \text{ mol dm}^{-3}$  and higher the rate of electropolymerisation was essentially constant.

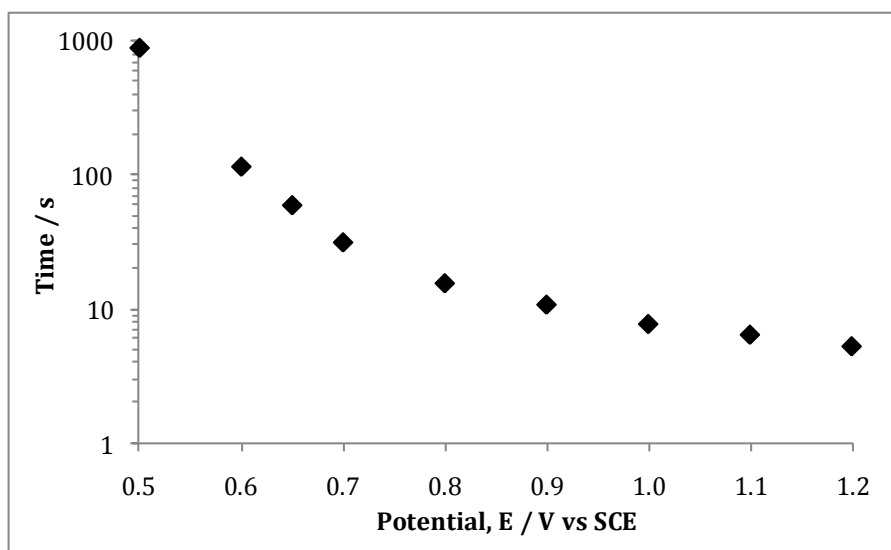


Figure 3.9: Electropolymerisation time to reach a charge density of  $0.35 \text{ C cm}^{-2}$  as a function of applied potential required. The PPy films doped with sul- $\beta$ CD were grown from a solution of  $0.20 \text{ mol dm}^{-3}$  Py monomer and  $0.02 \text{ mol dm}^{-3}$  sul- $\beta$ CD in distilled  $\text{H}_2\text{O}$ .

Combining these data it is possible to evaluate the magnitude of each variant on the rate-determining step of the electropolymerisation by calculating the partial orders of the reaction in accordance with the rate law, illustrated in Equation 3.7<sup>36</sup>.  $R$  is the rate of the electropolymerisation reaction,  $k$  is the rate constant,  $E$  is the applied potential,  $Py$  depicts the monomer,  $sul-\beta CD$  is the dopant and  $\alpha$ ,  $\beta$  and  $\gamma$  represent the respective partial orders. The rate ( $R$ ) is given as  $dQ/dt$  and Equation 3.8 is expressed in terms of the rate of polymer deposition. Taking the logarithm of Equation 3.8, Equation 3.9 simplifies the evaluation of the partial orders for each variable, as the partial order corresponds to the slope of the corresponding charge-time plot.

$$R = k[E]^\alpha [Py]^\beta [sul - \beta CD]^\gamma \quad (3.7)$$

$$\frac{dQ}{dt} = k[E]^\alpha [Py]^\beta [sul - \beta CD]^\gamma \quad (3.8)$$

$$\log \left( \frac{dQ}{dt} \right) = \log k + \alpha \log[E] + \beta \log[Py] + \gamma \log[sul - \beta CD] \quad (3.9)$$

The data depicted in Figure 3.9, in which the Py and sul- $\beta$ CD concentrations were held constant and the applied potential was varied, were modified to generate the linear relationship, as shown in Figure 3.10. The slope of this plot equates to the partial order,  $\alpha$ , as illustrated in Equation 3.9. A similar approach was used to evaluate the partial orders of  $\beta$  and  $\gamma$ . The slope of the line in Figure 3.11 was used to determine  $\beta$  and this plot was generated from experiments with a fixed applied potential of 0.5 V vs. SCE and sul- $\beta$ CD concentration at 0.01 mol dm<sup>-3</sup>. Similarly, Figure 3.12 depicts the relationship of the rate of polymerisation on the sul- $\beta$ CD concentration. Again, the applied potential was fixed at 0.5 V vs. SCE and the Py concentration was held constant at 0.20 mol dm<sup>-3</sup>.

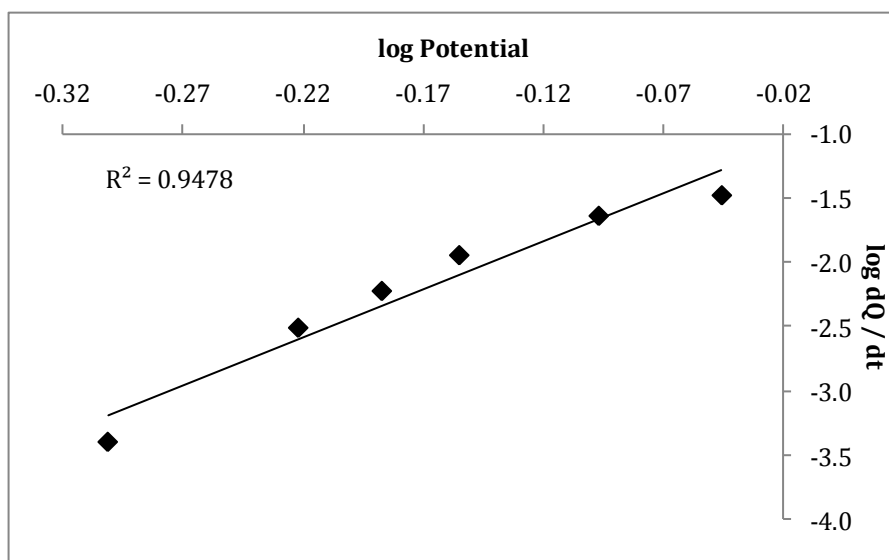


Figure 3.10: Logarithmic plot of the rate of polymerisation,  $dQ/dt$ , as a function of applied potential for the polymerisation of Py from 0.20 mol dm<sup>-3</sup> Py monomer and 0.02 mol dm<sup>-3</sup> sul- $\beta$ CD.

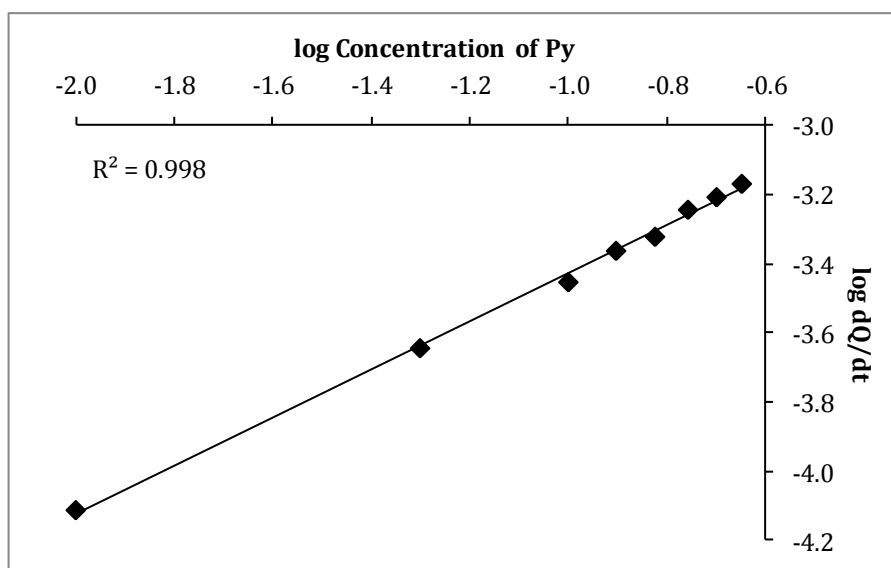


Figure 3.11: Logarithmic plot of the rate of polymerisation,  $dQ/dt$ , as a function of Py concentration at 0.5 V vs. SCE in 0.01 mol dm<sup>-3</sup> sul- $\beta$ CD. This experiment was carried out by Dr. Claire Harley<sup>37</sup>.

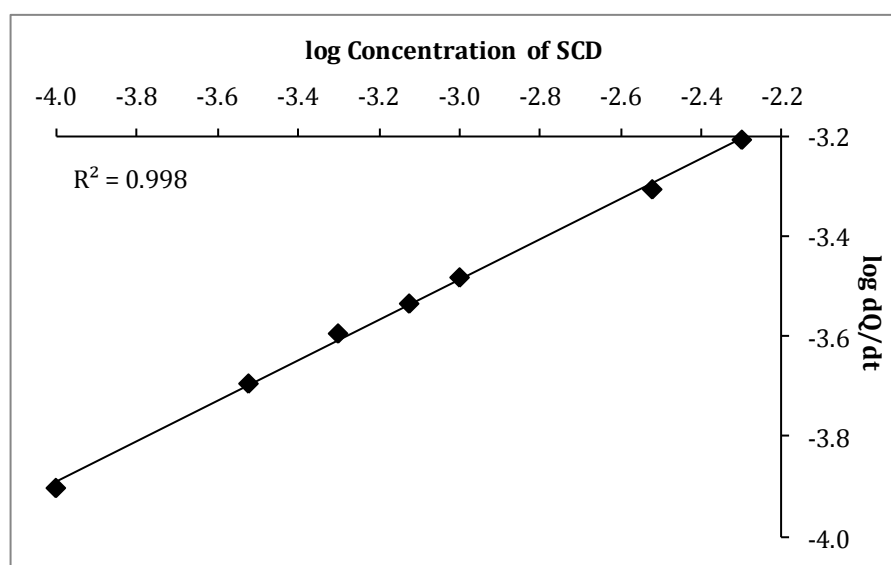


Figure 3.12: Logarithmic plot of the rate of polymerisation,  $dQ/dt$ , as a function of sul- $\beta$ CD concentration at 0.5 V vs. SCE in 0.20 mol dm<sup>-3</sup> Py. This experiment was carried out by Dr. Claire Harley<sup>37</sup>.

The evaluated partial orders for  $\alpha$ ,  $\beta$  and  $\gamma$  were 7.5, 0.7 and 0.4, respectively. These results clearly show the high dependence that the applied potential has on the rate-determining step in the electropolymerisation process. Another

point of interest is that the partial orders are of fractional values. This confirms the complexity of polymerisation. Also, the applied potential has consequential effects on the rate of reaction. A potential too low is not sufficient to overcome the activation barrier and initiate polymerisation, on the other hand an applied potential too high will overoxidise PPy and will cause a loss in its conducting properties. In reference to the literature, Ayad<sup>38</sup> evaluated a partial order of 1.2 for the dopant, ferric nitrate, and previous studies from this group yielded first order kinetics with respect to the Py monomer concentration for the electropolymerisation process<sup>39-41</sup>. Thus, it was concluded that the reaction obeyed 2<sup>nd</sup> order kinetics. However, as postulated by Salmon and co-workers<sup>42</sup>, the size of the anion can affect the oxidation and reduction of PPy<sup>43</sup>. In relation to the solution species, the partial order for sul- $\beta$ CD is lower than that of the Py monomer by a factor of approximately 2:1. This is somewhat different to values found in the literature with smaller dopants where the ratio is closer to 1:1<sup>36,38</sup>. This may be related to the large size of sul- $\beta$ CD and the number of ionised groups on the dopant. Thus, it is highly unlikely that the sul- $\beta$ CD will give rise to the same doping level as smaller dopants.

### 3.3.3 Effect of Charge/Film Thickness on the Polypyrrole films

Charge is often associated with film thickness and surface coverage<sup>44</sup>. Increasing charge leads to an increased surface coverage and hence a larger surface area for the detection of analyte species<sup>45</sup>. Secondly, thicker polymers can lead to a decrease in diffusion of ions to the interface due to the increased polymer network. However, if the polymer is sufficiently porous this should not have a counter effect on the diffusion rate to the metal surface<sup>46</sup>. In this section the influence of charge on the porosity of the polymer and the movement of ions to the interface will be discussed.

As shown in Table 3.3, the polymerisation of Py at a fixed potential, monomer and dopant concentration but with varying charge of deposition has no significant impact on the slope of the charge-time curves. The charge-time plots remained linear and were similar to that presented for the sul- $\beta$ CD in Figure 3.8,

with a slope of  $4.00 \times 10^{-4} \text{ C s}^{-1}$  or  $5.66 \times 10^{-3} \text{ C cm}^{-2} \text{ s}^{-1}$ . This indicates that PPy retains its conductivity irrespective of charge and thickness and grows at a near constant rate. However, as the surface area increases and the morphology changes with increasing charge, the signals from the reduction of the polymer are modified, as shown in Figure 3.13.

Table 3.3: Data recorded in varying the charge for the polymerisation of PPy doped with sul- $\beta$ CD. The monomer, dopant and applied potential were maintained constant.

Charge / C	Slope / $\text{C s}^{-1}$	Oxidative Potential / V vs. SCE	Py / $\text{mol dm}^{-3}$	Sul- $\beta$ CD / $\text{mol dm}^{-3}$
0.010	$4 \times 10^{-4}$	0.65	0.2	0.02
0.020	$4 \times 10^{-4}$	0.65	0.2	0.02
0.025	$4 \times 10^{-4}$	0.65	0.2	0.02
0.030	$4 \times 10^{-4}$	0.65	0.2	0.02
0.040	$4 \times 10^{-4}$	0.65	0.2	0.02
0.050	$5 \times 10^{-4}$	0.65	0.2	0.02
0.200	$5 \times 10^{-4}$	0.65	0.2	0.02

In these experiments the polymer was cycled between -0.1 and -1.4 V vs. SCE so as to observe the redox properties of the polymer. Reduction of the polymer, which is accompanied by the influx of  $\text{Na}^+$ , appears as a broad reduction wave centred at about -0.4 V vs. SCE for polymer charges up to 50 mC. The corresponding oxidation of the polymer and release of  $\text{Na}^+$  is seen as an oxidation wave with a peak potential at about -0.3 V vs. SCE, giving a peak separation of about 100 mV. Interestingly, the cathodic peak potential remains essentially constant, but there is a clear shift in the anodic peak potential with increasing charge up to 50 mC. This indicates that the oxidation of the polymer and the release of  $\text{Na}^+$  become increasingly more difficult with higher electropolymerisation charges. The red trace in Figure 3.13, which depicts the polymer electrodeposited to a higher charge of 0.2 C, shows an increased current for the reduction of the polymer due to the increased polymer thickness. However, a significant negative potential shift of the cathodic peak and a higher

peak separation are also observed. This is consistent with a much slower rate of polymer reduction/oxidation and influx and release of  $\text{Na}^+$ . Similar results were recorded by Almario *et al.*<sup>45</sup> for PPy doped with  $\text{SO}_4^{2-}$  in KCl solution. Clearly, the large increase in thickness from 50 to 200 mC can cause changes in morphology and create a more globular structure which can affect the electro-activity of the polymer<sup>47</sup>.

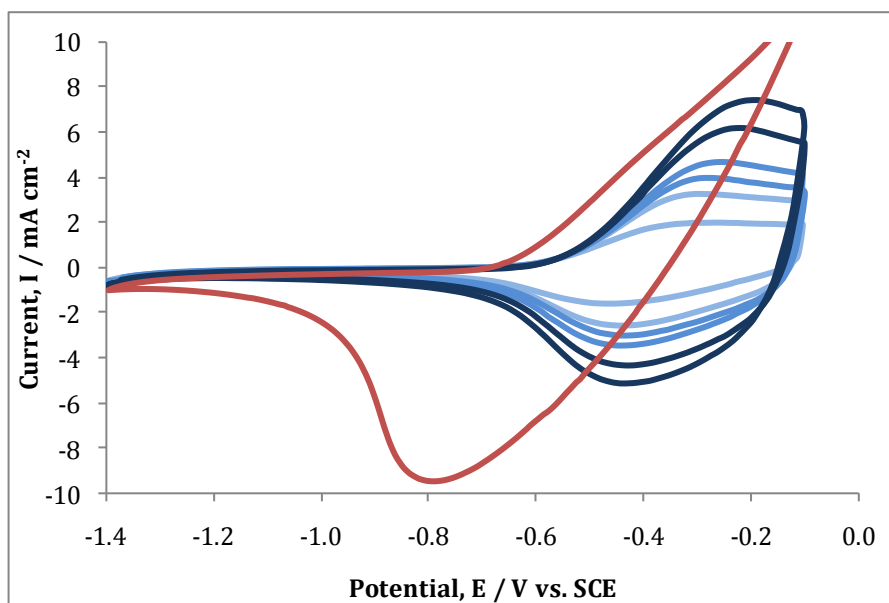


Figure 3.13: Cyclic voltammogram (CV) of PPy modified with sul- $\beta$ CD polymerised to 0.65 V vs. SCE, electrodeposited to the following charges; (—) 10, (—) 20, (—) 25, (—) 30, (—) 40, (—) 50 and (—) 200 mC and cycled in  $0.1 \text{ mol dm}^{-3}$  NaCl at a scan rate of  $100 \text{ mV s}^{-1}$  in a potential window of  $-0.1 \rightarrow -1.4 \text{ V vs. SCE}$ . The monomer solution contained  $0.20 \text{ mol dm}^{-3}$  Py monomer and  $0.02 \text{ mol dm}^{-3}$  sul- $\beta$ CD.

### 3.3.4 SEM and EDX

Another aspect in the characterisation of the polymer matrix is to examine its morphology and the distribution of the dopant anion along the polymer backbone. This can be done using a range of microscopy techniques, for example, optical microscopy (OM), atomic force microscopy (AFM) or scanning electron microscopy (SEM).

Figure 3.14 (a) and (b) show the SEM micrographs of PPy doped with  $\text{Cl}^-$  and PPy doped with sul- $\beta$ CD, respectively. It should be noted that these polymers

are progressively thicker (grown to a charge of 0.2 C) than those discussed previously in Section 3.3.3 and this will certainly influence the morphology, as evident in Figure 3.13. Globular structures are present on each micrograph, but it appears that the PPy doped with sul- $\beta$ CD has a higher density of globular structures and has a somewhat rougher morphology. This is consistent with the larger dopant anion. These globular structures are similar to those described in the literature<sup>48,49</sup>. For example, Kaplin *et al.*<sup>49</sup> documented that PPy films containing perchlorate as a dopant have a very rough surface, often referred to as cauliflower-like<sup>50</sup>. Hence, the collection of globular structures contributes to the “cauliflower”-like morphology.

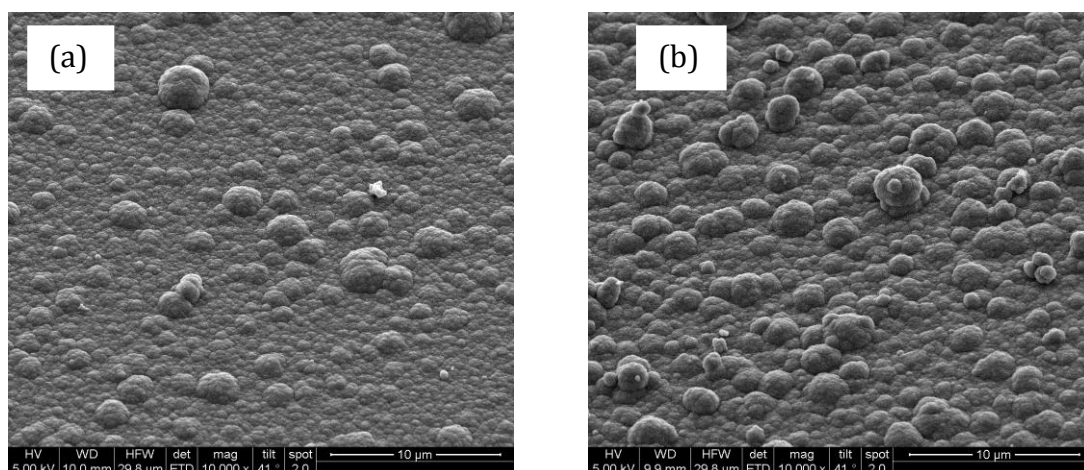


Figure 3.14: SEM micrographs of (a) PPy doped with  $\text{Cl}^-$  and (b) PPy doped with sul- $\beta$ CD. The polymers were polymerised from a solution containing  $0.20 \text{ mol dm}^{-3}$  Py monomer and  $0.10 \text{ mol dm}^{-3}$  NaCl for polymer (a) and  $0.02 \text{ mol dm}^{-3}$  sul- $\beta$ CD for polymer (b). The polymers were electrodeposited onto a GC interface, with a diameter of 4 mm, at 0.65 V vs. SCE until a charge of 0.2 C was reached.

To confirm the presence of the dopants within the polymer, energy dispersive X-ray analysis (EDX) was carried out. The EDX spectra shown in Figure 3.15 and 3.16 correspond to PPy doped with  $\text{Cl}^-$  and PPy doped with sul- $\beta$ CD, respectively. As illustrated in each spectrum, there is the presence of C, which pertains to PPy. The X-ray signal of Cl corresponds to PPy doped with  $\text{Cl}^-$  and similarly, the signals of S and O are indicative of sul- $\beta$ CD dopants present within PPy. Hence, the presence of these specific signals confirms clearly that the

dopants are incorporated within the polymer matrix. As EDX is not a good quantitative technique no further information on the level of doping can be obtained.

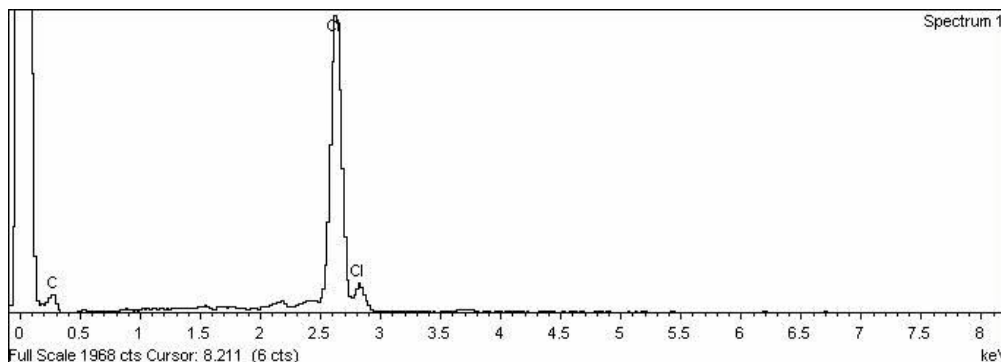


Figure 3.15: EDX spectrum of PPy doped with Cl<sup>-</sup>. The polymer was prepared potentiostatically at 0.60 V vs. SCE to a charge of 0.20 C onto GC. The diameter of the electrode was 4 mm and the polymer was synthesised from a solution containing 0.20 mol dm<sup>-3</sup> Py monomer and 0.10 mol dm<sup>-3</sup> NaCl.

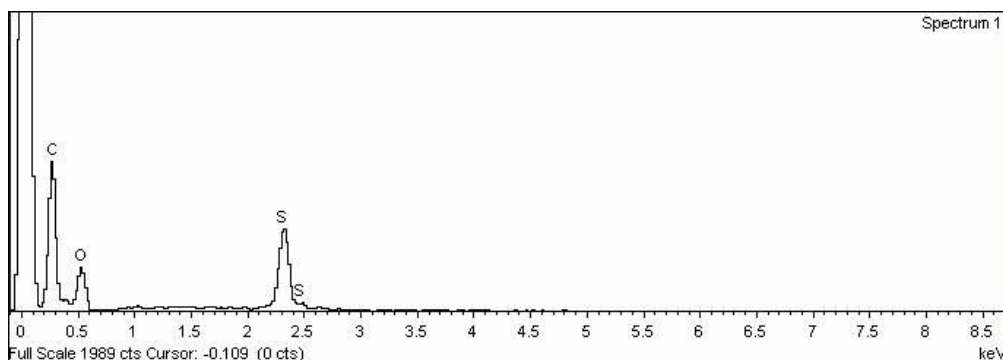


Figure 3.16: EDX spectrum of PPy doped with sul- $\beta$ -CD. The polymer was prepared potentiostatically at 0.65 V vs. SCE to a charge of 0.2 C onto GC. The diameter of the electrode was 4 mm and the polymer was synthesised from a solution containing 0.20 mol dm<sup>-3</sup> Py monomer and 0.02 mol dm<sup>-3</sup> sul- $\beta$ -CD.

The eventual application of PPy doped with sul- $\beta$ -CD is for the sensing and capture of paraquat in solution. As previously mentioned in Section 3.2, paraquat is electrochemically active at electronegative potentials. However, at these potentials, PPy becomes reduced to a neutral state and in most cases the anionic dopant is expelled from the polymer matrix, as it is no longer required

to maintain electron-neutrality<sup>27</sup>. Nevertheless with large bulky anions, they are retained within the polymer due to their large size<sup>51,52</sup>. To confirm this hypothesis for the sul- $\beta$ CD, EDX was used as a means of analysis and changes in the X-ray signals for the dopant were compared with that of oxidised and reduced PPy to ascertain if the dopant had been expelled or maintained within the polymer. This was done by placing a freshly prepared polymer into a 0.1 mol dm<sup>-3</sup> solution of NaCl and applying a reduction potential of -0.8 V vs. SCE for 60 minutes. This potential is sufficiently electronegative to reduce the polymer without causing degradation. It was anticipated that for PPy doped with Cl<sup>-</sup> the X-ray signal for Cl<sup>-</sup> would be diminished or completely removed upon reducing the polymer and expelling the small, mobile dopants. However, reduction of the X-ray signal for sul- $\beta$ CD should not be observed if the sul- $\beta$ CD remained within the polymer matrix.

As shown in Figure 3.17, when a reduction potential is applied to PPy doped with Cl<sup>-</sup>, the chloride signal is significantly reduced. However, there are still traces of Cl<sup>-</sup> within the polymer. As the polymer is significantly thicker, there is a larger amount of polymer to reduce and reduction of the polymer is not complete, even at -0.8 V vs. SCE. Initially, reduction of the polymer occurs at the compact layers closest to the interface. Therefore, as the polymer is reduced, polymer closest to the electrode surface becomes insulating. As a result the ease at which electrons are transferred through the polymer film, to reduce subsequent layers further away from the surface, becomes slower. Hence, the Cl<sup>-</sup> dopant is not completely removed. However, there is no evidence for Na, which shows that reduction of the polymer is indeed accompanied by the release of Cl<sup>-</sup>.

Figure 3.18 illustrates the results obtained for the reduction of PPy doped with sul- $\beta$ CD. Although the S signal is slightly reduced when Figure 3.18 is compared to Figure 3.16, it is difficult to make a quantitative deduction based on this comparison, as different polymers were used. The presence of the S and O signals indicate the presence of sul- $\beta$ CD within the polymer. Of more interest is the X-ray signal corresponding to Na. This confirms that sul- $\beta$ CD is immobilised

within the PPy matrix and  $\text{Na}^+$  is required to balance the negative charge of the sul- $\beta$ CD upon reduction of the polymer backbone. This is in good agreement with the work of Zanganeh *et al.*<sup>27</sup> who presented similar findings upon the incorporation of Eriochrome Blue-black (EBB) into PPy.

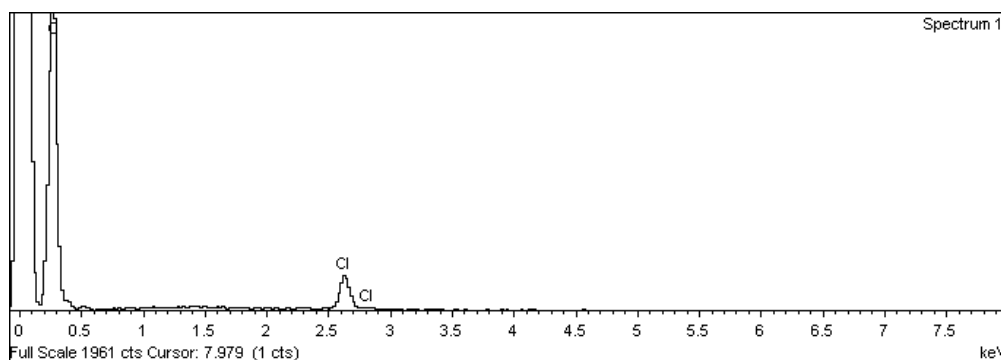


Figure 3.17: EDX spectrum of PPy doped with  $\text{Cl}^-$  reduced at  $-0.8$  V vs. SCE for 60 minutes in  $0.1 \text{ mol dm}^{-3}$  NaCl solution. This polymer was prepared potentiostatically at  $0.60$  V vs. SCE to a charge of  $0.2$  C onto GC. The diameter of the electrode was  $4$  mm and the polymer was synthesised from a solution containing  $0.2 \text{ mol dm}^{-3}$  Py monomer and  $0.1 \text{ mol dm}^{-3}$  NaCl.

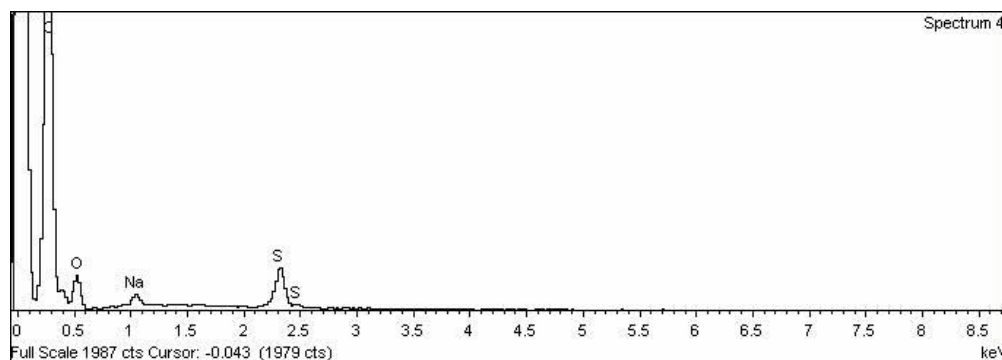


Figure 3.18: EDX spectrum of PPy doped with sul- $\beta$ CD reduced at  $-0.8$  V vs. SCE for 60 minutes in  $0.1 \text{ mol dm}^{-3}$  NaCl solution. This polymer was prepared potentiostatically at  $0.65$  V vs. SCE to a charge of  $0.2$  C onto GC. The diameter of the electrode was  $4$  mm and the polymer was synthesised from a solution containing  $0.2 \text{ mol dm}^{-3}$  Py monomer and  $0.02 \text{ mol dm}^{-3}$  sul- $\beta$ CD.

Following characterisation of the polymer with respect to the growth kinetics and morphology, Section 3.4 discusses the interaction of paraquat at the modified surface.

### 3.4. Paraquat at the Modified Electrode Surface

Following electropolymerisation of Py doped with sul- $\beta$ CD, the polymer was cycled in  $5.0 \times 10^{-3}$  mol dm<sup>-3</sup> paraquat and a 0.1 mol dm<sup>-3</sup> Na<sub>2</sub>SO<sub>4</sub> solution, at a slightly alkaline pH of 8.0. A potential window in the range of -0.1  $\rightarrow$  -1.4 V vs. SCE was used so that the redox chemistry of paraquat could be observed. The recorded CV is shown in Figure 3.19 (a), as the blue trace. The red trace represents a similar experiment, at a concentration of  $2.5 \times 10^{-3}$  mol dm<sup>-3</sup> paraquat in 0.1 mol dm<sup>-3</sup> Na<sub>2</sub>SO<sub>4</sub> at a pH of 8.0. The redox couple at approximately -0.2 V vs. SCE for both traces corresponds to the redox activity of PPy, as shown earlier in Figure 3.13. As Na<sub>2</sub>SO<sub>4</sub> is the supporting electrolyte and in large excess in contrast to the paraquat concentration, there is cationic exchange of Na<sup>+</sup> into and out of the polymer matrix in addition to any interaction with the cationic paraquat. For the higher concentration of paraquat, there are two reduction peaks at approximately -0.7 and -1.1 V vs. SCE, respectively. This corresponds to the reduction of MV<sup>2+</sup> to MV<sup>+</sup> and MV<sup>+</sup> to MV<sup>0</sup>. However, there is only one oxidation peak at approximately -0.6 V vs. SCE, corresponding to the oxidation of MV<sup>+</sup> to MV<sup>2+</sup>. Hence, the oxidation of MV<sup>0</sup> to MV<sup>+</sup> is not observed at the polymer surface. This may be a concentration effect or the modified polymer shows poor sensitivity for the neutral species, MV<sup>0</sup>. Also, there is no evidence of any adsorbed species. The large current for the reduction of MV<sup>+</sup> to MV<sup>0</sup> depicts a strong affinity for the radical species, MV<sup>+</sup>. This preference in the detection of MV<sup>+</sup> is further verified from the CV recorded at the lower concentration of  $2.5 \times 10^{-3}$  mol dm<sup>-3</sup> paraquat. In this case there is only one reduction peak observed at approximately -1.1 V vs. SCE.

The signals at the modified interface were then compared with the redox signals at the bare Au and GC electrodes. This is shown in Figure 3.19 (b), in which an identical concentration of analyte ( $2.5 \times 10^{-3}$  mol dm<sup>-3</sup> paraquat in 0.1 mol dm<sup>-3</sup> Na<sub>2</sub>SO<sub>4</sub> solution), pH, scan rate and potential window were used. The CVs at the Au and GC interface show two redox couples at similar redox potentials, in accordance with Equations 3.1 and 3.2. There is also an additional peak due to adsorption, in accordance with Equation 3.3. This was previously discussed in

Section 3.2. On the other hand, the CV for paraquat at the modified surface of PPy/sul- $\beta$ CD is very different. Only one reduction peak recorded at -1.18 V vs. SCE is observed. The peak current for this signal is higher than the corresponding signals recorded at Au or GC, as depicted in Table 3.4. This clearly confirms that the PPy/sul- $\beta$ CD polymer has an ability to detect paraquat in solution.

In order to establish the role of the sul- $\beta$ CD in the sensing of paraquat, two other large dopants were employed, PSS and SDS and a smaller anionic dopant of  $\text{SO}_4^{2-}$ . These modified polymers were cycled in  $2.5 \times 10^{-3}$  mol  $\text{dm}^{-3}$  paraquat in 0.1 mol  $\text{dm}^{-3}$   $\text{Na}_2\text{SO}_4$  solution at a pH of 8.0, and the results are shown in Figure 3.19 (c) and (d), respectively. It is evident, that no detection of paraquat occurs at the PPy/PSS surface or at the PPy/ $\text{SO}_4^{2-}$  film, as shown in Figure 3.19 (c). Only the redox activity of the polymer is observed. However, there is a reduction signal recorded for the PPy/SDS at a similar potential to that of PPy/sul- $\beta$ CD, as illustrated in Figure 3.19 (d). The peak current is similar in magnitude, as documented in Table 3.4. Although this peak current is high, the background current is considerably larger than that measured for PPy/sul- $\beta$ CD, making the detection of paraquat difficult, particularly at lower concentrations.

SDS is a surfactant, with a charged sulfate head and a hydrocarbon tail. Above a particular concentration, known as the critical micelle concentration (cmc), aggregates of the surfactant form in solution<sup>53</sup>. This is the arrangement of the hydrophobic tails towards each other to protect from solvent molecules. As a result of this, the charged heads are exposed to the solvent<sup>54</sup>. The cmc for SDS at room temperature is  $8.0 \times 10^{-3}$  mol  $\text{dm}^{-3}$ , implying that these aggregates or large molecules, are concentrated with negative charge on the perimeter of the dopant.<sup>54</sup> Hence, surfactants have a high affinity for cationic species. Using SDS as an anionic dopant in the formation of PPy has proved beneficial in regards to conductivity, stability and the mechanical properties of the polymer film<sup>55</sup>. As reported by Saidman and Vela<sup>56</sup>, in which they deposited PPy/SDS onto an Al electrode to produce a porous film, the presence of the surfactant increased the

deposition rate and  $\text{Na}^+$  transport from the electrolyte solution to the polymer film. Hence, the large redox peak at  $-0.75$  V vs. SCE corresponds to the redox activity of the PPy/SDS polymer as shown in Figure 3.19 (d). Given that SDS has a high affinity for cationic species and detects the reduced  $\text{MV}^+$  species at the modified electrode, this is a suitable sensor. However, the large background current at  $-0.75$  V vs. SCE due to  $\text{Na}^+$  exchange may interfere with the detection at low concentrations of paraquat.

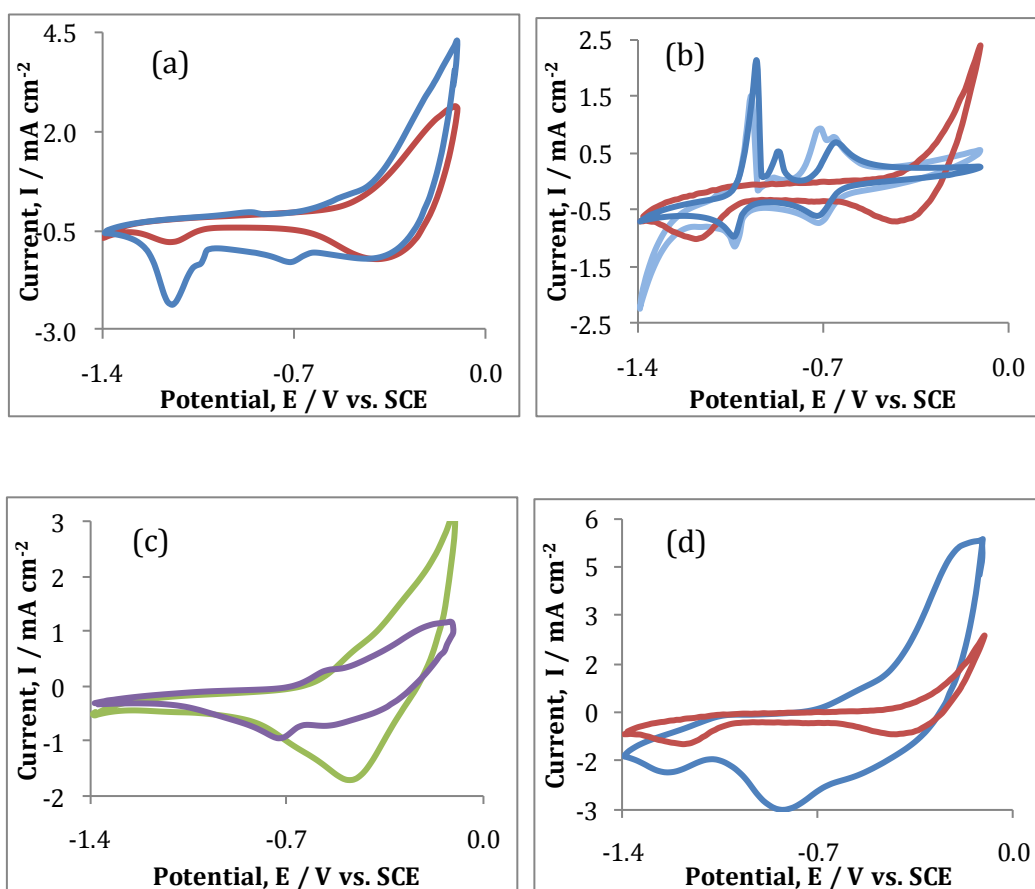


Figure 3.19: CVs of the following; (a) (—)  $5.00 \times 10^{-3}$  mol  $\text{dm}^{-3}$  and (—)  $2.50 \times 10^{-3}$  mol  $\text{dm}^{-3}$  paraquat in  $0.10$  mol  $\text{dm}^{-3}$   $\text{Na}_2\text{SO}_4$ , at PPy doped with sul- $\beta$ CD. (b)  $2.50 \times 10^{-3}$  mol  $\text{dm}^{-3}$  paraquat at (—) GC, (—) Au and (—) PPy doped with sul- $\beta$ CD. (c)  $2.50 \times 10^{-3}$  mol  $\text{dm}^{-3}$  paraquat at modified electrodes of (—) PPy/PSS and (—) PPy/ $\text{SO}_4^{2-}$  and (d)  $2.50 \times 10^{-3}$  mol  $\text{dm}^{-3}$  paraquat at modified electrodes of (—) PPy/SDS and (—) PPy/sul- $\beta$ CD. All analyte solutions were adjusted to a pH of 8.0 using  $0.1$  mol  $\text{dm}^{-3}$  NaOH. All CVs were carried out within a potential window of  $-0.10 \rightarrow -1.40$  V vs. SCE at a scan rate of  $100$   $\text{mV s}^{-1}$ . The polymer were synthesised electrochemically at  $0.65$  V vs. SCE to a charge of  $0.2$  C, at a Au interface of  $3$  mm in diameter. The solution for polymerisation contained  $0.20$  mol  $\text{dm}^{-3}$  Py monomer and  $0.02$  mol  $\text{dm}^{-3}$  of the required dopant.

Table 3.4: Data illustrating the peak currents,  $I_p$ , and peak potentials,  $E_p$ , of  $2.5 \times 10^{-3}$  mol dm<sup>-3</sup> paraquat in a 0.1 mol dm<sup>-3</sup> Na<sub>2</sub>SO<sub>4</sub> solution, obtained from CVs recorded and illustrated in Figure 3.19 (b), (c) and (d).

Substrate	$I_p / \text{mA cm}^{-2}$	$E_p / \text{V vs. SCE}$
Bare Au	0.247	-1.03
Bare GC	0.239	-1.03
PPy / sul- $\beta$ CD	0.321	-1.18
PPy / SDS	0.360	-1.24
PPy / PSS	-	-
PPy / SO <sub>4</sub> <sup>2-</sup>	-	-

It is clear that PPy doped with sul- $\beta$ CD shows promise for the detection of paraquat. Given the high signals obtained from PPy/sul- $\beta$ CD coupled with the low background current, this film was further optimised for the detection of paraquat. Then, in a later section of this chapter, Section 3.7, a comparative study of the polymer, PPy/SDS and its ability to detect paraquat will be discussed.

### 3.5 Optimisation of Paraquat at the Polymer Film

As discussed in Chapter 1, Section 1.5, paraquat is a toxic herbicide with a slow degradation time and it is hazardous for the environment<sup>5,57</sup>. In light of this, an effective sensor is required for its detection. The promising results obtained from the PPy doped with sul- $\beta$ CD required further analysis in order to optimise the sensor for paraquat detection. Some of the parameters investigated were pH, potential and charge consumed during the growth and the nature of the supporting electrolyte. The sensitivity of PPy/sul- $\beta$ CD with respect to  $2.5 \times 10^{-3}$  mol dm<sup>-3</sup> paraquat in 0.1 mol dm<sup>-3</sup> Na<sub>2</sub>SO<sub>4</sub> solution was analysed as a function of varying conditions, so that optimum conditions could be determined prior to carrying out a full calibration curve.

### 3.5.1 Effect of pH and Potential Window on the Paraquat signal

As described in Section 3.4 the pH of the paraquat-containing solutions were adjusted to a slightly alkaline pH of 8.0. The conductivity of the polymer within an alkaline solution is reduced, which is an important factor in minimising the charging capacitance of the conducting polymer. The CVs of  $2.5 \times 10^{-3}$  mol dm<sup>-3</sup> paraquat in 0.1 mol dm<sup>-3</sup> Na<sub>2</sub>SO<sub>4</sub> solution recorded at different pH values are shown in Figure 3.20 (a). The blue trace illustrates the CV recorded in a paraquat solution at a pH of 5.0 while the red trace depicts the electrochemistry of paraquat at a pH of 8.0. Even though the CVs are recorded in different potential windows, it is clearly evident that an increase in pH from 5.0 to 8.0 reduces considerably the electrochemical activity of the polymer. There is a clear reduction in the capacitance current at a pH of 8.0. At a pH of 5.0, the redox wave corresponding to the reduction and oxidation of the polymer is very broad making the detection of paraquat difficult. Hence, the optimum pH for sensing paraquat in Na<sub>2</sub>SO<sub>4</sub> solution was deemed as 8.0. These variations in the electrochemistry of the polymer can be explained in terms of the conductivity of the polymer. For example, Michalska *et al.*<sup>58</sup> reported similar findings for PPy doped with Cl<sup>-</sup> that was conditioned in an alkaline solution for short periods. The slight decrease in conductivity is due to partial deprotonation at an increased pH<sup>59,60</sup>.

In conjunction with optimising the pH, the influence of the potential window at the optimum pH of 8.0 is illustrated in Figure 3.20 (b). It is evident that the peak current at -1.2 V vs. SCE for the blue trace is larger than that of the red trace. The blue and red traces correspond to a potential window of -0.1 → -1.4 V and -0.4 → -1.3 V vs. SCE, respectively. Although, the redox activity of the polymer is larger at the wider potential window, it is sufficiently far enough away to monitor the reduction of MV<sup>+</sup> → MV<sup>0</sup>. Also, a peak current of  $3.3 \times 10^{-4}$  A cm<sup>-2</sup> and  $3.1 \times 10^{-5}$  A cm<sup>-2</sup> was recorded for the blue and red trace, respectively, indicating that the peak current is almost ten-fold higher for the potential window of -0.1 → -1.4V vs. SCE.

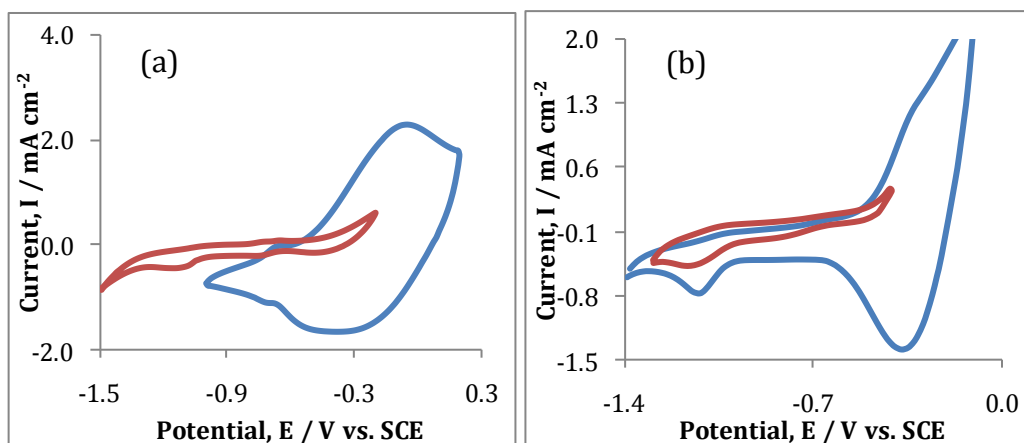


Figure 3.20: (a) CVs of  $2.50 \times 10^{-3}$  mol dm<sup>-3</sup> paraquat in 0.10 mol dm<sup>-3</sup> Na<sub>2</sub>SO<sub>4</sub> at pH (—) 8.0 and (—) 5.0 at a modified polymer film of PPy doped with sul-βCD. The potential was swept from (—) -0.2 → -1.5 V vs. SCE and (—) 0.2 → -1.0 V vs. SCE at a scan rate of 50 mV s<sup>-1</sup>. (b) CVs of  $2.50 \times 10^{-3}$  mol dm<sup>-3</sup> paraquat in 0.10 mol dm<sup>-3</sup> Na<sub>2</sub>SO<sub>4</sub> at a pH of 8.0 at a modified PPy/sul-βCD film. The potential was swept from (—) -0.1 → -1.4 V and (—) -0.4 → -1.3 V vs. SCE at a scan rate of 100 mV s<sup>-1</sup>. All polymers were prepared from a solution of 0.20 mol dm<sup>-3</sup> Py monomer and 0.01 mol dm<sup>-3</sup> sul-βCD electropolymerised at a potential of 0.5 V vs. SCE to a charge of 0.35 C cm<sup>-2</sup> at Au.

### 3.5.2 Influence of Applied Potential in Forming the Polymer

The influence of the potential applied in electrodepositing PPy/sul-βCD at Au was explored. The polymer films were grown to a constant charge of 0.35 C cm<sup>-2</sup> at formation potentials between 0.50 and 1.10 V vs. SCE. The polymer films were then tested for the sensing of paraquat in  $2.5 \times 10^{-3}$  mol dm<sup>-3</sup> paraquat dissolved in 0.1 mol dm<sup>-3</sup> Na<sub>2</sub>SO<sub>4</sub>, adjusted to a pH of 8.0. Representative voltammograms are shown in Figure 3.21. These data are further summarised in Table 3.5, showing the peak currents and potentials for the reduction of MV<sup>+</sup> to MV<sup>0</sup>. As the potential applied during polymerisation increases from 0.50 to 0.65 V vs. SCE, the current signal recorded for the reduction of MV<sup>+</sup> to MV<sup>0</sup> also increases. This increasing current is consistent with an increasing doping level. It is well known that the doping level in polypyrrole increases with an increase in the formation potential<sup>49</sup>. Accordingly, the doping level at 0.65 V vs. SCE is higher, with an increased number of sul-βCD anions, in contrast to those films polymerised at lower potentials. Thus, this trend implies an increasing number of sul-βCD sites to sense the reduced, MV<sup>+</sup> species at -1.18 V vs. SCE. However,

at applied potentials of 0.80 V vs. SCE and above, the current signal begins to decrease. At these higher oxidation potentials, PPy tends to be over-oxidised and as a result becomes insulating<sup>45,61</sup>. Hence, the conductivity of the polymer is reduced. Indeed, the reduction wave centred at about -0.4 V vs. SCE, which corresponds to the reduction of the polymer, is nearly absent for the films grown at 1.1 V vs. SCE. Hence, the optimum potential for the formation of PPy doped with sul- $\beta$ CD is 0.65 V vs. SCE, in order to obtain an enhanced signal for the reduction of MV<sup>+</sup> to MV<sup>0</sup>.

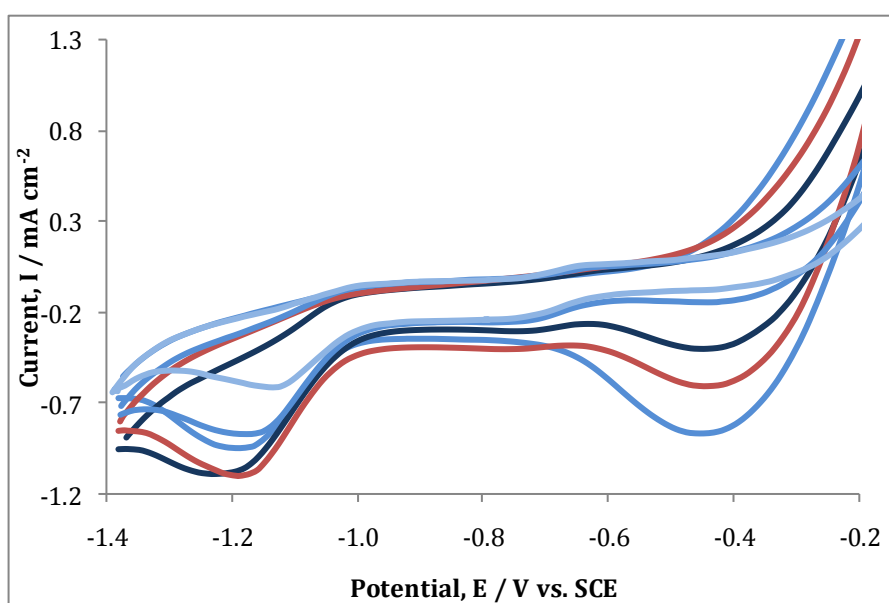


Figure 3.21: CVs of PPy/sul- $\beta$ CD cycled in  $2.50 \times 10^{-3}$  mol dm<sup>-3</sup> paraquat in 0.10 mol dm<sup>-3</sup> Na<sub>2</sub>SO<sub>4</sub> at a pH of 8.0. The potential was swept from -0.1 → -1.4 V vs. SCE at a scan rate of 100 mV s<sup>-1</sup>. Polymers were electropolymerised at Au at applied potentials of (—) 0.50, (—) 0.60, (—) 0.65, (—) 0.80 and (—) 1.10 V vs. SCE to a charge density of 0.35 C cm<sup>-2</sup>, from a solution containing 0.20 mol dm<sup>-3</sup> Py monomer and 0.02 mol dm<sup>-3</sup> sul- $\beta$ CD in distilled H<sub>2</sub>O.

Table 3.5: Peak currents ( $I_p^C$ ) and peak potentials ( $E_p^C$ ) for the reduction of  $MV^+ \rightarrow MV^0$  at the PPy/sul- $\beta$ CD modified Au electrode cycled in  $2.50 \times 10^{-3}$  mol  $dm^{-3}$  paraquat and 0.10 mol  $dm^{-3}$   $Na_2SO_4$ . Corresponding data are illustrated in Figure 3.21.

Applied Potential / V vs. SCE	$I_p^C$ ( $MV^+ \rightarrow MV^0$ ) / A $cm^{-2}$	$E_p^C$ ( $MV^+ \rightarrow MV^0$ ) / V vs. SCE
0.50	$2.6 \times 10^{-4}$	-1.19
0.60	$3.0 \times 10^{-4}$	-1.24
0.65	$3.1 \times 10^{-4}$	-1.19
0.80	$2.0 \times 10^{-4}$	-1.17
1.10	$8.0 \times 10^{-5}$	-1.14

### 3.5.3 Electropolymerisation Charge

The impact of the electropolymerisation charge on the ability of the modified polymer to sense paraquat was investigated by varying the electropolymerisation charge from 0.28 to 0.70 C  $cm^{-2}$ . Typical results are presented in Figure 3.22, where the polymer films were cycled in a  $2.5 \times 10^{-3}$  mol  $dm^{-3}$  solution of paraquat. As the electropolymerisation charge increases, there is an increasing reduction wave observed for the reduction of the polymer. The reduction wave is also displaced to more cathodic potentials in agreement with the data presented in Figure 3.13. This reduction is accompanied by the ingress of cations from the electrolyte solution and as the concentration of  $Na^+$  is in excess of  $MV^{2+}$ , much of the negative charge of the sul- $\beta$ CD is balanced by the ingress of  $Na^+$  species on reduction of the polymer. The  $Na^+$  is smaller and more mobile than either the  $MV^{2+}$  or  $MV^+$  species, giving rise to more efficient diffusion of the  $Na^+$  species within the polymer matrix.

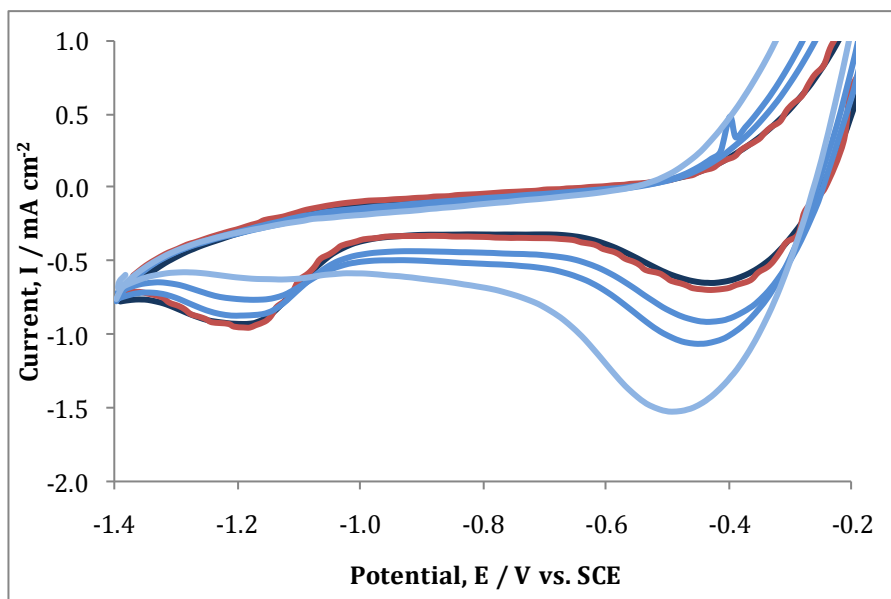


Figure 3.22: CVs recorded for PPy/sul- $\beta$ CD films in  $2.50 \times 10^{-3} \text{ mol dm}^{-3}$  paraquat and  $0.10 \text{ mol dm}^{-3} \text{ Na}_2\text{SO}_4$  solution at a pH of 8.0. The films were prepared at Au at a constant potential of 0.65 V vs. SCE and to charge densities of (—) 0.28, (—) 0.35, (—) 0.42, (—) 0.57, (—) 0.70 C  $\text{cm}^{-2}$ . The films were prepared from a solution of  $0.20 \text{ mol dm}^{-3}$  Py monomer and  $0.02 \text{ mol dm}^{-3}$  sul- $\beta$ CD.

It is well known that electropolymerisation at higher charge density produces thicker polymers with enhanced porosity and surface area<sup>45</sup>. It appears that these more porous polymers facilitate the transport of the mobile  $\text{Na}^+$  species and this, in turn, reduces the interactions between the polymer and the  $\text{MV}^{2+}$  and  $\text{MV}^+$  species. Nevertheless, the  $\text{MV}^{2+}$  species is reduced at the polymer film at approximately -0.7 V vs. SCE (not evident in Figure 3.22, but shown in Figure 3.19 (a)) and the resulting  $\text{MV}^+$  is reduced to  $\text{MV}^0$  at -1.2 V vs. SCE to give a peak current of  $3.23 \times 10^{-4} \text{ A cm}^{-2}$  at the film grown to a charge density of  $0.35 \text{ C cm}^{-2}$ . The background current is also minimised at this electropolymerisation charge, compared to the thicker polymers where the reduction wave broadens and extends into the potential window at which the reduction of  $\text{MV}^+$  occurs.

### 3.5.4 Influence of the supporting electrolyte

As shown in Figure 3.22, there is competition between the  $\text{Na}^+$  and the cationic forms of paraquat. In an attempt to gain more information on the nature of this competition, the supporting electrolyte was altered. Potassium chloride (KCl) was chosen as a comparative electrolyte, as  $\text{K}^+$  is larger in size compared to  $\text{Na}^+$ .

This in turn will affect the mobility of the competitor ions. The larger  $K^+$  is less hydrated by water molecules compared to the  $Na^+$ . The hydrated radii for  $Na^+$  and  $K^+$  are 2.76 and 2.32 Å, respectively<sup>55</sup>. Accordingly, the mobility of  $K^+$  is higher than  $Na^+$  and the hydrated  $K^+$  will diffuse more efficiently within the polymer matrix.

Cyclic voltammograms comparing the electrochemical detection of  $7.5 \times 10^{-4}$  mol  $dm^{-3}$  paraquat at the PPy/sul- $\beta$ CD modified electrode cycled in supporting electrolytes of 0.1 mol  $dm^{-3}$   $Na_2SO_4$  and KCl are displayed in Figure 3.23. There is a considerable increase in the reduction wave of the polymer in the presence of the KCl, which is consistent with the higher mobility of the  $K^+$  ions. Interestingly, the reduction wave for the conversion of  $MV^+$  to  $MV^0$  is almost absent in the KCl solution, highlighting the significant role of the competitor cation in the supporting electrolyte. It is clear that cations with lower mobility are more appropriate and consequently  $Na_2SO_4$  was chosen as the optimum electrolyte for sensing paraquat.

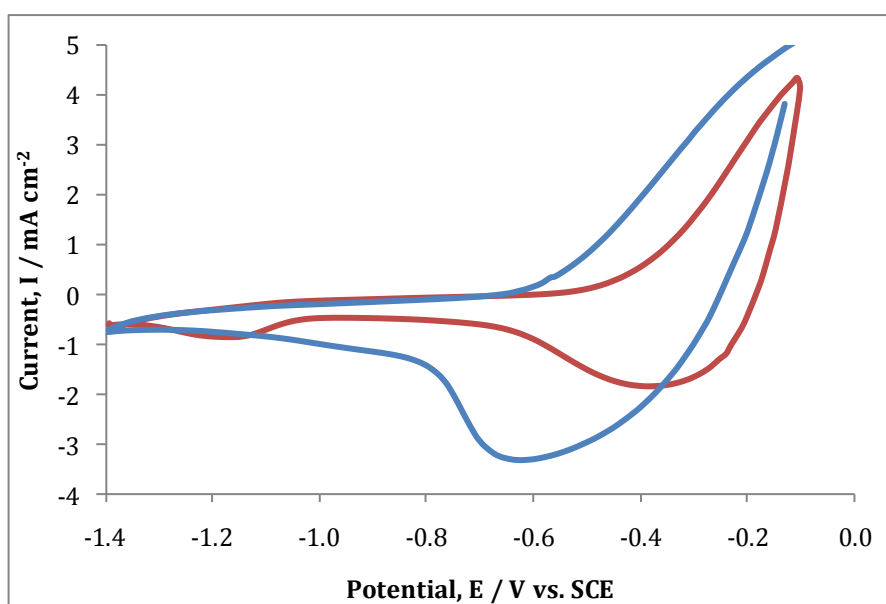


Figure 3.23: CVs recorded in  $7.50 \times 10^{-4}$  mol  $dm^{-3}$  paraquat in 0.10 mol  $dm^{-3}$  (—)  $Na_2SO_4$  and (—) KCl at a pH of 8.0 at PPy doped with sul- $\beta$ CD. The polymer was swept within a potential window of  $-0.1 \rightarrow -1.4$  V vs. SCE at  $100$   $mV$   $s^{-1}$ . Each polymer was prepared from a solution of  $0.20$  mol  $dm^{-3}$  Py monomer and  $0.02$  mol  $dm^{-3}$  sul- $\beta$ CD electropolymerised at an applied potential of  $0.65$  V vs. SCE until a charge density of  $0.35$  C  $cm^{-2}$  was reached.

### 3.5.5 Optimum Conditions

In addition to the parameters presented in Section 3.5.1 to 3.5.4, various conditioning parameters were used to optimise further the sensing of paraquat. As reported by Lu and Sun<sup>62</sup> accumulation of paraquat at the surface can occur by simply immersing the sensor in a paraquat sample. Also, Zanganeh *et al.*<sup>27</sup> found that pre-concentration of copper species within a PPy/EBB film depended on the application of a pre-conditioning potential. Various potentials were applied to the PPy/sul- $\beta$ CD in an attempt to reduce the competition between the  $\text{Na}^+$  and the cationic paraquat species. In these experiments the film was polarised at different potentials in a paraquat solution, at a fixed concentration relevant to the subsequent CVs to be carried out. Then the CVs were recorded in a fresh paraquat-containing solution. These data are summarised in Table 3.6, where the peak currents for the reduction of  $\text{MV}^+$  to  $\text{MV}^0$  are given as a function of the prior conditioning. It is clear that the optimum conditioning is achieved by polarising the polymer at -0.2 V vs. SCE for 15 mins in a fixed concentration of paraquat relevant to the following CVs carried out.

Table 3.6: Peak currents for the reduction of  $\text{MV}^+$  to  $\text{MV}^0$  for  $2.5 \times 10^{-3} \text{ mol dm}^{-3}$  paraquat in  $0.1 \text{ mol dm}^{-3} \text{ Na}_2\text{SO}_4$  solution at the PPy/sul- $\beta$ CD film, recorded using CV. The potential was swept from  $-0.1 \rightarrow -1.4 \text{ V vs. SCE}$  at  $100 \text{ mV s}^{-1}$ . Prior to carrying out the CVs, the PPy/sul- $\beta$ CD films were polarised at the potentials listed. All PPy/sul- $\beta$ CD films were prepared at  $0.65 \text{ V vs. SCE}$  to a charge density of  $0.35 \text{ C cm}^{-2}$  from a solution containing  $0.20 \text{ mol dm}^{-3}$  Py monomer and  $0.02 \text{ mol dm}^{-3}$  sul- $\beta$ CD.

Potentials of Polarisation / V vs. SCE	$I_p^c, \text{MV}^+ \rightarrow \text{MV}^0 / \text{A cm}^{-2}$
-0.1	$5.67 \times 10^{-5}$
-0.2	$3.25 \times 10^{-4}$
-0.3	$3.06 \times 10^{-4}$

Once the optimum conditions were fixed, a calibration study was carried out to establish the detection limit and sensitivity of PPy/sul- $\beta$ CD towards paraquat. These optimum conditions are summarised in Table 3.7.

Table 3.7: Optimum conditions for the sensing paraquat at the PPy film doped with sul- $\beta$ CD.

Parameter	Optimum Result
Concentration of Py monomer	0.20 mol dm <sup>-3</sup>
Concentration of sul- $\beta$ CD	0.02 mol dm <sup>-3</sup>
Electropolymerisation potential	0.65 V vs. SCE
Electropolymerisation charge	0.35 C cm <sup>-2</sup>
pH of paraquat solution	8.0
Supporting electrolyte	Na <sub>2</sub> SO <sub>4</sub>
Scan rate	100 mV s <sup>-1</sup>
Potential window	-0.1 $\rightarrow$ -1.4 V vs. SCE
Conditioning step	Cycle in 0.1 mol dm <sup>-3</sup> Na <sub>2</sub> SO <sub>4</sub> for 10 cycles and Condition at -0.2 V vs. SCE for 15 min

### 3.6 Calibration study

Three methods were used to establish the detection limit and the sensitivity of the modified polymer to paraquat namely, cyclic voltammetry (CV), differential pulse voltammetry (DPV) and constant potential amperometry (CPA).

#### 3.6.1 Cyclic Voltammetry

Cyclic voltammograms were recorded using the optimum conditions in Table 3.7 in solutions containing different concentrations of paraquat. The peak currents were obtained as a function of the concentration of paraquat. The results of the calibration curve are displayed in Figure 3.24. There is a linear relationship, with a correlation coefficient of 0.986, between the peak current for the reduction of MV<sup>+</sup> to MV<sup>0</sup> and the concentration of paraquat. The detection limit was calculated as  $3.75 \times 10^{-4}$  mol dm<sup>-3</sup>. This was obtained from the experimental data, as the lowest concentration that gave a reproducible peak current. This limit is considerably higher than the legislative limits given by the Environmental Protection Agency (EPA) and the European Union (EU) of  $3.0 \mu\text{g L}^{-1}$  ( $1.2 \times 10^{-9}$  mol dm<sup>-3</sup>) and  $0.1 \mu\text{g L}^{-1}$  ( $3.9 \times 10^{-10}$  mol dm<sup>-3</sup>) respectively<sup>5</sup>.

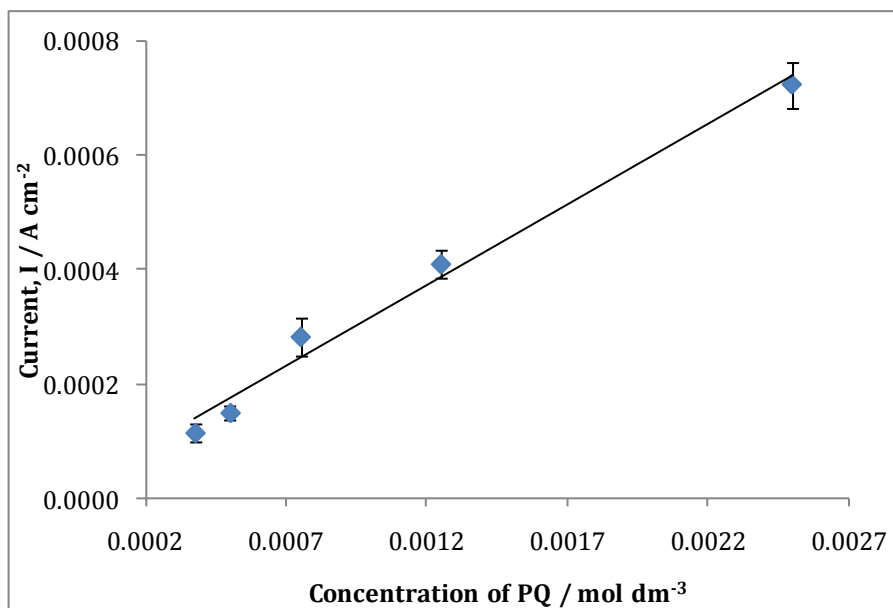


Figure 3.24: Calibration curve (correlation coefficient of 0.986) of the peak current as a function of the paraquat concentration recorded at PPy/sul- $\beta$ CD under the optimum conditions summarised in Table 3.7.

The sensitivity of this polymer was  $0.30 \text{ A cm}^{-2} \text{ M}^{-1}$ . A linear regression equation of  $I_p^C = 0.30c_{\text{paraquat}}$  was obtained from Figure 3.24. As previously discussed in Chapter 2, Section 2.4.1, the sensitivity of CV in comparison to some other voltammetric techniques is limited by the presence of a capacitance current, which increases in a linear manner with increasing scan rate. In an attempt to detect lower concentrations of paraquat both, DPV and CPA techniques were used. These results are presented and discussed in Sections 3.6.2 and 3.6.3.

### 3.6.2 Differential Pulse Voltammetry

To further enhance the detection of paraquat at the modified electrode, DPV was used. As discussed in Chapter 2, Section 2.4.3, DPV applies a set of pulses to distinguish between capacitance and faradaic current. The aim of DPV is to minimise the charging current and only measure the faradaic current, which can enhance the detection limit of the analyte.

The preparation of the PPy/sul- $\beta$ CD films and the detection of paraquat at the modified electrode were carried out in accordance with the optimum conditions outlined in Table 3.7. In addition to this, optimum parameters for sensing

paraquat at the PPy/sul- $\beta$ CD film using DPV were evaluated and are listed in Table 3.8. As illustrated in Figure 3.25, the current response of  $5 \times 10^{-4} \text{ mol dm}^{-3}$  paraquat at the modified electrode is significantly enhanced, in contrast to current response using CV. Current responses were recorded for the reduction of  $\text{MV}^{2+}$  and  $\text{MV}^+$ , respectively. Even though the oxidation and reduction waves were difficult to monitor at concentrations below  $10^{-4} \text{ mol dm}^{-3}$ , experimentally a detection limit of  $7.5 \times 10^{-5} \text{ mol dm}^{-3}$  for the reduction of  $\text{MV}^+$  to  $\text{MV}^0$  was evaluated. This is a notable improvement to  $3.75 \times 10^{-4} \text{ mol dm}^{-3}$  recorded using CV. Indeed, DPV has lowered the capacitance of the polymer, in respect that all redox states of paraquat are detected at the modified electrode. However, at lower concentrations, i.e., below  $10^{-4} \text{ mol dm}^{-3}$ , the redox activity of the polymer begins to dominate. This induces a subsequent masking of the first reduction wave. Hence, at lower concentrations, DPV resembles a CV profile for paraquat at PPy/sul- $\beta$ CD. This eventual loss of the analyte signal is evident by the increase in the reduction potential of the polymer at  $-0.5 \text{ V vs. SCE}$ , as depicted in Figure 3.25. This increases as the concentration of paraquat decreases. This indicates that the large excess of  $\text{Na}_2\text{SO}_4$  in comparison to paraquat is preferentially diffusing to the PPy/sul- $\beta$ CD film. DPV is a positive alternative for sensing applications, but given the high capacitance of this polymer, another method of analysis is required.

Table 3.8: Optimum conditions for detecting paraquat at PPy/sul- $\beta$ CD using DPV.

Optimal parameters for the detection of paraquat using DPV	
Increment, E / mV vs. SCE	3.00
Amplitude / mV vs. SCE	50.00
Pulse width / s	0.10
Pulse period / s	0.30
Sample width / s	0.06

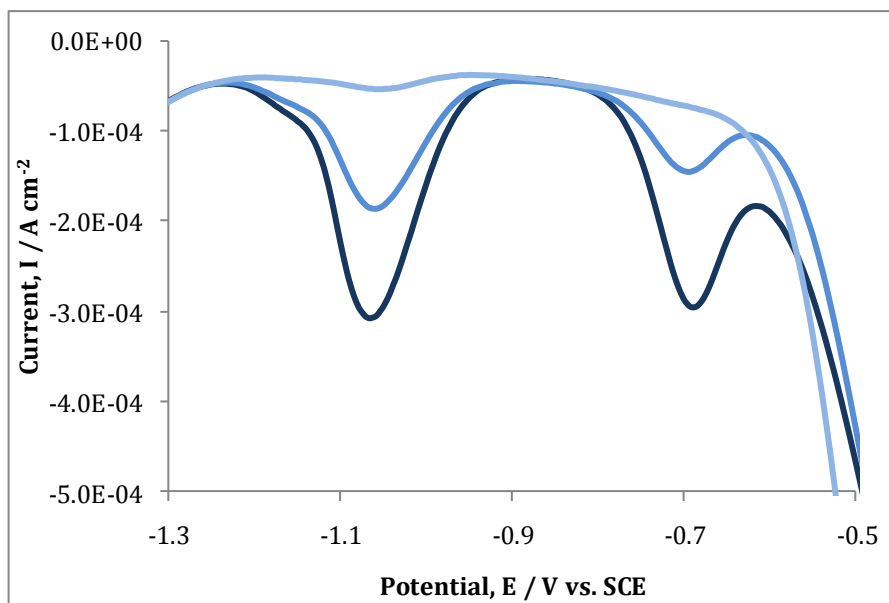


Figure 3.25: DPV of (—)  $5.00 \times 10^{-4}$ , (—)  $4.00 \times 10^{-4}$  and (—)  $3.00 \times 10^{-4}$  mol dm<sup>-3</sup> paraquat in 0.10 Na<sub>2</sub>SO<sub>4</sub> solution at PPy/sul-βCD. The potential was swept from -0.1 → -1.4 V vs. SCE and in accordance with the parameters listed in Table 3.8. Prior to carrying out the DPVs, the formation and conditioning of PPy/sul-βCD was carried out in accordance with the parameters listed in Table 3.7.

### 3.6.3 Constant Potential Amperometry

Constant potential amperometry (CPA) is frequently used as an electrochemical technique to assess the efficiency of an electrode coating or membrane<sup>63</sup>. In this study, it was used to optimise the detection of paraquat. This experiment was carried out by polarising the PPy/sul-βCD film at a reduction potential of -0.9 V vs. SCE in 0.1 mol dm<sup>-3</sup> Na<sub>2</sub>SO<sub>4</sub>. Aliquot additions of paraquat were added to the electrolyte solution and, to ensure efficient mixing, the working electrode was rotated at a fixed speed of 2,000 rpm. Incidentally, by fixing the applied potential at -0.9 V vs. SCE, the reduction of MV<sup>2+</sup> to MV<sup>+</sup> was monitored instead of the reduction of MV<sup>+</sup> to MV<sup>0</sup>, as was followed using CV.

Accordingly, this does not serve as a direct comparison to the CV measurements. The CPA measurements were limited to this first redox transition of paraquat to avoid the common comproportionation reaction between MV<sup>2+</sup> and MV<sup>0</sup> to generate MV<sup>+</sup>, as illustrated in Equation 3.4. Hence, only the reduction of the dicationic species was monitored to give a direct relationship between the signal

and the concentration of the paraquat analyte. The characteristic CPA plot is depicted in Figure 3.26. Clear steps are evident on addition of paraquat to the solution. As the electrode is rotated, the added paraquat reaches the polymer film, is reduced and gives a clear limiting current. The step sizes depend on the concentration of the stock solution added. The response time of the polymer, in which a steady-state current was reached following addition of paraquat was 36 s. Although this is a slow response time in comparison to the literature, the time at which the polymer was polarised at a reduction potential of -0.9V vs. SCE was over a longer time frame. This was to minimise the capacitance current. At reduction potentials, PPy is less conducting and this can affect the response time. These raw data were used to generate a calibration curve. A representative calibration curve is shown in Figure 3.27. Santhiago *et al.*<sup>64</sup> reported a response time of less than 1 s for the detection of  $\beta$ -nicotinamide adenine dinucleotide (NADH) at an amine rich polymer.

It is evident from this plot that at lower concentrations of paraquat there is a linear relationship. However, this is lost at higher concentrations. The currents recorded at lower concentrations are presented in Figure 3.28, with a correlation coefficient of 0.9904, confirming the linear relationship. This technique showed increased sensitivity, with a current to concentration ratio of  $1.87 \text{ A cm}^{-2} \text{ M}^{-1}$ . Using the slope of this plot, the limit of detection was calculated in accordance with Equation 3.10<sup>65</sup>, in which  $C_m$  is the limit of detection in  $\text{mol dm}^{-3}$ ,  $S_b$  is the standard deviation of the background current in  $\text{A cm}^{-2}$  and  $m$  is the slope of the linear calibration curve in  $\text{A cm}^{-2} \text{ M}^{-1}$ .

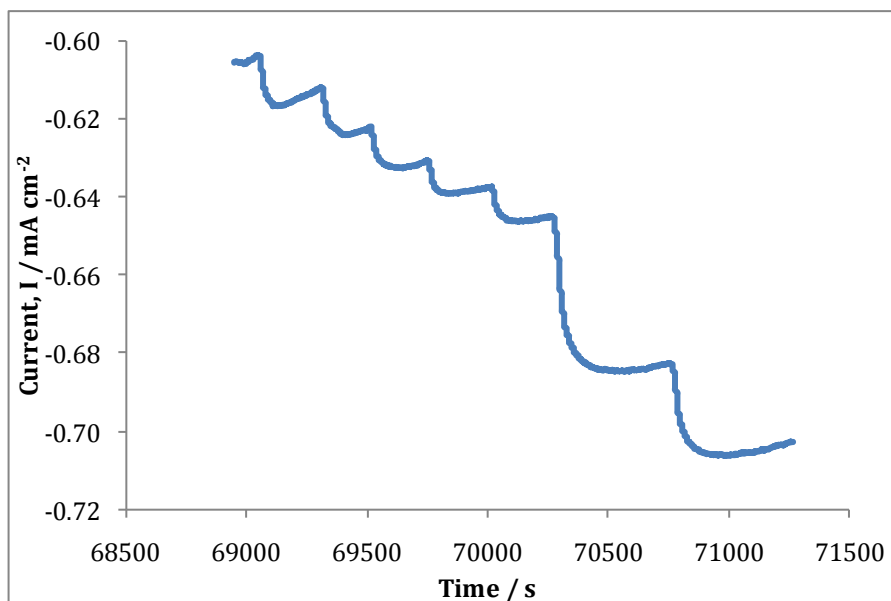


Figure 3.26: CPA plot recorded as a function of time with aliquot additions ranging from 50  $\mu\text{l}$  to 5 ml of  $2.0 \times 10^{-3} \text{ mol dm}^{-3}$  paraquat in  $0.1 \text{ mol dm}^{-3} \text{ Na}_2\text{SO}_4$  to an electrolyte solution of  $0.1 \text{ mol dm}^{-3} \text{ Na}_2\text{SO}_4$ . The PPy/sul- $\beta$ CD was prepared in accordance with the optimum conditions in Table 3.7. The PPy/sul- $\beta$ CD was polarised at  $-0.9 \text{ V}$  vs. SCE and rotated at 2,000 rpm.

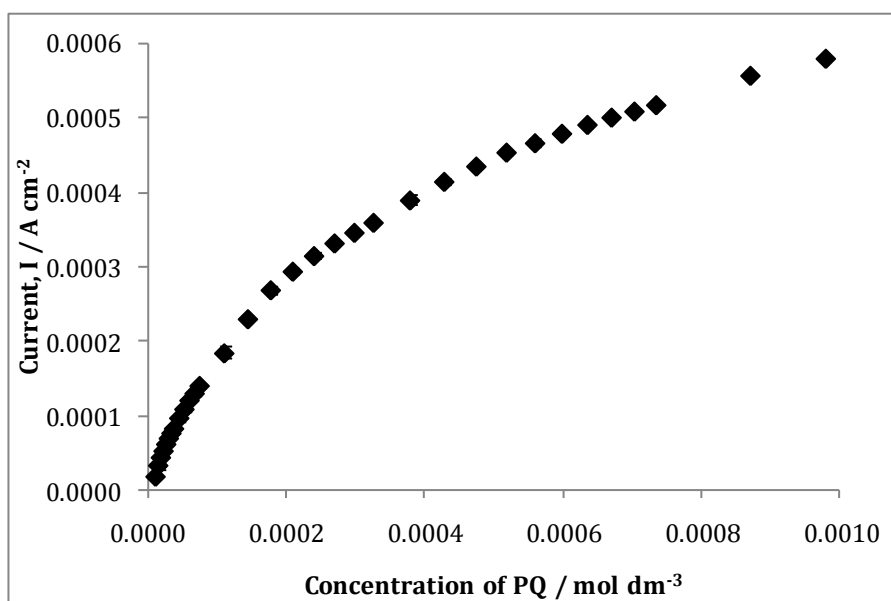


Figure 3.27: Limiting currents obtained from Figure 3.26 as a function of the concentration of paraquat for the reduction of  $\text{MV}^{2+} \rightarrow \text{MV}^+$  at PPy/sul- $\beta$ CD.

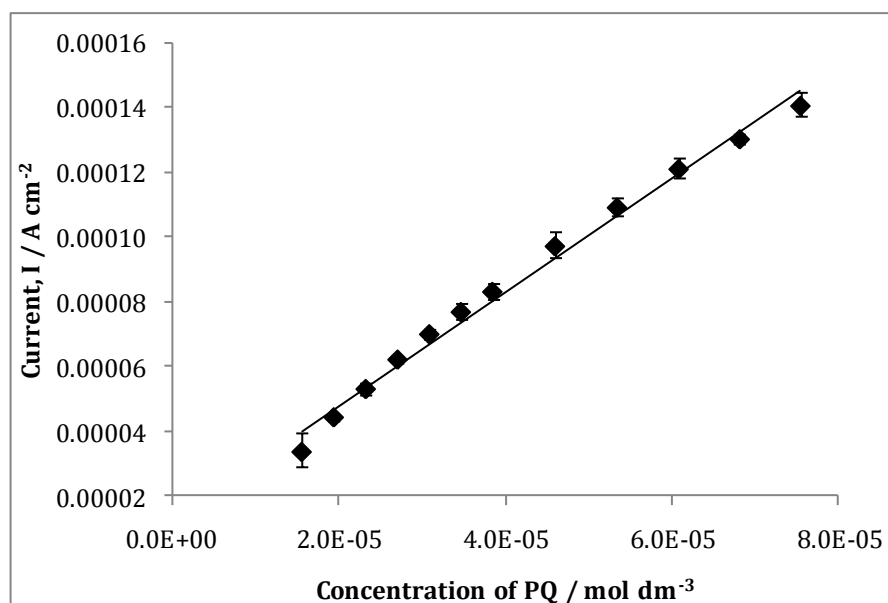


Figure 3.28: Limiting currents obtained from Figure 3.26 as a function of the low concentrations of paraquat recorded at PPy/sul- $\beta$ CD.

$$C_m = \frac{3S_b}{m} \quad (3.10)$$

A computed detection limit of  $1.28 \times 10^{-5}$  mol dm<sup>-3</sup> was obtained. This compares well with the experimentally observed detection limit of  $1.56 \times 10^{-5}$  mol dm<sup>-3</sup>. This latter value was obtained directly from Figure 3.26 as the minimum concentration required to give a reproducible and clear step. These detection limits correspond to a greater than 10-fold increase over the detection limit obtained with the CV technique, of  $3.75 \times 10^{-4}$  mol dm<sup>-3</sup>. This highlights the efficiency of the CPA technique in reducing the contribution of the background current.

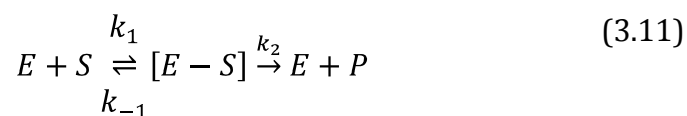
On comparing the data recorded using CV and CPA there is a significant improvement in the detection limit upon applying the CPA technique. Also, in regards the sensitivity, CPA shows increased sensitivity in contrast to CV. The sensitivity of PPy/sul- $\beta$ CD for paraquat using CPA was  $1.87$  A cm<sup>-2</sup> M<sup>-1</sup> and  $0.3$  A cm<sup>-2</sup> M<sup>-1</sup>. However, in contrast to previously developed and reported sensors in the literature, this sensor can only be categorised as average in the sensing of paraquat. For example, Chang *et al.*<sup>66</sup> obtained a detection limit of  $1.0 \times 10^{-4}$  mol

dm<sup>-3</sup> for MV<sup>2+</sup> using a polyviologen modified gold/quartz electrode. In terms of high sensitivity, Zen *et al.*<sup>6</sup> recorded a detection limit of  $8.0 \times 10^{-10}$  mol dm<sup>-3</sup> for MV<sup>2+</sup> at a clay modified electrode. This was done by spin coating a layer of clay colloides and appropriate amounts of Nafion onto a glassy carbon electrode and detection was optimised using square wave voltammetry.

Although the PPy/sul-βCD sensor has been optimised, further work is required to enhance its detection limit and meet the required legislative limits outlined by the EPA and the EU, of  $1.2 \times 10^{-9}$  and  $3.9 \times 10^{-10}$  mol dm<sup>-3</sup>, respectively<sup>5</sup>.

### 3.6.4 Michaelis-Menten Kinetics and Lineweaver-Burk Analysis

Michaelis-Menten kinetics measures the rate of catalytic conversion of the enzyme-substrate complex (*E-S*) to form the product (*P*) as denoted in Equation 3.11<sup>67</sup>. There is an initial reaction between the enzyme (*E*) and the substrate (*S*) to generate the enzyme-substrate complex in which  $k_1$  and  $k_{-1}$  represent the rate constants for the association and dissociation of the enzyme and the substrate. Also,  $k_2$  is the rate constant for the conversion of the enzyme substrate complex to form the product. Two assumptions are made upon applying Michaelis-Menten kinetics. Firstly, the enzyme concentration remains unchanged and secondly, the enzyme substrate complex concentration remains constant indicating that the rate of association and disassociation of E and S are equal, obeying steady-state conditions.



Thus, from these kinetic assumptions, the Michaelis-Menten equation is derived which relates the initial reaction rate, *V* and the substrate concentration, *S*, as depicted in Equation 3.12<sup>67</sup>.  $V_{\max}$  is the rate at which the enzyme has been “saturated” by an infinite concentration of substrate or the maximum conversion rate as expressed in Equation 3.13<sup>67</sup>.  $K_m$  corresponds to the Michaelis constant, which is the substrate concentration equivalent to half the

value of  $V_{\max}$ <sup>68</sup>. It is also related to the rate constants of Equation 3.11 and can be expressed as shown in Equation 3.14<sup>69</sup>.

$$V = \frac{V_{\max}[S]}{K_m + [S]} \quad (3.12)$$

$$V_{\max} = k_2([E] + [E - S]) \quad (3.13)$$

$$K_m = \frac{k_{-1} + k_2}{k_1} \quad (3.14)$$

A typical Michaelis-Menten plot has a characteristic hyperbolic curve as depicted in Figure 3.29. The initial linear response represents the catalytic first-order reaction. With a continued increase in substrate concentration the rate of conversion becomes slower, indicative of the transition from first to zero-order kinetics<sup>70,71</sup>. The constant,  $K_m$ , correlates to the strength of binding between the enzyme and the substrate<sup>72</sup>. A large value of  $K_m$  (typically  $10^{-3}$  mol dm<sup>-3</sup>) indicates weak binding and a small value (typically  $10^{-6}$  mol dm<sup>-3</sup>) is consistent with a strong interaction<sup>72</sup>.

Although Michaelis-Menten kinetics pertains to enzyme-substrate interactions, this analysis can be applied to assess the interaction between PPy/sul- $\beta$ CD and MV<sup>2+</sup>. In this case the sul- $\beta$ CD doped polymer represents the enzyme,  $E$ , MV<sup>2+</sup> corresponds to the substrate,  $S$ , while the current represents the rate of conversion,  $V$ , and  $V_{\max}$  is equivalent to  $I_{\max}$  which is the maximum change in current. Shu and Wilson<sup>73</sup> documented the use of amperometry to calculate  $K_m$ , from a plot of current as a function of analyte concentration. Hence, an identical plot was generated from the data recorded in Section 3.6.3 and this is depicted in Figure 3.29.

The experimental data were fit to the Michaelis-Menten equation, Equation 3.12. The simulated data are shown as the continuous trace, while the experimental data are shown as symbols. A correlation coefficient of 0.998 was obtained for the simulated curve, indicating good agreement between the experimental data and Equation 3.12. The Michaelis-Menten parameters,  $I_{\max}$  and  $K_m$  were evaluated at  $7.58 \times 10^{-4}$  A cm<sup>-2</sup> and  $3.41 \times 10^{-4}$  mol dm<sup>-3</sup>,

respectively. The magnitude of  $K_m$  indicates weak binding between  $MV^{2+}$  and PPy/sul- $\beta$ CD. Another means of determining  $K_m$  and  $V_{max}$  is using the Lineweaver-Burk plot. This is often used to support Michaelis-Menten kinetics.

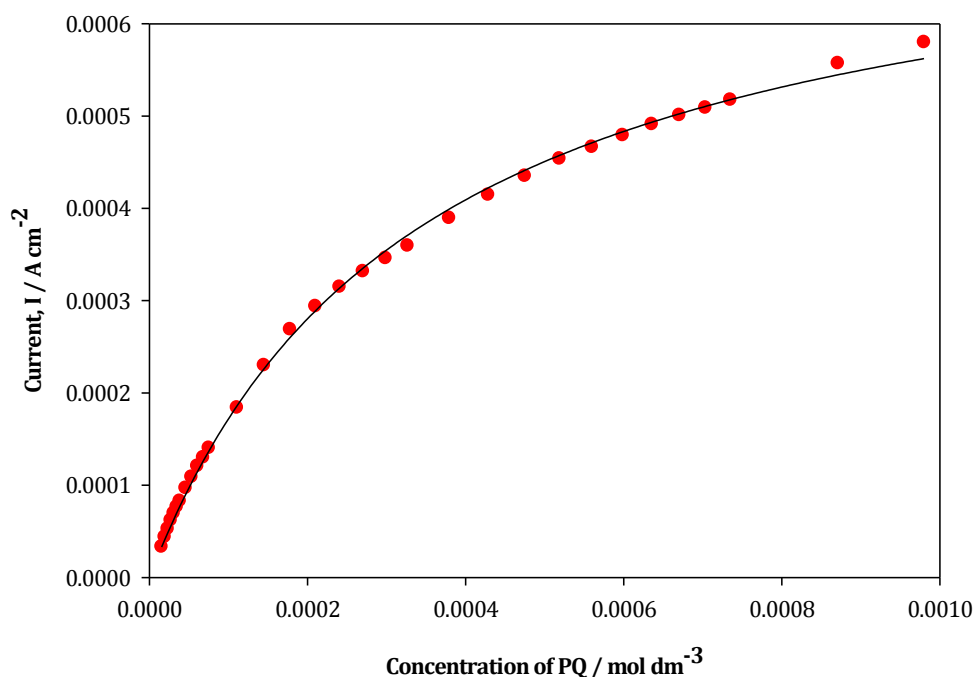


Figure 3.29: Michaelis-Menten plot of current density,  $I$ , as a function of  $MV^{2+}$  concentration. These data were obtained from Figure 3.26. A non-linear curve was fitted to the data, with a correlation coefficient of 0.998.

The Lineweaver-Burk equation is given by Equation 3.15<sup>74</sup> and is simply a plot of the reciprocal of the initial rate of conversion,  $V$ , and the reciprocal of the substrate concentration,  $[S]$ . A representative plot is shown in Figure 3.30, where the inverse of current,  $1/I$ , is plotted as a function of the inverse of the concentration of paraquat,  $1/MV^{2+}$ . Now,  $I_{max}$  and the Michaelis-Menten constant,  $K_m$ , can be calculated from the intercept and slope, respectively. Thus from the equation of the line, with a correlation coefficient of 0.997, values of  $7.41 \times 10^{-4}$  A cm<sup>-2</sup> and  $3.12 \times 10^{-4}$  mol dm<sup>-3</sup> were calculated for  $I_{max}$  and  $K_m$ , respectively. On comparing these values with those obtained from applying the Michaelis-Menten equation, the results show exceptional agreement, indicating the validity of using either equation to quantify  $I_{max}$  and  $K_m$ . Also, it confirms the close proximity in which  $I$  is approaching the asymptote  $I_{max}$ , as illustrated in

Figure 3.29. Moreover, the high  $K_m$  value recorded using both Michaelis-Menten and the Lineweaver-Burk analyses confirms that a weak interaction occurs between the charged species of paraquat,  $MV^{2+}$ , and the modified electrode of PPy/sul- $\beta$ CD.

$$\frac{1}{V} = \frac{1}{V_{max}} + \frac{K_m}{V_{max} [S]} \quad (3.15)$$

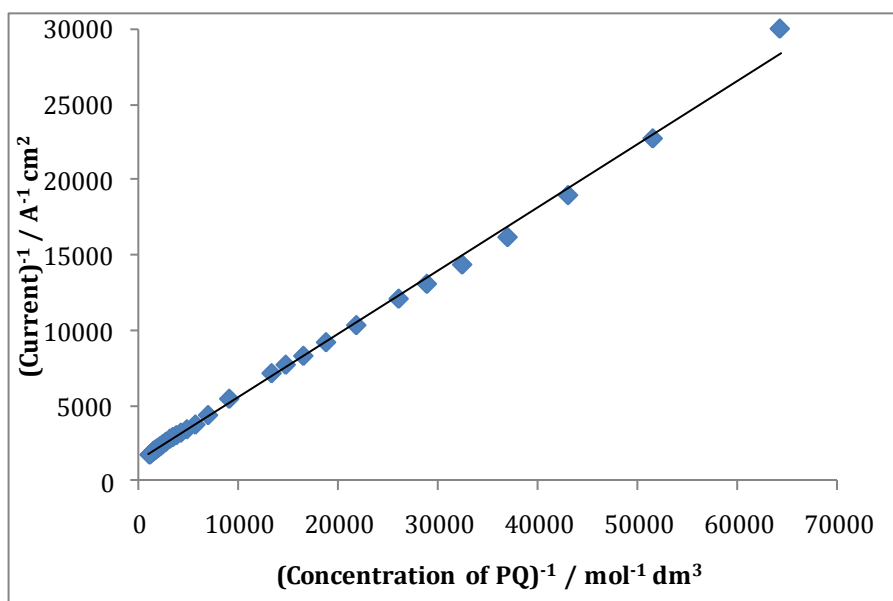


Figure 3.30: Lineweaver-Burk plot of the inverse of current plotted as a function of the inverse of paraquat concentration (linear regression constant of 0.997). These data were taken from Figure 3.26.

Based on the high  $K_m$  value obtained from Michaelis-Menten kinetics and the Lineweaver-Burk analysis, of  $10^{-4}$  mol dm<sup>-3</sup>, this is indicative of a weak interaction. This should imply that the complex of PPy/sul- $\beta$ CD and  $MV^{2+}$  dissociates with relative ease to regenerate PPy/sul- $\beta$ CD and the reduced paraquat species of  $MV^+$ . Although this interaction is suggestive of a weak complex, this may be due to the immobilisation of sul- $\beta$ CD within the polymer matrix. In general, a higher  $K_m$  value is obtained when the enzyme is immobilised. However, it can also be the reverse situation. As reported by Manso *et al.*<sup>75</sup>, a  $K_m$  value of  $14.9 \times 10^{-3}$  mol dm<sup>-3</sup> was recorded for the

interaction of glucose at a modified electrode of carbon nanotubes, glucose oxidase and gold colloides. A value of  $21.33 \times 10^{-3} \text{ mol dm}^{-3}$  was calculated for free glucose. The interaction of sul- $\beta$ CD and paraquat in solution will be pursued further in Chapter 6, to interpret the structural interaction.

### **3.7 Comparative study of PPy doped with SDS**

As illustrated in Section 3.4, the PPy modified with sodium dodecyl sulfate (SDS) gave a clear reduction wave in  $2.5 \times 10^{-3} \text{ mol dm}^{-3}$  paraquat. However, the capacitance current was very large for this polymer compared to that measured with the PPy/sul- $\beta$ CD system. In an attempt to reduce the capacitance current differential pulse voltammetry (DPV) was chosen as the electrochemical technique. As discussed in Section 3.6.2, DPV essentially measures faradaic current and minimises the capacitance current which has a big impact on limiting the sensitivity<sup>76</sup>. Thus, the following section outlines the optimisation of the paraquat signal at the modified PPy/SDS electrode and the detection level recorded with this technique and this will be compared to the sensitivity of PPy/sul- $\beta$ CD.

#### **3.7.1 Differential Pulse Voltammetry**

The procedure in electropolymerising and conditioning the polymer for sensing measurements as described in Table 3.7 was followed in the preparation of PPy/SDS for the detection of paraquat. Prior to carrying out a calibration study using DPV, additional parameters that required optimisation included the pulse period, pulse width, increment and amplitude. Experiments were carried out under different conditions and the optimal conditions obtained are tabulated in Table 3.9.

Table 3.9: Optimal parameters recorded for the detection of paraquat at the modified electrode of PPy/SDS using DPV.

Optimal parameters for the detection of paraquat using DPV	
Increment, E / mV vs. SCE	2.00
Amplitude / mV vs. SCE	50.00
Pulse width / s	0.09
Pulse period / s	0.30
Sample width / s	0.06

Using these conditions, a calibration study was then carried out within a concentration range of  $1.00 \times 10^{-5}$  to  $4.14 \times 10^{-4}$  mol dm<sup>-3</sup> paraquat in 0.10 mol dm<sup>-3</sup> Na<sub>2</sub>SO<sub>4</sub> solution. The recorded peak currents for the reduction of MV<sup>+</sup> to MV<sup>0</sup> showed linearity as a function of paraquat concentration, as illustrated in Figure 3.31. A detection limit of  $5.0 \times 10^{-5}$  mol dm<sup>-3</sup> was obtained which is slightly lower than that obtained for the PPy/sul-βCD sensor, of  $7.45 \times 10^{-5}$  mol dm<sup>-3</sup>, as discussed in Section 3.6.3. Also, the sensitivity PPy/SDS is slightly higher than that of PPy/sul-βCD, which is highlighted in Table 3.10. This indicates that with increased sensitivity, the detection limit increases also.

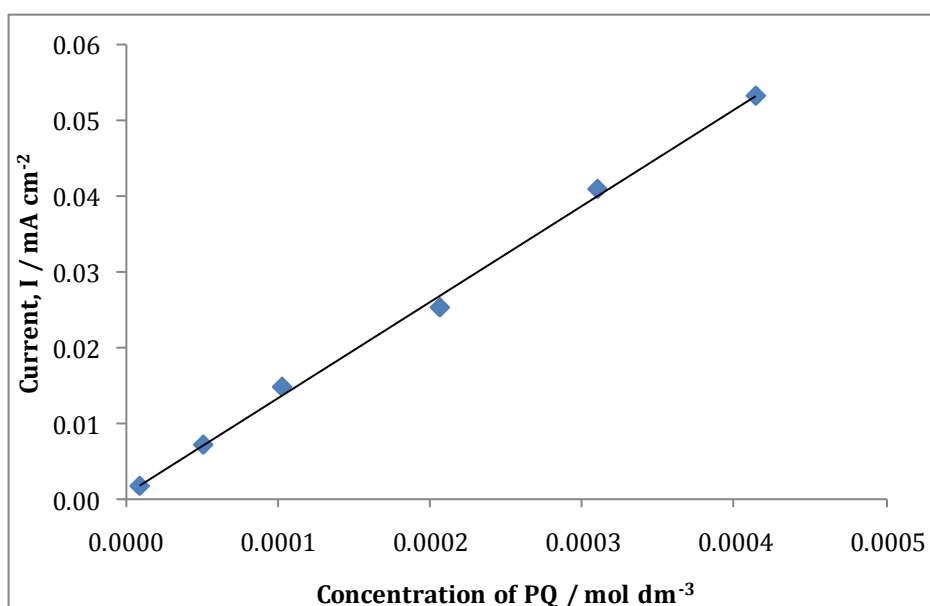


Figure 3.31: Peak current for the reduction of MV<sup>+</sup> → MV<sup>0</sup> as a function of concentration of paraquat using DPV, illustrating a linear relationship with a correlation coefficient of 0.997.

Table 3.10: Data of the detection limits and sensitivity of PPy/sul- $\beta$ CD and PPy/SDS in the detection of paraquat, for the reduction of MV<sup>+</sup> to MV<sup>0</sup>.

Sensor	Detection Limit / mol dm <sup>-3</sup>	Sensitivity / A cm <sup>-2</sup> M <sup>-1</sup>
PPy/sul $\beta$ CD	$7.45 \times 10^{-5}$	0.10
PPy/SDS	$5.00 \times 10^{-5}$	0.13

### 3.8 Interference Studies

The development of a sensor generally has two dependable parameters which are a measure of its efficiency and success. They are sensitivity and selectivity. As discussed earlier, the optimisation of the PPy/sul- $\beta$ CD sensor for the charged species of paraquat, MV<sup>2+</sup>, has a limit of detection of  $1.56 \times 10^{-5}$  mol dm<sup>-3</sup> as recorded from the amperometric data in Section 3.6.3. The concluding aspect of this sensor study was to assess the sensing properties of PPy/sul- $\beta$ CD towards paraquat in the presence of other harmful analytes, namely those of ametryn and diquat. Hence, these interfering compounds will serve as a means of determining the selectivity of the PPy/sul- $\beta$ CD.

#### 3.8.1 Interference of Ametryn

Ametryn is a type of triazine, with a chemical name of 2-ethylamino-4-isopropylamino-6-methylthio-s-triazine<sup>77,78</sup>. It is a herbicide with similar applications to that of paraquat, in which it is used in the control of broadleaf and weeds in the cultivation of sugarcane, corn, citrus, pineapple, tea and other crops<sup>77,79</sup>. The chemical structure is shown in Figure 3.32.

In order to monitor the selectivity of PPy/sul- $\beta$ CD towards paraquat, the redox signals for paraquat in the absence and presence of varying concentrations of ametryn were compared. DPV was the chosen technique to assess the interference of ametryn, as it is highly sensitive and minimises the capacitance current, hence both reduction processes of MV<sup>2+</sup> can be easily monitored. Figure 3.33 shows the recorded DPVs of  $1.0 \times 10^{-3}$  mol dm<sup>-3</sup> paraquat in 0.1 mol dm<sup>-3</sup> Na<sub>2</sub>SO<sub>4</sub> at the PPy/sul- $\beta$ CD in the presence of 0.0, 1.0 and  $50.0 \times 10^{-3}$  mol dm<sup>-3</sup> ametryn. It is evident from the illustrated voltammograms that ametryn has no

significant impact on the reduction of  $MV^+$  to  $MV^0$ . This suggests that ametryn has little interference on the sensitivity of PPy/sul- $\beta$ CD. This is clearly illustrated in Table 3.11 which depicts a minimal change in peak current and peak potential upon the addition of ametryn to a fixed concentration of paraquat.

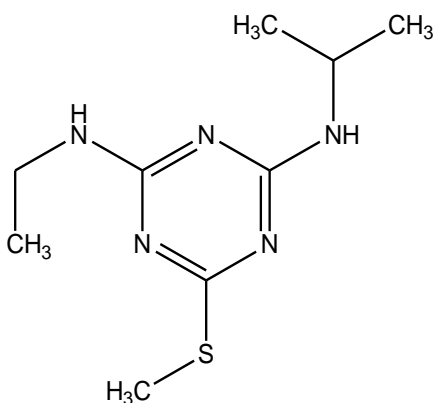


Figure 3.32: Chemical structure of 2-ethylamino-4-isopropylamino-6-methylthio-s-triazine, otherwise known as ametryn.

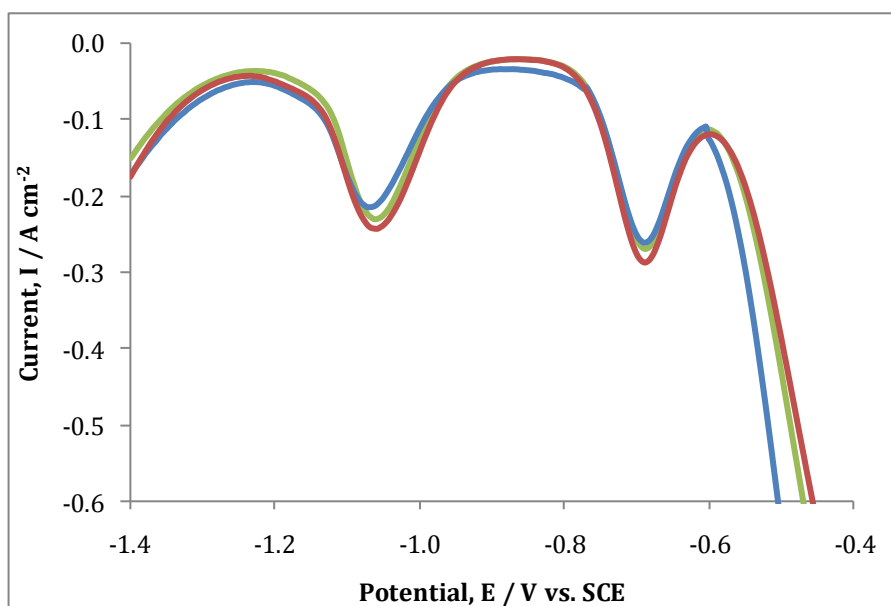


Figure 3.33: DPVs of  $1.00 \times 10^{-3}$  mol  $\text{dm}^{-3}$  paraquat and  $0.10$  mol  $\text{dm}^{-3}$   $\text{Na}_2\text{SO}_4$  at PPy/sul- $\beta$ CD in the presence of (—)  $0.00$ , (—)  $1.00$  and (—)  $50.00 \times 10^{-3}$  mol  $\text{dm}^{-3}$  ametryn. The samples were scanned in a potential window from  $-0.1 \rightarrow -1.4$  V vs. SCE, using the optimal conditions in Table 3.8. The PPy/sul- $\beta$ CD was prepared from a monomer solution of  $0.20$  mol  $\text{dm}^{-3}$  Py monomer and  $0.02$  mol  $\text{dm}^{-3}$  sul- $\beta$ CD and electropolymerised at Au, using the optimum conditions outlined in Table 3.7.

Table 3.11: Data depicting the peak potentials,  $E_p$ , and peak currents,  $I_p$ , for the reduction of  $MV^{2+} \rightarrow MV^+$  and  $MV^+ \rightarrow MV^0$  in  $1.0 \text{ mol dm}^{-3}$  paraquat in  $0.1 \text{ mol dm}^{-3}$   $\text{Na}_2\text{SO}_4$  at PPy/sul- $\beta$ CD.

Concentration / $\text{mol dm}^{-3}$	$E_p^c$ / V vs. SCE	$I_p^c$ / $\text{A cm}^{-2}$
$1 \times 10^{-3} \text{ mol dm}^{-3}$ Paraquat	-0.7	$2.00 \times 10^{-4}$
$0 \text{ mol dm}^{-3}$ Ametryn	-1.1	$1.82 \times 10^{-4}$
$1 \times 10^{-3} \text{ mol dm}^{-3}$ Paraquat	-0.7	$2.00 \times 10^{-4}$
$1 \times 10^{-3} \text{ mol dm}^{-3}$ Ametryn	-1.1	$2.10 \times 10^{-4}$
$1 \times 10^{-3} \text{ mol dm}^{-3}$ Paraquat	-0.7	$1.87 \times 10^{-4}$
$5 \times 10^{-2} \text{ mol dm}^{-3}$ Ametryn	-1.1	$2.02 \times 10^{-4}$

### 3.8.2 Interference of Diquat

1,1'-ethylene-2,2'-bipyridinium, more commonly known as diquat, is structurally quite similar to paraquat, as shown in Figure 3.34. Diquat is a dication and it contains a 2,2'-bipyridyl residue<sup>80</sup>. It is also used for pre-harvest desiccation and weed control of various crops<sup>3</sup>. Given the close comparison between each of the chemical structures, Luque *et al.*<sup>1</sup> referred to diquat as the most serious interferent in the determination of paraquat.

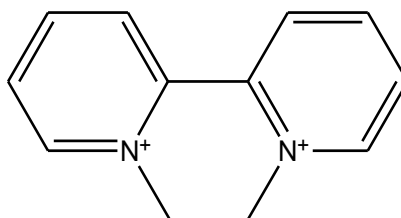


Figure 3.34: Chemical structure of 1,1'-ethylene-2,2'-bipyridinium, more commonly known as diquat.

Diquat has an almost identical electrochemistry to paraquat, as shown by the red trace in Figure 3.35. This trace was recorded in  $1.0 \times 10^{-3} \text{ mol dm}^{-3}$  diquat in the presence of  $0.1 \text{ mol dm}^{-3}$   $\text{Na}_2\text{SO}_4$  as supporting electrolyte at the PPy/sul- $\beta$ CD interface. Reduction of the dicationic diquat,  $V^{2+}$ , occurs at  $-0.6 \text{ V vs. SCE}$  as apposed to  $-0.7 \text{ V vs. SCE}$  for the reduction of the dication of paraquat. Likewise,

reduction of the  $V^+$  to the neutral species occurs at  $-1.0$  V for diquat compared with  $-1.1$  V vs. SCE for paraquat. As there is little variation in these reduction potentials interference is expected. Indeed this was observed as evident from the DPV traces shown in Figure 3.35.

When a large excess of diquat (50-fold excess) was added to a fixed concentration of  $1.0 \times 10^{-3}$  mol  $\text{dm}^{-3}$  solution of paraquat, there was a significant increase in the reduction current in the vicinity of the first reduction peak, corresponding to the conversion of  $V^{2+}$  to  $V^+$ . The current increase was less for the reduction of  $V^+$  to  $V^0$ , as indicated by the green trace in Figure 3.35. There was also a shift in the peak potential for the reduction of  $V^{2+}$  to  $V^+$  from  $-0.7$  to  $-0.6$  V vs. SCE, characteristic of the peak potentials for the first stage of reduction for diquat. This clearly indicates that the sensor is not selective for the detection of paraquat. As both cationic species compete for the interaction with the anionic cyclodextrin, increasing the interferent concentration (diquat) causes a notable increase in the peak current. This is particularly clear in Table 3.12 where the peak currents and peak potentials are compared for paraquat, diquat and a mixture of paraquat and diquat. Thus PPy doped with sul- $\beta$ CD shows excellent selectivity for paraquat in the presence of ametryn, but poor selectivity is observed in the presence of diquat. This is not surprising as diquat has very similar electrochemistry to paraquat.

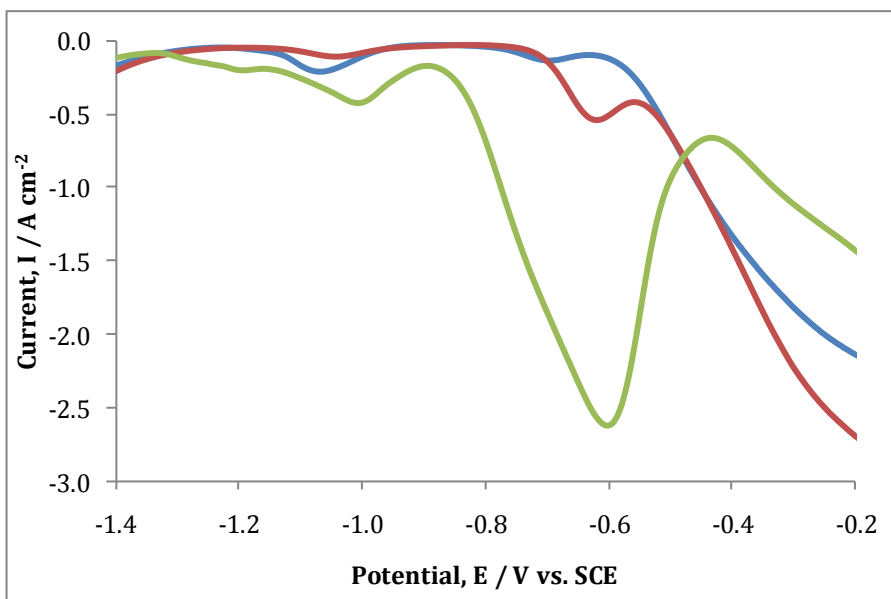


Figure 3.35: DPVs recorded for PPy/sul- $\beta$ CD in  $1.0 \times 10^{-3} \text{ mol dm}^{-3}$  paraquat (—),  $1.0 \times 10^{-3} \text{ mol dm}^{-3}$  diquat (—) and  $1.0 \times 10^{-3} \text{ mol dm}^{-3}$  paraquat in the presence of  $50.0 \times 10^{-3} \text{ mol dm}^{-3}$  diquat (—). All solutions were prepared in a  $0.1 \text{ mol dm}^{-3} \text{ Na}_2\text{SO}_4$  electrolyte solution. The potential was swept from  $-0.1 \rightarrow -1.4 \text{ V vs. SCE}$  using the optimum conditions outlined in Table 3.8. The polymer was prepared from a monomer solution of  $0.20 \text{ mol dm}^{-3}$  Py monomer and  $0.02 \text{ mol dm}^{-3}$  sul- $\beta$ CD and electropolymerised to the optimum conditions outlined in Table 3.7.

Table 3.12: Peak current values,  $I_p$ , and peak potentials,  $E_p$ , recorded for the reduction of  $V^{2+}$  to  $V^+$  and  $V^+$  to  $V^0$  for solutions of paraquat and diquat in  $0.1 \text{ mol dm}^{-3} \text{ Na}_2\text{SO}_4$  at the PPy/sul- $\beta$ CD electrode.

Concentration / $\text{mol dm}^{-3}$	$E_p^c$ / V vs. SCE	$I_p^c$ / $\text{A cm}^{-2}$
$1.0 \times 10^{-3} \text{ mol dm}^{-3}$ Paraquat	-0.7	$5.60 \times 10^{-5}$
$0.0 \text{ mol dm}^{-3}$ Diquat	-1.1	$1.72 \times 10^{-4}$
$1.0 \times 10^{-3} \text{ mol dm}^{-3}$ Diquat	-0.6	$2.10 \times 10^{-4}$
$0.0 \text{ mol dm}^{-3}$ Paraquat	-1.1	$6.88 \times 10^{-5}$
$1.0 \times 10^{-3} \text{ mol dm}^{-3}$ Paraquat	-0.6	$2.11 \times 10^{-3}$
$5.0 \times 10^{-2} \text{ mol dm}^{-3}$ Diquat	-1.1	$2.45 \times 10^{-4}$

### 3.9 Summary of Results

In summary, the results presented in this chapter illustrate the ease of electropolymerisation of pyrrole in the presence of a highly charged cyclodextrin. As shown in Section 3.3 the rate of electropolymerisation is high regardless of the size of the sul- $\beta$ CD. Moreover, no supporting electrolyte was used, ensuring that the only anion to dope the polypyrrole film was the anionic sul- $\beta$ CD. The ease of electropolymerisation was explained in terms of the high conductivity and high ionic strength of the solution of sul- $\beta$ CD. The applied potential, the concentration of pyrrole and the concentration of sul- $\beta$ CD all influenced the rate of electropolymerisation, with increasing potential, dopant and monomer concentration giving rise to higher rates of electropolymerisation. This is in good agreement with the extensive literature on the growth of polypyrrole in the presence of other dopants<sup>36,81</sup>. Using a rate law expression, the partial orders for the monomer and dopant were computed as 0.7 and 0.4, respectively. These fractional values confirmed the complexity of the polymerisation process.

The presence of the sul- $\beta$ CD was confirmed using EDX analysis. It was also shown that the large sul- $\beta$ CD was not expelled on reduction of the polymer. Instead, the film behaved as a cationic exchanger with reduction of the polymer accompanied by the ingress of cations from the supporting electrolyte. Using CV, a broad reduction wave, centred at about -0.4 V, was observed and this was attributed to the reduction of the polymer in the sodium containing electrolyte,  $\text{Ppy}^+ \text{ sul-}\beta\text{CD}^- + e^- \rightarrow \text{Ppy}^0 \text{ sul-}\beta\text{CD}^- \text{Na}^+$ . These cation exchange properties and the maintenance of the highly charged sul- $\beta$ CD within the polymer matrix are important as paraquat is electrochemically active in the potential window where polypyrrole is reduced.

In Section 3.4, results on the performance of the PPy/sul- $\beta$ CD in sensing paraquat are presented and discussed. As shown in Section 3.2, paraquat has complex electrochemistry with the reduction of  $\text{MV}^{2+}$  to  $\text{MV}^+$ , followed by the reduction of  $\text{MV}^+$  to  $\text{MV}^0$ . The reduced  $\text{MV}^0$  species is insoluble and forms an

adsorbed layer,  $MV^0_{(ads)}$ , which is oxidised at more electropositive potentials than the soluble  $MV^0_{(aq)}$  species. When the sul- $\beta$ CD doped polypyrrole film was cycled in a solution of paraquat, the reduction of  $MV^+$  to  $MV^0$  was clearly visible with a reduction wave centred at -1.1 V vs. SCE. The peak currents for this redox transition were higher at the polymer modified electrode than at gold or glassy carbon electrodes, giving enhanced detection of paraquat. Reduction of  $MV^{2+}$  to  $MV^+$  at the polymer-modified electrode was also visible using CV, CPA and DPV. Interestingly, polypyrrole films doped with PSS and  $SO_4^{2-}$  showed no signals for the reduction of paraquat, highlighting the significance of the sul- $\beta$ CD in the sensing of paraquat. When the polypyrrole was doped with SDS, which has surfactant properties, reduction of the paraquat was also observed indicating that there is some interaction between the cationic paraquat species and the SDS surfactant.

Using Michaelis-Menten kinetics, the interactions between  $MV^{2+}$  and the PPy/sul- $\beta$ CD were modelled in terms of enzyme kinetics. Using the measured current to represent the velocity of the reaction, Michaelis-Menten and Lineweaver-Burk plots were generated to give a  $K_m$  value of  $3.41 \times 10^{-4}$  mol  $dm^{-3}$ , suggesting a weak binding interaction between the  $MV^{2+}$  and the polymer modified electrode. Moreover, the fit between the electrochemistry data and the Michaelis-Menten theory suggest that once the viologen is reduced, the binding site, most likely the sul- $\beta$ CD dopant, is regenerated and available for further binding.

The optimisation of the PPy/sul- $\beta$ CD sensor included studies on the thickness and the potential at which the polymer was grown, the pH of the electrolyte and the supporting electrolyte. The optimal conditions are outlined in Table 3.7, and these were used throughout the remainder of the chapter. The optimum potential for forming the polymer was determined as 0.65 V vs. SCE. Lower peak currents for the reduction of paraquat were observed with lower formation potentials. This highlights again the role of the sul- $\beta$ CD dopant, as the dopant concentration increases with increasing formation potential. At higher

potentials, where overoxidation of the polymer occurs, the sensing was lost, indicating that the nature of the polymer network is also important. CV, DPV and CPA were used to determine the detection limit and sensitivity of the sensor. A detection limit of  $1.15 \times 10^{-5} \text{ mol dm}^{-3}$  was obtained for the reduction of  $\text{MV}^{2+} \rightarrow \text{MV}^+$  using CPA, while the sensitivity was determined as  $1.87 \text{ A cm}^{-2} \text{ M}^{-1}$ . The selectivity of the sensor was also investigated in the presence of both diquat and ametryn. Very good selectivity was obtained with an excess of ametryn, however poor selectivity was observed with an excess of diquat. This was explained by the fact that diquat has a similar electrochemistry to paraquat.

A comparative study with the PPy/SDS system was also undertaken. Using DPV a detection limit of  $1.00 \times 10^{-5} \text{ mol dm}^{-3}$  and a sensitivity of  $0.1 \text{ A cm}^{-2} \text{ M}^{-1}$  was obtained. In light of the similarity between the detection limits of paraquat using PPy/sul- $\beta$ CD and PPy/SDS, it poses the question as to whether paraquat is interacting electrostatically with sul- $\beta$ CD, forming an inclusion complex with the hydrophobic cavity, or alternatively a combination of both. This interaction will be studied at length in Chapter 6.

While the detection limits of approximately  $10 \mu\text{mol dm}^{-3}$  are good, they are still significantly higher than the permitted quantities within solution, as outlined by the EPA and EU<sup>5</sup>. Thus Chapter 4, looks at a further attempt to increase the detection limit of paraquat at a modified surface, by using another type of macrocyclic dopant, sulfonated-calix[4]arene. As reported by Guo *et al.*<sup>82</sup> paraquat shows a strong binding affinity for the anionic calixarene in solution, with an association constant,  $K_a$  of  $10^4 \text{ mol}^{-1} \text{ dm}^3$ .

### 3.10 References

1. M. Luque, A. Rios, and M. Valcarcel, *Analyst*, **123**, 2383, (1998).
2. M. A. El Mhammedi, M. Bakasse, and A. Chtaini, *J. Hazard. Mater.*, **145**, 1, (2007).
3. A. Walcarius and L. Lamberts, *J. Electroanal. Chem.*, **406**, 59, (1996).
4. P. Smith and D. Heath, *CRC Crit. Rev. Toxicol.*, **4**, 411, (1976).
5. U. M. F. de Oliveira, J. Lichtig, and J. C. Masini, *J. Braz. Chem. Soc.*, **15**, 735, (2004).
6. J. M. Zen, S. H. Jeng, and H. J. Chen, *Anal. Chem.*, **68**, 498, (1996).

7. Calderba.A and S. H. Yuen, *Analyst*, 90, 99, (1965).
8. S. H. Yuen, J. E. Bagness, and D. Myles, *Analyst*, 92, 375, (1967).
9. M. Ganesan, S. Natesan, and V. Ranganathan, *Analyst*, 104, 258, (1979).
10. P. Shivhare and V. K. Gupta, *Analyst*, 116, 391, (1991).
11. V. A. Simon and A. Taylor, *J. Chromatogr.*, 479, 153, (1989).
12. G. J. Moody, R. K. Owusu, and J. D. R. Thomas, *Analyst*, 112, 121, (1987).
13. G. J. Moody, R. K. Owusu, and J. D. R. Thomas, *Analyst*, 112, 1347, (1987).
14. G. J. Moody, R. K. Owusu, and J. D. R. Thomas, *Analyst*, 113, 65, (1988).
15. M. S. Ibrahim, I. S. Shehatta, and A. A. Al-Nayeli, *J. Pharm. Biomed. Anal.*, 28, 217, (2002).
16. D. Hallen, A. Schon, I. Shehatta, and I. Wadso, *J. Chem. Soc., Faraday Trans.*, 88, 2859, (1992).
17. I. Shehatta, *Reactive & Functional Polymers*, 28, 183, (1996).
18. P. M. S. Monk, C. Turner, and S. P. Akhtar, *Electrochim. Acta*, 44, 4817, (1999).
19. L. Xiao, G. G. Wildgoose, and R. G. Compton, *New J. Chem.*, 32, 1628, (2008).
20. C. L. Bird and A. T. Kuhn, *Chem. Soc. Rev.*, 10, 49, (1981).
21. Y. Matsui and A. Okimoto, *Bulletin of the Chemical Society of Japan*, 51, 3030, (1978).
22. P. M. S. Monk, *Fundamentals of Electroanalytical Chemistry*, J. Wiley & Sons LTD, Manchester, 2001.
23. P. H. Rieger, *Electrochemistry*, Chapman & Hall, Inc., New York, 1994.
24. B. Saad, M. Tahir, M. N. Ahmad, M. I. Saleh, and M. S. Jab, *Anal. Chim. Acta*, 285, 271, (1994).
25. A. Mirzoian and A. E. Kaifer, *Chemistry-a European Journal*, 3, 1052, (1997).
26. A. Ramanavicius, A. Ramanaviciene, and A. Malinauskas, *Electrochim. Acta*, 51, 6025, (2006).
27. A. R. Zanganeh and M. K. Amini, *Sens. Actuators, B*, 135, 358, (2008).
28. P. Chandrasekhar, *Conducting Polymers, Fundamentals and Applications, A Practical Approach*, Kluwer Academic Publishers, 3300 AH Dordrecht, THE NETHERLANDS, 1999.
29. W. Schuhmann, R. Lammert, B. Uhe, and H. L. Schmidt, *Sens. Actuators, B*, 1, 537, (1990).
30. J. Tamm, A. Alumaa, A. Hallik, and V. Sammelselg, *J. Electroanal. Chem.*, 448, 25, (1998).
31. P. C. Pandey, G. Singh, and P. K. Srivastava, *Electroanalysis*, 14, 427, (2002).
32. D. A. Reece, S. F. Ralph, and G. G. Wallace, *J. Membr. Sci.*, 249, 9, (2005).
33. T. Hernandez-Perez, M. Morales, N. Batina, and M. Salmon, *J. Electrochem. Soc.*, 148, C369, (2001).
34. D. A. McQuarrie and J. D. Simon, *Physical Chemistry, A Molecular Approach*, University Science Books, Sausalito, CA, 1997.
35. N. J. Selley, *Experimental Approach to Electrochemistry*, Edward Arnold (Publishers) Ltd., London, 1977.
36. S. M. Sayyah, S. S. Abd El-Rehim, and M. M. El-Deeb, *J. Appl. Polym. Sci.*, 90, 1783, (2003).
37. C. C. Harley, *Ph.D Thesis*, NUIM, 2009.

38. M. M. Ayad, *J. Mater. Sci. Lett.*, **22**, 1577, (2003).
39. M. M. Ayad, *J. Polym. Sci., Part A: Polym. Chem.*, **32**, 9, (1994).
40. M. M. Ayad, *J. Appl. Polym. Sci.*, **53**, 1331, (1994).
41. M. M. Ayad, *Polym. Int.*, **35**, 35, (1994).
42. M. Salmon, A. F. Diaz, A. J. Logan, M. Krounbi, and J. Bargon, *Mol. Cryst. Liq. Cryst.*, **83**, 265, (1982).
43. L. A. Samuelson and M. A. Druy, *Macromolecules*, **19**, 824, (1986).
44. J. M. Fonner, L. Forciniti, H. Nguyen, J. D. Byrne, Y. F. Kou, J. Syeda-Nawaz, and C. E. Schmidt, *Biomed. Mater.*, **3**, (2008).
45. A. A. A. Almario and R. L. T. Caceres, *J. Chil. Chem. Soc.*, **54**, 14, (2009).
46. G. Garcia-Belmonte, *Electrochem. Commun.*, **5**, 236, (2003).
47. T. V. Vernitskaya and O. N. Efimov, *Usp. Khim.*, **66**, 443, (1997).
48. T. Silk, Q. Hong, J. Tamm, and R. G. Compton, *Synth. Met.*, **93**, 59, (1998).
49. D. A. Kaplin and S. Qutubuddin, *Polymer*, **36**, 1275, (1995).
50. F. T. A. Vork, B. Schuermans, and E. Barendrecht, *Electrochim. Acta*, **35**, 567, (1990).
51. M. Hepel, *Electrochim. Acta*, **41**, 63, (1996).
52. J. Migdalski, T. Blaz, and A. Lewenstam, *Anal. Chim. Acta*, **322**, 141, (1996).
53. J. Gao, Y. Ren, and W. Ge, *Chin. J. Chem. Eng.*, **17**, 654, (2009).
54. S. Jalili and M. Akhavan, *Colloids Surf., A*, **352**, 99, (2009).
55. E. L. Kupila, J. Lukkari, and J. Kankare, *Synth. Met.*, **74**, 207, (1995).
56. S. B. Saidman and M. E. Vela, *Thin Solid Films*, **493**, 96, (2005).
57. O. Nunez, J. B. Kim, E. Moyano, M. T. Galceran, and S. Terabe, *J. Chromatogr. A*, **961**, 65, (2002).
58. A. Michalska and K. Maksymiuk, *Electroanalysis*, **10**, 177, (1998).
59. Q. Pei and R. Qian, *Synth. Met.*, **45**, 35, (1991).
60. O. Inganas, R. Erlandsson, C. Nylander, and I. Lundstrom, *J. Phys. Chem. Solids*, **45**, 427, (1984).
61. X. Du and Z. Wang, *Electrochim. Acta*, **48**, 1713, (2003).
62. T. H. Lu and I. W. Sun, *Talanta*, **53**, 443, (2000).
63. J. N. Ennis and P. C. Buxton, *Current Separations*, **17**, 75, (1998).
64. M. Santhiago, P. R. Lima, W. D. R. Santos, A. B. de Oliveira, and L. T. Kubota, *Electrochim. Acta*, **54**, 6609, (2009).
65. J. Njagi and S. Andreescu, *Biosens. Bioelectron.*, **23**, 168, (2007).
66. C. Hsien-Chang, C. Tzong-Jih, and C. Rong-Jyh, *Electroanalysis*, **10**, 1275, (1998).
67. S. W. Runge, B. J. F. Hill, and W. M. Moran, *CBE-Life Sciences Education*, **5**, 348, (2006).
68. J. E. Dowd and D. S. Riggs, *J. Biol. Chem.*, **240**, 863, (1965).
69. K. Kosmidis, V. Karalis, P. Argyrakis, and P. Macheras, *Biophys. J.*, **87**, 1498, (2004).
70. J. B. Houston and K. E. Kenworthy, *Drug Metab. Dispos.*, **28**, 246, (2000).
71. P. Wang, S. Q. Li, and J. Q. Kan, *Sens. Actuators, B*, **137**, 662, (2009).
72. E. A. Khudaish and W. R. Al-Farsi, *Electrochim. Acta*, **53**, 4302, (2008).
73. F. R. Shu and G. S. Wilson, *Anal. Chem.*, **48**, 1679, (1976).
74. C. J. Halkides and R. Herman, *J. Chem. Educ.*, **84**, 434, (2007).
75. J. Manso, M. L. Mena, P. Yáñez-Sedeño, and J. Pingarrón, *J. Electroanal. Chem.*, **603**, 1, (2007).

76. S. E. Group, Instrumental Methods in Electrochemistry, Eilis Horwood Limited, 1985.
77. B. Xu, N. Y. Gao, H. F. Cheng, C. Y. Hu, S. J. Xia, X. F. Sun, X. J. Wang, and S. G. Yang, *J. Hazard. Mater.*, 169, 586, (2009).
78. M. E. D. G. Azenha, H. D. Burrows, M. Canle, R. Coimbra, M. I. Fernandez, M. V. Garcia, M. A. Peiteado, and J. A. Santaballa, *J. Phys. Org. Chem.*, 16, 498, (2003).
79. E. A. Asongalem and A. Akintonwa, *Pestic. Sci.*, 53, 1, (1998).
80. H. M. Colquhoun, E. P. Goodings, J. M. Maud, J. F. Stoddart, J. B. Wolstenholme, and D. J. Williams, *J. Chem. Soc., Perkin Trans.* 2,607, (1985).
81. D. Kumar and R. C. Sharma, *Eur. Polym. J.*, 34, 1053, (1998).
82. D. S. Guo, L. H. Wang, and Y. Liu, *J. Org. Chem.*, 72, 7775, (2007).

**Calixarene Modified Polypyrrole for the Detection of Paraquat****4.1 Introduction**

The focus of this thesis centres on the characterisation and optimisation of a modified polypyrrole sensor for the electrochemical detection of harmful analytes. In particular, methyl viologen also known as paraquat (PQ) was chosen as the analyte. The results presented in Chapter 3 discussed in detail the behaviour of a modified PPy/sul- $\beta$ CD film and its sensing properties towards paraquat. The reduction of  $MV^+$  to  $MV^0$  at -1.18 V vs. SCE was monitored using cyclic voltammetry (CV), as the signal for the reduction of  $MV^{2+}$  to  $MV^+$  was lost at low concentrations of paraquat. This was due to the redox activity of the polymer masking the signal. Using constant potential amperometry (CPA), a detection limit of  $1.56 \times 10^{-5}$  mol dm<sup>-3</sup> was recorded for the reduction of  $MV^{2+}$  to  $MV^+$ . However, this limit of detection is still above the range of acceptable levels within the environment<sup>1</sup>.

Interestingly, Guo *et al.*<sup>2,3</sup> reported a strong binding affinity between *p*-sulfonated-calix[4]arene (sul-calix[4]) and the dicationic species of paraquat,  $MV^{2+}$ . As mentioned in Chapter 3, Section 3.3.3, polymer films generally offer a larger surface area than metallic substrates and modification with a suitable dopant can promote a higher sensitivity<sup>4</sup>. No prior knowledge is available regarding the interaction of sul- $\beta$ CD and paraquat, but this will be discussed at length in Chapter 6. The complex formed between sul-calix[4] and paraquat is encouraging with respect to further improvement in sensing paraquat. Hence, this chapter serves as a comparative study between the properties and sensitivity of PPy/sul- $\beta$ CD and PPy/sul-calix[4] towards paraquat. The initial section of this chapter investigates the formation and characterisation of the PPy/sul-calix[4] film. Then, the response of paraquat is monitored at the modified electrode. This is followed by the optimisation of the sensor to a fixed concentration of  $5.0 \times 10^{-3}$  mol dm<sup>-3</sup> paraquat in a 0.1 mol dm<sup>-3</sup> Na<sub>2</sub>SO<sub>4</sub>

electrolyte solution. Due to the strong interaction reported between paraquat and sul-calix[4]<sup>2</sup>, it was hypothesised that this large measure of complexation would inhibit interference and thus, generate a selective sensor.

#### 4.2 Formation and Characterisation of the PPy/sul-calix[4] films

As discussed in Chapter 3, Section 3.3.1, PPy doped with sul- $\beta$ CD shows a much higher growth rate in contrast to other simple dopants like  $\text{Cl}^-$  upon electropolymerisation. This is depicted in Chapter 3, Section 3.3.1, Figure 3.7. The increase in the rate of electropolymerisation is attributed to the highly charged nature of sul- $\beta$ CD, in which an average of 7-11 sulfonated groups are completely ionised within solution. In this chapter, the sul-calix[4] dopant as illustrated in Figure 4.1, was used. This negatively-charged macrocyclic cage is similar to that of sul- $\beta$ CD. It has an internal cavity of approximately 5.2 Å in size<sup>5</sup>. The upper rim is completely ionised with four negative sites at almost the entire pH range and also a hydroxyl group on the lower rim is dissociated with a  $\text{p}K_a$  of 3.26<sup>6</sup>. The dissociation of a second hydroxyl group has a  $\text{p}K_a$  of 12.30<sup>6</sup>, indicating that over a large pH range sul-calix[4] is penta-anionic, as shown in Figure 4.1.

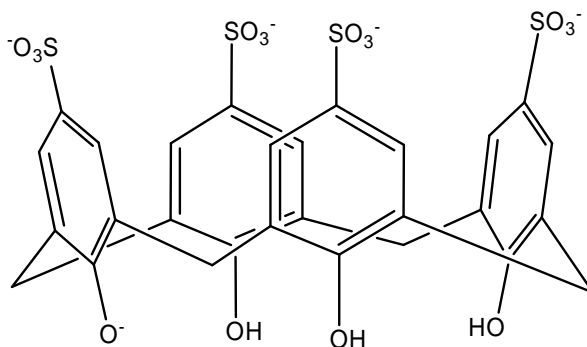


Figure 4.1: Chemical structure of sul-calix[4].

Electropolymerisation of Py occurs upon the application of an anodic potential which oxidises the monomer in the presence of a dopant anion generating a polymer film on a substrate<sup>7</sup>. Analysis of the current-time plots for the

formation of PPy/sul-calix[4], shows a steady state current value of  $2 \text{ mA cm}^{-2}$ . This is illustrated by the red trace in Figure 4.2 (a). In contrast, the steady state current recorded for PPy/sul- $\beta$ CD was  $5 \text{ mA cm}^{-2}$ . Thus, there is a change in current by more than half for the PPy/sul-calix[4] polymer. The blue trace in Figure 4.2 (a) depicts the growth curve for the polymer of PPy doped with sul- $\beta$ CD. Both polymers were formed at a fixed potential of  $0.65 \text{ V vs. SCE}$ , to a fixed charge of  $25 \text{ mC}$ . The difference in current for the growth of each polymer is not unexpected given that sul-calix[4] has fewer anionic sites than sul- $\beta$ CD. This is evident by quantifying the ionic strength for identical concentrations of each dopant, which are displayed in Table 4.1. The ionic strength was calculated in accordance with Equation 3.5. Moreover, the ionic strength for sul-calix[4] is still higher than small mobile anions for example,  $\text{Cl}^-$  or  $\text{SO}_4^{2-}$  at equivalent concentrations. Thus, this is a suitable choice of dopant for the detection of paraquat.

Continuing with the analysis regarding the formation of PPy/sul-calix[4], another important parameter in polymerisation is the applied potential. As reported by Otero and co-workers<sup>8,9</sup> and Satoh *et al.*<sup>10</sup>, this can have an impact on the formation and properties of the film. A further consideration is that sulfonated calixarenes are well known electroactive reagents<sup>11,12</sup>. It is imperative that oxidation of sul-calix[4] does not occur simultaneously to polymerisation of Py. Diao and Liu<sup>13</sup> reported that sulfonated-calix[6]arene (sul-calix[6]), is oxidised at approximately  $0.8 \text{ V vs. SCE}$  and as the pH increases, the oxidation shifts to more negative potentials. This is connected with the degree of protonation at lower pH values. Also, it has been reported that the oxidation of sul-calix[4] is not as difficult as sul-calix[6] or sul-calix[8]<sup>14</sup>. Based on this information, the applied potential for the formation of PPy/sul-calix[4] was confined to a range of  $0.55$  to  $0.75 \text{ V vs. SCE}$ . The influence of the applied potential on the rate of polymerisation is illustrated in Figure 4.2 (b). The rate at which a charge density of  $0.13 \text{ C cm}^{-2}$  is achieved increases with higher applied potentials. Similar findings were recorded by Du *et al.*<sup>15</sup> for the electro-polymerisation of 3,4-ethylenedioxythiophene (EDOT) doped with  $\text{ClO}_4^-$  with an increase in current and rate of polymerisation upon increasing the applied

potential. Prior to assessing the morphology at a range of film thicknesses, the influence of charge on the PPy/sul-calix[4] film was analysed.

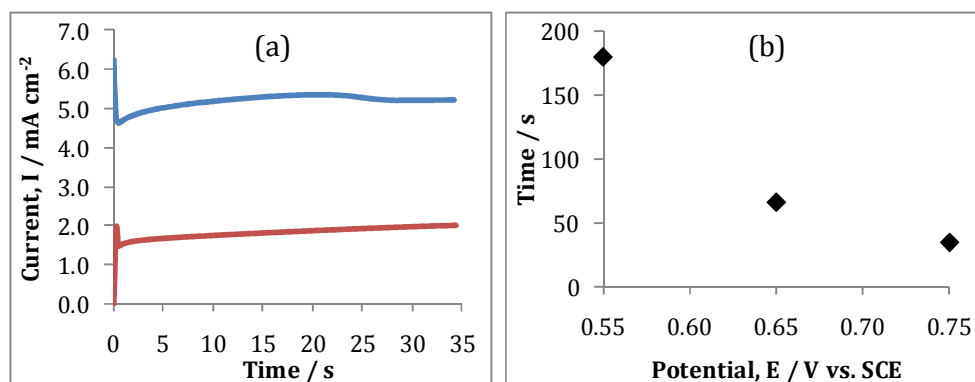


Figure 4.2: (a) Current-time plots for the formation of (—) PPy/sul-βCD and (—) PPy/sul-calix[4] at a fixed applied potential of 0.65 V vs. SCE to a charge of 25 mC. The polymers were deposited on Au, from a monomer solution containing 0.20 mol dm<sup>-3</sup> Py monomer and 0.02 mol dm<sup>-3</sup> sul-βCD or 0.02 mol dm<sup>-3</sup> sul-calix[4]. (b) Time to reach a charge density of 0.13 C cm<sup>-2</sup> as a function of applied potential for the formation of PPy/sul-calix[4].

Table 4.1: Ionic strength values calculated in accordance with Equation 3.5, Section 3.3.1, Chapter 3, for equal concentrations of sul-calix[4] and sul-βCD.

Dopant	Concentration / mol dm <sup>-3</sup>	Ionic Strength / mol dm <sup>-3</sup>
sul-calix[4]	0.02	0.30
sul-βCD	0.02	0.56
NaCl	0.02	0.02
Na <sub>2</sub> SO <sub>4</sub>	0.02	0.06

The effect of varying the charge density during the formation of PPy/sul-calix[4] on its response in a 0.10 mol dm<sup>-3</sup> Na<sub>2</sub>SO<sub>4</sub> electrolyte solution is shown in Figure 4.3. Each polymer was formed at a fixed potential of 0.55 V vs. SCE from a solution containing 0.20 mol dm<sup>-3</sup> Py monomer and 0.02 mol dm<sup>-3</sup> sul-calix[4]. The plot clearly shows an increase in peak current as a function of electropolymerisation charge consumed during the formation for Ppy/sul-calix[4]. Since film thickness is associated with electropolymerisation charge,

increased charge yields a thicker film and hence a larger surface area<sup>4</sup>. The broad reduction wave centred at about -0.4 to -0.6 V vs. SCE corresponds to the reduction of PPy/sul-calix[4]. As this dopant is large, this polymer is likely to exhibit cation exchange properties<sup>16</sup>. Therefore, reduction is accompanied by the ingress of Na<sup>+</sup> cations from the electrolyte solution. As documented by Silk *et al.*<sup>17</sup>, polymer thickness also has an influence on the surface morphology and porosity. The reduction wave increases in intensity and there is a corresponding cathodic shift in the peak potential with increasing film thickness. This indicates that the reduction of the polymer and ingress of Na<sup>+</sup> becomes hindered with thicker polymer films.

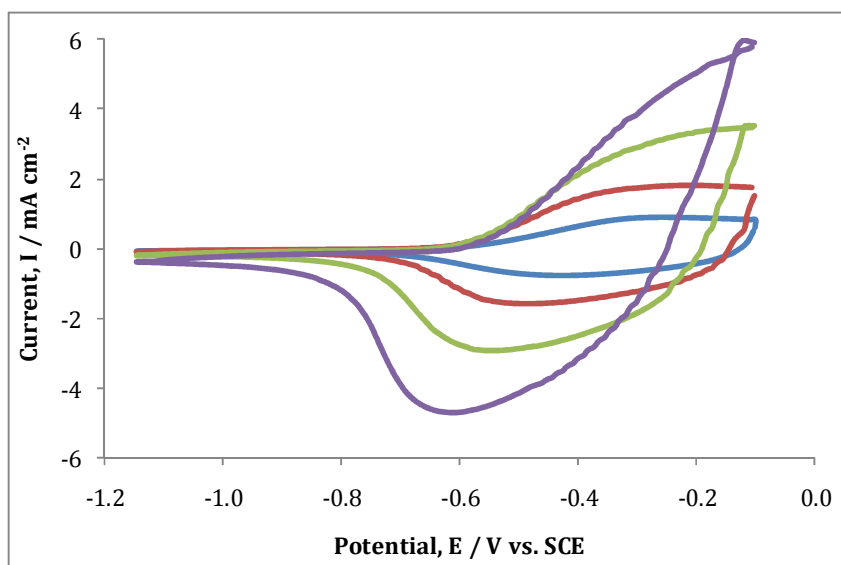


Figure 4.3: CVs of PPy/sul-calix[4] in 0.10 mol dm<sup>-3</sup> Na<sub>2</sub>SO<sub>4</sub> solution, measuring a pH of 7.0. The potential was swept from -0.10 V → -1.15 V vs. SCE at 50 mV s<sup>-1</sup>. Each polymer was prepared from a 0.20 mol dm<sup>-3</sup> Py monomer and 0.02 mol dm<sup>-3</sup> sul-calix[4] solution on Au. The applied potential was fixed at 0.55 V vs. SCE until the following charge densities were reached; (—) 0.13, (—) 0.26, (—) 0.51 and (—) 1.02 C cm<sup>-2</sup>.

#### 4.2.1 SEM and EDX

The morphology of the PPy/sul-calix[4] film was imaged using scanning electron microscopy (SEM) and the results are shown in Figure 4.4 and Figure 4.5. The SEM micrographs in Figure 4.4 were carried out at Tyndall National

Institute, University College Cork. The PPy/sul-calix[4] film was grown to a charge density of  $1.8 \text{ C cm}^{-2}$  at an applied potential of  $0.70 \text{ V vs. SCE}$  on a Au surface. It is evident from Figure 4.4 (a) that this polymer has a rough surface in contrast to that of PPy/Cl<sup>-</sup>. However, it is similar to a PPy/sul- $\beta$ CD film, as illustrated in Chapter 3, Section 3.3.4, Figure 3.14. At higher magnification, as shown in Figure 4.4 (b), it appears that the PPy/sul-calix[4] polymer is quite porous. This is in contrast to the rough compact polymer obtained for PPy/sul- $\beta$ CD. Given the similarity between sul-calix[4] and sul- $\beta$ CD in terms of both being macrocyclic structures, this difference in surface morphology is unexpected. As mentioned in Section 4.2, the ease of oxidation of sulfonated calixarenes, increases with fewer phenolic rings. As reported by Diao *et al.*<sup>11</sup>, the oxidation of sul-calix[4] shows an anodic wave when the potential ranges from  $0.70$  to  $0.90 \text{ V vs. SCE}$ . Thus, a consequence of electropolymerising at an applied potential of  $0.70 \text{ V vs. SCE}$  may be the oxidation of the dopant, which in turn, may alter the morphology of the polymer. To assess the influence of potential on the morphological properties of PPy/sul-calix[4], an SEM micrograph was recorded for PPy/sul-calix[4] prepared at  $0.55 \text{ V vs. SCE}$  to a similar charge density of  $1.6 \text{ C cm}^{-2}$ . As shown in Figure 4.5 (a), a similar rough morphology comparable to that of Figure 4.4 (a) is observed. However, upon closer inspection, Figure 4.5 (b) shows a more compact polymer comparable to that of PPy/sul- $\beta$ CD, but slightly different to that of Figure 4.4 (b). Hence, the applied potential of electropolymerisation has an impact on the morphology of the polymer. Moreover, it is for this reason that the applied potential was kept below  $0.70 \text{ V vs. SCE}$ , but was still sufficiently high for polymerisation to occur at  $0.55 \text{ V vs. SCE}$ .

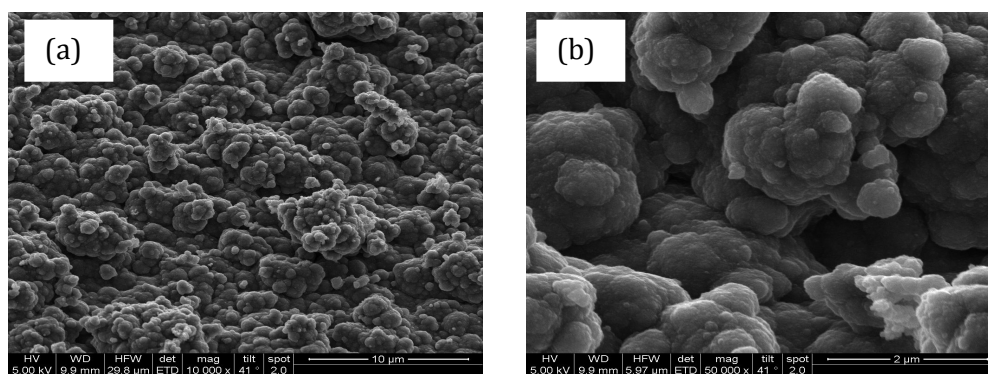


Figure 4.4: SEM micrographs of PPy/sul-calix[4] at the following magnifications; (a) 10,000 and (b) 50,000. This polymer was prepared from a  $0.20 \text{ mol dm}^{-3}$  Py and  $0.02 \text{ mol dm}^{-3}$  sul-calix[4] solution. Electropolymerisation was carried out at  $0.70 \text{ V}$  vs. SCE on Au until a charge density of  $1.8 \text{ C cm}^{-2}$  was reached.

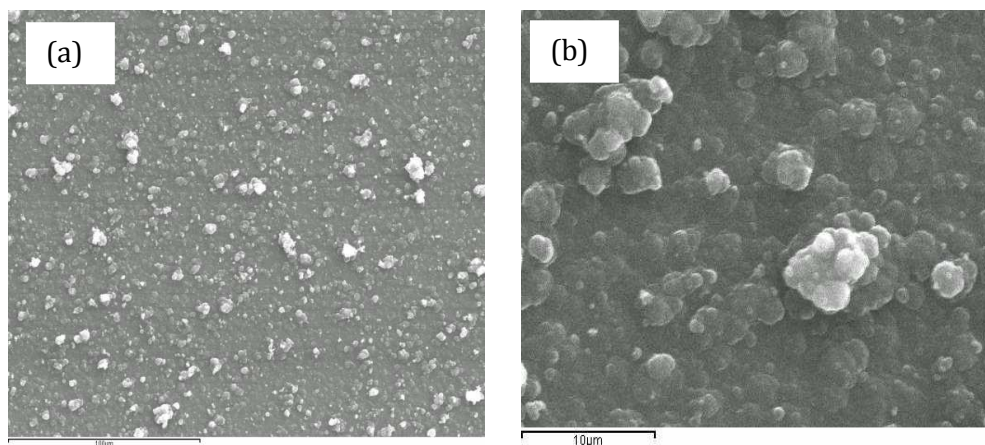


Figure 4.5: SEM micrographs of a PPy/sul-calix[4] film electropolymerised on GC. An applied potential of  $0.55 \text{ V}$  vs. SCE was used until a charge density of  $1.6 \text{ C cm}^{-2}$  was reached. The polymer was analysed at the following magnifications: (a) 1,000 and (b) 10,000. The polymer was prepared from a  $0.20 \text{ mol dm}^{-3}$  Py and  $0.02 \text{ mol dm}^{-3}$  sul-calix[4] solution.

As the solution of sul-calix[4] is sufficiently conducting similar to sul- $\beta$ CD, it does not require the presence of a supporting electrolyte in the monomer solution. This ensures that only sul-calix[4] is doped along the PPy backbone during polymerisation. To confirm the presence of sul-calix[4] energy dispersive X-ray analysis (EDX) was carried out on a freshly oxidised polymer and the spectrum is shown in Figure 4.6. The monomer solution contains 10 fold excess of Py monomer to sul-calix[4]. Hence, identification of PPy is evident from the

large broad C and N X-ray signals recorded within a range of 0-400 electron Volts (eV). Definitive evidence that sul-calix[4] is within the polymer is through the S and O peaks at 500 and 2,300 eV, respectively, which are evident from this EDX analysis.

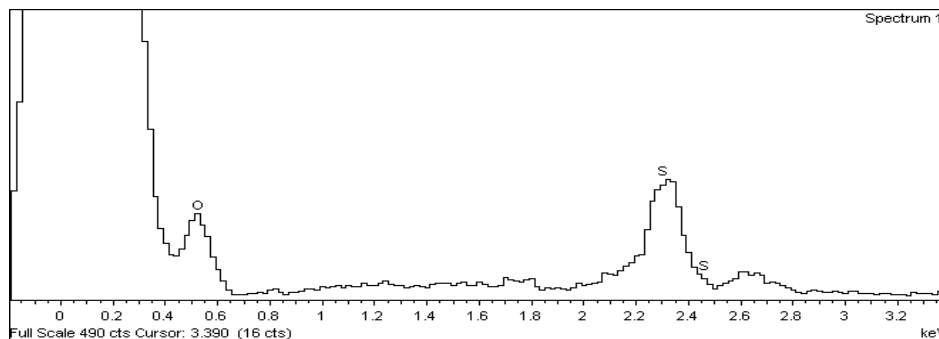
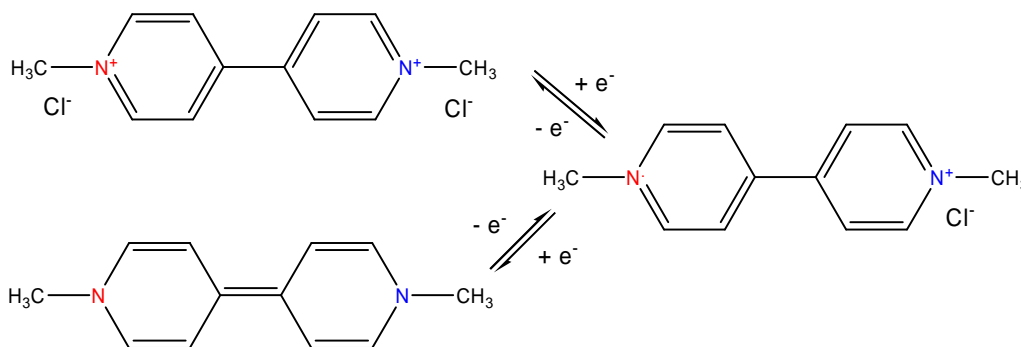


Figure 4.6: EDX analysis of a PPy/sul-calix[4] polymer electropolymerised at an applied potential of 0.55 V vs. SCE to a charge density of 1.6 C cm<sup>-2</sup> on Au. The polymer was prepared from a 0.20 mol dm<sup>-3</sup> Py and 0.02 mol dm<sup>-3</sup> sul-calix[4] solution.

As indicated earlier, PPy/sul-calix[4] may act as a cation exchanger. It has been proposed by Temsamani *et al.*<sup>18</sup> that when PPy is reduced to a neutral state, large anionic dopants are not released from the polymer matrix. This was confirmed in Chapter 3, Section 3.3.4 for the PPy/sul-βCD polymer using EDX analysis. The X-ray signal corresponding to Na<sup>+</sup> indicated that the dopant was immobilised within the polymer and required the ingress of the mobile cations to neutralise the polymer. Sul-calix[4] and sul-βCD are referred to as macrocyclic molecules<sup>14</sup>. In comparing the current responses with CV of PPy/sul-βCD and PPy/sul-calix[4] in 0.1 mol dm<sup>-3</sup> Na<sub>2</sub>SO<sub>4</sub> solution, they exhibit similar redox activity at approximately -0.4 V vs. SCE. The similarity of the peak currents and peak potentials corresponds to the influx of Na<sup>+</sup> into the polymer matrix. These CVs are depicted in Chapter 3, Section 3.3.3, Figure 3.13 and Figure 4.3, respectively. Hence, sul-calix[4] is retained within the polymer upon reduction. Indeed, the data presented in Figure 4.3 are consistent with cation exchange. This is in good agreement with the literature, in which Bidan and co-workers<sup>19-21</sup>, stated that sul-calix[4] can be immobilised in a PPy film and retain recognition properties.

### 4.3 Paraquat at the Modified Electrode

Paraquat exhibits redox activity at a reduction potential window<sup>22,23</sup>. Within this window, additional processes of adsorption and comproportionation can occur<sup>24</sup>. The two step redox process of  $MV^{2+}$  to  $MV^+$  and  $MV^+$  to  $MV^0$ , as depicted in Scheme 4.1 is discussed in detail in Chapter 3, Section 3.2.



Scheme 4.1: Schematic illustration for the reduction of paraquat from  $MV^{2+}$  to  $MV^+$  and  $MV^+$  to  $MV^0$ .

The response recorded upon cycling the sul-calix[4] doped polymer in a  $5.0 \times 10^{-3}$  mol  $dm^{-3}$  paraquat solution in 0.1 mol  $dm^{-3}$   $Na_2SO_4$  electrolyte solution is shown in Figure 4.7. The response of paraquat at the PPy/sul-calix[4] film shows two clearly identifiable reduction peaks at -0.78 and -1.12 V vs. SCE and two corresponding oxidation peaks at -0.60 and -0.90 V vs. SCE. There is also a low capacitance current. On comparing the response for an identical concentration of paraquat at a PPy/sul- $\beta$ CD film, (Chapter 3, Section 3.4, Figure 3.19 (a)) the signals are clearly different. The response of paraquat at the PPy/sul- $\beta$ CD film shows two reduction peaks and relatively small oxidation peaks, with a background signal. The redox signals for paraquat recorded at the PPy/sul-calix[4] film indicates an interaction of each redox state with PPy/sul-calix[4]. However, the peak potentials are quite characteristic of that recorded at Au. This is depicted in Table 4.2. This poses the question as to whether it is Au or the polymer film which is detecting the redox species of  $MV^{2+}$ ,  $MV^+$  and  $MV^0$ . Even though, there is no characteristic peak of adsorption which occurs at -0.90 V vs. SCE at bare Au, as discussed in Chapter 3, Section 3.2, a further study was

carried out using a Pt substrate. This was employed as the working electrode. As  $\text{H}_{2(\text{g})}$  evolution commonly occurs at negative potentials at a platinum surface<sup>25</sup>, modification at the surface with a polymer film prevents this phenomenon. This is illustrated by the red trace in Figure 4.8. The blue trace corresponds to the current responses of paraquat at bare Pt, in which  $\text{H}_2$  evolution occurs at negative potentials greater than  $-1.1$  V vs. SCE. Both CVs were carried out under identical conditions, whereby only the surface of the working electrode differed. The notable difference between the CVs indicates that indeed paraquat is interacting with the polymer film and not at the bare substrate.

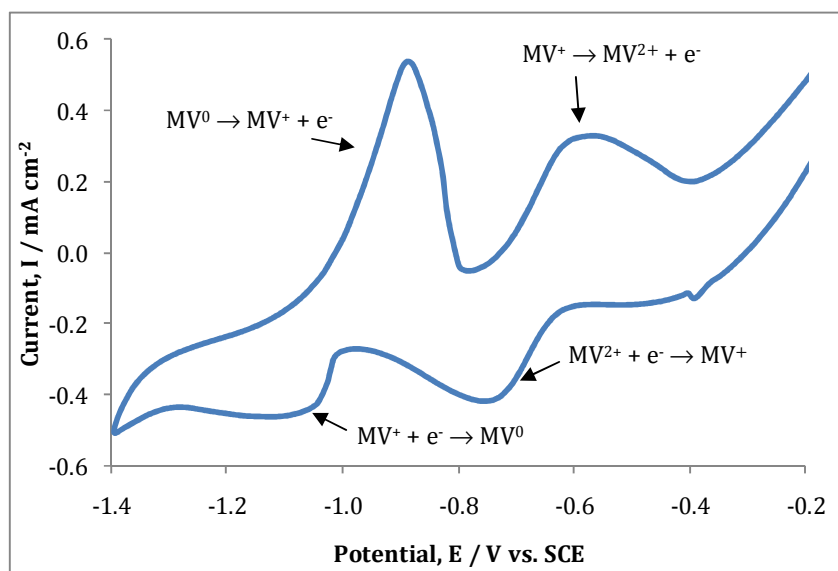


Figure 4.7: CV recorded for  $5.00 \times 10^{-3}$  mol  $\text{dm}^{-3}$  paraquat in  $0.10$  mol  $\text{dm}^{-3}$   $\text{Na}_2\text{SO}_4$  electrolyte solution measuring a pH of 7.0 at the PPy/sul-calix[4] film. The potential was swept from  $-0.10 \rightarrow -1.40$  V vs. SCE at  $100$   $\text{mV s}^{-1}$ . The polymer film was prepared from a  $0.20$  mol  $\text{dm}^{-3}$  Py monomer and  $0.02$  mol  $\text{dm}^{-3}$  sul-calix[4] solution, in which an oxidative potential was applied of  $0.55$  V vs. SCE at Au until a charge of  $0.13$   $\text{C cm}^{-2}$  was reached.

Table 4.2: Peak potentials,  $E_p$ , for the oxidation and reduction of  $5.00 \times 10^{-3}$  mol dm<sup>-3</sup> paraquat in 0.1 mol dm<sup>-3</sup> Na<sub>2</sub>SO<sub>4</sub> electrolyte solutions at Au and a modified Au surface with PPy/sul-calix[4].

Substrate	$E_p^C$ / V vs. SCE	$E_p^A$ / V vs. SCE
Au	-0.71	-0.72
	-1.01	-0.89
PPy/sul-calix[4]	-0.78	-0.57
	-1.12	-0.88

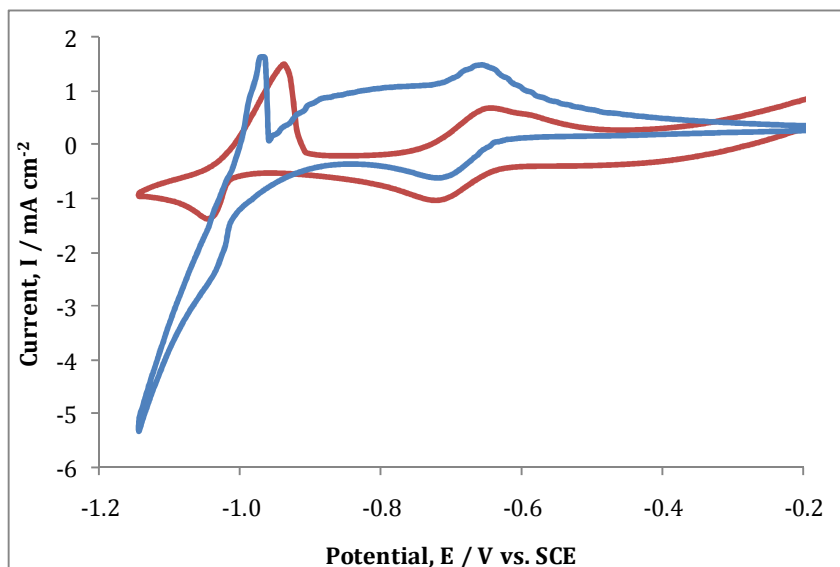


Figure 4.8: CV of  $5.00 \times 10^{-3}$  mol dm<sup>-3</sup> paraquat in 0.10 mol dm<sup>-3</sup> Na<sub>2</sub>SO<sub>4</sub> solution, measuring a pH of 7.0, at Pt (—) and a modified Pt substrate with PPy/sul-calix[4] (—). The potential was swept from -0.10 → -1.15 V vs. SCE at a scan rate of 50 mV s<sup>-1</sup>. The polymer film was prepared from a solution of 0.20 mol dm<sup>-3</sup> Py monomer and 0.02 mol dm<sup>-3</sup> sul-calix[4]. A potential of 0.55 V vs. SCE was applied for the electropolymerisation of PPy/sul-calix[4] until a charge of 0.2 C cm<sup>-2</sup> was reached.

#### 4.4 Optimisation of Paraquat at the Polymer film

Clearly the polymer film shows an affinity for all redox states of paraquat, in contrast to the PPy/sul-βCD which has a preference for the reduction of MV<sup>+</sup> to MV<sup>0</sup>. In light of these differences, the optimum conditions for sensing may not be identical for both polymers. Hence, this section investigates the influence of the applied potential of polymerisation, charge density, pH and scan rate in

sensing a fixed concentration of  $5.0 \times 10^{-3} \text{ mol dm}^{-3}$  paraquat in  $0.1 \text{ mol dm}^{-3}$   $\text{Na}_2\text{SO}_4$  electrolyte solution at the modified electrode.

#### 4.4.1 Potential Window

Figure 4.9 depicts the response of PPy/sul-calix[4] towards paraquat at varying potential windows. As shown in Figure 4.9 (a), applying a scan rate of  $100 \text{ mV s}^{-1}$  and sweeping within a smaller potential window to that of the optimised window for PPy/sul- $\beta$ CD ( $-0.10 \rightarrow -1.40 \text{ V vs. SCE}$ ), enhances the peak current for the reduction of  $\text{MV}^{2+}$  and  $\text{MV}^+$ . Reducing the potential window further was assessed and the results are shown in Figure 4.9 (b). When the potential window is confined to the first reduction process of  $\text{MV}^{2+}$  to  $\text{MV}^+$ , this shows no increased benefit and so the optimum potential window for detection is  $-0.10 \rightarrow -1.15 \text{ V vs. SCE}$ . The next section investigates the influence of the applied potential on the formation of PPy/sul-calix[4].

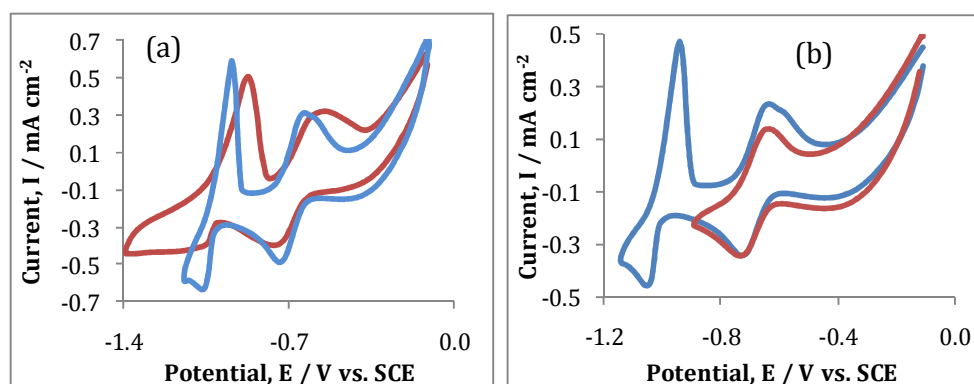


Figure 4.9: CVs recorded in  $5.0 \times 10^{-3} \text{ mol dm}^{-3}$  paraquat in  $0.1 \text{ mol dm}^{-3}$   $\text{Na}_2\text{SO}_4$  electrolyte solution at a pH of 7.0 at PPy/sul-calix[4], at the following conditions; (a) scan rate of  $100 \text{ mV s}^{-1}$  and a potential window of (—)  $-0.10 \rightarrow -1.40 \text{ V vs. SCE}$  and (—)  $-0.10 \rightarrow -1.15 \text{ V vs. SCE}$ , (b) scan rate of  $50 \text{ mV s}^{-1}$  within a potential window of (—)  $-0.10 \rightarrow -1.15 \text{ V vs. SCE}$  and (—)  $-0.10 \rightarrow -0.90 \text{ V vs. SCE}$ . Each polymer was prepared from a  $0.20 \text{ mol dm}^{-3}$  Py monomer and  $0.02 \text{ mol dm}^{-3}$  sul-calix[4] solution. Polymerisation was carried out at an applied potential of  $0.55 \text{ V vs. SCE}$  at Au until a charge density of  $0.13 \text{ C cm}^{-2}$  was reached.

#### 4.4.2 Applied Potential for the Polymerisation of Py

Given the redox properties of sul-calix[4] as previously discussed in Section 4.2, sul-calix[4] is prone to oxidation within a range of 0.7 → 0.9 V vs. SCE<sup>11</sup>. Hence, the range of applied potentials for electropolymerisation is somewhat limited. Potentials lower than 0.5 V vs. SCE are generally quite poor at initiating nucleation and hence polymerisation<sup>26,27</sup>. The current signals recorded for  $5.0 \times 10^{-3}$  mol dm<sup>-3</sup> paraquat, in which Ppy/sul-calix[4] films were prepared at different electropolymerisation potentials are shown in Figure 4.10. It is evident from the overlaid CVs that polymer growth at 0.55 V vs. SCE produces the largest currents in sensing paraquat. This is further illustrated with the summary of peak currents and peak potentials listed in Table 4.3. Increasing the applied potential to within close proximity of the oxidation of sul-calix[4] may effect the quantity of anionic calixarene available to dope the polymer matrix. Moreover, the detection of paraquat can be compromised if sul-calix[4] is oxidised during the formation of PPy/sul-calix[4].

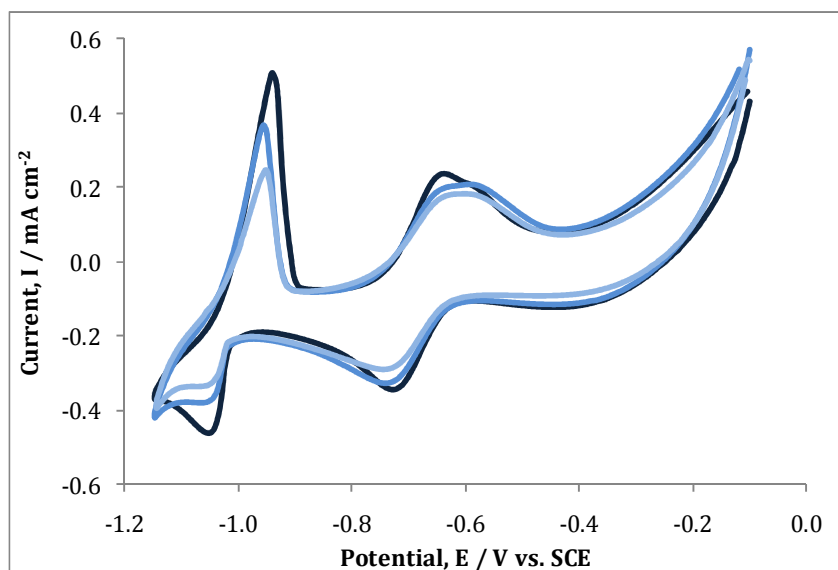


Figure 4.10: CVs of  $5.0 \times 10^{-3}$  mol dm<sup>-3</sup> paraquat in 0.1 mol dm<sup>-3</sup> Na<sub>2</sub>SO<sub>4</sub> solution at a pH of 7.0. The potential was swept from -0.10 → -1.15 V vs. SCE applying a scan rate of 50 mV s<sup>-1</sup>. Each polymer was prepared from a 0.20 mol dm<sup>-3</sup> Py monomer and 0.02 mol dm<sup>-3</sup> sul-calix[4] solution. Electropolymerisation occurred at the applied potentials of (—) 0.55 V, (—) 0.65 V and (—) 0.75 V vs. SCE until a charge density of 0.13 C cm<sup>-2</sup> was reached.

Table 4.3: Data outlining the cathodic and anodic peak currents ( $I_p$ ) and peak potentials ( $E_p$ ) for the redox reactions of  $MV^{2+}$  to  $MV^+$  and  $MV^+$  to  $MV^0$ , taken from the results illustrated in Figure 4.10.

Applied Potential / V vs. SCE	$E_p^C$ / V vs. SCE	$I_p^C$ / A cm <sup>-2</sup>	$E_p^A$ / V vs. SCE	$I_p^A$ / A cm <sup>-2</sup>
0.55	-0.73	$1.4 \times 10^{-4}$	-0.64	$2.3 \times 10^{-4}$
	-1.10	$1.1 \times 10^{-4}$	-0.95	$5.6 \times 10^{-4}$
0.65	-0.74	$1.2 \times 10^{-4}$	-0.63	$2.1 \times 10^{-4}$
	-1.10	$9.2 \times 10^{-5}$	-0.96	$4.2 \times 10^{-4}$
0.75	-0.74	$8.2 \times 10^{-5}$	-0.63	$1.8 \times 10^{-4}$
	-1.10	$4.3 \times 10^{-5}$	-0.96	$3.0 \times 10^{-4}$

#### 4.4.3 Electropolymerisation Charge

The dependency of charge density involved in the electro-deposition of PPy/sul-calix[4] on Au and its effect in detecting a fixed concentration of  $5.0 \times 10^{-3}$  mol dm<sup>-3</sup> paraquat is illustrated in Table 4.4. Electropolymerisation charge is linked with polymer thickness<sup>28</sup>. According to Holdcroft and Funt<sup>29</sup>, as the charge density increases, there is a corresponding increase in film thickness. This provides a larger surface area for sensing, in theory enhancing the current density responses. The current responses of paraquat at PPy/sul-calix[4], prepared at varying charge densities, show no significant variation in current. Hence, a charge density of 0.13 C cm<sup>-2</sup> was chosen as the optimum, since the time taken for Py doped with sul-calix[4] to electropolymerise to this charge was the shortest.

Table 4.4: Peak currents ( $I_p$ ) and peak potentials ( $E_p$ ) corresponding to the redox states of  $MV^{2+} \rightarrow MV^+$  and  $MV^+ \rightarrow MV^0$  for  $5.0 \times 10^{-3}$  mol  $dm^{-3}$  paraquat in 0.1 mol  $dm^{-3}$   $Na_2SO_4$  solution at a pH of 7.0, recorded at a PPy/sul-calix[4]. The CVs were recorded within a potential window of -0.10  $\rightarrow$  -1.15 V vs. SCE at a scan rate of 50  $mV s^{-1}$ . Each polymer was prepared from a 0.20 mol  $dm^{-3}$  Py monomer and 0.02 mol  $dm^{-3}$  sul-calix[4] solution using an applied potential of 0.55 V vs. SCE until a charge density of either 0.13, 0.26, 0.51 or 1.02  $C cm^{-2}$  was reached.

Charge Density/ $C cm^{-2}$	$E_p^C /$ V vs. SCE	$I_p^C /$ $A cm^{-2}$	$E_p^A /$ V vs. SCE	$I_p^A /$ $A cm^{-2}$
0.13	-0.73	$1.4 \times 10^{-4}$	-0.64	$2.3 \times 10^{-4}$
	-1.10	$1.1 \times 10^{-4}$	-0.94	$5.6 \times 10^{-4}$
0.26	-0.72	$1.9 \times 10^{-4}$	-0.65	$2.6 \times 10^{-4}$
	-1.10	$9.4 \times 10^{-5}$	-0.94	$6.0 \times 10^{-4}$
0.51	-0.72	$1.8 \times 10^{-4}$	-0.65	$2.4 \times 10^{-4}$
	-1.10	$1.3 \times 10^{-4}$	-0.95	$5.7 \times 10^{-4}$
1.02	-0.72	$1.7 \times 10^{-4}$	-0.65	$2.2 \times 10^{-4}$
	-1.10	$1.4 \times 10^{-4}$	-0.96	$5.6 \times 10^{-4}$

#### 4.4.4 Effect of pH on the Paraquat signal

As PPy is highly conducting in acidic media and becomes insulating at alkaline pHs<sup>30</sup>, monitoring the pH over the pH spectrum is useful in optimising the faradaic current response for paraquat at the modified electrode. The results shown in Figure 4.11 illustrate that there is no significant influence of pH in the range between 5.0 and 11.0. However, at an acidic pH of 3.3, there is an obvious effect on the redox responses of paraquat at the PPy/sul-calix[4] interface. At this pH, PPy is highly conducting and the reduction wave of PPy/sul-calix[4] at approximately -0.4 V vs. SCE is much larger in contrast to higher pH values. This may account for recording only one reduction peak, in that the reduction of PPy/sul-calix[4] is masking the first reduction process of  $MV^{2+}$  to  $MV^+$ . As shown by the red trace, maintaining the pH of the paraquat solution at 7.0 yielded the highest current densities.

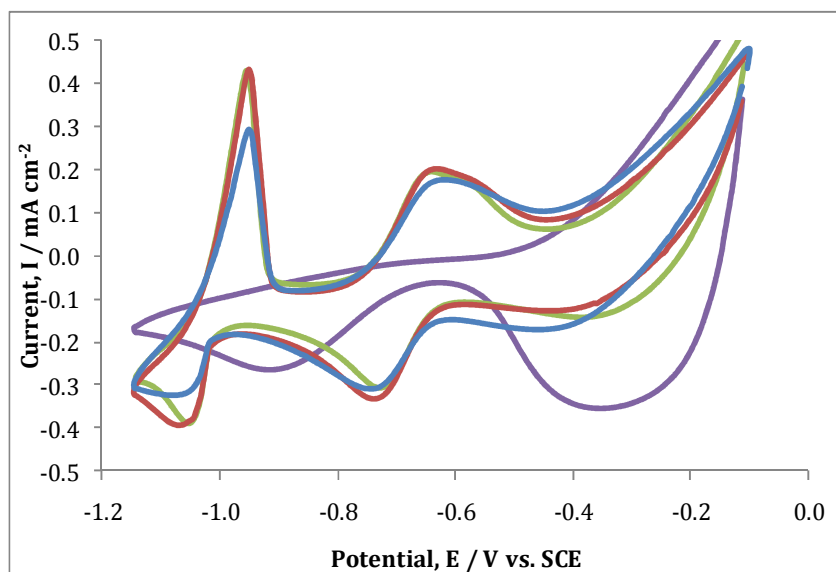


Figure 4.11: CVs of  $5.0 \times 10^{-3} \text{ mol dm}^{-3}$  paraquat in  $0.1 \text{ mol dm}^{-3} \text{ Na}_2\text{SO}_4$  electrolyte solutions, at PPY/sul-calix[4]. The analyte solution of paraquat and  $\text{Na}_2\text{SO}_4$  were adjusted to pH values of: (—) 3.3, (—) 4.8, (—) 7.0 and (—) 10.6. The potential was swept from  $-0.10 \text{ V} \rightarrow -1.15 \text{ V}$  vs. SCE at a scan rate of  $50 \text{ mV s}^{-1}$ . Each polymer was prepared from a  $0.20 \text{ mol dm}^{-3}$  Py monomer and  $0.02 \text{ mol dm}^{-3}$  sul-calix[4] solution. An applied potential of  $0.55 \text{ V}$  vs. SCE was used to electrodeposit PPY/sul-calix[4] until a charge density of  $0.13 \text{ C cm}^{-2}$  was reached.

#### 4.4.5 Influence of Scan Rate

The influence of scan rate on the diffusion of the redox species of paraquat to the PPY/sul-calix[4] solution interface was analysed by varying the scan rate from  $10 \rightarrow 250 \text{ mV s}^{-1}$ . The results are presented in Figure 4.12 and it is evident from the voltammograms that current increases as a function of scan rate for each redox reaction. Using these raw data it is possible to decipher if the reduction reactions occur by either an electron transfer process or a reactant diffusion process. The log of the peak current for the reduction of  $\text{MV}^{2+}$  to  $\text{MV}^+$  is plotted as a function of the log of the scan rate. This relationship stems from the power-law type, as illustrated in Equation 4.1 and 4.2, respectively<sup>31</sup>, whereby  $I_p^c$  is the peak reduction current in  $\text{A cm}^{-2}$ ,  $k$  is the proportional constant,  $\nu$  is the scan rate in  $\text{V s}^{-1}$  and  $x$  is the exponent of the scan rate. From the data illustrated in Figure 4.12, for the reduction of  $\text{MV}^{2+}$  to  $\text{MV}^+$ , a plot of the logarithm of current as a function of scan rate was generated, as shown in

Figure 4.13. A linear relationship is observed with a slope of 0.454 and correlation coefficient of 0.999. Similar values of 0.400 and 0.990 for the slope and correlation coefficient, were recorded for the reduction of  $MV^+$  to  $MV^0$ , respectively. According to Gal *et al.*<sup>31</sup>, a slope value corresponding to 1 indicates an electron transfer process and a slope of 0.5 indicates a diffusion process. As the exponent of the scan rate,  $x$ , is within the range of 0.5, this confirms that the reduction of  $MV^{2+}$  and  $MV^+$  is diffusion controlled.

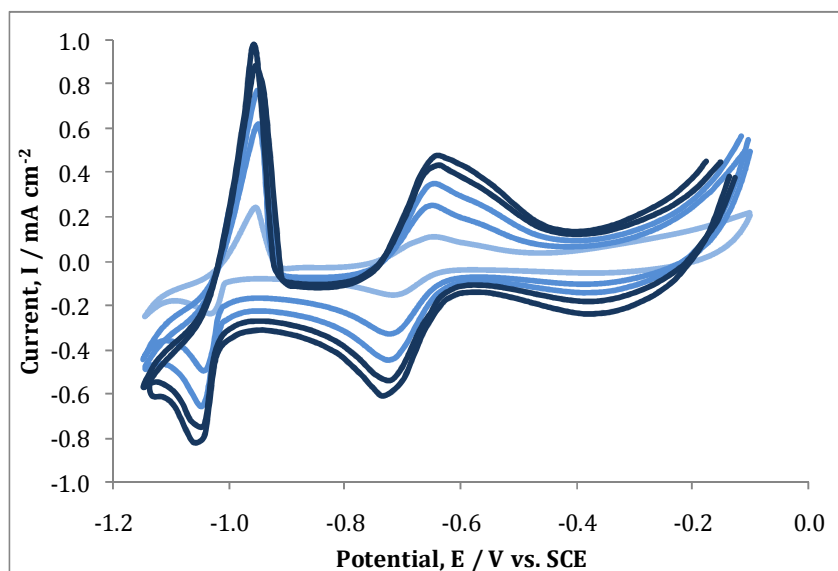


Figure 4.12: CVs recorded for  $5.0 \times 10^{-3} \text{ mol dm}^{-3}$  paraquat in  $0.1 \text{ mol dm}^{-3} \text{ Na}_2\text{SO}_4$  electrolyte solution at a pH of 7.0 at PPy/sul-calix[4]. The potential was swept from  $-0.10 \rightarrow -1.15 \text{ V vs. SCE}$  at the following scan rates: (—) 10, (—) 50, (—) 100, (—) 150 and (—) 200  $\text{mV s}^{-1}$ . Each polymer was prepared from a  $0.20 \text{ mol dm}^{-3}$  Py monomer and  $0.02 \text{ mol dm}^{-3}$  sul-calix[4] solution. An applied potential of  $0.55 \text{ V vs. SCE}$  was used to electro-deposit PPy/sul-calix[4] until a charge density of  $0.13 \text{ C cm}^{-2}$  was reached.

$$I_{p,c} = kv^x \quad (4.1)$$

$$\log I_{p,c} = \log k + x \log v \quad (4.2)$$

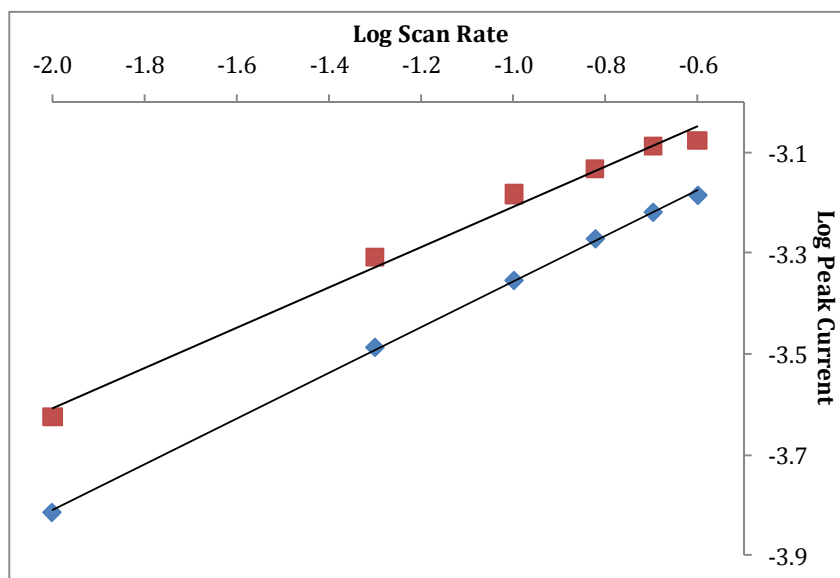


Figure 4.13: Logarithmic plot of scan rate as a function of peak current for the reduction of (—)  $MV^{2+} \rightarrow MV^+$  at  $-0.71$  V and (—)  $MV^+ \rightarrow MV^0$  at  $-1.10$  vs. SCE. These data were compiled from the raw data recorded and depicted in Figure 4.11.

As the process of reduction is governed by diffusion, diffusion coefficients of  $MV^{2+}$  and  $MV^+$  at the polymer interface were calculated. Applying the Randles-Sevcik equation, Chapter 2, Section 2.4.1, Equation 2.2,  $D_c$  can be evaluated by plotting peak current,  $I_p$  as a function of the square root of the scan rate,  $v^{1/2}$ , in which  $D_c$  is determined from the slope. Figure 4.14 shows the linear plots corresponding to the Randles-Sevcik equation. To interpret the influence of the background current on the detection of  $MV^{2+}$  at the modified electrode, the peak currents with and without the background are depicted. Interestingly, better linearity is observed when the background currents are not subtracted. The slope values of  $0.0014$  and  $0.009 \text{ A cm}^{-2} (\text{V s}^{-1})^{-1/2}$ , translate to  $1.08 \times 10^{-6} \text{ cm}^2 \text{ s}^{-1}$  and  $4.48 \times 10^{-7} \text{ cm}^2 \text{ s}^{-1}$  for the diffusion coefficients, with and without the background subtracted, respectively. The  $D_c$  values were also calculated for the reduction of  $MV^+$  at the PPy/sul-calix[4] film. Similar values of  $1.99 \times 10^{-6}$  and  $4.47 \times 10^{-7} \text{ cm}^2 \text{ s}^{-1}$  were evaluated, with and without background subtracted, respectively. A higher  $D_c$  value by a factor of approximately 2.5 for the peak currents considering the inclusion of the background, indicates that the charging capacitance influences the detection of  $MV^{2+}$  at the PPy/sul-calix[4]

interface. However, literature depicts the  $D_c$  value for  $MV^{2+}$  is in the range of  $10^{-6}$   $\text{cm}^2 \text{s}^{-1}$ . Monk *et al.*<sup>32</sup> stated a  $D_c$  value of  $8.6 \times 10^{-6}$   $\text{cm}^2 \text{s}^{-1}$  for  $MV^{2+}$  in  $\text{H}_2\text{O}$ . Ferreyra *et al.*<sup>33</sup> recorded a similar value of  $7.2 \times 10^{-6}$   $\text{cm}^2 \text{s}^{-1}$  for  $MV^{2+}$  in a solution of  $\text{NaNO}_2$  and Ohsaka *et al.*<sup>34</sup> calculated a lower  $D_c$  value of  $4.8 \times 10^{-6}$   $\text{cm}^2 \text{s}^{-1}$  for  $MV^{2+}$  in DMSO. Thus, the capacitive current has an influence on the diffusion process and from the literature, it can be concluded that the true  $D_c$  for both  $MV^{2+}$  and  $MV^+$  is closer to  $10^{-6}$   $\text{cm}^2 \text{s}^{-1}$ .

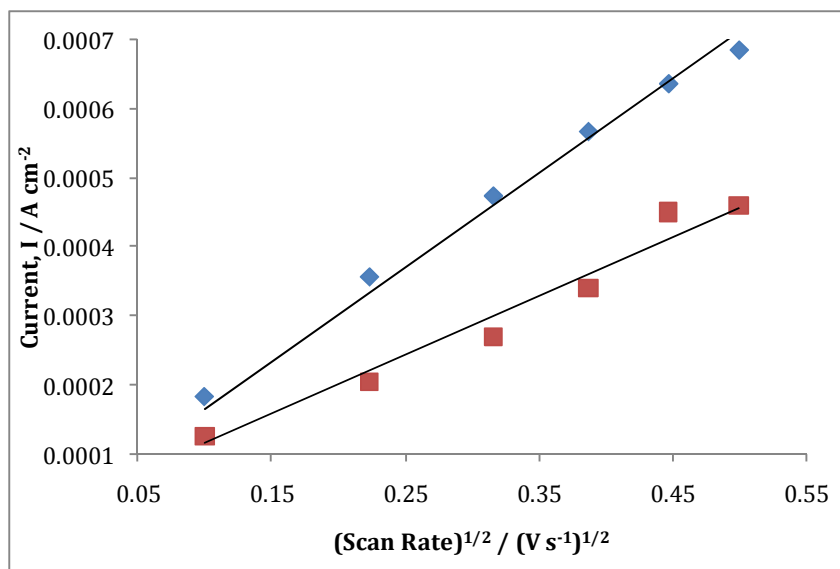


Figure 4.14: Randles-Sevcik plot of peak current ( $I_p$ ) at  $-0.7$  V vs. SCE as a function of the square root of the scan rate ( $\nu^{1/2}$ ) for  $MV^{2+}$ . The data for this plot originate from the plots depicted in Figure 4.12, in which ( $\blacklozenge$ ) is the peak current including the background and ( $\blacksquare$ ) is the peak current with the background subtracted.

#### 4.4.6 Optimum conditions

The series of variables explored to obtain an optimum signal for the reduction of  $MV^{2+}$  to  $MV^+$  at  $-0.7$  V vs. SCE are summarised in Table 4.5. Using this information, Section 4.5 investigates the detection limit of paraquat at the PPy/sul-calix[4] interface using CV and CPA.

Table 4.5: Summary detailing the optimum conditions for the detection of  $5.0 \times 10^{-3}$  mol dm<sup>-3</sup> paraquat in 0.1 mol dm<sup>-3</sup> Na<sub>2</sub>SO<sub>4</sub> electrolyte solution at PPy/sul-calix[4].

Varying Parameter	Optimum Condition
Py concentration	0.20 mol dm <sup>-3</sup>
Sul-calix[4] concentration	0.02 mol dm <sup>-3</sup>
Na <sub>2</sub> SO <sub>4</sub> electrolyte concentration	0.10 mol dm <sup>-3</sup>
Applied Potential	0.55 V vs. SCE
Charge Density	0.13 C cm <sup>-2</sup>
Potential window	-0.10 → -1.15 V vs. SCE
Scan Rate	50 mV s <sup>-1</sup>
pH of paraquat solution	7.0

#### 4.5 Calibration Study

As mentioned in Chapter 3, Section 3.6, CV is a useful technique to estimate the detection range of a sensor towards the analyte. CPA offers a larger appeal due to its ability to minimise background current, thus enhancing the detection limit<sup>35</sup>. Signals are also enhanced due to a thin diffusion layer at the modified electrode and solution interface.

##### 4.5.1 Cyclic Voltammetry

Using the optimum conditions outlined in Table 4.5, a calibration curve was carried out using CV. The recorded data are shown in Figure 4.15, which show an increasing peak current as a function of concentration. Interestingly, the currents corresponding to the redox couple of MV<sup>+</sup> → MV<sup>0</sup> diminish considerably at concentrations below  $1.0 \times 10^{-3}$  mol dm<sup>-3</sup>. The currents depicting the first redox couple of MV<sup>2+</sup> → MV<sup>+</sup> decrease with concentration and the characteristic traces of this redox reaction are more pronounced. Thus, the peak currents for the reduction of MV<sup>2+</sup> as a function of concentration were plotted. A linear relationship is obtained as depicted in Figure 4.16, illustrating an experimental detection limit of  $8 \times 10^{-4}$  mol dm<sup>-3</sup> for the MV<sup>2+</sup> species. This detection limit is somewhat poorer than that obtained for paraquat at the

PPy/sul- $\beta$ CD film. However, this is not a direct comparison, as the detection limit using PPy/sul- $\beta$ CD was relative to the reduction of  $MV^+$  to  $MV^0$ . On inspection of the second reduction wave, it is evident from Figure 4.15 that at paraquat concentrations lower than  $1.0 \times 10^{-3} \text{ mol dm}^{-3}$ , only a capacitive current is observed with no evidence of a faradaic current for the conversion of  $MV^+$  to  $MV^0$ . The sensitivity of PPy/sul-calix[4] for  $MV^{2+}$  was  $0.04 \text{ A cm}^{-2} \text{ M}^{-1}$  using CV. This is almost 10-fold lower than the sensitivity evaluated for PPy/sul- $\beta$ CD of  $0.30 \text{ A cm}^{-2} \text{ M}^{-1}$ .

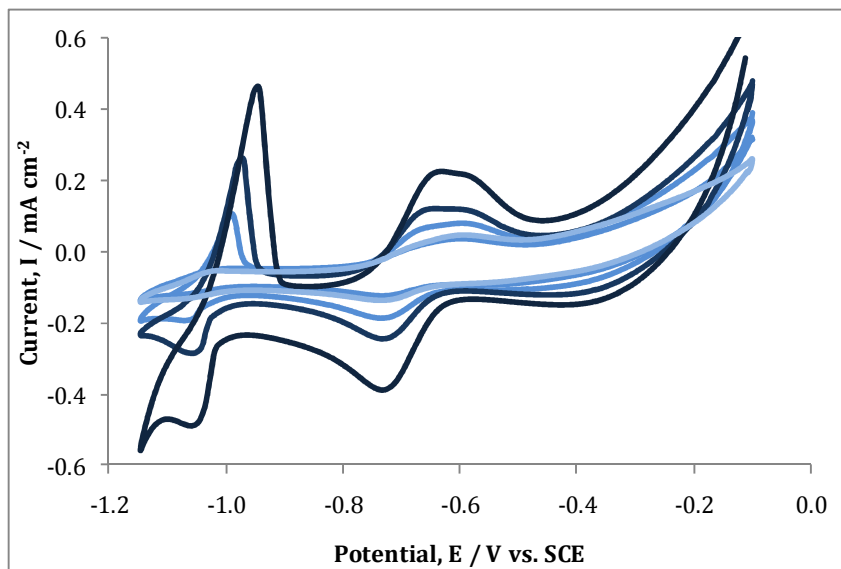


Figure 4.15: CV titration of current as a function of paraquat concentration. The following concentrations of paraquat were analysed at a PPy/sul-calix[4] film; (—)  $5.0 \times 10^{-3}$ , (—)  $2.0 \times 10^{-3}$ , (—)  $1.0 \times 10^{-3}$ , (—)  $9.0 \times 10^{-4}$  and (—)  $8.0 \times 10^{-4} \text{ mol dm}^{-3}$  in  $0.1 \text{ mol dm}^{-3} \text{ Na}_2\text{SO}_4$  solution at a pH of 7.0. The potential was swept from  $-0.10 \rightarrow -1.15 \text{ V vs. SCE}$  at  $50 \text{ mV s}^{-1}$ . Each polymer was prepared from a  $0.20 \text{ mol dm}^{-3}$  Py monomer and  $0.02 \text{ mol dm}^{-3}$  sul-calix[4] solution. Applying a potential of  $0.55 \text{ V vs. SCE}$  the polymer was electrodeposited at Au, until a charge density of  $0.13 \text{ C cm}^{-2}$  was reached.

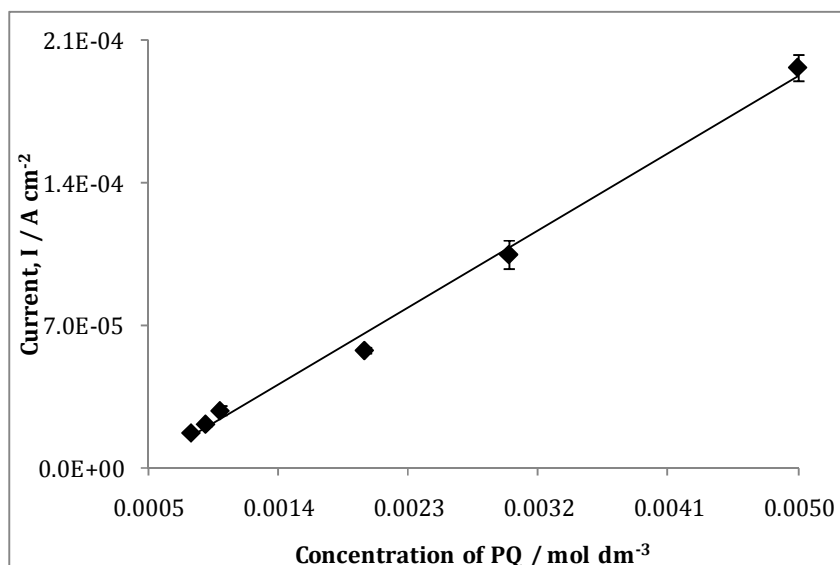


Figure 4.16: Plot of peak current for the reduction of  $MV^{2+}$  to  $MV^+$  as a function of the concentration of paraquat which depicts a linear relationship with correlation constant of 0.995. These peak currents correspond to the raw data displayed in Figure 4.15, recorded at Au modified with PPy/sul-calix[4].

#### 4.5.2 Constant Potential Amperometry

Constant potential amperometry (CPA), as previously discussed in Chapter 3, Section 3.6.3 is a useful technique for improving sensitivity due to the minimisation of the background current. An identical protocol in carrying out CPA was employed for the detection of paraquat at the PPy/sul-calix[4] interface as, to that described in Chapter 3, Section 3.6.3 for PPy/sul- $\beta$ CD. The potential was held at -0.9 V vs. SCE, with the working electrode rotated at a rate of 2,000 rpm and aliquots of  $2.0 \times 10^{-3}$  mol dm<sup>-3</sup> paraquat were added to a 0.1 mol dm<sup>-3</sup> Na<sub>2</sub>SO<sub>4</sub> solution. The polymer film of PPy/sul-calix[4] was prepared in accordance with the optimum conditions outline in Table 4.5. In addition to this study, the detection of  $MV^{2+}$  at the PPy/SO<sub>4</sub><sup>2-</sup> film was also investigated. Identical conditions in the formation of PPy/SO<sub>4</sub><sup>2-</sup> were adhered to as for the formation of PPy/sul-calix[4].

This served as a dual experiment for two reasons. Firstly, the current response of  $MV^{2+}$  at PPy/SO<sub>4</sub><sup>2-</sup> was investigated. As previously shown in Chapter 3,

Section 3.4 PPy/SO<sub>4</sub><sup>2-</sup> did not detect MV<sup>2+</sup> using CV. However, CV is not as sensitive as CPA. Secondly, this established whether small mobile dopants are retained within the polymer when a reduction potential is applied and exhibit anion exchange behaviour<sup>36</sup>. The results shown by the red trace in Figure 4.17 indicate that PPy/SO<sub>4</sub><sup>2-</sup> does not sense MV<sup>2+</sup> at -0.9 V vs. SCE. This is further confirmation that the small mobile dopant is released at reduction potentials. In comparing the SO<sub>4</sub><sup>2-</sup> dopant with sul-calix[4], this macrocycle is immobilised within the polymer matrix. Therefore, PPy/sul-calix[4] acts as a cation exchanger. This is verified by the current steps recorded for the reduction of MV<sup>2+</sup> at the modified surface, as shown by the blue trace in Figure 4.17. The response time of PPy/sul-calix[4] was much slower in contrast to the PPy/sul-βCD polymer, in which it took approximately 5 min for this polymer to respond to the addition of paraquat. This was attributed to the duration for which the polymer was polarised at reduction potentials. As illustrated in Figure 4.18, the peak current increases as a function of concentration, generating an initial linear region followed by a plateau shaped curve. Probing the initial current steps, the linear region, as depicted in Figure 4.19, shows an experimental detection limit of  $3.99 \times 10^{-6}$  mol dm<sup>-3</sup> for the reduction of MV<sup>2+</sup> to MV<sup>+</sup>. Moreover, this linear region was used to evaluate a limit of detection in accordance with Equation 3.10<sup>37</sup>. With a limit of detection of  $3.48 \times 10^{-6}$  mol dm<sup>-3</sup>, this is sufficiently close to the experimental limit. In contrast to the PPy/sul-βCD polymer, PPy doped with sul-calix[4] obtains a lower detection limit by a factor of 4. The sensitivity of this sensor is 2.22 A cm<sup>-2</sup> M<sup>-1</sup>. This is slightly higher than that of PPy/sul-βCD, which was 1.87 A cm<sup>-2</sup> M<sup>-1</sup>. This increase in sensitivity highlights the affinity PPy/sul-calix[4] has for the detection of MV<sup>2+</sup>. This is not surprising as it has been previously reported by Guo *et al.*<sup>2</sup> that a strong interaction occurs between the two species. Further analysis of the amperometric data using Michaelis-Menten kinetics and the Lineweaver-Burk plot gives an indication of the strength of this interaction.

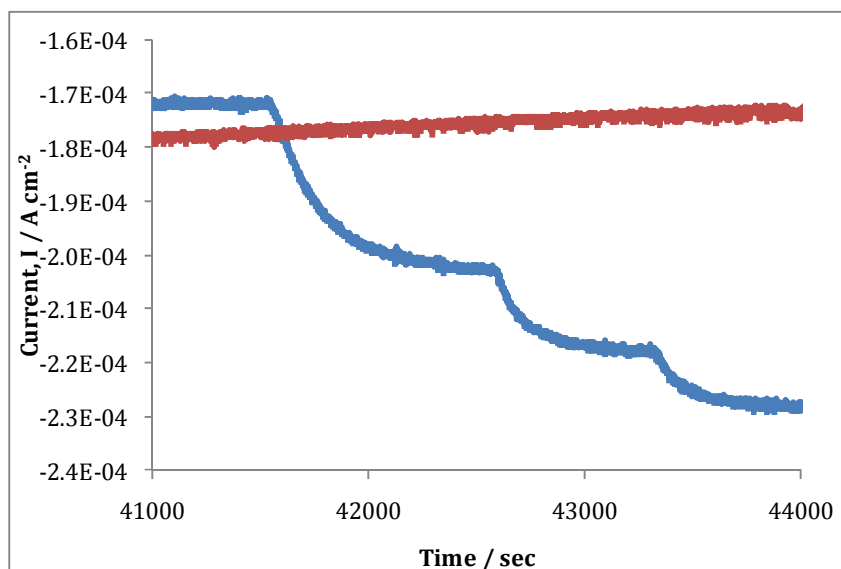


Figure 4.17: CPA plot of current as a function of time for the detection of  $2.0 \times 10^{-3} \text{ mol dm}^{-3}$  paraquat in a  $0.1 \text{ mol dm}^{-3} \text{ Na}_2\text{SO}_4$  electrolyte solution at (—) PPy/sul-calix[4] and (—) PPy/SO<sub>4</sub><sup>2-</sup>. Both polymers were prepared in accordance with the optimum conditions outlined in Table 4.5. Aliquot additions of the paraquat solution ranged from 5  $\mu\text{l}$  to 5 ml. The polymers were polarised at -0.9 V vs. SCE and rotated at 2,000 rpm.

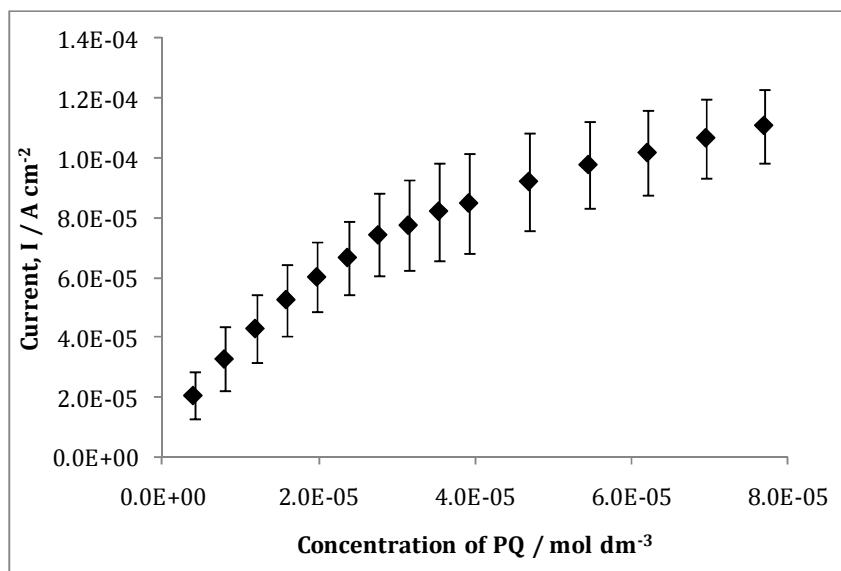


Figure 4.18: Limiting currents for the reduction of  $\text{MV}^{2+}$  to  $\text{MV}^+$  plotted as a function of paraquat concentration. The polymer was prepared using the optimum conditions illustrated in Table 4.5 and the amperometric data were recorded at a fixed potential of -0.9 V vs. SCE, whereby the working electrode was rotated at 2,000 rpm and aliquots in the range of 50-5000  $\mu\text{l}$  were added once a limiting current was achieved.

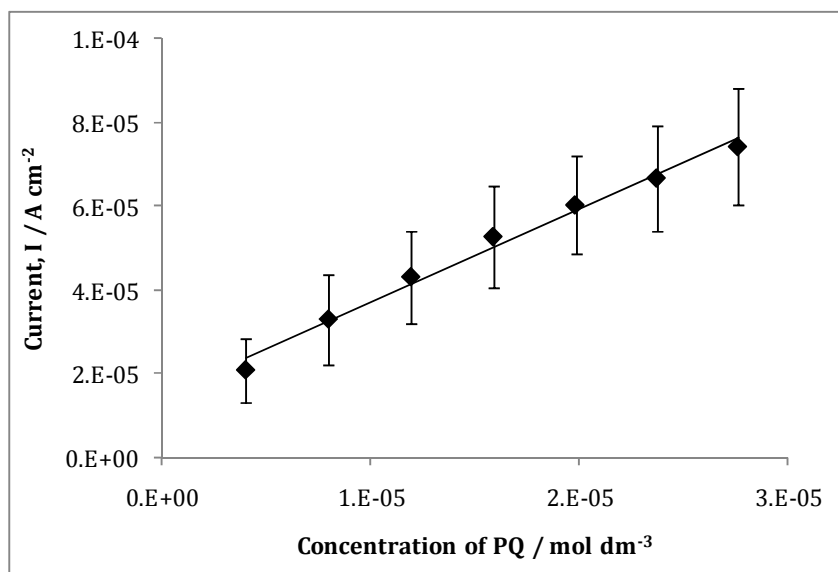


Figure 4.19: Linear region taken from the plotted CPA data illustrated in Figure 4.18. There is a proportional relationship between limiting current and  $MV^{2+}$  concentration, with a correlation coefficient of 0.9885.

#### 4.6 Michaelis-Menten Kinetics and Lineweaver-Burk analysis

As discussed in Chapter 3, Section 3.6.4, Michaelis-Menten kinetics is a basic enzyme kinetic scheme used extensively in chemistry and biology for the study of enzymatic catalysis, as it is a relatively simple model from a mathematical point of view<sup>38</sup>. The data recorded using CPA can be fitted to a hyperbolic curve and using the Michaelis-Menten equation, Equation 3.12<sup>39</sup>, the values for Michaelis constant,  $K_m$  and the maximum change in current,  $I_{max}$ , can be calculated. A useful comparative to Michaelis-Menten kinetics is the Lineweaver-Burk plot. As is the case for Michaelis-Menten kinetics, the asymptote of  $I_{max}$  is never reached. Thus, the Lineweaver-Burk plot can be used as an alternative means of determining  $K_m$  and  $I_{max}$ . The Lineweaver-Burk plot is simply a linear plot of the reciprocal of limiting current for the reduction of  $MV^{2+} \rightarrow MV^+$  as a function of the reciprocal of the paraquat concentration. The relationship on which this plot is based, is depicted in Chapter 3, Equation 3.15<sup>40</sup> and using the slope and the intercept,  $K_m$  and  $I_{max}$  can be calculated, respectively.

Gathering the relevant data from CPA, Michaelis-Menten and Lineweaver-Burk plots were constructed and are shown in Figure 4.20 and Figure 4.21, respectively. The values for  $K_m$  and  $I_{max}$  were calculated. As illustrated in Table 4.6, there is close agreement in the values of  $I_{max}$  and  $K_m$  calculated using both methods. The  $K_m$  values indicate an intermediate interaction, as strong interactions generally have  $K_m$  values in the range of  $\mu\text{mol dm}^{-3}$  or lower and weak interactions have  $K_m$  values of  $\text{mmol dm}^{-3}$ . For example, Cosiner *et al.*<sup>41</sup>, evaluated  $K_m$  values in the range of 1.9-2.6  $\mu\text{mol dm}^{-3}$  for the interaction of salicylate and a poly(amphiphilic pyrrole ammonium) film. They proposed this low value was an indication of the good permeability of the analyte diffusing through the polymer matrix. In comparing the interaction of PPy/sul- $\beta$ CD with  $MV^{2+}$  with that of PPy/sul-calix[4] and  $MV^{2+}$ , the  $K_m$  value depicts a somewhat stronger interaction between PPy/sul-calix[4] and  $MV^{2+}$ .  $K_m$  values of  $3.12 \times 10^{-4}$  and  $3.41 \times 10^{-4} \text{ mol dm}^{-3}$  were calculated using Michaelis-Menten analysis and the Lineweaver-Burk plot, respectively for PPy/sul- $\beta$ CD and  $MV^{2+}$ . These values are ten-fold lower than the  $K_m$  values displayed in Table 4.6 for PPy/sul-calix[4]. This again highlights the affinity  $MV^{2+}$  has for PPy/sul-calix[4]. As a means of measuring the strength of this interaction and selectivity, an interference study was carried out, in which the electrochemical response of paraquat was analysed in the presence of its main interferent, diquat.

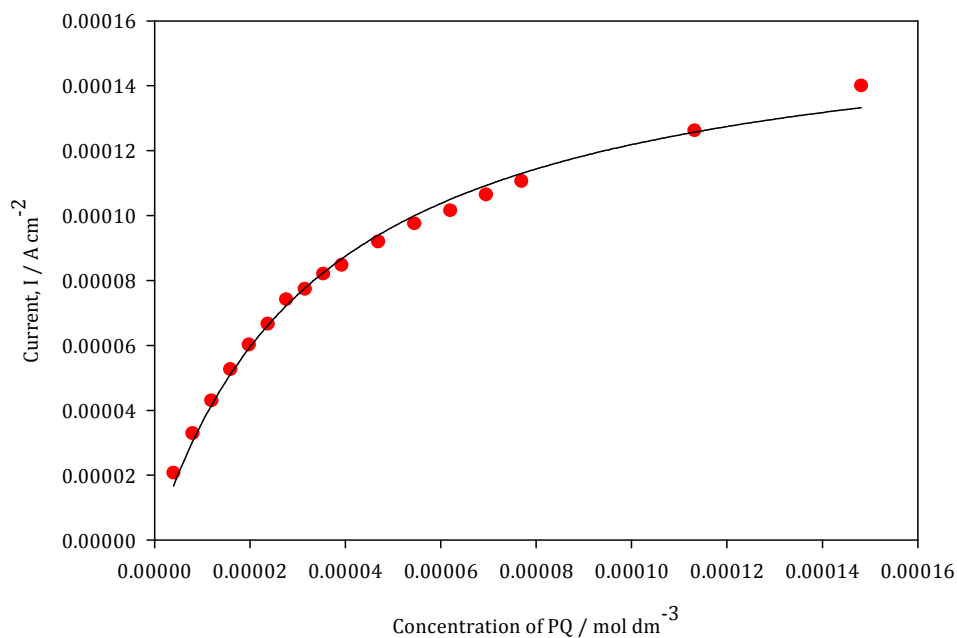


Figure 4.20: Michaelis-Menten plot of current density as a function of MV<sup>2+</sup> concentration. These data were obtained from Figure 4.18. A non-linear curve was fitted to the data, with a correlation coefficient of 0.993

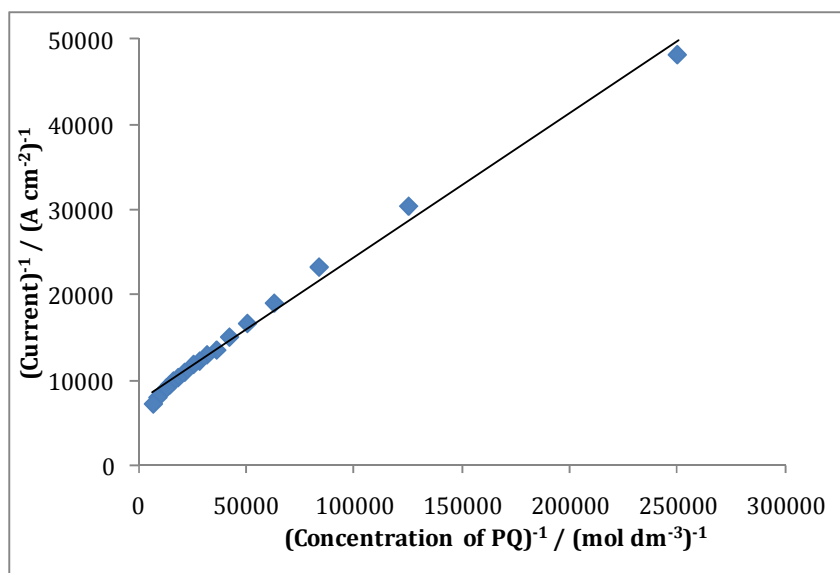


Figure 4.21: Lineweaver-Burk plot of the inverse of current as a function of the inverse of paraquat concentration (linear regression constant of 0.992). These data were obtained from Figure 4.18.

Table 4.6: Calculated values of  $K_m$  and  $I_{max}$  using Michaelis-Menten kinetics and Lineweaver-Burk plot for the interaction of  $MV^{2+}$  at the modified polymer film of PPy/sul-calix[4].

Technique	$K_m / \text{mol dm}^{-3}$	$I_{max} / \text{A cm}^{-2}$	$R^2$
Michaelis-Menten	$3.56 \times 10^{-5}$	$1.65 \times 10^{-4}$	0.993
Lineweaver-Burk	$2.30 \times 10^{-5}$	$1.36 \times 10^{-4}$	0.992

#### 4.7 Interference Study

As discussed at the outset of this chapter, the reported strong interaction between sul-calix[4] and  $MV^{2+}$  in solution<sup>2</sup>, introduced the possibility of a more sensitive and selective sensor using sul-calix[4] as a dopant. Given that diquat is the main interferent in the presence of paraquat<sup>42</sup>, a selective sensor is desirable. In Chapter 3, Section 3.8.2, the electrochemical signals for paraquat at the modified PPy/sul- $\beta$ CD showed no selectivity in the presence of diquat. Thus, this section outlines a brief analysis of the interference of diquat at the PPy/sul-calix[4] polymer in the presence of paraquat.

##### 4.7.1 Interference of Diquat

The CV results of  $5.0 \times 10^{-3} \text{ mol dm}^{-3}$  paraquat in the presence of  $5.0 \times 10^{-3} \text{ mol dm}^{-3}$  diquat in an electrolyte solution of  $0.1 \text{ mol dm}^{-3} \text{ Na}_2\text{SO}_4$  at a pH of 7.0 at PPy/sul-calix[4] are shown in Figure 4.22. Diquat has a very similar electrochemistry to paraquat, in terms of redox reactions, with similar peak potentials and peak currents. This is evident from the red trace in Figure 4.22 which corresponds to  $5.0 \times 10^{-3} \text{ mol dm}^{-3}$  diquat at the PPy/sul-calix[4] interface. The blue trace depicts the redox reactions of an identical concentration of paraquat at the modified polymer film. As shown by the green trace when identical concentrations of paraquat and diquat are present in solution, the effect on peak current is additive and PPy/sul-calix[4] shows no selectivity for paraquat in the presence of diquat.

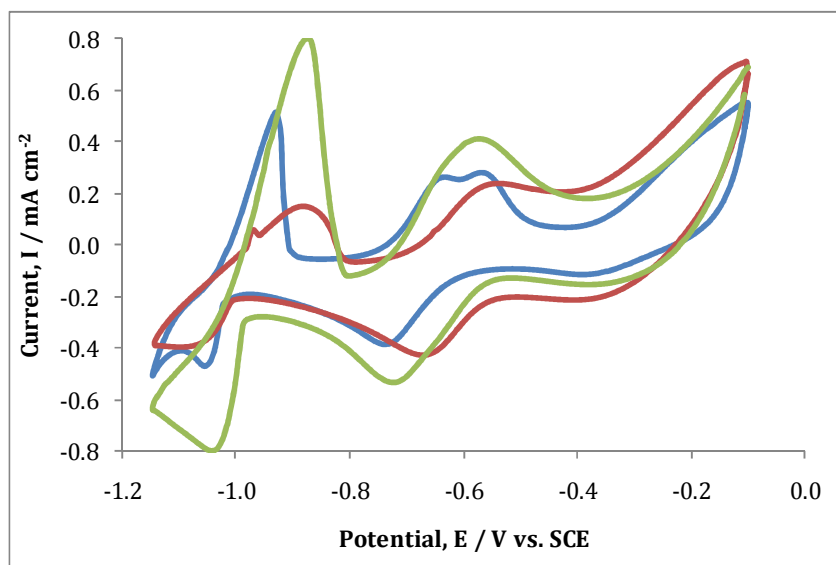


Figure 4.22: CV of (—)  $5.0 \times 10^{-3}$  paraquat, (—)  $5.0 \times 10^{-3}$  diquat and (—)  $5.0 \times 10^{-3}$  paraquat and  $5.0 \times 10^{-3}$  mol  $\text{dm}^{-3}$  diquat in  $0.1 \text{ mol dm}^{-3}$   $\text{Na}_2\text{SO}_4$  at a pH of 7.0, at the modified polymer film of PPy/sul-calix[4]. The potential was swept from  $-0.10 \rightarrow -1.15$  V vs. SCE at a scan rate of  $50 \text{ mV s}^{-1}$ . Each polymer was prepared from a  $0.20 \text{ mol dm}^{-3}$  Py monomer and  $0.02 \text{ mol dm}^{-3}$  sul-calix[4] solution. An applied potential of  $0.55$  V vs. SCE was used to electrodeposit the polymer until a charge density of  $0.13 \text{ C cm}^{-2}$  was reached.

Clearly, PPy/sul-calix[4] shows poor selectivity for paraquat in the presence of diquat. Given the strong interaction that forms between sul-calix[4] and paraquat as reported by Guo *et al.*<sup>2</sup>, the PPy/sul-calix[4] film was cycled in a solution of paraquat, followed by another CV in a separate solution of diquat. Thus, the formation of a strong complex may inhibit the detection of diquat at the modified electrode. The results of this experiment are shown in Figure 4.23. The red trace corresponds to the redox signals of diquat following an initial cycling period in  $5.0 \times 10^{-3}$  mol  $\text{dm}^{-3}$  paraquat solution. It is evident that exposing the modified surface to paraquat prior to diquat detection has no adverse effect on the peak potentials or currents of diquat.

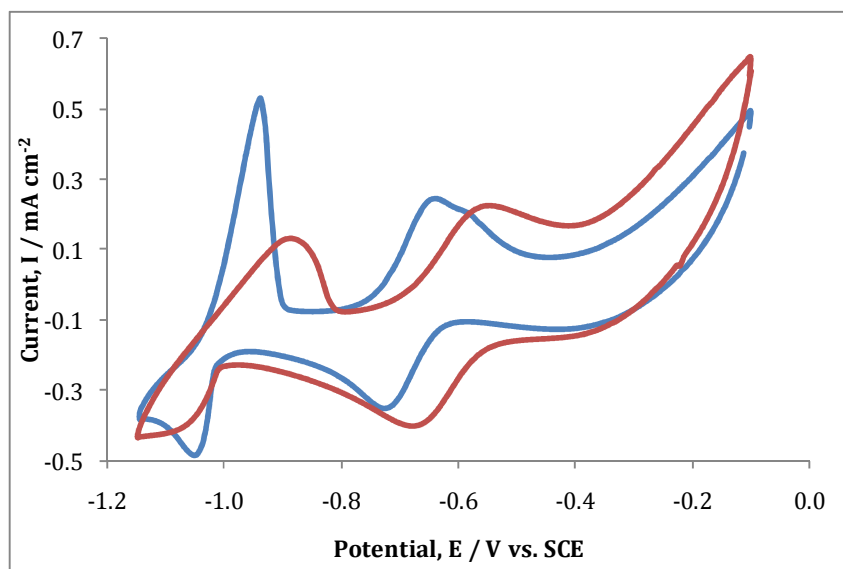


Figure 4.23: CV of (—)  $5.0 \times 10^{-3} \text{ mol dm}^{-3}$  paraquat and (—)  $5.0 \times 10^{-3} \text{ mol dm}^{-3}$  diquat in  $0.1 \text{ mol dm}^{-3} \text{ Na}_2\text{SO}_4$  electrolyte solution at a pH of 7.0 at a PPy/sul-calix[4] interface. Initially a CV of paraquat was carried out followed by a CV of diquat using the identical polymer film, with rinsing between experiments. The potential was swept from  $-0.10 \rightarrow -1.15 \text{ V vs. SCE}$  at a scan rate of  $50 \text{ mV s}^{-1}$ . The polymer was prepared using a  $0.20 \text{ mol dm}^{-3}$  Py monomer and  $0.02 \text{ mol dm}^{-3}$  sul-calix[4] solution. Electropolymerisation was carried out at  $0.55 \text{ V vs. SCE}$  until a charge density of  $0.13 \text{ C cm}^{-2}$  was reached.

To the best of our knowledge, no previous research has been carried out monitoring the behaviour of diquat at the modified PPy/sul-calix[4] interface. Given the structural similarity of diquat and paraquat, this indicates that the charged species of diquat may have an affinity for sul-calix[4] also. The behaviour of  $5.0 \times 10^{-3} \text{ mol dm}^{-3}$  diquat at the PPy/sul-calix[4] interface and its influence on subsequent CVs carried out in a paraquat solution at the same concentration was analysed and the recorded data are presented in Figure 4.24. The red trace depicts the characteristic redox couples of diquat at freshly prepared PPy/sul-calix[4] film. However, the redox activity of paraquat is significantly affected by initial cycling in diquat. This is evident by the decrease in peak current for the reduction of  $\text{MV}^{2+}$  to  $\text{MV}^+$  and also the loss of redox peaks characteristic of the second stage of reduction of paraquat, i.e.,  $\text{MV}^+$  to  $\text{MV}^0$ . Thus, it is clear that the interaction of diquat at the modified polymer surface is quite strong in light of its ability to hinder the redox activity of paraquat. This is

in contrast to the results as shown in Figure 4.23, since the diquat signal was unaffected by previous cycling of PPy/sul-calix[4] in paraquat. Furthermore, the paraquat signal is very much affected by diquat as shown in Figure 4.24. Although, this sensor is not selective for paraquat, the impressive interaction between PPy/sul-calix[4] and diquat requires further study to quantify and compare this interaction to that of paraquat and sul-calix[4]. Hence, Chapter 5 will analyse this interaction in more detail as a solution based study to determine the quantitative measure of interaction, as the results illustrated in Figure 4.24 clearly indicate the formation of a strong interaction.

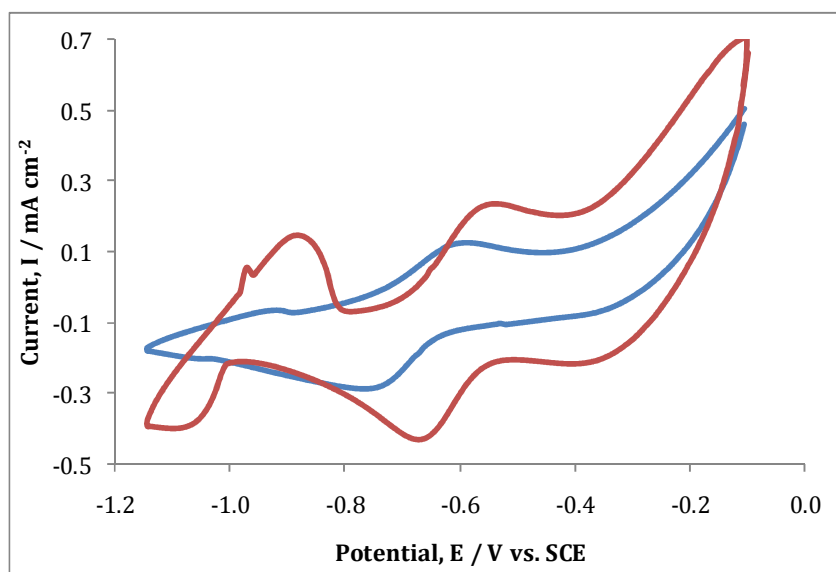


Figure 4.24: CV of (—)  $5.0 \times 10^{-3} \text{ mol dm}^{-3}$  paraquat and (—)  $5.0 \times 10^{-3} \text{ mol dm}^{-3}$  diquat in  $0.1 \text{ mol dm}^{-3} \text{ Na}_2\text{SO}_4$  electrolyte solution at a pH of 7.0, at a PPy/sul-calix[4] interface. Initially a CV of diquat was carried out followed by a CV of paraquat using the identical polymer film, with rinsing between experiments. The potential was swept from  $-0.10 \rightarrow -1.15 \text{ V vs. SCE}$  at a scan rate of  $50 \text{ mV s}^{-1}$ . The polymer was prepared using a  $0.20 \text{ mol dm}^{-3}$  Py monomer and  $0.02 \text{ mol dm}^{-3}$  sul-calix[4] solution. Electropolymerisation was carried out at  $0.55 \text{ V vs. SCE}$  until a charge density of  $0.13 \text{ C cm}^{-2}$  was reached.

#### 4.8 Summary of Results

The results presented in this chapter highlighted the enhanced sensitivity of paraquat at the modified interface of PPy/sul-calix[4] in comparison to that of PPy/sul- $\beta$ CD. Although, structurally sul-calix[4] and sul- $\beta$ CD are quite similar,

the variation in properties of the respective doped polymers is interesting. The most significant being the electroactivity of sul-calix[4] which impacts on the range of applied potentials available for electro-polymerisation. Subsequently, this also has an effect on the morphology of the polymer as discussed in Section 4.2.1, in that a much more porous polymer was grown at higher oxidation potentials of 0.70 V vs. SCE in contrast to those grown at 0.55 V vs. SCE.

In regards to sensing paraquat at the modified electrode, PPy/sul-calix[4] displayed an affinity for all redox states even at moderate concentrations of  $1.0 \times 10^{-3} \text{ mol dm}^{-3}$ . However, at concentrations lower than this value, it was the redox state of  $MV^{2+} \rightarrow MV^+$  that retained its characteristic reduction and oxidation wave, which further supports the literature documenting the host-guest inclusion properties of paraquat and sul-calix[4]<sup>2,3</sup>. The limit of detection of this sensor is  $3.48 \times 10^{-6} \text{ mol dm}^{-3}$  for the reduction of  $MV^{2+} \rightarrow MV^+$ , with a sensitivity of  $2.22 \text{ A cm}^{-2} \text{ M}^{-1}$ . This is a significant increase in comparison to the PPy/sul- $\beta$ CD sensor, in which a detection limit of  $1.28 \times 10^{-5} \text{ mol dm}^{-3}$  was recorded from the CPA data. Even though, this detection limit is still above those outlined by the EU and the EPA<sup>1</sup>, this increase in detection is certainly a step in the right direction. Further optimisation of this sensor could include the use of micro-electrodes<sup>43</sup> as they are efficient in reducing capacitance current and so enhance the faradaic current.

Finally, the selectivity of this sensor was assessed with respect to monitoring the influence of the interference of diquat at the polymer interface. Although, PPy/sul-calix[4] showed no apparent selectivity for paraquat, interestingly, the interaction between diquat and PPy/sul-calix[4] had an adverse effect on further detection of paraquat. On the other hand, paraquat had no such effect and hence this poses the requirement for further analysis of this interaction is required. A detailed study of the solution based interaction between diquat and sul-calix[4] will be discussed in Chapter 5 and a brief comparison will be made to that of paraquat and sul-calix[4] which has been previously reported in the literature<sup>2</sup>.

#### 4.9 References

1. U. M. F. de Oliveira, J. Lichtig, and J. C. Masini, *J. Braz. Chem. Soc.*, **15**, 735, (2004).
2. D. S. Guo, L. H. Wang, and Y. Liu, *J. Org. Chem.*, **72**, 7775, (2007).
3. D. S. Guo, K. Wang, and Y. Liu, *J. Inclusion Phenom. Macrocyclic Chem.*, **62**, 1, (2008).
4. A. A. A. Almario and R. L. T. Caceres, *J. Chil. Chem. Soc.*, **54**, 14, (2009).
5. S. J. Dalgarno, J. L. Atwood, and C. L. Raston, *Cryst. Growth Des.*, **6**, 174, (2006).
6. I. Yoshida, N. Yamamoto, F. Sagara, D. Ishii, K. Ueno, and S. Shinkai, *Bull. Chem. Soc. Jpn.*, **65**, 1012, (1992).
7. C. Weidlich, K. M. Mangold, and K. Jüttner, *Electrochim. Acta*, **47**, 741, (2001).
8. T. F. Otero and C. Santamaria, *Synth. Met.*, **51**, 313, (1992).
9. T. F. Otero, R. Tejada, and A. S. Elola, *Polymer*, **28**, 651, (1987).
10. M. Satoh, K. Kaneto, and K. Yoshino, *Synth. Met.*, **14**, 289, (1986).
11. G. W. Diao and Z. Wei, *J. Electroanal. Chem.*, **567**, 325, (2004).
12. J. Wang, S. P. Chen, and M. S. Lin, *J. Electroanal. Chem.*, **273**, 231, (1989).
13. G. W. Diao and Y. Liu, *Electroanalysis*, **17**, 1279, (2005).
14. M. Chen, H. L. Wang, J. Gu, and G. W. Diao, *J. Appl. Electrochem.*, **37**, 331, (2007).
15. X. Du and Z. Wang, *Electrochim. Acta*, **48**, 1713, (2003).
16. C. Weidlich, K. M. Mangold, and K. Juttner, *Electrochim. Acta*, **50**, 1547, (2005).
17. T. Silk, Q. Hong, J. Tamm, and R. G. Compton, *Synth. Met.*, **93**, 59, (1998).
18. K. R. Temsamani, H. B. Mark, W. Kutner, and A. M. Stalcup, *J. Solid State Electrochem.*, **6**, 391, (2002).
19. G. Bidan and M. A. Niel, *Synth. Met.*, **85**, 1387, (1997).
20. A. Buffenoir and G. Bidan, *Synth. Met.*, **102**, 1300, (1999).
21. K. Kaneto and G. Bidan, *Thin Solid Films*, **331**, 272, (1998).
22. J. Volke, *Collect. Czech. Chem. Commun.*, **33**, 3044, (1968).
23. L. Pospisil, J. Kuta, and J. Volke, *J. Electroanal. Chem.*, **58**, 217, (1975).
24. L. Xiao, G. G. Wildgoose, and R. G. Compton, *New J. Chem.*, **32**, 1628, (2008).
25. R. Gomez, A. Fernandez-Vega, J. M. Feliu, and A. Aldaz, *J. Phys. Chem.*, **97**, 4769, (2002).
26. S. Asavapiryanont, G. K. Chandler, G. A. Gunawardena, and D. Pletcher, *J. Electroanal. Chem.*, **177**, 229, (1984).
27. D. D. Ateh, H. A. Navsaria, and P. Vadgama, *J. R. Soc. Interface*, **3**, 741, (2006).
28. A. T. Lawal and S. B. Adeloju, *Journal of Molecular Catalysis B-Enzymatic*, **63**, 45, (2010).
29. S. Holdcroft and B. L. Funt, *J. Electroanal. Chem.*, **240**, 89, (1988).
30. S. Kuwabata, J. Nakamura, and H. Yoneyama, *J. Chem. Soc.-Chem. Commun.*, 779, (1988).
31. Y. S. Gal, W. C. Lee, W. S. Lyoo, S. H. Jin, K. T. Lim, Y. I. Park, and J. W. Park, *Int. J. Photoenergy*, **1**, (2008).

32. P. M. S. Monk, C. Turner, and S. P. Akhtar, *Electrochim. Acta*, 44, 4817, (1999).
33. N. F. Ferreyra, S. A. Dassie, and V. M. Solis, *J. Electroanal. Chem.*, 486, 126, (2000).
34. T. Ohsaka, Y. Shintani, F. Matsumoto, T. Okajima, and K. Tokuda, *Bioelectrochem. Bioenerg.*, 37, 73, (1995).
35. A. Salimi, K. Abdi, and G. R. Khayatian, *Microchimica Acta*, 144, 161, (2004).
36. M. Karthikeyan, K. K. Satheeshkumar, and K. P. Elango, *J. Hazard. Mater.*, 167, 300, (2009).
37. J. Njagi and S. Andreescu, *Biosens. Bioelectron.*, 23, 168, (2007).
38. K. Kosmidis, V. Karalis, P. Argyrakis, and P. Macheras, *Biophys. J.*, 87, 1498, (2004).
39. S. W. Runge, B. J. F. Hill, and W. M. Moran, *CBE-Life Sciences Education*, 5, 348, (2006).
40. C. J. Halkides and R. Herman, *J. Chem. Educ.*, 84, 434, (2007).
41. C. Serge, G. Chantal, and W. Jean-Christophe, *Electroanalysis*, 13, 906, (2001).
42. M. Luque, A. Rios, and M. Valcarcel, *Analyst*, 123, 2383, (1998).
43. D. De Souza and S. A. S. Machado, *Electroanalysis*, 18, 862, (2006).

## Complexation of Sulfonated Calix[4]arene with Diquat and Paraquat

## 5.1 Introduction

The results presented in Chapter 4 described the sensitivity of the doped polypyrrole film with sulfonated-calix[4]arene (sul-calix[4]) towards the analytes diquat ( $V^{2+}$ ) and paraquat ( $MV^{2+}$ ). As discussed in Chapter 4, this may indicate an interaction between the analyte and the sul-calix[4] dopant. Given the presence of anions on the upper rim of the macrocycle, as shown in Fig. 5.1 (a), and a respective positive charge on diquat, (Fig. 5.1(b)) and paraquat (Fig. 5.1(c)), there will be an electrostatic contribution to the interaction. Also, the presence of a cavity within the charged calix[4]arene introduces the possibility of an inclusion complex being formed upon sensing either diquat or paraquat<sup>1</sup>. The results presented in this chapter discuss the stoichiometry and the nature of the interactions between sul-calix[4] and diquat, and sul-calix[4] and paraquat in solution. Probing the interaction within the polymer system is hindered by the polymer support which is in large excess of the dopant, i.e., sul-calix[4]. However, analysing the interaction within solution can be useful in understanding the probable interaction within the polymer matrix.

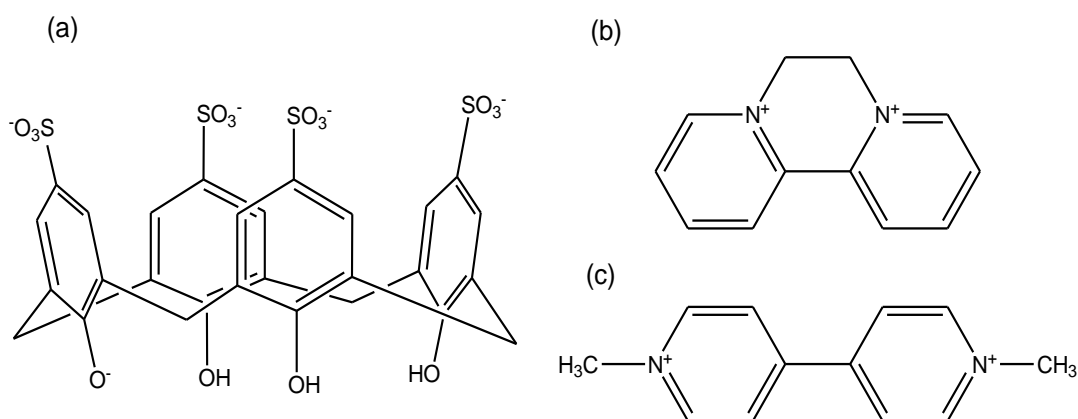


Figure 5.1: Chemical structures of (a) sul-calix[4], (b) diquat and (c) paraquat.

Within this chapter, the interactions and stoichiometry of the diquat and sul-calix[4] complex and that of the paraquat and sul-calix[4] complex are discussed and evaluated. The measure of interaction is quantified by an association constant,  $K_a^{2-4}$ . The influence of ionic strength of the solution on  $K_a$  is also investigated, as calixarenes have a high affinity for alkali cations<sup>5,6</sup>. Finally, a comparative study investigating the interactions of diquat and paraquat with neutral calix[4]arenes (calix[4]) is discussed.

Given the good detection of diquat at the sul-calix[4] doped polymer, the majority of this study was carried out on diquat and sul-calix[4] in order to understand this interaction. Previous research has been carried out investigating the complexation of diquat with a range of hosts<sup>7-9</sup>, including that of Gaeta *et al.*<sup>10</sup>, who reported a strong inclusion complex of diquat and *p*-sulfonatocalix[7]arenes. Previous work carried out by Guo *et al.*<sup>11</sup> reported a strong inclusion complex of paraquat and sul-calix[4]. Thus, a comparative study on the interaction of diquat with sul-calix[4] and paraquat with sul-calix[4] was carried out on this system, and the results are reported here.

Since the completion of this experimental work and during the writing period of this thesis, Wang *et al.*<sup>12</sup> published in September 2009 on the interaction of diquat and sul-calix[4], for the treatment of viologen poisoning. They confirmed that diquat interacts strongly with sul-calix[4]. Although this is a similar study to the results that are presented in this chapter, there are some notable differences. Firstly, the contribution of the ionic strength on the formation of the complex is thoroughly examined in this chapter. This is not discussed in this paper. Also, a range of techniques were used to quantify the measure of the interaction, in contrast to Wang *et al.*<sup>12</sup>, whereby only isothermal titration calorimetry (ITC) was used. Hence, this work aims to establish the similarities, but also to highlight the contrasts which exist between each study and the consequences of these differences.

## 5.2 Interaction of $V^{2+}$ and Sul-calix[4] using CV

Both diquat and sul-calix[4] are electrochemically active. However, the redox properties of diquat are observed at electro-negative potentials and sul-calix[4] is oxidised at a positive potential of approximately 0.8 V vs. SCE<sup>13</sup>. Thus, they are sufficiently far apart to analyse their redox activities separately. In this study, cyclic voltammetry (CV) was employed to study the redox properties of diquat in the absence and presence of sul-calix[4]. In general, in titrations quantifying the measure of interaction between two species, the concentration of one species is kept constant and monitored with respect to varying concentration of the other species. In this case, the diquat concentration was maintained at  $8.0 \times 10^{-4} \text{ mol dm}^{-3}$  and the sul-calix[4] concentration was varied.

Analysis of the interaction between diquat and sul-calix[4] was confined to the first electron reduction process of diquat ( $V^{2+} + e^- \rightarrow V^+$ ). This allowed for a valid comparison of the electrochemistry results with those obtained from <sup>1</sup>H NMR, UV-Vis and fluorescence spectroscopy, where the analyte is in a +2 oxidation state. Figure 5.2 shows the effect upon addition of sul-calix[4] to a fixed concentration of diquat. Initially, the current decreases along with potential shifts in a negative direction, as small amounts of sul-calix[4] are added. This trend indicates that  $V^{2+}$  is bound by the sul-calix[4] molecule and is not as readily available for reduction. The decrease in current is due to a slower rate of diffusion. The  $V^{2+}$  is surrounded by a large macrocycle and thus, the amount of  $V^{2+}$  reaching the interface is reduced in comparison to free  $V^{2+}$ . Similar results were recorded by Sorbransingh *et al.*<sup>14</sup> for the inclusion complex of ferrocenium and functionalised oxacalixarenes. A potential shift of 114 mV was recorded upon addition of an excess of host<sup>14</sup>. Also, Philip *et al.*<sup>15</sup> noted a four-fold decrease in current upon encapsulation of cobaltocenium with a modified resorcinarene molecule.

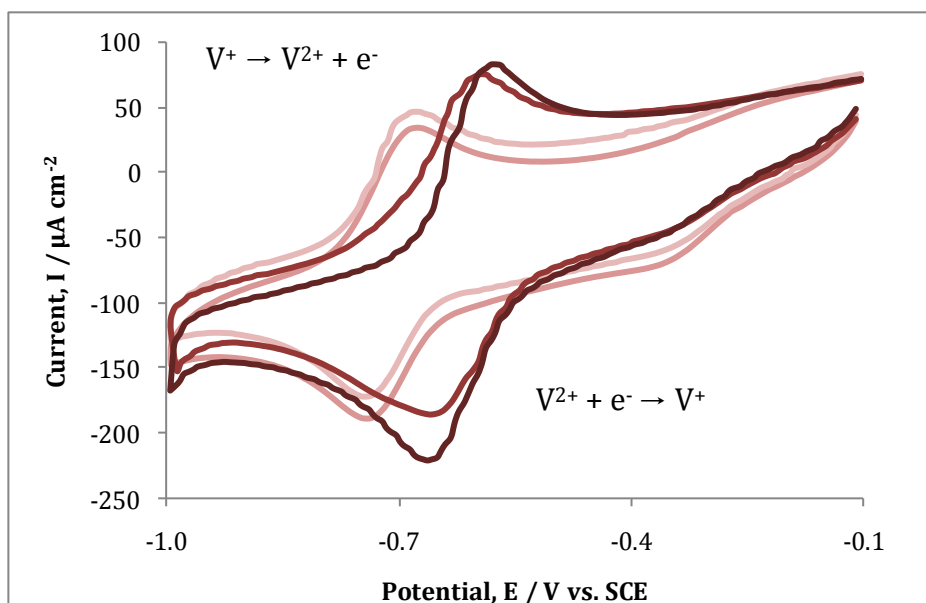


Figure 5.2: Cyclic voltammograms of  $8.0 \times 10^{-4}$  mol  $\text{dm}^{-3}$  diquat in  $0.1$  mol  $\text{dm}^{-3}$   $\text{Na}_2\text{SO}_4$  electrolyte in the presence of (—)  $0.0$ , (—)  $2.4 \times 10^{-4}$ , (—)  $2.4 \times 10^{-3}$  and (—)  $4.0 \times 10^{-3}$  mol  $\text{dm}^{-3}$  sul-calix[4]. The potential was swept from  $-0.1 \rightarrow -1.0$  V vs. SCE at  $50$   $\text{mV s}^{-1}$  at Au.

However, upon addition of equi-molar concentrations and above of sul-calix[4], there was an increase in the reduction current. This was attributed to a change in the conductivity of the solution given the charged nature of sul-calix[4]. This is clearly evident in Table 5.1, where an increase in conductance is observed upon addition of increasing concentration of sul-calix[4]. The increasing charge and ionic strength thus explain the increase in current as a function of sul-calix[4] concentration. The conductivity was calculated in accordance with Equation 5.1, where  $k$  is the conductivity of the solution in  $\Omega^{-1} \text{ m}^{-1}$ ,  $1/R$  is the conductance in  $\Omega^{-1}$  and  $l/A$  is the path length between the electrodes measured in  $\text{m}^{-1}$ .

$$k = \left(\frac{1}{R}\right) \frac{l}{A} \quad (5.1)$$

In order to maintain a constant ionic strength within each solution, the concentration of the supporting electrolyte,  $\text{Na}_2\text{SO}_4$ , was increased to  $0.5$  mol  $\text{dm}^{-3}$ . Figure 5.3 illustrates the effect of this increase on the voltammograms. The

current decreases with increasing sul-calix[4] concentration and also the potential at which  $V^{2+}$  is reduced is shifted to a greater negative value. This trend is now consistent with the formation of a complex. Table 5.2 illustrates that the conductivity of each solution is maintained within a constant range. Thus, the change observed electrochemically can be attributed to the interaction of  $V^{2+}$  and sul-calix[4] alone.

Table 5.1: Conductivity of  $0.1 \text{ mol dm}^{-3} \text{ Na}_2\text{SO}_4$  and  $8.0 \times 10^{-4} \text{ mol dm}^{-3}$  diquat containing varying amounts of sul-calix[4]. KCl was used as a standard reference to calculate the path length ( $l/A$ ), of  $1,033 \text{ m}^{-1}$ .

0.1 mol dm <sup>-3</sup> Na <sub>2</sub> SO <sub>4</sub> electrolyte and 8.0 × 10 <sup>-4</sup> mol dm <sup>-3</sup> V <sup>2+</sup>		
Sul-calix[4] / mmol dm <sup>-3</sup>	Conductance / Ω <sup>-1</sup>	Conductivity / Ω <sup>-1</sup> m <sup>-1</sup>
0.00	0.01000	10.33
0.80	0.01516	15.66
4.00	0.01594	16.46

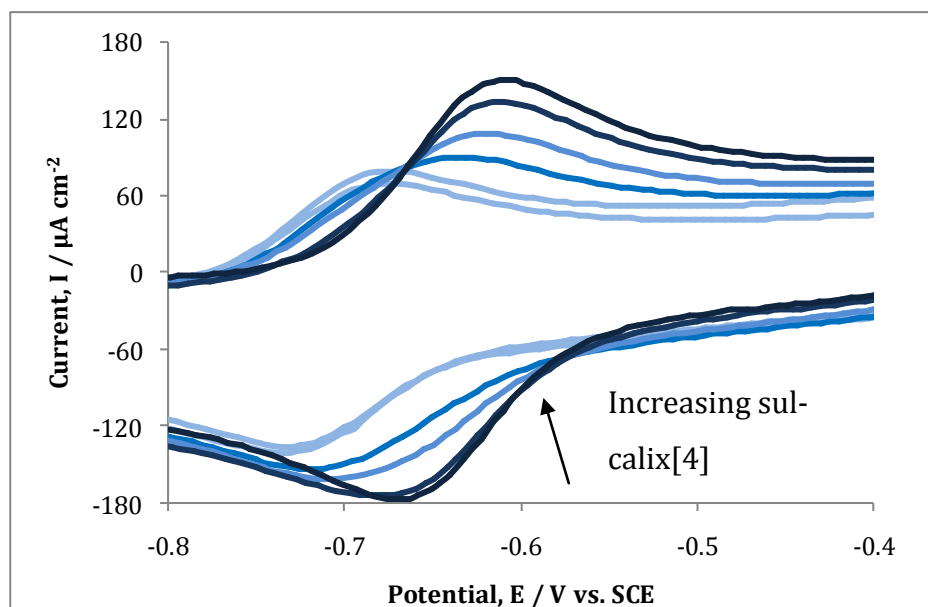


Figure 5.3: Cyclic voltammograms of  $8.0 \times 10^{-4} \text{ mol dm}^{-3} \text{ V}^{2+}$  in a  $0.5 \text{ mol dm}^{-3} \text{ Na}_2\text{SO}_4$  electrolyte in the presence of (—) 0.00, (—)  $2.38 \times 10^{-4}$ , (—)  $5.50 \times 10^{-4}$ , (—)  $7.94 \times 10^{-4}$ , (—)  $2.38 \times 10^{-3}$  and (—)  $3.97 \times 10^{-3} \text{ mol dm}^{-3}$  sul-calix[4]. The potential was swept from  $-0.1 \rightarrow -1.0 \text{ V vs. SCE}$  at a scan rate of  $50 \text{ mV s}^{-1}$  at Au.

Table 5.2: Conductivity of diquat in  $0.5 \text{ mol dm}^{-3} \text{ Na}_2\text{SO}_4$  with increasing amounts of sul-calix[4]. KCl was used as a reference to evaluate the path length,  $l/A$  of  $908 \text{ m}^{-1}$ .

0.5 mol dm <sup>-3</sup> Na <sub>2</sub> SO <sub>4</sub> electrolyte and $8.0 \times 10^{-4} \text{ mol dm}^{-3} \text{ V}^{2+}$		
Sul-calix[4] / mmol dm <sup>-3</sup>	Conductance / Ω <sup>-1</sup>	Conductivity / Ω <sup>-1</sup> m <sup>-1</sup>
0.00	0.0460	41.76
0.80	0.0462	41.95
4.00	0.0468	42.49

The changes observed in the reduction of  $\text{V}^{2+}$  with respect to the addition of sul-calix[4] indicate that there is an interaction. However, this interaction is influenced by ionic strength at the lower electrolyte solutions, as shown in Figure 5.4 (a). The plot shows an initial decrease in current, followed by an increase, where the sul-calix[4] concentration exceeds  $1.0 \times 10^{-3} \text{ mol dm}^{-3}$ . As discussed previously, the charged sul-calix[4] contributes to the increase in current, as shown by the conductivity values in Table 5.1. Figure 5.4 (b) shows that the reduction potential is not as affected as the current by the electrolyte concentration. A similar trend is observed for both the 0.1 and  $0.5 \text{ mol dm}^{-3}$  supporting electrolytes.

It is evident from Figure 5.4 (a) and (b) that the concentration of the supporting electrolyte influences the reduction of  $\text{V}^{2+}$  in the absence of sul-calix[4]. The reduction peak current is lower and the peak potential is at more negative potentials in the presence of  $0.5 \text{ mol dm}^{-3} \text{ Na}_2\text{SO}_4$  solution, compared to  $0.1 \text{ mol dm}^{-3} \text{ Na}_2\text{SO}_4$  electrolyte. This indicates that the electrochemical reduction of  $\text{V}^{2+}$  to  $\text{V}^+$  is hindered at the higher  $\text{Na}_2\text{SO}_4$  concentrations. At higher electrolyte concentrations, it appears that  $\text{V}^{2+}$  is stabilised by the ionic atmosphere of the  $\text{SO}_4^{2-}$  or  $\text{HSO}_4^-$  ions making the reduction less energetically favoured and more difficult, thereby slowing down the rate of diffusion of the  $\text{V}^{2+}$  species to the electrode interface.

This may have implications for the interaction of  $\text{V}^{2+}$  and sul-calix[4]. Indeed, there is some evidence for this from the data in Figure 5.4 (b), where the extent

of the potential shift between the free  $V^{2+}$  and the  $V^{2+}$  complexed with  $4.0 \times 10^{-3}$  mol dm $^{-3}$  sul-calix[4], is shown to depend on the concentration of the  $Na_2SO_4$  supporting electrolyte. The observed potential shift was 86 mV in the presence of 0.1 mol dm $^{-3}$   $Na_2SO_4$  and 63 mV in the presence of 0.5 mol dm $^{-3}$   $Na_2SO_4$ .

Interestingly, the excesses of sul-calix[4] relative to the fixed concentration of diquat in forming this complex were much lower than expected, as shown in Figure 5.4. In general, for the formation of a complex, large concentrations of the host species are required to shift the equilibrium towards the complex form. A plateau in both the current and potential is observed at about  $1.0 \times 10^{-3}$  mol dm $^{-3}$  of sul-calix[4], which corresponds to a 1.00:1.25 ratio of  $V^{2+}$  to sul-calix[4]. Colquhoun *et al.*<sup>16</sup> have shown that complexation occurs when one of the species is present in large excesses. Based on this, Pospisil *et al.*<sup>17</sup> reported a potential shift of approximately 30 mV upon a 5,000 fold excess of cyclodextrin host to difenzoquat guest. However, Bernardo *et al.*<sup>18</sup> recorded a potential shift of 50 mV upon the addition of a two-fold excess of sulfonated-calix[6]arene to paraquat. Given that the first case investigates the interaction of a charged guest and neutral host and the latter studies the binding of oppositely charged molecules, this indicates the importance of charge for a strong interaction.

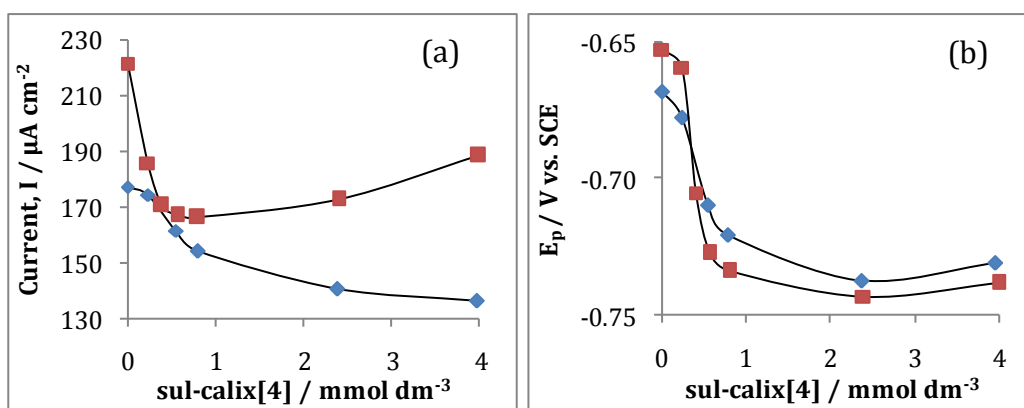


Figure 5.4: (a) Reduction peak current of  $8.0 \times 10^{-4}$  mol dm $^{-3}$   $V^{2+}$  in 0.1 mol dm $^{-3}$   $Na_2SO_4$  (■) and 0.5 mol dm $^{-3}$   $Na_2SO_4$  (◆) plotted as a function of increasing sul-calix[4] concentration. (b) The reduction peak potential of  $8.0 \times 10^{-4}$  mol dm $^{-3}$   $V^{2+}$  in 0.1 mol dm $^{-3}$   $Na_2SO_4$  (■) and 0.5 mol dm $^{-3}$   $Na_2SO_4$  (◆) plotted as a function of increasing sul-calix[4] concentration.

To investigate this interaction further, the stoichiometry of the complex was first evaluated, by means of a Job's plot. Secondly, the degree of interaction was measured upon calculation of an association constant,  $K_a$ .

### 5.3 Stoichiometry of $V^{2+}$ and Sul-calix[4]

As previously discussed in Chapter 2, Section 2.7.1, a Job's plot is a means of establishing the stoichiometry of two species within a complex<sup>19</sup>. During this experiment, the molar concentrations of sul-calix[4] and  $V^{2+}$  were kept constant, however the mole fraction was varied according to the mole fraction of  $V^{2+}$ . The stoichiometry of the  $V^{2+}$  and sul-calix[4] complex was investigated using  $^1\text{H}$  NMR and UV-Vis spectroscopy. As shown in Figure 5.5, upon increasing the mole fraction of  $V^{2+}$ , the absorbance band of  $V^{2+}$  with a  $\lambda_{\text{max}}$  at 310 nm increases. The absorption band in the range of 260-280 nm corresponds to the absorbance of sul-calix[4]. To ensure that only the absorbance of  $V^{2+}$  was measured, the absorbance was recorded at a fixed wavelength of 320 nm. At this wavelength sul-calix[4] does not absorb.

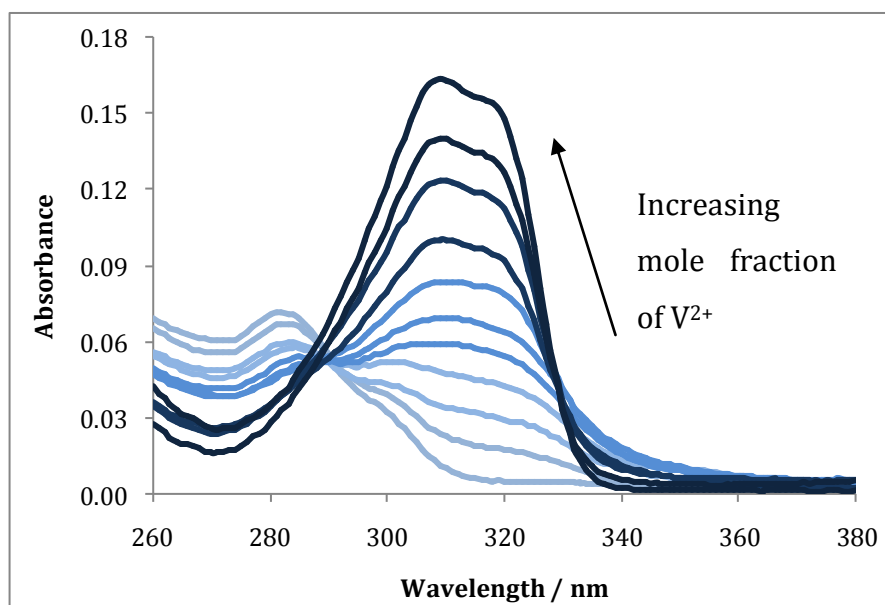


Figure 5.5: UV-Vis spectra of  $V^{2+}$  with increasing mole fractions of  $V^{2+}$  in a sul-calix[4] solution. The mole fraction ranged from 0.0  $\rightarrow$  1.0 with increments of 0.1. Each sample was prepared to a volume of 3.0  $\text{cm}^3$  in distilled  $\text{H}_2\text{O}$ , from stock solutions of  $1.0 \times 10^{-5} \text{ mol dm}^{-3}$   $V^{2+}$  and sul-calix[4], respectively.

The product of the change in absorbance and mole fraction of  $V^{2+}$  was calculated and then plotted as a function of the mole fraction of  $V^{2+}$  to generate a Job's plot as shown in Figure 5.6 (a). This bell shaped curve with a maximum of 0.5 is indicative of a 1:1 complex<sup>20,21</sup>. In order to verify this means of analysis, a Job's plot using  $^1\text{H}$  NMR data was also prepared. A similar method was applied in carrying out a Job's plot using  $^1\text{H}$  NMR data. The initial molar concentrations of  $V^{2+}$  and sul-calix[4] were identical and the mole fraction of  $V^{2+}$  was varied from 0.0 to 1.0, by combining different ratios of the two stock solutions. To generate a Job's plot using  $^1\text{H}$  NMR data, the changes in chemical shift ( $\delta$ ) of the signal due to  $V^{2+}$  with respect to increasing mole fraction was monitored. Throughout this analysis the  $\beta$ -H, which is the proton coupled to the secondary carbon, was monitored. This was chosen as there was no interference from solvent or sul-calix[4] signals. As shown in Table 5.3, at an increasing mole fraction of  $V^{2+}$ , the chemical shifts increase downfield. The change in chemical shift, ( $\Delta\delta$ ), of  $V^{2+}$  at a mole fraction of 1.0 and  $V^{2+}$  at varying mole fractions were multiplied by the corresponding mole fraction of  $V^{2+}$ . These values were then plotted as a function of mole fraction of  $V^{2+}$  as shown in Figure 5.6 (b). A bell shaped curve with a maximum of 0.5 was evident<sup>20,22</sup>. This is in good agreement with the plotted UV-Vis data in Figure 5.6 (a). This clearly shows that the interaction between  $V^{2+}$  and sul-calix[4] is in a 1:1 ratio.

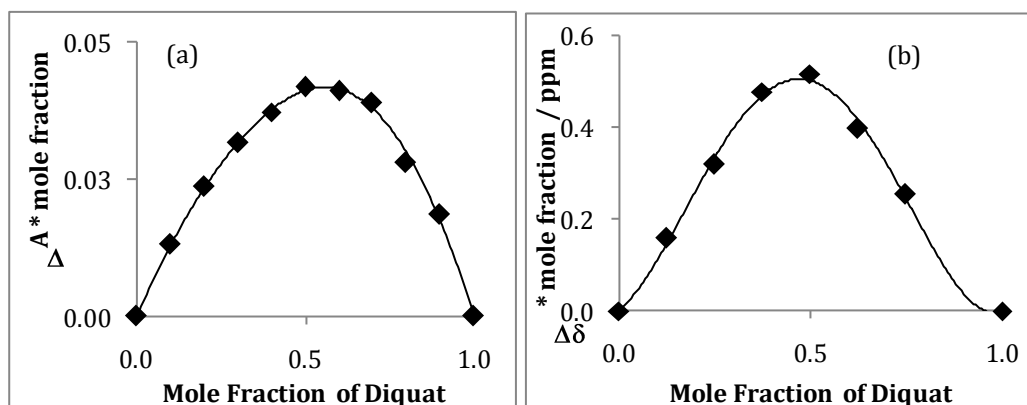


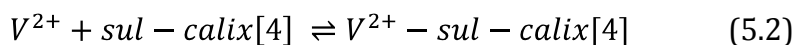
Figure 5.6: Job's plot of  $V^{2+}$  and sul-calix[4] using (a) UV-Vis spectroscopy and (b)  $^1\text{H}$  NMR spectroscopy. Each plot has a maximum absorption and chemical shift change at a mole fraction of 0.5. This corresponds to a stoichiometry of 1:1 for  $V^{2+}$  and sul-calix[4].

Table 5.3:  $^1\text{H}$  NMR recorded for  $\text{V}^{2+}$  as a function of the mole fractions of  $\text{V}^{2+}$  in sul-calix[4]. Each sample was prepared to  $0.4\text{ cm}^3$  in  $\text{D}_2\text{O}$ . The mole fraction of  $\text{V}^{2+}$  was calculated as  $[\text{V}^{2+}] / ([\text{V}^{2+}] + [\text{sul-calix[4]})$ . The change in chemical shift ( $\Delta\delta$ ) was calculated from the difference of the chemical shift of free  $\text{V}^{2+}$  at a mole fraction of 1.0 ( $\delta_f$ ) and the chemical shifts of  $\text{V}^{2+}$  in the presence of sul-calix[4] ( $\delta_c$ ).

Job's Plot – $^1\text{H}$ NMR		
Mole Fraction of $\text{V}^{2+}$	$\delta_{(\text{V}^{2+})} / \text{ppm}$	$\Delta\delta_{(\delta_f - \delta_c)} / \text{ppm}$
0.000	-	-
0.125	7.891	1.276
0.250	7.891	1.276
0.375	7.891	1.276
0.500	8.133	1.034
0.625	8.530	0.637
0.750	8.830	0.337
1.000	9.167	0.000

#### 5.4 Evaluation of the association constant, $K_a$ , for sul-calix[4] and $\text{V}^{2+}$

The stoichiometry evaluated by means of a Job's plot in Section 5.3 illustrated a 1:1 complex between  $\text{V}^{2+}$  and sul-calix[4]. In order to gain more information on the nature of this complex and the strength of the interaction, an association constant,  $K_a$ , was evaluated. The equilibrium between  $\text{V}^{2+}$ , sul-calix[4] and the complex,  $\text{V}^{2+}$ -sul-calix[4], can be represented by Equation 5.2, while the association constant is given by Equation 5.3<sup>23</sup>. The concentrations in Equation 5.2 represent the equilibrium concentrations of  $\text{V}^{2+}$ , sul-calix[4] and  $\text{V}^{2+}$ -sul-calix[4].



$$K_a = \frac{[\text{V}^{2+} - \text{sul-calix[4]}]}{[\text{V}^{2+}][\text{sul-calix[4]}]} \quad (5.3)$$

The association constant,  $K_a$ , can easily be obtained using electrochemical techniques, such as cyclic voltammetry (CV) and rotating disc voltammetry (RDV). This analysis is based on the fact that if a complex is formed, then  $V^{2+}$  will be more difficult to oxidise or reduce, leading to variations in the oxidation or reduction potentials. In addition, if the complex formed is larger in size than the free  $V^{2+}$ , then it will diffuse more slowly, giving rise to a lowering in the peak current<sup>3,24,25</sup>. In all cases, the equilibrium must be sufficiently shifted to that of the complex over the free sul-calix[4] and  $V^{2+}$  in solution.

The interaction of  $V^{2+}$  with sul-calix[4] appears to depend on the nature of the supporting electrolyte, as shown in Section 5.2. Accordingly, the electrochemical experiments were recorded in two supporting electrolytes, 0.1 and 0.5 mol dm<sup>-3</sup> Na<sub>2</sub>SO<sub>4</sub>, respectively. This dual experiment set out to investigate the influence of charge and ionic strength on the magnitude of  $K_a$ . Indeed, Sindelar *et al.*<sup>26</sup> found that an increase in the electrolyte concentration can lead to a decrease in the value of  $K_a$ . The authors confirmed competition between the sodium cation and anthraquinone for cucurbit[7]uril<sup>26</sup>. As an electrochemical approach is limited by the need for a supporting electrolyte, two other spectroscopic techniques, UV-Vis and fluorescence spectroscopy were used to study the interactions in low ionic strength. Finally, <sup>1</sup>H NMR spectroscopy was used to obtain structural information on the nature of the complex.

#### **5.4.1 Evaluation of $K_a$ for Sul-calix[4] with $V^{2+}$ using RDV**

As explained previously in Chapter 2, Section 2.4.5, RDV eliminates the time dependent processes of diffusion and instead controls the rate of mass transport by convection<sup>27</sup>. In the case of the CV technique, the diffusion process is time dependent. Furthermore, the CV approach may not be the most accurate in calculating the  $K_a$  value as the changes observed in the peak currents may not only be due to a binding interaction, but also due to changes in the viscosity of the solution on addition of sul-calix[4]<sup>28</sup>. However, the relatively small concentrations of sul-calix[4] used in this study will give rise to negligible changes in the viscosity of the solution. Nevertheless, the RDV technique was

chosen as it tends to produce better quality data with higher reproducibility. Typical RDV data recorded for  $V^{2+}$  in a  $0.5 \text{ mol dm}^{-3} \text{ Na}_2\text{SO}_4$  solution are presented in Figure 5.7. Reduction of diquat ( $V^{2+} + e^- \rightarrow V^+$ ) is observed at approximately  $-0.6 \text{ V}$  vs. SCE, which agrees well with the cyclic voltammograms depicted in Figure 5.3. Limiting currents are observed at potentials lower than  $-0.7 \text{ V}$  vs. SCE, indicating limiting mass transfer conditions. The limiting current clearly increases with rotation rate.

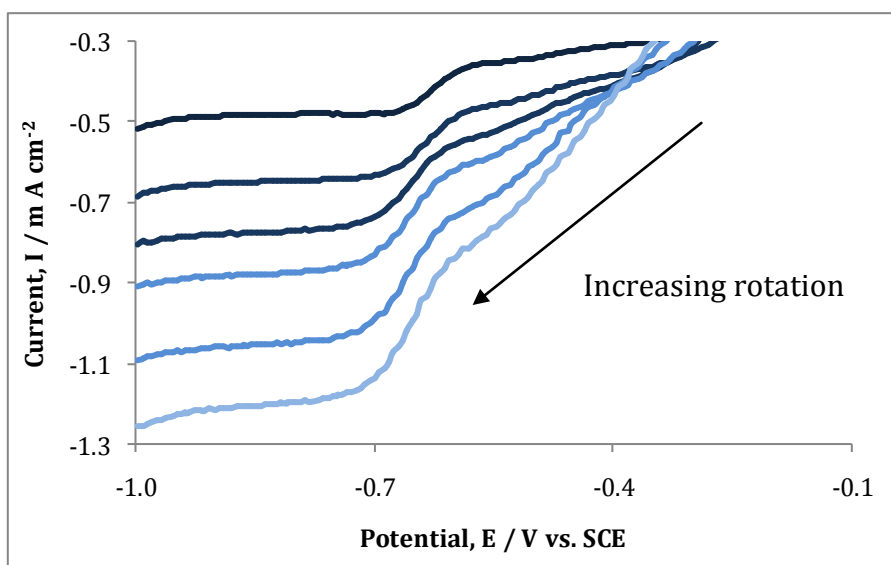


Figure 5.7: RDV of  $8.0 \times 10^{-4} \text{ mol dm}^{-3} V^{2+}$  in  $0.5 \text{ mol dm}^{-3} \text{ Na}_2\text{SO}_4$  solution at rotation rates of (—) 250 rpm, (—) 500 rpm, (—) 750 rpm, (—) 1,000 rpm, (—) 1,500 rpm and (—) 2,000 rpm. The potential was swept from  $-0.1 \text{ V} \rightarrow -1.0 \text{ V}$  vs. SCE at  $50 \text{ mV s}^{-1}$  at Au.

The influence of sul-calix[4] on the rotating disc voltammograms recorded for  $8.0 \times 10^{-4} \text{ mol dm}^{-3} V^{2+}$  in  $0.5 \text{ mol dm}^{-3} \text{ Na}_2\text{SO}_4$  at a fixed rotation rate of 250 rpm is clearly evident in Figure 5.8. There is a clear decrease in the limiting current as higher concentrations of sul-calix[4] are added. Moreover, there is a clear shift in the half-wave potentials ( $E_{1/2}$ ) to more negative values as the concentration of sul-calix[4] is increased. For example, the  $E_{1/2}$  is  $-642 \text{ mV}$  vs. SCE for pure  $V^{2+}$ , but is  $-677 \text{ mV}$  vs. SCE with a three-fold excess of sul-calix[4]. This trend corresponds to that shown in Figure 5.3 confirming the formation of a complex. Similar to the results presented in Section 5.2, small excesses of sul-

calix[4] give rise to large changes in the peak current and peak potentials, which indicates the strength of this interaction.

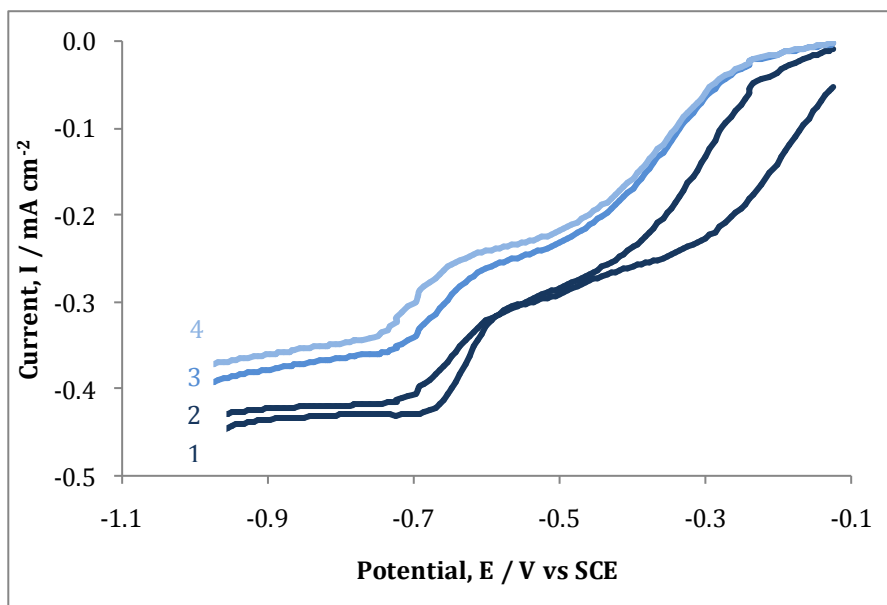


Figure 5.8: RDV of  $8.0 \times 10^{-4} \text{ mol dm}^{-3} \text{ V}^{2+}$  in  $0.5 \text{ mol dm}^{-3} \text{ Na}_2\text{SO}_4$  with additions of sul-calix[4], (1) 0.0, (2)  $5.6 \times 10^{-4}$ , (3)  $8.0 \times 10^{-4}$  and (4)  $2.4 \times 10^{-3} \text{ mol dm}^{-3}$ . The potential was swept from  $-0.1 \rightarrow -1.0 \text{ V vs. SCE}$ , at a fixed rotation of 250 rpm, at  $50 \text{ mV s}^{-1}$  at Au.

Voltammograms of samples containing varying amounts of sul-calix[4] and  $8.0 \times 10^{-4} \text{ mol dm}^{-3} \text{ V}^{2+}$ , in either  $0.1$  or  $0.5 \text{ mol dm}^{-3} \text{ Na}_2\text{SO}_4$ , were carried out at different rotation rates. Using these data, Levich plots were constructed as shown in Figure 5.9. The slope was used to evaluate the diffusion coefficient ( $D_c$ ) for all samples, in accordance with Equation 5.4<sup>29</sup>, where  $i_L$  is the limiting current in A,  $n$  is the number of electrons transferred through oxidation or reduction,  $F$  is the Faraday's constant of  $96,485.3415 \text{ C mol}^{-1}$ ,  $A$  is the surface area in  $\text{cm}^2$ ,  $\nu$  is kinematic viscosity in  $\text{cm}^2 \text{ s}^{-1}$ ,  $c$  is the concentration of the analyte in  $\text{mol cm}^{-3}$ ,  $\omega$  is the angular velocity in  $\text{rad s}^{-1}$  and  $D_c$  is the diffusion coefficient in  $\text{cm}^2 \text{ s}^{-1}$ .

$$i_L = 0.621nFAD_c^{2/3}\nu^{-1/6}c\omega^{1/2} \quad (5.4)$$

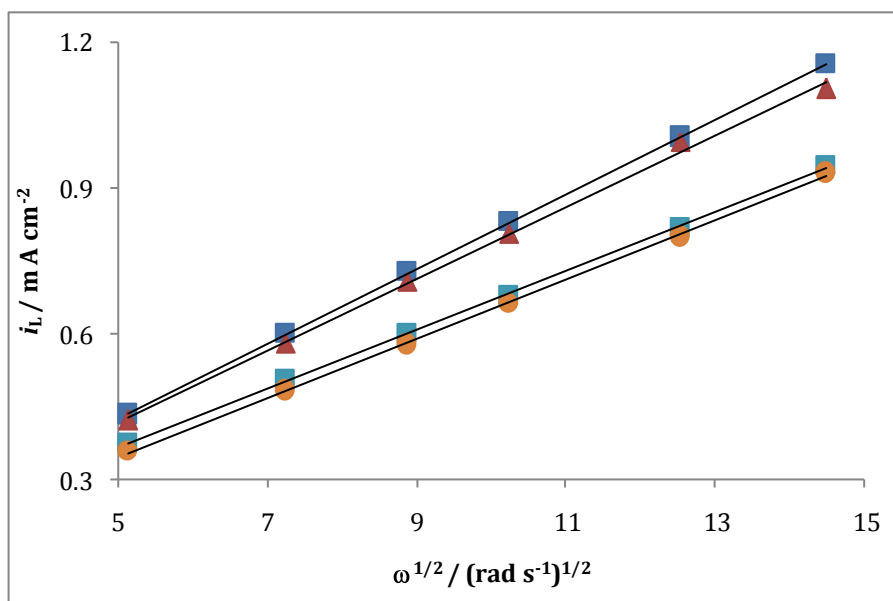


Figure 5.9: Levich plots of limiting current ( $i_L$ ) as a function of the square root of rotation speed ( $\omega^{1/2}$ ), for  $8.0 \times 10^{-4} \text{ mol dm}^{-3} \text{ V}^{2+}$  in the presence of (■) 0.0, (▲)  $5.6 \times 10^{-4}$ , (◻)  $8.0 \times 10^{-4}$  and (●)  $4.0 \times 10^{-3} \text{ mol dm}^{-3}$  sul-calix[4].

Each plot shows a linear relationship, with correlation coefficients ( $R^2$ ) in the range of 0.967 to 0.992. The  $D_c$  values decreased from  $2.05 \times 10^{-5} \text{ cm s}^{-1}$  for pure  $\text{V}^{2+}$  to a minimum of  $1.42 \times 10^{-5} \text{ cm}^2 \text{ s}^{-1}$  upon increasing the sul-calix[4] concentration. This minimum occurred when a five-fold excess of sul-calix[4] was added to  $\text{V}^{2+}$ , indicating that this was a sufficient excess to form a complex with  $\text{V}^{2+}$ . The recorded data corresponds to the literature wherein a  $D_c$  value of  $1.10 \times 10^{-5} \text{ cm}^2 \text{ s}^{-1}$  for  $\text{V}^{2+}$  was reported using CV<sup>30</sup>. The relative ratio of  $D_c$  of the free  $\text{V}^{2+}$  ( $\text{V}^{2+}_f$ ) with respect to the complexed  $\text{V}^{2+}$  ( $\text{V}^{2+}_{\text{com}}$ ) was calculated to be approximately 0.69. This value is consistent with the literature and is indicative of a binding interaction<sup>31</sup>.

Similar trends were observed using an electrolyte solution of  $0.1 \text{ mol dm}^{-3} \text{ Na}_2\text{SO}_4$ . However, the half-wave potentials and diffusion coefficients of  $\text{V}^{2+}$  in the presence and absence of sul-calix[4] were found to depend on the concentration of  $\text{Na}_2\text{SO}_4$ , as shown in Figure 5.10 (a) and (b). In general, a similar pattern was observed with increasing amounts of sul-calix[4] for both

concentrations of electrolyte, i.e., the decrease in  $D_c$  and the negative potential shift of  $E_{1/2}$ . However, further analysis of the potential shifts indicates that there is a larger overall potential shift for those samples in 0.1 mol dm<sup>-3</sup> Na<sub>2</sub>SO<sub>4</sub> in comparison to those in 0.5 mol dm<sup>-3</sup> solutions. This could imply competition between Na<sup>+</sup> and V<sup>2+</sup> with regard to the interaction with the anionic calixarene.

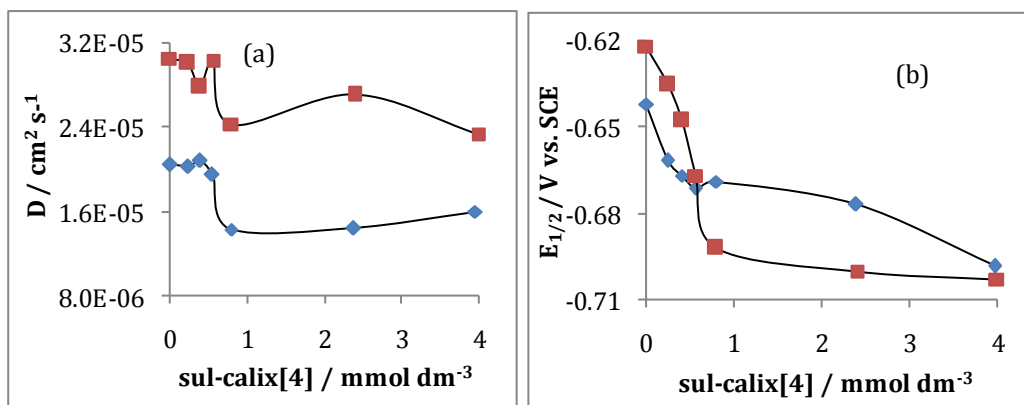


Figure 5.10: (a) Diffusion coefficients ( $D_c$ ) of  $8 \times 10^{-4}$  mol dm<sup>-3</sup> V<sup>2+</sup> in the presence of varying concentrations of sul-calix[4] in a (■) 0.1 mol dm<sup>-3</sup> and a (◆) 0.5 mol dm<sup>-3</sup> Na<sub>2</sub>SO<sub>4</sub> electrolyte solution. (b) Half-wave potentials ( $E_{1/2}$ ) of  $8 \times 10^{-4}$  mol dm<sup>-3</sup> V<sup>2+</sup> in the presence of varying concentrations of sul-calix[4] in a (■) 0.1 mol dm<sup>-3</sup> and a (◆) 0.5 mol dm<sup>-3</sup> Na<sub>2</sub>SO<sub>4</sub> electrolyte solution.

It has been well documented that cations have an affinity for negatively charged calixarenes<sup>32</sup>. Guo *et al.*<sup>32</sup> demonstrated the affinities that mono-valent and multi-valent cations have for the charged calix[4]arene using ITC (isothermal titration calorimetry). They found that the interaction was predominately electrostatic with the sulfonated groups on the upper rim, and in particular for Na<sup>+</sup> ions, there was inclusion due to the cation- $\pi$  interactions<sup>32</sup>.

The  $K_a$  values were calculated using the diffusion coefficients and the potential shifts using Equation 5.5<sup>3</sup>. In this equation,  $F$  is the Faraday's constant of 96,485.3415 C mol<sup>-1</sup>,  $R$  is the gas constant of 8.3145 J K<sup>-1</sup> mol<sup>-1</sup>,  $T$  is the temperature in K,  $E_{1/2app}$  and  $E_{1/2f}$  are the half-wave potentials of the complex and free V<sup>2+</sup>, in V vs. SCE,  $K_a$  is the binding constant in mol<sup>-1</sup> dm<sup>3</sup>, *sul-calix[4]* is

the concentration of sul-calix[4] in mol dm<sup>-3</sup>,  $D_c$  and  $D_f$  are the diffusion coefficients in cm<sup>2</sup> s<sup>-1</sup> of the complexed V<sup>2+</sup> and free V<sup>2+</sup>, respectively.

$$\left(\frac{F}{RT}\right) \left\{ (E_{\frac{1}{2}})_{app} - (E_{\frac{1}{2}})_f \right\} = \ln(1 + K_a[sul - calix[4]]) + \ln\left(\frac{D_c}{D_f}\right)^{1/2} \quad (5.5)$$

$K_a$  values of  $2.00 \times 10^3$  and  $7.95 \times 10^3$  mol<sup>-1</sup> dm<sup>3</sup> were obtained for the 0.5 and 0.1 mol dm<sup>-3</sup> electrolyte concentrations, respectively. The values depicted in Table 5.4 indicate the formation of a strong complex between V<sup>2+</sup> and sul-calix[4]. Also, the results show that  $K_a$  is almost quartered upon increasing the electrolyte concentration five-fold. This confirms the significant role charge and consequently the ionic strength has on the interaction of V<sup>2+</sup> and sul-calix[4]. This was also observed using CV and shown in Section 5.2. As these values are considerably larger than those reported in the literature<sup>7,16</sup>, for the interaction of V<sup>2+</sup> with a range of other molecules, it is clear that sul-calix[4] has a high affinity for V<sup>2+</sup>.

Table 5.4: Association constants,  $K_a$ , of V<sup>2+</sup> and sul-calix[4] at 0.1 and 0.5 mol dm<sup>-3</sup> Na<sub>2</sub>SO<sub>4</sub> electrolyte concentrations.

Association Constant, $K_a$ / mol <sup>-1</sup> dm <sup>3</sup>	
0.5 mol dm <sup>-3</sup> Na <sub>2</sub> SO <sub>4</sub> electrolyte	0.1 mol dm <sup>-3</sup> Na <sub>2</sub> SO <sub>4</sub> electrolyte
$(2.00 \pm 0.02) \times 10^3$ mol <sup>-1</sup> dm <sup>3</sup>	$(7.95 \pm 0.19) \times 10^3$ mol <sup>-1</sup> dm <sup>3</sup>

As published by Wang *et al.*<sup>12</sup>, analysis of the interaction of V<sup>2+</sup> and sul-calix[4] yielded much higher binding constants of  $5.40 \times 10^5$  and  $7.95 \times 10^5$  mol<sup>-1</sup> dm<sup>3</sup> at a pH of 2.0 and 7.0, respectively. Interestingly, a 0.1 mol dm<sup>-3</sup> phosphate buffer was used to maintain a constant pH of 7.0. In preparing the acidic solution, phosphoric acid was added to a previously prepared phosphate buffered solution at a pH of 7.0. Altering the pH of a buffer solution at a neutral pH value to an acidic pH value requires a significantly higher concentration of H<sup>+</sup> ions. Therefore, in this instance the ionic strength was not maintained constant

between the two pH studies. Cyclic voltammetry was also used by this group to investigate the interaction of diquat and sul-calix[4]. Similarly, they observed a decrease in current and a shift in the reduction potential of  $V^{2+}$  when 1.0 equivalents of sul-calix[4] was added to 1.0 equivalents of diquat. However, no further analysis was followed up from this result.

Aside from calculating the association constant using RDV, these data can also be used to calculate the rate constant,  $k$ , of  $V^{2+}$ . The rate constant corresponds to the kinetics of heterogeneous electron transfer at the interface upon either oxidation or reduction<sup>33</sup>. The Gibbs energy barrier ( $\Delta G$ ) of the electron transfer is dependent on the reorganisation energy and the work done in bringing the reactants to the reaction site<sup>34,35</sup>. Thus, low reorganisation energy with an increased rate at which the reactants are brought to the surface increases the electron transfer. The rate constant,  $k$ , can be calculated using the Koutechy-Levich equation, Equation 5.6<sup>36</sup>.

$$\frac{1}{i_L} = \frac{1}{nFAk_{DQC}} + \frac{1.61}{nFA\nu^{-1/6}D^{2/3}\omega^{1/2}c} \quad (5.6)$$

As shown in Figure 5.11, plotting the inverse of the limiting current,  $i_L^{-1}$ , as a function of the inverse of the square root of rotation frequency,  $(\omega^{1/2})^{-1}$ , gives a linear plot from which the rate constant can be evaluated.

Tables 5.5 and 5.6 show the change in the rate constant for the reduction of diquat ( $V^{2+} + e^- \rightarrow V^+$ ) with respect to increasing sul-calix[4] and also the concentration variant in the electrolyte solution. As shown for both electrolytes, there is a significant decrease in  $k$  upon addition of equi-molar quantities of sul-calix[4]. The higher reorganisation energy and the increased work to bring the diquat bound by a larger sul-calix[4] reduces the rate of transfer. Again, this is further evidence of an interaction between  $V^{2+}$  and sul-calix[4].

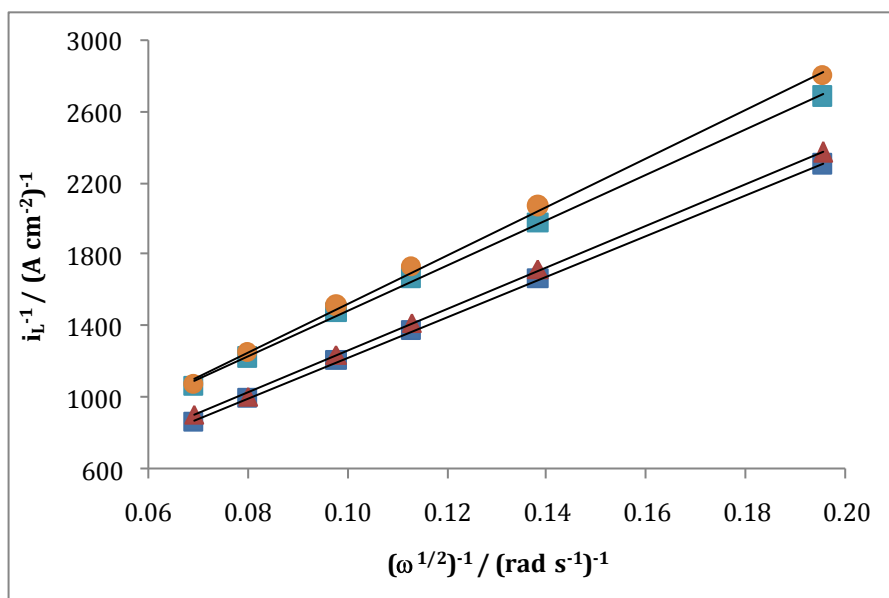


Figure 5.11: Koutechy-Levich plots of  $i_L^{-1}$  as a function of  $(\omega^{1/2})^{-1}$ . These data were plotted from RDVs carried out using  $8.0 \times 10^{-4} \text{ mol dm}^{-3} \text{ V}^{2+}$  in the presence of (■) 0.0, (▲)  $5.6 \times 10^{-4}$ , (■)  $8.0 \times 10^{-4}$  and (●)  $4.0 \times 10^{-3} \text{ mol dm}^{-3}$  sul-calix[4].

Table 5.5: Rate constant,  $k$ , of  $8.0 \times 10^{-4} \text{ mol dm}^{-3} \text{ V}^{2+}$  at varying concentrations of sul-calix[4] in  $0.5 \text{ mol dm}^{-3}$  solution of  $\text{Na}_2\text{SO}_4$ . The rate constant,  $k$ , was evaluated from the intercept of  $i_L^{-1}$  as a function of  $(\omega^{1/2})^{-1}$ . From these plots, correlation coefficients were found to be either 0.998 or 0.999, indicating the linearity and validity in using the Koutechy-Levich equation.

Rate Constants for $\text{V}^{2+}$ in the absence and presence of sul-calix[4]			
0.5 mol dm <sup>-3</sup> Na <sub>2</sub> SO <sub>4</sub> electrolyte			
sul-calix[4] / mol dm <sup>-3</sup>	[V <sup>2+</sup> ] : [sul-calix[4]]	Rate Constant, $k$ / cm s <sup>-1</sup>	Correlation coefficient / R <sup>2</sup>
0.00	1.0 : 0.0	0.140	0.999
$4.0 \times 10^{-4}$	1.0 : 0.5	0.078	0.999
$5.6 \times 10^{-4}$	1.0 : 0.7	0.056	0.998
$8.0 \times 10^{-4}$	1.0 : 1.0	0.039	0.998

Table 5.6: Rate constant,  $k$ , for the reduction of  $V^{2+}$  as a function of the concentrations of sul-calix[4] in  $0.1 \text{ mol dm}^{-3}$  solution of  $\text{Na}_2\text{SO}_4$ . Other conditions are identical to that in Table 5.5.

Rate Constants for $V^{2+}$ in the absence and presence of sul-calix[4]			
0.1 mol dm <sup>-3</sup> Na <sub>2</sub> SO <sub>4</sub> electrolyte			
sul-calix[4] / mol dm <sup>-3</sup>	[V <sup>2+</sup> ] : [sul- calix[4]]	Rate Constant, $k$ / cm s <sup>-1</sup>	Correlation coefficient / R <sup>2</sup>
0.0	1.0 : 0.0	0.138	0.999
$2.4 \times 10^{-4}$	1.0 : 0.3	0.122	0.999
$4.0 \times 10^{-4}$	1.0 : 0.5	0.115	0.999
$8.0 \times 10^{-4}$	1.0 : 1.0	0.090	0.999
$4.0 \times 10^{-3}$	1.0 : 5.0	0.078	0.998

Due to the influence and importance of charge in measuring the interaction of  $V^{2+}$  and sul-calix[4] electrochemically, the measure of interaction was further investigated spectroscopically using UV-Vis and fluorescence spectroscopy. As these techniques do not depend on the presence of a conducting solution to ensure the transfer of electrons, it was proposed that both these methods would give a true measure of the level of binding without the interference of  $\text{Na}^+$  ions.

#### 5.4.2. Evaluation of $K_a$ for Sul-calix[4] with $V^{2+}$ using UV-Vis Spectroscopy

Both  $V^{2+}$  and sul-calix[4] absorb within the UV region of the electromagnetic spectrum, as shown in Figure 5.12. However, the maximum absorption ( $\lambda_{\text{max}}$ ) of sul-calix[4] is at 280 nm and for  $V^{2+}$ , it is at 310 nm. Thus, they are sufficiently far apart to monitor one species over the other. In order to quantify the  $K_a$  value, the absorbance of  $V^{2+}$  at 320 nm was monitored with respect to varying concentrations of sul-calix[4]. Figure 5.12 clearly shows that at 320 nm there is no absorbance of sul-calix[4].

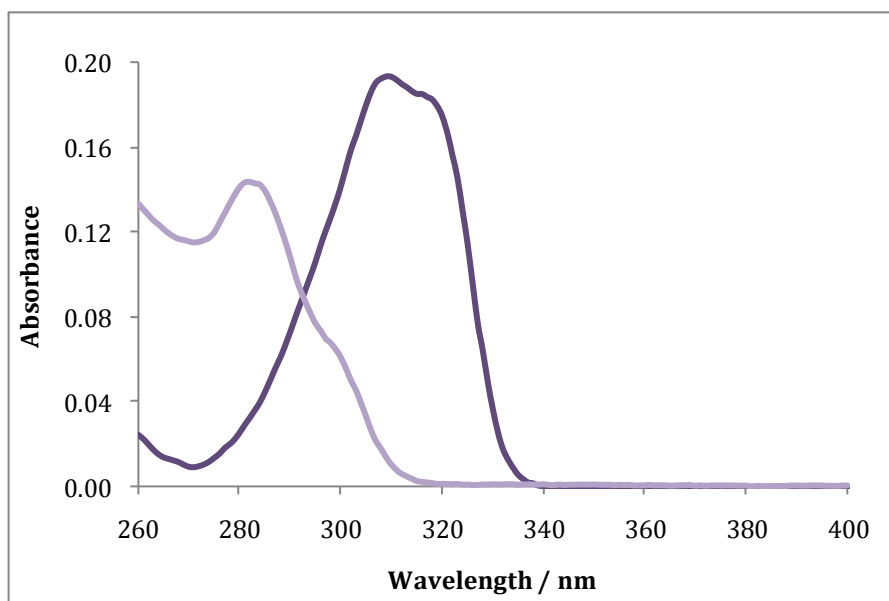


Figure 5.12: Absorbance of (---)  $1.92 \times 10^{-5} \text{ mol dm}^{-3} \text{ V}^{2+}$  and (—)  $2.04 \times 10^{-5} \text{ mol dm}^{-3} \text{ sul-calix[4]}$  in the UV region. The solutions were prepared in distilled  $\text{H}_2\text{O}$ . Each sample was scanned from 260 to 400 nm.

Using the relative ratios of sul-calix[4] to  $\text{V}^{2+}$  employed for the RDV measurements, a UV-Vis titration was carried out and the recorded data are shown in Figure 5.13. Upon addition of sul-calix[4], the absorbance of  $\text{V}^{2+}$  decreased. This trend, known as a hypochromic effect is due to a decrease in the extinction coefficient for the absorption band upon complexation. It is typical in the formation of complexes<sup>37</sup>. The slight shift of the  $\lambda_{\text{max}}$  of diquat to a longer wavelength is referred to a bathochromic shift or red-shift. Zhang *et al.*<sup>38</sup> recorded a similar effect upon complexing sul-calix[4] with diphenylamine-4-diazonium chloride.

The recorded data were used to generate a Heildebrand-Bensei plot<sup>39</sup>, as shown in Figure 5.14. This plot is based on Equation 5.7, in which the slope and the intercept are necessary to calculate  $K_a$ . Here,  $A$  and  $A_0$  are the absorbance values of  $\text{V}^{2+}$  in the presence and absence of sul-calix[4], respectively and  $\epsilon_{\text{H}}$  and  $\epsilon_{\text{G}}$  are the extinction coefficients of sul-calix[4] and  $\text{V}^{2+}$ , respectively.

$$\frac{A_0}{A - A_0} = \frac{\varepsilon_G}{\varepsilon_{H-G} - \varepsilon_G} + \frac{\varepsilon_G}{\varepsilon_{H-G} - \varepsilon_G} \times \frac{1}{K_a[\text{sul} - \text{calix}[4]]} \quad (5.7)$$

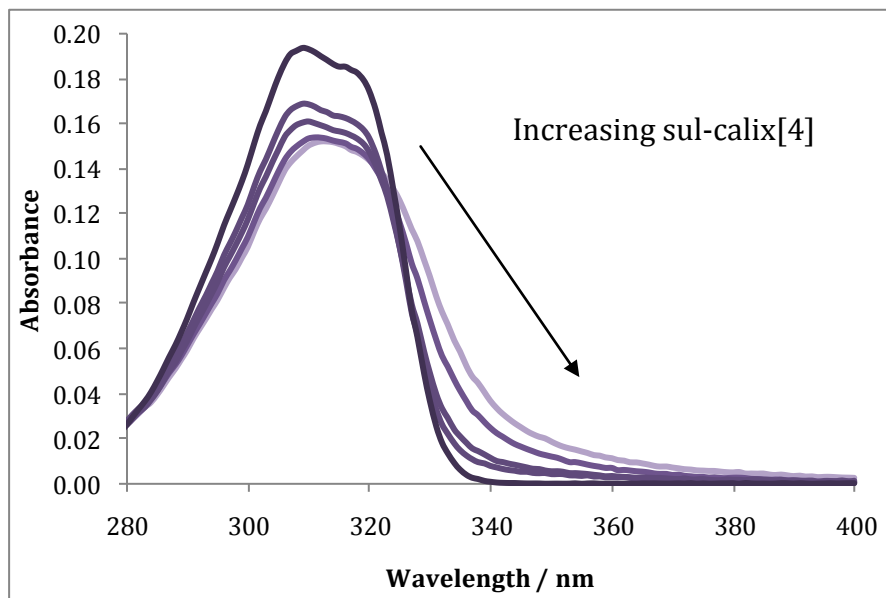


Figure 5.13: UV-titration of  $1.92 \times 10^{-5} \text{ mol dm}^{-3} \text{ V}^{2+}$  in the presence of (—) 0.00, (—)  $1.54 \times 10^{-5}$ , (—)  $7.68 \times 10^{-6}$ , (—)  $2.88 \times 10^{-6}$ , (—)  $1.44 \times 10^{-6} \text{ mol dm}^{-3}$  sul-calix[4]. All samples were prepared using distilled  $\text{H}_2\text{O}$ .

The value of  $K_a$  shown in Table 5.7 was  $2.14 \times 10^6 \text{ mol}^{-1} \text{ dm}^3$ , which is extremely high in comparison to that recorded for RDV, as shown in Table 5.4. However, as previously reported by Guo *et al.*<sup>32</sup>, monovalent cations have a high affinity for sul-calix[n]. Also, Gennady *et al.*<sup>40</sup> demonstrated that electrolytes tend to depress the magnitude of the binding constant in the formation of [1+1] cavitantd-calix[4]arene<sup>40</sup>. Given the absence of an electrolyte solution in carrying out the UV-Vis measurements, this study confirms the significant influence of the ionic strength on the value of  $K_a$ .

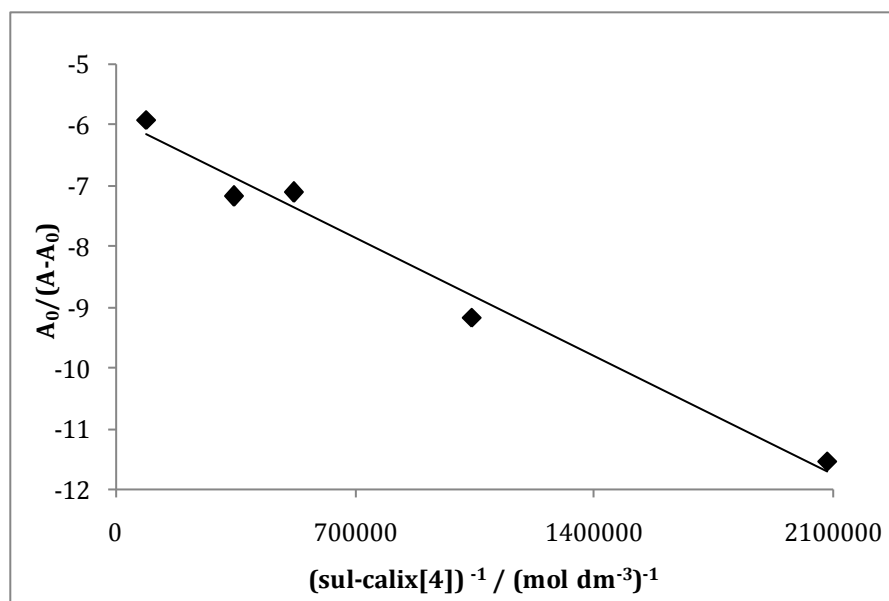


Figure 5.14: Heildebrand-Bensei plot of  $A_0/(A-A_0)$  as a function of  $(\text{sul-calix[4]})^{-1}$ . From the slope and intercept of this plot,  $K_a$  was evaluated. The correlation coefficient,  $R^2$ , was 0.981.

Table 5.7: Slopes of Heildebrand-Bensei plots and  $K_a$  values as a function of the diquat and  $\text{Na}_2\text{SO}_4$  concentrations.

UV-Vis Analysis			
$\text{Na}_2\text{SO}_4 / \text{mol dm}^{-3}$	$\text{V}^{2+} / \text{mol dm}^{-3}$	Slope / $\text{mol dm}^{-3}$	$K_a / \text{mol}^{-1} \text{dm}^3$
0.00	$1.00 \times 10^{-5}$	$-2.772 \times 10^{-6}$	$(2.14 \pm 0.26) \times 10^6$
$1.25 \times 10^{-3}$	$1.00 \times 10^{-5}$	$-4.144 \times 10^{-6}$	$(1.07 \pm 0.25) \times 10^6$
$5.00 \times 10^{-3}$	$4.00 \times 10^{-5}$	$-8.819 \times 10^{-5}$	$(8.12 \pm 0.86) \times 10^4$
$1.00 \times 10^{-1}$	$1.00 \times 10^{-5}$	$-7.789 \times 10^{-5}$	$(5.43 \pm 1.90) \times 10^4$

Further experiments were carried out to investigate the influential factors for obtaining such a large  $K_a$  value. The results of these experiments are tabulated in Table 5.7, which show that, upon addition of  $\text{Na}_2\text{SO}_4$  to the samples of  $\text{V}^{2+}$  and sul-calix[4], the strength of binding decreases. The concentration of  $\text{V}^{2+}$  was also varied to investigate the influence of concentration on the binding process. Although the level of association decreased upon increasing  $\text{V}^{2+}$  concentration, the quantity of  $\text{Na}_2\text{SO}_4$  was increased simultaneously. Thus, this effect is still as a result of increasing ionic strength. This is in good agreement with the

observations recorded for RDV, which resulted in a lower  $K_a$  value using a  $0.5 \text{ mol dm}^{-3} \text{ Na}_2\text{SO}_4$  solution, in comparison to a  $0.1 \text{ mol dm}^{-3} \text{ Na}_2\text{SO}_4$  supporting electrolyte solution. Given the sensitivity of UV-Vis spectroscopy in comparison to RDV, it was not possible to measure the absorbance of similar concentrations as those used in RDV. However, it is clear that UV-Vis is a useful method in probing the interaction of  $V^{2+}$  and sul-calix[4] without the influence of any ions in solution.

In order to verify this spectroscopic method as a means of analysis, fluorescence spectroscopy was also carried out under similar conditions and the evaluation of  $K_a$  is outlined in the following section.

#### **5.4.3 Evaluation of $K_a$ for Sul-calix[4] and $V^{2+}$ using Fluorescence Spectroscopy**

As previously explained in Chapter 2, Section 2.5.2, fluorescence spectroscopy records the emission of absorbed wavelengths of light. It is complementary to UV-Vis spectroscopy. Sul-calix[4] has an excitation wavelength of 280 nm, but the emission band at 310 nm is negligible. On the other hand,  $V^{2+}$  shows an emission band between 320 and 400 nm upon excitation at 310 nm. The fluorescence of  $V^{2+}$  was monitored with respect to varying amounts of sul-calix[4]. Experiments similar to those carried out for UV-Vis were performed using fluorescence spectroscopy. Figure 5.15 shows that the fluorescence of  $V^{2+}$  decreases upon increasing concentration of sul-calix[4]. Interestingly, with a five-fold excess of sul-calix[4] to  $V^{2+}$ , the fluorescence of  $V^{2+}$  was quenched. This effect of quenching was also reported by Li *et al.*<sup>41</sup>, upon addition of sul-calix[4] to a fixed concentration of L-tryptophan.

Applying the Heildebrand-Bensei analysis, the change in emission intensity was plotted as a function of the inverse of sul-calix[4] concentration<sup>42</sup>. The graph shown in Figure 5.16 is the plotted data from Figure 5.15. This linear relationship with a correlation coefficient of 0.994 gives a  $K_a$  value of  $4.29 \times 10^4 \text{ mol}^{-1} \text{ dm}^3$ , in the presence of a  $0.1 \text{ mol dm}^{-3} \text{ Na}_2\text{SO}_4$  electrolyte solution. In the

absence of  $\text{Na}_2\text{SO}_4$  a  $K_a$  value of  $7.05 \times 10^5 \text{ mol}^{-1} \text{ dm}^3$  was obtained. Although this is slightly below the value obtained from the UV-Vis measurements at similar concentrations of  $2.14 \times 10^{-6} \text{ mol}^{-1} \text{ dm}^3$ , all samples were thermostated according to room temperature. Hence, a slight variation in room temperature can have a bearing on the magnitude of  $K_a$ . The large  $K_a$  value highlights the influence of charge and ionic strength on the binding between  $\text{V}^{2+}$  and sul-calix[4]. These data are summarised in Table 5.8.

On comparing the electrochemical and spectroscopic data at the  $0.1 \text{ mol dm}^{-3}$  electrolyte concentration, there is a variation in the  $K_a$  value. However, the sensitivity of UV-Vis and fluorescence spectroscopy and the contrast of this technique to RDV may account for the discrepancies within the two techniques. Nonetheless, the impact of charge on the association constant is clear from all techniques and even at a high ionic strength, e.g.,  $1.25 \text{ mol dm}^{-3}$  with a  $K_a$  value in the vicinity of  $10^3 \text{ mol}^{-1} \text{ dm}^3$ , the measure of binding represents the formation of a strong complex.

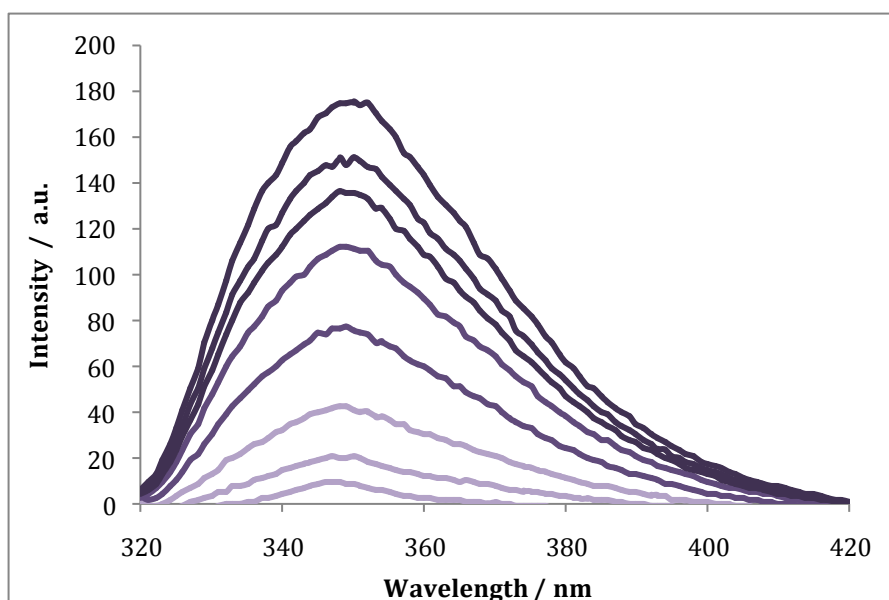


Figure 5.15: Fluorescence spectra of  $1.00 \times 10^{-5} \text{ mol dm}^{-3} \text{ V}^{2+}$  in  $0.10 \text{ mol dm}^{-3} \text{ Na}_2\text{SO}_4$  in the presence of (—)  $0.00$ , (—)  $2.32 \times 10^{-6}$ , (—)  $3.88 \times 10^{-6}$ , (—)  $6.48 \times 10^{-6}$ , (—)  $1.08 \times 10^{-5}$ , (—)  $1.80 \times 10^{-5}$ , (—)  $3.00 \times 10^{-5}$  and (—)  $5.00 \times 10^{-5} \text{ mol dm}^{-3}$  sul-calix[4]. The excitation wavelength was  $310 \text{ nm}$ .

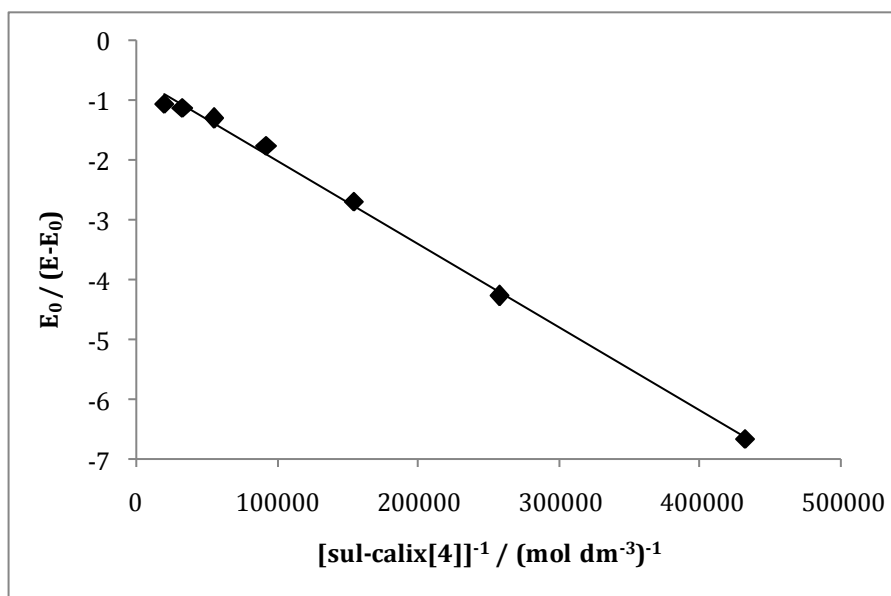


Figure 5.16: Heildebrand-Bensei plot of  $E_0 / (E_0 - E)$  as a function of  $(\text{sul-calix[4]})^{-1}$  in  $0.1 \text{ mol dm}^{-3} \text{ Na}_2\text{SO}_4$ . From this linear relationship,  $K_a$  was evaluated by calculating the ratio of the intercept with respect to the slope of the graph. The  $K_a$  value for this plot was  $4.29 \times 10^4 \text{ mol}^{-1} \text{ dm}^3$ .

Table 5.8:  $K_a$  values at constant  $V^{2+}$  concentrations with varying  $\text{Na}_2\text{SO}_4$  electrolyte concentrations. The varying quantities of sul-calix[4] added to the fixed concentration of  $1.0 \times 10^{-5} \text{ mol dm}^{-3} V^{2+}$ , as described in Figure 5.15.

Fluorescence Analysis			
$\text{Na}_2\text{SO}_4 / \text{mol dm}^{-3}$	$V^{2+} / \text{mol dm}^{-3}$	Slope / $\text{mol dm}^{-3}$	$K_a / \text{mol}^{-1} \text{ dm}^3$
0.00	$1.00 \times 10^{-5}$	$-1.687 \times 10^{-6}$	$(7.07 \pm 1.79) \times 10^5$
$1.25 \times 10^{-3}$	$1.00 \times 10^{-5}$	$-5.048 \times 10^{-6}$	$(1.51 \pm 0.11) \times 10^5$
$1.00 \times 10^{-1}$	$1.00 \times 10^{-5}$	$-1.401 \times 10^{-5}$	$(4.29 \pm 0.45) \times 10^4$

#### 5.4.4 Role of Charge and Ionic Strength

It is clearly evident from the data presented in Sections 5.4.1, 5.4.2 and 5.4.3 that the magnitude of the association constant varies with the concentration of the supporting electrolyte and indeed the concentration of diquat, as evident from Table 5.7. However, in all these cases, there is considerable variation in the ionic strength of the solution. Given that  $V^{2+}$  and sul-calix[4] are highly charged, it is more accurate to express the association constant in terms of the activities

of the charged species and accordingly the true thermodynamic association constant,  $K'_a$ , which is given below in Equation 5.8<sup>43</sup>, where  $a$  represents the activities of the charged species. This equation can be expressed in terms of the concentrations of the equilibrium species and the activity coefficients, as shown in Equation 5.9<sup>44</sup>. Thus,  $K_a$  and  $K'_a$  differ by the activities of the ions involved in the equilibrium, as shown in Equation 5.10<sup>44</sup>.

$$K'_a = \frac{a_{V^{2+}-sul-calix[4]}}{a_{V^{2+}}a_{sul-calix[4]}} \quad (5.8)$$

$$K'_a = \frac{[V^{2+} - sul - calix[4]]}{[V^{2+}][sul - calix[4]]} \cdot \frac{\gamma_{V^{2+}-sul-calix[4]}}{\gamma_{V^{2+}}\gamma_{sul-calix[4]}} \quad (5.9)$$

$$K'_a = K_a \cdot \frac{\gamma_{V^{2+}-sul-calix[4]}}{\gamma_{V^{2+}}\gamma_{sul-calix[4]}} \quad (5.10)$$

Taking logarithms of Equation 5.9<sup>44</sup>, gives Equation 5.11<sup>43</sup>, where the association constants are given as a function of the activity coefficients of the equilibrium species.

$$\log K'_a = \log K_a + \log \left[ \frac{\gamma_{V^{2+}-sul-calix[4]}}{\gamma_{V^{2+}}\gamma_{sul-calix[4]}} \right] \quad (5.11)$$

In order to calculate the activity coefficients, the ionic strength of the solution is required. The ionic strength is related to the concentration of the ions in solution through Equation 5.12<sup>45</sup>, where  $c_i$  represents the concentration of the  $i^{\text{th}}$  ion and  $z_i$  is the charge of the  $i^{\text{th}}$  ion.

$$I = \frac{1}{2} \sum_{i=0}^n c_i z_i^2 \quad (5.12)$$

Once the ionic strength is known, the activity coefficients may be obtained from the Debye-Hückel law, or the Debye-Hückel extended law. The Debye-Hückel

law, which is given by the expression in Equation 5.13<sup>45</sup>, works well only for dilute solutions, with concentrations typically of the order of  $1 \times 10^{-3}$  mol dm<sup>-3</sup>. Therefore, the Debye-Hückel extended law, which is given by the expression in Equation 5.14<sup>45</sup>, was used, as this gives a much better approximation of the activity coefficients in moderately concentrated solutions. In both these equations,  $A$  is a temperature dependent constant with a value of 0.59 at 25 °C.

$$\log \gamma_{\pm} = -A|z_+z_-|I^{1/2} \quad (5.13)$$

$$\log \gamma_{\pm} = \frac{-A|z_+z_-|\sqrt{I}}{1 + \sqrt{I}} \quad (5.14)$$

Using Equation 5.11<sup>43</sup> and 5.14<sup>45</sup> the association constant  $K'_a$  can be expressed in terms of  $K_a$  and the ionic strength of the solution to give Equation 5.15<sup>46</sup>. The  $n$  term in this expression is related to the charge,  $z$ , on the complex ( $V^{2+}$ -sul-calix[4]), the free  $V^{2+}$  and the free sul-calix[4], as shown in Equation 5.16<sup>46</sup>. Diquat is a di-cationic species with a charge of 2 and assuming that the four sulfonated groups on the calixarene are ionized together with one of the phenols, as depicted in Figure 5.1 (a), then the charge can be approximated as 5. This is a reasonable assumption as Scharff *et al.*<sup>47</sup> reported that all sulfonic groups are totally dissociated in aqueous solution. Also, Yoshida *et al.*<sup>48</sup> documented that the first acid dissociation of the hydroxyl groups occurs in a very acidic pH region, whereas the second to fourth acid dissociation occurs at a highly basic pH region. The pH range for all complexation studies carried out was approximately 6.0, thus the sul-calix[4] was penta-anionic in charge, as stated above. It is more difficult to estimate the charge of the inclusion complex, but taking the charge as 3, gives an  $n$  value of 4.

$$\log K_a = \log K'_a - \frac{nA\sqrt{I}}{1 + \sqrt{I}} \quad (5.15)$$

$$n = z(V^{2+} - sul - calix[4]) - z(V^{2+}) - z(sul - calix[4]) \quad (5.16)$$

The data obtained from the spectroscopy and electrochemistry experiments were combined and the ionic strength of the solutions were computed based on

the average concentration of sul-calix[4] used in measuring the association constant. These were then plotted in accordance with Equation 5.15<sup>46</sup>. The resulting plot is depicted in Figure 5.17. Although there is some scatter in the data, a linear plot is obtained with a slope of 4.8 and an intercept of 5.9. The slope value corresponds to an  $n$  value of 8, while the intercept can be used to compute the thermodynamic association constant,  $K'_a$ , as  $7.9 \times 10^5 \text{ mol}^{-1} \text{ dm}^3$  which agrees well with the values measured in low ionic strength, depicted in Table 5.7 and 5.8.

The slope and  $n$  values are quite far removed from the estimated values, which may indicate that the charge not only affects the ionic strength and the activity coefficients of the equilibrium species, but also plays a role in the formation of the complex.

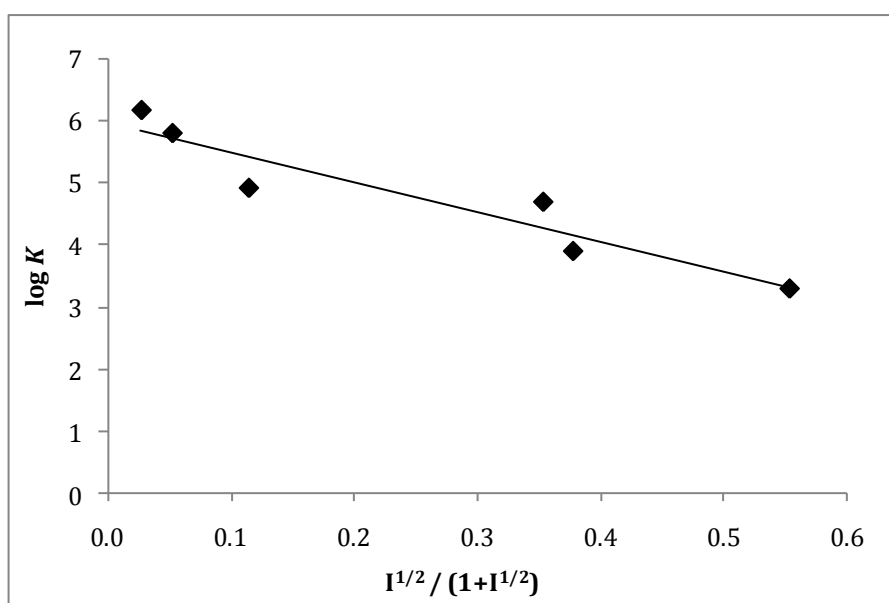


Figure 5.17: Plot of  $\log K$  as a function of ionic strength ( $I^{1/2}/1+I^{1/2}$ ). From this plot, the overall charge of the complex can be obtained from the slope, and the intercept gives the thermodynamic association constant,  $K'_a$ .

### 5.5 Conformations of Sul-calix[4]

The techniques of RDV, UV-Vis and fluorescence spectroscopy allowed for the quantitative evaluation of the interaction between  $V^{2+}$  and sul-calix[4].  $^1H$  NMR serves as another technique to evaluate  $K_a$ , but it can also be employed to gain structural information regarding the interaction. Prior to carrying out  $^1H$  NMR experiments, it was important to establish the most stable conformer of sul-calix[4]. An interesting feature of calixarenes is the range of conformations they can adopt due to the flexibility in each of the aromatic units<sup>49</sup>. Traditionally, the calix[4]arene tetramer has four conformations, either cone or alternate conformers as shown in Figure 5.18. The interchange of these conformations is quite fast at room temperature and structurally can be identified using  $^1H$  NMR, as a broad singlet at 3.90 ppm, which corresponds to the methylene bridging protons. At lower temperatures, the rate of the conformational change becomes sufficiently slow, so that  $^1H$  NMR can discriminate between each conformation<sup>50</sup>. Alternatively, slow exchange can occur at room temperature if a sufficiently strong complex forms and locks the calixarene into one conformation. This is known as the template effect, which can occur when the broad singlet characteristic of the methylene bridging protons ( $CH_2$ ) splits into two doublets. Experimentally, this was confirmed using  $^1H$  NMR spectroscopy, when  $4.0 \times 10^{-3} \text{ mol dm}^{-3}$  sul-calix[4], shown in Figure 5.19 (a), was added to  $4.0 \times 10^{-3} \text{ mol dm}^{-3} V^{2+}$ , shown in Figure 5.19 (b). The broad singlet split into a pair of doublets. This clearly shows the template effect and highlights the value of  $^1H$  NMR in probing the formation of the complex between  $V^{2+}$  and sul-calix[4].

Previous research shows that the cone conformation is the most stable in forming complexes. Shinkai *et al.*<sup>50</sup> illustrated that the cone conformation provides a cavity-shape more suitable to binding than the alternate conformation. This was demonstrated using X-ray crystallography<sup>50</sup>. Similarly, Barbour *et al.*<sup>51</sup> reported that of 102 calixarenes with at least three hydroxyl groups in the Cambridge Crystallographic Database, none deviated from the cone conformer. Also, the cone conformation is stabilized by intramolecular hydrogen bonding interactions among the OH groups on the lower rim<sup>49</sup>.

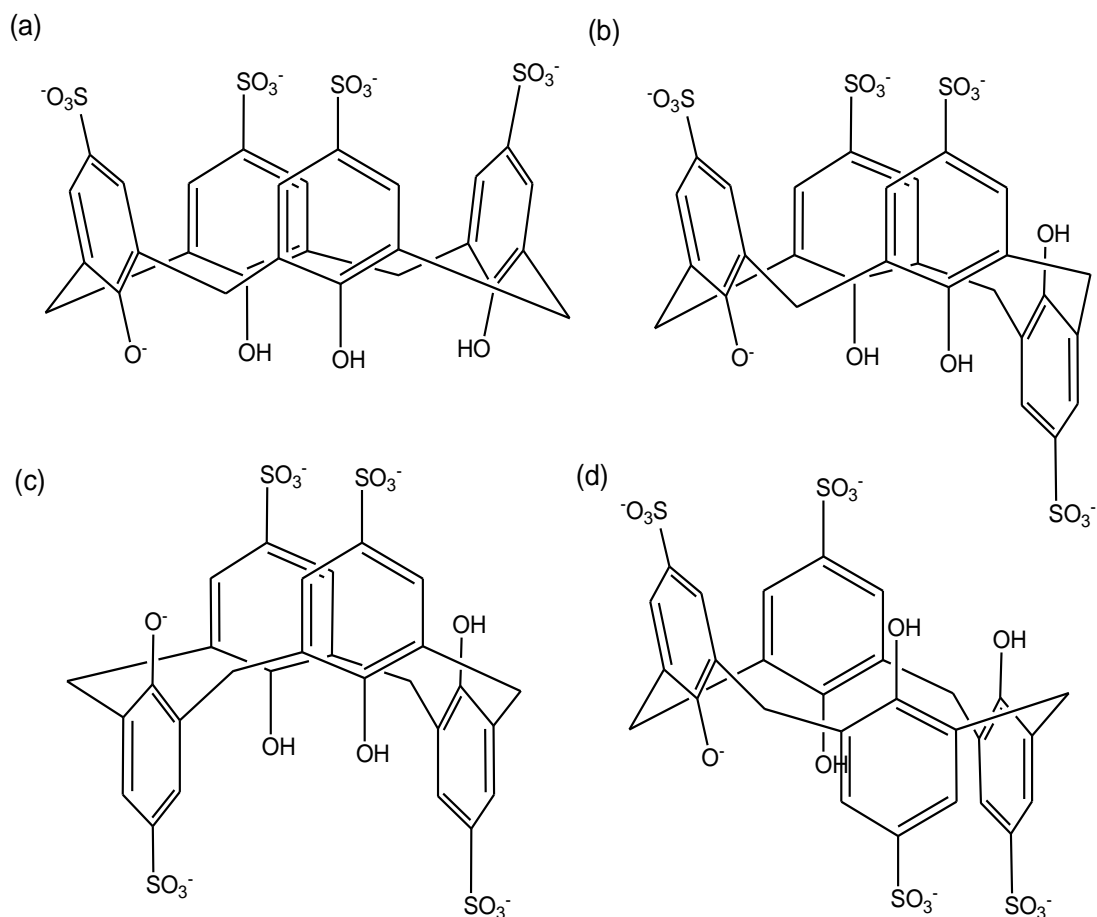


Figure 5.18: Conformations of sul-calix[4], (a) cone, (b) partial-cone, (c) 1,3-alternate and (d) 1,2-alternate.

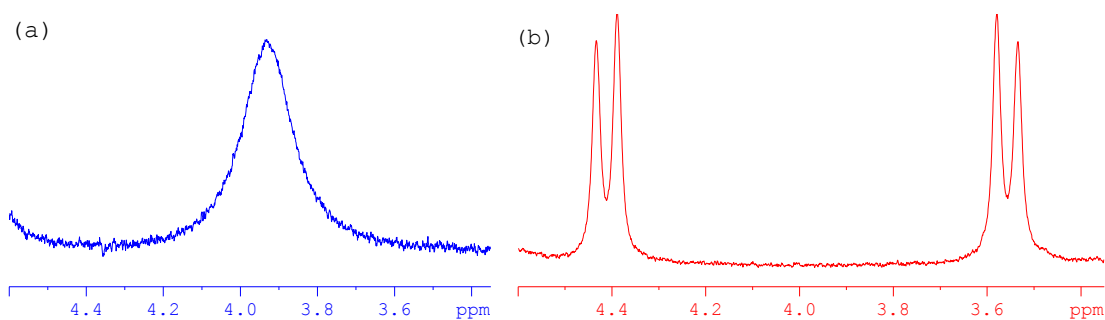


Figure 5.19:  $^1\text{H}$  NMR spectra of the methylene ( $\text{CH}_2$ ) bridging protons of  $4.0 \times 10^{-3} \text{ mol dm}^{-3}$  sul-calix[4], in which (a) shows the fast exchange process between the cone and alternate conformations represented by the broad singlet at approximately 3.9 ppm and (b) shows the template effect of the complex formed between  $4.0 \times 10^{-3} \text{ mol dm}^{-3} \text{ V}^{2+}$  and  $4.0 \times 10^{-3} \text{ mol dm}^{-3}$  sul-calix[4], illustrated by the pair of doublets at approximately 4.4 and 3.5 ppm.

### 5.5.1 Structural Interaction of $V^{2+}$ and Sul-calix[4]

From the quantitative analysis of RDV, UV-Vis and fluorescence spectroscopy it is clear that  $V^{2+}$  and sul-calix[4] are strongly bound. Based on this, a  $^1\text{H}$  NMR titration was carried out, maintaining a constant  $V^{2+}$  concentration and varying the sul-calix[4] concentration at an electrolyte concentration of  $0.1 \text{ mol dm}^{-3}$ . The changes in the chemical shift ( $\Delta\delta$ ) of  $V^{2+}$  were monitored with respect to increasing additions of sul-calix[4], to obtain structural information regarding the interaction.

It is important to note for strong interactions, the  $^1\text{H}$  NMR spectra are modified depending on whether a fast or slow exchange process is occurring. For fast-exchange processes, time averaged signals are recorded for the free and bound species of the complex. Thus, only changes in chemical shift of the averaged proton signals are observed. In slow-exchange processes, separate signals are recorded for the free and complexed species within solution<sup>52</sup>.

Prior to carrying out the titration,  $^1\text{H}$  NMR spectra were recorded for  $V^{2+}$  and sul-calix[4], as shown in Figure 5.20 (a) and (b), respectively. The chemical shifts ( $\delta$ ) were assigned to the equivalent protons of  $V^{2+}$  and sul-calix[4]. Table 5.9 and 5.10 outline the chemical shifts ( $\delta$ ) and multiplicity for the equivalent protons of both  $V^{2+}$  and sul-calix[4], respectively. Non-equivalent protons are labelled from  $\text{H}_a \rightarrow \text{H}_e$  in the case of  $V^{2+}$  and  $\text{H}_a \rightarrow \text{H}_c$  for sul-calix[4]. All samples were prepared in deuterium oxide ( $\text{D}_2\text{O}$ ). Traces of  $\text{H}_2\text{O}$  appeared in the spectra due to the hygroscopic nature of  $\text{D}_2\text{O}$ . This signal appeared as a broad singlet at approximately 4.6 ppm, as shown in Figure 5.20.

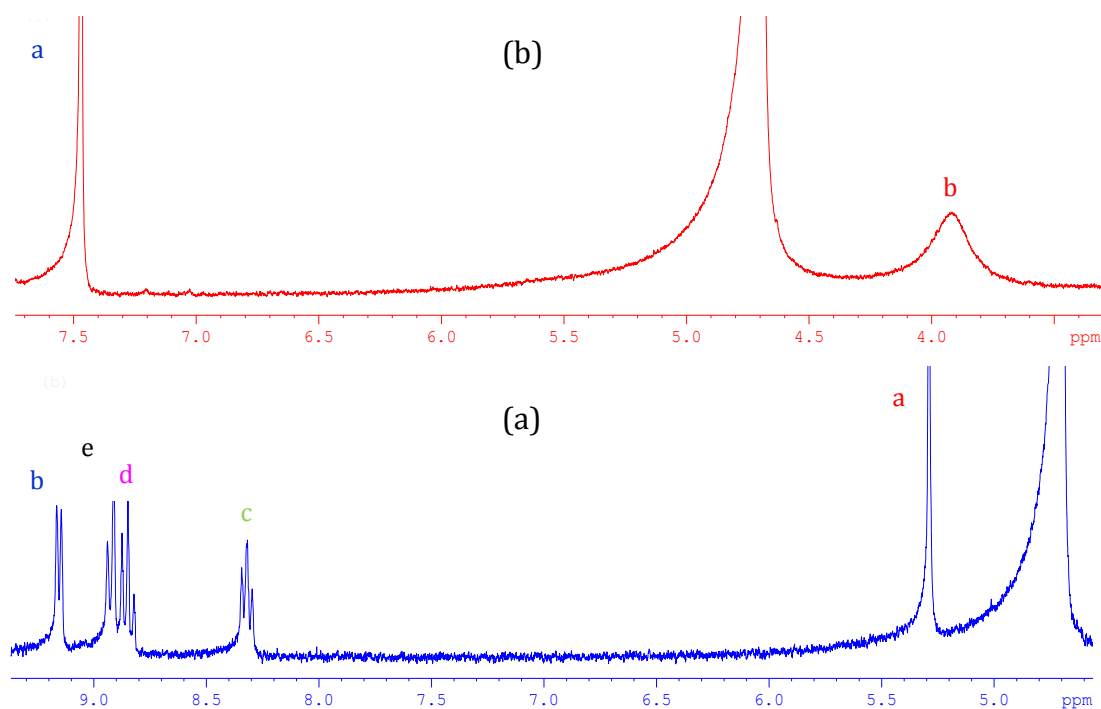


Figure 5.20:  $^1\text{H}$  NMR spectra of (a)  $4.86 \times 10^{-3} \text{ mol dm}^{-3} \text{ V}^{2+}$  and (b)  $1.00 \times 10^{-2} \text{ mol dm}^{-3}$  sul-calix[4] in  $0.10 \text{ mol dm}^{-3} \text{ KCl}$  and  $\text{D}_2\text{O}$ .

Table 5.9: Non-equivalent protons of  $\text{V}^{2+}$  ( $\text{H}_a \rightarrow \text{H}_e$ ) are identified and the chemical structure of  $\text{V}^{2+}$  is shown on the right, with the equivalent protons characterised by the same colour.

$^1\text{H}$ NMR data for $4.86 \times 10^{-3} \text{ mol dm}^{-3} \text{ V}^{2+}$		
$\text{V}^{2+}$		
Proton / H	$\delta / \text{ppm}$	Multiplicity
$\text{CH}_2 / \text{a}$	5.38	Singlet / s
$\text{CH} / \text{c}$	8.40	Multiplet / m
$\text{CH} / \text{d}$	8.93	Multiplet / m
$\text{CH} / \text{e}$	9.01	Doublet / d
$\text{CH} / \text{b}$	9.24	Doublet / d

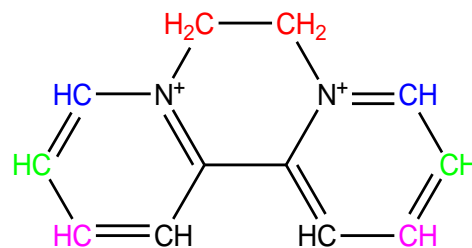
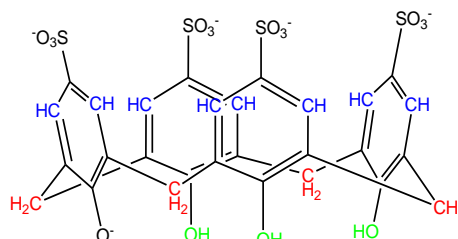


Table 5.10: Equivalent protons are indicated by means of identical colour and non-equivalent protons by differing colour, with three non-equivalent protons of H<sub>a</sub>, H<sub>b</sub> and H<sub>c</sub>, as shown in the accompanying chemical structure of sul-calix[4].

<sup>1</sup> H NMR data for 1.00 × 10 <sup>-2</sup> mol dm <sup>-3</sup> sul-calix[4]		
Proton / H	δ / ppm	Multiplicity
CH <sub>2</sub> / b	3.92	Broad singlet / bs
CH / a	7.47	Singlet/ s
OH / c	-	-



Following identification of the respective proton signals of  $4.86 \times 10^{-3} \text{ mol dm}^{-3} \text{ V}^{2+}$  and  $1.00 \times 10^{-2} \text{ mol dm}^{-3} \text{ sul-calix[4]}$ , a <sup>1</sup>H NMR titration was carried out. The samples were prepared in D<sub>2</sub>O and a  $0.10 \text{ mol dm}^{-3} \text{ KCl}$  electrolyte solution. The proton signals of V<sup>2+</sup> were monitored with respect to increasing sul-calix[4] concentration. As all the recorded spectra contained one set of resonances, this indicated a fast exchange process occurring between the free and complexed species<sup>53</sup>. Figure 5.21 (a) shows the <sup>1</sup>H NMR spectrum of free V<sup>2+</sup>. As can be seen from Figure 5.21 (b) the addition of  $4.86 \times 10^{-3} \text{ mol dm}^{-3} \text{ sul-calix[4]}$  induces an upfield shift in the chemical shift ( $\Delta\delta$ ) position of the signals, H<sub>b</sub>, H<sub>c</sub>, H<sub>d</sub> and H<sub>e</sub>. As documented by Wheate *et al.*<sup>54</sup>, this upfield shift or shielding effect is consistent with the formation of a complex. The maximum changes in chemical shift ( $\Delta\delta$ ) recorded for H<sub>b</sub> and H<sub>e</sub> were approximately 1.00 ppm. For H<sub>c</sub> and H<sub>d</sub>,  $\Delta\delta$  was approximately 1.60 ppm. Figure 5.21 (c) and (d) illustrates the effect of adding  $1.55 \times 10^{-2}$  and  $2.43 \times 10^{-2} \text{ mol dm}^{-3} \text{ sul-calix[4]}$  to  $4.86 \times 10^{-3} \text{ mol dm}^{-3}$  of V<sup>2+</sup>. It is clear from the saturation in chemical shifts that a complex is formed<sup>38</sup>. The chemical shift changes for H<sub>a</sub> at 5.40 ppm were somewhat difficult to monitor, given the close proximity of the signals to the broad HOD peak at approximately 5.00 ppm. Nonetheless, the maximum  $\Delta\delta$  was approximately 0.47 ppm, as shown in Figure 5.22.

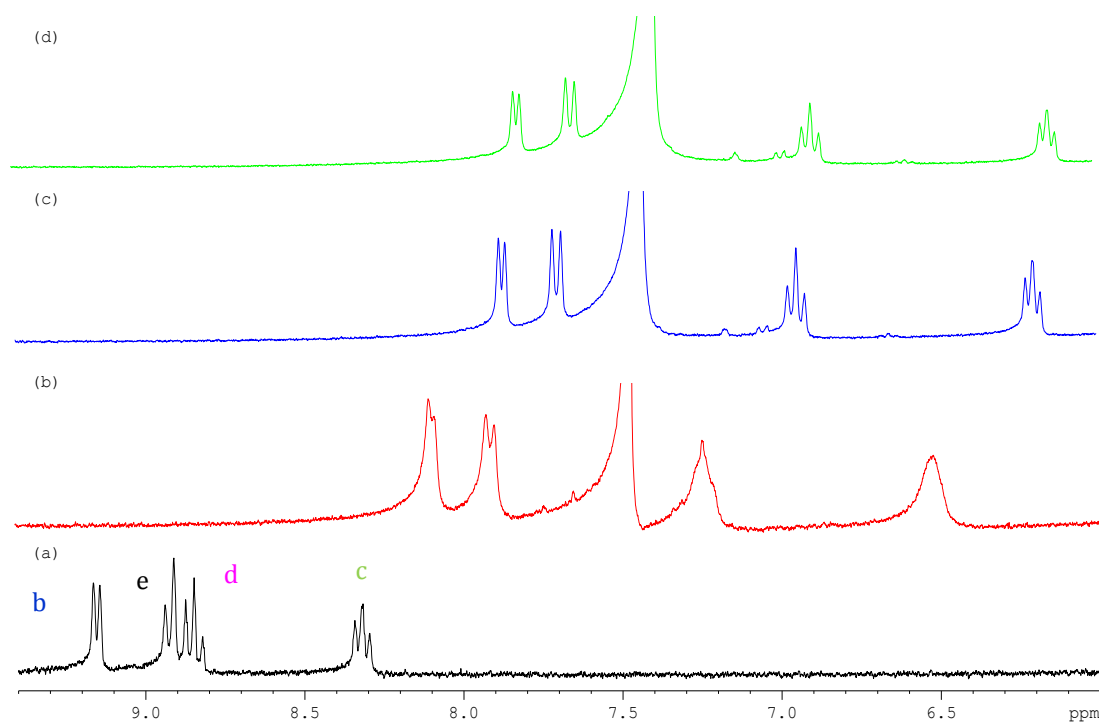


Figure 5.21:  $^1\text{H}$  NMR spectra of  $4.86 \times 10^{-3} \text{ mol dm}^{-3} \text{ V}^{2+}$  and  $0.10 \text{ mol dm}^{-3} \text{ KCl}$  in  $\text{D}_2\text{O}$  with the following additions of sul-calix[4]; (a) 0.00, (b)  $4.86 \times 10^{-3}$ , (c)  $1.55 \times 10^{-2}$  and (d)  $2.43 \times 10^{-2} \text{ mol dm}^{-3}$ .

It has been reported that the extent of  $\Delta\delta$  is an indication of the orientation of two species with respect to each other<sup>55</sup>. This combined with the calculated sizes of the host cavity and guest molecule can illustrate the probable geometry for the complex.

The results recorded from the  $^1\text{H}$  NMR titration indicate that  $\text{H}_b$ ,  $\text{H}_c$ ,  $\text{H}_d$  and  $\text{H}_e$  of  $\text{V}^{2+}$  showed a large change in chemical shift in the presence of sul-calix[4], in particular  $\text{H}_c$  and  $\text{H}_d$ , with a change in chemical shift of 1.60 ppm. This suggests that  $\text{H}_c$  and  $\text{H}_d$  are effected most by the presence of sul-calix[4], followed by  $\text{H}_b$  and  $\text{H}_e$ .  $\text{H}_a$ , on the other hand, was effected minimally due to the small change in chemical shift recorded. This suggests that  $\text{H}_a$  is not bound to the same extent by sul-calix[4]. Hence,  $\text{V}^{2+}$  adopts a slanted orientation with respect to its position within sul-calix[4] and  $\text{H}_a$  is pointing furthest away from sul-calix[4], as shown in Figure 5.23.

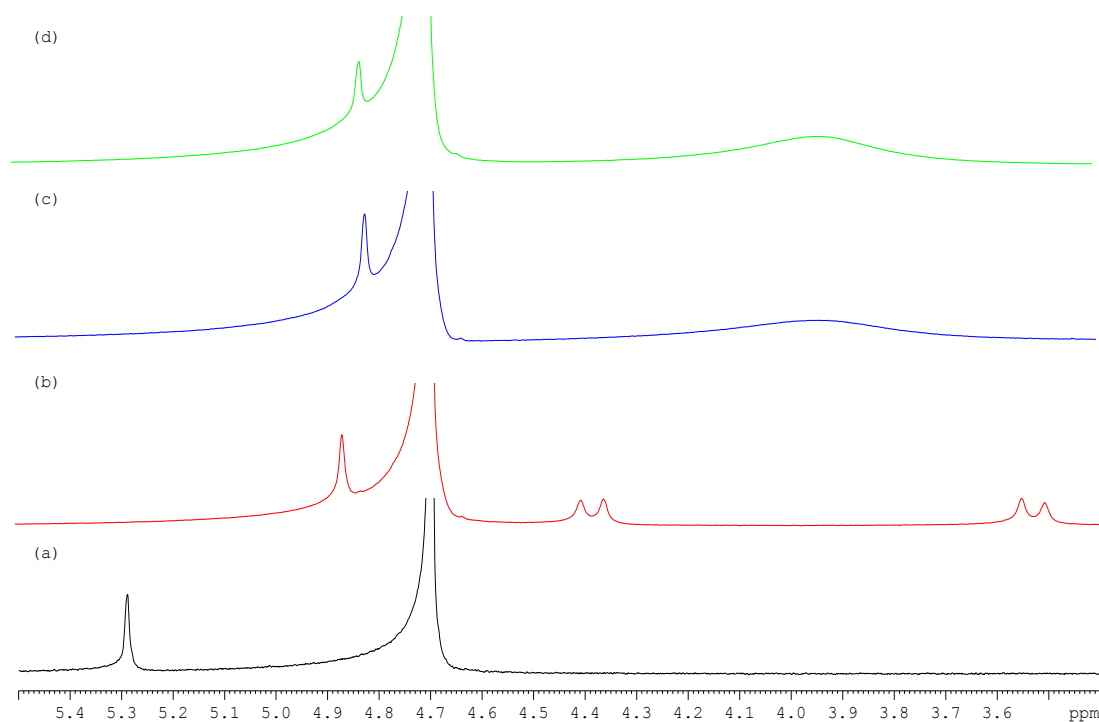


Figure 5.22:  $^1\text{H}$  NMR spectra of  $4.86 \times 10^{-3} \text{ mol dm}^{-3} \text{ V}^{2+}$  and  $0.10 \text{ mol dm}^{-3} \text{ KCl}$  in  $\text{D}_2\text{O}$  with the following additions of sul-calix[4]; (a) 0.00, (b)  $4.86 \times 10^{-3}$ , (c)  $1.55 \times 10^{-2}$  and (d)  $2.43 \times 10^{-2} \text{ mol dm}^{-3}$ .

Figure 5.23 also shows the relative dimensions of  $\text{V}^{2+}$ , the cavity distance of sul-calix[4] and the distance between the sulfonated groups on the upper rim. Some basic molecular modelling was also carried out using Chem 3D Pro 9.0 to establish an energy-minimised structure. The obtained structure was similar to that depicted in Figure 5.23, which agrees well with the predicted structure from the  $^1\text{H}$  NMR data. It has been documented that the symmetry of the calixarene is compromised upon interacting with molecules similar in size to diquat<sup>10</sup>. The structure becomes distorted, accounting for the increased distance between two of the sulfonated groups<sup>10,56-58</sup>. The structure indicates partial inclusion, as it is not possible for the dicationic species,  $\text{V}^{2+}$ , to be completely included within the cavity given the shorter distance on the lower rim. In terms of charge interaction it is more favourable for  $\text{V}^{2+}$  to be partially included given the electrostatic attraction of the cationic diquat to anionic sul-calix[4]. Thus, the electrostatic interaction holds two of the sulfonated groups in close proximity to  $\text{V}^{2+}$ . The remaining sulfonated groups are distorted slightly to

accommodate  $V^{2+}$ , but also there is electrostatic repulsion between the neighbouring sulfonated groups.

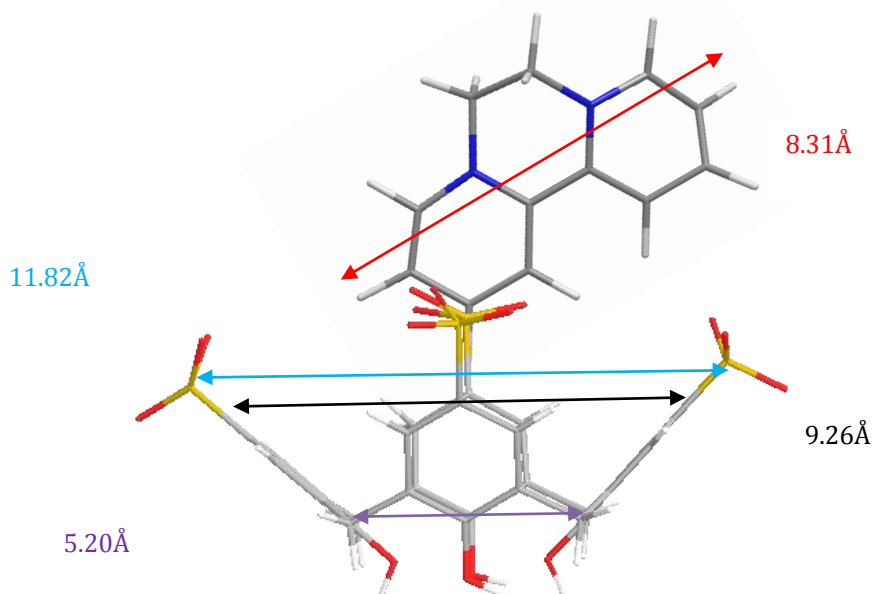


Figure 5.23: Energy-minimised structure of the complex of  $V^{2+}$  and sul-calix[4].

### 5.5.2 Quantitative Interaction of $V^{2+}$ and Sul-calix[4]

As the concentrations of  $V^{2+}$ , sul-calix[4] and the supporting electrolyte were similar in the  $^1\text{H}$  NMR and RDV experiments, the level of agreement between the two techniques was tested. The  $K_a$  value evaluated at a  $0.1 \text{ mol dm}^{-3} \text{ Na}_2\text{SO}_4$  electrolyte concentration using RDV and the respective ratios of sul-calix[4] to  $V^{2+}$  used in  $^1\text{H}$  NMR were used to generate a simulated plot. This was done using Equations 5.17<sup>2</sup> and 5.18<sup>2</sup>, where  $K_a$  is the association constant evaluated from the RDV measurements of  $7.95 \times 10^3 \text{ mol}^{-1} \text{ dm}^3$ ,  $\text{sul-calix[4]}_0$  is the initial concentration of sul-calix[4] in  $\text{mol dm}^{-3}$ ,  $V^{2+}_0$  is the initial concentration of diquat, in  $\text{mol dm}^{-3}$  and  $R$  is the ratio of  $V^{2+}_0$  to  $\text{sul-calix[4]}_0$ . In Equation 5.18,  $\Delta\delta$  is the maximum change in chemical shift observed for free  $V^{2+}$  and  $V^{2+}$  in the presence of sul-calix[4] in ppm,  $\delta$  is the chemical shift of  $V^{2+}$  in the presence of sul-calix[4] and  $\delta_g$  is the chemical shift of free  $V^{2+}$ , in ppm. The values obtained from Equation 5.18 were plotted as a function of  $R$  as shown in Figure 5.24 as previously demonstrated by Macomber<sup>2</sup>. These simulated data are shown as the

continuous trace. The experimentally obtained  $^1\text{H}$  NMR data are shown as symbols. Only the proton signals of  $\text{H}_b$  and  $\text{H}_e$  were plotted, as protons  $\text{H}_c$  and  $\text{H}_d$  were difficult to identify due to the overlapping signal of the  $\text{H}_a$  protons of sul-calix[4] at 7.5 ppm. As shown in Figure 5.24, the plotted experimental data aligns well with the curve, indicating that the observed changes in chemical shift of  $\text{V}^{2+}$  from  $^1\text{H}$  NMR agree well with the changes observed electrochemically from the RDV measurements. Thus,  $7.95 \times 10^3 \text{ mol}^{-1} \text{ dm}^3$  is a reasonable estimate of the  $K_a$  value in a  $0.1 \text{ mol dm}^{-3}$  supporting electrolyte.

$$b = 1 + R + \frac{1}{(K_a[\text{V}^{2+}]_0)} \quad (5.17)$$

$$|\delta - \delta_g| = \left| \left( \frac{\Delta\delta}{2} \right) (b - \sqrt{b^2 - 4R}) \right| \quad (5.18)$$

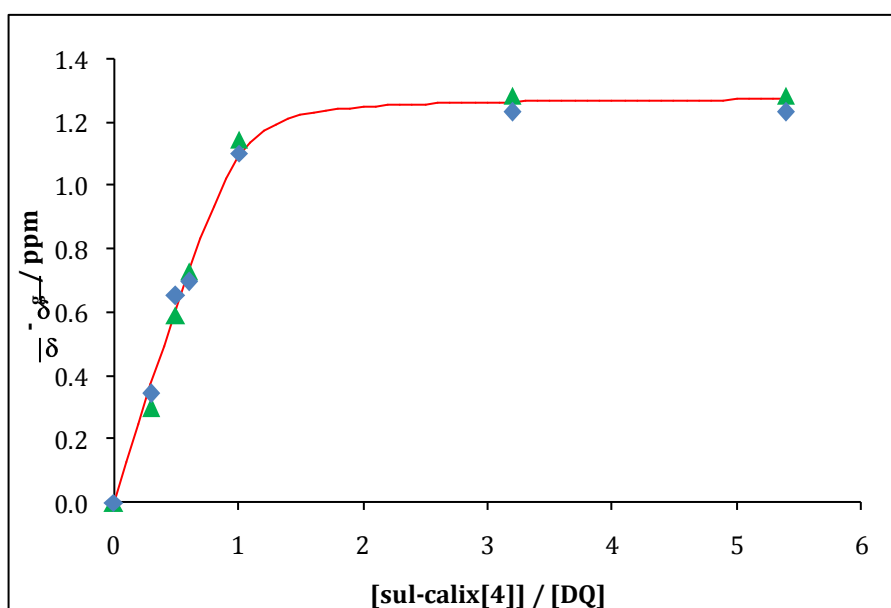


Figure 5.24: Non-linear plot generated from the  $K_a$  value obtained from the RDV data of  $7.95 \times 10^3 \text{ mol}^{-1} \text{ dm}^3$  as calculated from Equation 5.18 as a function of the ratio of sul-calix[4] to  $\text{V}^{2+}$ , (—). The observed change in chemical shift recorded for  $\text{H}_b$  (▲) and  $\text{H}_e$  (◆) plotted as a function of the ratio of sul-calix[4] to diquat (DQ).

In comparison to the  $^1\text{H}$  NMR studies carried out by Wang *et al.*<sup>12</sup> regarding the interaction of  $\text{V}^{2+}$  and sul-calix[4], there is excellent agreement recorded in our study, with the chemical shift for the proton signals of  $\text{V}^{2+}$  in the presence of sul-calix[4] at a pH of 7.0. The changes in chemical shift are not comparable at an acidic pH. The authors proposed that  $\text{V}^{2+}$  is immersed into the sul-calix[4] cavity in a acclivitous orientation, which was confirmed using X-ray crystallography. Similarly, this agrees with the structural interaction depicted in Section 5.5.1.

### 5.6 Interaction of $\text{MV}^{2+}$ and Sul-calix[4]

Given the structural similarity between diquat ( $\text{V}^{2+}$ ) and paraquat ( $\text{MV}^{2+}$ ), i.e., both di-cationic and each composed of a bipyridine unit, as previously shown in Figure 5.1 (b) and (c), it was proposed that the interaction of  $\text{MV}^{2+}$  with sul-calix[4] would be comparable to that of  $\text{V}^{2+}$  with sul-calix[4]. As previously documented by Guo *et al.*<sup>11</sup>, an inclusion complex between  $\text{MV}^{2+}$  and sul-calix[4] is formed. However, the influence of ionic strength is not documented within this paper. Thus, the following section establishes the stoichiometry between  $\text{MV}^{2+}$  and sul-calix[4] and investigates the interaction between the host and guest at two different ionic strengths.

#### 5.6.1 Stoichiometry of the Interaction of $\text{MV}^{2+}$ and Sul-calix[4]

The stoichiometry of the complex formed between  $\text{MV}^{2+}$  and sul-calix[4] was established by means of a Job's plot using  $^1\text{H}$  NMR spectroscopy. An identical procedure was carried out to that of  $\text{V}^{2+}$  and sul-calix[4], in which the mole fraction of  $\text{MV}^{2+}$  was varied from 0.0 to 1.0. The change in chemical shift of the  $\alpha\text{-H}$  or  $\text{H}_a$ , adjacent to the nitrogen atom as shown in the inset of Figure 5.25, was monitored.  $\text{H}_a$  has a chemical shift of 8.99 ppm, as shown in Figure 5.25 (d). At a mole fraction of 0.5, the largest change in chemical shift upfield was recorded at 8.02 ppm, as illustrated in Figure 5.25 (b). These changes in chemical shift combined with a varying mole fraction of  $\text{MV}^{2+}$  were plotted as a function of mole fraction of  $\text{MV}^{2+}$ . The Job's plot, shown in Figure 5.26 with a maximum of 0.5, clearly indicates the formation of a 1:1 complex<sup>59</sup>.

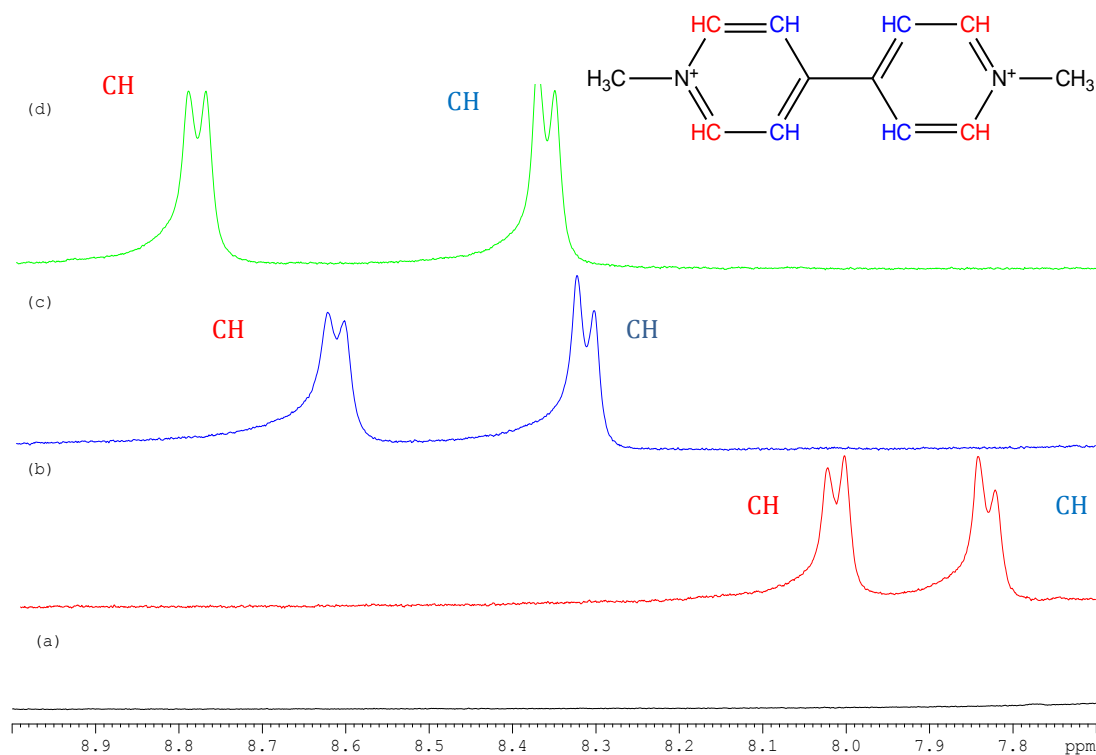


Figure 5.25:  $^1\text{H}$  NMR spectra of  $\text{MV}^{2+}$  and sul-calix[4] at the following mole fractions of  $\text{MV}^{2+}$ , (a) 0.00, (b) 0.50, (c) 0.75 and (d) 1.00. The inset shows the chemical structure of  $\text{MV}^{2+}$ , with the equivalent protons of **CH** corresponding to the  $\alpha$ -H and **CH** which represents the  $\beta$ -H.

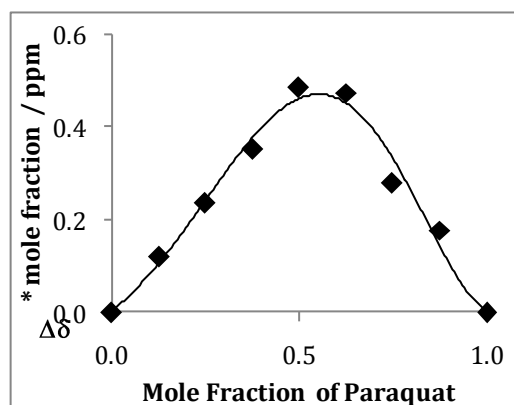


Figure 5.26: Job's plot of  $\text{MV}^{2+}$  and sul-calix[4] using  $^1\text{H}$  NMR. The plot shows the product of the change in chemical shift and the mole fraction of  $\text{MV}^{2+}$  plotted as a function of the mole fraction of  $\text{MV}^{2+}$  (PQ).

### 5.6.2 Evaluation of $K_a$ for the Interaction of $MV^{2+}$ and Sul-calix[4] using CV

The stoichiometry indicated a 1:1 interaction of  $MV^{2+}$  with sul-calix[4]. From this, electrochemical methods of CV and RDV were used to evaluate the measure of this interaction. Prior to this, it was important to establish the electrochemical properties of paraquat. Paraquat exhibits similar chemistry to that of diquat, in that it is oxidised and reduced in a potential window from -0.1 to -1.4 V vs. SCE. It is a two-step redox process, in which  $MV^{2+} + e^- \rightarrow MV^+$  occurs at approximately -0.75 V and  $MV^+ + e^- \rightarrow MV^0$  occurs at approximately -1.0 V. To obtain a valid comparison to the formed complex of  $V^{2+}$  and sul-calix[4], the electrochemical study was confined to the first redox process, i.e.,  $MV^{2+} + e^- \rightarrow MV^+$ .

Typical CVs recorded of  $8.0 \times 10^{-4}$  mol dm<sup>-3</sup>  $MV^{2+}$  maintained in a 0.1 mol dm<sup>-3</sup>  $Na_2SO_4$  electrolyte solution are shown in Figure 5.27. The reduction peak at -0.75 V vs. SCE was monitored with respect to the addition of sul-calix[4] in the range of 0.0 to  $4.0 \times 10^{-3}$  mol dm<sup>-3</sup>. As shown in Figure 5.27, there was a decrease in the peak current and a shift in the peak potential ( $E_p$ ) upon increasing the concentration of sul-calix[4]. Kim *et al.*<sup>60</sup> documented a similar trend which is indicative of the formation of a complex, due to an increase in reduction potential and a slower rate of diffusion, as the  $MV^{2+}$  is bound by the sul-calix[4]. The importance of ionic strength in the formation of complexes with charged calixarenes is evident in Figure 5.27. A slight increase in current was recorded when concentrations greater than equi-molar quantities were added. This is shown by the blue trace in Figure 5.27. Although this effect is not as large as that recorded for  $V^{2+}$  and sul-calix[4] (Figure 5.3), nevertheless ionic strength is a factor within these measurements. Thus, the  $K_a$  values were calculated using two different concentrations of  $Na_2SO_4$  electrolyte solution, 0.1 and 0.5 mol dm<sup>-3</sup>, respectively.

Figure 5.28 illustrates the appropriate plot to evaluate  $K_a$ , as shown in Equation 5.19<sup>25</sup>, in which  $K_a$  is the association constant in mol<sup>-1</sup> dm<sup>3</sup>,  $i$  and  $i_0$  correspond to the peak current, in A cm<sup>-2</sup> of  $MV^{2+}$  in the presence and absence of sul-calix[4]

and  $A$  is the proportional constant. This equation quantifies  $K_a$  based on the change in current, essentially the change in the rate of diffusion of the analyte, to the electrode surface. However, as shown in Figure 5.27, there is a potential shift in the reduction of  $MV^{2+} + e^- \rightarrow MV^+$ . This highlights the increased potentials required to reduce the di-cationic species, as it was bound by sul-calix[4]. Osella *et al.*<sup>61</sup> also reported similar findings upon the complexation of ferrocene and  $\beta$ -cyclodextrin.

$$\frac{1}{\text{sul-calix}[4]} = K \frac{(1-A)}{1-i/i_0} - K \quad (5.19)$$

The calculated  $K_a$  values using CV at the different electrolyte concentrations are presented in Table 5.11. From this evaluated data, it is evident that the ionic strength has an impact on the measure of association of  $MV^{2+}$  and sul-calix[4].

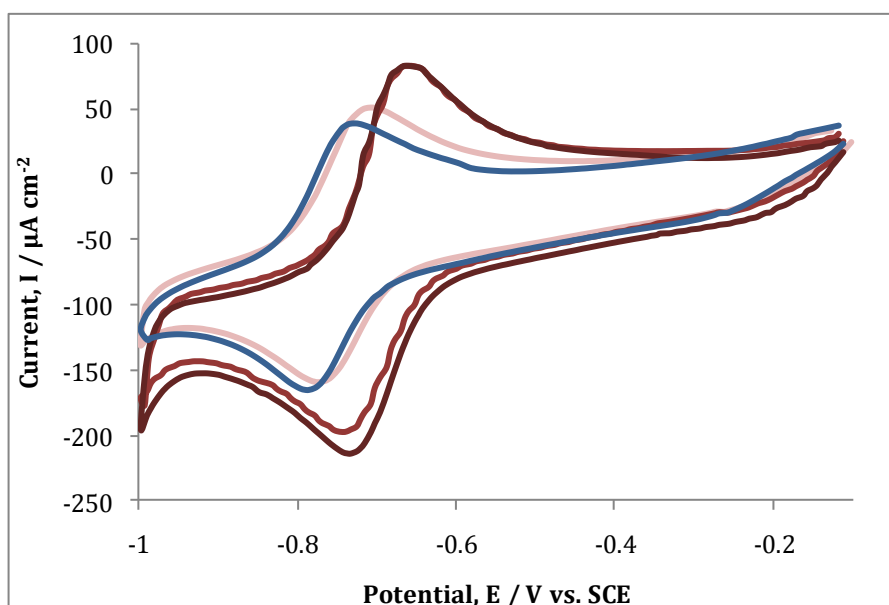


Figure 5.27: Cyclic voltammograms of  $8.0 \times 10^{-4} \text{ mol dm}^{-3} MV^{2+}$  in  $0.1 \text{ mol dm}^{-3} Na_2SO_4$  electrolyte solution in the presence of (—)  $0.0$ , (—)  $1.6 \times 10^{-4}$ , (—)  $9.6 \times 10^{-4}$  and (—)  $4.0 \times 10^{-3} \text{ mol dm}^{-3}$  sul-calix[4]. The potential was swept from  $-0.1 \rightarrow -1.0 \text{ V vs. SCE}$  at a scan rate of  $50 \text{ mV s}^{-1}$  at Au.

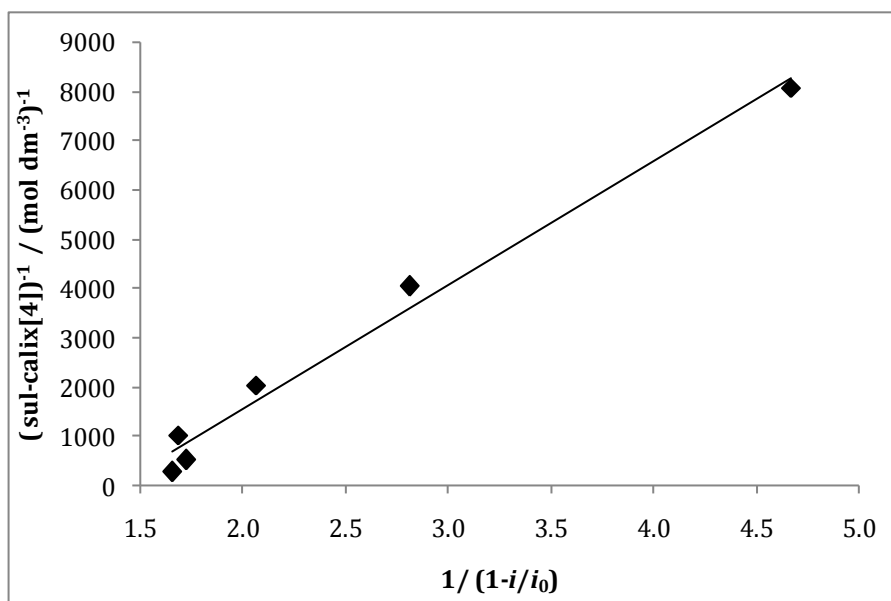


Figure 5.28: Plot of  $1/(\text{sul-calix[4]})$  as a function of  $1/(1-i/i_0)$ . This linear relationship with a correlation coefficient of 0.985 corresponds to the recorded data of  $\text{MV}^{2+}$  and additives of sul-calix[4] in a  $0.1 \text{ mol dm}^{-3} \text{ Na}_2\text{SO}_4$  electrolyte solution.

As this system has been previously studied, the values in Table 5.11 were compared to the work of Guo *et al.*<sup>11</sup>. The  $K_a$  value obtained by the authors of  $9.33 \times 10^5 \text{ mol}^{-1} \text{ dm}^3$  was almost three hundred times larger than the values presented in Table 5.11. Further analysis of the study by Guo *et al.*<sup>11</sup> showed that a phosphate buffer was used as the supporting electrolyte. This variation in electrolyte will have an effect on the ionic strength and as previously mentioned this has a significant influence on the  $K_a$  value, which may explain the variation between this study and that previously published. In order to further verify the results obtained from CV, RDV was carried out to quantify  $K_a$ .

Table 5.11:  $K_a$  values for the complex formation of  $\text{MV}^{2+}$  and sul-calix[4] at 0.1 and  $0.5 \text{ mol dm}^{-3} \text{ Na}_2\text{SO}_4$  electrolyte solutions. These values were calculated using CV data.

CV Analysis	
Electrolyte / $\text{Na}_2\text{SO}_4$	Association Constant, $K_a / \text{mol}^{-1} \text{ dm}^3$
$0.1 \text{ mol dm}^{-3}$	$(3.46 \pm 0.41) \times 10^3 \text{ mol}^{-1} \text{ dm}^3$
$0.5 \text{ mol dm}^{-3}$	$(4.19 \pm 0.34) \times 10^2 \text{ mol}^{-1} \text{ dm}^3$

### 5.6.3 Evaluation of $K_a$ for the Interaction of $MV^{2+}$ and Sul-calix[4] using RDV

RDV is proposed to be a more reproducible technique in comparison to CV as it eliminates the time dependent process of diffusion and instead controls it by convection<sup>27</sup>. RDV was therefore used as the accompanying technique to quantify  $K_a$  for  $MV^{2+}$  and sul-calix[4].

Initially,  $8.0 \times 10^{-4} \text{ mol dm}^{-3} MV^{2+}$  in a  $0.5 \text{ mol dm}^{-3} Na_2SO_4$  electrolyte solution was scanned within a potential window at a constant scan rate but at varying rotation speeds as depicted in Figure 5.29. The reduction of paraquat ( $MV^{2+} + e^- \rightarrow MV^+$ ) occurred at approximately  $-0.7 \text{ V vs. SCE}$ . The limiting current observed between  $-0.7$  and  $-1.0 \text{ V vs. SCE}$  indicated that the process was mass transport controlled. The Levich equation, Equation 5.4<sup>29</sup>, gives the proportional relationship of the limiting current and rotation speed. From this, the diffusion coefficient ( $D_c$ ) was evaluated for free  $MV^{2+}$  and  $MV^{2+}$  in the presence of various concentrations of sul-calix[4]. The concentrations of sul-calix[4] used were similar to those employed in the CV analysis.

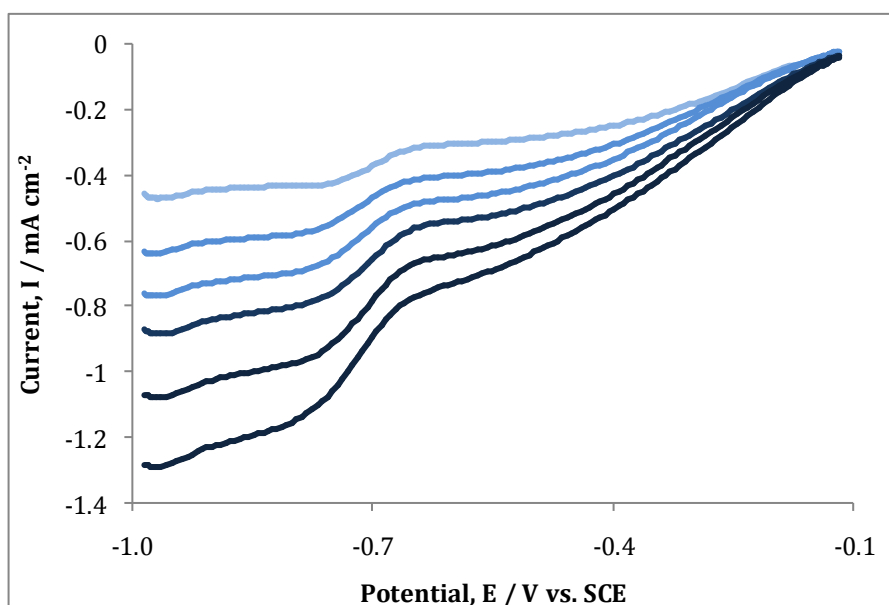


Figure 5.29: RDV of  $8.0 \times 10^{-4} \text{ mol dm}^{-3} MV^{2+}$  in  $0.5 \text{ mol dm}^{-3} Na_2SO_4$  at the following rotation speeds; (—) 250 rpm, (—) 500 rpm, (—) 750 rpm, (—) 1,000 rpm, (—) 1,500 rpm and (—) 2,000 rpm. The potential was swept from  $-0.1$  to  $-1.0 \text{ V vs. SCE}$  at a scan rate of  $50 \text{ mV s}^{-1}$  at Au.

The changes in current and half-wave potentials ( $E_{1/2}$ ) of  $MV^{2+}$  were monitored in the absence and presence of sul-calix[4]. As shown in Figure 5.30, there was a decrease in current and a shift in the half-wave potential at which  $MV^{2+}$  was being reduced. Similar to the analysis of  $V^{2+}$  and sul-calix[4], this trend indicates the formation of a complex<sup>3</sup>. The recorded RDVs for  $MV^{2+}$  in the presence and absence of sul-calix[4], at varying rotation speeds and employing an electrolyte solution of  $0.5 \text{ mol dm}^{-3} \text{ Na}_2\text{SO}_4$  were combined to generate Levich plots, as shown in Figure 5.31. From the Levich plots shown in Figure 5.31, the slope of each plot was used to calculate the diffusion coefficient ( $D_c$ ) of  $MV^{2+}$  in accordance with Equation 5.4<sup>29</sup>. Table 5.12 illustrates the calculated values, in which the diffusion coefficient of  $MV^{2+}$  decreases as a function of increasing sul-calix[4] concentration.

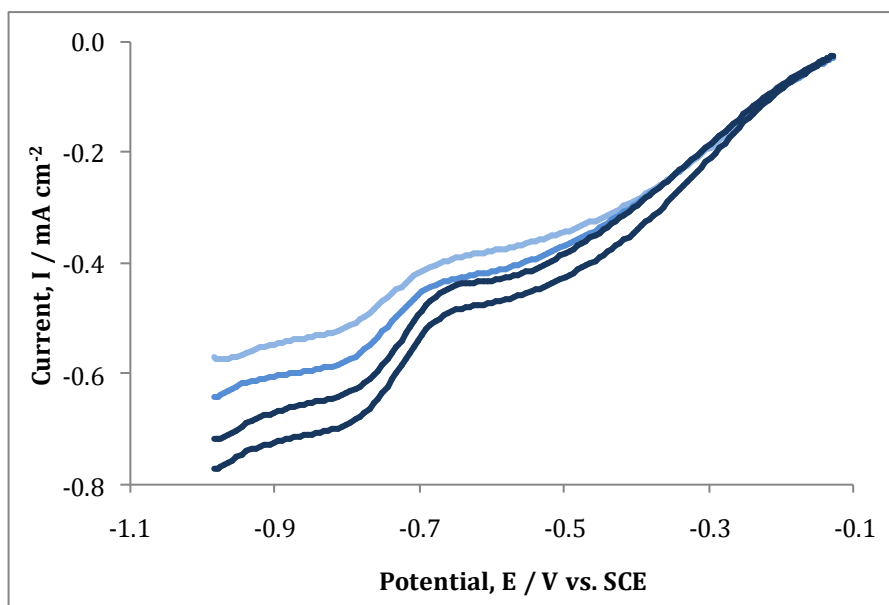


Figure 5.30: RDVs of  $8.0 \times 10^{-4} \text{ mol dm}^{-3} \text{ MV}^{2+}$  in  $0.5 \text{ mol dm}^{-3} \text{ Na}_2\text{SO}_4$ , with the following additions of sul-calix[4]; (—)  $0.0$ , (—)  $1.6 \times 10^{-4}$ , (—)  $4.8 \times 10^{-4}$  and (—)  $4.0 \times 10^{-3} \text{ mol dm}^{-3}$ . The potential was swept from  $-0.1$  to  $-1.0 \text{ V vs. SCE}$  at  $50 \text{ mV s}^{-1}$  at a fixed rotation speed of  $750 \text{ rpm}$  at Au.

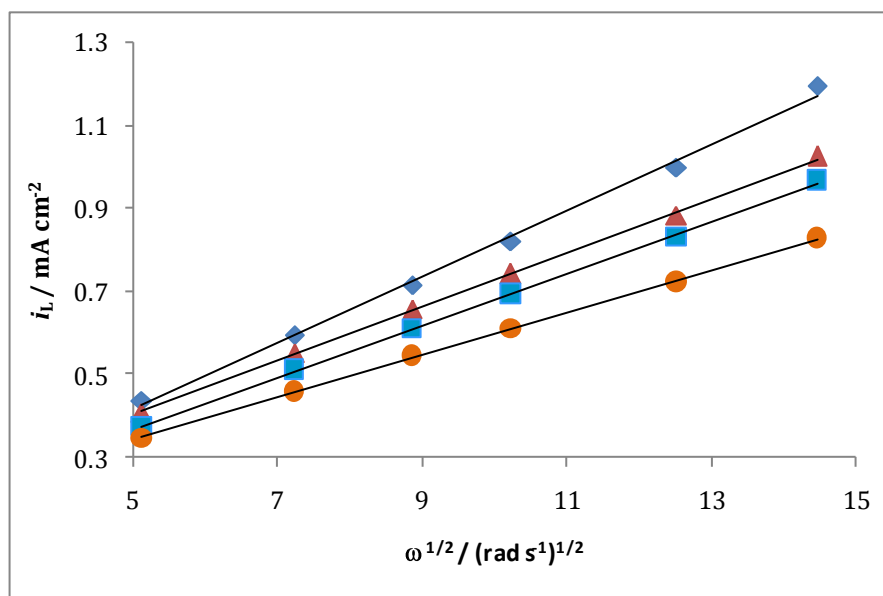


Figure 5.31: Levich plots of limiting current ( $i_L$ ) as a function of the square root of rotation speed ( $\omega^{1/2}$ ). The data correspond to RDVs of  $8.0 \times 10^{-4} \text{ mol dm}^{-3} \text{ MV}^{2+}$  in  $0.5 \text{ mol dm}^{-3} \text{ Na}_2\text{SO}_4$  with the following additions of sul-calix[4]; ( $\blacklozenge$ )  $0.0$ , ( $\blacktriangle$ )  $1.6 \times 10^{-4}$ , ( $\blacksquare$ )  $2.4 \times 10^{-4}$  and ( $\bullet$ )  $1.0 \times 10^{-3} \text{ mol dm}^{-3}$ .

Table 5.12: Data outlining the influence of sul-calix[4] on  $8.0 \times 10^{-4} \text{ mol dm}^{-3} \text{ MV}^{2+}$  in a  $0.5 \text{ mol dm}^{-3} \text{ Na}_2\text{SO}_4$  electrolyte solution. There was a decrease in  $D_c$  upon addition of sul-calix[4] to  $\text{MV}^{2+}$ .  $D_c$  of the complexed  $\text{MV}^{2+}$ ,  $D_{c(\text{complex})}$ , and sul-calix[4] is compared with that of  $D_c$  of the uncomplexed  $\text{MV}^{2+}$ ,  $D_{c(\text{free PQ})}$ .

$\text{MV}^{2+} / \text{mol dm}^{-3}$	Sul-calix[4] / $\text{mol dm}^{-3}$	$D_c / \text{cm}^2 \text{ s}^{-1}$	$D_{c(\text{complex})} / D_{c(\text{free MV}^{2+})}$
$8.0 \times 10^{-4}$	0.0	$2.16 \times 10^{-5}$	0.00
$8.0 \times 10^{-4}$	$1.2 \times 10^{-4}$	$1.58 \times 10^{-5}$	0.73
$8.0 \times 10^{-4}$	$2.5 \times 10^{-4}$	$1.52 \times 10^{-5}$	0.70
$8.0 \times 10^{-4}$	$5.0 \times 10^{-4}$	$1.35 \times 10^{-5}$	0.63
$8.0 \times 10^{-4}$	$1.0 \times 10^{-3}$	$1.10 \times 10^{-5}$	0.51

Combining these data and the shifts in reduction potential,  $K_a$  was evaluated, in accordance with Equation 5.5<sup>3</sup>. The values are shown in Table 5.13. This analysis was further verified in regards the influence of ionic strength on the degree of complexation. In general, these data show good agreement with the analysis using CV, as evident from the values listed in Tables 5.11 and 5.13,

respectively. In comparison to the complex of  $V^{2+}$  with sul-calix[4], the  $K_a$  value for  $MV^{2+}$  and sul-calix[4] was slightly lower.

In addition to calculating  $K_a$ , the rate constant,  $k$ , of  $MV^{2+}$  was also calculated using the Koutechy-Levich equation, Equation 5.6<sup>36</sup>. As explained previously in Section 5.4.1,  $k$  is the kinetics of heterogeneous electron transfer at the interface upon either oxidation or reduction<sup>33</sup>. As illustrated in Figure 5.32, when the inverse of the limiting current was plotted as a function of the inverse of scan rate, a linear relationship was obtained with correlation coefficients in the range of 0.997 to 0.999. The intercept of this relationship was then used to calculate the rate constant of  $MV^{2+}$  in solution. Tabulated values are shown in Table 5.14. On inspection of the data, it is clear that as the concentration of sul-calix[4] increases with respect to a fixed concentration of  $MV^{2+}$ , the rate constant decreases. This again points in the direction of the formation of a complex.

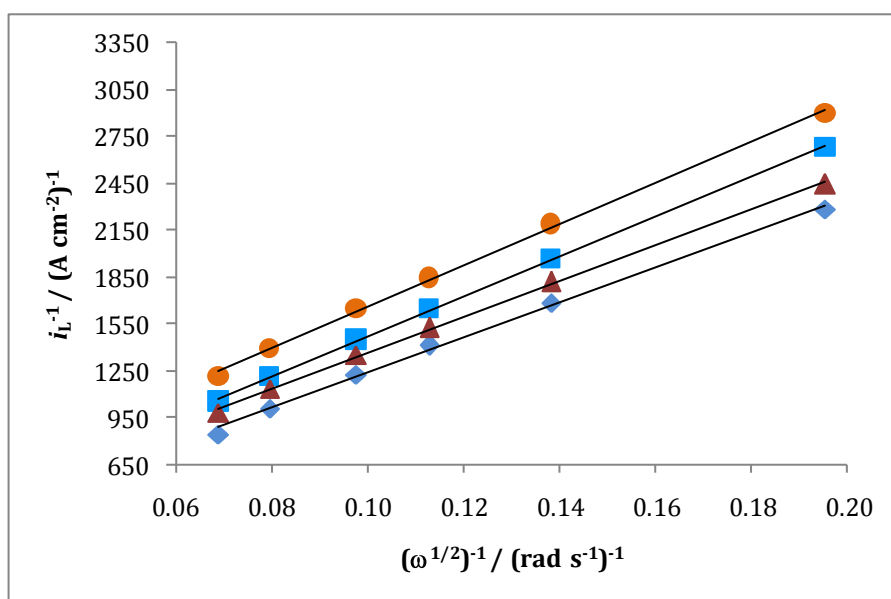


Figure 5.32: Koutechy-Levich plots of  $i_L^{-1}$  as a function of  $(\omega^{1/2})^{-1}$ . These data were plotted from RDVs carried out using  $8.0 \times 10^{-4} \text{ mol dm}^{-3} MV^{2+}$  in  $0.5 \text{ mol dm}^{-3} Na_2SO_4$ , with the following additions of sul-calix[4]; ( $\blacklozenge$ ) 0.0, ( $\blacktriangle$ )  $1.6 \times 10^{-4}$ , ( $\blacksquare$ )  $2.4 \times 10^{-4}$  and ( $\bullet$ )  $1.0 \times 10^{-3} \text{ mol dm}^{-3}$ .

Table 5.13:  $K_a$  values for the complex of  $MV^{2+}$  and sul-calix[4] in the presence of 0.1 and 0.5 mol  $dm^{-3}$   $Na_2SO_4$ .

Association Constant, $K_a$	
0.1 mol $dm^{-3}$ $Na_2SO_4$ / mol $^{-1}$ $dm^3$	0.5 mol $dm^{-3}$ $Na_2SO_4$ / mol $^{-1}$ $dm^3$
$(2.42 \pm 0.59) \times 10^3$ mol $^{-1}$ $dm^3$	$(5.24 \pm 0.17) \times 10^2$ mol $^{-1}$ $dm^3$

Table 5.14: Rate constants,  $k$ , of  $8.0 \times 10^{-4}$  mol  $dm^{-3}$   $MV^{2+}$  in 0.5 mol  $dm^{-3}$  and 0.1 mol  $dm^{-3}$   $Na_2SO_4$  electrolyte solution at varying concentrations of sul-calix[4]. The rate constant,  $k$ , was evaluated from the intercept of  $i_L^{-1}$  as a function of  $(\omega^{1/2})^{-1}$ . From these plots, correlation coefficients were in the range of 0.997 to 0.999.

0.5 mol $dm^{-3}$ $Na_2SO_4$ electrolyte			
sul-calix[4] / mol $dm^{-3}$	[PQ] : [sul-calix[4]]	Rate Constant, $k$ / $cm\ s^{-1}$	Correlation coefficient, $R^2$
0.00	1.0 : 0.0	0.140	0.997
$1.24 \times 10^{-4}$	1.0 : 0.2	0.062	0.998
$2.49 \times 10^{-4}$	1.0 : 0.3	0.078	0.999
$4.98 \times 10^{-4}$	1.0 : 0.6	0.056	0.999
$9.90 \times 10^{-4}$	1.0 : 1.3	0.039	0.998

0.1 mol $dm^{-3}$ $Na_2SO_4$ electrolyte			
sul-calix[4] / mol $dm^{-3}$	[PQ] : [sul-calix[4]]	Rate Constant, $k$ / $cm\ s^{-1}$	Correlation coefficient, $R^2$
0.00	1.0 : 0.0	0.275	0.999
$1.24 \times 10^{-4}$	1.0 : 0.2	0.154	0.999
$2.49 \times 10^{-4}$	1.0 : 0.3	0.127	0.999
$9.90 \times 10^{-4}$	1.0 : 1.3	0.122	0.999
$4.00 \times 10^{-3}$	1.0 : 5.0	0.065	0.998

### 5.6.4 Structural Interaction of MV<sup>2+</sup> and Sul-calix[4]

<sup>1</sup>H NMR spectroscopy, has previously been used to gather information regarding the stoichiometry of the interaction between MV<sup>2+</sup> and sul-calix[4], as shown in Section 5.6.1. It can also be applied to obtain structural information for the complex of sul-calix[4] and MV<sup>2+</sup>. A <sup>1</sup>H NMR titration was carried out maintaining a constant MV<sup>2+</sup> concentration and a varying sul-calix[4] concentration. The proton signals of MV<sup>2+</sup> were then monitored in the presence and absence of sul-calix[4]. It is these changes in chemical shift that indicate the change in environment for MV<sup>2+</sup> and consequently the formation of a complex<sup>62</sup>. As the proton signals for sul-calix[4] have already been identified and explained in Section 5.5.1, initially the non-equivalent proton signals for MV<sup>2+</sup> were assigned. A <sup>1</sup>H NMR spectrum of MV<sup>2+</sup> was carried out in D<sub>2</sub>O and the following signals were assigned, as depicted in Figure 5.33. As mentioned previously, D<sub>2</sub>O is extremely hygroscopic and traces of H<sub>2</sub>O were seen as a broad singlet at approximately 4.60 ppm. The α-H, i.e., H<sub>a</sub> appeared as a doublet at 8.99 ppm. The β-H, i.e., H<sub>b</sub> appeared as a doublet at 8.45 ppm. The methyl protons, designated as H<sub>c</sub>, appeared as a singlet at 4.44 ppm. The signals for the aromatic protons on the sul-calix[4] were sufficiently far apart from the signals for the aromatic protons of MV<sup>2+</sup>. Thus, these protons were monitored throughout the titration.

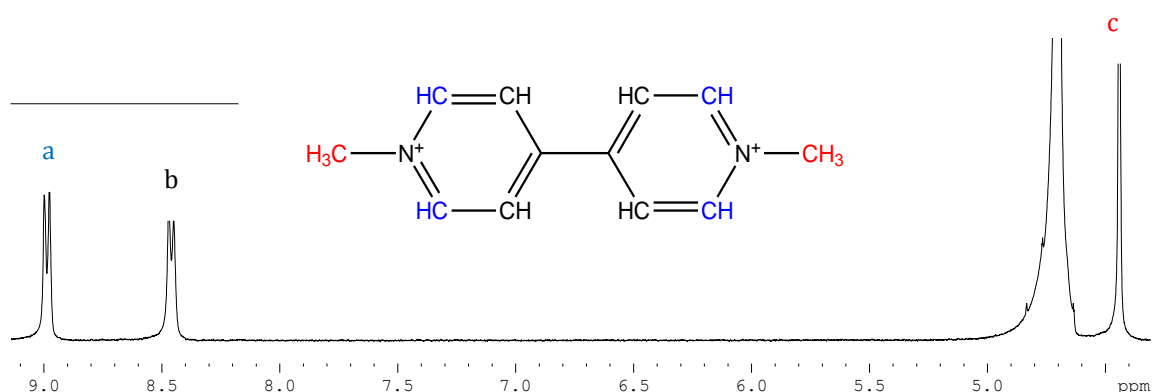


Figure 5.33: <sup>1</sup>H NMR spectrum of  $4.0 \times 10^{-3} \text{ mol dm}^{-3}$  MV<sup>2+</sup> in  $0.1 \text{ mol dm}^{-3}$  KCl and D<sub>2</sub>O solvent, with the appropriate proton signals characterised by varying colour as shown by the inset, which illustrates the chemical structure of MV<sup>2+</sup>.

Upon carrying out the  $^1\text{H}$  NMR titration, the methylene bridging protons of sul-calix[4] were analysed, to investigate if a similar splitting pattern occurred to that presented in Section 5.5 for  $\text{V}^{2+}$  and sul-calix[4]. The broad singlet of sul-calix[4] at 4.00 ppm is shown in Figure 5.34 (a). Upon interacting with  $\text{MV}^{2+}$ , the signal splits into a pair of doublets, as shown in Figure 5.34 (b). Although the signal to noise ratio was reasonably high despite carrying out the  $^1\text{H}$  NMR at 128 scans, it was observed that the broad singlet split and became two sharper signals. This occurred at concentrations of between  $2.1 \times 10^{-3}$  and  $4.3 \times 10^{-3}$  mol  $\text{dm}^{-3}$  sul-calix[4], in the presence of  $4.0 \times 10^{-3}$  mol  $\text{dm}^{-3}$   $\text{MV}^{2+}$ .

At concentrations greater than  $4.3 \times 10^{-3}$  mol  $\text{dm}^{-3}$  sul-calix[4], the broad singlet appears again, as shown in Figure 5.34 (c). This indicates that there is now a surplus of sul-calix[4] in solution and an average of the signals for the cone and alternate conformation is recorded. This splitting of the broad singlet of sul-calix[4] agrees with the guest template effect, in which one conformation is predominant over the other. In this case, the complex of  $\text{MV}^{2+}$  and sul-calix[4], maintains the sul-calix[4] in the cone conformation. According to Shinkai *et al.*<sup>50</sup>, the conformation of water-soluble calixarenes is fixed to the cone conformation upon interaction with a guest molecule<sup>63</sup>. Also, this sharpening of the broad singlet, due to the guest template effect is consistent with the analysis obtained from the complex formed between  $\text{V}^{2+}$  and sul-calix[4], as illustrated in Figure 5.19.

From this analysis, it is clear that the  $\text{MV}^{2+}$  is interacting with sul-calix[4]. In order to obtain further information of its possible orientation within the cavity, the changes in chemical shift of the aromatic and methyl protons of  $\text{MV}^{2+}$  were analysed.

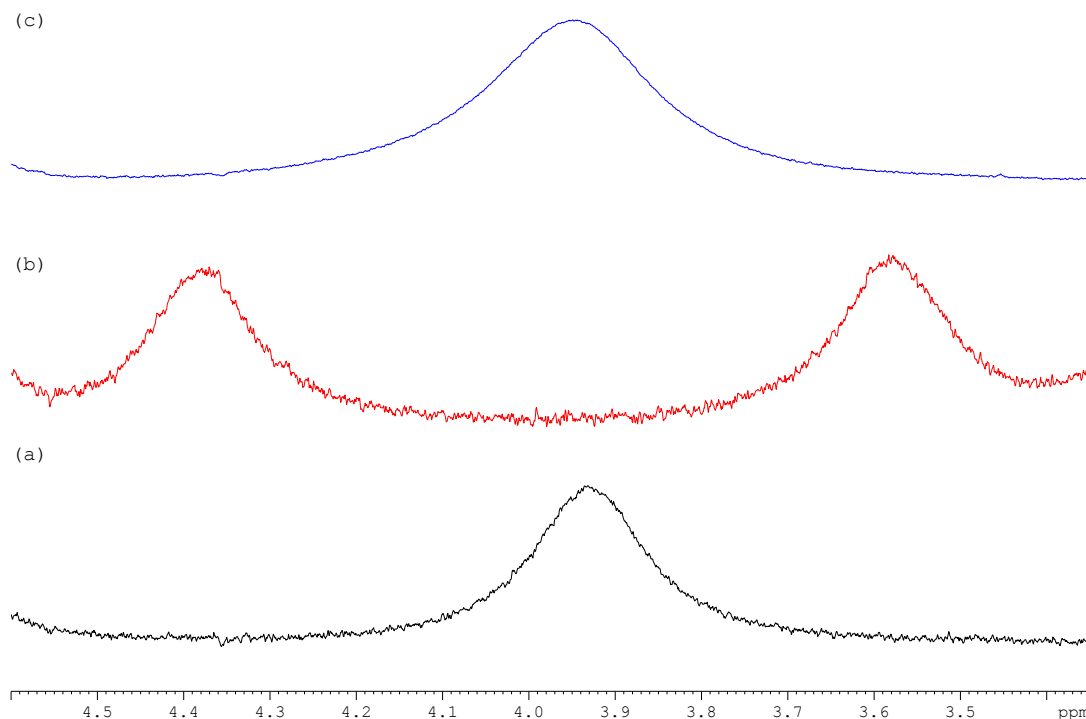


Figure 5.34:  $^1\text{H}$  NMR spectra of the following samples prepared in  $0.1 \text{ mol dm}^{-3}$  KCl and  $\text{D}_2\text{O}$  solvent: (a)  $1.0 \times 10^{-2} \text{ mol dm}^{-3}$  sul-calix[4], (b)  $4.0 \times 10^{-3} \text{ mol dm}^{-3}$   $\text{MV}^{2+}$  and  $4.3 \times 10^{-3} \text{ mol dm}^{-3}$  sul-calix[4] and (c)  $4.0 \times 10^{-3} \text{ mol dm}^{-3}$   $\text{MV}^{2+}$  and  $1.3 \times 10^{-2} \text{ mol dm}^{-3}$  sul-calix[4].

Figure 5.35 shows the recorded spectra of the  $^1\text{H}$  NMR titration carried out in  $\text{D}_2\text{O}$  solvent using  $0.1 \text{ mol dm}^{-3}$  KCl and  $4.0 \times 10^{-3} \text{ mol dm}^{-3}$   $\text{MV}^{2+}$  with varying concentrations of sul-calix[4]. Figure 5.35 (a) shows the doublets of  $\text{H}_a$  and  $\text{H}_b$  of  $\text{MV}^{2+}$  at approximately 9.0 and 8.5 ppm, respectively. Upon addition of  $2.0 \times 10^{-3} \text{ mol dm}^{-3}$  sul-calix[4], there was a change in the chemical shift of both protons in an upfield direction. This is depicted in Figure 5.35 (b). Moreover, a further addition of  $2.2 \times 10^{-2} \text{ mol dm}^{-3}$  sul-calix[4] induced an upfield shift of the proton signals of  $\text{H}_a$  and  $\text{H}_b$  of  $\text{MV}^{2+}$ , as shown in Figure 5.35 (c). As recorded for the interaction of  $\text{V}^{2+}$  and sul-calix[4], upfield shifts are indicative of complex formation<sup>54</sup>.

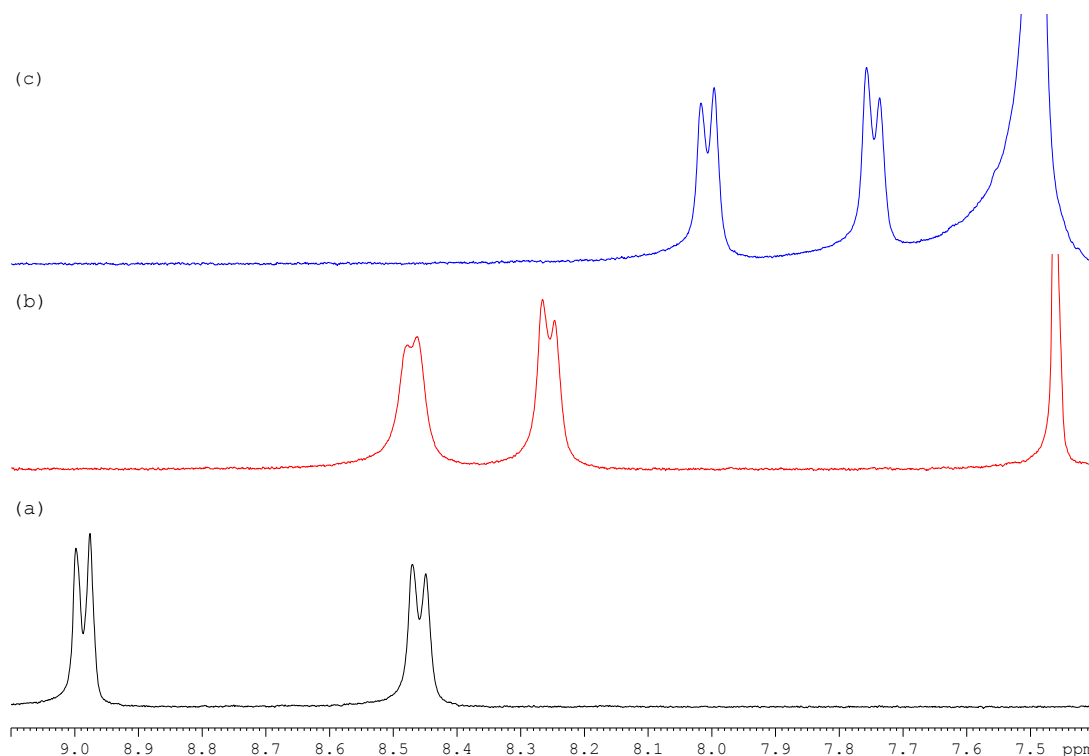


Figure 5.35:  $^1\text{H}$  NMR spectra of  $4.0 \times 10^{-3} \text{ mol dm}^{-3} \text{ MV}^{2+}$  in  $0.1 \text{ mol dm}^{-3} \text{ KCl}$  in  $\text{D}_2\text{O}$  solvent, in the presence of (a) 0.0, (b)  $2.0 \times 10^{-3}$  and (d)  $2.2 \times 10^{-2} \text{ mol dm}^{-3}$  sul-calix[4].

Analysis of the methyl protons,  $\text{H}_c$ , of  $\text{MV}^{2+}$  at 4.45 ppm also showed a change in chemical shift. Although this signal was a little harder to monitor in comparison to  $\text{H}_a$  and  $\text{H}_b$ , due to the interference of the methylene bridging protons at 3.92 ppm of sul-calix[4], a general trend was observed. Table 5.15 shows the changes in chemical shift ( $\Delta\delta$ ) as a function of sul-calix[4] concentration. Given the change in chemical shift experienced by the non-equivalent protons of  $\text{MV}^{2+}$ , this indicated that all protons were interacting with the sul-calix[4]. In order to establish the possible interaction, the dimensions of  $\text{MV}^{2+}$  and the cavity size of sul-calix[4] were calculated.

Analysis of the  $^1\text{H}$  NMR titration showed a maximum  $\Delta\delta$  of 1.00 ppm for  $\text{H}_a$ , 0.70 ppm for  $\text{H}_b$  and 1.60 ppm for  $\text{H}_c$ , the methyl protons. As previously mentioned in Section 5.5.1, the extent of  $\Delta\delta$  is an indication of the orientation of the two molecules with respect to each other<sup>55</sup>. Thus, it is probable that  $\text{MV}^{2+}$  is orientated axially within the sul-calix[4] as shown in Figure 5.36. Although  $\text{MV}^{2+}$

could also interact equatorially with sul-calix[4], the magnitude of the change in chemical shift is greatest for H<sub>c</sub> and H<sub>b</sub>. This suggests that these protons are more effected by the presence of sul-calix[4], hence axial insertion. The complex of MV<sup>2+</sup> and sul-calix[4] has been previously studied by Guo *et al.*<sup>11,64</sup>, in solid-state phase and in solution. They depicted a similar orientation from <sup>1</sup>H NMR data. This corresponds well with the recorded <sup>1</sup>H NMR data illustrated previously in this section.

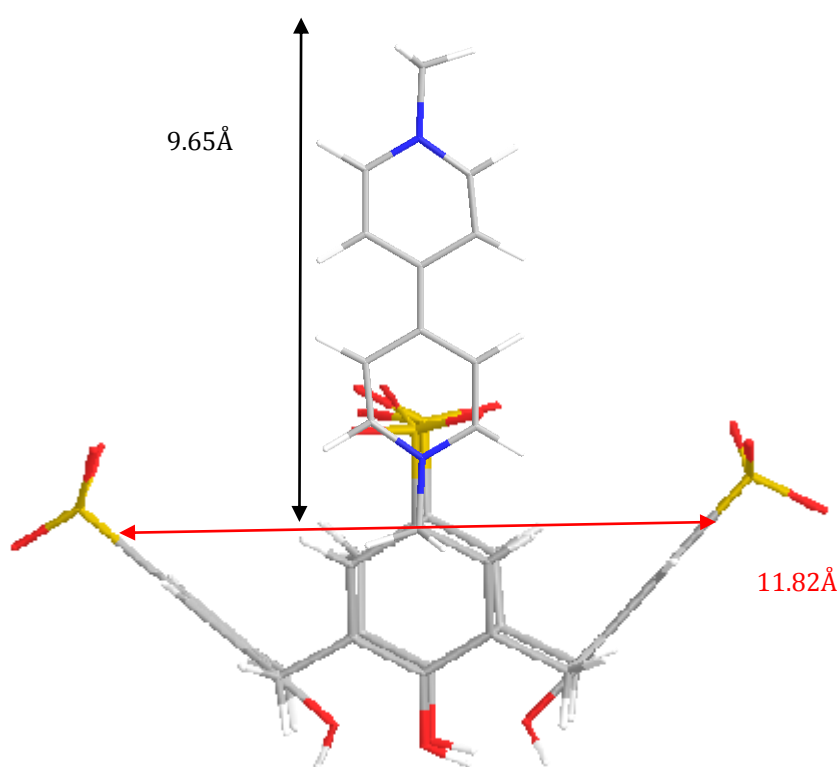


Figure 5.36: Schematic illustration of the interaction of MV<sup>2+</sup> and sul-calix[4].

Table 5.15: Chemical shifts ( $\delta$ ) and the changes in chemical shifts ( $\Delta\delta$ ) in ppm of the methyl protons,  $H_c$  of  $MV^{2+}$  in the absence and presence of sul-calix[4].

$^1H$ NMR titration of $MV^{2+}$ /sul-calix[4]		
Sul-calix[4] / mol dm $^{-3}$	Chemical shift, $\delta$ / ppm	$\Delta\delta$ / ppm
0.0	4.45	0.00
$4.0 \times 10^{-4}$	4.18	0.27
$2.0 \times 10^{-3}$	3.77	0.68
$4.4 \times 10^{-3}$	2.94	1.51
$1.3 \times 10^{-2}$	2.81	1.64
$2.2 \times 10^{-2}$	2.77	1.68

### 5.6.5 Evaluation of $K_a$ of $MV^{2+}$ and Sul-calix[4] using $^1H$ NMR

The techniques available to quantify  $K_a$  for  $MV^{2+}$  and sul-calix[4] were confined to electrochemical and  $^1H$  NMR methods. As both species absorbed in the same range of the UV-Vis spectrum, it was not possible to analyse the interactions using UV-Vis spectroscopy. Also, both  $MV^{2+}$  and sul-calix[4] are weakly fluorescent, thus fluorescence spectroscopy could not be carried out to obtain quantitative information on the interaction of  $MV^{2+}$  and sul-calix[4].

Using the approach described in Section 5.5.2, the  $K_a$  value recorded from RDV, of  $2.42 \times 10^3$  mol $^{-1}$  dm $^3$  for  $MV^{2+}$  and sul-calix[4], was combined with the recorded changes in chemical shift of  $MV^{2+}_{free}$  and  $MV^{2+}_{complexed}$  from  $^1H$  NMR spectra, to construct a non-linear plot. This is shown in Figure 5.37. Data were plotted in accordance with Equation 5.17<sup>2</sup>. The plot shows reasonable agreement with the changes in chemical shifts recorded using  $^1H$  NMR spectra and the calculated  $K_a$  value from RDV measurements.

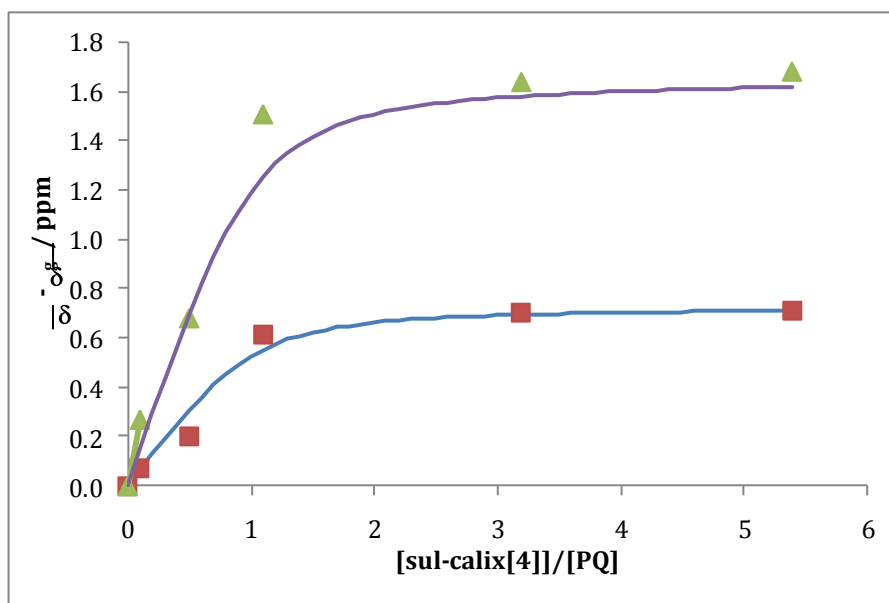


Figure 5.37: Non-linear plot generated from the chemical shift as calculated from Equation 5.18, using a  $K_a$  value of  $2.42 \times 10^{-3} \text{ mol}^{-1} \text{ dm}^3$ , as a function of the ratios of sul-calix[4] to paraquat (PQ), (—) for  $H_a$  and (—) for the methyl protons,  $H_c$  of  $MV^{2+}$ . The changes in chemical shifts for  $H_b$  (■) and  $CH_3$  (▲) in the presence of the following concentrations of sul-calix[4];  $0.0$ ,  $4.0 \times 10^{-4}$ ,  $2.0 \times 10^{-3}$ ,  $4.4 \times 10^{-3}$ ,  $1.3 \times 10^{-2}$  and  $2.2 \times 10^{-2} \text{ mol dm}^{-3}$ .

### 5.7 Interaction of $V^{2+}$ and $MV^{2+}$ with Calix[4]arene

The data presented clearly indicates the formation of a strong complex formed between sul-calix[4] and the analytes of  $V^{2+}$  and  $MV^{2+}$ . However, the influence of ionic strength on the measure of the binding constant, indicates the affinity charged species have for sul-calix[4]. In order to quantify the influence that the electrostatic interaction has on the formation of the above mentioned complexes, the interaction of neutral calix[4]arene (calix[4]) with  $V^{2+}$  and  $MV^{2+}$  was investigated using  $^1\text{H}$  NMR spectroscopy. It was proposed, from this method of analysis that  $K_a$  would be reduced and the decrease in  $K_a$  would be equivalent to the driving force of the electrostatic interactions between the sulfonated groups and the cationic species of  $V^{2+}$  or  $MV^{2+}$ .

Figure 5.38 illustrates the chemical structure of the uncharged calix[4]. As shown, the upper rim remains un-substituted and the lower rim remains fully protonated. The difficulty with handling neutral calixarenes is the poor

solubility of the linked phenolic rings in aqueous based systems and therefore the majority of research of calix[4] is based on solid state interactions<sup>10,13,65</sup>. Thus, the initial barrier to overcome was to find a suitable solvent in which calix[4],  $V^{2+}$  and  $MV^{2+}$  were soluble. Dimethyl sulfoxide (DMSO) was sufficiently non polar to dissolve the hydrophobic calix[4] and the charged species of  $V^{2+}$  and  $MV^{2+}$ . However, as reported by Sueishi *et al.*<sup>66</sup> changing the solvent can have an impact on inclusion and the measure of complexation. More specifically for calixarenes, the hydroxyl groups on the lower rim, which are involved in hydrogen bonding, contribute to the stable cone conformation adopted by the calixarene. Thus, reducing these interactions by changing the solvent system from aqueous to non-aqueous can have an impact on the preferred conformation within solution. Therefore, to provide a valid comparison, the changes in chemical shift of  $V^{2+}$  and  $MV^{2+}$  in the presence of calix[4] or sul-calix[4] were monitored in deuterated DMSO ( $d_6$ -DMSO) solvent.

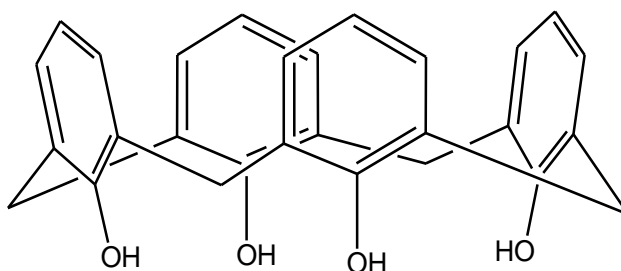


Figure 5.38: Schematic illustration of calix[4]. The molecule is un-charged with the upper rim un-substituted.

Figure 5.39 illustrates the recorded results from the  $^1H$  NMR spectra of  $V^{2+}$  in the absence and presence of calix[4] and sul-calix[4]. The spectra recorded for  $V^{2+}$  in  $d_6$ -DMSO were similar to those recorded in  $D_2O$  (Figure 5.20 (a)). Thus, only the protons in the range relative to  $V^{2+}$  are presented in Figure 5.39 (a). Figure 5.39 (b) shows the influence of  $4.0 \times 10^{-3} \text{ mol dm}^{-3}$  calix[4] on the proton signals of  $8.0 \times 10^{-4} \text{ mol dm}^{-3} V^{2+}$ . It is clear that there is no change in the chemical shift of  $V^{2+}$ . Thus, there are no or very weak interactions between calix[4] and  $V^{2+}$ . Figure 5.39 (c) shows the change in chemical shift upon the addition of  $4.0 \times 10^{-3} \text{ mol dm}^{-3}$  sul-calix[4] to  $8.0 \times 10^{-4} \text{ mol dm}^{-3} V^{2+}$ . In this case,

significant shifts in the proton signals are seen. These results are similar to those recorded in  $D_2O$ , showing a comparable change in the chemical shift for  $H_b$ ,  $H_c$ ,  $H_d$  and  $H_e$  between the free and complexed  $V^{2+}$  with sul-calix[4].

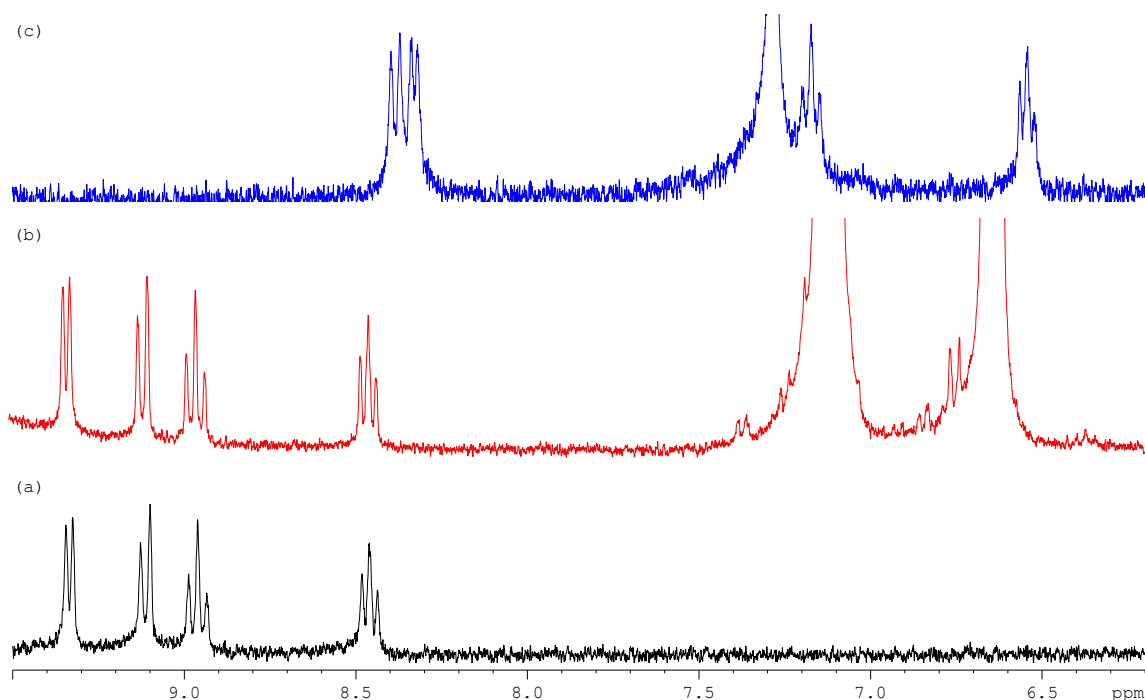


Figure 5.39:  $^1H$  NMR spectra of  $8.0 \times 10^{-4} \text{ mol dm}^{-3} V^{2+}$  in  $d_6$ -DMSO and the following additions of calixarene, (a) 0.0, (b)  $4.0 \times 10^{-3} \text{ mol dm}^{-3}$  calix[4] and (c)  $4.0 \times 10^{-3} \text{ mol dm}^{-3}$  sul-calix[4].

Similar results were recorded for the  $MV^{2+}$  system. As shown in Figure 5.40 (a), the chemical shifts of the aromatic protons of  $MV^{2+}$  in  $d_6$ -DMSO are comparable to those in  $D_2O$  (Figure 5.33) and so only  $H_a$  and  $H_b$  of  $MV^{2+}$  were monitored in the absence and presence of the functionalised calixarenes. Figure 5.40 (b), shows the chemical shifts of  $8.0 \times 10^{-4} \text{ mol dm}^{-3} MV^{2+}$  in the presence of  $4.0 \times 10^{-3} \text{ mol dm}^{-3}$  calix[4]. Similar to the interaction of  $V^{2+}$  and calix[4], there is no change in the spectra. However the addition of  $4.0 \times 10^{-3} \text{ mol dm}^{-3}$  sul-calix[4], as shown in Figure 5.40 (c), induced a change in chemical shift of approximately 1.0 ppm for  $H_a$  and approximately 0.7 ppm for  $H_b$ . Again, this is comparable to the results recorded for  $MV^{2+}$  and sul-calix[4] in  $D_2O$  solvent.

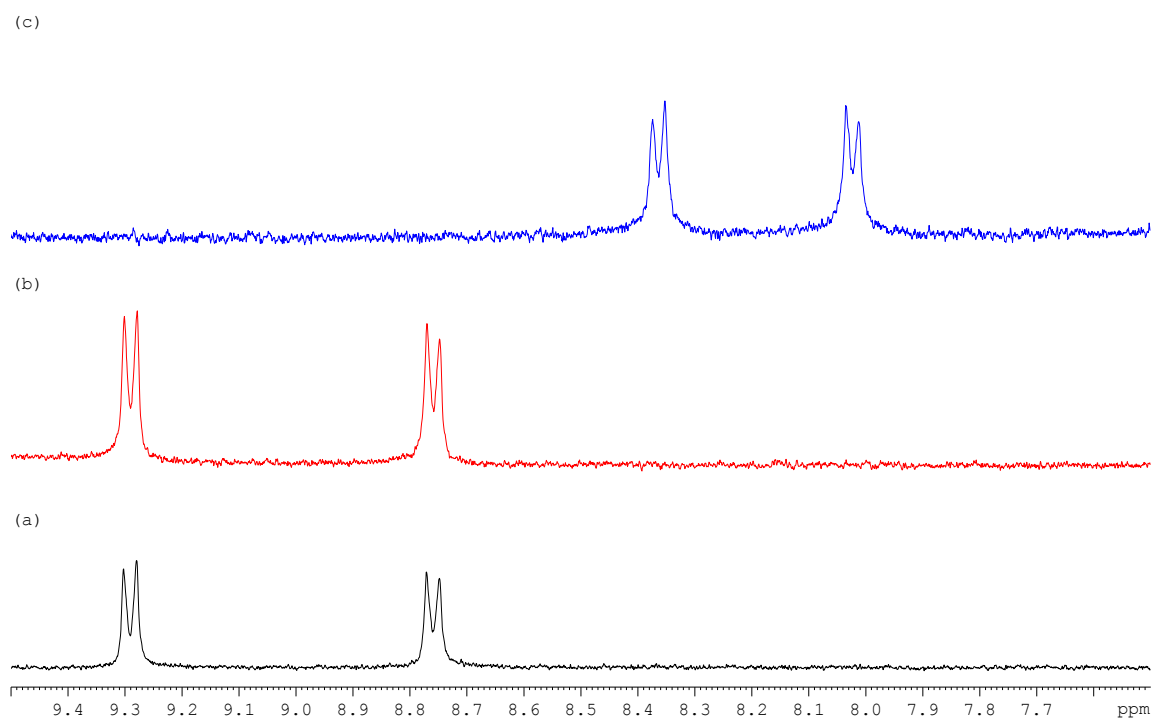


Figure 5.40:  $^1\text{H}$  NMR spectra of  $8.0 \times 10^{-4} \text{ mol dm}^{-3} \text{ MV}^{2+}$  in  $\text{d}_6\text{-DMSO}$  with the following additions of calixarene; (a) 0.0, (b)  $4.0 \times 10^{-3} \text{ mol dm}^{-3}$  calix[4] and (c)  $4.0 \times 10^{-3} \text{ mol dm}^{-3}$  sul-calix[4].

It is evident from the recorded  $^1\text{H}$  NMR spectra that the strong complex formed between  $\text{V}^{2+}$  or  $\text{MV}^{2+}$  and sul-calix[4] is dominated by an electrostatic interaction. Thus, the complex formed involves partial inclusion and is highly dependent on the presence of charged sulfonate groups.

### 5.8 Summary of results

The results presented in this chapter illustrate clearly that a strong complex is formed between  $\text{V}^{2+}$  and sul-calix[4] and between  $\text{MV}^{2+}$  and sul-calix[4]. Initially, the formation of the complex was confirmed by applying the Job's method in which the interaction of  $\text{V}^{2+}$  and sul-calix[4] and  $\text{MV}^{2+}$  and sul-calix[4] were evaluated to be 1:1. Through the use of electrochemical and spectroscopic techniques, the strength of binding was calculated and expressed in terms of a binding constant,  $K_a$ . These methods of analyses also highlighted the importance of ionic strength and the influence that ions have on the measure of association between sul-calix[4] and either  $\text{V}^{2+}$  or  $\text{MV}^{2+}$ . It was observed that upon

increasing the ionic strength of the electrolyte solution,  $K_a$  decreased from values in the vicinity of  $10^6$  to  $10^3$  mol<sup>-1</sup> dm<sup>3</sup>. This was explained in terms of competition between Na<sup>+</sup> and either V<sup>2+</sup> or MV<sup>2+</sup>.

Using <sup>1</sup>H NMR spectroscopy, information of the structure of the bound V<sup>2+</sup> or MV<sup>2+</sup> with sul-calix[4] was obtained. Combining these data with the size of the analytes and the cavity of sul-calix[4], this analysis confirmed partial inclusion of V<sup>2+</sup> with sul-calix[4] as shown in Figure 5.23. The structural analysis of MV<sup>2+</sup> with sul-calix[4] is consistent with the axial interaction which has previously been reported in the literature<sup>11,64</sup>. Analysis of  $K_a$  for V<sup>2+</sup> and MV<sup>2+</sup>, showed a slightly stronger interaction between V<sup>2+</sup> and sul-calix[4] in comparison to MV<sup>2+</sup> and sul-calix[4]. This was initially confirmed by the larger changes in peak potential ( $\Delta E_p$ ) recorded for reduction of diquat (V<sup>2+</sup> + e<sup>-</sup> → V<sup>+</sup>). Although similar changes were recorded for the reduction of paraquat (MV<sup>2+</sup> + e<sup>-</sup> → MV<sup>+</sup>), the shifts of peak potentials in the negative direction for this reduction process were not as large as for V<sup>2+</sup>.

Finally, it was concluded that the interaction of V<sup>2+</sup> and MV<sup>2+</sup> with sul-calix[4] was dominated by charge, as both analytes showed no evidence of inclusion with the neutral calix[4]. This supporting evidence confirmed the importance of ionic strength within the interaction. This was previously concluded as a result of the large variations in  $K_a$  due to a varying electrolyte concentration. In contrast to the results published by Wang *et al.*<sup>12</sup>, the  $K_a$  values for the interaction of V<sup>2+</sup> and sul-calix[4] reported in this chapter were significantly lower. However, this paper employed a phosphate buffer as the supporting electrolyte. As discussed throughout this chapter the combined influence of ionic strength and the presence of ions had a significant impact on the complex formed, thus it is not unusual to obtain a variation in the  $K_a$  values when the supporting electrolyte is varied. Interestingly, the level of agreement of the <sup>1</sup>H NMR data in both studies is excellent and the obtained X-ray crystal structure provided in the paper supports the proposed structural interaction of V<sup>2+</sup> and sul-calix[4].

## 5.9 References

1. S. Kunsági-Máté, G. Nagy, and L. Kollár, *Anal. Chim. Acta*, **428**, 301, (2001).
2. R. S. Macomber, *Chem. Educ.*, **69**, 375, (1992).
3. E. Coutouli-Argyropoulou, A. Kelaidopoulou, C. Sideris, and G. Kokkinidis, *J. Electroanal. Chem.*, **477**, 130, (1999).
4. Z. Yunyou, L. Chun, Y. Huapeng, X. Hongwei, L. Qin, and W. Lun, *Spectrosc. Lett.*, **39**, 409, (2006).
5. W. Ong and A. E. Kaifer, *J. Org. Chem.*, **69**, 1383, (2004).
6. Z. Asfari, J. Harrowfield, P. Thuery, and J. Vicens, *Supramol. Chem.*, **15**, 69, (2003).
7. Y. H. Ling, J. T. Mague, and A. E. Kaifer, *Chemistry-a European Journal*, **13**, 7908, (2007).
8. H. Mansikkamaki, M. Nissinen, and K. Rissanen, *Chem. Commun.*, 1902, (2002).
9. T. Han and C. F. Chen, *Org. Lett.*, **9**, 4207, (2007).
10. C. Gaeta, T. Caruso, M. Mincoelli, F. Troisi, E. Vasca, and P. Neri, *Tetrahedron*, **64**, 5370, (2008).
11. D. S. Guo, L. H. Wang, and Y. Liu, *J. Org. Chem.*, **72**, 7775, (2007).
12. K. Wang, D. S. Guo, H. Q. Zhang, D. Li, X. L. Zheng, and Y. Liu, *J. Med. Chem.*, **52**, 6402, (2009).
13. G. Diao and W. Zhou, *J. Electroanal. Chem.*, **567**, 325, (2004).
14. D. Sobransingh, M. B. Dewal, J. Hiller, M. D. Smith, and L. S. Shimizu, *New J. Chem.*, **32**, 24, (2008).
15. I. Philip and A. E. Kaifer, *J. Org. Chem.*, **70**, 1558, (2005).
16. H. M. Colquhoun, E. P. Goodings, J. M. Maud, J. F. Stoddart, J. B. Wolstenholme, and D. J. Williams, *J. Chem. Soc., Perkin Trans. 2*, 607, (1985).
17. L. Pospisil, J. Hanzlik, R. Fuoco, and M. P. Colombini, *J. Electroanal. Chem.*, **368**, 149, (1994).
18. A. R. Bernardo, T. B. Lu, E. Cordova, L. T. Zhang, G. W. Gokel, and A. E. Kaifer, *J. Chem. Soc., Chem. Commun.*, 529, (1994).
19. A. Sayago, M. Boccio, and A. G. Asuero, *Int. J. Pharm.*, **295**, 29, (2005).
20. M. Masson, J. F. Sigurjonsdottir, S. Jonsdottir, and T. Loftsson, *Drug Dev. Ind. Pharm.*, **29**, 107, (2003).
21. K. A. Connors, Binding Constants. The Measurement of Molecular Complex Stability, Wiley, New York, 1987.
22. E. Bruneau, D. Lavabre, G. Levy, and J. C. Micheau, *J. Chem. Educ.*, **69**, 833, (1992).
23. A. A. Rafati, N. Hamnabard, E. Ghasemian, and Z. B. Nojini, *Mater. Sci. Eng., C*, **29**, 791, (2009).
24. M. S. Ibrahim, I. S. Shehatta, and A. A. Al-Nayeli, *J. Pharm. Biomed. Anal.*, **28**, 217, (2002).
25. G.-C. Zhao, J.-J. Zhu, J.-J. Zhang, and H.-Y. Chen, *Anal. Chim. Acta*, **394**, 337, (1999).
26. V. Sindelar, S. E. Parker, and A. E. Kaifer, *New J. Chem.*, **31**, 725, (2007).
27. S. E. Group, Instrumental Methods in Electrochemistry, Eilis Horwood Limited, 1985.
28. R. Isnin, C. Salam, and A. E. Kaifer, *J. Org. Chem.*, **56**, 35, (1991).

29. C. M. A. Brett and A. M. O. Brett, Electrochemistry: Principles, Methods and Applications, Oxford University Press, 1993.
30. T. Ikeda, R. Schmehl, P. Denisevich, K. Willman, and R. W. Murray, *J. Am. Chem. Soc.*, **104**, 2683, (1982).
31. M. C.-S. Juan, O.-S. Emilia, J. G.-M. Juan, G.-F. Luís, F. C.-V. Luís, S.-G. Francisco, and V.-B. Antonio, *Chemistry - A European Journal*, **15**, 710, (2009).
32. D. S. Guo, K. Wang, and Y. Liu, *J. Inclusion Phenom. Macrocyclic Chem.*, **62**, 1, (2008).
33. N. K. Bhatti, M. S. Subhani, A. Y. Khan, R. Qureshi, and A. Rahman, *Turk. J. Chem.*, **30**, 165, (2006).
34. M. Muzikar and W. R. Fawcett, *J. Phys. Chem. B*, **110**, 2710, (2006).
35. R. A. Marcus, *J. Chem. Phys.*, **43**, 679, (1965).
36. F. Brusciotti and P. Duby, *Electrochim. Acta*, **52**, 6644, (2007).
37. C. Topala, G. Ionita, V. Meltzer, E. Pincu, and C. Draghici, *Arkivoc*, **87**, (2002).
38. Y. J. Zhang, G. Z. Tu, and W. X. Cao, *Supramol. Chem.*, **14**, 473, (2002).
39. H. A. Benesi and J. H. Hildebrand, *J. Am. Chem. Soc.*, **71**, 2703, (1949).
40. V. O. Gennady, N. R. David, and V. Willem, *Eur. J. Org. Chem.*, **2006**, 2810, (2006).
41. W. Y. Li, H. Li, G. M. Zhang, J. Bin Chao, L. X. Ling, S. M. Shuang, and C. Dong, *J Photoch Photobio A*, **197**, 389, (2008).
42. Y. Zhou, Q. Lu, C. Liu, S. She, and L. Wang, *Anal. Chim. Acta*, **552**, 152, (2005).
43. D. A. McQuarrie and J. D. Simon, Physical Chemistry: A Molecular Approach, University Science Books, Sausalito, CA, 1997.
44. C. Hannachi, B. Hamrouni, and M. Dhahbi, *Ionics*, **15**, 445, (2009).
45. H. Li, F. Lai, and R. Luo, *Langmuir*, (2009).
46. M. Farkova, P. Lubal, and J. Havel, *Chem. Pap. - Chem. Zvesti*, **58**, 299, (2004).
47. J. P. Scharff, M. Mahjoubi, and R. Perrin, *New J. Chem.*, **15**, 883, (1991).
48. I. Yoshida, N. Yamamoto, F. Sagara, D. Ishii, K. Ueno, and S. Shinkai, *Bull. Chem. Soc. Jpn.*, **65**, 1012, (1992).
49. S. Shinkai, K. Araki, M. Kubota, T. Arimura, and T. Matsuda, *J. Org. Chem.*, **56**, 295, (1991).
50. S. Shinkai, K. Araki, T. Matsuda, and O. Manabe, *Bull. Chem. Soc. Jpn.*, **62**, 3856, (1989).
51. L. J. Barbour and J. L. Atwood, *Chem. Commun.*, 2020, (2001).
52. R. Ficarra, P. Ficarra, M. R. Di Bella, D. Raneri, S. Tommasini, M. L. Calabro, M. C. Gamberini, and C. Rustichelli, *J. Pharm. Biomed. Anal.*, **23**, 33, (2000).
53. S. M. Ali, S. K. Upadhyay, and A. Maheshwari, *J. Inclusion Phenom. Macrocyclic Chem.*, **59**, 351, (2007).
54. N. J. Wheate, G. M. Abbott, R. J. Tate, C. J. Clements, R. Edrada-Ebel, and B. F. Johnston, *J. Inorg. Biochem.*, **103**, 448, (2009).
55. P. Sompornpisut, N. Deechalao, and J. Vongsvivut, *ScienceAsia*, **28**, 263, (2002).
56. G. L. Zheng, H. J. Zhang, S. Y. Song, Y. Y. Li, and H. D. Guo, *Eur. J. Inorg. Chem.*, 1756, (2008).

57. P. Thuery, Z. Asfari, J. Vicens, V. Lamare, and J. F. Dozol, *Polyhedron*, 21, 2497, (2002).
58. G. L. Zheng, Y. Y. Li, R. P. Deng, S. Y. Song, and H. J. Zhang, *Cryst. Eng. Comm.*, 10, 658, (2008).
59. J. T. Bien, M. J. Eschner, and B. D. Smith, *J. Org. Chem.*, 60, 4525, (1995).
60. H. J. Kim, W. S. Jeon, Y. H. Ko, and K. Kim, *Proc. Natl. Acad. Sci. U. S. A.*, 99, 5007, (2002).
61. D. Osella, A. Carretta, C. Nervi, M. Ravera, and R. Gobetto, *Organometallics*, 19, 2791, (2000).
62. C. Cabaleiro-Lago, M. Nilsson, and O. Soderman, *Langmuir*, 21, 11637, (2005).
63. S. Shinkai, T. Arimura, H. Satoh, and O. Manabe, *J. Chem. Soc., Chem. Commun.*, 1495, (1987).
64. D.-S. Guo, X. Su, and Y. Liu, *Cryst. Growth Des.*, 8, 3514, (2008).
65. O. I. Kalchenko, F. Perret, N. Morel-Desrosiers, and A. W. Coleman, *J. Chem. Soc., Perkin Trans. 2*, 258, (2001).
66. Y. Sueishi and K. Asano, *J. Inclusion Phenom. Macrocyclic Chem.*, 63, 37, (2009).

### Complexation of Sulfonated $\beta$ -Cyclodextrin with Paraquat and Diquat

#### 6.1 Introduction

The results presented in Chapter 3 discussed the sensitivity of polypyrrole (PPy) doped with sulfonated- $\beta$ Cyclodextrin (sul- $\beta$ CD) towards the analytes paraquat and diquat. In order to probe this interaction further, this chapter focuses on establishing the nature and strength of the interaction in solution, between sul- $\beta$ CD and paraquat, and sul- $\beta$ CD and diquat. As discussed in Chapter 5, the interaction of paraquat and diquat with sulfonated-calix[4]arene (sul-calix[4]) was dominated by electrostatic interactions, in which ionic strength played a significant role on the measure of complexation. Given the charged nature of the sul- $\beta$ CD macrocycle due to the presence of ionised sulfonic groups, electrostatic interactions will contribute to the interaction of sul- $\beta$ CD with paraquat and diquat. Also, sul- $\beta$ CD has a cavity similar to that of sul-calix[4], as shown in Figure 6.1. Therefore, an inclusion complex may form between the sul- $\beta$ CD and the paraquat or diquat guest molecules.

As previously discussed in Chapter 1, Section 1.4.1, sul- $\beta$ CD is highly charged, with sulfonate groups on both the primary rim and some substitution on the secondary rim. As reported by Chen *et al.*<sup>1</sup> about 7 to 11 hydroxyl groups are substituted with  $\text{SO}_3^-$  groups. Thus, sul- $\beta$ CD has a minimum of 7 sulfonate groups present. There is a higher charge in comparison to the penta-anionic sul-calix[4]. Also, the large ring structure of sul- $\beta$ CD as a result of the linkage of 7 gluco-pyranose units, provides a larger cavity for inclusion in contrast to sul-calix[4]<sup>2</sup>.

To the best of our knowledge, no previous research has investigated the interactions between either paraquat or diquat and sul- $\beta$ CD. Matsue *et al.*<sup>3</sup> have studied the interactions between paraquat and neutral  $\beta$ cyclodextrin ( $\beta$ CD).

They found that the reduced species of paraquat,  $MV^0$ , was included within the cavity of  $\beta$ CD.

In this chapter the interactions between the dicationic species of paraquat and diquat, i.e.,  $MV^{2+}$  and  $V^{2+}$  and the macrocycle, sul- $\beta$ CD, are considered and discussed. The stoichiometries of the complexes formed are established first. Then the level of association is determined by computing an association constant,  $K_a$ . The study is extended further, in analysing the interaction of lower reduction states of paraquat and diquat, i.e., the cationic and neutral species, with sul- $\beta$ CD. Finally, the interaction is evaluated as a function of the pH of the solution.

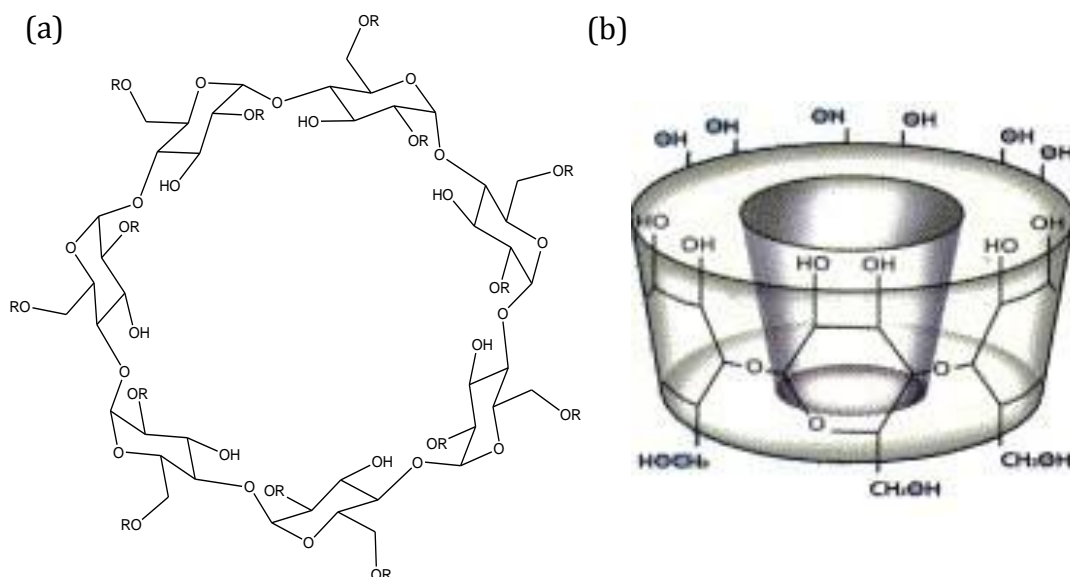


Figure 6.1: Chemical structure of (a) functionalised  $\beta$ CD, in which  $R = SO_3^- Na^+$  or  $H^+$ , in which the degree of substitution is between 7 and 11 of the hydroxyl groups and (b) 3-D illustration of  $\beta$ CD, a cone-shaped macrocycle.

## 6.2 Stoichiometry of Sul- $\beta$ CD and Paraquat

There are many different techniques, such as  $^1H$  NMR, UV-Vis and fluorescence spectroscopies, which can be used to evaluate the stoichiometry of a complex that forms between two species. The mole ratio of the analyte is varied and the recorded raw data are then used to generate a Job's plot. Depending on where

the maximum occurs on the characteristic bell-shaped curve, this indicates the stoichiometry of the complex<sup>4</sup>.

In the case of paraquat and sul- $\beta$ CD, the Job's plot was constructed from electrochemical data recorded using cyclic voltammetry (CV). The mole fraction was calculated in accordance with Equation 6.1, in which  $n$  represents the number of moles.

$$\frac{n_{PQ}}{n_{PQ} + n_{sul-\beta CD}} \quad (6.1)$$

As the stoichiometry was recorded according to the mole fraction of paraquat in a mixture of paraquat and sul- $\beta$ CD, it was important that there was no interference from sul- $\beta$ CD in the electrochemical window used. Representative data are shown in Figure 6.2, where the voltammogram recorded in a solution of  $3.75 \times 10^{-2} \text{ mol dm}^{-3}$  sul- $\beta$ CD is compared to that recorded in  $2.5 \times 10^{-3} \text{ mol dm}^{-3}$  paraquat. It is clear that sul- $\beta$ CD shows no redox activity within this window, as depicted by the blue trace in Figure 6.2. Paraquat exhibits a two-step redox process between the potential of -0.4 and -1.1 V vs. SCE, as shown by the red trace in Figure 6.2. As previously discussed in Chapter 3, Section 3.2, paraquat displays a well-behaved reversible redox process for the  $MV^{2+}/MV^+$  couple,  $MV^{2+} + e^- \rightleftharpoons MV^+$  (Equation 6.2<sup>5</sup>) at approximately -0.7 V vs. SCE. However, the redox couple corresponding to the second electron transfer,  $MV^+ + e^- \rightleftharpoons MV^0$  (Equation 6.3<sup>5</sup>) at approximately -1.0 V vs. SCE is made complicated by the adsorbed  $MV^0$  species and also the comproportionation process<sup>6-9</sup>. These reactions and corresponding redox peaks are illustrated in Figure 6.2 and Equations 6.2 – 6.6<sup>5,6</sup>. The primary investigation of the interaction between paraquat and sul- $\beta$ CD was confined to the first redox couple at about -0.7 V vs. SCE. This also served as a viable comparison to other spectroscopic techniques, e.g.,  $^1\text{H}$  NMR spectroscopy, in which  $MV^{2+}$  is the predominant species in solution.

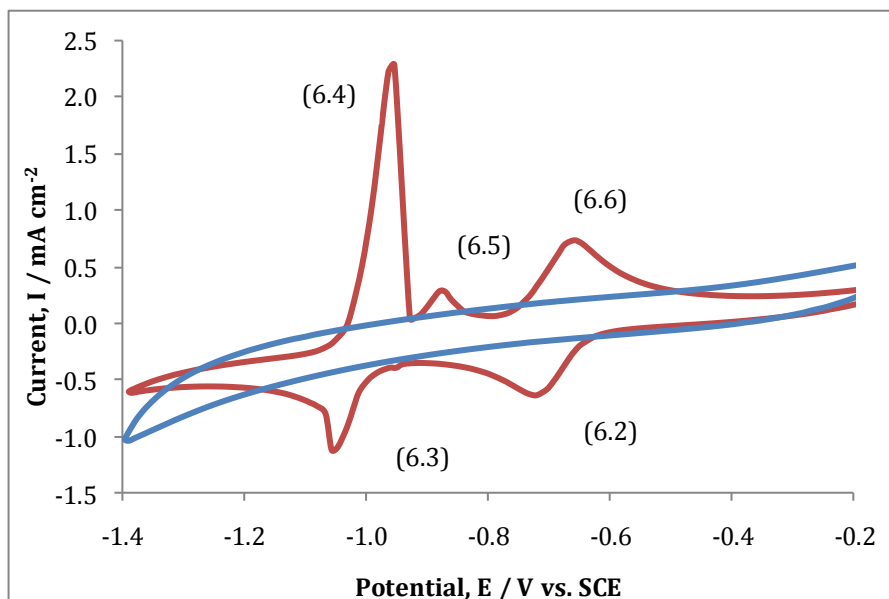
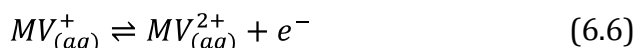
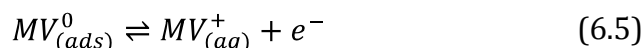
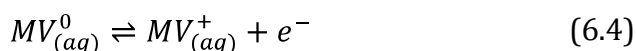
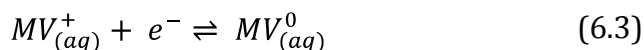
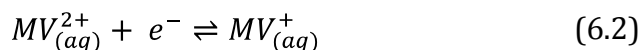


Figure 6.2: Cyclic voltammograms (CV) of (—)  $2.50 \times 10^{-3} \text{ mol dm}^{-3}$  paraquat and (—)  $3.75 \times 10^{-2} \text{ mol dm}^{-3}$  sul- $\beta$ CD in  $0.10 \text{ mol dm}^{-3} \text{ Na}_2\text{SO}_4$  solution. The potential was swept from  $-0.1 \rightarrow -1.4 \text{ V}$  vs. SCE at  $100 \text{ mV s}^{-1}$  at GC.



The mole fraction of paraquat was varied from 0.0 to 1.0 in a solution of paraquat and sul- $\beta$ CD and the voltammograms were recorded within a potential window of  $-0.1$  to  $-1.0 \text{ V}$  vs. SCE. The recorded data displayed in Figure 6.3, illustrates an increase in the peak current for the reduction of  $MV^{2+}$  to  $MV^{+}$  with increasing mole fraction of paraquat. A Job's plot was then constructed by calculating the difference in the peak reduction currents of paraquat in the absence and presence of the sul- $\beta$ CD ( $\Delta i_p = i_p(MV^{2+}) - i_p(MV^{+}/\text{sul-}\beta\text{CD})$ ). Using the corresponding mole fractions, a Job's plot was generated. This is shown in Figure 6.4. The bell-shaped plot with a maximum of 0.5 is indicative of a 1:1 complex<sup>10,11</sup>.

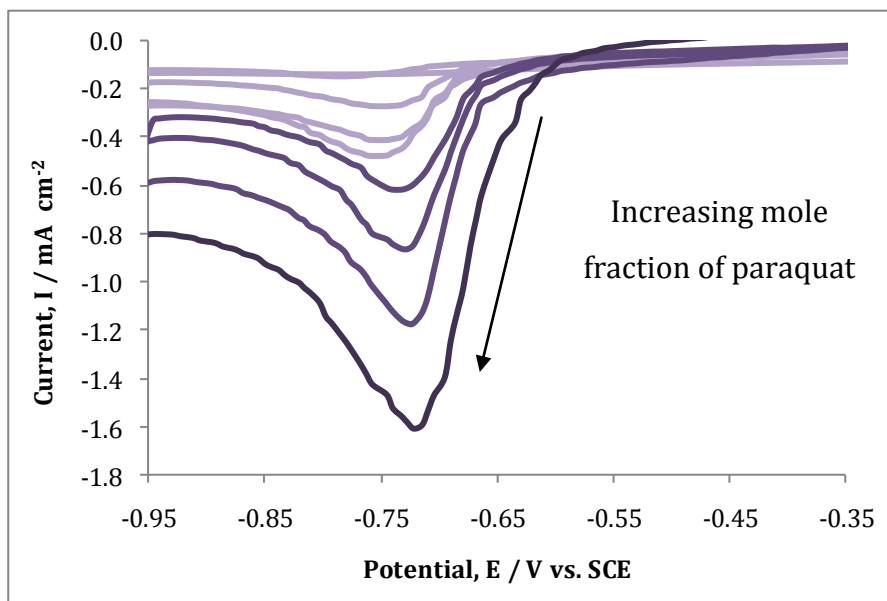


Figure 6.3: CVs recorded for paraquat at mole fractions between 0.0 and 1.0 in a supporting  $0.10 \text{ mol dm}^{-3} \text{ Na}_2\text{SO}_4$  electrolyte. The potential was swept from  $-0.1 \rightarrow -1.0 \text{ V}$  vs. SCE at  $50 \text{ mV s}^{-1}$ , at Au. Stock solutions used were  $1.00 \times 10^{-3} \text{ mol dm}^{-3}$  paraquat and  $1.00 \times 10^{-3} \text{ mol dm}^{-3}$  sul- $\beta$ CD.

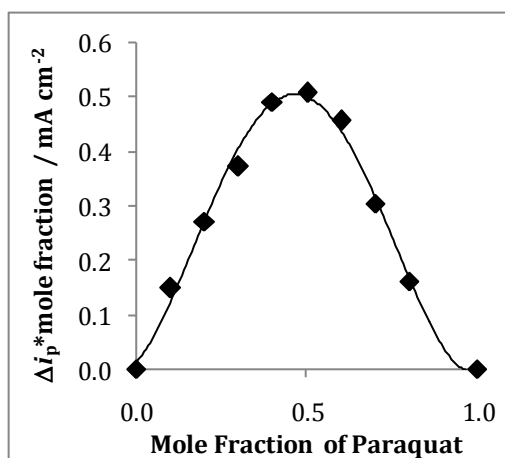


Figure 6.4: Job's plot of paraquat and sul- $\beta$ CD, generated from data recorded using CV, Figure 6.3. The plot shows a maximum at 0.5, which corresponds to a stoichiometry of 1:1 for the paraquat and sul- $\beta$ CD complex.

### 6.3 Evaluation of $K_a$ for Sul- $\beta$ CD and $\text{MV}^{2+}$

From the preliminary analysis carried out there is a clear solution phase interaction between sul- $\beta$ CD and the dicationic form of paraquat,  $\text{MV}^{2+}$ , as illustrated from the Job's plot in Section 6.2. It is also evident in Figure 6.3 that

the peak potential is influenced by the presence of sul- $\beta$ CD, with the peak potential being shifted to more electronegative values with increasing mole fraction of sul- $\beta$ CD. Again, this indicates some interaction between the species. The extent of this interaction was quantified by measuring an association constant,  $K_a$ , as outlined in Chapter 5. Three approaches were used to compute  $K_a$ ; these included cyclic voltammetry (CV), rotating disc voltammetry (RDV) and  $^1\text{H}$  NMR spectroscopy.

### 6.3.1 Evaluation of $K_a$ for Sul- $\beta$ CD and $\text{MV}^{2+}$ using CV

It is well known that an association between two species can be easily monitored using CV if one of the species is electroactive. For example, Sun *et al.*<sup>12</sup> used CV to illustrate the formation of a strong complex, based on the electrostatic interaction of negatively charged pyronine B and positively charged heparin. The complex interaction caused a significant decrease in  $i_p$  and a shift in the  $E_p$  of heparin.

A titration was carried out, by maintaining a constant concentration of paraquat ( $\text{MV}^{2+}$ ) in  $0.1 \text{ mol dm}^{-3}$   $\text{Na}_2\text{SO}_4$  electrolyte solution and excess quantities of sul- $\beta$ CD were added. Figure 6.5 shows the CVs recorded for paraquat in the absence and presence of different concentrations of sul- $\beta$ CD. There is a clear decrease in the peak current ( $i_p$ ) for the reduction of  $\text{MV}^{2+}$  ( $\text{MV}^{2+} + e^- \rightleftharpoons \text{MV}^+$ ), upon addition of sul- $\beta$ CD. This drop in current is consistent with the formation of a complex between sul- $\beta$ CD and the dicationic paraquat<sup>13</sup>. Mendoza *et al.*<sup>14</sup> demonstrated a decrease in peak currents for a functionalised ferrocene dimer in the presence of neutral  $\beta$ CD, which was attributed to the formation of an inclusion complex. However, as detailed by Sun *et al.*<sup>12</sup>, this drop in the peak current is also consistent with the formation of a complex through electrostatic interactions. In both cases, the complexed  $\text{MV}^{2+}$  is large and bulky compared to the free  $\text{MV}^{2+}$ , giving rise to lower rates of diffusion to the electrode surface. There is also a clear shift in the peak potential,  $E_p$ , with increasing concentrations of sul- $\beta$ CD.

These data indicate that the reduction of the complexed  $MV^{2+}$ , compared with that of the free  $MV^{2+}$  is more difficult.

In contrast to the  $MV^{2+}$  and sul-calix[4] complex, higher concentrations of sul- $\beta$ CD were required to form the complex and hence, shift the equilibrium preferentially to the right, as shown in Equation 6.7. This insured that the complexed electroactive species was predominant electroactive species within the solution.

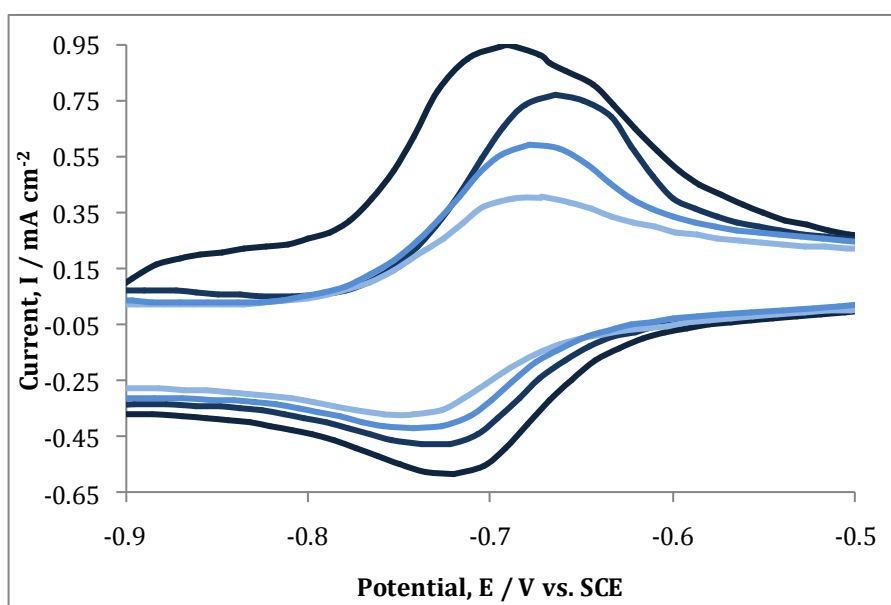


Figure 6.5: CVs of  $2.5 \times 10^{-3} \text{ mol dm}^{-3} MV^{2+}$  in  $0.1 \text{ mol dm}^{-3} Na_2SO_4$ . The following concentrations of sul- $\beta$ CD were added; (—)  $0.00$ , (—)  $2.50 \times 10^{-3}$ , (—)  $1.25 \times 10^{-2}$  and (—)  $4.25 \times 10^{-2} \text{ mol dm}^{-3}$ . The potential was swept from  $-0.1 \rightarrow -1.0 \text{ V vs. SCE}$  at  $100 \text{ mV s}^{-1}$  at GC.

In contrast to the voltammetry recorded for diquat in solutions of sul-calix[4] Section 5.2, Chapter 5, there was no notable increase in current upon the addition of large excesses of sul- $\beta$ CD to a fixed concentration of  $MV^{2+}$ . This suggests that a  $0.1 \text{ mol dm}^{-3} Na_2SO_4$  solution is sufficient in maintaining a near constant ionic strength and the changes observed in current are due to an interaction between  $MV^{2+}$  and sul- $\beta$ CD and not as a result of increased

conductivity of the solution. The changes in peak current were then plotted in accordance with Equation 5.19<sup>15</sup>. A linear plot with a correlation coefficient of 0.999 was obtained, as shown in Figure 6.6. From the equation of the line,  $K_a$  was evaluated as  $141.3 \pm 13.1 \text{ mol}^{-1} \text{ dm}^3$ . This value is much lower than the  $K_a$  value of  $3.46 \times 10^3 \text{ mol}^{-1} \text{ dm}^3$  obtained for paraquat and sul-calix[4] in  $0.1 \text{ mol dm}^{-3} \text{ Na}_2\text{SO}_4$ , indicating that the complex formed between paraquat and sul- $\beta$ CD is not as strongly bound. To ensure the validity of this result, RDV and  $^1\text{H}$  NMR spectroscopy were carried out to evaluate  $K_a$ , and  $^1\text{H}$  NMR spectroscopy was also used to assess the structure of the complex formed.

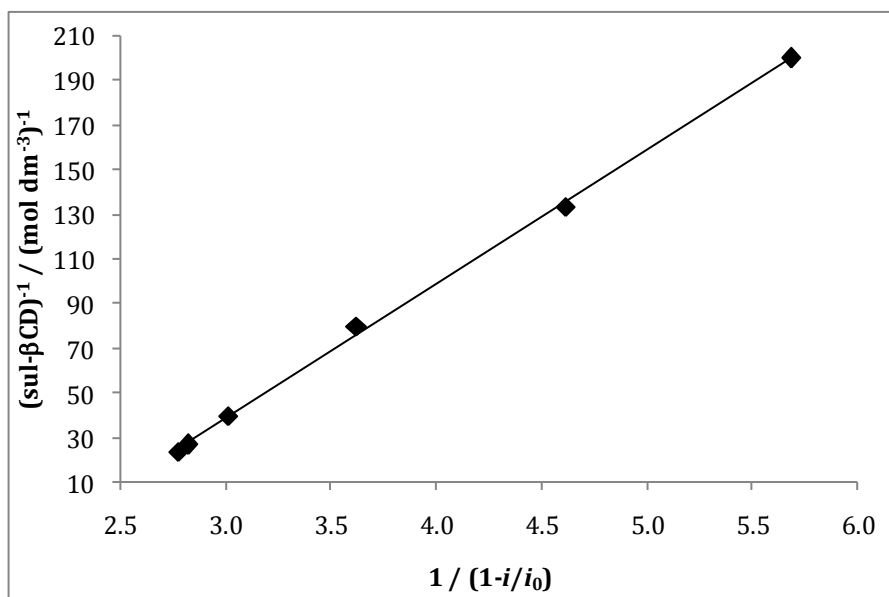


Figure 6.6: Plot of  $1/\text{sul-}\beta\text{CD}$  as a function of  $1/(1-i/i_0)$ . This linear relationship with a correlation coefficient of 0.999 corresponds to the raw data recorded in Figure 6.5 using CV for a  $2.5 \times 10^{-3} \text{ mol dm}^{-3} \text{ MV}^{2+}$  solution in a  $0.1 \text{ mol dm}^{-3} \text{ Na}_2\text{SO}_4$  electrolyte solution, in the absence and presence of sul- $\beta$ CD.

### 6.3.2 Evaluation of $K_a$ for Sul- $\beta$ CD and $\text{MV}^{2+}$ using RDV

As discussed in Chapter 5, Section 5.8.2,  $K_a$  can be calculated using RDV measurements. Similar to CV, RDV records voltammograms within a potential window, however the working electrode is rotated. Thus, the process of diffusion is controlled by convection and is no longer time dependent<sup>16</sup>. Figure 6.7 shows voltammograms recorded for  $1.0 \times 10^{-3} \text{ mol dm}^{-3}$  paraquat in a  $0.1$

$\text{mol dm}^{-3}$   $\text{Na}_2\text{SO}_4$  solution at varying rotation rates. As the voltammograms show, the limiting current at approximately  $-0.85$  V vs. SCE increases with rotation speed, in accordance with the Levich equation, Equation 5.4<sup>17</sup>. This is depicted by the inset shown in Figure 6.7.

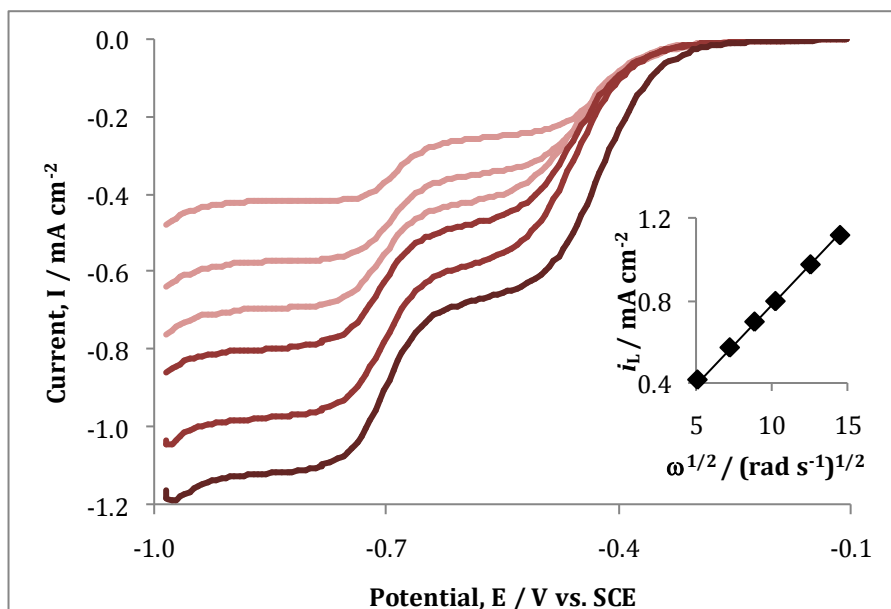


Figure 6.7: RDVs of  $1.0 \times 10^{-3}$  mol  $\text{dm}^{-3}$   $\text{MV}^{2+}$  in  $0.1$  mol  $\text{dm}^{-3}$   $\text{Na}_2\text{SO}_4$  solution at the following rotation speeds, (—) 2,000 rpm, (—) 1,500 rpm, (—) 1,000 rpm, (—) 750 rpm, (—) 500 rpm and (—) 250 rpm. The potential window was swept from  $-0.1 \rightarrow -1.0$  V vs. SCE at  $50$   $\text{mV s}^{-1}$ , at GC. The inset depicts the relationship of limiting current,  $i_L$ , as a function of rotation speed,  $\omega^{1/2}$ . This is a linear relationship in accordance with the Levich equation.

Upon closer inspection of Figure 6.7, two limiting current regions can be seen. There is an initial increase in the reduction current at  $-0.3$  V vs. SCE. This gives rise to a limiting current at approximately  $-0.5$  V vs. SCE. Then a second wave is observed resulting in a limiting current at about  $-0.8$  V vs. SCE. This second wave corresponds to the reduction of  $\text{MV}^{2+}$  to  $\text{MV}^+$  and the half-wave reduction potential of  $-0.7$  V vs SCE agrees well with the CV data presented in Figure 6.5. As the first reduction wave occurs at potentials where  $\text{MV}^{2+}$  is stable, additional experiments were carried out to in an attempt to identify the processes which result in this wave. On comparing Figure 6.7 with the data recorded in Chapter 5, Section 5.6.3, it is clear that the nature of the substrate has an influence on the

shape of the RDVs and on the reduction of  $MV^{2+}$ . In Section, 5.6.3, the reduction of  $MV^{2+}$  at Au was shown to yield a half-wave reduction potential at -0.7 V vs. SCE followed by a limiting current at lower reduction potentials. This difference is highlighted in Figure 6.8 (a), in which the red trace corresponds to the reduction of  $MV^{2+}$  at Au and the blue trace is the reduction of  $MV^{2+}$  at GC. The reduction of  $MV^{2+}$  at Au is governed by an initial sloping current followed by a potential step indicative of the conversion of  $MV^{2+}$  to  $MV^+$ . However, at GC there are two clear potential steps. It has been documented by Kostela *et al.*<sup>18</sup> that the peak at around -0.4 V vs. Ag/AgCl (-0.45 V vs. SCE) is believed to be caused by reorganisation of the surface structure. They reported the presence of a similar peak for the reduction of N-tetradecyl-N'-methylviologen at GC using CV. The CVs of paraquat at GC produced no such peak. However, as RDV is a more sensitive technique, it may be able to detect the presence of structural reorganisation.

Methyl viologen has also been used to catalyse oxygen reduction. In a study by Jin and co-workers<sup>19</sup>, the authors observed that oxygen reduction, which occurs at -0.66 V vs. SCE at a bare gold disk microelectrode, occurred at a higher potential of -0.45 V vs. SCE at a modified electrode of Nafion and  $MV^{2+}$ . The influence of dissolved  $O_2$  on the shape of the voltammograms can be seen in Figure 6.8 (b). The blue trace depicts the reduction of  $MV^{2+}$  at GC in the presence of  $O_2$  and the green trace represents the reduction of a completely deoxygenated sample of  $MV^{2+}$  (purged with nitrogen for 60 min). This indicates that the first redox wave is associated with the presence of dissolved  $O_2$ .

Thus, the presence of this first reduction step is a combination of the substrate effect and the reduction of dissolved  $O_2$ . Although this can introduce errors in measuring the true limiting current for the reduction of  $MV^{2+}$ , this wave was constant over cycle number and in addition it was highly reproducible. Consequently, the limiting currents for the reduction of  $MV^{2+}$  to  $MV^+$  were computed between -0.8 and -1.0 V vs SCE. As the oxygen contribution is

constant and reproducible it will have little impact on the calculation of diffusion coefficients or in the determination of  $K_a$ .

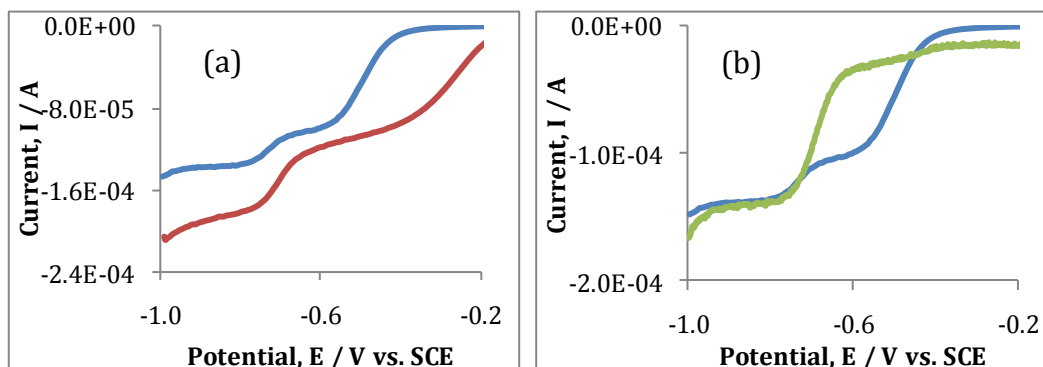


Figure 6.8: (a) RDVs of  $1.0 \times 10^{-3} \text{ mol dm}^{-3}$  paraquat in  $0.1 \text{ mol dm}^{-3} \text{ Na}_2\text{SO}_4$  at (-) Au and (-) GC. (b) RDVs of  $1.0 \times 10^{-3} \text{ mol dm}^{-3}$  paraquat in a (-) oxygenated solution of  $0.1 \text{ mol dm}^{-3} \text{ Na}_2\text{SO}_4$  at GC and a (-)  $0.1 \text{ mol dm}^{-3} \text{ NaCl}$  deoxygenated solution at GC. For both RDVs, the potential was swept from  $-0.1 \rightarrow -1.4 \text{ V vs. SCE}$  at  $50 \text{ mV s}^{-1}$ , at a fixed rotation of  $2,000 \text{ rpm}$ . The diameter of Au and GC was  $4$  and  $5 \text{ mm}$ , respectively. The deoxygenated RDVs were carried out by Ms. Valeria Annibaldi.

The changes in the limiting current and half-wave potential for the reduction of  $\text{MV}^{2+} + \text{e}^- \rightleftharpoons \text{MV}^+$  were monitored in the absence and presence of sul- $\beta$ CD at varying rotation rates. Figure 6.9 illustrates the influence of sul- $\beta$ CD on the limiting current of  $\text{MV}^{2+}$ . There is a decrease in current with increasing sul- $\beta$ CD concentration, indicating a decreased rate in diffusion and hence the formation of a complex. Isnin *et al.*<sup>20</sup> recorded similar results for the complex of a modified ferrocene compound with  $\beta$ CD. Also, Zhang *et al.*<sup>21</sup> reported that the complexation of calixarene with ferrocene derivatives decreases the diffusion coefficient ( $D_c$ ), as the ferrocene derivatives are much bulkier than the free guests and hence their diffusion to the interface is compromised.

The limiting currents ( $i_L$ ) of  $\text{MV}^{2+}$ , in the absence and presence of sul- $\beta$ CD, were plotted as a function of rotation speed ( $\omega^{1/2}$ ) to generate Levich plots, as shown in Figure 6.10. Linear plots, with correlation coefficients between  $0.982$  and  $0.998$ , were obtained in each case, in agreement with the Levich equation,

Equation 5.4<sup>17</sup>. Based on this, the slope of each plot was then used to evaluate the diffusion coefficients,  $D_c$ . The diffusion coefficient,  $D_{c(\text{free})}$ , of free  $MV^{2+}$  in solution was computed as  $1.41 \times 10^{-5} \text{ cm}^2 \text{ s}^{-1}$ . However, a  $D_{c(\text{complex})}$  value of  $6.83 \times 10^{-6} \text{ cm}^2 \text{ s}^{-1}$  was obtained when a 40-fold excess of sul- $\beta$ CD was added to the solution. As mentioned above, a decrease in the rate of diffusion<sup>22</sup> is consistent with the formation of a complex species between the  $MV^{2+}$  and sul- $\beta$ CD.

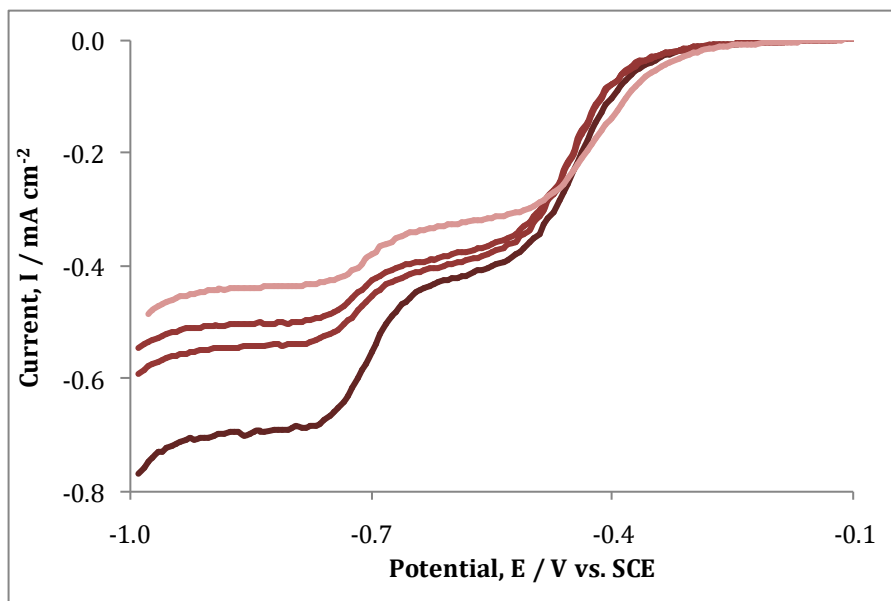


Figure 6.9: RDVs of  $1.0 \times 10^{-3} \text{ mol dm}^{-3} MV^{2+}$  in  $0.1 \text{ mol dm}^{-3} Na_2SO_4$ , in the presence of the following concentrations of sul- $\beta$ CD; (—) 0.0, (—)  $5.0 \times 10^{-3}$ , (—)  $1.0 \times 10^{-2}$  and (—)  $4.0 \times 10^{-2} \text{ mol dm}^{-3}$ . The potential window was swept from  $-0.1 \rightarrow -1.0 \text{ V vs. SCE}$ , at a fixed rotation of 750 rpm at 50  $\text{mV s}^{-1}$  at GC.

In Figure 6.9, there is a small shift in the half-wave potential for the reduction of  $MV^{2+}$  to  $MV^+$  when a large excess of sul- $\beta$ CD is added. In contrast to the potential shifts recorded for the first reduction of paraquat in the presence of sul-calix[4], in which the maximum shift was 50 mV, the largest shift recorded in the presence of a 40-fold excess of sul- $\beta$ CD was 23 mV. This indicates a much weaker binding interaction between  $MV^{2+}$  and sul- $\beta$ CD. The diffusion coefficients,  $D_{c(\text{free})}$  and  $D_{c(\text{complex})}$ , were used together with the half-wave potentials for the reduction of  $MV^{2+}$  in the absence and presence of sul- $\beta$ CD to evaluate  $K_a$  using Equation 5.5<sup>22</sup>. The lower potential shift for  $MV^{2+}$  and sul- $\beta$ CD

had a bearing on the lower  $K_a$  value obtained from RDV as indicated in Table 6.1. In spite of the low  $K_a$  value obtained, the concurrence between CV and RDV is clear from the similar values recorded for both techniques.

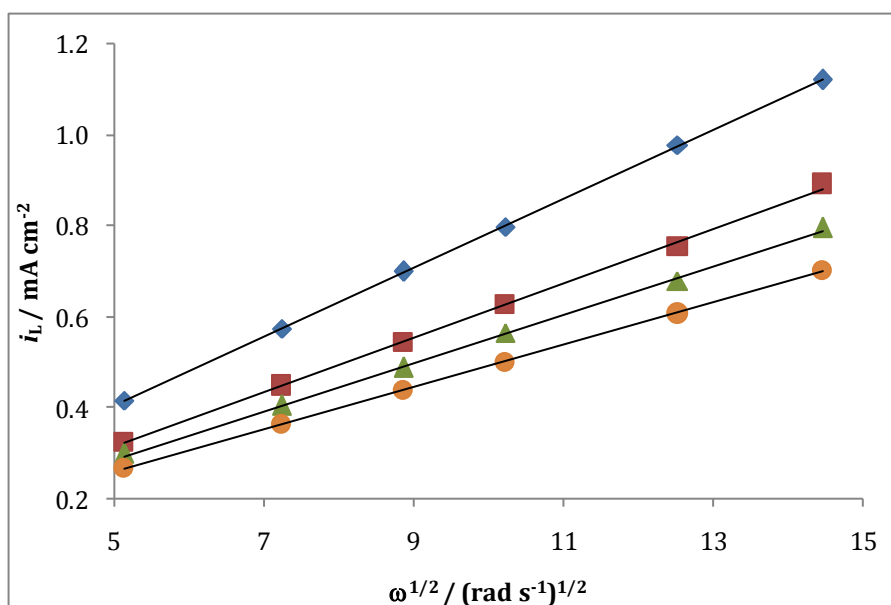


Figure 6.10: Levich plots of the limiting current ( $i_L$ ) of  $1.0 \times 10^{-3} \text{ mol dm}^{-3} \text{ MV}^{2+}$  in  $0.1 \text{ mol dm}^{-3} \text{ Na}_2\text{SO}_4$  as a function of the square root of the rotation speed ( $\omega^{1/2}$ ) with the following additions of sul- $\beta$ CD; ( $\blacklozenge$ )  $0.0$ , ( $\blacksquare$ )  $5.0 \times 10^{-3}$ , ( $\blacktriangle$ )  $2.0 \times 10^{-2}$  and ( $\bullet$ )  $4.0 \times 10^{-2} \text{ mol dm}^{-3}$ .

Table 6.1:  $K_a$  values for the complex of  $\text{MV}^{2+}$  and sul- $\beta$ CD, evaluated using CV and RDV.

$K_a$ for $\text{MV}^{2+}$ and sul- $\beta$ CD in $0.1 \text{ mol dm}^{-3} \text{ Na}_2\text{SO}_4$ electrolyte solution	
CV analysis / $\text{mol}^{-1} \text{ dm}^3$	RDV analysis / $\text{mol}^{-1} \text{ dm}^3$
$141.3 \pm 13.1$	$122.0 \pm 9.7$

The limiting currents,  $i_L$ , coupled with the rotation speed can also be used to evaluate the rate constant,  $k$ , for the reduction of free and complexed  $\text{MV}^{2+}$  in solution. This was done using the Koutechy-Levich equation, Equation 5.6<sup>22</sup>, in which  $i_L^{-1}$  was plotted as a function of  $(\omega^{1/2})^{-1}$ . These linear plots are shown in Figure 6.11. The intercepts were computed using a linear regression analysis and then used to calculate  $k$  at varying concentrations of sul- $\beta$ CD. The rate constants are shown in Table 6.2 and indicate a decrease in the rate of heterogeneous electron transfer upon increasing the sul- $\beta$ CD concentration.

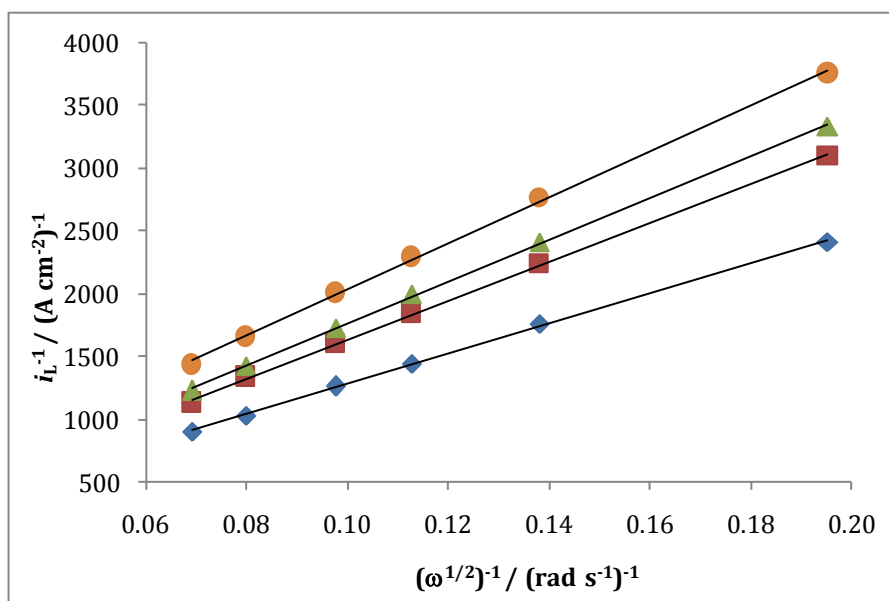


Figure 6.11: Koutechy-Levich plots of  $i_L^{-1}$  as a function of  $(\omega^{1/2})^{-1}$  for  $1.0 \times 10^{-3} \text{ mol dm}^{-3} \text{ MV}^{2+}$  in  $0.1 \text{ mol dm}^{-3} \text{ Na}_2\text{SO}_4$ . These data were plotted using the RDVs in Figure 6.10 for  $1.0 \times 10^{-3} \text{ mol dm}^{-3} \text{ MV}^{2+}$  with the following quantities of sul- $\beta$ CD; ( $\blacklozenge$ ) 0, ( $\blacksquare$ )  $5.0 \times 10^{-3}$ , ( $\blacktriangle$ )  $2.0 \times 10^{-2}$  and ( $\bullet$ )  $4.0 \times 10^{-2} \text{ mol dm}^{-3}$ .

Table 6.2: Rate constants,  $k$ , for the reduction of  $\text{MV}^{2+}$  to  $\text{MV}^+$  recorded in  $1.0 \times 10^{-3} \text{ mol dm}^{-3} \text{ MV}^{2+}$  at varying concentrations of sul- $\beta$ CD in  $0.1 \text{ mol dm}^{-3} \text{ Na}_2\text{SO}_4$ . The rate constant,  $k$ , was evaluated from the intercept of  $i_L^{-1}$  as a function of  $(\omega^{1/2})^{-1}$ . From these plots, correlation coefficients were found to range from 0.998 or 0.999 indicating the linearity and validity in using the Koutechy-Levich equation.

Sul- $\beta$ CD / $\text{mol dm}^{-3}$	[Paraquat] : [sul- $\beta$ CD]	Rate constant, $k$ / $\text{cm}^2 \text{ s}^{-1}$	Correlation coefficient, $R^2$
0.0	1 : 0	0.138	0.999
$5.0 \times 10^{-3}$	1 : 5	0.121	0.999
$1.0 \times 10^{-2}$	1 : 10	0.115	0.999
$2.0 \times 10^{-2}$	1 : 20	0.067	0.998
$3.0 \times 10^{-2}$	1 : 30	0.076	0.999
$4.0 \times 10^{-2}$	1 : 40	0.054	0.999

Both electrochemical techniques of CV and RDV gave similar results and the recorded data are consistent with the formation of a weak complex between  $MV^{2+}$  and sul- $\beta$ CD. As the  $MV^{2+}$  bound by the sul- $\beta$ CD is larger in size compared to the free  $MV^{2+}$ , this will give rise to an increase in the activation energy and a lower rate constant for the electron transfer of the large and bulky complexed  $MV^{2+}$ . This is clearly evident from Table 6.2. It is also clear from the  $K_a$  value recorded here and that presented in Chapter 5, Sections 5.6.2 and 5.6.3, that the binding between  $MV^{2+}$  and sul-calix[4] is stronger than that between  $MV^{2+}$  and sul- $\beta$ CD.

### 6.3.3 $^1H$ NMR Studies on the Interaction of $MV^{2+}$ and sul- $\beta$ CD

To analyse the structural interaction between  $MV^{2+}$  and sul- $\beta$ CD, a  $^1H$  NMR titration was carried out in which the signals for a fixed concentration of  $MV^{2+}$  were monitored with respect to a varying concentration of sul- $\beta$ CD. Prior to carrying out the titration, it was important to identify the relevant signals for both the  $MV^{2+}$  and sul- $\beta$ CD and to determine if there was any overlap between the signals.

Figure 6.12 (a) and (b) shows the equivalent protons of sul- $\beta$ CD and  $MV^{2+}$ , respectively. The signals for sul- $\beta$ CD, as shown in Figure 6.12 (a), are quite broad and confined to the range of 3.50 and 6.00 ppm on the  $^1H$  NMR spectra. This broadening of the signals is attributed to the fact that the sul- $\beta$ CD has varying degrees of substitution of the sulfonate groups. Therefore, an average signal is recorded which appears broad. As previously described in Chapter 5, Section 5.6.4, the aromatic protons of  $MV^{2+}$  appear at 8.45 ( $H_b$ ) and 9.00 ppm ( $H_a$ ) and the methyl protons ( $H_c$ ) at 4.44 ppm. The large broad singlet at approximately 4.60 ppm corresponds to  $H_2O$  present in  $D_2O$ , due to its hygroscopic properties. From this initial inspection, it is clear that it is indeed possible to carry out the  $^1H$  NMR titration and monitor the aromatic signals,  $H_b$  and  $H_a$ , of  $MV^{2+}$  at 8.45 and 9.00 ppm, respectively.

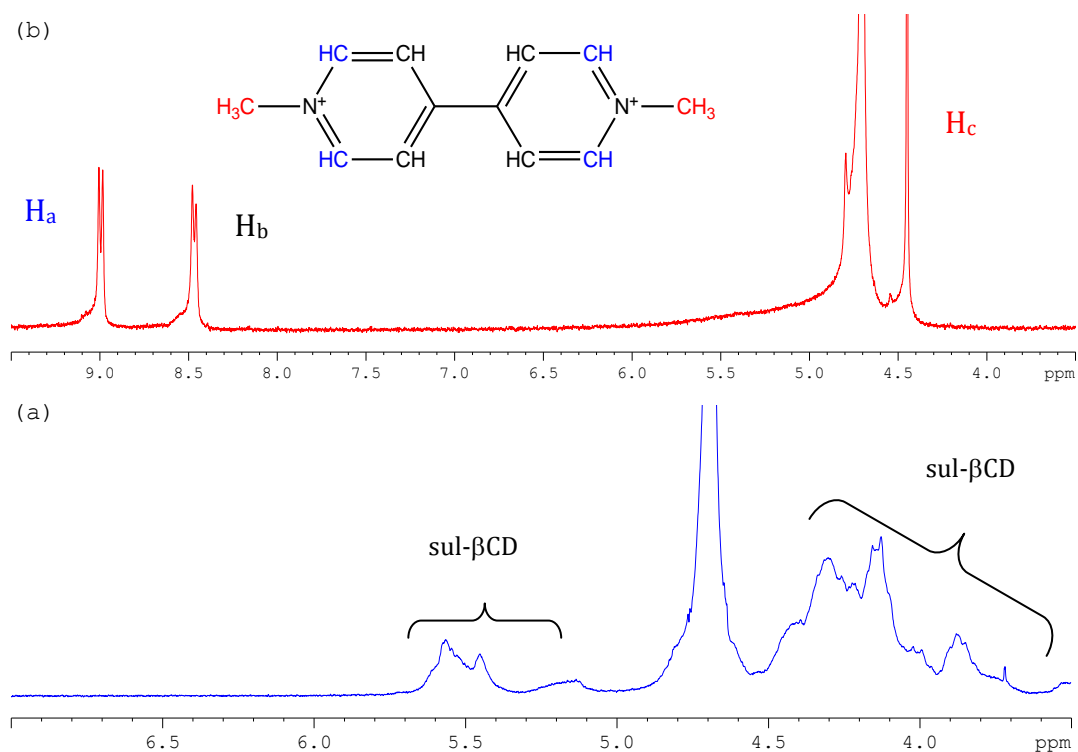


Figure 6.12:  $^1\text{H}$  NMR spectra of (a) sul- $\beta$ CD and (b) MV $^{2+}$  in 0.1 mol dm $^{-3}$  KCl and D $_2$ O solvent. The inset shows the chemical structure of MV $^{2+}$ .

Figure 6.13 illustrates the  $^1\text{H}$  NMR titration carried out, using a fixed concentration of  $5.0 \times 10^{-3}$  mol dm $^{-3}$  MV $^{2+}$  in 0.1 mol dm $^{-3}$  KCl and in D $_2$ O solvent, in the absence and presence of sul- $\beta$ CD. The KCl was added to buffer the ionic strength. As depicted in Figure 6.13 (b), there is a downfield shift of the aromatic protons, when equimolar quantities of MV $^{2+}$  and sul- $\beta$ CD are present within solution. Addition of a 5-fold (Figure 6.13 (c)) and 20-fold excess (Figure 6.13 (d)) of sul- $\beta$ CD to MV $^{2+}$ , induce a further downfield shift for the H $_a$  and H $_b$  protons of MV $^{2+}$ . As all the spectra contain one set of resonances, this indicates a fast reversible exchange between the free and complexed MV $^{2+}$  on the  $^1\text{H}$  NMR time scale $^{23}$ . In general, changes in the chemical shift of a proton signal indicate a change in the environment for that proton and it signifies an interaction $^{24}$ . The magnitude of  $\Delta\delta$  for the corresponding protons, also gives an indication of the strength of the interaction $^{25}$ . As shown in Figure 6.13, the maximum change in chemical shift ( $\Delta\delta$ ) was approximately 0.10 ppm for H $_a$  and H $_b$ . Of the limited analysis that could be carried out on the methyl protons, H $_c$ , due to the

overlapping signals of sul- $\beta$ CD, it was clear that the initial changes in chemical shift were comparable to those of H<sub>a</sub> and H<sub>b</sub>.

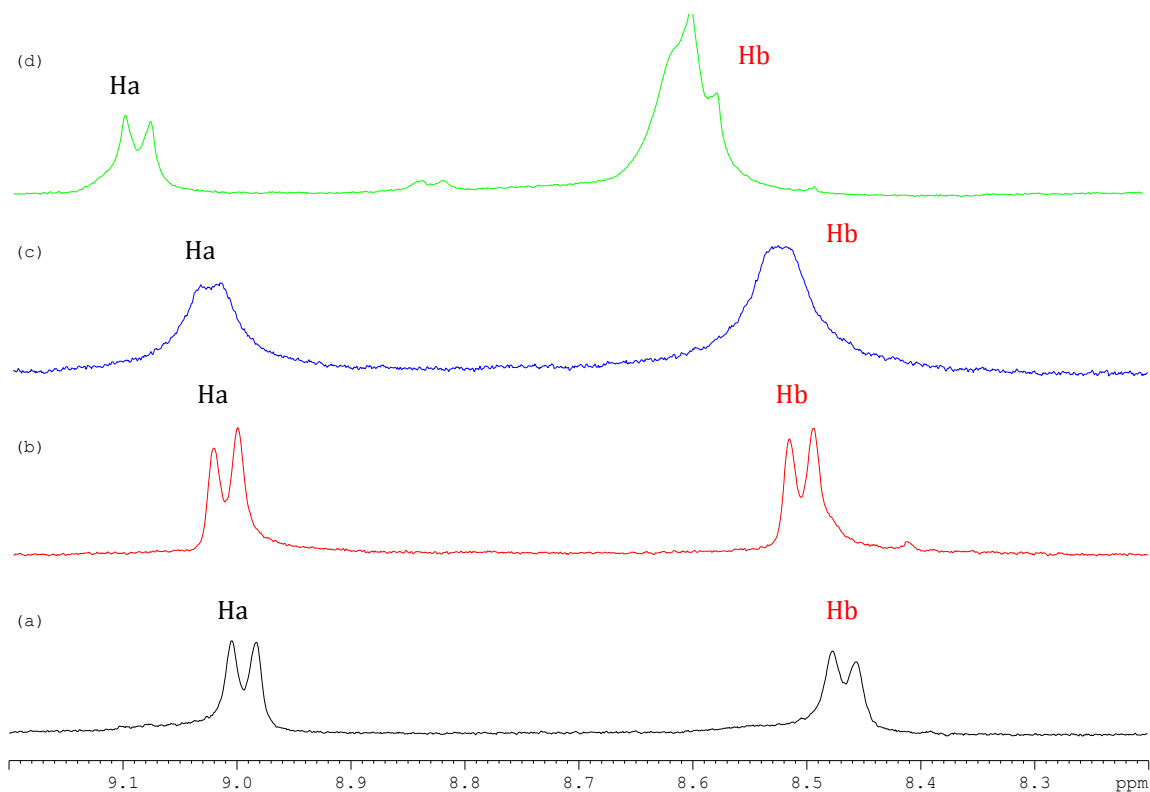


Figure 6.13:  $^1\text{H}$  NMR titration of  $5.0 \times 10^{-3} \text{ mol dm}^{-3} \text{ MV}^{2+}$  in  $0.1 \text{ mol dm}^{-3} \text{ KCl}$  and in  $\text{D}_2\text{O}$  solvent with the following additions of sul- $\beta$ CD; (a) 0.0, (b)  $5.0 \times 10^{-3}$ , (c)  $2.5 \times 10^{-2}$  and  $0.1 \text{ mol dm}^{-3}$ .

These changes are significantly lower than the recorded  $\Delta\delta$  for the complex of  $\text{MV}^{2+}$  and sul-calix[4], in which the maximum change was 1.60 ppm for H<sub>c</sub> and 1.00 ppm for H<sub>a</sub> and H<sub>b</sub>, indicating the formation of a strong complex. As proposed in Chapter 5, Section 5.6.4, the methyl protons of  $\text{MV}^{2+}$  were most affected by the sul-calix[4] evident by the magnitude of  $\Delta\delta$ . However, for the interaction of  $\text{MV}^{2+}$  and sul- $\beta$ CD, all protons are affected equally. This implies that all protons have the same level of interaction with sul- $\beta$ CD and the magnitude of such is quite small indicating that the force of association is governed by charge.

As the concentrations of  $\text{MV}^{2+}$ , sul- $\beta$ CD and the supporting electrolyte were similar in the CV, RDV and  $^1\text{H}$  NMR experiments, the level of agreement between

these techniques was tested. The  $K_a$  value calculated from RDV of  $122.0 \pm 9.7$  mol<sup>-1</sup> dm<sup>3</sup> in Table 6.1 was coupled with the maximum change in chemical shift of MV<sup>2+</sup> in the absence and presence of sul- $\beta$ CD. Using Equations 5.17<sup>26</sup> and 5.18<sup>26</sup>, a non-linear curve was plotted, as shown by the blue trace in Figure 6.14. Also shown in this plot as symbols, are the experimental data. Poor agreement is observed between the experimental data and the data simulated using a  $K_a$  value of  $122.0 \pm 9.7$  mol<sup>-1</sup> dm<sup>3</sup>. In fact, the <sup>1</sup>H NMR spectral data are well below the simulated curve in Figure 6.14, indicating that the  $K_a$  value determined using <sup>1</sup>H NMR is lower than that evaluated from the electrochemical data. Thus, simulated curves were generated using  $K_a$  values below  $122.0 \pm 9.7$  mol<sup>-1</sup> dm<sup>3</sup>. Good agreement between the experimental and simulated data was obtained using a  $K_a$  value of 50.0 mol<sup>-1</sup> dm<sup>3</sup>, as shown in Figure 6.14.

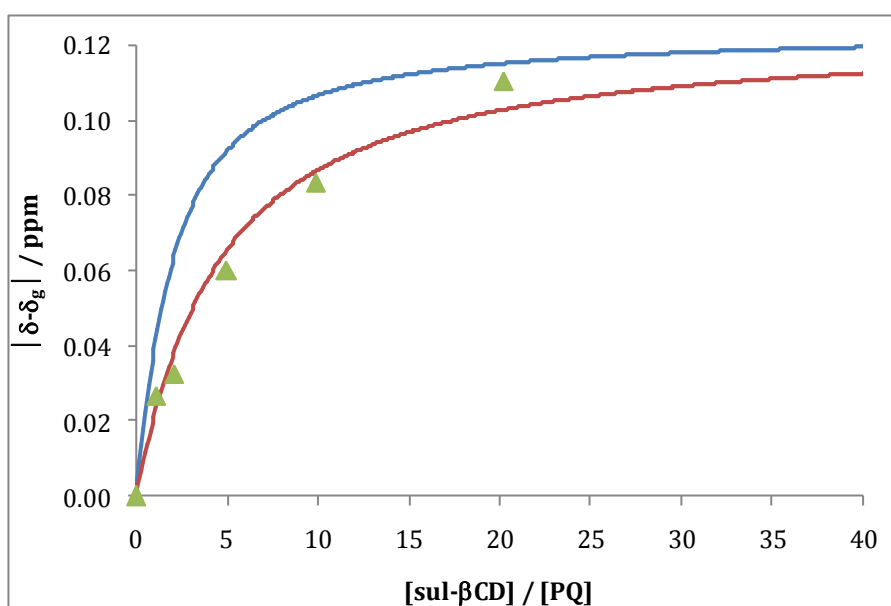


Figure 6.14: Non-linear plots generated from the  $K_a$  of 122.0 mol<sup>-1</sup> dm<sup>3</sup> (—) and 50.0 mol<sup>-1</sup> dm<sup>3</sup> (—) as calculated from Equation 5.18 as a function of the ratio of sul- $\beta$ CD to MV<sup>2+</sup>. The observed changes in chemical shift recorded for Hb ( $\blacktriangle$ ) of MV<sup>2+</sup> were plotted as a function of the ratio of sul- $\beta$ CD to MV<sup>2+</sup>.

Analysis of the complex formed between MV<sup>2+</sup> and sul- $\beta$ CD clearly shows a weak interaction. Although there is a slight difference in the  $K_a$  values obtained

electrochemically and from the  $^1\text{H}$  NMR data, the overall conclusion is similar, in that a weak interaction occurs between  $\text{MV}^{2+}$  and sul- $\beta$ CD. To complement these studies a series of experiments was designed to explore the interactions between  $\text{MV}^+$  and sul- $\beta$ CD, and between  $\text{MV}^0$  and sul- $\beta$ CD. In addition, a comparative study was carried out using the neutral  $\beta$ cyclodextrin.

#### 6.4 Interaction of $\text{MV}^+$ and $\text{MV}^0$ with Sul- $\beta$ -CD and $\beta$ -CD

Electrochemistry is the most practical technique to examine the interaction of  $\text{MV}^0$  or  $\text{MV}^+$  with sul- $\beta$ CD, as in the spectroscopic techniques of UV-Vis or  $^1\text{H}$  NMR, paraquat is maintained in a +2 oxidation state throughout the analysis. In order to generate the  $\text{MV}^0$  and  $\text{MV}^+$  species the electrochemical window was extended to a vertex potential of -1.4 V vs. SCE. Typical data of the peak currents and peak potentials for the reduction of  $\text{MV}^+$  to  $\text{MV}^0$  in the absence and presence of varying concentrations of sul- $\beta$ CD are shown in Table 6.3. To complement these data and isolate the oxidation of the adsorbed species of  $\text{MV}^0$ , voltammograms were recorded using RDV. RDV data of a  $1.0 \times 10^{-3}$  mol  $\text{dm}^{-3}$  paraquat solution in the absence and presence of  $2.0 \times 10^{-2}$  mol  $\text{dm}^{-3}$  sul- $\beta$ CD are shown in Figure 6.15.

Table 6.3: CV data corresponding to the peak potentials and peak currents for the reduction of  $\text{MV}^+$  to  $\text{MV}^0$  in the absence and presence of sul- $\beta$ CD.

CV Data for $2.5 \times 10^{-3}$ mol $\text{dm}^{-3}$ paraquat in 0.1 mol $\text{dm}^{-3}$ $\text{Na}_2\text{SO}_4$		
sul- $\beta$ CD	$E_p^c$ / V vs. SCE	$I_p^c$ / A $\text{cm}^{-2}$
0.0	-1.04	$9.36 \times 10^{-4}$
$5.0 \times 10^{-3}$	-1.06	$7.11 \times 10^{-4}$
$6.3 \times 10^{-3}$	-1.06	$6.90 \times 10^{-4}$
$7.5 \times 10^{-3}$	-1.06	$6.10 \times 10^{-4}$
$2.5 \times 10^{-2}$	-1.06	$6.00 \times 10^{-4}$

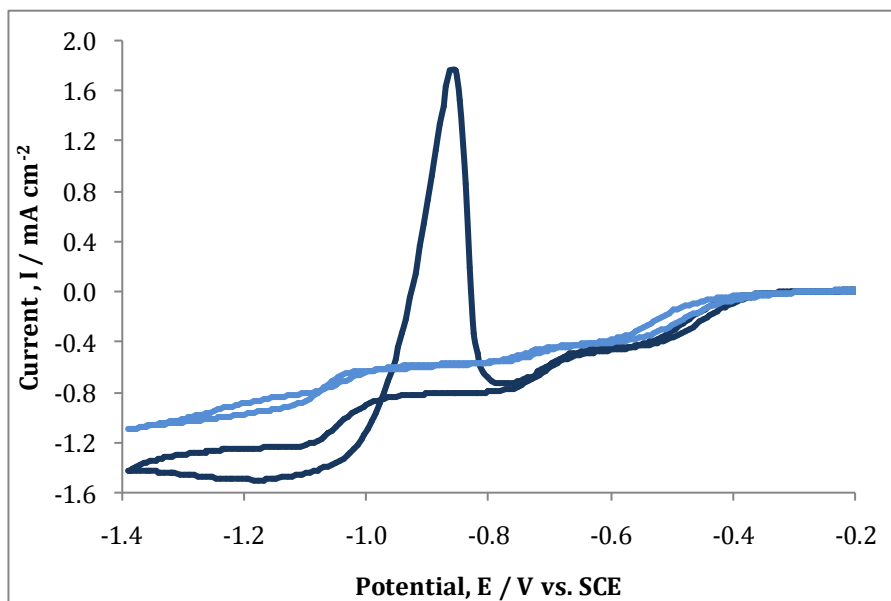


Figure 6.15: RDVs of  $1.0 \times 10^{-3}$  mol dm $^{-3}$  paraquat in 0.1 mol dm $^{-3}$  Na $_2$ SO $_4$  solution with the following additions of sul- $\beta$ CD; (—) 0.0 and (—)  $2.0 \times 10^{-2}$  mol dm $^{-3}$ . The potential was swept from -0.1  $\rightarrow$  -1.4 V vs. SCE at a fixed rotation of 1,000 rpm, at 50 mV s $^{-1}$  at GC.

The reduction of MV $^+$  to MV $^0$  occurs in the potential interval from about -1.0 to -1.4 V vs. SCE. It is clear from the data shown in Table 6.3 that there is a decrease in currents for the reduction of MV $^+$  to MV $^0$  in the presence of sul- $\beta$ CD. This is also evident in Figure 6.15 and Table 6.4 where the limiting current for the conversion of MV $^+$  to MV $^0$  is lower in the presence of sul- $\beta$ CD. There is a notable decrease in the limiting current on addition of  $8.0 \times 10^{-4}$  mol dm $^{-3}$  sul- $\beta$ CD and on further additions there is a smaller reduction in the currents. However, as shown in Table 6.3, from the recorded CV data there is only a small shift in the cathodic peak potential. This is supported by the data shown in Table 6.4 in which there is little variation, about 20 mV, in the half-wave potentials in the absence and presence of sul- $\beta$ CD. This, combined with the lower limiting currents, suggests the formation of a weak complex between the MV $^+$  and sul- $\beta$ CD. The  $K_a$  value was calculated in accordance with Equation 5.5. This equation quantifies the binding interaction based on potential shifts and the ratio of the diffusion coefficients of the free and complexed MV $^+$ . Although, the exact concentration of MV $^+$  in solution was unknown, the ratio of the diffusion coefficients of free MV $^+$  and complexed MV $^+$  was quantified from the limiting currents and rotation speed in accordance with the Levich equation.

Hence, the concentration of  $MV^+$  in solution was not required. The  $K_a$  value was computed to be  $43.1 \pm 8.6 \text{ mol}^{-1} \text{ dm}^3$ . Although, this value is lower than that calculated for the interaction of  $MV^{2+}$  and sul- $\beta$ CD, Table 6.1, the magnitude of association for each cationic state indicates a weak interaction with sul- $\beta$ CD that is influenced by charge.

Table 6.4: Recorded data of peak currents of the oxidation of  $MV^0_{(ads)}$  and the data corresponding to the reduction of  $MV^+$  in which the changes in limiting current ( $i_L$ ) and half-wave potential ( $E_{1/2}$ ) are presented.

RDV analysis of $1 \text{ mmol dm}^{-3} MV^0_{(ads)}$ in $0.1 \text{ mol dm}^{-3} Na_2SO_4$ at 1,000 rpm			
sul- $\beta$ CD / $\text{mol dm}^{-3}$	$i_p, MV^0_{(ads)} / \text{A cm}^{-2}$	$i_L, MV^+ / \text{A cm}^{-2}$	$E_{1/2} / \text{V vs. SCE}$
0.0	$2.67 \times 10^{-3}$	$1.50 \times 10^{-3}$	-1.04
$8.0 \times 10^{-4}$	$5.62 \times 10^{-4}$	$1.02 \times 10^{-3}$	-1.04
$2.4 \times 10^{-3}$	$4.48 \times 10^{-4}$	$9.44 \times 10^{-4}$	-1.05
$2.0 \times 10^{-2}$	-	$9.20 \times 10^{-4}$	-1.05
$3.0 \times 10^{-2}$	-	$8.21 \times 10^{-4}$	-1.05
$4.0 \times 10^{-2}$	-	$7.28 \times 10^{-4}$	-1.06

Also, in Figure 6.15, on the reverse cycle there is a large anodic wave, indicative of the oxidation of the adsorbed  $MV^0$  species which is deposited at the electrode surface during the forward cycle. The assignment of this peak was previously discussed in Chapter 3, Section 3.2. Small additions of sul- $\beta$ CD resulted in a drop in this peak current and the peak is completely lost upon addition of a 20-fold excess of sul- $\beta$ CD, as summarised in Table 6.4. As shown, excesses of 20-fold and above caused complete disappearance of the adsorption peak, indicating that at a sufficient excess of sul- $\beta$ CD the adsorbed species,  $MV^0$ , was not deposited onto the electrode surface. This is evident from the raw data depicted in Figure 6.15.

There are two possible explanations for this phenomenon. Firstly, the neutral species of paraquat forms an inclusion complex with sul- $\beta$ CD, increasing the

solubility of  $MV^0$  and hindering the oxidation of the adsorbed species. Alternatively, the interaction of  $MV^+$  and sul- $\beta$ CD reduces the amount of  $MV^0$  being produced in solution and hence there is less  $MV^0$  to adsorb onto the electrode surface. Also, a combination of the latter two situations could be occurring. In the event that the sul- $\beta$ CD has an affinity for the neutral species,  $MV^0$ , it must be attributed to inclusion, as this cannot occur due to an electrostatic interaction.

In order to explore the influence of the charged sulfonated groups on the interactions between the reduced paraquat species and the cyclodextrin, a series of complementary experiments was carried out using the neutral  $\beta$ CD. Similar excesses of  $\beta$ CD were used as for the analysis of  $MV^{2+}$  and sul- $\beta$ CD. However, given the poor solubility of  $\beta$ CD, concentrations were lowered to maintain comparable excesses. As discussed in Chapter 3, Section 3.2, the oxidation of the adsorbed species,  $MV^0$ , is recorded at slow scan rates and is also concentration dependent. Thus, the CV shown in Figure 6.16 illustrates the 2-step oxidation process of  $MV^0 \rightleftharpoons MV^+ + e^-$  and  $MV^+ \rightleftharpoons MV^0 + e^-$  using a  $5.0 \times 10^{-4}$  mol  $dm^{-3}$  solution of paraquat.

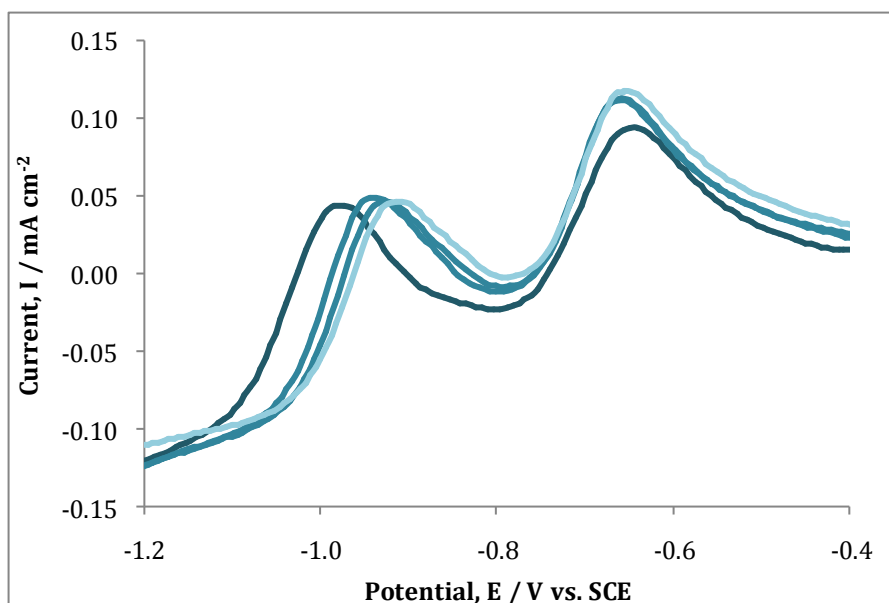


Figure 6.16: CV of  $5 \times 10^{-4}$  mol  $dm^{-3}$   $MV^{2+}$  in  $0.1$  mol  $dm^{-3}$   $Na_2SO_4$  with the following concentrations of  $\beta$ CD: (—)  $0.0$ , (—)  $5.0 \times 10^{-3}$ , (—)  $1.0 \times 10^{-2}$  and (—)  $1.5 \times 10^{-2}$  mol  $dm^{-3}$ . The potential was swept from  $-0.1 \rightarrow -1.4$  V vs. SCE at  $50$   $mV s^{-1}$  at GC.

Upon addition of a 10-fold excess of  $\beta$ CD to a fixed concentration of paraquat, the peak potential for the oxidation of  $MV^0$  to  $MV^+$  shifted to a more electropositive value. Further shifts in the peak oxidation potential were observed on the addition of a 20-fold and 30-fold excess, as illustrated in Table 6.5. This shift corresponding to 50 mV is indicative of the formation of an inclusion complex between the  $MV^0$  species and the neutral  $\beta$ CD.

Table 6.5: Data of the peak currents and peak potentials for the oxidation of  $MV^0$  and  $MV^+$  in  $Na_2SO_4$  solution in the absence and presence of varying concentrations of  $\beta$ CD.

CV data of $5.0 \times 10^{-4} \text{ mol dm}^{-3} MV^{2+}$ in $0.1 \text{ mol dm}^{-3} Na_2SO_4$ solution				
$\beta$ CD / $\text{mol dm}^{-3}$	$i_p^A, MV^0 /$ $\text{mA cm}^{-2}$	$E_p^A, MV^0 /$ V vs. SCE	$i_p^A, MV^+ /$ $\text{mA cm}^{-2}$	$E_p^A, MV^+ /$ V vs. SCE
0.0	0.12	-0.97	0.11	-0.65
$5.0 \times 10^{-3}$	0.12	-0.94	0.11	-0.66
$1.0 \times 10^{-2}$	0.11	-0.92	0.11	-0.66
$1.5 \times 10^{-2}$	0.11	-0.92	0.11	-0.66

A difficulty in quantifying this interaction is defining the precise concentration of  $MV^0$  within solution. Even though the original concentration of  $MV^{2+}$  is known, the precipitation and adsorption of the reduced species makes it quite difficult to quantify the concentration of  $MV^0$  within solution<sup>27</sup>. Thus, an association constant was not computed. As there is no charge associated with either the  $MV^0$  or  $\beta$ CD, the main force of interaction is a host-guest inclusion. Mendoza *et al.*<sup>14</sup> recorded a similar effect for the complexation of a functionalised ferrocene compound with  $\beta$ CD, where inclusion was evident by the redox potential shift of the functionalised ferrocene to more electropositive values. Also, there is a slight decrease in the peak current upon increasing the concentration of  $\beta$ CD. Again, this is characteristic of an inclusion complex as the  $MV^0$  species is now bound by the  $\beta$ CD cavity which creates a reduction in the diffusion coefficients<sup>27</sup>. These findings are in good agreement with the work of

Matsue *et al.*,<sup>3</sup> in which it was found that the fully reduced  $MV^0$  formed an inclusion complex with neutral  $\beta$ CD.

Examination of the oxidation wave for the conversion of  $MV^+$  to  $MV^{2+}$  ( $MV^+ \rightleftharpoons MV^{2+} + e^-$ ) in the absence and presence of  $\beta$ CD showed no obvious effect on the peak current,  $i_p$ , or peak potential  $E_p$ . This is illustrated in Table 6.5, which shows the peak oxidation potentials,  $E_p$ , and peak oxidation currents  $i_p$ , for  $MV^0$  and  $MV^+$  in the absence and presence of  $\beta$ CD. These data clearly show that the charged  $MV^+$  species has no affinity for the hydrophobic cavity of  $\beta$ CD, but the fully reduced  $MV^0$  species forms an inclusion complex with the  $\beta$ CD.

### 6.5 Influence of pH

The quantitative information obtained in the previous sections indicates the formation of a weak complex between  $MV^+$  and sul- $\beta$ CD and between  $MV^{2+}$  and sul- $\beta$ CD. Given the charged nature of  $MV^{2+}$ ,  $MV^+$  and sul- $\beta$ CD, changing the level of ionisation can have an impact on the binding constant<sup>28</sup>. Therefore, another aspect of the interaction that was investigated was the influence of pH. Thus, a titration was carried out at a different pH value using the same electrolyte concentrations of  $MV^{2+}$  and similar excesses of sul- $\beta$ CD to those experiments documented in Section 6.3.1. However, in this instance, the pH value of all solutions was altered using  $H_2SO_4$  to a pH of 4.0. RDV measurements were employed to study the influence of pH using the same conditions, electrochemical window, rotation rate and scan rate as that detailed in Section 6.3.1.

RDV data for the reduction of  $MV^{2+}$  to  $MV^+$  and for the conversion of  $MV^+$  to  $MV^0$  at the pH values of 6.0 and 4.0 are summarised in Table 6.6 and 6.7, respectively. It is clear that the variation in pH from 6.0 to 4.0 has little effect on the half-wave potentials or on the limiting currents. Similar results are obtained at both pH 4.0 and 6.0. This is further confirmed by the evaluation of  $K_a$  for  $MV^{2+}$  and sul- $\beta$ CD at both pH values, as shown in Table 6.8. Thus, the influence of pH

within the range of 4.0 to 6.0 does not impact significantly on the measure of interaction between the  $MV^{2+}$  and sul- $\beta$ CD or between the  $MV^+$  and sul- $\beta$ CD.

Table 6.6: Half-wave potentials ( $E_{1/2}$ ) and limiting currents ( $i_L$ ) for the reduction of  $1.0 \times 10^{-3}$  mol dm $^{-3}$   $MV^{2+}$  in 0.1 mol dm $^{-3}$   $Na_2SO_4$  solution in the absence and presence of sul- $\beta$ CD at pH 4.0 and pH 6.0.

RDV Analysis for the reduction of $1.0 \times 10^{-3}$ mol dm $^{-3}$ $MV^{2+}$ in 0.1 mol dm $^{-3}$ $Na_2SO_4$				
sul- $\beta$ CD / mol dm $^{-3}$	$E_{1/2}$ / V vs. SCE,	$E_{1/2}$ / V vs. SCE,	$i_L$ / A cm $^{-2}$ ,	$i_L$ / A cm $^{-2}$ ,
	pH: 6.0	pH: 4.0	pH: 6.0	pH: 4.0
0	-0.700	-0.705	$7.98 \times 10^{-4}$	$8.02 \times 10^{-4}$
$2 \times 10^{-2}$	-0.716	-0.723	$5.63 \times 10^{-4}$	$6.67 \times 10^{-4}$
$3 \times 10^{-2}$	-0.720	-0.723	$5.26 \times 10^{-4}$	$5.36 \times 10^{-4}$
$4 \times 10^{-2}$	-0.722	-0.723	$5.01 \times 10^{-4}$	$5.05 \times 10^{-4}$

Table 6.7: Half-wave potentials ( $E_{1/2}$ ) and limiting currents ( $i_L$ ) for the reduction of  $MV^+$  to  $MV^0$ . Data were recorded using  $1.0 \times 10^{-3}$  mol dm $^{-3}$   $MV^{2+}$  in 0.1 mol dm $^{-3}$   $Na_2SO_4$  in the absence and presence of sul- $\beta$ CD at pH 4.0 and pH 6.0.

RDV Analysis for the reduction of $1.0 \times 10^{-3}$ mol dm $^{-3}$ $MV^+$ in 0.1 mol dm $^{-3}$ $Na_2SO_4$				
sul- $\beta$ CD / mol dm $^{-3}$	$E_{1/2}$ / V vs. SCE,	$E_{1/2}$ / V vs. SCE,	$i_L$ / A cm $^{-2}$ ,	$i_L$ / A cm $^{-2}$ ,
	pH: 6.0	pH: 4.0	pH: 6.0	pH: 4.0
0	-1.037	-1.021	$1.26 \times 10^{-3}$	$1.04 \times 10^{-3}$
$2 \times 10^{-2}$	-1.041	-1.022	$8.56 \times 10^{-4}$	$8.33 \times 10^{-4}$
$3 \times 10^{-2}$	-1.043	-1.050	$7.23 \times 10^{-4}$	$6.92 \times 10^{-4}$
$4 \times 10^{-2}$	-1.047	-1.050	$6.76 \times 10^{-4}$	$6.11 \times 10^{-4}$

Table 6.8:  $K_a$  values for the interaction of  $MV^{2+}$  and  $MV^+$  with sul- $\beta$ CD at pH 4.0 and 6.0.

$K_a$ values for $MV^{2+}$ and $MV^+$ with sul- $\beta$ CD calculated from RDV analysis		
pH	$K_a (MV^{2+}) / \text{mol}^{-1} \text{dm}^3$	$K_a (MV^+) / \text{mol}^{-1} \text{dm}^3$
4.0	$114.3 \pm 3.1$	$51.0 \pm 8.7$
6.0	$122.0 \pm 9.7$	$43.1 \pm 8.6$

## 6.6 Interaction of Diquat and sul- $\beta$ CD

Given the structural similarity of paraquat and diquat, a comparison was carried out to investigate the interaction of diquat with sul- $\beta$ CD.

### 6.6.1 Stoichiometry of $V^{2+}$ with sul- $\beta$ CD

As discussed in Section 6.2, the stoichiometry of any interaction can be established by carrying out a Job's plot. As diquat absorbs in the UV region, UV-Vis spectroscopy was used to generate the Job's plot. The mole fraction of diquat was varied from 0.0 to 1.0. Stock solutions of  $1.0 \times 10^{-5} \text{ mol dm}^{-3}$  diquat and  $1.0 \times 10^{-5} \text{ mol dm}^{-3}$  sul- $\beta$ CD were prepared in distilled  $\text{H}_2\text{O}$ . Different volumes of the two stock solutions were combined to give the desired mole fractions of diquat. Then the absorbance of the solutions was measured between 280 and 400 nm as diquat absorbs in this region. Typical UV spectra of the absorbance region, from 280 to 330 nm of diquat are presented in Figure 6.17. Each spectra recorded had an overlapping baseline. As shown in Figure 6.17, the absorbance increases with increasing mole fraction of diquat.

The difference in the absorbance of free diquat and diquat in the presence of sul- $\beta$ CD was computed and then multiplied by the corresponding mole fraction of diquat and plotted as a function of the mole fraction of diquat, as shown in Figure 6.18. The characteristic bell-shaped Job's plot, with a maximum of 0.5, indicates a 1:1 stoichiometry between diquat in the dicationic state and sul- $\beta$ CD.

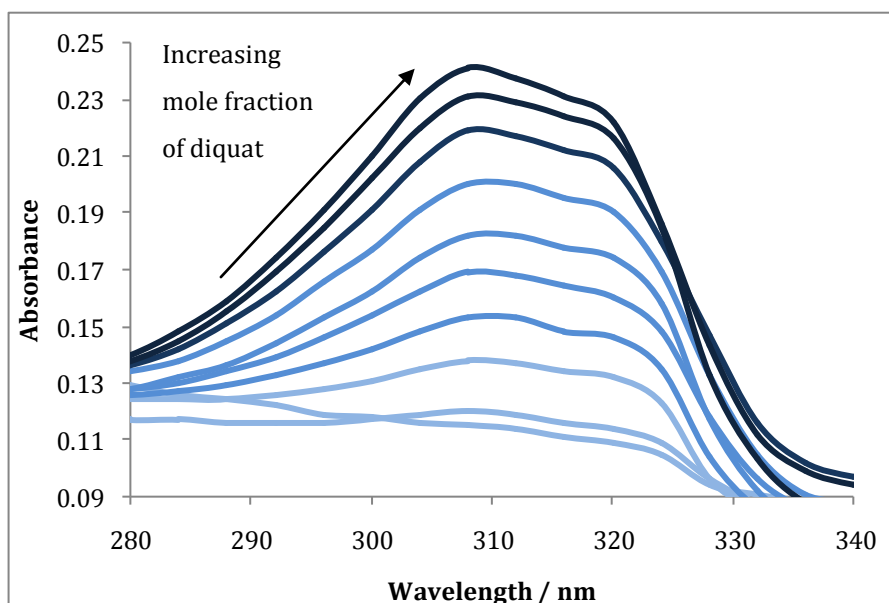


Figure 6.17: UV-Vis spectra of the absorbance of diquat in the presence and absence of sul- $\beta$ CD. Mole fractions of diquat were varied from 0.0  $\rightarrow$  1.0, increasing in increments of 0.1.

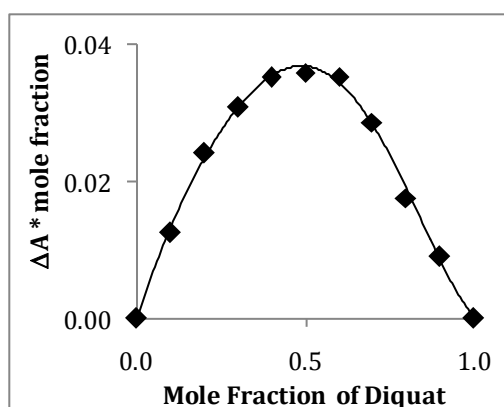


Figure 6.18: Job's plot illustrating the stoichiometry for the interaction of diquat and sul- $\beta$ CD, with a maximum at 0.5, indicating a 1:1 interaction.

### 6.6.2 Evaluation of $K_a$ for Sul- $\beta$ -CD and Diquat

Figure 6.19 illustrates the influence of the sul- $\beta$ CD on the electrochemistry of diquat. In the absence of the sul- $\beta$ CD, the characteristic electrochemistry of diquat is seen. The first reduction wave is observed at about -0.66 V vs. SCE and this corresponds to the reduction of the dicationic  $V^{2+}$  to  $V^+$ . This  $V^{2+}/V^+$  couple shows good reversibility. The second reduction wave appears at -1.03 vs. SCE

and this corresponds to the reduction of  $V^+$  to  $V^0$ . The CV illustrates the decrease in peak current and shift in peak potential upon increasing sul- $\beta$ CD concentration to a fixed concentration of diquat in  $0.1 \text{ mol dm}^{-3} \text{ Na}_2\text{SO}_4$ . The sul- $\beta$ CD has an influence on both the  $V^{2+}$  and  $V^+$  oxidation states of diquat. In both cases, there is a decrease in the peak reduction currents and a shift in the peak reduction potentials to more electronegative values. There is, in both cases, a decrease in redox couple peak currents, and an electronegative shift in the redox couple potentials.

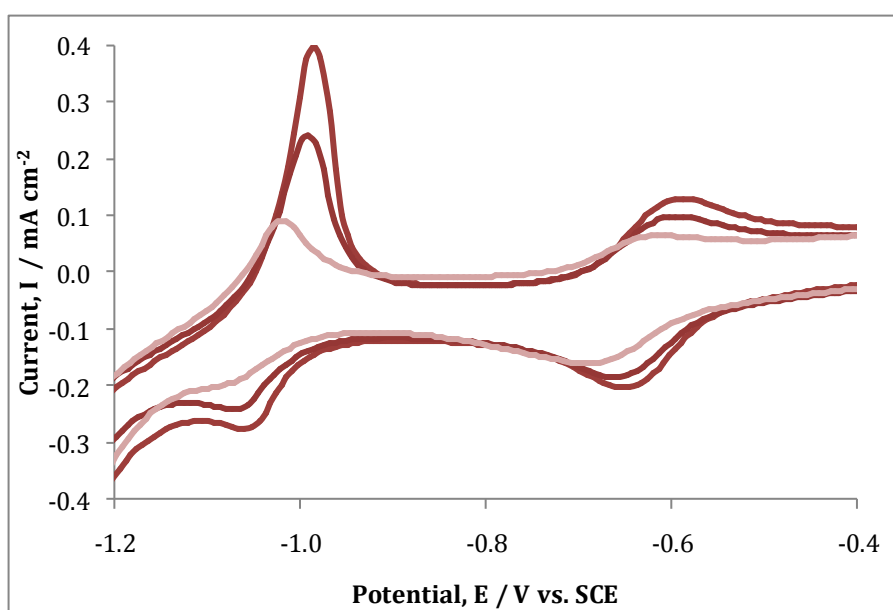


Figure 6.19: CVs of  $8.0 \times 10^{-4} \text{ mol dm}^{-3}$  diquat in  $0.1 \text{ mol dm}^{-3} \text{ Na}_2\text{SO}_4$  in the presence of the following concentrations of sul- $\beta$ CD; (—) 0.0, (—)  $6.0 \times 10^{-4}$  and (—)  $4.0 \times 10^{-3} \text{ mol dm}^{-3}$ . The potential was swept from  $-0.1 \rightarrow -1.4 \text{ V vs. SCE}$  at  $50 \text{ mV s}^{-1}$  at Au.

The changes in current of the free and complexed  $V^{2+}$  and  $V^+$  species of diquat with sul- $\beta$ CD were plotted in accordance with Equation 5.19, in which the intercept is a measure of  $K_a$ . The linear plots are displayed in Figure 6.20 with correlation coefficients of 0.997 and 0.996, respectively. Using Equation 5.19, a  $K_a$  value of  $(1.19 \pm 0.11) \times 10^3 \text{ mol}^{-1} \text{ dm}^3$  was computed for the  $V^{2+}$  and sul- $\beta$ CD, while a  $K_a$  value of  $(1.15 \pm 0.08) \times 10^3 \text{ mol}^{-1} \text{ dm}^3$  was obtained for the  $V^+$  species with sul- $\beta$ CD. These are significantly higher than the corresponding values for the  $MV^{2+}$  or  $MV^+$  and sul- $\beta$ CD complex, indicating that the charged species of

diquat have a higher affinity for the anionic cyclodextrin in terms of binding. These experiments were carried out using different concentrations of diquat and sul- $\beta$ CD in contrast to the analyses of paraquat and sul- $\beta$ CD. This however should have little influence on the binding constant.

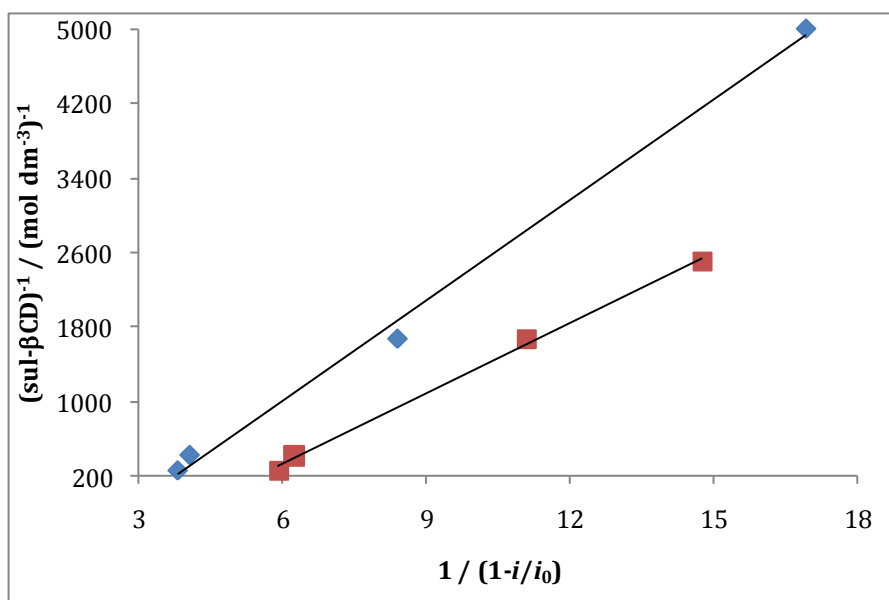


Figure 6.20: Plot of  $1/(\text{sul-}\beta\text{CD})$  as a function of  $1/(1-i/i_0)$ . These linear relationships with correlation coefficients of 0.997 and 0.996, correspond to the recorded electrochemical data for the reduction of (■)  $V^{2+}$  and (♦)  $V^+$  in the absence and presence of sul- $\beta$ CD in a  $0.1 \text{ mol dm}^{-3}$   $\text{Na}_2\text{SO}_4$  solution (Figure 6.18).

This analysis of  $K_a$  concentrates primarily on the changes in current, which in turn are related to changes in the rate of diffusion of the free and complexed  $V^{2+}$  or  $V^+$  species to the electrode surface. However, as shown in Table 6.9, there are corresponding changes in the peak potentials for the reduction of  $V^{2+}$  to  $V^+$  and for the further reduction of  $V^+$  to  $V^0$ . A potential shift of 40 mV and 30 mV is observed for the reduction of  $V^{2+}$  to  $V^+$  and  $V^+$  to  $V^0$ , on adding  $1.25 \times 10^{-2} \text{ mol dm}^{-3}$  sul- $\beta$ CD to a  $2.5 \times 10^{-3} \text{ mol dm}^{-3}$  diquat solution. The higher affinity of the sul- $\beta$ CD for the dicationic diquat compared to the dicationic paraquat is clearly evident from the data presented in Table 6.9 (a). The change in peak potential for the complex of paraquat ( $\text{MV}^{2+}$ ) and sul- $\beta$ CD is 20 mV, but the change for the complex of diquat ( $V^{2+}$ ) and sul- $\beta$ CD is double this value, with a change of 40

mV. Similar data was recorded for the reduction of  $V^+$  and  $MV^+$ , which is illustrated in Table 6.9 (b). This shift in peak potential is closely related to the potential shifts recorded for the complex of paraquat ( $MV^{2+}$ ) and sul-calix[4], as discussed in Chapter 5, Section 5.6.3 in which the potential shift for the complex was approximately 50 mV. Likewise, on comparing the currents of the free and complexed species, the drop in current is larger for the complex formed with diquat than for that formed with paraquat, indicating the predominant shift in equilibrium due to a stronger interaction.

Table 6.9: (a) Tabulated data comparing the reduction of  $MV^{2+} + e^- \rightarrow MV^+$  for  $2.5 \times 10^{-3} \text{ mol dm}^{-3}$  paraquat and the reduction of  $V^{2+} + e^- \rightarrow V^+$  for  $2.5 \times 10^{-3} \text{ mol dm}^{-3}$  diquat in  $0.1 \text{ mol dm}^{-3} \text{ Na}_2\text{SO}_4$  solution. (b) Tabulated data comparing the reduction of  $MV^+ + e^- \rightarrow MV^0$  for  $2.5 \times 10^{-3} \text{ mol dm}^{-3}$  paraquat and the reduction of  $V^+ + e^- \rightarrow V^0$  for  $2.5 \times 10^{-3} \text{ mol dm}^{-3}$  diquat in  $0.1 \text{ mol dm}^{-3} \text{ Na}_2\text{SO}_4$  solution, respectively.

(a)

sul- $\beta$ CD / mol $\text{dm}^{-3}$	$E_{p(MV^{2+} \rightarrow MV^+)}$ / V vs. SCE	$E_{p(V^{2+} \rightarrow V^+)}$ / V vs. SCE	$i_p^C (MV^{2+}) /$ A $\text{cm}^{-2}$	$i_p^C (V^{2+}) /$ A $\text{cm}^{-2}$
0.00	-0.72	-0.66	$6.5 \times 10^{-4}$	$6.8 \times 10^{-4}$
$1.25 \times 10^{-2}$	-0.74	-0.70	$4.4 \times 10^{-4}$	$4.3 \times 10^{-4}$

(b)

sul- $\beta$ CD / mol $\text{dm}^{-3}$	$E_{p(MV^+ \rightarrow MV^0)}$ / V vs. SCE	$E_{p(V^+ \rightarrow V^0)}$ / V vs. SCE	$i_p^C (MV^+) /$ A $\text{cm}^{-2}$	$i_p^C (V^+) /$ A $\text{cm}^{-2}$
0.00	-1.03	-1.03	$1.1 \times 10^{-3}$	$1.1 \times 10^{-3}$
$1.25 \times 10^{-2}$	-1.05	-1.06	$6.2 \times 10^{-4}$	$7.2 \times 10^{-4}$

The dimensions of diquat, paraquat and sul- $\beta$ CD are illustrated in Figure 6.21. Diquat is somewhat smaller than paraquat laterally, however axially it is larger. The inner cavity of  $\beta$ CD, as reported by Astray *et al.*<sup>29</sup> and Szejtli<sup>30</sup>, is approximately 7.8 Å. Cyclodextrins are similar in shape to calixarenes adopting a truncated cone conformation. Thus, there is some flexibility within the macrocyclic structure and per-substitution of the upper rim with sulfonated

groups can cause electron repulsion between the negatively charged groups which can lead to a slight expansion of the upper rim<sup>31</sup>. In spite of this expansion of the upper rim, neither paraquat nor diquat can include within the cyclodextrin cavity laterally. However, axially, inclusion is possible for both. As previously mentioned in Section 6.4.3, cyclodextrins preferably include neutral molecules due to their hydrophobic cavity<sup>20,32</sup>. The weak binding interactions observed between both  $MV^+$  and  $MV^{2+}$  and the sul- $\beta$ CD are not consistent with the formation of an inclusion complex. Instead, the weak binding interactions can be attributed to the formation of a complex driven by electrostatic interactions.

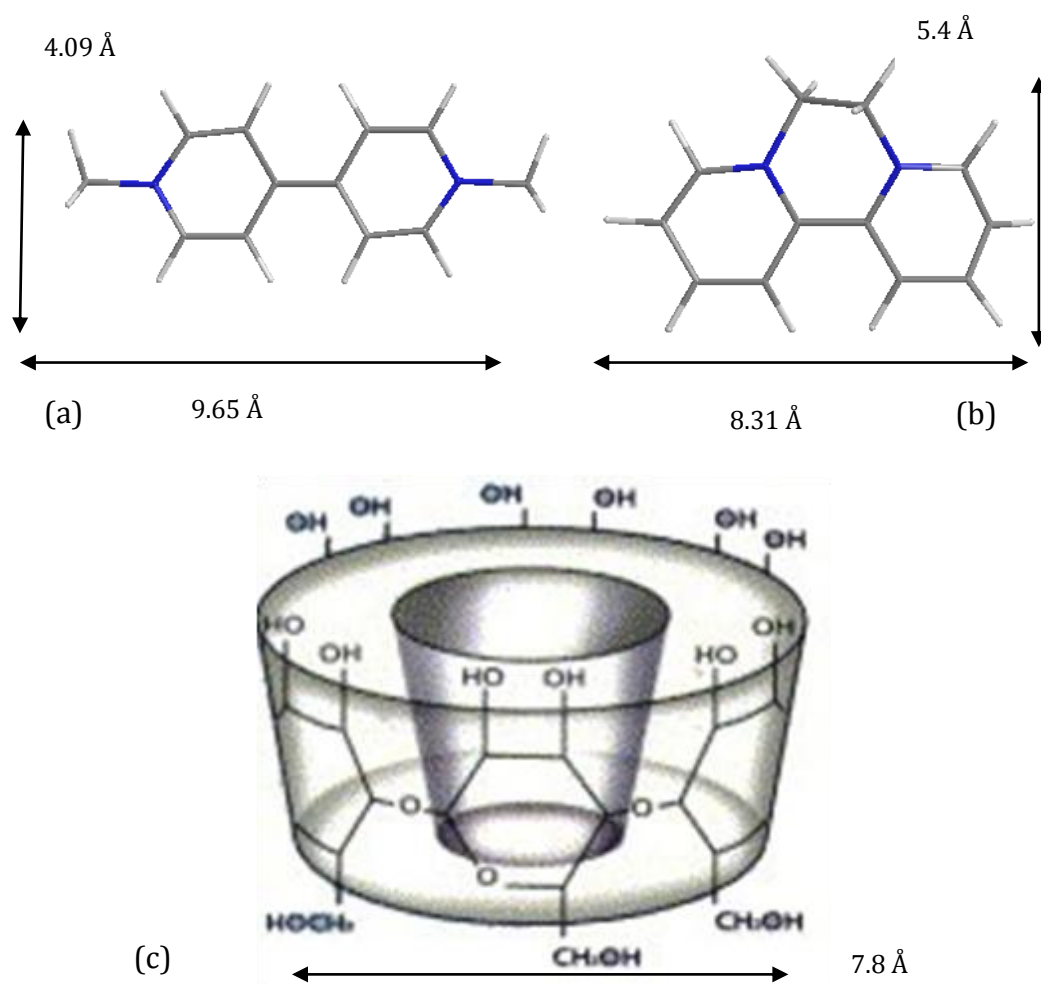


Figure 6.21: Chemical structures of (a) paraquat, (b) diquat and (c)  $\beta$ CD and their respective dimensions.

Higher association constants are computed for the diquat system. Again, diquat is charged and electrostatic interactions will exist between the anionic sulfonated groups and the charged diquat molecule. However, given the sites of positive charge on diquat, it is possible for diquat to form a partial inclusion complex while the positive sites are maintained outside the hydrophobic cavity. This would explain why the binding between the charged diquat and sul- $\beta$ CD is stronger than that between the charged paraquat and sul- $\beta$ CD, which is based on weak electrostatic interactions. Similar findings were reported by Wang *et al.*<sup>33</sup> on comparing the complexation of  $V^{2+}$  with sul-calix[4] and  $MV^{2+}$  with sul-calix[4]. They attributed the larger  $K_a$  values on the position of the nitrogen atom in the viologen, which exerts a certain influence on the stability of the complex.

### 6.7 Summary of Results

In summary, the results depicted in this chapter described the interactions of sul- $\beta$ CD with the charged and neutral species of paraquat and diquat, respectively. Interestingly, the interactions between both analytes and the charged cyclodextrin are quite different and certainly are much weaker than those with sul-calix[4], as discussed in Chapter 5.

The majority of this study focused on the complex of  $MV^{2+}$  and sul- $\beta$ CD. Electrochemical data recorded using CV and RDV displayed typical characteristics of complex formation with a reduction in the peak currents and a shift in the reduction potential. However, in contrast to the complexes formed with sul-calix[4], the changes in potential and current were not as large and also the excesses of sul- $\beta$ CD required to form the complex were much higher in contrast to the complexes with sul-calix[4]. The  $K_a$  values obtained from this analysis indicated the formation of a weak complex which was further verified from the information recorded using  $^1H$  NMR. The  $^1H$  NMR spectra showed that the maximum change in chemical shift was about 0.10 ppm for all protons of  $MV^{2+}$  on addition of an excess of sul- $\beta$ CD. This indicates a similar change in the environment of the methyl protons,  $H_c$  and the protons  $H_a$  and  $H_b$  is consistent

with a complex where the  $MV^{2+}$  and sul- $\beta$ CD are bound by electrostatic forces. There was no evidence for the formation of an inclusion complex between  $MV^{2+}$  or  $MV^+$  and the anionic sul- $\beta$ CD. The influence of pH on the interaction was also analysed in which no profound effect was recorded as similar  $K_a$  values were calculated at a pH of 4.0 and 6.0.

The interaction of the neutral species of paraquat,  $MV^0$  and  $\beta$ CD was then analysed using CV. The potential shifts were greater than those recorded for  $MV^{2+}$  or  $MV^+$  and sul- $\beta$ CD and it was concluded that an inclusion complex is indeed formed between  $MV^0$  and  $\beta$ CD. This is in good agreement with previous work by Matsue *et al.*<sup>3</sup>, in which it was documented the formation of an inclusion complex. However, no inclusion complex was formed between the charged  $MV^+$  or  $MV^{2+}$  and  $\beta$ CD. Furthermore, the inclusion of  $MV^0$  with sul- $\beta$ CD was of sufficient magnitude to prevent the oxidation of the adsorbed species,  $MV^0$  at the electrode surface which was clearly shown from the RDV data in Section 6.4.

Finally, a comparative study of the interaction of diquat with sul- $\beta$ CD was carried out to assess the variation, regarding the interaction, as structurally paraquat and diquat are very similar. The results showed the formation of a stronger complex and a much larger  $K_a$  value was calculated. The tabulated data shows greater shifts in peak potential for the reduction of  $V^{2+}$  to  $V^+$  and a larger decrease in peak current in contrast to that for the corresponding oxidation states of paraquat and sul- $\beta$ CD. Structurally, it is possible for both paraquat and diquat to include axially within sul- $\beta$ CD to form an inclusion complex. However, the relative positions of the positively charged nitrogen on each structure dictate whether an inclusion complex is formed. It is proposed that the complex formed between  $MV^{2+}$  or  $MV^+$  and sul- $\beta$ CD is electrostatic in nature, while a partial inclusion complex is formed between the charged diquat and sul- $\beta$ CD.

## 6.8 References

1. F. T. A. Chen, G. Shen, and R. A. Evangelista, *J. Chromatogr. A*, **924**, 523, (2001).
2. P. Sun, F. M. MacDonnell, and D. W. Armstrong, *Inorg. Chim. Acta*, **362**, 3073, (2009).
3. T. Matsue, T. Kato, U. Akiba, and T. Osa, *Chem. Lett.*, 1825, (1985).
4. A. Sayago, M. Boccio, and A. G. Asuero, *Int. J. Pharm.*, **295**, 29, (2005).
5. C. L. Bird and A. T. Kuhn, *Chem. Soc. Rev.*, **10**, 49, (1981).
6. L. Xiao, G. G. Wildgoose, and R. G. Compton, *New J. Chem.*, **32**, 1628, (2008).
7. P. M. S. Monk, C. Turner, and S. P. Akhtar, *Electrochim. Acta*, **44**, 4817, (1999).
8. D. De Souza and S. A. S. Machado, *Electroanalysis*, **18**, 862, (2006).
9. D. De Souza and S. A. S. Machado, *Anal. Chim. Acta*, **546**, 85, (2005).
10. M. Masson, J. F. Sigurjonsdottir, S. Jonsdottir, and T. Loftsson, *Drug Dev. Ind. Pharm.*, **29**, 107, (2003).
11. E. Bruneau, D. Lavabre, G. Levy, and J. C. Micheau, *J. Chem. Educ.*, **69**, 833, (1992).
12. W. Sun, K. Jiao, Y. Q. Ding, and C. Z. Zhao, *Can. J. Anal. Sci. Spectros.*, **52**, 57, (2007).
13. M. S. Ibrahim, I. S. Shehatta, and A. A. Al-Nayeli, *J. Pharm. Biomed. Anal.*, **28**, 217, (2002).
14. S. Mendoza, E. Castano, Y. Meas, L. A. Godinez, and A. E. Kaifer, *Electroanalysis*, **16**, 1469, (2004).
15. G.-C. Zhao, J.-J. Zhu, J.-J. Zhang, and H.-Y. Chen, *Anal. Chim. Acta*, **394**, 337, (1999).
16. S. E. Group, *Instrumental Methods in Electrochemistry*, Eilis Horwood Limited, 1985.
17. C. M. A. Brett and A. M. O. Brett, *Electrochemistry: Principles, Methods and Applications*, Oxford University Press, 1993.
18. J. Kostela, M. Elmgren, P. Hansson, and M. Almgren, *J. Electroanal. Chem.*, **536**, 97, (2002).
19. W. L. Sun, J. Xue, J. S. Chen, L. Q. Mao, L. T. Jin, K. Yamamoto, S. G. Tao, and J. Y. Jin, *Talanta*, **49**, 345, (1999).
20. R. Isnin, C. Salam, and A. E. Kaifer, *J. Org. Chem.*, **56**, 35, (1991).
21. L. Zhang, A. Macias, T. B. Lu, J. I. Gordon, G. W. Gokel, and A. E. Kaifer, *J. Chem. Soc., Chem. Commun.*, 1017, (1993).
22. E. Coutouli-Argyropoulou, A. Kelaidopoulou, C. Sideris, and G. Kokkinidis, *J. Electroanal. Chem.*, **477**, 130, (1999).
23. S. M. Ali, S. K. Upadhyay, and A. Maheshwari, *J. Inclusion Phenom. Macrocyclic Chem.*, **59**, 351, (2007).
24. I. Alfonso, M. I. Burguete, F. Galindo, S. V. Luis, and L. Vigara, *J. Org. Chem.*, **74**, 6130, (2009).
25. L. X. Song, P. Xu, H. M. Wang, and Y. Yang, *Nat. Prod. Res.*, **23**, 789, (2009).
26. R. S. Macomber, *Chem. Educ.*, **69**, 375, (1992).
27. A. Mirzoian and A. E. Kaifer, *Chemistry-a European Journal*, **3**, 1052, (1997).

28. H. Park, Y. Choi, S. Kang, S. Lee, C. Kwon, and S. Jung, *Carbohydr. Polym.*, 64, 85, (2006).
29. G. Astray, C. Gonzalez-Barreiro, J. C. Mejuto, R. Rial-Otero, and J. Simal-Gandara, *Food Hydrocolloids*, 23, 1631, (2009).
30. J. Szejtli, *Chem. Rev.*, 98, 1743, (1998).
31. J. J. Wang, G. J. Zheng, L. Yang, and W. R. Sun, *Analyst*, 126, 438, (2001).
32. A. Diaz, P. A. Quintela, J. M. Schuette, and A. E. Kaifer, *J. Phys. Chem.*, 92, 3537, (1988).
33. K. Wang, D. S. Guo, H. Q. Zhang, D. Li, X. L. Zheng, and Y. Liu, *J. Med. Chem.*, 52, 6402, (2009).

**Aging and Electro-regeneration of Carbon Membranes****7.1 Introduction**

The focus of this research has been the development and optimisation of environmental technologies. In Chapters 3-6, sensor development towards pollutants which exist primarily in aqueous based systems were analysed and discussed. Another aspect of this research was to study pollutants in gaseous systems. The most common hazardous gas is CO<sub>2</sub>. As previously mentioned in Chapter 1, Section 1.1, the influence of CO<sub>2</sub> on climate change has increased the demand for technologies to combat this pollutant. One such technology is membrane technology. Membranes have been used in a range of applications, but only since the 1980s have they been used in gas separation<sup>1</sup>. Thus, the focus of this chapter is to develop and optimise a membrane for the separation of CO<sub>2</sub> from N<sub>2</sub> gas. This is useful in the application of flue gas separation in which CO<sub>2</sub> is the main source of emission from power plants<sup>2,3</sup>. The results presented in this chapter were carried out during a five month visit to the Norwegian University of Science and Technology, Trondheim, Norway.

The preparation and gas testing methods of the carbon molecular sieve membranes (CMSMs) are outlined in Chapter 2, Section 2.8. Firstly, the membranes are characterised with respect to the material and pore size using scanning electron microscopy (SEM) and energy dispersive X-ray analysis (EDX). Then, the permeation of both CO<sub>2</sub> and N<sub>2</sub> gas and the selectivity of the hollow fibre carbon membranes towards each of these gases are assessed. A significant problem with carbon membranes and their productivity is, that over time permeation decreases due to aging of the membrane in which the predominant factor is the adsorption of O<sub>2</sub> on the membrane surface, blocking the pores necessary for permeation<sup>4-6</sup>. Hence, the results of an aging study are also presented to understand the influence of various air flow systems on the productivity of the membrane. Finally, a developed method to combat the

process of aging is investigated using electro-regeneration. Other methods of regeneration include, thermal, chemical and microwave<sup>7-9</sup>. However, electro-regeneration of membranes is a relatively new and promising technique. Previous research by Lie *et al.*<sup>10</sup> showed that the electro-regeneration of flat sheet carbon membranes can increase the permeability of CO<sub>2</sub>. Interestingly, when the flat-sheet membranes contain metal, such as Fe, Ni or Cu, there is increased conductivity of the membrane and hence the application of an electrical current has an enhanced effect in the process of regeneration. A similar principle was applied to the electro-regeneration of hollow fibre carbon membranes. Carbon membranes containing no additional compounds and those with a range of metal additives incorporated were tested and their permeability and selectivity values were compared. These results are presented in Section 7.5.

## 7.2 Characterisation of CMSMs

As discussed in Chapter 1, Section 1.6.4, the material properties of the membranes have a significant impact on their permeation and selectivity<sup>11</sup>. In general, the carbon membranes prepared throughout this research were hollow fibre asymmetric membranes with a dense selective outer layer and a porous inner layer. The materials used to prepare these hollow fibres were the polymers, cellulose acetate (CA) and poly-vinyl pyrrolidone (PVP), in a solvent, non-solvent mixture of N-methyl-pyrrolidone (NMP) and H<sub>2</sub>O. CA is a precursor of cellulose and is an environmentally acceptable renewable resource. It was the main component in the mixture used in hollow-fibre spinning. This was the technique used to prepare the hollow fibres by phase inversion. The presence of PVP in small quantities was sufficient to inhibit the formation of macrovoids. Macrovoids are large pores which jeopardise the mechanical integrity of a polymeric membrane support by acting as sites of increased local stress<sup>12</sup>. In essence, they compromise the permeability of particular gases, in that all gaseous molecules permeate through the large pores. Thus, there is a significant loss in selectivity as a result of the presence of macrovoids. Regarding the preparation of metal enhanced fibres, small amounts of metal nitrates were

added, including  $\text{Ni}(\text{NO}_3)_2$ ,  $\text{Fe}(\text{NO}_3)_3$  or  $\text{Cu}(\text{NO}_3)_2$ . Carbon nanotubes (CNTs) were also added, in which multiwalled CNTs were used to enhance the hollow fibres.

Following hollow fibre spinning, the fibres were further modified through deacetylation and carbonisation before arriving at the final product of graphene sheets, arranged to form a carbon hollow fibre membrane. They are arranged in a disordered manner to provide a pore size in the range of 3-5 Å. Hence, the mechanism of transport is molecular sieving. A schematic of the pore size and arrangement of the graphite sheets of the membrane is shown in Figure 7.1.

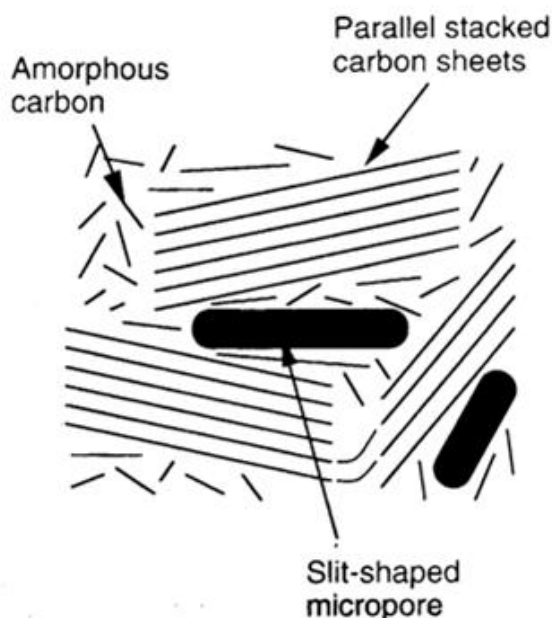


Figure 7.1: Micropore of a carbon molecular sieve membrane (CMSM)<sup>13</sup>.

The properties of the hollow fibres at the various stages of preparation were analysed using SEM. The changes in dimensions of the wall thicknesses and the porosity of the fibres were examined following hollow fibre spinning, deacetylation and carbonisation. The variations in the SEM micrographs provided a good indication of the loss of functional groups from the carbon precursor within the fibre. All SEM micrographs were recorded by Cathrine

Karlsen, at the Norwegian University of Science and Technology (NTNU), Trondheim, Norway.

Figure 7.2 (a) and (b), presents SEM micrographs of the cross sectional area of the fibre and of the middle section of the fibre wall, respectively. These fibres correspond to those prepared using hollow fibre spinning. It is clear from these SEM micrographs, the thickness of the fibre wall. As shown in more detail in Figure 7.2 (b) the middle section of the fibre wall combines a porous layer on the inner section and a dense selective layer on the outer section of the fibre. This is characteristic of an asymmetric membrane<sup>1</sup>. Following the synthesis of the hollow fibres, they were then de-acetylated to remove the functional acetate groups. De-acetylation causes shrinkage in length of the fibre wall ( $l_w$ ) as shown in Figure 7.3 (a) and also, a more compact fibre forms as depicted in Figure 7.3 (b). The wall now appears to have a dense layer as it becomes increasingly difficult to magnify the small pores, which are predominant on the inner layer of the membrane. The final pre-treatment step prior to module assembly and gas testing was carbonisation. There was a further decrease in the diameter of the fibre ( $d_0$ ) as tabulated in Table 7.1. Similarly, the structure becomes quite dense as all particles other than carbon are removed and the pore size has an average of between 3-5 Å. The compactness of the fibre is shown in Figure 7.4 (a). There is some evidence of the presence of pores on the inner wall, but the outer wall of the fibre is much denser and more compact as shown in Figure 7.4 (b).

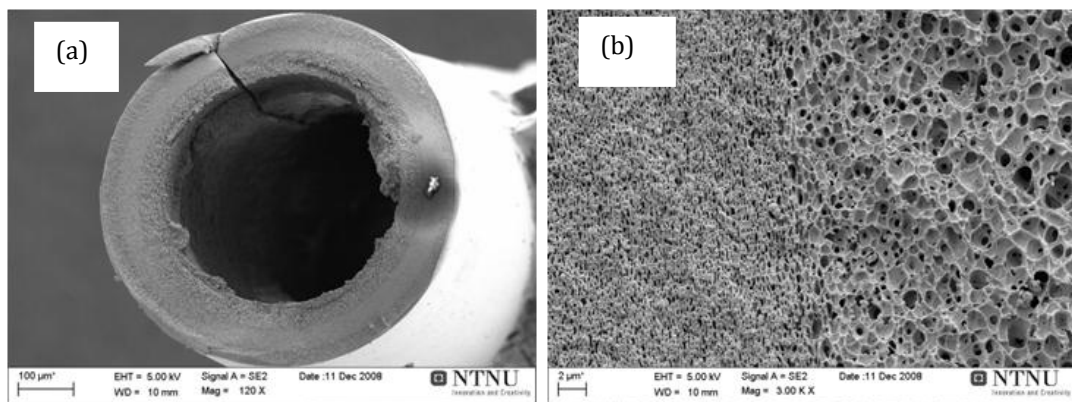


Figure 7.2: SEM micrographs of cellulose acetate (CA) fibre depicting (a) the cross sectional area of the fibre and (b) the cross sectional area of the middle section of the fibre.

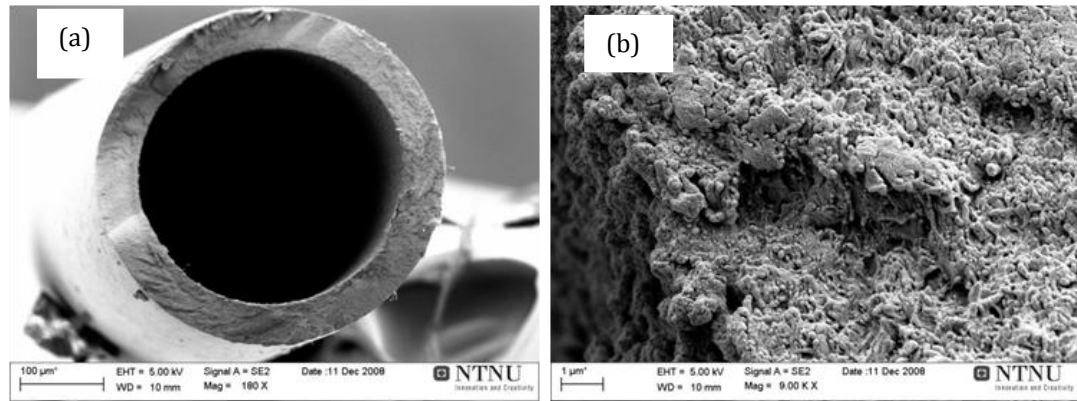


Figure 7.3 SEM images of de-acetylated (DCA) fibres showing (a) cross sectional of the fibre and (b) a magnification of the inner wall.

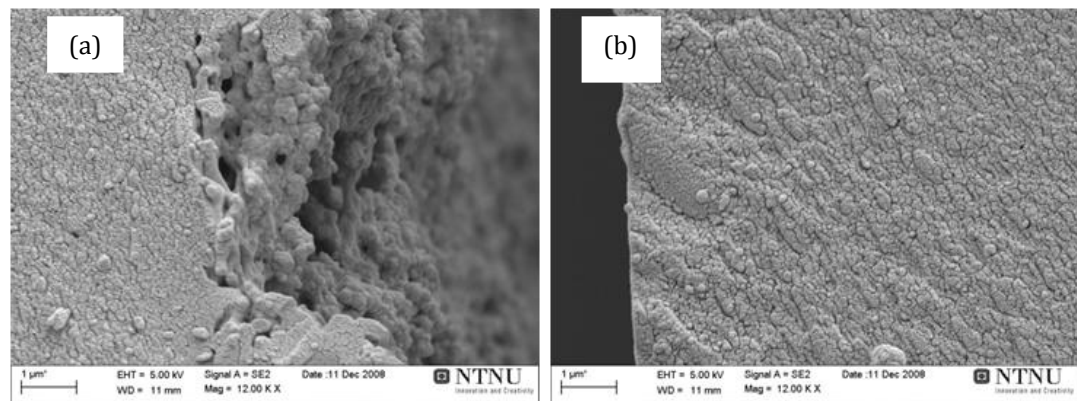


Figure 7.4: SEMs of carbon membrane following carbonisation illustrating (a) inner wall of the fibre and (b) outer wall of the fibre.

Table 7.1: Data outlining the decrease in length of the cell wall ( $l_w$ ) of the fibres and also the change in diameter ( $d_0$ ) of the entire cross sectional area of the fibres following the various treatment methods.

Fibre	$l_w / \mu\text{m}$	$d_0 / \mu\text{m}$
CA	120.0	712.5
DCA	50.0	407.0
Carbon	27.2	290.0

It is apparent from the various treatment methods that the fibres become more compact and there is shrinkage in diameter and length from synthesis to

carbonisation. However, the morphology of the porous inner layer and dense selective layer are maintained. Koresh *et al.*<sup>14-16</sup> reported similar findings upon carbonisation of cellulose membranes. EDX analysis was carried out to complement the micrographs recorded using SEM. Figure 7.5 illustrates the spectrum of a carbonised hollow fibre carbon membrane. As mentioned previously, carbonisation is the removal of functional groups associated with the polymeric material, in which the end product is disordered graphite sheets, similar to the orientation depicted in Figure 7.1. Thus, the X-ray signal of carbon which occurs at approximately 400 eV, as shown in Figure 7.5, indicates that carbon is the predominant element within the hollow fibre following carbonisation. Although, there is an X-ray signal for oxygen (O) this may be due to chemical adsorption of O<sub>2</sub> upon exposure of the membranes to the atmosphere. The definitive feature of this spectrum shows that all elemental traces aside from carbon are removed, which highlights the efficiency of the protocol used in the carbonisation of the deacetylated hollow fibre membranes.

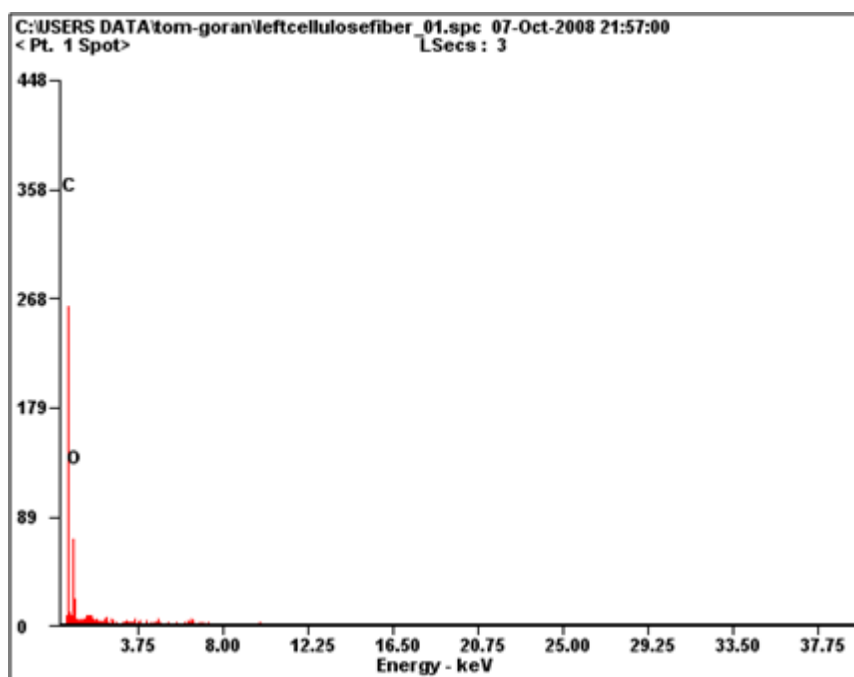


Figure 7.5: EDX spectrum of the CSM. The membrane was prepared in the following sequence, hollow fibre spinning, deacetylation and carbonisation.

The carbon membranes containing metals were characterised in a similar way according to their morphology using SEM and elemental analysis using EDX. From the SEM micrographs recorded of the fibres containing an added metal, a similar pattern emerged as for the CMSMs. Following each stage, which induced a further reduction of functional groups attached to the carbon precursor, there was a decrease in the wall thickness and the inner diameter of the bore of the membrane. Losses of 77% and 60% were recorded for the wall thickness and inner diameter of the fibre, respectively. These are almost identical to those losses for the CMSM shown in Table 7.1. As it is impossible to locate the metal within the membrane using SEM, as a result of the low concentration used in hollow fibre spinning, EDX was the only method of analysis to determine the presence of the metal within the membrane. As shown in Figure 7.6, EDX analysis of the CMSM containing  $\text{Fe}(\text{NO}_3)_3$ , illustrates the X-ray signals for C, O and Fe. The C signal is due to the carbon sheets of the membrane, the O signal is due to prior exposure of the membrane and possible adsorption of  $\text{O}_2$  and the X-ray signal for Fe, indeed suggests that the metal is incorporated within the membrane. Trace elements of Na appear within the spectra, which may be due to the NaOH solution used for deacetylation of the hollow fibres, which may not have been sufficiently removed upon rinsing the membranes prior to carbonisation. Fibres containing  $\text{Ni}(\text{NO}_3)_2$  were characterised in the same way. Although, quantitative information cannot be obtained using this method, it was a clear indication that the metal was incorporated within the membranes.

Modification of the carbon membranes with additives of either  $\text{Ni}(\text{NO}_3)_2$  or CNTs has a three-fold effect. Firstly, added compounds, e.g., PVP or nitrates that burn off during carbonisation leave a high micropore volume and can create a high capacity membrane. Thus, the pore size is expanded slightly to enhance permeability. These added compounds are referred to as porogens. Secondly, stable compounds within the membrane can enhance the transport rate of the gas through the membrane. As reported by Barsema *et al.*<sup>17</sup>, adding Ag-nanoclusters to a CMS membrane increases the selectivity of  $\text{O}_2$  over  $\text{N}_2$  by a factor of 1.6 compared to a non-functionalised CMS membrane prepared by the

same carbonisation method. Thirdly, adding metals to the precursor, i.e., cellulose acetate may increase the micropore volume of the resulting carbon and cause electronic interactions such as, surface diffusion with permeants like  $\text{CO}_2$ <sup>18</sup>. Also, as the  $\text{Ni}^{2+}$  and  $\text{Fe}^{3+}$  are added in the form of nitrates, the released  $\text{NO}_3^-$  during carbonisation can also be classified as a porogen.

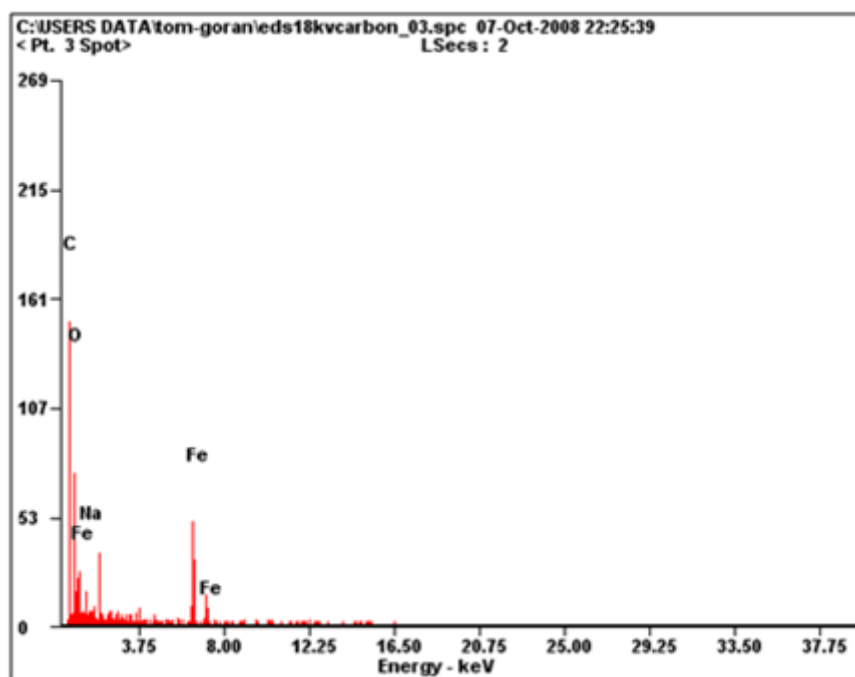


Figure 7.6: EDX analysis of a CMSM doped with  $\text{Fe}(\text{NO}_3)_3$ . This membrane was prepared by phase inversion using hollow fibre spinning. It was then deacetylated and carbonised to remove functional groups of the carbon precursor, i.e., cellulose acetate.

Upon establishing the morphology of the membranes, they were then assembled into a module and the membranes were tested using the methodology described in Chapter 2, Sections 2.8.2 and 2.8.3. As previously mentioned in Chapter 1, Section 1.6.6, single gas tests were employed throughout this study, in which the permeability of  $\text{N}_2$  and  $\text{CO}_2$  were measured separately. The permeability of each gas was then compared to obtain a measure of the selectivity of the membrane. The following section outlines the recorded results.

### 7.3 Permeation of CO<sub>2</sub> and N<sub>2</sub>

In general, the prepared carbon membranes showed an increased pressure flow for CO<sub>2</sub> over N<sub>2</sub> as a function of time. This indicated selectivity of the membrane for CO<sub>2</sub>. This is shown in Figure 7.7 (a) and (b) by the respective scale on the y-axis. The slope of each plot depicts a higher rate of diffusion of CO<sub>2</sub> in comparison to N<sub>2</sub> from the feed to the permeate side of the membrane, which is illustrated by the slope values in Table 7.2. To ensure an accurate measurement of pressure, a leak test was carried out. The difference in these pressure values of the carbon membrane in the presence of either CO<sub>2</sub> or N<sub>2</sub> were used to calculate the permeability of each gas towards the membrane. Then, from the ratios of the permeability values, the selectivity was calculated.

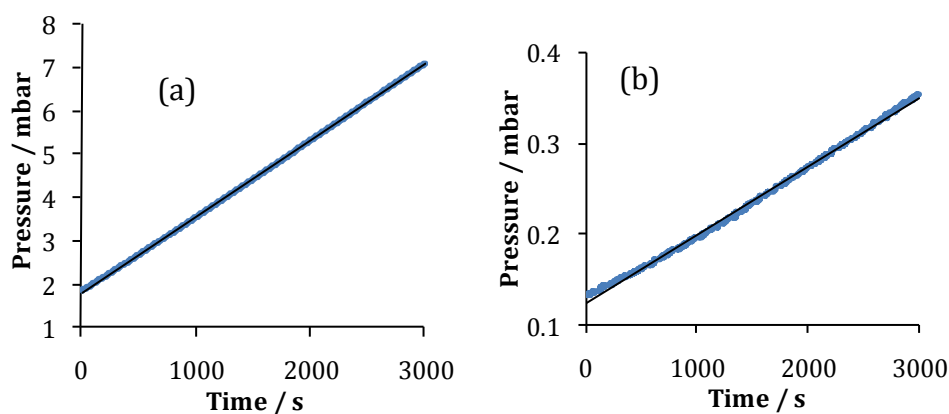


Figure 7.7: Plot of pressure as a function of time for (a) CO<sub>2</sub> gas and (b) N<sub>2</sub> gas diffusing through the carbon membrane.

Table 7.2: Pressure rates of CO<sub>2</sub> and N<sub>2</sub> through carbon membranes. These rates are obtained from the slope of pressure as a function of time, in which a linear relationship is obtained as illustrated by the correlation coefficient,  $R^2$ .

Gas	Slope / mbar s <sup>-1</sup>	$R^2$
CO <sub>2</sub>	$1.76 \times 10^{-3}$	0.999
N <sub>2</sub>	$7.00 \times 10^{-5}$	0.997

Selectivity is dependent on the pre-testing stages of hollow-fibre spinning, deacetylation and carbonisation, whereby the pore size is tailored for selective permeation of one gas over others. However, the type of gas test can also affect permeability. Mixed-gas tests which, measure the experimental selectivity of the membrane permeating a mixture of gases may not always compare identically to the calculated selectivity values from single-gas tests. This can happen as a result of adsorption of the slower permeating gas onto the membrane surface and within the pores. Hence, this can interfere with the permeation rate over time and have an impact on the selectivity. On the other hand, if the selective gas has a sufficiently higher rate of diffusion, this can prevent adsorption, as is the case for the studied gas pair of CO<sub>2</sub>/N<sub>2</sub>. Moreover, the selectivity evaluated from the single-gas test then resembles the probable values that would be recorded for mixed-gas tests. Also, this creates a more realistic situation for the potential use of membranes in industry.

In order to calculate the permeability of the membrane towards each gas separately, parameters of volume, area, pressure, temperature and length were considered. The permeability is calculated in accordance with Equation 7.1, whereby,  $P$  is the permeability of the membrane in Barrer,  $V$  is the volume of the chamber on the permeate side in cm<sup>3</sup>,  $l$  is the membrane thickness in cm,  $A$  is the effective area of the membrane in cm<sup>2</sup>,  $T$  is the operating temperature in K,  $p$  is the feed gas pressure in bar and  $dp/dt$  is the pressure rate at which the gas flows through the membrane, in mbar/min<sup>19</sup>. From quantifying the permeability of each gas, the selectivity of the membrane is then found by applying Equation 7.2, in which  $P_A$  and  $P_B$  are the permeability values of gas A and B, respectively<sup>19</sup>.

$$P = \frac{273.15 \times 10^{10} V l}{76 A T (p \times 75)} \left( \frac{dp}{dt} \times \frac{0.075}{60} \right) \quad (7.1)$$

$$\alpha_{A/B} = \frac{P_A}{P_B} \quad (7.2)$$

Table 7.3 illustrates the permeability and selectivity of hollow fibre carbon membranes prepared from cellulose acetate. As shown, the membranes display

selectivity towards the permeability of CO<sub>2</sub> by a factor of  $24.7 \pm 10.2$  over the permeability of N<sub>2</sub>. In regards to the literature, Park *et al.*<sup>20</sup> recorded a minimum permeability of 71 Barrer and selectivity ( $\alpha_{\text{CO}_2/\text{N}_2}$ ) of 71 using a carbon precursor of polyimide. In contrast, Hosseini *et al.*<sup>19</sup> documented the permeability of carbon membranes synthesised from matrimid at 7 Barrer and selectivity of 25 in favour of CO<sub>2</sub>. Thus, clearly the precursor, from which the carbon membranes are prepared from, is an influencing factor on the permeability and selectivity of the membrane towards CO<sub>2</sub>. Also, the protocol of carbonisation has a bearing on the transport properties and measure of permeability of the membrane<sup>14,19-24</sup>. This is clearly depicted by Lie *et al.*<sup>10</sup> in which, the final carbonisation temperature of the carbon membranes influences the permeability of a range of gases including, N<sub>2</sub>, H<sub>2</sub> and CO<sub>2</sub>. Thus, it is difficult to make a valid comparison on the permeability of similar membranes, as varying one parameter on the membrane synthesis has a significant impact on the membranes performance.

Table 7.3: Permeability and selectivity of the carbon membranes for CO<sub>2</sub> and N<sub>2</sub>. The membrane shows selectivity for the permeability of CO<sub>2</sub>.

Gas	Permeability / Barrer	Selectivity, $\alpha_{(\text{CO}_2 / \text{N}_2)}$
CO <sub>2</sub>	$24.43 \pm 9.85$	$24.7 \pm 10.2$
N <sub>2</sub>	$1.03 \pm 0.44$	-

In terms of selectivity a general trend is observed, in that CO<sub>2</sub> is selectively permeated over N<sub>2</sub>. This can be explained in terms of kinetic diameters of the gaseous molecules of CO<sub>2</sub> and N<sub>2</sub>, as shown in Figure 7.8 (a) and (b), which are 3.30 and 3.64 Å, respectively<sup>25,26</sup>. The kinetic diameter is a scale used to quantify the size of gaseous molecules<sup>27</sup>. Although CO<sub>2</sub> is a larger molecule than N<sub>2</sub>, the rationale for a smaller kinetic diameter was observed by Breck<sup>26</sup>, in which it was observed that CO<sub>2</sub> adsorbed on micro-porous zeolites, but N<sub>2</sub> did not. In general, a higher diffusion coefficient is associated with a smaller kinetic diameter<sup>1</sup>. Permeability can also be expressed in terms of diffusion coefficient and solubility constant. The proportional relationship between permeability

and diffusion is illustrated in Equation 7.3, in which  $P$  is the permeability coefficient in Barrer,  $D$  is the diffusion coefficient in  $\text{m}^2 \text{s}^{-1}$  and  $S$  is the solubility constant in  $\text{m}^3(\text{STP})/(\text{m}^3(\text{bar}))^{28,29}$ . This highlights the increased permeability of  $\text{CO}_2$  and hence selectivity towards  $\text{CO}_2$  permeation.

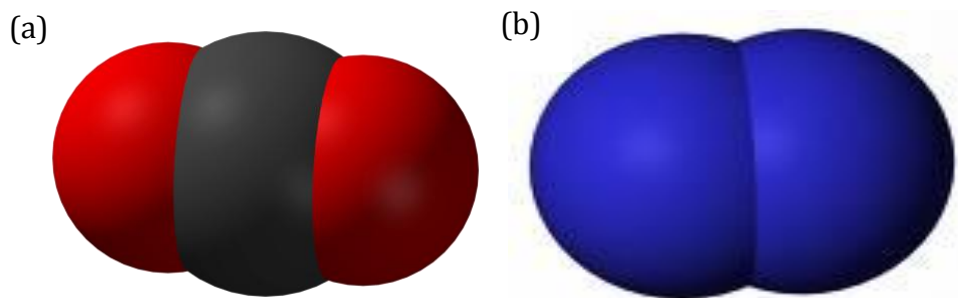


Figure 7.8: Space-fill illustrations of (a)  $\text{CO}_2$  and (b)  $\text{N}_2$ .

$$P = DS \quad (7.3)$$

It has been reported that for a membrane to be successful in gas separation as well as cost competitive, selectivity of  $\text{CO}_2/\text{N}_2$  should be in the range of 120<sup>30,31</sup>. Although, when the  $\text{CO}_2$  content is greater than 20% as in industrial processes, the selectivity decreases to approximately 60<sup>30</sup>. To date, there are no commercially available membranes achieving this criterion<sup>32</sup>. However, as previously mentioned, the chosen precursor and protocol as to which the membranes are synthesised has an impact on the permeability and in turn on the selectivity. Also, it should be noted at this stage, that the de-acetylated cellulose acetate (DCA) membranes tested above had previously been exposed to the atmosphere and hence a period of aging had occurred. Carbon molecular sieve membranes are sensitive to oxidation, humidity and blockage of the pore system and so the permeability can be affected by this process<sup>4-6</sup>. Furthermore, the aging process occurs primarily in the initial hours following carbonisation. If these aspects are addressed correctly, a higher selectivity may be obtained.

## 7.4 Influence of Aging on Carbon Membranes

As previously discussed in Chapter 1, Section 1.6.7, carbon membranes are susceptible to two types of aging, physical and chemical<sup>4</sup>. Physical aging or physical adsorption is the intermolecular interactions caused by the adsorption of water molecules from moisture in the atmosphere<sup>33</sup>. Chemical adsorption on the other hand, is the formation of chemical C-O bonds, which are significantly stronger than Van der Waals forces or hydrogen bonds of physically adsorbed H<sub>2</sub>O on the membrane<sup>33,34</sup>. It has been suggested that physical aging enhances the adsorption of further molecules. The majority of adsorption occurs at edge sites of the membrane as these are more reactive than the interior graphene sheets<sup>35,36</sup>. This explains the decline in the permeability of the membrane over time, as generally the gas is fed into the membrane using an outside-in flow pattern, as opposed to through the bore of hollow fibre, which is known as the inside-out flow pattern. This section investigates the most influential conditions which promote aging and the most critical time period for aging depending on the environment the membrane is exposed to.

### 7.4.1 Dynamic Study

As previously described in Chapter 2, Section 2.8.5.1, two identical modules (1 and 2) were prepared and tested using a dynamic flow of air. The means as to which the air was transported from the module to the membrane was done using an inside-out pattern. This pattern is where the flow of air enters on the inside of the fibre, i.e., through the bore. This induces a better mass transfer along the membrane compared with the outside-in flow, whereby air enters from the outside of the fibre. Although, applying this flow pattern at high pressures can cause the membrane to rupture, the feed pressure used in this study was only slightly above 1 atmosphere. However, the most common flow pattern is the outside-in flow, which consequently was used for all other permeability tests concerning CO<sub>2</sub> or N<sub>2</sub>. Permeability tests were carried out on each module separately and were recorded at different time intervals. Each test was carried out over a short period of time until linearity was established. This ensured that the aging process continued with a constant flow of air through the

system. As depicted from the graph in Figure 7.9, there is only a slight change in permeability over a time period of 795 hours or 34 days. The slight changes between each module is attributed to the variation in fibre diameter and hence wall thickness, as slight variations in the pre-treatment stages can result in variations of the membranes permeability. It is evident that there is no decrease in permeability, indicating that this dynamic source of air has an inhibitory effect on aging. Following, approximately 100 hours of aging, there is an increase in permeability and after 200 hours of aging, there is a stabilization period, in which the permeability remains within a range of 50-60 Barrer.

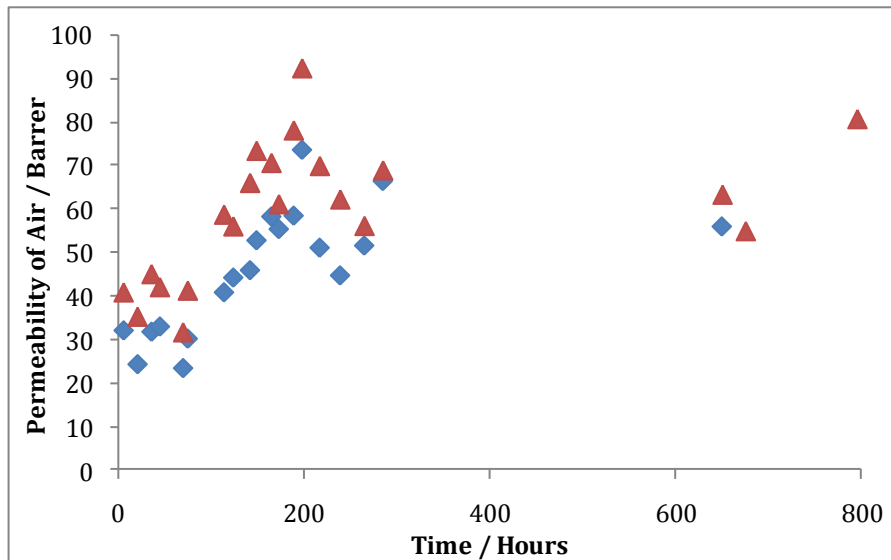


Figure 7.9: Data of the permeability values for air as a function of time. Two similar modules were tested to ensure validity of the study, and labelled module 1 (♦) and module 2 (▲). Two hollow fibre carbon membranes were placed in each module measuring approximately 15 cm in length.

No selectivity values were evaluated for these membranes, since no other gases were tested. Useful information that can be obtained from this study is a calculation of the flow rate in accordance with the Reynolds number ( $R_e$ ). Using this information, the pressure drop can also be calculated due to a change in thickness of the boundary layer<sup>1</sup>. Prior to evaluating the Reynolds number, the velocity of air flow through the membranes was determined. This was done by measuring the volume velocity, in which the time was recorded for the air to fill

a volume of 9 cm<sup>3</sup>. This procedure was repeated a number of times and the average volume velocities for each module are depicted in Table 7.4. These values were used to quantify the velocity in accordance with Equation 7.4, in which  $dV/dt$  is the volume velocity in m<sup>3</sup> s<sup>-1</sup> and  $A$  is the area of the space where the gas flows through the hollow fibre in m<sup>2</sup>. A velocity of 34.54 and 36.06 m s<sup>-1</sup> were calculated for Module 1 and 2, respectively. The velocity was then used to calculate the Reynolds number. The Reynolds number ( $R_e$ ) was calculated using Equation 7.5<sup>37</sup>, in which,  $d_i$  is the inner diameter of the hollow fibre in m,  $v$  is the velocity of the air flow in m s<sup>-1</sup>,  $\rho_{\text{air}}$  is the density of air, 1.184 kg m<sup>-3</sup> and  $\mu_{\text{air}}$  is the viscosity of air,  $1.98 \times 10^{-5}$  Pa s<sup>-1</sup>. Given the similarity in velocity and inner diameters of both modules the Reynolds number of 423 and 442 were evaluated for Module 1 and 2, respectively. The Reynolds numbers are useful in discriminating between laminar and turbulent flow. When the Reynolds number is below 2,000, the flow is classed as laminar and above this denotes a turbulent flow system<sup>1</sup>. A laminar flow is when the streamlines remain distinct from one another over the entire length of the surface<sup>38,39</sup>. Turbulent flow, on the other hand is when eddies produced in the initial zone of instability spread rapidly throughout the medium, producing a disruption to the entire flow pattern<sup>38,39</sup>. This laminar flow protects the membrane from damage, as disruption of the flow pattern within quite a small surface area, can rupture the membrane. Also, from this laminar flow rate, it is assumed that the permeate flow is less than the feed flow.

Table 7.4: Average values obtained from a gas bubble flow-meter, in which the time was measure to fill a volume of 9 cm<sup>3</sup>, from which the volume velocity was calculated.

Volume Velocity / m <sup>3</sup> s <sup>-1</sup>	
Module 1	Module 2
$1.14 \times 10^{-6} \pm 1.99 \times 10^{-8}$	$1.19 \times 10^{-6} \pm 1.56 \times 10^{-8}$

$$v = \frac{\dot{v}}{A} = \frac{dV/dt}{\pi d_i^2/4} \quad (7.4)$$

$$R_e = \frac{d_i v \rho_{air}}{\mu_{air}} \quad (7.5)$$

The pressure at the feed end including the pressure loss was estimated and compared to that of the experimental feed pressure applied to assess the pressure loss due to aging. Three different types of pressure are considered when evaluating the estimated feed pressure. They are, the pressure loss due to sudden contraction, i.e., the flow going from the inlet tube to the entrance of the membrane. Secondly, the friction losses within the membrane due to the gas flow through the fibre. Thirdly, the loss due to the expansion from the permeate side to the atmosphere. The estimated feed pressure at the feed side was calculated using a Fanning-type expression as shown in Equation 7.6, 7.8 and 7.9<sup>40</sup>. Equation 7.6 pertains to the pressure across the membrane, whereby,  $f$  is a friction factor as defined in Equation 7.7<sup>40</sup>, which is valid for laminar flow only.  $G$  is the product of the velocity and density of air in  $\text{kg m}^{-2} \text{s}^{-1}$ ,  $d_i$  is the internal diameter of the membrane in m and  $M$  is the weight of the gas flowing inside the membrane in  $\text{g mol}^{-1}$ . Equation 7.8 and 7.9 correspond to the evaluation of the pressures at the permeate and feed sides, respectively. The quantification of these pressure values considers the loss due to expansion and contraction as the gas exits and enters the membrane. In these equations,  $A_1$  is the cross sectional area of the membrane in  $\text{m}^2$ ,  $A_2$  is the cross sectional area of the tubing housing the membrane in  $\text{m}^2$ ,  $G$  is the product of velocity and density in air in  $\text{kg m}^{-2} \text{s}^{-1}$  and  $a$  is a constant of 0.55 for laminar flow.

$$\Delta p_f^2 = \frac{4f\Delta L G^2}{d_i M} \quad (7.6)$$

$$f = \frac{16}{R_e} \quad (7.7)$$

$$\Delta p_{ex} = \left(1 - \frac{A_1}{A_2}\right)^2 \frac{G^2}{2a} \quad (7.8)$$

$$\Delta p_c = 0.55 \left(1 - \frac{A_1}{A_2}\right)^2 \frac{G^2}{2a} \quad (7.9)$$

The quantified pressure values at various points of the membrane in accordance with Equation 7.6, 7.8 and 7.9 are correlated to give  $\Delta p^2$  in Pa<sup>2</sup>, as shown in Table 7.5. From the data shown in Table 7.5, it is evident that the estimated feed pressures,  $p_{\text{est}}$ , of  $1.35 \times 10^5$  and  $1.38 \times 10^5$  Pa are within close range of the experimental feed pressures,  $p_{\text{exp}}$ , of  $1.40 \times 10^5$  Pa for module 1 and 2, respectively. This indicates that the flow rate is maintained and the accumulation of a boundary layer due to adsorption of molecules such as O<sub>2</sub> present in the air flow is minimised. Hence, aging of the membrane is reduced using this type of flow system.

Table 7.5: Data correlating the pressures at various sections of the membrane. These values have been used to estimate the feed pressure,  $p_{\text{est}}$  and compared with the experimental feed pressure,  $p_{\text{exp}}$ .

Module	$f$	$G /$ $\text{kg m}^{-2} \text{s}^{-1}$	$\Delta p^2 / \text{Pa}^2$	$\Delta p / \text{Pa}$	$p_{\text{est}} / \text{Pa}$	$p_{\text{exp}} / \text{Pa}$
1	0.0756	20.8	$8.35 \times 10^9$	$9.14 \times 10^4$	$1.35 \times 10^5$	$1.40 \times 10^4$
2	0.0724	21.8	$9.16 \times 10^9$	$9.57 \times 10^4$	$1.38 \times 10^5$	$1.40 \times 10^4$

#### 7.4.2 Intermediate Study

Following a period of 28 days, permeation tests were concluded on Module 1 as a function of dynamic aging. The pump was then disconnected from the module at the feed end and it was exposed to the atmosphere, undergoing a period of static aging. A vacuum still remained on the permeate side of the module, to prevent the adsorption of air on the remainder of the gas unit. Thus, this combination of dynamic and static aging was termed intermediate aging.

As shown in Figure 7.10, there was no significant change in permeability over a 6 day period following a 28 day period of dynamic aging. This is also illustrated in Table 7.6, in which the permeability values were corrected for the variation in temperature, as the fibres were not thermostatted. The temperature was then monitored and recorded in accordance with the room temperature at the time of each experiment. From the tabulated results in Table 7.6, it is clear that the

dynamic atmosphere had an inhibitory effect on the aging process. In order to confirm this, another aging study was carried out in which other membranes prepared from the same batch were exposed to the lab atmosphere and the permeability was recorded over a 30 day period. Hence, the membranes were exposed to a static atmosphere and not a dynamic or intermediate air flow, to which the results are presented in the following section.

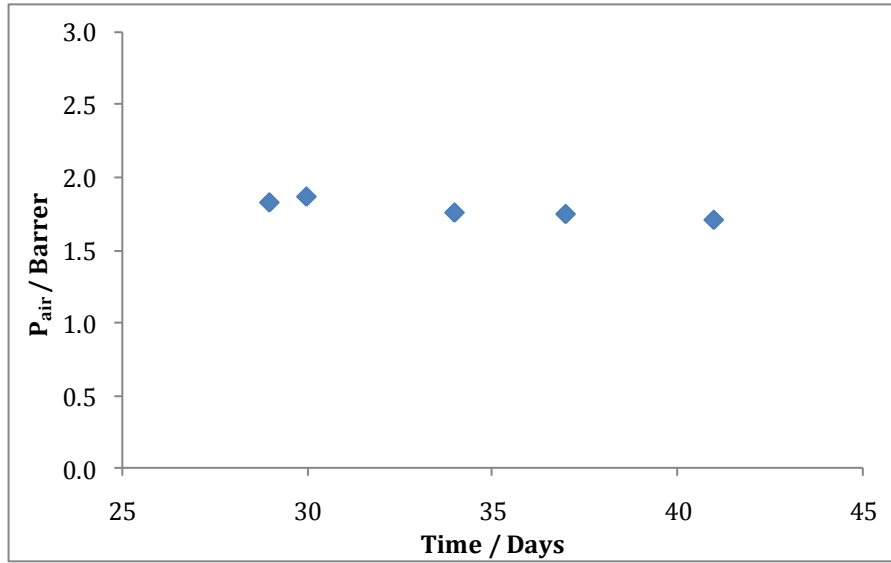


Figure 7.10: Permeability values of air as a function of time for Module 1 containing carbon membranes previously used in the dynamic aging study.

Table 7.6: Data recorded from the permeance values of the intermediate aging study

Day	Time / hr	$P_h / \text{Pa}$	$(dP/dt) / (\text{Pa/s})$	$P_{\text{air},T_{\text{corr}}} / \text{Barrer}$
29	675	$1 \times 10^5$	$6.86 \times 10^{-3}$	1.83
30	699	$1 \times 10^5$	$7.04 \times 10^{-3}$	1.87
34	795	$1 \times 10^5$	$6.61 \times 10^{-3}$	1.76
37	867	$1 \times 10^5$	$6.58 \times 10^{-3}$	1.75
41	963	$1 \times 10^5$	$6.46 \times 10^{-3}$	1.71

### 7.4.3 Static Study

The procedure for this experiment is outlined in Chapter 2, Section 2.7.8.2. The difficulty in carrying out any type of aging experiment is that the membranes

cannot be tested immediately after carbonisation, as the time required to prepare the modules is a minimum of 6 hours. The epoxy resin requires this duration of time to set, otherwise placing the module directly in the gas testing unit under vacuum, would cause distortion of the epoxy resin, break the seal and hence the gas would permeate through the fibres as well as the module resulting in an inaccurate evaluation of permeability.

Figure 7.11 illustrates the data recorded for the static aging experiment. The first permeation test was not carried out until 9 days of aging had occurred. It has been reported by Menendez *et al.*<sup>33</sup> that the permeability values of carbon membranes drops by nearly 50% after 1 day due to aging and following a certain period of time, the aging process is saturated and the permeability remains constant. Hence, this particular type of aging study investigated the saturation point. Also, in order for this to be a viable application for industrial use, membranes in which the permeability varies due to the process of aging, is not a potential option for large-scale use. Thus, following module assembly, mounting the module into the gas permeation unit and allowing time for a short evacuation period, the fibres had undergone a significant period of aging. The fibres used to prepare this module, Module 3, were prepared from the same batch as those used in Module 1 and 2, and so had similar properties. As depicted Figure 7.11, the fibres underwent a further period of aging between day 10 and day 28. However, from day 28 to day 41, the permeability remained constant. This is also illustrated in Table 7.7, with the pressure rate values and the permeability data calculated according to the corrected temperature. The relatively small fluctuation in permeability from day 28 to 41 indicates that the largest effect of aging had occurred and the permeability was relatively stable for this membrane after day 28.

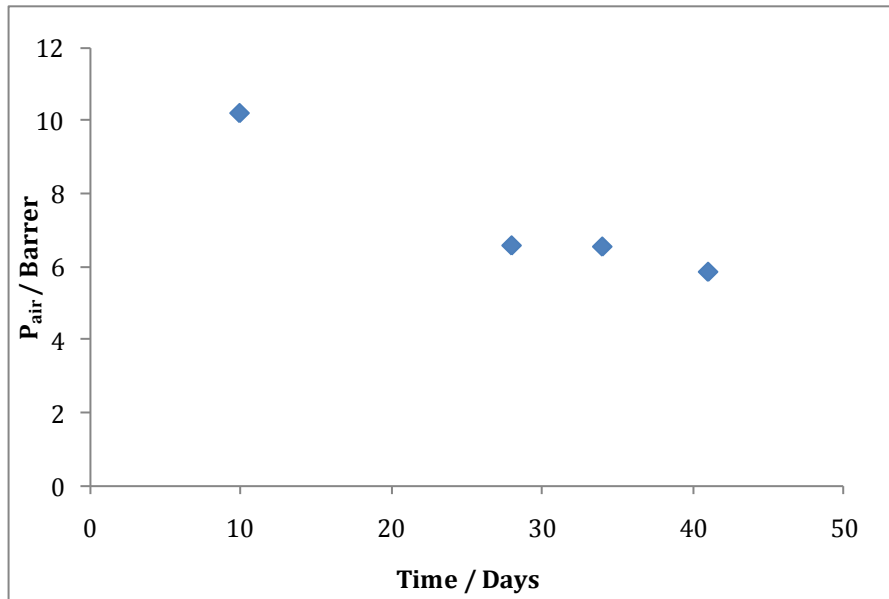


Figure 7.11: Permeability data plotted as a function of time, for the static aging study.

Table 7.7: Pressure rates at the corresponding days of aging, recorded for the static aging study.

Time / Day	$P_h / \text{Pa}$	$dP/dt / \text{Pa s}^{-1}$	$P_{\text{air}, T_{\text{corr}}}$
10	$1 \times 10^{-5}$	$3.83 \times 10^{-2}$	10.20
28	$1 \times 10^{-5}$	$2.46 \times 10^{-2}$	6.57
34	$1 \times 10^{-5}$	$2.45 \times 10^{-2}$	6.54
41	$1 \times 10^{-5}$	$2.19 \times 10^{-2}$	5.84

Analysis of the changes in permeability from day 28 to day 41 appears quite similar for the membranes exposed to intermediate aging and static aging. However, the average decrease in permeability for the module exposed to a static environment was  $-5.73 \times 10^{-2}$  Barrer / day, whereas the average decrease for the membranes exposed to the intermediate aging is  $-1.21 \times 10^{-2}$  Barrer / day. This decrease in permeability due to intermediate or static aging was determined from the slope of the plots of permeability as a function of time, shown in Figure 7.10 and 7.11, respectively. From these data, it is clear that the membranes exposed to static environment are aging at a rate approximately 5 times faster than those previously exposed to a dynamic air supply and then to a static environment. Hence, this confirms the positive effect that a dynamic air

source has on slowing down the aging process. However, as mentioned previously, in order for this to be a viable process for industry, the process of aging should be kept to a minimum. Although, a dynamic air flow has this effect, financially, this is not a feasible option. Another method used to reduce aging, is regeneration. The following section discusses the results recorded for the electro-regeneration of various types of carbon membranes.

### **7.5 Electro-regeneration of Carbon Membranes**

As previously discussed in Chapter 1, Section 1.6.8, there are a range of regeneration techniques from thermal, chemical to electrochemical<sup>7-10,33</sup>. These techniques partially restore the permeability to those values of an un-aged membrane. One example is the use of thermal regeneration which requires heat treatments of 600-800 °C. Although, applying these high temperatures can change the microporosity of the membrane. The energy required to heat the membranes to this temperature creates an additional cost in the production of the membranes<sup>7</sup>. However, as reported by Lie *et al.*<sup>10</sup> the use of electricity for the regeneration of flat sheet carbon membranes, proved a more economical method to use. A relatively low voltage supplied directly to a flat sheet carbon membrane containing metal caused an instant increase in permeability, while the membrane remained stable.

The preliminary gas tests carried out and discussed in Section 7.3 illustrated a selectivity of the carbon membranes for CO<sub>2</sub> over N<sub>2</sub>. With a selectivity of  $24.7 \pm 10.2$  and a permeability of  $24.43 \pm 9.85$  Barrer for CO<sub>2</sub>, the importance of electro-regeneration was to minimise the effect of aging on the membranes, which has a significant effect on the permeability of gases over time. Considering the gas pair, CO<sub>2</sub>/N<sub>2</sub>, a larger effect has been recorded on the decreased permeability of N<sub>2</sub> due to aging, which causes the selectivity to increase slightly<sup>4</sup>. The importance for flue gas removal was to maintain a constant permeability of CO<sub>2</sub>, thus maintaining the performance of the membrane. This inexpensive method of electro-regeneration which can be carried out during gas testing was applied to carbon hollow fibre membranes

and carbon membranes containing either  $\text{Ni}(\text{NO}_3)_2$  or CNTs. The direct method of applying current similar to that applied to flat sheet carbon membranes was not possible hence initial tests were required to establish the most productive method in applying this current. This was done by applying the current to the module in 3 different ways. As described in Chapter 2, Section 2.8.1, three types of modules were prepared. They were module A, B and C. The material used in the construction of these modules was different for each and hence the application of current to the module varied. For module A, the materials used to encase the membranes were, steel housing and epoxy resin. Module B was assembled with steel housing and conducting epoxy resin. Finally, for module C, insulating material and conducting epoxy resin was used in constructing the module.

### **7.5.1 Electro-regeneration of CMSMs**

For these preliminary studies, gas tests were carried out as single gas tests on the carbon molecular sieve membranes, containing no  $\text{Ni}(\text{NO}_3)_2$  or CNTs. Following a stabilisation period in which the pressure flow was constant, a potential of 5 V was applied to the module. Given, the high resistance of carbon, the currents recorded were in the range of  $\mu\text{A}$ . The potential was applied for approximately 1 hour and was then switched off and the experiment continued for approximately another hour. This protocol was followed for both the  $\text{N}_2$  and  $\text{CO}_2$  test, in which the permeability was calculated, before, during and after the potential was applied.

The results depicted in Table 7.8 correspond to the calculated permeability values from the electro-regeneration studies carried out using carbon membranes. It is evident from the recorded values that the application of a potential has an influence on the permeability. It has been documented that the application of an electrical current supplies sufficient energy to remove adsorbed species from the membrane<sup>41</sup>. The notable difference between the tests was the module material encasing the fibres. In the first incidence, for module A, the applied potential acted on the housing material of the module,

there was essentially an electric field surrounding the fibres. There was a 9.8% increase in N<sub>2</sub> permeation and a 7.3% increase in permeation of CO<sub>2</sub>. More importantly, the contribution of current induced a sustained rate in permeation even when the potential was no longer applied. The second scenario was when both the fibres and the housing surrounding the membranes were conducting due to the application of current (module B). Similar to the results recorded for module A there was an increase in the permeability which was sustained. For N<sub>2</sub> permeability, there was a 7.4 % increase and for CO<sub>2</sub>, there was a slight decrease of 7.1%. The third type of module tested, module C, was one in which the potential was applied to the fibres only. As depicted in Table 7.8, there was an increase of 23.6% in N<sub>2</sub> permeation and a 9.1% increase in CO<sub>2</sub> permeation.

Table 7.8: Permeability values measured in Barrer for the N<sub>2</sub> and CO<sub>2</sub> gas permeation tests carried out using three types of module. The permeability is tabulated for three points of the experiment; before applying a 5 V potential, during the potential being applied and after.

Type of Module	Gas Test	Permeability/ Barrer	Permeability (applied potential) / Barrer	Permeability (after applied potential) / Barrer	Selectivity after 5 V / $\alpha_{(CO_2/N_2)}$
A	N <sub>2</sub>	1.10	1.22	1.22	25.4
	CO <sub>2</sub>	28.74	31.00	31.00	
B	N <sub>2</sub>	1.00	1.08	1.09	24.4
	CO <sub>2</sub>	28.64	27.62	26.60	
C	N <sub>2</sub>	1.20	1.46	1.57	11.0
	CO <sub>2</sub>	15.68	17.25	17.41	

It is evident that when the current is applied to the fibres only, in module C, this has the optimum effect on increasing the N<sub>2</sub> and CO<sub>2</sub> permeability. It can be generalised that, the influence of a potential of 5 V has a positive effect on the permeation of both N<sub>2</sub> and CO<sub>2</sub>, for all types of modules. However, this increase in permeability did not enhance selectivity. As discussed in Chapter 1, Section 1.6.6, the ideal membrane combines permeability and selectivity<sup>30</sup>. As the

parameters influencing electro-regeneration are quite vast, to design the optimum protocol for the combined enhancement of permeability and selectivity is challenging. It was proposed that applying a potential during evacuation and for a certain period during the CO<sub>2</sub> gas test, were the optimum conditions for enhancing permeability. The concept of applying the potential during evacuation provided an added advantage. Given the high vacuums that are acquired between gas tests, it is probable that the low pressure can successfully remove adsorbed molecules. In the presence of an applied potential, it has the ability to improve desorption of gaseous molecules from the membrane surface, thereby reducing the effect of aging.

For the modified membranes the module assembly involved plastic housing and conducting epoxy resin, identical to the construction used for module C. The modified carbon membranes with added Ni(NO<sub>3</sub>)<sub>2</sub> or CNTs were tested as a function of CO<sub>2</sub> permeability. A potential of 5 V was applied during the gas test and the change in permeability was calculated before and after the application of potential. These results are depicted in Table 7.9, which shows clearly a slight decrease in permeability for the fibres with Ni(NO<sub>3</sub>)<sub>2</sub> added. Interestingly, the CMSM doped with CNTs showed an increase of 17.29 % upon application of 5 V. Also, these membranes showed the optimum permeability and selectivity for CO<sub>2</sub>, which is depicted on the Robeson plot, in Figure 7.12.

Table 7.9: Data corresponding to the permeability of CO<sub>2</sub> through the modified carbon membranes. The permeability of the gas before and after a potential of 5 V is applied is listed.

Modified CMSM	Permeability CO <sub>2</sub> before 5 V / Barrer	Permeability CO <sub>2</sub> after 5 V / Barrer	% Change
Ni(NO <sub>3</sub> ) <sub>2</sub>	59.05	57.70	2.20 % ↓
CNTs	59.70	72.18	17.29% ↑

The Robeson upper bound relates the permeability and selectivity of particular gas pairs. It is well recognised that permeability and selectivity are trade-off parameters, to which a decrease in separation factor generally leads to an

increase in the more permeable gas component<sup>42</sup>. In 2008, Robeson<sup>43</sup> published on the upper bound, in which the relationship of permeability and selectivity is governed by Equation 7.10<sup>43</sup>. In this equation,  $P_i$  is the permeability of the more permeable gas,  $\alpha$  is the separation factor and  $n$  is the slope of the log-log limit. In this article, the slope for the gas pair of CO<sub>2</sub>/N<sub>2</sub> is given and values that are above this slope, as depicted by the upper bound line are referred to as successful membranes in maintaining selectivity and permeability. The upper bound for a large range of gas pairs is also given in this publication. These limits were calculated from permeability values of a sample containing a large variety of polymeric membranes (approximately 300) prepared from different precursors.

$$P_i = k\alpha_{ij}^n \quad (7.10)$$

In comparing the modified CMSMs with the unmodified CMSMs, it is clear that an applied potential has a positive effect on the permeability of CO<sub>2</sub>. Given, the novelty of this technique, the process of electro-regeneration is still unclear. There are a few publications in the literature describing the effects of an applied potential, but the effects are poorly understood. Huotari *et al.*<sup>44</sup> employed hollow carbon fibres for the separation of oily wastewater. The flux increased about 4.5 times with an electric field applied. Also, Visvanathan and Benaim<sup>45</sup> carried out a study on minimising the accumulation of particles and colloids on the membrane surface with a cross-flow electrofiltration technique. They found this to be a better method in reducing membrane fouling by using charged colloids and particles.

In general, an increased rate of permeation can prevent the adsorption of molecules on the membrane surface. In the case of electro-regeneration, ohmic heating may be the predominant effect in increasing the desorption rate. As the energy supplied to the fibre through current generates heat and hence there should be an increase in the permeability. The application of current can also generate a magnetic field, which may cause orientation of the diffusing polar

molecules and lessen the degree of rotation. Similarly, this can lead to increased permeability. Increased permeability can lead to a decrease in selectivity, as previously discussed in regards the upper bound relationship. However, the affinity of CO<sub>2</sub> for selectively permeating the membrane over N<sub>2</sub> and the polarity of CO<sub>2</sub> can have an increased effect on the selectivity.

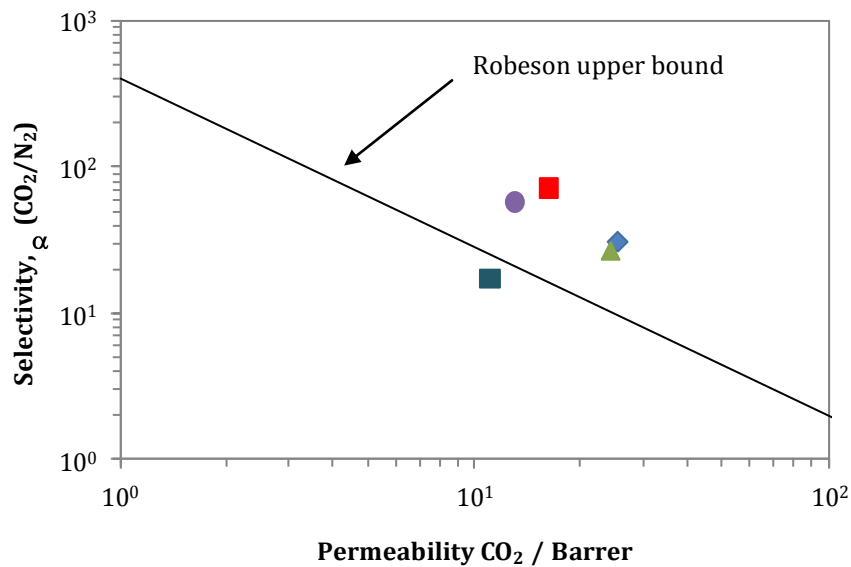


Figure 7.12: A log-log plot of the selectivity of the CMSMs as a function of permeability. The following modified carbon membranes were tested for electroregeneration; (●) CMSM/Ni<sup>2+</sup> and (■) CMSM/CNT. The following correspond to module (◆) A, (▲) B and (■) C, in which electro-regeneration was carried out during the gas permeation tests. The equation of the line corresponds to the Robeson upper bound for CO<sub>2</sub>/N<sub>2</sub> pair.

## 7.6 Summary of Results

In summary, the results presented in this chapter gave a brief description of the development of an environmental technology for the selective permeation of CO<sub>2</sub> over N<sub>2</sub>, using CMSMs. The formation of the carbon molecular sieve membranes (CMSMs) were tailored towards the kinetic diameter of CO<sub>2</sub>, thereby enhancing its permeation. The SEM micrographs provided information regarding the characterisation of CMSMs following each stage of treatment. A significant decrease in wall thickness and in length was observed after hollow

fibre spinning, de-acetylation and carbonisation. This loss was due to the removal of the functional groups from the carbon precursor, in which a final membrane of disordered graphene sheets was used in the permeation tests. For the modified fibres, characterisation of the presence of the metal was done using EDX analysis. As shown in Figure 7.6, the X-ray signal of Fe was evident with signals of C and traces of O and Na, for the fibres containing  $\text{Fe}(\text{NO}_3)_3$ . The presence of the latter atoms is most likely as a result of exposure to the atmosphere and insufficient rinsing of the fibres following deacetylation.

The selective permeation of CMSMs for  $\text{CO}_2$  was evaluated at  $24.71 \pm 10.21$ . This was slightly lower than the reported selectivity values in the range of 30 and above however, the membranes had undergone a period of aging. In light of this, an aging study using three different means of exposure to the atmosphere, indicated that exposure to a static atmosphere had the biggest effect on the aging of the membrane. A dynamic flow was found to be the most successful at minimising the period of aging, in which the laminar flow prevented the permeating molecules from adsorbing on the membrane surface. This was confirmed in comparing the experimental feed pressure with an estimated feed pressure, which considered the pressure loss throughout the membrane in accordance with the Fanning equation.

To prevent the aging process occurring on the CMSMs, electro-regeneration of the carbon fibres was carried out, by applying a potential during the permeation test. Preliminary results indicated a positive effect, sustaining a constant rate of permeation. Direct application of the potential to the fibres and during an initial  $\text{N}_2$  test inhibited the adsorption of these molecules. The modified membranes also showed an enhanced effect on the minimisation of aging in which the CMSMs containing CNTs showed the most promise of improving the rate of permeation. Finally the permeability and selectivity values were plotted on a Robeson plot, which showed good performance in regards, all of the membranes were above or located on the upper bound of the  $\text{CO}_2/\text{N}_2$  gas pair.

## 7.7 References

1. M. Mulder, Basic Principles of Membrane Technology, Kluwer Academic Publishers, Dordrecht, 1996.
2. E. Favre, R. Bounaceur, and D. Roizard, *Sep. Purif. Technol.*, **68**, 30, (2009).
3. G. Xomeritakis, C. Y. Tsai, Y. B. Jiang, and C. J. Brinker, *J. Membr. Sci.*, **341**, 30, (2009).
4. S. Lagorsse, F. D. Magalhaes, and A. Mendes, *J. Membr. Sci.*, **310**, 494, (2008).
5. S. M. Saufi and A. F. Ismail, *Carbon*, **42**, 241, (2004).
6. B. McEnaney, E. Alain, Y. F. Yin, and T. J. Mays, *Design and Control of Structure of Advanced Carbon Materials for Enhanced Performance*, **374**, 295, (2001).
7. D. Q. Vu, W. J. Koros, and S. J. Miller, *Ind. Eng. Chem. Res.*, **42**, 1064, (2003).
8. C. W. Jones and W. J. Koros, *Carbon*, **32**, 1427, (1994).
9. P. M. Coss and C. Y. Cha, *J. Air Waste Manage. Assoc.*, **50**, 529, (2000).
10. J. A. Lie and M. B. Hagg, *J. Membr. Sci.*, **284**, 79, (2006).
11. A. F. Ismail and L. I. B. David, *J. Membr. Sci.*, **193**, 1, (2001).
12. S. A. McKelvey and W. J. Koros, *J. Membr. Sci.*, **112**, 29, (1996).
13. K. Kusakabe, M. Yamamoto, and S. Morooka, *J. Membr. Sci.*, **149**, 59, (1998).
14. J. E. Koresh and A. Soffer, *Sep. Sci. Technol.*, **22**, 973, (1987).
15. J. E. Koresh and A. Soffer, *J. Chem. Soc., Faraday Trans. I*, **82**, 2057, (1986).
16. J. E. Koresh and A. Soffer, *Sep. Sci. Technol.*, **18**, 723, (1983).
17. J. N. Barsema, J. Balster, V. Jordan, N. F. A. van der Vegt, and M. Wessling, *J. Membr. Sci.*, **219**, 47, (2003).
18. T. Horiuchi, H. Hidaka, T. Fukui, Y. Kubo, M. Horio, K. Suzuki, and T. Mori, *Applied Catalysis a-General*, **167**, 195, (1998).
19. S. S. Hosseini and T. S. Chung, *J. Membr. Sci.*, **328**, 174, (2009).
20. H. B. Park, Y. K. Kim, J. M. Lee, S. Y. Lee, and Y. M. Lee, *J. Membr. Sci.*, **229**, 117, (2004).
21. J. E. Koresh and A. Soffer, *J. Chem. Soc. Faraday*, **176**, 2457, (1980).
22. V. C. Geiszler and W. J. Koros, *Ind. Eng. Chem. Res.*, **35**, 2999, (1996).
23. H. Suda and K. Haraya, *J. Phys. Chem. B*, **101**, 3988, (1997).
24. P. S. Tin, T. S. Chung, and A. J. Hill, *Ind. Eng. Chem. Res.*, **43**, 6476, (2004).
25. D. Q. Vu, W. J. Koros, and S. J. Miller, *Ind. Eng. Chem. Res.*, **41**, 367, (2002).
26. D. W. Breck, Zeolite Molecular Sieves: Structure, Chemistry and Use, John Wiley & Sons, New York, 1974.
27. S. Matteucci, Y. Yampolskii, B. D. Freeman, and I. Pinnau, Material Science of Membranes for gas and vapor separation, Wiley, West Sussex, 2006.
28. B. D. Freeman, *Macromolecules*, **32**, 375, (1999).
29. L. M. Robeson, *Curr. Opin. Solid State Mat. Sci.*, **4**, 549, (1999).
30. C. A. Scholes, S. E. Kentish, and G. W. Stevens, *Recent Patents on Chemical Engineering* **1**, 52, (2008).
31. E. Favre, *J. Membr. Sci.*, **294**, 50, (2007).
32. C. Roberts, J. R. Gibbins, R. Panesar, and G. Kelsall, in IEA Greenhouse Gas R & D Programme, Cheltenham, 2004.
33. I. Menendez and A. B. Fuertes, *Carbon*, **39**, 733, (2001).

34. J. S. Mattson and H. B. Mark, Activated carbon, Marcel Dekker, New York, 1971.
35. S. Lagorsse, M. C. Campo, F. D. Magalhaes, and A. Mendes, *Carbon*, 43, 2769, (2005).
36. M. A. Montes-Moran, D. Suarez, J. A. Menendez, and E. Fuente, *Carbon*, 42, 1219, (2004).
37. D. Van Gauwbergen, S. Jamar, and J. Baeyens, *Filtr. Sep.*, 37, 59, (2000).
38. E. S. o. M. S. Technology, Nomenclature & Symbols in Membrane Science & Technology, 1995.
39. Perry, Chilton, and Kirkpatrick, Perry's Chemical Engineers Handbook, McGraw-Hill.
40. N. C. Mehta, J. M. Smith, and E. W. Comings, *Ind. Eng. Chem.*, 49, 986, (1957).
41. M. Petkovska and M. Mitrovic, *Chem. Eng. J.*, 53, 157, (1994).
42. L. M. Robeson, *J. Membr. Sci.*, 62, 165, (1991).
43. L. M. Robeson, *J. Membr. Sci.*, 320, 390, (2008).
44. H. M. Huotari, I. H. Huisman, and G. Tragardh, *J. Membr. Sci.*, 156, 49, (1999).
45. C. Visvanathan and R. Benaim, *Sep. Sci. Technol.*, 24, 383, (1989).

### Conclusions

#### 8.1 General Conclusions

The results presented in this thesis described the development of environmental technologies for aqueous and gaseous based systems. Initially, the formation and characterisation of a modified polypyrrole (PPy) sensor, for the detection of the harmful pollutant, paraquat was investigated. A short study followed, with the production and characterisation of carbon membranes. These membranes were then used in single gas permeation tests, from which it was evaluated that CO<sub>2</sub> was selectively permeated over N<sub>2</sub>.

The major goal of this thesis was to design a sensor for the detection and capture of the harmful herbicide, paraquat. This dicationic species displays a two-step redox process for the reduction of MV<sup>2+</sup> to MV<sup>+</sup> and MV<sup>+</sup> to MV<sup>0</sup> within a potential window of -0.1 → -1.4 V vs. SCE. The proposed material for the detection of paraquat was a PPy film which was electrodeposited onto a metal substrate by applying an anodic potential. PPy was modified with the incorporation of a large anionic dopant, sulfonated-βcyclodextrin (sul-βCD). This CD contains a hydrophobic cavity, an ionised primary face and a partial ionised secondary face. It was postulated that the means of detection and capture would occur through electrostatic interactions and the formation of an inclusion complex.

In Chapter 3, studies characterising the PPy doped with sul-βCD were described. Due to the highly charged nature of sul-βCD the rate of electropolymerisation was much higher in comparison to using small dopants e.g. Cl<sup>-</sup> or SO<sub>4</sub><sup>2-</sup>. Hence, the monomer solution of Py and sul-βCD did not require the presence of a supporting electrolyte for electropolymerisation. This ensured that only the negatively charged sul-βCD was incorporated within the polymer matrix upon oxidation of the monomer. The application of this sensor was to detect paraquat electrochemically at reduction potentials. It has been reported that when large

anionic dopants are immobilised within the PPy matrix, the polymer acts as a cation exchanger causing, the ingress of cations from solution<sup>1,2</sup>. This proved to be the case for the PPy/sul- $\beta$ CD. Energy dispersive X-ray analysis (EDX) carried out on an oxidised PPy film showed the presence of X-rays for S and O atoms, indicative of the sulfonate groups of sul- $\beta$ CD. More importantly when the polymer was potentiostically reduced at -0.8 V vs. SCE in NaCl signals for S and O atoms were still observed along with an X-ray signal corresponding to Na.

As outlined in Chapter 3, the performance of the PPy/sul- $\beta$ CD polymer showed higher current responses for the reduction of  $MV^+$  to  $MV^0$  in contrast to the bare electrode. Optimisation of the sensor for the detection of this redox couple was carried out at a fixed concentration of paraquat using cyclic voltammetry (CV). The techniques of differential pulse voltammetry (DPV) and constant potential amperometry (CPA) were used to minimise the capacitance current of the polymer. The detection limits obtained from monitoring the reduction of  $MV^+$  using DPV and CPA were  $7.50 \times 10^{-5}$  mol dm<sup>-3</sup> and  $1.28 \times 10^{-5}$  mol dm<sup>-3</sup>, respectively. A comparative study was also carried out using PPy doped with sodium dodecyl sulfate (SDS). A detection limit for the reduction of  $MV^+$  to  $MV^0$  of  $5.00 \times 10^{-5}$  mol dm<sup>-3</sup> was obtained using DPV. The similarity in detection between PPy/sul- $\beta$ CD and PPy/SDS for the reduction of paraquat indicated that electrostatic attraction was the major contributor to the interaction between the paraquat and the polymer and there was no evidence for inclusion. A study to investigate the interaction between sul- $\beta$ CD and paraquat in solution using CV, rotating disc voltammetry (RDV) and <sup>1</sup>H NMR spectroscopy was described in Chapter 6. Analysis of the data indicated that paraquat forms a 1:1 complex with the sul- $\beta$ CD. Association constant ( $K_a$ ) values of 122.0 and 43.1 mol<sup>-1</sup> dm<sup>3</sup> were evaluated for the complexes of  $MV^{2+}$  and sul- $\beta$ CD and  $MV^+$  and sul- $\beta$ CD respectively. This indicated the formation of a weak complex between  $MV^{2+}$  and sul- $\beta$ CD which was consistent the data obtained from the <sup>1</sup>H NMR experiments.

The results presented in Chapter 4 examined the use of a another modified PPy film doped with sulfonated-calix[4]arene (sul-calix[4]) for the detection of paraquat in solution. This polymer film showed an affinity for all redox states

above a concentration of  $1.00 \times 10^{-3}$  mol dm<sup>-3</sup> paraquat. Following optimisation of the polymer for the detection of MV<sup>2+</sup>, CPA was carried out and a detection limit of  $3.48 \times 10^{-6}$  mol dm<sup>-3</sup> was recorded. This was a significant improvement in detection compared to that obtained from CPA for PPy/sul-βCD ( $1.28 \times 10^{-5}$  mol dm<sup>-3</sup>). The selectivity of this sensor was also tested. Diquat, which is structurally similar to paraquat is also a commonly used herbicide and is the main interferent for paraquat<sup>3</sup>. Unfortunately the PPy/sul-calix[4] polymer was not selective for paraquat over diquat. When equimolar concentrations of paraquat and diquat were present in solution, the current response of PPy/sul-calix[4] to the mixed solution was additive, implying that both species were interacting at the modified surface. Interestingly, the interaction between diquat and PPy/sul-calix[4] had an adverse effect on further detection of paraquat. However, paraquat had no such effect on the sensing of diquat. To probe this interaction further, the complex formation of diquat and sul-calix[4] in solution was investigated.

The results presented in Chapter 5 probe the strong interaction formed between diquat and sul-calix[4] in solution. The most significant aspect of this study was the influence of ionic strength and subsequently the presence of ions within solution. The  $K_a$  values decreased from  $10^6$  to  $10^3$  mol<sup>-1</sup> dm<sup>3</sup> in the absence and presence of an electrolyte solution. This was explained in terms of the competition between Na<sup>+</sup> from the electrolyte and the dicationic species of diquat, V<sup>2+</sup> to complex with sul-calix[4]. The data obtained using <sup>1</sup>H NMR spectroscopy, were consistent with the a strong interaction occurring between the diquat and the sul-calix[4]. To interpret the dominant force for this interaction, a comparative study was carried out using <sup>1</sup>H NMR spectroscopy to investigate the inclusion properties of V<sup>2+</sup> with neutral calix[4]arene (calix[4]). The results showed that additions of calix[4] had no effect on the chemical shift of the proton signals of diquat. On the other hand, shifts of approximately 1 ppm were observed upon addition of sul-calix[4] to a fixed concentration of diquat. This indicated that electrostatic forces were the driving force for the interaction of sul-calix[4]. Similar results were recorded for the interaction of MV<sup>2+</sup> with

sul-calix[4] and these results showed good agreement with those published by Guo and co-workers<sup>4</sup>.

Another aspect of this research focused on use of membrane technology for the separation of gases. In this work, the gas pair chosen was CO<sub>2</sub>/N<sub>2</sub>, with a potential application for flue gas separation, using carbon molecular sieve membranes (CMSMs). The membranes were characterised using scanning electron microscopy (SEM), in which the loss of functional groups from the carbon precursor were deduced from the decrease in wall thickness and the bore diameter of the membrane. The membrane was tailored to selectively permeate CO<sub>2</sub> over N<sub>2</sub>, in which a selectivity of CO<sub>2</sub>:N<sub>2</sub> of 24.7:1.0 was quantified. Although, this value was slightly lower than the normal value of 30.0:1.0, the membranes had undergone a period of aging. Aging is a decrease in the membranes permeability over time due to either chemical or physical adsorption on the membrane surface<sup>5</sup>. In light of this, an aging study using three different means of exposing the membranes to the atmosphere was carried out. The results indicated that exposure to a static atmosphere had the biggest effect on the aging of the membrane while a dynamic flow was found to be the most successful at minimising aging. Electro-regeneration was carried out in an effort to combat aging. This was done by applying a potential of 5 V during the permeation test and the permeability was determined before, during and after the application of electricity to the membranes. The results showed a positive increase in permeability, in spite of the high resistance of the carbon membranes. The most significant improvement was a 17.29% increase in permeability of CO<sub>2</sub> using a modified carbon membrane with multi-walled carbon nanotubes (CNTs) incorporated. The Robeson plot determined for this membrane indicates that electroregeneration is a successful means of combating aging.

## 8.2 Conference Presentations

59<sup>th</sup> Irish Universities Chemistry Research Colloquium, Dublin City University 2007.

“Conducting Polymers Modified with Cyclodextrins and their ability to detect pollutants: Nitrophenol and Paraquat”, Sinéad Mc Dermott, Carmel B. Breslin and Denise A. Rooney; National University of Ireland, Maynooth.

6<sup>th</sup> Spring Meeting of the International Society of Electrochemistry, Foz do Iguaçu, Brazil, March 16-19, 2008.

“Conducting Polypyrrole Modified with Anionic Dopants and its Ability to Detect the Pollutant Paraquat”, Sinéad Mc Dermott, Carmel B. Breslin and Denise A. Rooney; National University of Ireland, Maynooth.

1<sup>st</sup> Regional Symposium on Electrochemistry of South- East Europe, Crveni Otok, Rovinj, Istria, Croatia, May 4-8, 2008.

“Host Guest Interactions of Methyl Viologen with Modified Polypyrrole Films”, Sinéad Mc Dermott, Carmel B. Breslin and Denise A. Rooney; National University of Ireland, Maynooth.

6<sup>th</sup> Spring Meeting of the International Society of Electrochemistry, Foz do Iguaçu, Brazil, March 16-19, 2008.

“Polypyrrole modified with Supramolecular Cages: Applications in the Electrochemical Sensing of Herbicides”, Carmel B. Breslin, Valeria Annibaldi, Sinéad Mc Dermott, Denise A. Rooney; National University of Ireland, Maynooth.

## 8.3 References

1. P. C. Pandey, G. Singh, and P. K. Srivastava, *Electroanalysis*, 14, 427, (2002).
2. J. Tamm, A. Alumaa, A. Hallik, and V. Sammelselg, *J. Electroanal. Chem.*, 448, 25, (1998).
3. M. Luque, A. Rios, and M. Valcarcel, *Analyst*, 123, 2383, (1998).
4. D. S. Guo, L. H. Wang, and Y. Liu, *J. Org. Chem.*, 72, 7775, (2007).
5. S. Lagorsse, F. D. Magalhaes, and A. Mendes, *J. Membr. Sci.*, 310, 494, (2008).